Functionalized Hydrazone-Crosslinked Hyaluronic Acid Hydrogels for Tissue Repair

by

Alycia Nicole Galindo

A dissertation accepted and approved in partial fulfillment of the

requirements for the degree of

Doctor of Philosophy

In Bioengineering

Dissertation Committee:

Paul D. Dalton, Chair

Marian H. Hettiaratchi, Advisor

Gabriella Lindberg, Core Member

Morgan Giers, Core Member

Ashley Walker, Institutional Representative

University of Oregon
&
Oregon State University

Summer 2026

© 2026 Alycia Nicole Galindo
This work is openly licensed via CC BY-ND 4.0.



DISSERTATION ABSTRACT

Alycia Nicole Galindo
Doctor of Philosophy in Bioengineering
Title: Functionalized Hydrazone-Crosslinked Hyaluronic Acid Hydrogels for Tissue Repair

Polymers have been used in biomedical engineering for over 75 years. Hydrogels are water-swollen crosslinked polymer chains that form a three-dimensional (3D) network. Due to their high-water content, structure, and porosity, hydrogels can resemble living tissues and are attractive biomaterials for tissue engineering and regenerative medicine. Hydrogels fabricated from hyaluronic acid (HA) are attractive biomaterials because HA is a major component of the extracellular matrix in several tissues and interacts with multiple cellular receptors to regulate migration, proliferation, and differentiation. HA can easily be modified for crosslinking to form hydrogels with a range of physicochemical properties. Specifically, hydrazone-crosslinked HA hydrogels are promising candidates due to their dynamic covalent crosslinking, injectability, tunable mechanical properties, and capacity for functionalization with bioactive molecules. The overall objective of this dissertation was to engineer functionalized HA hydrazone-crosslinked hydrogels that support tissue repair through tunable mechanical properties, controlled protein delivery, and enhanced cell-material interactions.

We first used design of experiments to statistically optimize the physicochemical properties of hydrazone-crosslinked HA hydrogels for controlled therapeutic protein delivery. By evaluating the effects of HA molecular weight and polymer concentration on hydrogel gelation time, compressive modulus, and stability, an optimized hydrogel formulation was identified that exhibited a fast gelation time, a maximum compressive modulus, and stability over 28 days. The optimized hydrogel was further functionalized with affibody affinity proteins specific to bone morphogenetic protein-2 (BMP-2), enabling sustained protein release over 28 days and demonstrating their use for controlled therapeutic delivery.

To promote skeletal muscle regeneration, hydrazone-crosslinked HA hydrogels were combined with aligned melt electrowritten (MEW) poly(ε-caprolactone) scaffolds to create a

composite scaffold that combined biochemical and topographical cues. Hyaluronic acid was further functionalized with norbornene groups to enable conjugation of fibronectin-derived peptides (RGD). The composite scaffolds promoted C2C12 myoblast attachment, alignment, and myotube formation. These findings demonstrated that combining aligned MEW scaffolds with a dynamic HA hydrogel coating provides an effective strategy for engineering aligned composite scaffolds for muscle tissue repair.

We further expanded the applicability of HA hydrazone crosslinked hydrogels to neural tissue engineering, where a comprehensive review of biomaterial strategies for modulating neuroinflammation highlighted recent advances in nanoparticles, injectable hydrogels, implantable scaffolds, and neural probe coatings. Building on these concepts, a hydrazone-crosslinked HA-alginate (HA-Alg) hydrogel was developed to more closely match the mechanical properties of neural tissue. The functionalization of HA with fibronectin-derived peptides (RGD) and laminin-derived peptides (IKVAV) was evaluated for the generation of V2a interneurons from mouse embryonic stem cells embedded in hydrogels. All hydrogels supported the generation of V2a interneurons; however, hydrogels functionalized with IKVAV significantly enhanced neuronal adhesion and neurite extension. These results demonstrated the importance of incorporating the appropriate adhesion cues to engineer permissive environments for neural regeneration.

Finally, the versatility of the hydrogel platform was leveraged to enable controlled delivery of glial cell line-derived neurotrophic factor (GDNF) in a 3D *in vitro* glioblastoma microenvironment. Affibody-mediated GDNF delivery was combined with aligned MEW scaffolds to recreate key biochemical and biophysical features of the brain extracellular matrix. Sustained GDNF release promoted glioblastoma cell migration along aligned fibers, providing a physiologically relevant platform for investigating tumor progression and evaluating future therapeutic strategies.

Collectively, this dissertation establishes functionalized hydrazone-crosslinked HA biomaterials as a versatile platform for tissue engineering and regenerative medicine applications. Through the statistical optimization of hydrogels, affinity-mediated protein delivery, extracellular matrix-derived peptide functionalization, and engineered tissue-specific

composite scaffolds, this work demonstrates the multifunctional use of HA hydrogels that address challenges in tissue engineering and regenerative medicine. Ultimately, these findings provide a foundation for the continued development of HA-hydrazone crosslinked hydrogels for biomedical engineering applications.

This dissertation includes previously published and unpublished co-author material.

CURRICULUM VITAE

NAME OF AUTHOR: Alycia Nicole Galindo

GRADUATE AND UNDERGRADUATE SCHOOLS ATTENDED:

University of Oregon, Eugene, Oregon
University of New Mexico, Albuquerque, New Mexico
Central New Mexico Community College, Albuquerque, New Mexico

DEGREES AWARDED:

Doctor of Philosophy, Bioengineering, Innovation and Entrepreneurship Specialization, **2026**, University of Oregon
Bachelor of Science, Chemical Engineering, Bioengineering Concentration, **2021**, University of New Mexico
Associate of Arts, Liberal Arts, **2017**, Central New Mexico Community College

AREAS OF SPECIAL INTEREST:

Regenerative Medicine
Tissue Engineering
Biomaterials
Drug Delivery

PROFESSIONAL EXPERIENCE:

Undergraduate Research Assistant, Brinker Lab, November 2019 – May 2021

GRANTS, AWARDS, AND HONORS:

Giustina Fellowship, Knight Campus, University of Oregon, Eugene, Oregon, 2025-2026

NIH Tissue Engineering and Regenerative Medicine International Society Travel Award, Seattle, Washington, 2024

Best Ph.D. Student Seminar Presentation, Knight Campus, University of Oregon, Eugene, Oregon, 2024

Knight Campus Undergraduate Scholars Mentor, Knight Campus, University of Oregon, Eugene, Oregon, 2024

Honorable Mention for Most Innovative, Human Performance Alliance Symposium, Stanford University, Palo Alto, California, 2023

First Year Fellow, Knight Campus, University of Oregon, Eugene, Oregon, 2021

Aim to Achieve Scholarship, University of New Mexico, Albuquerque, New Mexico, 2021

Dean's List, School of Engineering, University of New Mexico, Albuquerque, New Mexico, 2021

Leonard Engineering Scholarship, University of New Mexico, Albuquerque, New Mexico, 2021

PUBLICATIONS:

A. Mozipo, E. and N. Galindo, A.; D. Khachatourian, J.; G. Harris, C.; Dorogin, J.; R. Spaulding, V.; R. Ford, M.; Singhal, M.; C. Fogg, K.; H. Hettiaratchi, M. Statistical Optimization of Hydrazone-Crosslinked Hyaluronic Acid Hydrogels for Protein Delivery. *Journal of Materials Chemistry B* **2024**, *12* (10), 2523–2536. https://doi.org/10.1039/D3TB01588B.

Galindo, A. N. and Frey Rubio, D. A.; Hettiaratchi, M. H. Biomaterial Strategies for Regulating the Neuroinflammatory Response. Mater. Adv. **2024**, 5 (10), 4025–4054. https://doi.org/10.1039/D3MA00736G.

Galindo, A. N.; Chi, A. K.; Liashenko, I.; O'Neill, K. L.; Asnes, C. L.; Sharma, R.; Khachatourian, J. D.; Hajarizadeh, A.; Dalton, P. D.; Hettiaratchi, M. H. Hyaluronic Acid-Coated Melt Electrowritten Scaffolds Promote Myoblast Attachment, Alignment, and Differentiation. *Cel. Mol. Bioeng.* **2025**. https://doi.org/10.1007/s12195-025-00865-y.

Galindo, A. and McLaren, M. E.; Chi, A. K.; Khachatourian, J. D.; Butts, J. C.; Hettiaratchi, M. H. Hyaluronic Acid-Alginate Hydrazone Crosslinked Hydrogels Support the Generation and Maturation of V2a Interneurons. *bioRxiv* **2026**, 2026–06.

ACKNOWLEDGMENTS

First, thank you, Dr. Hettiaratchi, for welcoming me into your lab. It has been amazing watching both the lab and you grow over the years. Thank you for always giving your time and feedback, especially for staying up all night, commenting back and forth with me on a paper due the next day. I am grateful for the creative space you have given me for my dissertation project and for always being on the hunt for our next collaboration. I am grateful to have been mentored by a strong leader in science and engineering. My time here will always be a positive experience because of you.

To my mother Patricia, thank you for all the sacrifices you made to get me here. I know I wasn't always the easiest child to raise but thank you for always giving us your unconditional love. I promise it will all be worth it. Kristina, thank you for forever being my best and sometimes only friend. I appreciate you moving 41 hours away from the sunny beaches to be here with me; you truly give me a sense of security and a feeling of being home. You are the best aunty that Malayah could ever have asked for.

Gianni, thank you always for moving away from home with me to go follow my dreams. This would not have been easy without you. Thank you for giving me our beautiful daughter and building this beautiful life that we have together. I wouldn't want to do it with anyone else. Thank you to Angel for helping me this last year. I couldn't have finished this without your support. Father, Luke, Onecima, and Rachel, thank you for always reminding me to live in the moment and for the importance of family.

Now for the official acknowledgments, this work was supported by the Collins Medical Trust; the National Institutes of Health (R21-EB032112); the Wu Tsai Human Performance Alliance; the Joe and Clara Tsai Foundation; the Donald E. and Delia B. Baxter Foundation; and the National Science Foundation CAREER Award (2237240). Additional support was provided by the Giustina Knight Campus Fellowship Program and Knight Campus Innovation Fellowship to Alycia and through the Lary Simpson Professorship to Dr. Hettiaratchi.

Individual co-author support was provided through several fellowship and scholarship programs. J.D. was supported by the Natural Sciences and Engineering Research Council of Canada (NSERC). A.K.C. was supported by a Wu Tsai Performance Undergraduate Fellowship. E.A.M. and J.D.K. were supported by the Knight Campus Undergraduate Scholars Program.

M.F. was supported by the University of Oregon Summer Program for Undergraduate Research (SPUR) and the Vice President for Research and Innovation (VPRI) Fellowship. P.D.D. was supported by the Bradshaw and Holzapfel Research Professorship in Transformational Science and Mathematics.

In addition we gratefully acknowledge Dr. Casey Check and Professor Willie ("Skip") Rochefort for their guidance on rheology; Dr. Patrick Hall for guidance on scanning electron microscopy; Dr. David Johnson and Dr. Danielle Benoit for technical support with and access to the RSA-G2 Solids Analyzer, as well as Dr. Benoit for guidance on gel permeation chromatography; Adam Fries and Chandler Asnes for technical support with confocal imaging and image analysis; and Justin Svendsen for technical support with protein modeling analysis.

DEDICATION

This work is dedicated to my grandmother, Elizabeth Cecilia Hale, and my daughter, Malayah Amber Slay. Thank you for being my reason to love science and for giving me a new perspective on the meaning of life.

TABLE OF CONTENTS

Chapter Page

1. HYALURONIC ACID HYDROGELS FOR BIOMEDICAL ENGINEERING 25

1.1 Polymers for Biomedicine 25

1.1.1 Hydrogels for Tissue Engineering and Regenerative Medicine 27

1.2 Hyaluronic Acid Hydrogels 27

1.2.1 Hyaluronic Acid (HA) 27

1.2.2 HA Modifications 29

1.2.3 Hyaluronic Acid Hydrogel Crosslinking 30

1.2.3.1 Physical Crosslinking..... 30

1.2.3.2 Covalent Crosslinking..... 30

1.2.3.3 Dynamic Covalent Crosslinking 32

1.2.3.4 Hydrazone Crosslinked HA Hydrogels 35

1.3 Hydrazone-Crosslinked HA Hydrogels for Tissue Repair 36

1.3.1 Norbornene-Modified HA (HA-Nor) 37

1.3.2 ADH-Modified HA (HA-ADH) 39

1.3.3 Oxidized HA (HA-Ox) 39

1.3.4 Oxidized Alginate (Alg-Ox) 40

1.3.5 Peptide and Small Protein Functionalization of HA..... 40

2. STATISTICAL OPTIMIZATION OF HYDRAZONE-CROSSLINKED HYALURONIC ACID HYDROGELS FOR PROTEIN DELIVERY 42

2.1 Abstract 42

2.2 Graphical Abstract 43
2.3 Introduction 43
2.4 Materials and Methods 46
2.4.1 Materials 46
2.4.2 Synthesis of Adipic Acid Dihydrazide HA (HA-ADH) 46
2.4.3 Synthesis of Oxidized HA (HA-Ox) 46
2.4.4 Synthesis of HA Norbornene (HA-Nor) 47
2.4.5 Oxidization of HA Norbornene (HA-Nor-Ox) 47
2.4.6 Molecular Weight Analysis of Modified HA 47
2.4.7 Affibody Bioconjugation 48
2.4.8 Degree of Modification (DOM) Determination 48
2.4.9 Preparation of HA Hydrogels 49
2.4.10 Physicochemical Characterization of Hydrogels 49
2.4.10.1 Gelation Time 49
2.4.10.2 Compressive Modulus 49
2.4.10.3 Mass Change Over Time 50
2.4.11 Release of BMP-2 from HA Hydrogels 50
2.4.12 Design of Experiments 51
2.4.13 Hydrogel Morphology 52
2.5 Results and Discussion 53
2.5.1 Functionalization of HA Polymers 53
2.5.2 Hydrogel Gelation Time 55
2.5.3 Hydrogel Compressive Modulus 56

2.5.4 Hydrogel Mass Change Over Time 57
2.5.5 Design of Experiments Analysis 59
2.5.6 Optimal and Pessimal Hydrogel Predictions 62
2.5.7 BMP-2 Release from Affibody-Containing Hydrogels 64
2.6 Conclusion 67
2.7 Bridging Paragraph 68
3. HYALURONIC ACID-COATED SCAFFOLDS PROMOTE MYOBLAST ATTACHMENT, ALIGNMENT, AND DIFFERENTIATION 69
3.1 Abstract 69
3.1.1 Purpose 69
3.1.2 Methods 69
3.1.3 Results 70
3.1.4 Conclusion 70
3.1.5 Keywords 70
3.2 Introduction 70
3.3 Materials and Methods 73
3.3.1 Oxidized HA (HA-Ox) 73
3.3.2 HA-Norbornene (HA-Nor) 73
3.3.3 HA-Norbornene-Adipic Acid Dihydrazide (HA-Nor-ADH) 74
3.3.4 Determination of Degree of Modification (DOM) 74
3.3.5 RGD Conjugation to HA-Nor-ADH (HA-RGD) 75
3.3.6 Fabrication of Melt Electrowritten (MEW) Scaffolds 76
3.3.7 Etching and Sterilization of MEW Scaffolds 77

3.3.8 HA Coating of MEW Scaffolds 77
3.3.9 SEM Imaging and Fiber Measurements of MEW Scaffolds 77
3.3.10 C2C12 Myoblast Culture 77
3.3.11 Myoblast Culture on Scaffolds 77
3.3.12 Immunocytochemistry 78
3.3.13 Imaging of Scaffolds 79
3.3.14 Nuclei Count Analysis 79
3.3.15 Directionality Analysis 79
3.3.16 Creatine Kinase (CK) Activity Assay 80
3.3.17 Mechanical Properties 80
3.3.18 Myogenic Gene Expression Analysis via RT-qPCR 80
3.3.19 Statistical Analysis 81
3.4 Results 81
3.4.1 Fabrication of HA-coated MEW Scaffolds 81
3.4.2 Morphology of Non-coated and HA-coated MEW Scaffolds 83
3.4.3 Myoblast Attachment on MEW Scaffolds 83
3.4.4 Myotube Formation on MEW Scaffolds 85
3.4.5 Mechanical Properties 88
3.4.6 Creatine Kinase Activity 88
3.4.7 Myogenic Gene Expression 91
3.4.8 Sarcomere Staining 92
3.5 Discussion 92
3.6 Conclusion 95

3.7 Bridging Paragraph 96
4. BIOMATERIAL STRATEGIES FOR REGULATING THE NEUROINFLAMMATORY RESPONSE 97
4.1 Abstract 97
4.2 Graphical Abstract 98
4.3 Introduction 98
4.4 Background 99
4.4.1 Resident Cells of the Central Nervous System 99
4.4.2 The Role of Peripheral Immune Cells in Maintaining Tissue Homeostasis 100
4.4.3 The Inflammatory Response to Central Nervous System Injury 101
4.4.3.1 Acute Inflammation (Hours After Injury) 104
4.4.3.2 Sub-Acute Inflammation (Days to Weeks After Injury) 106
4.4.3.3 Chronic Inflammation (Months to Years After Injury) 107
4.4.3.4 Resolution of Inflammation 108
4.4.4 Neuroinflammation During Disease 109
4.4.4.1 Stroke 111
4.4.4.2 Multiple Sclerosis 111
4.4.4.3 Glioblastoma 112
4.4.4.4 Cerebral Palsy 112
4.4.4.5 Parkinson's Disease 113
4.5 Biomaterials for Modulating Neuroinflammation 113
4.5.1 Nanoparticles 113

4.5.1.1 Exosomes 115
4.5.1.2 Dendrimers 117
4.5.1.3 Polymeric nanoparticles 118
4.5.2 Hydrogels 120
4.5.3 Implantable scaffolds 126
4.5.4 Neural probe coatings 130
4.6 Future Outlook 135
4.7 Conclusion 138
4.8 Bridging Paragraph 138
5. HYALURONIC ACID-COATED SCAFFOLDS PROMOTE MYOBLAST ATTACHMENT, ALIGNMENT, AND DIFFERENTIATION 140
5.1 Abstract 140
5.2 Graphical Abstract 141
5.3 Introduction 141
5.4 Materials and Methods 145
5.4.1 Synthesis of Norbornene-HA (HA-Nor) 145
5.4.2 Synthesis of Adipic Acid Dihydrazide Norbornene HA (HA-Nor-ADH) 145
5.4.3 Synthesis of Oxidized Alginate (Alg-Ox) 146
5.4.4 Peptide Conjugation and Quantification 146
5.4.5 Degree of Modification (DOM) Determination 146
5.4.6 Preparation of HA Alginate (HA-Alg) Hydrogels 147
5.4.7 Physicochemical Characterization of Hydrogels 147

5.4.7.1 Gelation Time 147
5.4.7.2 Compressive Modulus 148
5.4.7.3 Mass Change 148
5.4.8 Ab2.2 Mouse Embryonic Stem Cell Culture 149
5.4.9 Preparing Embryoid Bodies (EBs) 149
5.4.10 Embedding Embryoid Bodies (EBs) into Hydrogels 149
5.4.11 Differentiation and Maturation of V2a Interneurons 150
5.4.12 Live/Dead Assay 151
5.4.13 RNA Extraction and Purification 151
5.4.14 cDNA Synthesis 151
5.4.15 Quantitative Real-Time PCR (qPCR) 151
5.4.16 Immunocytochemistry 152
5.4.17 Live/Dead Image Analysis 153
5.4.18 Neurite Length Analysis 154
5.5 Results 154
5.5.1 Polymer Modifications for the Synthesis of Hydrazone Crosslinked HA-Alg Hydrogels 154
5.5.2 HA-Alg Hydrogels Exhibit a Range of Physicochemical Properties 155
5.5.3 HA-Alg Hydrogels Support V2a Interneuron Viability 156
5.5.4 Evaluation of V2a Interneuron Differentiation in HA-Alg Hydrogels 158
5.5.5 IKVAV-modified HA-Alg Hydrogels Enhance V2a Interneuron Neurite Outgrowth 160
5.6 Discussion 162

5.7 Conclusion 166
5.8 Bridging Paragraph 166
6. CONTROLLED RELEASE OF GLIAL CELL LINE-DERIVED NEUROTROPHIC FACTOR PROMOTES GLIOBLASTOMA MIGRATION ON ALIGNED MELT ELECTROWRITTEN MICROFIBER SCAFFOLDS 168
6.1 Abstract 168
6.2 Introduction 169
6.3 Materials and Methods 172
6.3.1 Isolation of GDNF Specific Affibodies from a Yeast Surface Display Library 172
6.3.1.1 Yeast Induction Check 172
6.3.1.2 Magnetic Activated Cell Sorting 173
6.3.1.3 Fluorescence Activated Cell Sorting 173
6.3.2 Gene Sequencing of GDNF-Specific Affibodies 174
6.3.3 GDNF-Affibody Yeast-Bound Specificity and Affinity 174
6.3.4 Solid Phase Peptide Synthesis 174
6.3.5 GDNF-Affibody Characterization 175
6.3.5.1 Circular Dichroism 175
6.3.5.2 Biolayer Interferometry 175
6.3.6 HA Hydrogel Fabrication 176
6.3.6 Conjugation of GDNF-Affibodies for Controlled Delivery of Glial Cell Line-Derived Neurotrophic Factor 176
6.3.7 Controlled Release of GDNF 176

6.3.8 U-87 Glioblastoma Cell Culture 177
6.3.9 U-87 Glioblastoma Spheroid Formation 177
6.3.10 Aligned Melt-Electrowritten Scaffold Fabrication 177
6.3.11 Soluble GDNF Delivery to Glioblastoma Spheroids 178
6.3.12 Controlled GDNF Factor Delivery to Glioblastoma Spheroids 178
6.3.13 Immunocytochemistry and Image Analysis 178
6.4 Results 179
6.4.1 Discovery and Isolation of GDNF Affibodies 179
6.4.2 Characterization of GDNF Affibody 180
6.4.3 Affibody Conjugated HA Hydrogels Sustain GDNF Release 182
6.4.4 Localized GDNF Delivery Enhances Glioblastoma Migration Along Aligned Fibers 184
6.5 Discussion 185
6.6 Conclusion 188
7. CONCLUSIONS AND FUTURE DIRECTIONS 189
7.1 Conclusions 189
7.1.1 Statistical Optimization of HA Hydrogels 189
7.1.2 HA-Coated Scaffolds Promote Myoblast Attachment, Alignment, and Differentiation 189
7.1.3 HA Hydrogels for the Generation and Maturation of V2a Interneurons 190
7.1.4 Controlled GDNF Delivery from HA Hydrogels 190
7.2 Future Directions 191

7.2.1 HA-Coated Scaffolds for Muscle Tissue Repair 191
7.2.2 Central Nervous System Tissue Repair following Injury and Disease 191
7.2.2.1 GDNF Delivery for Parkinson's Disease 191
7.2.2.2 Multiple Neurotrophic Factor Delivery for CNS Tissue Repair 192
7.2.1.3 Aligned Composite Scaffolds for Spinal Cord Injury 193
7.2.3 Neuromuscular Junctions 194
APPENDICES 197
A. STATISTICAL OPTIMIZATION OF HYDRAZONE-CROSSLINKED HYALURONIC ACID HYDROGELS FOR PROTEIN DELIVERY 195
B. HYALURONIC ACID-COATED SCAFFOLDS PROMOTE MYOBLAST ATTACHMENT, ALIGNMENT, AND DIFFERENTIATION 227
C. HYALURONIC ACID-ALGINATE HYDRAZONE CROSSLINKED HYDROGELS SUPPORT THE GENERATION AND MATURATION OF V2A INTERNEURONS 230
REFERENCES CITED 235

LIST OF FIGURES

Figure Page

1.1. Number of records for publications for biomaterials for tissue regeneration. 26

1.2. Summary of hyaluronic acid crosslinking strategies. 31

1.3. Example of a Diels-Alder crosslinked HA hydrogel functionalized with RGD. 33

1.4. Summary of dynamic covalent crosslinking chemistry. 35

1.5. Norbornene-modified HA 37

1.6. ADH-Modified HA. 39

1.7. Oxidized HA. 39

1.8. Oxidized alginate. 40

1.9. Functionalization of HA with ECM-derived peptides. 40

2.1. Functionalization of HA and hydrogel formation via hydrazone crosslinking. 55

2.2. Physicochemical properties for each of the 15 hydrogel formulations for the D-optimal design. 57

2.3 Three-dimensional response surfaces demonstrating the effect of input parameters on different output responses. 62

2.4 Validation of predictive models to optimize HA hydrogels. 64

2.5. Synthesis of HA-Nor, HA-Nor-Ox, and HA-Nor-Ox-Affibody. 66

2.6. Release of BMP-2 from HA hydrogel. 67

3.1. HA modifications for hydrazone crosslinking. 82

3.2. Coating of MEW scaffolds with HA. 83
3.3. SEM images of noncoated and HA-coated MEW scaffolds. 84
3.4. C2C12 myoblasts attach and align on MEW scaffolds. 85
3.5. HA and HA-RGD-coatings increase myoblast attachment and anisotropic alignment on MEW scaffolds. 87
3.6. C2C12 myoblasts form aligned myotubes on MEW scaffolds. 88
3.7. MEW scaffolds support anisotropic myotube formation, while HA and HA-RGD coatings increase cellular attachment. 90
3.8. Creative kinase (CK) activity of myoblasts during differentiation. 91
3.9. Alpha-actinin staining reveals presence of myotubes containing striations on HA-coated MEW scaffolds. 92
4.1. Composition of central nervous system parenchymal tissue during homeostasis. 102
4.2. The stages of the inflammatory response to injury in the CNS. 110
4.3. Nanoparticle-based delivery vehicles and their transport mechanisms through CNS tissue. 115
4.4. Examples of recent advances in hydrogels to modulate CNS inflammation. 123
4.5. Examples of recent advances in implantable scaffolds to modulate CNS inflammation. 128
4.6. Different types of coatings for improving neural probe integration. 132
5.1. Polymer modifications for the fabrication of HA-Alg hydrogels. 155
5.2. Physiochemical properties of HA-Alg hydrogels. 157

5.3. V2a interneurons remain viable and express neural marker expression in HA-Alg and HA-HA hydrogels. 159
5.4. Immunostaining assessing V2a interneuron maturation and neurite length. 161
6.1. Sorting of an affibody-displaying yeast surface display library identified one GDNF affibody.. 180
6.2. Synthesis of affibody and characterization of secondary structure. 181
6.3. Affinity characterization of GDNF affibody. 182
6.4. Computational binding interface of affibody and GDNF with respect to GFRα1 receptor. 183
6.5. Controlled release of GDNF from affibody-conjugated HA hydrogels. 184
6.6. Fabrication of HA MEW 3D glioblastoma model. 185
6.7. Migration of glioblastoma cells on scaffolds with soluble GDNF. 186

LIST OF TABLES

Table Page

2.1. HA hydrogel formulations evaluated to generate D-optimal multilinear regression model. 53

2.2. Ranges of physicochemical properties exhibited by HA hydrogels. 59

2.3. ANOVA assessment of regression models. 60

2.4. Formulations for optimal and pessimal hydrogels. 64

3.1. MEW printing parameters and fiber characteristics for each scaffold design 76

4.1. Role of glial cells in neuroinflammation. 103

5.1. Table of hydrogel formulations for physicochemical characterization. 148

5.2. Table of primer pairs for qPCR listed 5' to 3'. 152

5.3. Table of antibodies used for immunostaining. 153

CHAPTER 1
HYALURONIC ACID HYDROGELS FOR BIOMEDICAL ENGINEERING

1.1 Polymers for Biomedicine

Both synthetic polymers and biologically derived polymers have been used in biomedical applications for over 75 years. The first reported polymer used as an implantable material was cellophane, a plant-derived polymer, introduced in 1939 to wrap blood vessels and contain aneurysms through a fibrotic response.[1] In 1948, cellophane was interestingly used to contain Albert Einstein's abdominal aorta aneurysm, which helped sustain his life for seven years.[2] The use of nylon, poly(methyl methacrylate), and polyethylene in humans shortly followed. After World War II, the need for biomaterials to repair damaged tissues was even more apparent, sparking the era of biomaterial research. Within a year, Sir Harold Ridley invented the intraocular lens made from poly(methyl methacrylate) to treat cataracts and implanted it in humans in 1949.[3] It proved highly biocompatible and improved the quality of life for millions, transforming the trajectory of biomaterials. In 1974, the Society for Biomaterials was established and defined biomaterials as a "systematically, pharmacologically inert substance designed for implantation within or incorporation with a living system", which was later updated to include the overall goal of a biomaterial to "maintain or improve the quality of life of the individual".[2] Over the years, biomaterial research has advanced significantly, with a growing number of publications focused on regenerative medicine and tissue engineering. In 2020, more than 1,200 papers were published on biomaterials for tissue regeneration (**Figure 1.1**).[2]

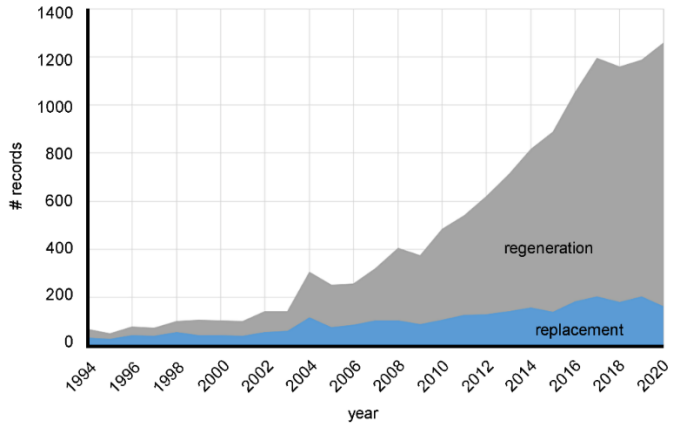

Figure 1.1. Number of records for publications for biomaterials for tissue regeneration. Reported number of Scopus records from 1994 to 2020 for keywords "biomaterial replacement" and "biomaterial regeneration". Reproduced from Todros *et al.*, Processes, (2021), under the terms of the Creative Commons Attribution 4.0 License (CC BY 4.0).

Biomaterials used in tissue engineering can be fabricated from synthetic or natural polymers and can act as an extracellular matrix (ECM) support to repair or regenerate damaged tissue. Polymers must be biocompatible with the tissue environment, including matching the tissue's mechanical properties, being bioabsorbable or biodegradable, exhibiting a minimal foreign-body response, and, overall, displaying low cytotoxicity.[4] The modification of synthetic and natural polymers is advancing, enabling the production of biomaterials for tissue engineering, drug delivery, and cell transplantation in regenerative medicine applications.

Synthetic polymers, including polyethylene glycol (PEG), poly(ε-caprolactone) (PCL), poly(lactic acid), and poly(glycolic-co-lactic acid), are common in tissue engineering to create biomaterials.[5,6] While synthetic polymers are highly homogeneous with reproducible properties, they lack the biological signals present in the ECM. Many efforts have been made to modify synthetic polymers with ECM molecules, such as small proteins and peptides, to improve cellular-material interactions and improve polymer degradability.

Conversely, biopolymers are natural polymers derived from plants and animals and are often preferred over synthetic polymers due to their presence in the body's ECM. In addition to their recognition by the body, biopolymers are highly biocompatible, supporting cell-material interactions and tissue regeneration. Most biopolymers are also readily degraded into smaller,

absorbable monomers by native biological enzymes, which may be required for certain biomedical applications.

Common biopolymers can be categorized into polysaccharides and polypeptides.[7] Polysaccharides are complex chains of monosaccharides or disaccharide repeating units linked together by glycosidic bonds. Many polysaccharides are glycosaminoglycans, characterized by long, unbranched repeating disaccharide units that are highly polar and negatively charged. Of these glycosaminoglycans, the most used in tissue engineering are hyaluronic acid, chondroitin sulfate, and heparin. Other common polysaccharides are dextran, alginate, cellulose, and chitin/chitosan. Polypeptides are repeating units of amino acids. Polypeptide-based biomaterials have the potential to mimic the native ECM for several biomedical engineering applications. Common polypeptides include gelatin, silk fibroin, albumin, elastin, and keratin.

1.1.1 Hydrogels for Tissue Engineering and Regenerative Medicine

Hydrogels are water-swollen crosslinked polymer chains that form a three-dimensional (3D) network.[8] Hydrogels have high water absorbability due to the hydrophilic groups on the crosslinked polymers. Due to their high-water content, structure, and porosity, hydrogels can resemble living tissues and are attractive biomaterials for tissue engineering and regenerative medicine. Hydrogels were first developed in 1960 from poly-2-hydroxyethyl methacrylate (PHEMA) for eye enucleation and contact lenses.[9] Since then, hydrogels have evolved over the years for a range of applications, even extending beyond biomedical engineering. In 2020, over 6,000 publications on hydrogels for biomedical applications alone were published.[8] Hydrogels can be formed either by a single network (one polymer chain) or an interpenetrating polymer network (two or more polymer chains). Semi-interpenetrating polymer networks combine these ideas with a single crosslinked polymer that entraps an uncrosslinked polymer chain. Hydrogels can be engineered to be implantable, injectable, or sprayable for various biomedical applications. Injectable hydrogels are highly attractive in tissue engineering and regenerative medicine for minimally invasive drug delivery and three dimensional (3D) printing applications.

1.2 Hyaluronic Acid Hydrogels

1.2.1 Hyaluronic Acid (HA)

HA is the only non-sulfated glycosaminoglycan and is found in multiple tissues, including cartilage, muscle, skin, eyes, and the central nervous system.[7] HA is an anionic linear

polysaccharide composed of repeating disaccharide units of β-1,4-D-glucuronic acid and β-1,3-N-acetyl-D-glucosamine linked together by alternating glycosidic bonds. HA has been sourced from animals since the 1950s, including umbilical cords, bovine vitreous humor, and rooster combs, for biomedical applications.[10] Although high yields of hyaluronic acid can be obtained from animal extraction, the polydispersity of hyaluronic acid polymer chains is high, and the extracted products may contain contaminants, including endotoxins and proteins, which can cause adverse effects. Modern production methods use bacterial fermentation by *Streptococcus* species to produce HA, enabling greater control over purity and molecular weight, which can range from 5 kDa to 1.8 MDa.[11] Bacterial fermentation is currently the most widely used method for producing HA for biomedical applications; however, extensive downstream purification is required and can be costly. Alternative methods, including synthetic and enzymatic approaches, have been employed to address the drawbacks of bacterial fermentation, but they are often time-consuming, limited to small-scale production, and restricted to producing low-molecular-weight HA.

In the body, HA is synthesized as a high-molecular-weight polymer ranging from ~1-8 MDa; however, degradation by hyaluronidase or reactive oxygen species can fragment polymer chains, resulting in a range of polymer molecular weights.[12,13] For instance, in healthy tissues such as skin, the molecular weight of hyaluronic acid ranges from 4-6 MDa. In contrast, in remodeled tissue and tumor environments, low-molecular-weight HA is predominant.[12] The molecular weight of HA has shown to modulate the immune response; for instance, high molecular weight HA (>1,250 kDa) has been shown to suppress the immune response of lipopolysaccharide stimulated murine macrophages.[14] Others have reported that high molecular weight HA (>500 kDa) has immunosuppressive and anti-inflammatory properties, whereas low molecular weight HA (<500 kDa) elicits a pro-inflammatory immune response.[13,15] Depending on the application, introducing biomaterials composed of low-molecular-weight HA may be preferred to promote an immune response that stimulates angiogenesis and tissue healing.

HA is mostly known to interact with the cluster of differentiation-44 (CD44) receptor and the receptor for hyaluronan-mediated motility (RHAMM). HA can also interact with other receptors, including toll-like receptors 2 and 4 (TLR2 and TLR4), the lymphatic vessel endothelial receptor (LYVE-1), and the HA receptor for endocytosis (HARE), depending on its molecular weight and location within the body. For example, low molecular weight HA is mostly

known to interact with CD44 and RHAMM receptors and, directly or indirectly, with TLR receptors.[12]

1.2.2 HA Modifications

The available carboxyl, hydroxyl, and N-acetyl groups in HA can be readily modified. Modifications on the carboxyl group include amidation, Ugi condensation, and esterification. Among these approaches, amidation is the most commonly used, occurring through a two-step mechanism in which the carboxyl group is first activated using coupling agents, such as carbodiimides or (4-(4,6-dimethoxy-1,3,5-triazin-2-yl)-4-methylmorpholinium chloride) (DMTMM), forming a reactive intermediate, followed by a nucleophilic attack from a primary amine group, resulting in an amide bond.[10] For example, carbodiimide activation with (1-Ethyl-3-(3-dimethylaminopropyl)carbodiimide) (EDC) in the presence of N-Hydroxysuccinimide (NHS) or 1-hydroxybenzotriazole (HOBt) is often used due to the water solubility of these reagents.[16] Carbodiimide chemistry has been used to modify HA with hydrazides, thiols, and tyramine functional groups to produce hydrogels.

Modification to the hydroxyl groups on HA includes etherification, esterification, sulfation, oxidation, hemiacetal formation, and carbamate formation.[10,16] Etherification can be achieved with common crosslinkers such as glutaraldehyde or divinyl sulfone. In basic solutions, epoxides such as 1,4-butanediol diglycidyl ether can undergo an etherification reaction to form hydrogels. Esterification of HA with methacrylic anhydride yields the commonly used methacrylate hyaluronic acid, which can then undergo photoinitiated reactions to form hydrogels. Oxidation of HA can occur using sodium periodate ($NaIO_4$) or 2,2,6,6-tetramethylpiperidin-1-yl)oxyl. Oxidation of HA using $NaIO_4$ targets the vicinal hydroxyl groups, cleaving the C2-C3 bond of the D-glucuronic acid unit, revealing two aldehyde groups. Although this method is often used to produce hydrogels, the reaction can cause oxidative cleavage of polymer chains, significantly reducing hyaluronic acid molecular weight and increasing polymer polydispersity.[10,17,18]

Lastly, modifications of the N-acetyl are deacetylation and amidation. Deacetylation can occur through two methods, including chemical and enzymatic, and results in an available amino group. Chemical deacetylation proceeds in strong basic or acidic conditions. However, in both cases, HA can experience chain fragmentation via hydrolytic cleavage of the glycosidic bonds or partial fragmentation of the N-acetyl-D-glucosamine unit.

1.2.3 Hyaluronic Acid Hydrogel Crosslinking

1.2.3.1 Physical Crosslinking

Several methods have been used to crosslink HA to produce hydrogels (**Figure 1.2**).[16,19,20] Depending on the crosslinking strategy, hydrogels can exhibit different physicochemical properties, such as shear-thinning and self-healing properties. Physical crosslinked hydrogels do not form covalent bonds; they are rather formed through physical interactions such as electrostatic interactions, chain entanglement, hydrophobic/hydrophilic interactions, or hydrogen bonds. Physical interactions can produce injectable hydrogels with shear-thinning and self-healing properties, which can be used for minimally invasive therapeutic delivery or extrusion bioprinting. Common physical crosslinking methods use the natural properties of HA to form hydrogels. For example, because HA is anionic, a blend of cationic polymers, such as chitosan, can be used to create hybrid hydrogels.[21] Other natural properties of HA, including its hydrophilic properties, can enable hydrogel formation through the addition of hydrophilic drugs. Host-guest hydrogels can additionally be formed from modifying HA with host/guest monomers that self-assemble to crosslink and form hydrogels driven by molecular recognition.[22,23] The modification of HA with catechol functional groups, such as dopamine, can also facilitate metal coordination crosslinking. For instance, dopamine-modified HA was crosslinked with methacrylate-modified HA via Fe^{3+}-mediated coordination of dopamine, producing self-healing, adhesive hydrogels inspired by mussels.[24]

1.2.3.2 Covalent Crosslinking

Covalent crosslinked hydrogels form irreversible bonds between polymers and result in more stable and elastic hydrogels compared to physical crosslinked hydrogels. Covalent crosslinked HA hydrogels can be formed through condensation reactions, radical polymerization, click chemistry, enzymatic crosslinking, or oxidation reactions.[16] Common condensation reactions include amidation of the carboxyl group of HA or etherification of the hydroxyl group. For example, divinyl sulfone can be used to crosslink HA via its hydroxyl groups, resulting in an enzymatically stable and biocompatible hydrogel. For example, a HA hydrogel crosslinked with divinyl sulfone, containing fibrin, supported tissue remodeling and vascularization in a mouse subcutaneous model after 12 weeks.[25] Other condensation reactions include crosslinking the

carboxyl group on HA; for example, adipic acid dihydrazide (ADH) has been used as a crosslinker in the presence of EDC.[26,27]

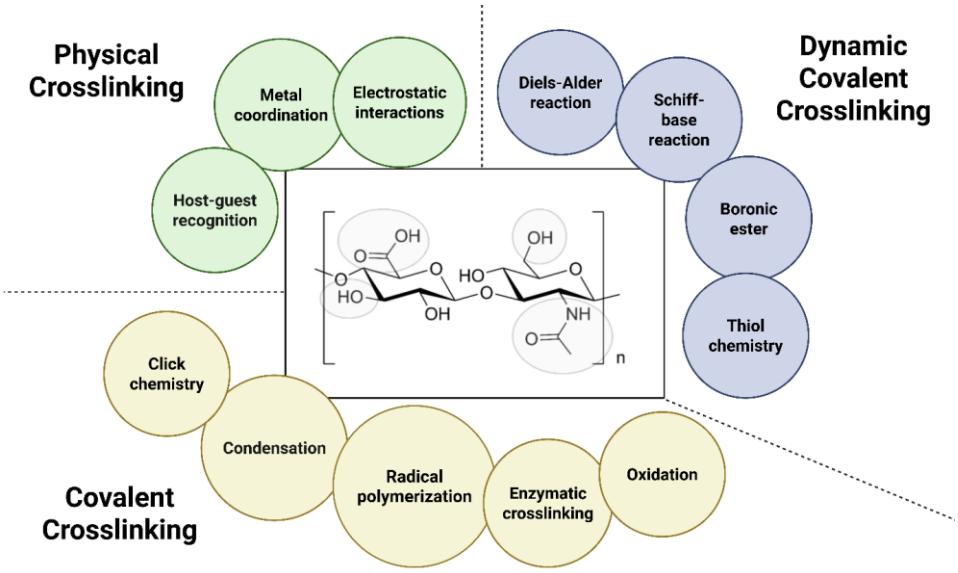

Figure 1.2. Summary of hyaluronic acid crosslinking strategies. Reproduced from Luo et al., Smart Medicine, (2023), under the terms of CC BY-NC 4.0 license. Figure created with BioRender.com.

Radially polymerized hydrogels can be formed through exposure to light, heat, or oxidative reactions, resulting in hydrogels with tunable mechanical properties. Photoinitiated polymerization is a common method for forming HA hydrogels. HA can be modified with alkene, alkyne, or thiol groups to form photoinitiated hydrogels, but the most widely used modification is the addition of methacrylate or thiol groups. By varying the photoinitiator, its concentration, exposure time, or light intensity, a range of hydrogel physicochemical properties can be achieved. For example, the pore size and mechanical properties of methacrylate-modified HA photocrosslinked hydrogels were controlled by varying the crosslinking density from fine-tuning the reaction conditions.[28] Common photoinitiators used to form these hydrogels include Irgacure 2959 and lithium phenyl-2,4,6-trimethylbenzoylphosphinate. However, high concentrations of crosslinkers can be toxic and result in free radicals *in vivo*, which can trigger an inflammatory response.

Azide-alkyne cycloaddition, thiol-yne addition, and Diels-Alder reactions can be used to form hydrogels using click chemistry. For example, HA modified with either alkyne or azide

functional groups was prepared via a strain-promoted azide-alkyne cycloaddition reaction, thereby eliminating the need for a toxic metal catalyst and yielding a compatible hydrogel with tunable mechanical and biochemical properties.[29] HA hydrogels formed via thiol-yne click chemistry are stable and non-toxic, with promising potential in biomedical engineering.[16,30]

Lastly, enzymatically covalent-crosslinked HA hydrogels can be formed in the presence of catalysts such as horseradish peroxidase and galactose oxidase, or of hydrogen peroxide and hematin.[31,32] A well-known enzymatic crosslinked HA hydrogel is a blend of tyramine-modified HA and silk fibroin, formed in the presence of horseradish peroxidase and hydrogen peroxide.[33] Lastly, oxidation crosslinking can occur between catechol- or thiol-modified HA in the presence of an oxidant, such as $NaIO_4$.[16]

1.2.3.3 Dynamic Covalent Crosslinking

Dynamic covalent crosslinked hydrogels are formed by reversible covalent bonds that allow them to deform under stress and regain their macroscopic characteristics after the applied force is removed, resulting in viscoelastic hydrogels with tunable physicochemical properties. These hydrogels exhibit shear-thinning, stress-relaxation, self-healing, and shape-adaptability properties.[16] Together, these properties result in injectable and printable hydrogels that are of great interest in tissue engineering applications. Dynamic covalent crosslinked hydrogels are also favored in biomedical applications because their viscoelastic behavior can promote cell spreading, migration, proliferation, and differentiation.[20] Dynamic covalent hydrogels can also be designed to respond to stimuli such as pH, light, or temperature. Common dynamic covalent crosslinking chemistries include Diels-Alder, Schiff-base, thiol, and boronic ester reactions.

The Diels-Alder reaction is a click cycloaddition between a diene and a substituted alkene (dienophile), forming a carbon-carbon bond. This exothermic reaction can occur without a catalyst in physiological conditions with electron-rich functional groups, making it suitable for biomedical applications. For example, HA modified with maleimide functional groups has been crosslinked with furan-modified polymers, such as PEG, to form HA-PEG hydrogels. However, this crosslinking combination can be energy-intensive and result in long gelation times; therefore, other crosslinking methods have been used, including a Diels-Alder reaction between tetrazine and norbornene functional groups. Hydrogels fabricated from HA modified with norbornene or tetrazine functional groups resulted in fast gelation times of less than 5 minutes and a range of elastic moduli.[34] Norbornene-modified HA was additionally functionalized with

methacrylate groups to conjugate cysteine-terminal fibronectin-derived peptides (RGD) via a pH-driven Michael addition, prior to crosslinking with tetrazine-modified HA (**Figure 1.3**). The addition of RGD adhesive peptides to hydrogels enhanced mesenchymal stem cell adhesion and, depending on the hydrogel's stiffness or degradability, led to different morphologies, spreading, and differentiation.[34]

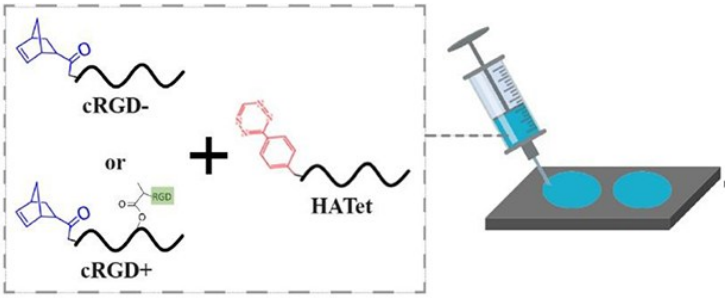

Figure 1.3. Example of a Diels-Alder crosslinked HA hydrogel functionalized with RGD. Norbornene (cRGD-) and norbornene methacrylate modified HA hydrogels conjugated with RGD (cRGD+) crosslinked with tetrazine modified HA (HATet) to form injectable HA hydrogels. Reproduced with permission from Gultian et al., Macromolecular Bioscience (2023), Wiley-VCH GmbH.

Schiff-base reactions occur between a nucleophilic amine and an active carbonyl group, forming reversible oxime, acylhydrazone, hydrazone, or imine bonds.[16] Imine reactions require acidic conditions and occur between a nucleophilic amine and an aldehyde or ketone, eliminating water, and resulting in hydrogels with reversible imine-amine exchange. However, imine-based hydrogels exhibit poor hydrolytic stability in acidic conditions, which can limit their use in biomedical applications. Oxime reactions occur between an alkoxyamine and an aldehyde or ketone, forming an oxime bond. The allylhydrazone and hydrazone reactions occur between a hydrazide or hydrazine and an aminooxy group (aldehyde or ketone), forming hydrazone bonds. Both oxime and hydrazone reactions are condensation reactions that produce water as a byproduct and form reversible covalent bonds. In oxime and hydrazone reactions, the nucleophilic amine is more reactive, yielding more efficient and stable hydrogels than those formed via imine reactions. However, the hydrolytic stability of the resulting hydrogel can vary depending on the hydrazide and aminooxy groups selected. For instance, HA modified with various hydrazide groups, including carbodihydrazide, oxalyldihydrazide, or ADH, was

crosslinked with pendent aldehyde-modified HA, and the hydrogel hydrolytic stability was directly compared, where carbodihydrazide-modified HA formed more stable hydrazone bonds compared to other hydrazide groups.[35] These hydrogels were then used to deliver bone morphogenetic protein-2 (BMP-2) for bone repair. Compared with oxime reactions, hydrazone reactions are generally faster, especially when the hydrazone-reactive group is near an acidic group, thereby increasing its reactivity.

Other dynamic covalent reactions between an active disulfide and a thiolated ion can form reversible bonds via thiol-disulfide exchange, thereby producing stable, self-healing hydrogels.[36] For instance, vinyl- or thiol-modified HA can undergo thiol-Michael additions under specific pH conditions, yielding dynamic hydrogels. These hydrogels can also be dual-crosslinked via photoinitiated reactions; for example, a dynamic silk fibroin-HA hydrogel was formed via thiol-disulfide linkages and then further crosslinked to produce a hydrogel for bone repair.[37] Since free thiols may interfere with encapsulated proteins, exhausting all free thiols using dual-crosslinked hydrogels may be necessary for protein delivery.[20,38]

Hydrogels produced between boronic acid and diols can also result in reversible covalent boronic ester bonds due to the exchange between boronic acid/diol and boronate esters. Boronic esters can vary in stability with pH, such that hydrolysis can occur under acidic conditions, but the extent of hydrolysis varies greatly with the substrate structure. For instance, acyclic boronic esters undergo rapid hydrolysis, whereas hindered esters hydrolyze more slowly. Furthermore, when the pH is near the pKa of the boronic acid reactive group, the exchange between boronic acid/diol and boronate esters is most effective. In one study, phenylboronic acid and benzoboroxole-modified HA were directly compared to form hydrogels with saccharide-modified HA, where the hydrogels' viscoelastic properties varied depending on the boronic acid and sugar groups.[39] A summary of HA dynamic covalent crosslinking chemistries and reaction conditions for forming reversible covalent bonds is shown in **Figure 1.4**.

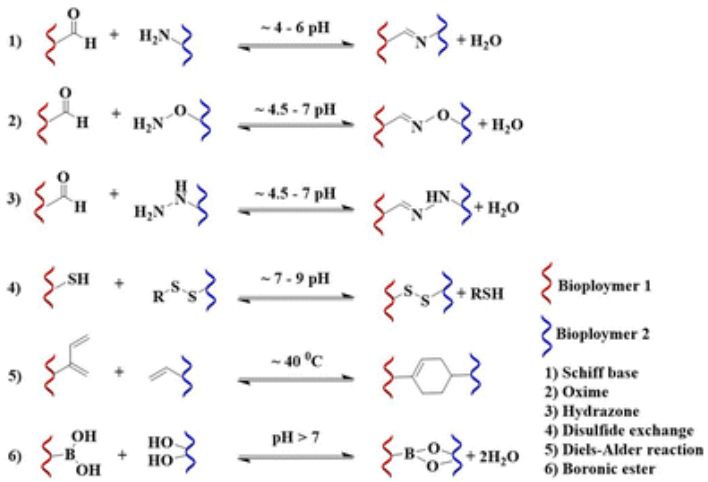

Figure 1.4. Summary of dynamic covalent crosslinking chemistry. Reproduced from Wang et al. (2022), Biomaterials Science, under the terms of the Creative Commons Attribution 3.0 License (CC BY 3.0).

1.2.3.4 Hydrazone Crosslinked HA Hydrogels

HA hydrogels formed via Schiff base hydrazone crosslinking are stable and have been used in several biomedical applications.[17,40–43] These hydrogels can form reversible hydrazone linkages, resulting in multifunctional, self-healing, injectable hydrogels with a range of physicochemical properties by tuning the polymer concentration and crosslinking density. Compared with other crosslinking chemistries, hydrazone-crosslinked hydrogels are ideal for biomedical engineering applications, including protein delivery, due to their viscoelastic, self-healing, and tunable properties. For instance, HA hydrogels crosslinked via hydrazone crosslinking were compared to hydrogels formed via thiol-Michael addition for BMP-2 delivery, where hydrazone crosslinked HA hydrogels significantly improved bone formation in a rat subcutaneous model compared to thiol-Michael HA hydrogels.[38] However, choosing the correct hydrazide functional group is shown to be critical for downstream applications. As described earlier, carbodihydrazide-modified HA hydrogels crosslinked with pendent aldehyde-modified HA were more stable when compared to other hydrazide functional groups.[35,44] However, previous members in the Hettiaratchi Lab showed that both the aldehyde group and the hydrazide group can influence the biocompatibility of the hydrogel.[45] Briefly, various combinations of hydrazone-crosslinked hydrogels, including ADH- or carbodihydrazide-modified HA crosslinked with either pendant oxidized HA or oxidized HA, were used to form hydrogels and evaluated *in*

vitro. Interestingly, individual modified HA polymers, including oxidized HA and carbodiimide-modified HA, showed a decrease in the number of live cells after 4 days of exposure to cultured skeletal myoblasts, whereas ADH-modified HA and oxidized HA hydrogels supported myoblast viability.[45] Further suggesting that hydrazone crosslinked hydrogels formed by ADH-modified HA and oxidized HA were the most compatible hydrogel. Supporting this are several publications reporting the use of ADH-modified and oxidized HA to fabricate hydrogels for biomedical applications. Specifically, ADH-modified HA and oxidized HA crosslinked hydrogels have been evaluated for nucleus pulposus regeneration, a vitreous substitute, and cell microcarriers for tissue repair, demonstrating biocompatibility and promising results.[40–42,46–48] Furthermore, when comparing hydrazone HA hydrogels formed via host-guest chemistry that exhibit similar shear-thinning, self-healing, and viscoelastic properties, hydrazone-crosslinked hydrogels generally can form more stable hydrogels due to the presence of dynamic covalent bonds. This increased stability can make them more favorable for long-term use while retaining dynamic behavior.[20] Conversely, host-guest interactions rely on noncovalent physical interactions, which can readily dissociate under physiological conditions, leading to rapid swelling and a burst release of a drug payload, thereby limiting their use in drug delivery applications.[49] Additionally, depending on the environment, molecular steric hindrance and competitive binding can block host-guest interactions.[50] While host-guest hydrogels have many of the same desirable physicochemical properties as hydrazone-crosslinked hydrogels, dynamic covalent crosslinked hydrogels were preferred for their stability and controllable swelling rates. Lastly, to build upon this platform, Davidson et al. formed a dual-crosslinked fibrous hydrogel using norbornene-modified and oxidized HA crosslinked with ADH, which was further photo-crosslinked via thiol-ene chemistry using the available norbornene functional groups.[51] Further modification of HA with norbornene-functional groups can enable tunable functionality by incorporating thiol-terminal crosslinkers, dyes, peptides, and small proteins.[52]

1.3 Hydrazone-Crosslinked HA Hydrogels for Tissue Repair

The development of two HA hydrazone crosslinked hydrogels was evaluated throughout this dissertation for their use in tissue engineering and regenerative medicine applications across multiple tissues, including bone, muscle, and central nervous system. The research on these hydrogels has yielded two previously published manuscripts (**Chapters 2 and 3**), one review

article (**Chapter 4**), and one manuscript currently under review (**Chapter 5**). Hydrazone crosslinking of HA was chosen as the preferred crosslinking chemistry because it can produce injectable hydrogels with shear-thinning and self-healing properties, and tunable physicochemical properties by varying the crosslinked polymer concentration, making it an ideal platform for several applications. In Mozipo and Galindo et al., design of experiments was applied to build a statistical model of HA hydrazone crosslinked hydrogels. We varied the concentrations of the two modified polymers and their molecular weight to determine an optimal hydrogel formulation for protein delivery for bone repair.[18] In a separate application, we combined HA hydrogels functionalized with fibronectin-derived peptides (RGD) with aligned, 3D-printed PCL melt-electrowritten (MEW) scaffolds to create HA-coated scaffolds to investigate myoblast alignment and differentiation for muscle tissue repair.[53] In our third application, we explored a blend of HA and alginate to form hydrazone crosslinked hydrogels for neural tissue engineering applications, since alginate biomaterials can provide neuroprotective properties.[54] HA-alginate hydrogels were modified with ECM-derived peptides (IKVAV and RGD) and evaluated for V2a interneuron viability and maturation. Lastly, HA hydrogels were used to control the delivery of glial cell line-derived neurotrophic factor (GDNF), a potent neurotrophic factor that promotes neural tissue repair following injury or disease. This platform was used to engineer an HA composite scaffold that mimics the microenvironment of glioblastoma. These hydrogels were used in several applications, highlighting their tunability and multifunctional use in tissue engineering and regenerative medicine, including protein delivery, cell transplantation, implantable composite scaffolds, and engineering of 3D *in vitro* models.

1.3.1 Norbornene-Modified HA (HA-Nor)

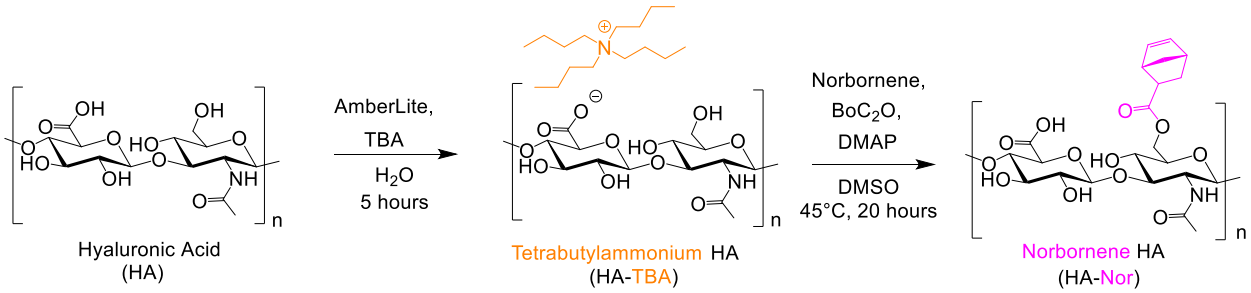

Figure 1.5. Norbornene-modified HA. Synthesis of norbornene-modified HA for functionalization of thiol-terminal peptides, proteins, and molecules.

To fabricate HA hydrazone crosslinked hydrogels, HA was first modified with norbornene functional groups through di-tert-butyl dicarbonate (Boc_2O) activated coupling (**Figure 1.5**).[51,52] To carry out this reaction, HA is converted to an intermediate salt, tetrabutylammonium HA (HA-TBA), using an ion-exchange resin and titration with tetrabutylammonium hydroxide. Because HA is highly polar and hydrophilic, this intermediate is needed for HA to be soluble in organic solvents such as dimethyl sulfoxide (DMSO). Anhydrous organic solvents are required for Boc_2O-activated coupling to prevent activated carboxylic acid intermediates from hydrolyzing. HA-TBA is then dissolved in DMSO for Boc_2O activated coupling with 5-norbornene-2-carboxylic acid, which occurs under a N_2 atmosphere at 45 °C in the presence of a nucleophilic catalyst, (4-dimethylaminopyridine) (DMAP) for 20 hours.[52] The reaction is quenched with cold water and dialyzed against water for 3 days to remove unreacted byproducts, after which the product is precipitated by adding salt and acetone. Depending on the application, the molar excess of coupling agents may need to be optimized to reduce the degree of modification of norbornene functional groups on HA, thereby favoring downstream thiol-ene norbornene reactions. Recent studies have shown that HA modified with norbornene with a high degree of modification can undergo homopolymerization during photoinitiated reactions, resulting in limited cell spreading *in vitro*.[55] One suggested method to mitigate this occurrence was to reduce the degree of norbornene modification to favor the thiol-ene reaction with norbornene. However, this can subsequently limit the ability to achieve high degrees of functionalization of thiol-terminal peptides, small proteins, or molecules for downstream applications.

1.3.2 ADH-Modified HA (HA-ADH)

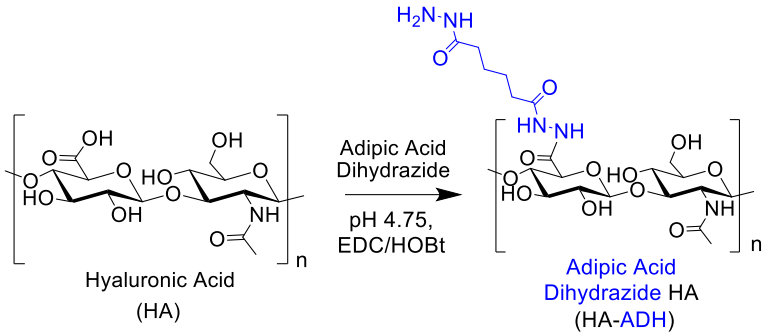

Figure 1.6. ADH-modified HA. Synthesis of ADH-modified HA for crosslinking using carbodiimide chemistry.

To functionalize HA with ADH, carbodiimide chemistry was used to modify the carboxyl group on HA (**Figure 1.6**). Specifically, EDC/HoBt coupling was performed at pH 4.75 to achieve optimal coupling conditions. However, as evidenced by a drastic increase in polymer molecular weight and polydispersity, high ADH molar excesses are required in this reaction due to ADH's bifunctional nature, which can result in covalent crosslinking of HA.

1.3.3 Oxidized HA (HA-Ox)

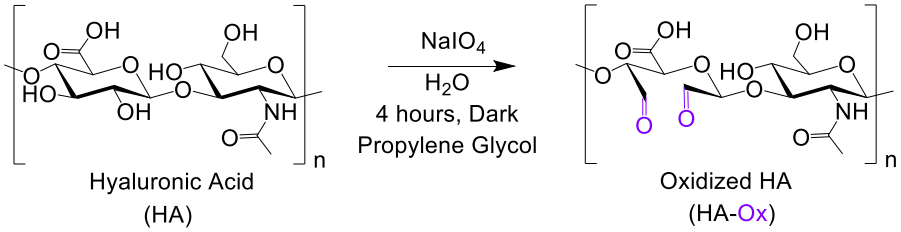

Figure 1.7. Oxidized HA. Oxidation of HA using $NaIO_4$ for crosslinking with ADH-modified HA.

Lastly, HA is oxidized using $NaIO_4$. However, depending on the oxidation reaction duration, cleavage of the HA chain can occur, resulting in low yields and reduced polymer molecular weight.[56,57] By varying the molar excess of $NaIO_4$ and the oxidation duration, we found that 4 hours of oxidation was ideal for achieving sufficient degrees of modification and yield. In addition, because the oxidation reaction cleaves the D-glucuronic acid unit of HA, exposing aldehydes, the nuclear magnetic resonance polymer spectrum is altered, necessitating secondary modifications or titration-based assays to quantify the degree of oxidation.

1.3.4 Oxidized Alginate (Alg-Ox)

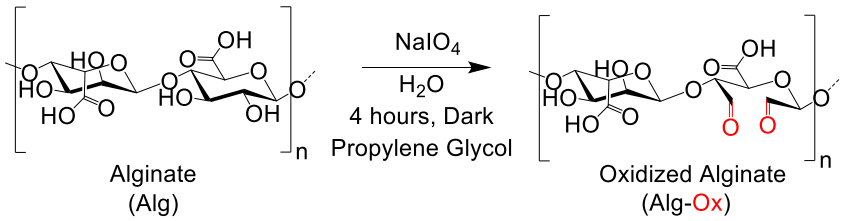

Figure 1.8. Oxidized alginate. Oxidation of alginate with $NaIO_4$ for crosslinking with ADH-modified HA.

In addition to HA, alginate can be oxidized under similar reaction conditions and crosslinked with ADH-modified HA to form a HA-alginate hydrogel blend. In addition to strengthening the mechanical properties of hydrogels, HA-alginate hydrogel systems may provide neuroprotection properties for neural tissue engineering applications.[54]

1.3.5 Peptide and Small Protein Functionalization of HA

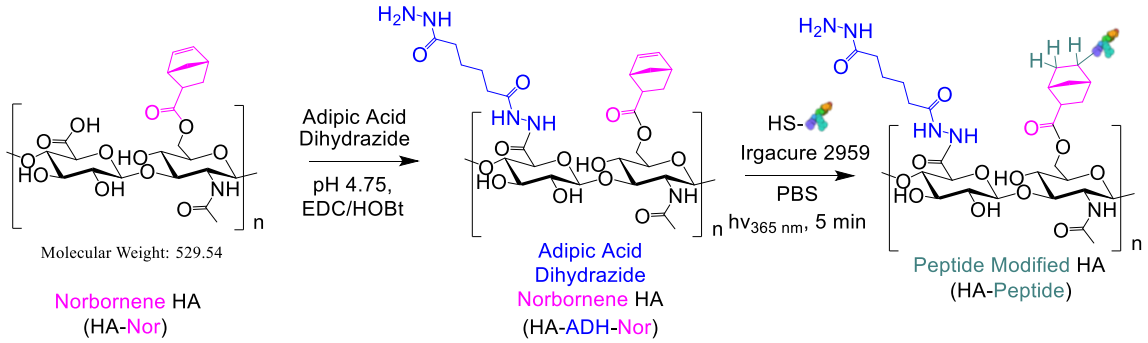

Figure 1.9. Functionalization of HA with ECM-derived peptides. Representative functionalization of norbornene and ADH-modified HA with cysteine terminal peptides and/or small proteins via photoinitiated thiol-ene norbornene click chemistry.

Norbornene-modified HA can be further modified with aldehydes or ADH functional groups, then functionalized with peptides or small proteins via photoinitiated thiol-ene norbornene click chemistry to form functionalized HA hydrazone crosslinked hydrogels for various tissue engineering and regenerative medicine applications (**Figure 1.9**). For example, norbornene- and ADH-modified HA have been functionalized with cysteine-terminal RGD to enhance myoblast attachment to HA-coated scaffolds.[53] Norbornene-modified HA has also been

used to conjugate thiol-terminal molecules and dyes, such as Rhodamine, and to form dual-crosslinked hydrogels.[51,52]

The above modifications were used to fabricate HA hydrogels for various tissue engineering and regenerative medicine applications, shown throughout this dissertation. Overall, we demonstrated the multifunctional use of HA hydrazone hydrogels across multiple tissue types and applications. HA hydrazone crosslinked hydrogels have proven to be a promising candidate for tunable functionalization of HA hydrogels for tissue repair. Although we have proposed several avenues for the use of HA hydrazone crosslinked hydrogels in this dissertation, many applications remain to be explored and will be touched upon in the future directions.

CHAPTER 2

STATISTICAL OPTIMIZATION OF HYDRAZONE-CROSSLINKED HYALURONIC ACID HYDROGELS FOR PROTEIN DELIVERY

From Esther A. Mozipo, Alycia N. Galindo, Jenna D. Khachatourian, Conor G. Harris, Jonathan Dorogin, Veronica R. Spaulding, Madeleine R. Ford, Malvika Singhal, Kaitlin C. Fogg, and Marian H. Hettiaratchi. Statistical optimization of hydrazone-crosslinked hyaluronic acid hydrogels for protein delivery. Journal of Materials Chemistry B 12 (10), 2523-2536 (2024). *This manuscript is under the terms of the Creative Commons Attribution-NonCommercial 3.0 Unported License (CC BY-NC 3.0).*

2.1 Abstract

Hydrazone-crosslinked hydrogels are attractive protein delivery vehicles for regenerative medicine. However, each regenerative medicine application requires unique hydrogel properties to achieve an ideal outcome. The properties of a hydrogel can be impacted by numerous factors involved in its fabrication. We used design of experiments (DoE) statistical modeling to efficiently optimize the physicochemical properties of a hyaluronic acid (HA) hydrazone-crosslinked hydrogel for protein delivery for bone regeneration. We modified HA with either adipic acid dihydrazide (HA-ADH) or aldehyde (HA-Ox) functional groups and used DoE to evaluate the interactions of three input variables, the molecular weight of HA (40 or 100 kDa), the concentration of HA-ADH (1–3% w/v), and the concentration of HA-Ox (1–3% w/v), on three output responses, gelation time, compressive modulus, and hydrogel stability over time. We identified 100 kDa HA-$ADH_{3.00}$HA-$Ox_{2.33}$ as an optimal hydrogel that met all of our design criteria, including displaying a gelation time of 3.7 minutes, compressive modulus of 62.1 Pa, and minimal mass change over 28 days. For protein delivery, we conjugated affinity proteins called affibodies that were specific to the osteogenic protein bone morphogenetic protein-2 (BMP-2) to HA hydrogels and demonstrated that our platform could control the release of BMP-2 over 28 days. Ultimately, our approach demonstrates the utility of DoE for optimizing hydrazone-crosslinked HA hydrogels for protein delivery

2.2 Graphical Abstract

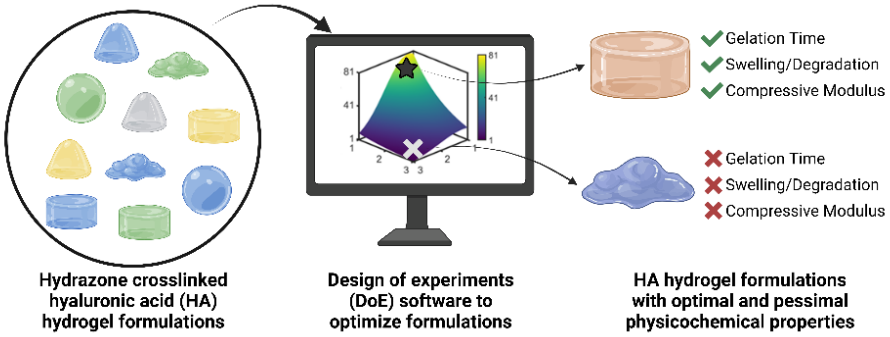

2.3 Introduction

Recombinant protein delivery is a promising strategy for the repair of injured or damaged tissues including bone, muscle, nerves, vasculature, and skin.[58] Specifically in the case of bone repair, the delivery of bone morphogenetic protein-2 (BMP-2) has demonstrated success as a bone regeneration strategy in both animal models and human patients.[59] A wide variety of biomaterials have been investigated for protein delivery to the body, and their properties have been tuned to enable control over protein release rate, material degradation rate, material compressive modulus, and injectability. However, tuning all of these properties simultaneously to develop the ideal biomaterial for protein delivery is challenging. Furthermore, biomaterial delivery vehicles must be individually optimized for different clinical applications, as unique properties may be necessary to control the release of different proteins to different tissues. Hydrogels are chemically or physically crosslinked water swollen polymer networks that can be effective vehicles for the delivery of a variety of cells, proteins, and drugs due to their ability to support cell viability, provide sustained release of cargo, and mimic the mechanical and biochemical properties of tissues.[58,60–62] The relative ease in which a variety of natural and synthetic polymers can be chemically modified with different functional groups has facilitated the fabrication of diverse hydrogels with a wide array of properties suitable for numerous applications. Varying individual input parameters to create a hydrogel, such as polymer concentration, crosslinking ratio, and molecular weight of the polymer, one at a time to determine the combination of parameters that yields a hydrogel with the optimal properties can be time-intensive and expensive. While extensive prior work has been performed to determine the ideal physicochemical properties of hydrogels for a variety of biomedical applications, there

has been limited investigation of the collective, combinatorial effects of varying multiple input parameters on the properties of hydrogels in the context of protein delivery.

To tackle this challenge, we used a statistical optimization technique known as design of experiments (DoE) to efficiently screen the effects of multiple input parameters on several hydrogel properties and create a mathematical model to predict the optimal and pessimal hydrogel formulations given a specific set of design criteria. Design of experiments (DoE) is a method of experimental design in which a combination of factors are varied simultaneously instead of the typical ‘‘one factor at a time’’ approach. The responses to each set of input parameters is mapped to generate a model for how the different input parameters collectively influence each hydrogel property (i.e., the output responses), known as the response surface methodology.[63,64] Mathematical models can then be used to define the response surface and predict expected outcomes. DoE was originally developed in the 1920s for agricultural purposes, but has since been used in a broad array of applications, including the development and optimization of biomaterials.[64–67] It lends itself particularly well to applications such as hydrogel design, in which it is highly likely that multiple input parameters will have interactive effects on hydrogel properties, which makes individually varying input parameters less informative. We and others have used DoE to predict responses of hydrogels and cells within hydrogels in systems with multiple input variables.[65,68–71] This approach can be widely used in regenerative medicine applications such as scaffold design, cell culture optimization, and the development of *in vitro* model systems, accelerating the timeframe in which new platforms can be optimized.[72–74]

In this study, we were specifically interested in tuning the properties of hyaluronic acid hydrogels formed via hydrazone crosslinking. Hyaluronic acid (HA) is an abundant biopolymer found throughout the body. It is a critical extracellular matrix component of connective tissue, skin, and the brain that functions by creating a hydrated polymer matrix for cells to migrate and proliferate.[75–77] HA also exists at a range of molecular weights, which can activate different cell signaling pathways.[78,79] Although HA itself is soluble in aqueous media, modifications can be made to the carboxylic acid, adjacent alcohol, and secondary alcohol groups on the HA backbone to form crosslinks throughout the polymer, resulting in a stable three-dimensional, water-swollen network. HA hydrogels have been used successfully in several biomedical applications, including protein and cell delivery and tissue regeneration.[80–82]

While there are numerous criteria that may be considered important for the design of a hydrogel for protein delivery, we narrowed down our desired hydrogel properties to three essential criteria for optimization: compressive modulus, gelation time, and mass change over four weeks. Compressive modulus can have a profound effect on cell differentiation,[83,84] while the bulk stiffness of an implanted material must be matched to the target tissue to avoid eliciting mechanical irritation and subsequent inflammation. Hydrogel gelation time should allow for sufficient time to mix components (different polymers, proteins, cells) before gelation. Typically, hydrogel gelation times of less than 10 minutes are preferred.[85,86] Finally, the mass change of the hydrogel due to swelling or degradation of the crosslinked network can impact cellular responses over time, such cell spreading, cell-cycle progression, and differentiation.[87–89]

We formed HA hydrogels using dynamic covalent hydrazone crosslinks as this approach can yield a wide range of physicochemical properties, making them an attractive hydrogel platform for numerous regenerative medicine applications.[40,42,43,90–94] The properties of hydrazone-crosslinked HA hydrogels can be easily tuned by adjusting the ratios of the two dynamic covalent crosslinking polymers: oxidized HA (HA-Ox) and HA adipic acid dihydrazide (HA-ADH). Thus, we narrowed our input parameters to HA molecular weight, HA-Ox concentration, and HA-ADH concentration. We then used DoE to identify the contributions and combinatorial effects of the concentration of HA-ADH, the concentration of HA-Ox, and the molecular weight of HA on hydrogel compressive modulus, gelation time, and mass change over time. We then created a statistical model that predicted physicochemical properties as a function of input parameters. This model was validated by evaluating the hydrogels predicted to be the optimal and pessimal delivery vehicles. Finally, as a proof-of-concept for protein delivery, we conjugated a protein-binding peptide known as an affibody to the HA hydrogels using thiol–ene click chemistry to enable affinity-controlled delivery of bone morphogenetic protein-2 (BMP-2), which is a potent osteogenic protein that is clinically used as a bone graft substitute. Overall, we developed a hydrogel platform and used DoE analysis to optimize the vast tunability of hydrazone-crosslinked HA hydrogels for protein delivery for tissue regeneration.

2.4 Materials and Methods

2.4.1 Materials

Sodium hyaluronate (HA, 40 kDa and 100 kDa) was purchased from Lifecore Biomedical LLC (Chaska, MN). Adipic acid dihydrazide (ADH) was purchased from Spectrum Chemical (Gardena, CA). Hydroxybenzotriazole (HOBt) was purchased from Chem Impex (Wood Dale, IL). 1-Ethyl-3-(3-dimethylaminopropyl)carbodiimide (EDC) was purchased from G Biosciences (St. Louis, MO). Sodium Periodate, AmberLite® MB Ion Exchange Resin, tetrabutylammonium hydroxide (TBA-OH), DMSO, 4-dimethylaminopyridine (DMAP), di-tert-butyl decarbonate (BoC2O) and 5-norbornene-2-carboxylic acid were purchased from Sigma Aldrich (St. Louis, MO). Irgacure 2959 was purchased from Advanced Biomatrix (Carlsbad, CA). Recombinant human bone morphogenetic protein-2 (BMP-2) and the human BMP-2 DuoSet enzyme-linked immunosorbent assay (ELISA) were purchased from R&D Systems (Minneapolis, MN).

2.4.2 Synthesis of Adipic Acid Dihydrazide HA (HA-ADH)

HA (200 mg, 0.527 mmol) was dissolved in 20 mL of diH_2O to form a 1% w/v solution. Adipic acid dihydrazide (183.75 mg, 1.05 mmol) and hydroxy-benzotriazole (142.53 mg, 1.05 mmol) were added to the HA solution and the pH was adjusted to 4.75. EDC was added (91.00 mg, 0.47 mmol) to the solution, and the pH was monitored and maintained at 4.75 for 4 hours using 1 M HCl and 1 M NaOH. The solution was stirred for 24 hours at room temperature and dialyzed against 0.1 M NaCl in diH2O for 2 days followed by diH_2O for 2 days. The solution of HA functionalized with ADH (HA-ADH) was sterile filtered through a 0.22 µm filter, frozen at -80 °C, and lyophilized using a VirTis BenchTop Pro lyophilizer (SP Scientific, Warminster, PA).

2.4.3 Synthesis of Oxidized HA (HA-Ox)

HA (200 mg, 0.561 mmol) was dissolved in 10 mL of diH_2O to form a 2% w/v solution. Sodium periodate (322.00 mg, 0.281 mmol) was added to the solution and stirred for 4 hours at room temperature protected from light. The reaction was quenched with 1 mL of propylene glycol and dialyzed against diH_2O for 3 days. The oxidized HA solution (HA-Ox) was sterile filtered through a 0.22 µm filter, frozen at -80 °C, and lyophilized.

2.4.4 Synthesis of HA Norbornene (HA-Nor)

A (1.01 g, 2.506 mmol) was dissolved in 50 mL diH_2O to form a 2% w/v solution. AmberLitet MB Ion Exchange Resin (3.03 g) was added to the reaction and stirred at room temperature for 5 hours. The resin was vacuum-filtered, and the filtrate was titrated to pH of 7 with TBA-OH and dialyzed against diH_2O for 3 days. The HA-TBA solution was sterile filtered through a 0.22 µm filter, frozen at -80 °C, and lyophilized.

HA-TBA (153 mg, 0.35 mmol) was dissolved in 0.75 L DMSO to form a 2% w/v solution. The flask was purged with N_2 for 5 minutes, then 5-norbornene-2-carboxylic acid (145 mg, 1.05 mmol) and DMAP (145 mg, 1.049 mmol) was added to the reaction flask. Boc_2O was added via syringe (32 µL, 0.14 mmol). The solution was stirred at 45 °C for 20 hours, then quenched with cold diH_2O (10 mL) before being dialyzed against diH_2O for 3 days. Norbornene-functionalized HA (HA-Nor) was precipitated from the solution by adding NaCl and cold acetone (30 mL), then filtered and dialyzed against diH_2O for 3 days. The solution was sterile filtered through a 0.22 µm filter, frozen at -80 °C, and lyophilized.

2.4.5 Oxidization of HA Norbornene (HA-Nor-Ox)

HA-Nor (91.75 mg, 0.18 mmol) was dissolved in diH_2O to form a 1% w/v solution. Sodium periodate (10.57 mg, 0.049 mmol) was dissolved in diH_2O to create a 0.5 M solution and added to the HA-Nor solution. The solution was stirred overnight at room temperature protected from light. The reaction was quenched with 1 mL of propylene glycol and dialyzed against diH_2O for 3 days. The oxidized HA-Nor solution (HA-Nor-Ox) was sterile filtered through a 0.22 µm filter, frozen at -80 °C, and lyophilized.

2.4.6 Molecular Weight Analysis of Modified HA

Gel permeation chromatography (GPC) was used to determine the molecular weight of unmodified and modified HA at both 40 kDa and 100 kDa. Lyophilized HA samples were sent to Polyanalytik, Inc. (London, ON, Canada) for analysis using a Viscotek TDA 305 and GPCmax (Malvern Panalytical Ltd, Malvern, United Kingdom) fitted with PAA-202 and PAA-206M aqueous columns. Samples were diluted to 1.00–2.50 mg mL^{-1} in a mobile phase of 8.5 g L^{-1} NaCl in ultrapure water, allowed to dissolve at room temperature for several hours, and then filtered through a 0.22 µm Nylon syringe filter prior to injection. Samples were run in triplicate at a flow rate of 0.7 mL min^{-1} and temperature of 30 °C.

2.4.7 Affibody Bioconjugation

BMP-2-specific affibodies were expressed in E. coli and purified as previously described.[95] HA-Nor-Ox (14.5 mg) was dissolved in 1.5 mL of 0.71 mg mL^{-1} affibody in PBS (1.45 104 mmol) to create a solution with 1:1 ratio of affibody to HA-Nor-Ox. 15 µL of 10% w/v Irgacure 2595 in methanol was added to the reaction vial, stirred, and illuminated with 365 nm light for 10 minutes. The solution was dialyzed against HEPES buffer pH 7.0 for 1 day and diH_2O for 2 days. The affibody-conjugated solution of HA (HA-Nor-Ox-Affibody) was sterile filtered through a 0.22 µm filter, frozen at -80 °C, and lyophilized. The amount of affibody conjugated to the polymer was quantified by dissolving 2–3 mg of HA-Nor-Ox-Affibody in PBS at 2% w/v and determining the protein concentration of the solution using a Pierce 660 Protein Assay Kit (Thermo Fisher Scientific).

2.4.8 Degree of Modification (DOM) Determination

The degree of chemical modification of HA-ADH and HA-Nor was quantified using proton nuclear magnetic resonance spectroscopy (^{1}H NMR, 500 Hz, Bruker, USA). 2–5 mg of modified polymer was dissolved in 600 µL of deuterium oxide (D_2O) for ^{1}H NMR (256 scans). To calculate the degree of modification for HA-ADH, the peaks from the aliphatic chain were integrated from 2.5–2.1 ppm and 1.7–1.44 ppm (8H) and normalized to the n-acetyl methyl group peaks from 1.8–2 ppm (3H) (**Figure A1**).[96] The degree of modification for HA-Nor was calculated by integrating the vinyl peaks from 5.7–6.3 ppm and normalizing to the n-acetyl methyl group from 1.8–2 ppm (3H) (**Figure A2**).[96]

The degree of oxidation for HA-Ox was determined by hydroxylamine hydrochloride titration.[97,98] Briefly, 100 mg of oxidized polymer was dissolved in 0.25 N hydroxylamine hydrochloride containing 0.05% w/v methyl orange reagent for 2 hours. The solution was then titrated with 0.1 M NaOH while monitoring the pH until the pH indicator changed from red to yellow at a pH of 4. The reaction of hydroxylamine hydrochloride with the aldehydes on oxidized HA is shown below.

$$HA-(CHO)_n + H_2N-OH \cdot HCl \rightarrow HA-(CH=N-OH)_n + H_2O + HCl$$

Equation 2.1 was used to calculate the percent degree of modification (% DOM) or the percentage of HA disaccharide units that contain aldehydes.

Equation 2.1.

$$\%DOM = (\frac{379.2\ g}{mol} HA \times 0.1M\ NaOH \times \left(\frac{V_f - V_0}{m_{HA-Ox}}\right)) \times 100$$

where 379.2 g mol-[1] is the monomeric molecular weight of HA, 0.1 M is the molarity of NaOH used to adjust the solution pH, V_f is the final volume of NaOH in the burette after titration recorded in liters, V_0 is the initial volume of NaOH in the burette before titration recorded in liters, and $m_{HA\text{-}Ox}$ is the mass in g of HA-Ox used in the titration.

2.4.9 Preparation of HA Hydrogels

HA-ADH and oxidized HA (HA-Ox, HA-Nor-Ox, or HA-Nor-OxAffibody) were each reconstituted at 1–3% w/v in PBS. Hydrogels were then prepared by mixing 50 µL of each polymer in 2 mL microcentrifuge tube or 8 mm diameter cylindrical silicone mold to create 100 µL hydrogels.

2.4.10 Physicochemical Characterization of Hydrogels

2.4.10.1 Gelation Time

Due to the rapid nature of hydrazone crosslinking between HA-Ox and HA-ADH, in which bonds form too rapidly to measure the gelation point using rheology, the gelation time of each hydrogel was determined using the inverted tube test, which measures the point at which the hydrogel reaches a fully gelled state.[99–101] 50 µL each of HA-ADH and HA-Ox were pipetted into 2 mL microcentrifuge tubes to create 100 µL hydrogels and inverted every minute until gelation occurred. The time at which there was no viscous flow was recorded as the gelation time.

2.4.10.2 Compressive Modulus

Compressive moduli of the hydrogels were evaluated using a Discovery Hybrid Rheometer-2 (DHR-2) (TA Instruments, New Castle, DE). 100 µL hydrogels were formed in 8 mm cylindrical silicone molds. The hydrogels were crosslinked overnight at room temperature before being removed from the molds and placed on the rheometer. Hydrogels were compressed within an 8 mm parallel plate to 15% of their original height at 37 °C, and the slope of the linear stress versus strain curve was used to calculate the compressive modulus.[102] Representative stress–strain curves used to determine the compressive moduli of the hydrogels can be found in **Appendix A** (**Figure A4**).

2.4.10.3 Mass Change Over Time

Hydrogels were formed overnight in pre-weighed 2 mL microcentrifuge tubes and incubated in 100 µL of 1 PBS. At 0 hours, 24 hours, 4, 7, 10, 14, 21, and 28 days, the supernatant was removed, hydrogels were blotted of excess PBS with a KimWipe, and the tube containing the hydrogel was weighed. The mass of the hydrogel was recorded, and fresh PBS was added to the tube. The percentage mass change was calculated using **Equation 2.2**.

Equation 2.2.

$$\%Mass\ Change = \frac{m_t - m_0}{m_0} \times 100\%$$

where m_t is the mass of the hydrogel at time t and m_0 is the initial mass of the hydrogel immediately after it was formed.

2.4.11 Release of BMP-2 from HA Hydrogels

Release of BMP-2 was assessed from HA hydrogels with and without conjugated BMP-2-specific affibodies over 28 days. To load BMP-2 into the hydrogels, BMP-2 was added to the HA-Ox and HA-Nor-Ox Affibody solutions and then crosslinked with HA-ADH. For hydrogels without affibodies, 200 ng of BMP-2 were added to a 50 µL solution of 2% w/v HA-Ox. For affibody-conjugated HA hydrogels, BMP-2 was added to a 50 µL solution of 2% w/v HANor-Ox-Affibody, which resulted in 1000 molar excess of affibody to BMP-2. For each hydrogel, 50 µL of HA-ADH were added to the HA-Nor-Ox or HA-Nor-Ox-Affibody solutions to create 100 µL HA hydrogels in 2 mL microcentrifuge tubes. 900 µL of 0.1% w/v BSA in PBS was added to each tube, and the hydrogels were incubated at 37 °C. 300 µL aliquots of supernatant were collected and replenished with fresh 0.1% w/v BSA in PBS at multiple time points over 28 days. BMP-2 in the supernatant was quantified using a BMP-2-specific ELISA. Cumulative BMP2 release was calculated by adding the total mass of BMP-2 in each collected aliquot. Cumulative fractional release versus the square root of time was plotted, and the data were fit to a short time approximation of one-dimensional diffusion from a thin sheet, and the slope of Fickian diffusion, k, was determined using **Equation 2.3**.[103,104]

Equation 2.3:

$$\frac{M_t}{M_\infty} = kt^{\frac{1}{2}}$$

where M_t is the mass of BMP-2 released at time t, M_t is the total mass of BMP-2 released at the end of the experiment, and k is the slope of Fickian diffusion.

2.4.12 Design of Experiments

Design of experiments (DoE) statistical optimization was used to investigate how the chemical composition of the hydrogels influenced their physicochemical properties. More specifically, D-optimal design was used to generate a design matrix of 15 hydrogel formulations with 1 centrally repeated condition (**Table 2.1**). We used a D-optimal design due to the constrained range of polymer concentrations from 1 to 3% w/v and the use of two distinct molecular weights of HA, either 40 kDa or 100 kDa, which resulted in a categorical variable in our model. The input variables for HA hydrogel composition were the concentration of HA-ADH (1–3% w/v), the concentration of HA-Ox (1–3% w/v), and the molecular weight of HA (40 kDa or 100 kDa) used to synthesize the hydrogel. The concentrations of HA-ADH and HA-Ox were continuous variables that were examined at equidistant low, medium, and high levels, whereas the molecular weight was a categorical variable that was examined at either 40 kDa or 100 kDa. The physicochemical properties quantified as response variables were gelation time, compressive modulus, and mass change at 1, 7, 14, 21, and 28 days after hydrogel fabrication.

MODDE-Pro 13.0 software (Sartorius, Fremont, CA) was used to generate the D-optimal experimental matrix of 15 hydrogel formulations and analyze the experimental data obtained. Experimental data were collected from each of the hydrogel formulations then used to fit a multiple linear regression model for each response variable as a function of the statistically

significant input variables. An input variable was considered statistically significant if it had a p-value of < 0.05 as determined by ANOVA. The model performance was further assessed using R^2, adjusted R^2, and Q^2. R^2 describes the variation of the response explained by the model for every variable. Adjusted R^2 describes the variation of the response explained by the model only for the variables that affect the response. Q^2 describes the variation of the response predicted by the model for new data. R^2 and adjusted R^2 values close to 1.0 indicate a high correlation between observed and predicted values. Q^2 above 0.50 and a difference between R^2 and Q^2 values below 0.30 validate that the model works independently of the specific data used to train the model.[105,106] Residual plots, Box–Cox plots, and ANOVA tables were used to diagnose outliers, trends, or lack of fit. The model was then refined by removing any outliers and input variables that were not statistically significant to increase the validity of our model.

Our overall engineering objective was to maximize the compressive modulus, set the gelation time to a value within 1–10 min, and set the mass change at all time points to 0%. Thus, to validate the predictive models, we generated hydrogels predicted to either fulfill these optimization parameters (optimal hydrogels) or fulfill reciprocal objectives (pessimal hydrogels). Specifically, the pessimal hydrogels were predicted to minimize the compressive modulus, maximize the gelation time, and either maximize or minimize the hydrogel mass change at all time points (i.e., induce hydrogel swelling or degradation).

2.4.13 Hydrogel Morphology

Scanning electron microscopy (SEM) was performed on the optimal hydrogel formulation, HA-$ADH_{3.00}$ HA-$Ox_{2.33}$, using a ThermoFisher Apreo 2 SEM. A 100 µL hydrogel was formed in an 8 mm mold, frozen at -80 °C, and lyophilized for imaging. Images were taken at 100 times magnification at 0.80 nA and 10.00 kV.

Table 2.1. HA hydrogel formulations evaluated to generate D-optimal multilinear regression model. 15 Unique hydrogel formulations were evaluated in triplicate with a centrally repeating condition at 100 kDa HA-$ADH_{2.00}$HA-$Ox_{2.00}$ evaluated with 9 replicates to determine the system's variance. The centrally repeated condition is bolded.

HA-ADH (% w/v)	HA-Ox (% w/v)	Molecular Weight
1.00	1.00	40 kDa
1.00	3.00	40 kDa
1.67	1.00	40 kDa
2.00	2.00	40 kDa
3.00	1.00	40 kDa
3.00	3.00	40 kDa
1.00	1.00	100 kDa
1.00	3.00	100 kDa
1.00	1.67	100 kDa
1.67	3.00	100 kDa
2.00	**2.00**	**100 kDa**
2.00	**2.00**	**100 kDa**
2.00	**2.00**	**100 kDa**
2.33	1.00	100 kDa
3.00	1.00	100 kDa
3.00	3.00	100 kDa
3.00	2.33	100 kDa

2.5 Results and Discussion

2.5.1 Functionalization of HA Polymers

HA was modified with either aldehyde (HA-Ox) or ADH functional groups (HA-ADH) for hydrazone crosslinking (**Figure 2.1**). Because polymer molecular weight can influence crosslinking density and subsequent physicochemical properties of the hydrogel,[85] we functionalized both 40 kDa and 100 kDa HA for hydrogel fabrication and evaluation. To expose

aldehyde groups on HA, we oxidized the polymer in the presence of sodium periodate (NaIO4) for 4 h in the dark before quenching the reaction with propylene glycol. Using the same starting material, we added ADH to HA in the presence of EDC at a pH of 4.75 for 24 h to create HA-ADH. The degree of oxidization was characterized using titration with hydroxylamine hydrochloride and was found to be 27.5±5.9% and 41.4±12.8% of HA repeating disaccharide units for 40 kDa and 100 kDa HA-Ox, respectively. The degree of modification of the ADH functional groups on the polymer was 67.6±1.2% for 40 kDa HA-ADH and 50.6±10.1% for 100 kDa HA-ADH as characterized by 1 H NMR (**Figure A1**). The degrees of modification and yields of all modified polymers are summarized in **Table A1**. Degrees of oxidation between 27–82%[107,108]and degrees of modification with ADH between 30–49%[109,110] have been previously reported, which is consistent with our results. Gel permeation chromatography was used to determine how the modifications to the HA polymer changed its molecular weight and polydispersity (**Table A2**). Our results revealed a decrease in molecular weight during the oxidation reaction due to the ring break on HA; however, the size of the polymer backbone was not greatly affected by hydrolysis as observed in other HA oxidation reactions.[17] Furthermore, the polydisperity indices of the two oxidized HA polymers were similar to unmodified HA. Interestingly, the average molecular weights of both the 40 kDa and 100 kDa HA-ADH were much larger than expected at 366±16.8 kDa and 332±9.58 kDa, respectively, suggesting that ADH reacted with multiple HA polymer chains during synthesis, resulting in larger polymer chains. Similar results have been documented in a previous HA-ADH synthesis in the presence of EDC and a low molar excess of ADH due to the bifunctionality of ADH.[111] This finding was further supported by the higher polydispersity indices for both 40 kDa and 100 kDa HA-ADH at 2.02±0.03 and 2.18±0.10, respectively, compared to unmodified HA, which indicate a larger distribution of polymer chain molecular weights.

We then used these modified HA polymers to fabricate the 15 hydrogels in **Table 2.1** and evaluated their gelation time, compressive moduli, and mass change over time to generate a predictive model for DoE analysis.

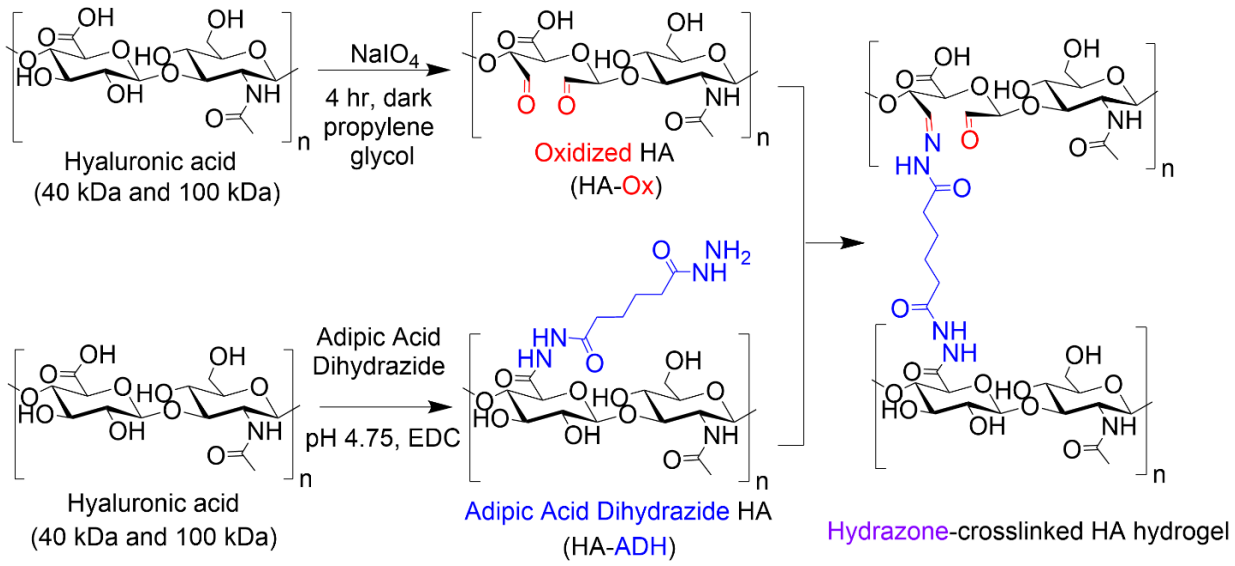

Figure 2.1. Functionalization of HA and hydrogel formation via hydrazone crosslinking. Hyaluronic acid (40 kDa or 100 kDa) was either stirred with sodium periodate in water for 4 h in the dark to oxidize the polymer and reveal aldehyde functional groups (HA-Ox) or mixed with adipic acid dihydrazide (ADH) and 1-ethyl-3-(3-dimethylaminopropyl)carbodiimide (EDC) in water and maintained at pH 4.75 for 24 h to create ADH-functionalized HA (HA-ADH). All polymers were dialyzed, filtered, and lyophilized before use. HA-Ox and HA-ADH were re-dissolved in phosphate buffered saline (PBS) and mixed at room temperature and pH 7.4 to form hydrazone-crosslinked HA hydrogels.

2.5.2 Hydrogel Gelation Time

HA hydrogels were fabricated by mixing 50 µL of HA-ADH and 50 µL of HA-Ox at different polymer concentrations and molecular weights. Inversion tests were used to quantify the gelation time of each of the HA hydrogel formulations. As expected, increasing the polymer content of the hydrogels increased the crosslinking density of the polymer network and subsequently decreased the gelation time (**Figure 2.2A**). Changing the polymer concentrations of the 40 kDa hydrogels had a greater effect on gelation time compared to the 100 kDa hydrogels, such that the 40 kDa hydrogels had a larger range of average gelation times ranging from 4.5 to 292.7 min. Additionally, increasing the HA-ADH content in the 40 kDa hydrogels decreased the gelation time of the hydrogels, except for the HA-$ADH_{1.00}$HA-$OX_{3.00}$ hydrogel. The gelation times of the 100 kDa hydrogels all fell between 1.4 and 71.5 min. The 100 kDa HA hydrogels

similarly exhibited decreasing gelation time in response to increasing HA-ADH content, except for the HA-$ADH_{1.67}$HA-$OX_{3.00}$ and HA-$ADH_{1.00}$HA-$OX_{3.00}$hydrogels, which demonstrated faster gelation times than the HA-$ADH_{2.00}$HA-$OX_{2.00}$ hydrogel. Excess HA-Ox content compared to HA-ADH content also resulted in shorter gelation times in both the 40 kDa and 100 kDa hydrogels. Overall, the 100 kDa hydrogels gelled faster than 40 kDa hydrogels, potentially due to increased entanglement of the longer polymer chains.[112] Gelation time of the centrally repeated hydrogel condition (100 kDa HA-$ADH_{2.00}$HA-$Ox_{2.00}$) was evaluated using 50 µL, 100 µL, and 200 µL hydrogels to determine if the hydrogel size had an effect on the gelation time (**Figure A3**). As the hydrogel volume increased, gelation time also increased. This was likely due to the increased time required to establish more crosslinks to effect complete gelation of a larger hydrogel.

2.5.3 Hydrogel Compressive Modulus

The compressive moduli of the hydrogels ranged from 4.5 to 42.2 Pa (**Figure 2.2B**). The compressive moduli of all the 100 kDa HA hydrogels fell within a narrow range of 20–40 Pa except for the HA-$ADH_{1.00}$HA-$Ox_{1.00}$ hydrogel, which exhibited an average compressive modulus of 13.6 Pa, which was significantly lower than HA-$ADH_{3.00}$HA-$Ox_{2.33}$ and HA-$ADH_{2.00}$HA-$Ox_{2.00}$ hydrogels and likely due to the lower polymer concentration. In contrast, the compressive moduli of all of the 40 kDa HA hydrogels fell within 4.5 to 20 Pa. Increasing the overall polymer content and HA-ADH content of the 40 kDa HA hydrogels resulted in higher compressive moduli, which was similar to the trends of increasing polymer concentration and HA-ADH content decreasing gelation time.

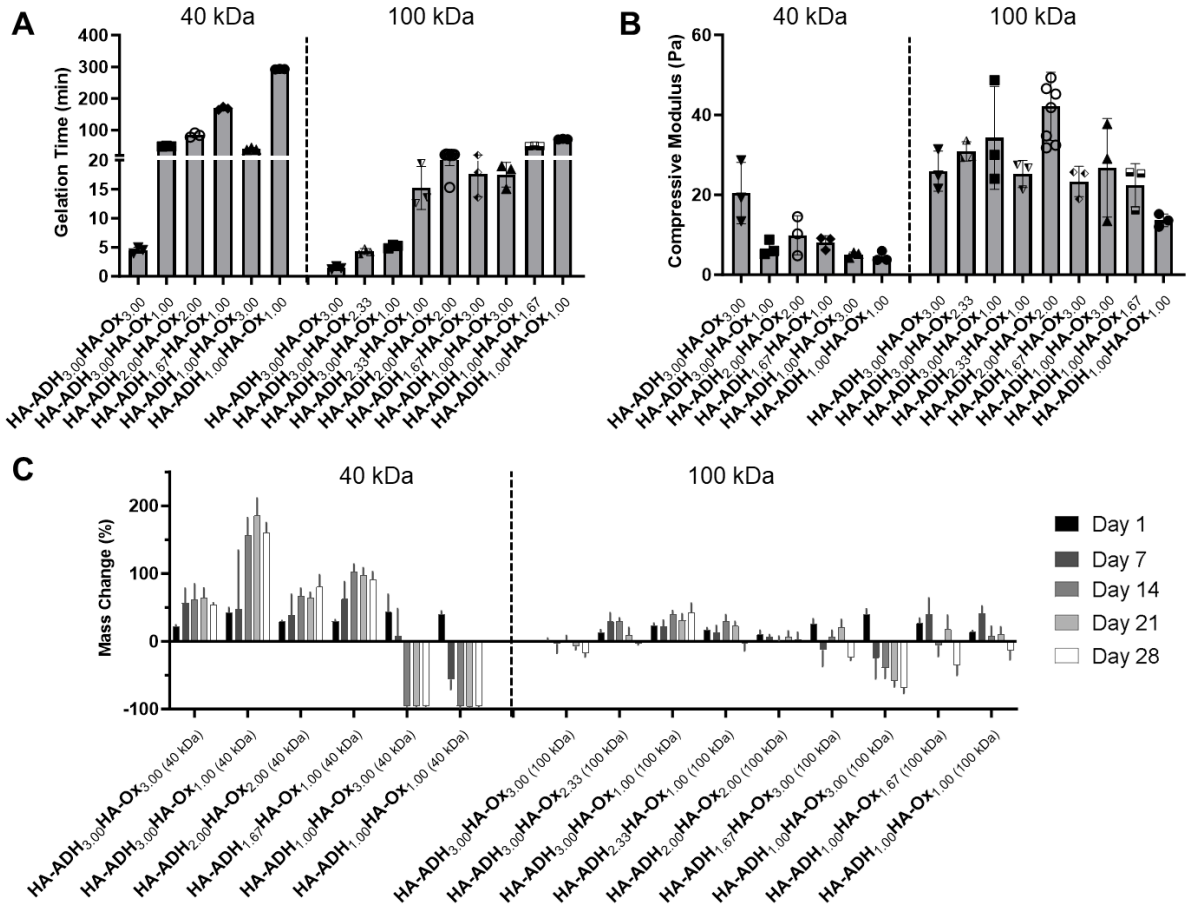

Figure 2.2. Physicochemical properties for each of the 15 hydrogel formulations for the D-optimal design. HA hydrogels were fabricated using 40 kDa or 100 kDa HA-Ox and HA-ADH at different polymer weight percentages. A) Gelation time of HA hydrogels. B) Compressive moduli of HA hydrogels. C) Mass change of HA hydrogels incubated in phosphate-buffered saline at room temperature for 28 days. Data presented as mean ±SD with 3 replicates for all hydrogel formulations, except for the centrally repeated condition, HA-$ADH_{2.00}$HA-$Ox_{2.00}$ (100 kDa), which had 9 replicates. A summary of statistical significance for gelation time, compressive modulus, and mass change can be found in **Tables A3–A5**, respectively.

2.5.4 Hydrogel Mass Change Over Time

The hydrogels were incubated in PBS at room temperature for 28 days, and their masses were periodically measured to observe swelling and/or degradation over time. For the 40 kDa HA hydrogels, the HA-$ADH_{3.00}$HA-$Ox_{1.00}$ hydrogel exhibited the maximum swelling of 185% of

its original mass at 21 days (**Figure 2.2C**). The HA-$ADH_{1.00}$HA-$Ox_{3.00}$ and HA-$ADH_{1.00}$HA-$Ox_{1.00}$ hydrogels demonstrated complete degradation (i.e., minimum mass change of 100%) at 14 days. For the 100 kDa HA hydrogels, the HA-$ADH_{1.00}$HA-$Ox_{3.00}$ hydrogel demonstrated the greatest degradation of 68% at 28 days, while the HA-$ADH_{2.33}$HA-$Ox_{1.00}$hydrogel demonstrated the maximum swelling of 62% at 4 days (**Figure 2.2D**). Overall, the 40 kDa HA hydrogels demonstrated larger changes in mass (swelling or degradation) than the 100 kDa HA hydrogels. This may be due to the lower degree of modification achieved for 40 kDa HA-Ox compared to 100 kDa HA-Ox, which may have resulted in lower crosslinking densities of the polymer network and less stable hydrogels. Hydrogels that contained either excess ADH or aldehyde content also demonstrated increased degradation or swelling, likely due to lower crosslinking density and a less stable crosslinked polymer network.

Our results corroborate the findings of other groups who have fabricated hydrazone-crosslinked HA hydrogels. Similar to the results of our study, others have demonstrated a large range of gelation times, an inverse relationship between gelation time of their HA hydrogels and concentration of ADH crosslinker, and less stable hydrogels with excess aldehydes.[43] In another study exploring hydrazone-crosslinked HA hydrogels for a vitreous substitute, the use of higher amounts of free ADH crosslinker stabilized the hydrogels;[108] however, we found that excess HA-ADH increased hydrogel swelling at early time points. A wide range of Young's moduli have been observed with hydrazone-crosslinked HA hydrogels with values ranging between 1–2000 Pa reported in the literature.[42] In comparison, our HA hydrogels exhibited relatively low compressive moduli within a narrow range of 4.5–42.2 Pa. Others have found that a higher degree of modification for HA-ADH led to stiffer hydrogels, which was similar to what we observed for the 40 kDa hydrogels.[90]

Ultimately, our method of fabricating hydrazone-crosslinked HA hydrogels yielded hydrogels with a wide range of physicochemical properties, including large ranges in hydrogel gelation time and mass change, with the capacity to swell, degrade, or maintain a relatively constant mass over 28 days depending on the molecular weight and concentrations of HA-ADH and HA-Ox used (**Table 2.2**).

Table 2.2. Ranges of physicochemical properties exhibited by HA hydrogels.

Property	Range
Gelation Time	1.4 – 292.7 min
Compressive Modulus	4.5 – 42.2 Pa
Mass Change Day 1	1.0 – 43.1 %
Mass Change Day 7	-56.3 – 62.2 %
Mass Change Day 14	-100 – 156.9 %
Mass Change Day 21	-100 – 185.3 %
Mass Change Day 28	-100 – 160.7 %

2.5.5 Design of Experiments Analysis

After obtaining response data for our 15 hydrogel formulations, we used this data to generate a multivariate model for DoE analysis to better understand how HA-Ox concentration, HA-ADH concentration, and HA molecular weight interacted to produce a wide range of physicochemical properties demonstrated by our platform and to predict the hydrogel formulations that would yield responses that met our desired design criteria. We fit second order multiple linear regression models for each response (gelation time, compressive modulus, mass change at 1, 7, 14, 21, and 28 days) and eliminated the terms that were not statistically significant unless they contributed to square terms or interaction terms that were statistically significant ($p < 0.05$) (**Table 2.3**). There was a significant effect of HA-ADH concentration on all responses except for mass change at day 7 and a significant effect of HA-Ox concentration on all responses except for mass change at day 1. The molecular weight of the HA had a significant effect on all responses. Notably, several squared and interaction terms also had significant effects on individual responses. We found that all of our models fit the success criteria of R^2 and adjusted R^2 values close to 1.0, Q^2 above 0.50, and the difference between R^2 and Q^2 values below 0.30. The models with the lowest R^2 and Q^2 values, indicating the poorest fit, were for mass change at days 1 and 7. This may be due to large variations in the initial swelling of the hydrogel network when incubated in PBS resulting in unpredictable short-term changes in mass compared to hydrogels that have swollen to a stable, more predictable equilibrium at later time points (days 14, 21, and 28).[113]

Table 2.3. ANOVA assessment of regression models. Excluded non-significant values are indicated with a dash (-)

Response	Gelation Time	Compressive Modulus	Mass Change Day 1	Mass Change Day 7	Mass Change Day 14	Mass Change Day 21	Mass Change Day 28
			p-values				
[HA-ADH]	<0.0001	0.0258	0.0136	0.612	<0.0001	<0.0001	<0.0001
[HA-Ox]	<0.0001	0.173	0.725	0.000539	<0.0001	<0.0001	<0.0001
Molecular Weight (MW)	<0.0001	0.00122	0.000702	0.000222	0.000494	0.00107	0.000234
$[HA\text{-}ADH]^2$	0.000985	0.00375	0.0399	-	-	-	-
$[HA\text{-}Ox]^2$	-	0.000782	-	-	-	-	-
MW^2	-	-	-	-	-	-	-
[HA-ADH]* [HA-Ox]	-	-	0.00213	0.00237	-	-	-
[HA-ADH]* MW	-	-	-	-	0.00166	0.000823	0.0125
[HA-Ox]* MW	-	-	-	-	0.000964	0.00304	0.00763
Lack of Fit	0.177	0.363	0.948	0.213	0.410	0.472	0.548
Total Sample Size (N)	17	13	17	16	16	16	16
Degrees of Freedom (DF)	12	7	11	11	10	10	10
R^2	0.964	0.970	0.828	0.852	0.950	0.937	0.936
R^2-adjusted	0.952	0.903	0.750	0.799	0.926	0.905	0.904
Q^2	0.918	0.949	0.601	0.683	0.710	0.840	0.792

Three-dimensional response surface plots of gelation time for the 40 kDa HA hydrogels demonstrated that higher polymer content resulted in faster gelation with the shortest gelation time occurring at HA-$ADH_{3.00}$HA-$Ox_{3.00}$ and longest gelation time occurring at HA-$ADH_{1.00}$HA-$Ox_{1.00}$ (**Figure 2.3A**). This response surface was identical but smaller in magnitude for the 100 kDa HA hydrogels (**Figure 2.3B**). These plots indicate that gelation time was dependent on the concentrations of both HA-ADH and HAOx. The response surfaces of compressive modulus for 40 kDa and 100 kDa HA hydrogels both depicted a negative quadratic dependence on the HA-Ox and HA-ADH concentrations with a maximum compressive modulus predicted to occur at HA-$ADH_{2.21}$HA-$Ox_{2.08}$. For the 40 kDa HA hydrogels, this maximum compressive modulus was predicted to be 39.2 Pa (**Figure 2.3C**), while, for the 100 kDa HA hydrogels, the maximum compressive modulus was predicted to be 27.3 Pa (**Figure 2.3D**). The relationship between mass change and input parameters was different at different time points. Mass change at day 1 was dependent on interactions between HA-ADH and HA-Ox concentrations and demonstrated a positive quadratic dependence on HA-ADH. The minimal mass change for both 40 kDa and 100 kDa hydrogels occurred at HA-$ADH_{3.00}$HA-$Ox_{3.00}$ and was found to be at 4.65% and 21.1%, respectively (**Figure 2.3E and F**). Mass change at day 7 demonstrated a linear dependence on HA-ADH and HA-Ox concentrations, suggesting there were no interactions between HA-ADH and HA-Ox concentrations for this response. For both 40 kDa and 100 kDa hydrogels, the minimum mass change occurred at HA-$ADH_{1.00}$HA-$Ox_{3.00}$; however, the predicted minimum was 9.49% for 40 kDa hydrogels (**Figure 2.3G**), and -22.61% for 100 kDa hydrogels (**Figure 2.3H**). At day 14, the model predicted a minimum mass change of 74.87% at HA-$ADH_{1.00}$HA-$Ox_{3.00}$ and a maximum mass change of 174.16% at HA-$ADH_{3.00}$HA-$OX_{1.00}$ for 40 kDa hydrogels (**Figure 2.3I**). Minimum and maximum mass changes occurred at the same polymer compositions for 100 kDa hydrogels on day 14, with a minimum at 26.63% and a maximum of 40.23% (**Figure 2.3J**). The response surfaces for 40 kDa and 100 kDa HA hydrogels at day 28 demonstrated linear dependences on HA-ADH and HA-Ox concentrations similar to response surfaces at day 14 (**Figure 2.3K and L**). Overall, the response surfaces and ANOVA table demonstrate that gelation time, compressive modulus, and mass change at day 1 were dependent on interactions between HA-ADH concentration and HA-Ox

concentration, while no interactions of the input parameters were observed with mass changes at the other time points.

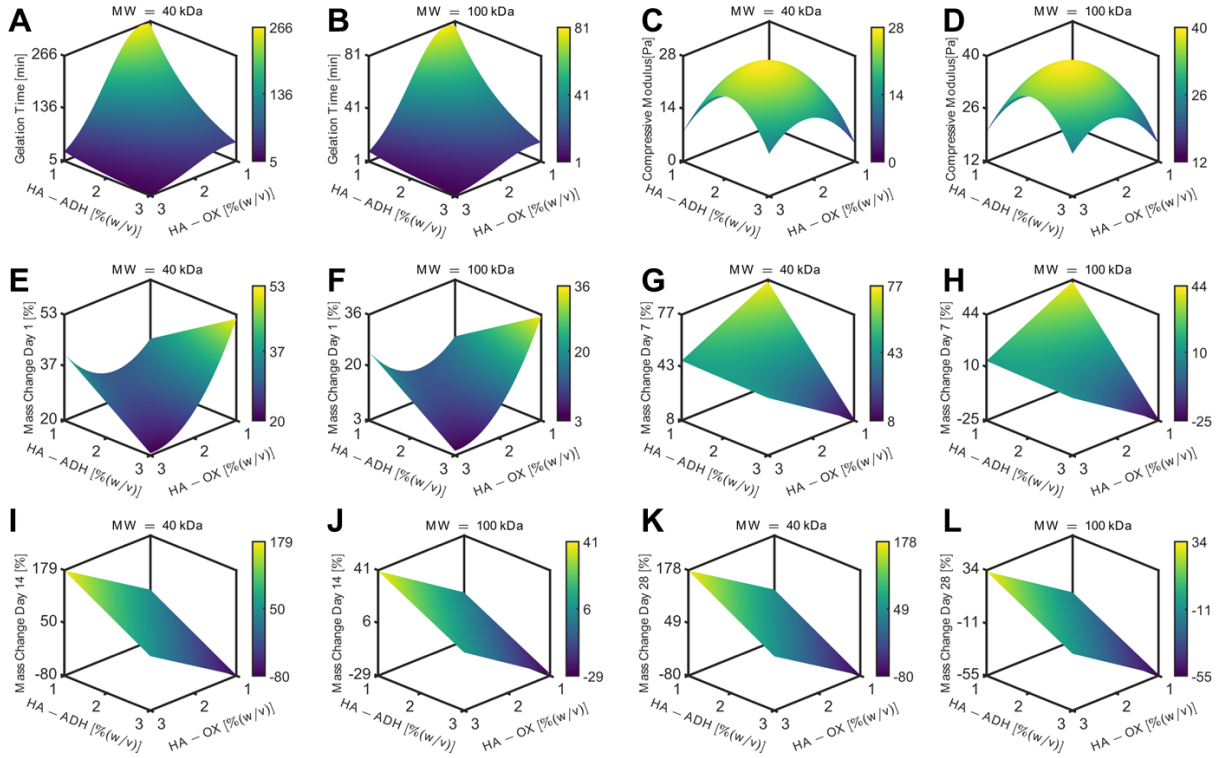

Figure 2.3. Three-dimensional response surfaces demonstrating the effect of input parameters on different output responses. Polymer weight percentages of HA-ADH and HA-Ox are on the x- and y-axes respectively, and output responses are on the z-axes. Responses for 40 kDa and 100 kDa HA hydrogels are plotted separately. The colored bars represent the magnitude of the response from low (blue) to high (yellow) for each response surface. Response surfaces for gelation time for A) 40 kDa HA and B) 100 kDa HA, compressive moduli for C) 40 kDa HA and D) 100 kDa HA, mass change at day 1 for E) 40 kDa HA and F) 100 kDa HA, mass change at day 7 for G) 40 kDa HA and H) 100 kDa HA, mass change at day 14 for I) 40 kDa HA and J) 100 kDa HA, and mass change at day 28 for, K) 40 kDa HA and L) 100 kDa HA.

2.5.6 Optimal and Pessimal Hydrogel Predictions

Our overall objective was to use DoE to optimize HA hydrogels for protein delivery for bone regeneration. We aimed to formulate a hydrogel that exhibited a gelation time between 1–10 minutes, minimal mass change (i.e., 0%) over 28 days, and the maximum possible

compressive modulus. D-Optimal design generated predictive models describing how HA-ADH polymer concentration, HA-Ox polymer concentration, and HA molecular weight influenced compressive modulus, gelation time, and mass change.

To validate this model, we generated a hydrogel formulation that was predicted to optimize our target parameters (Optimal) as well as two hydrogels that were optimized with opposite objectives (Pessimal 1 and 2) (**Table 2.4**). More specifically, Pessimal 1 was set to degrade over 28 days, while Pessimal 2 was set to swell over 28 days. Our optimal formulation had a molecular weight of 100 kDa while both pessimal formulations had a molecular weight of 40 kDa. This may be due to the longer gelation times, softer compressive moduli, and larger mass changes over time that were observed in our 40 kDa hydrogels. The optimal formulation, HA-$ADH_{3.00}$HA-$OX_{2.33}$, met our targeted responses with a gelation time of 3.7 min (**Figure 2.4A**), compressive modulus of 62.1 Pa (**Figure 2.4B**), and minimal mass change ranging between -22.2 to 5.5% over 28 days (**Figure 2.4C**). Conversely, our Pessimal 1 formulation, HA-$ADH_{1.17}$HA-$OX_{1.02}$, displayed a gelation time of 262.2 min, compressive modulus of 23.1 Pa, and swelling up to 85.3% of its initial mass on day 4, followed by full degradation by day 21. The Pessimal 2 formulation, HA-$ADH_{1.70}$HA-$OX_{1.80}$ displayed a gelation time of 100 min, a compressive modulus of 70.6 Pa, and swelling up to 172.3% by day 28 with no degradation.

The gelation time of the optimal formulation was significantly lower than that of the pessimal formulations. Mass change for the optimal formulation was closer to the 0% target mass change at all timepoints, while both pessimal formulations exhibited initial swelling before either degrading completely or continuing to swell excessively. However, there were no significant differences between the compressive moduli of the optimal formulation and the two pessimal formulations. Thus, trying to independently target each of our desired physicochemical properties with our hydrogel formulation would not have been successful, highlighting the importance of using DoE to simultaneously optimize multiple output responses. Scanning electron microscopy of the optimal hydrogel formulation revealed interconnected pores of different sizes (**Figure A5**). This porous morphology resembles the morphology observed in other HA hydrogels.[114]

Table 2.4. Formulations for optimal and pessimal hydrogels.

	HA-ADH (%w/v)	HA-Ox (%w/v)	Molecular Weight
Optimal	3.00	2.33	100 kDa
Pessimal 1	1.17	1.02	40 kDa
Pessimal 2	1.70	1.80	40 kDa

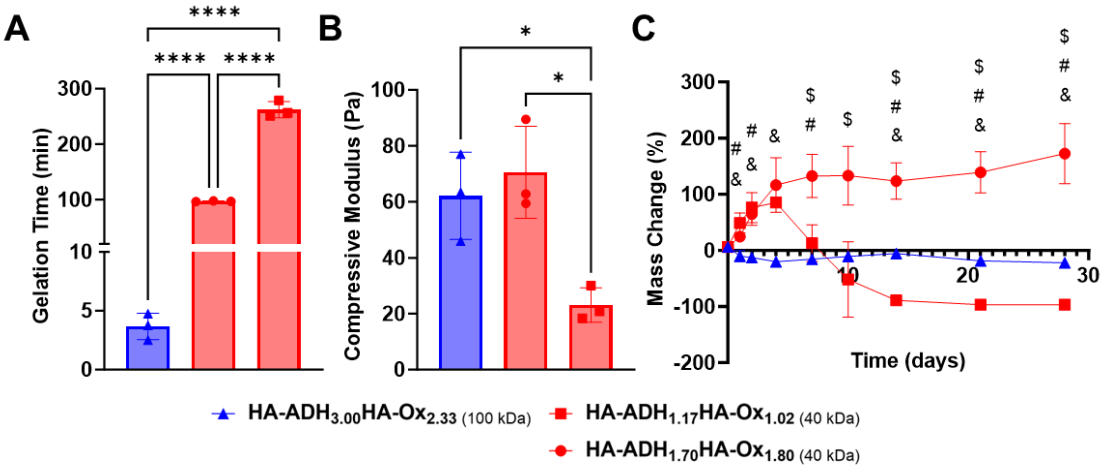

Figure 2.4 Validation of predictive models to optimize HA hydrogels. (A) Gelation time of optimal (blue) and pessimal (red) hydrogels. One-way ANOVA, post hoc Tukey's multiple comparisons. n = 3; ** $p < 0.01$, **** $p < 0.0001$. (B) Compressive modulus of optimal and pessimal hydrogels. One-way ANOVA, post hoc Tukey's multiple comparisons. n = 3; * $p < 0.05$. (C) Mass change over 28 days of optimal and pessimal hydrogels. Two-way ANOVA, post-hoc Tukey's multiple comparisons. n = 3; & $p < 0.05$ HA-ADH$_{3.00}$HA-Ox$_{2.33\ (100\ kDa)}$ vs. HA-ADH$_{1.17}$HA-Ox$_{1.02\ (40\ kDa)}$, # $p < 0.05$ HA-ADH$_{3.00}$HA-Ox$_{2.33\ (100\ kDa)}$ vs. HA-ADH$_{1.70}$HA-Ox$_{1.80\ (40\ kDa)}$, and \$ $p < 0.05$ HA-ADH$_{1.17}$HA-Ox$_{1.02\ (40\ kDa)}$ vs. HA-ADH$_{1.70}$HA-Ox$_{1.80\ (40\ kDa)}$.

2.5.7 BMP-2 Release from Affibody-Containing Hydrogels

As proof-of-concept of affinity-controlled protein delivery from our HA hydrogels, we modified HA-Ox to contain a norbornene functional group for bioconjugation of a previously discovered BMP-2-specific affibody with high affinity for BMP-2 (dissociation constant, K_D = 10.7 nM).[95] Affibodies are small proteins with 58 amino acids folded into a bundle of three α-helices.[115,116] Affibodies can be engineered to bind to different proteins with a range of affinities

and can be used to release proteins at various rates by tuning the strength of the affinity interactions.[95,117,118] HA was functionalized with norbornene through BoC_2O activated coupling (**Figure 2.5A**). The resulting product was then modified a second time by the previously described oxidation reaction, resulting in oxidized, norbornene-functionalized HA (HA-Nor-Ox; **Figure 2.5B**). Two times molar excess affibody to HA was then added to HA-Nor-Ox in the presence of a photoinitiator and exposed to light at 365 nm to create affibody-conjugated HA-Nor-Ox (HA-Nor-Ox-Affibody). The average concentration of affibody conjugated to HA-Nor-Ox was 2.80±1.95 nmol mg^{-1} HA polymer (**Figure A6**). This modified polymer was crosslinked with HA-ADH to form a hydrazone-crosslinked, affibody-containing HA hydrogel.

Release of BMP-2 was evaluated over 28 days from unmodified HA hydrogels or hydrogels conjugated with affibodies with high affinity and specificity for BMP-2 (dissociation constant, K_D = 10.7 nM).[95] Hydrogels were formed with BMP-2 and incubated in 1% w/v BSA in PBS. Aliquots were taken from the supernatant over 28 days to evaluate a release profile of BMP-2 from the HA hydrogel. The HA hydrogel with BMP-2 affibody reduced the release of BMP-2 compared to a HA hydrogel without affibody (**Figure 2.6A**). After 28 days, 11.7% of BMP-2 was released from the hydrogel without the affibodies, whereas 3.5% of BMP-2 was released from the hydrogel with the BMP-2-specific affibodies. **Figure 2.6B** depicts the cumulative fraction release at each time point (M_t/M_∞) as a function of the square root of time of the linear region of the BMP-2 release profile. The diffusivity (i.e., release rate) or the Fickian diffusion slope, k, was calculated using the slope of the cumulative fractional release (**Equation 2.3**) demonstrating that the release rate of BMP-2 was significantly slower in the affibody-containing hydrogel compared to the hydrogel without affibodies (**Figure 2.6C**). Our goal was to use BMP-2-specific affibodies to increase BMP-2 retention within the HA hydrogel for future applications in bone regeneration, since increased BMP-2 retention has been shown to stimulate localized bone formation within an injury site.[119] In other work, we have demonstrated that BMP-2 release from polyethylene glycol (PEG) hydrogels can be tuned over a range of release rates and amounts by changing the affinity between the affibodies and BMP-2.[120] In the future, we plan to further explore how changes to the HA hydrogel formulation, affibody amount, and affibody affinity strength can influence BMP-2 release to enhance bone regeneration.

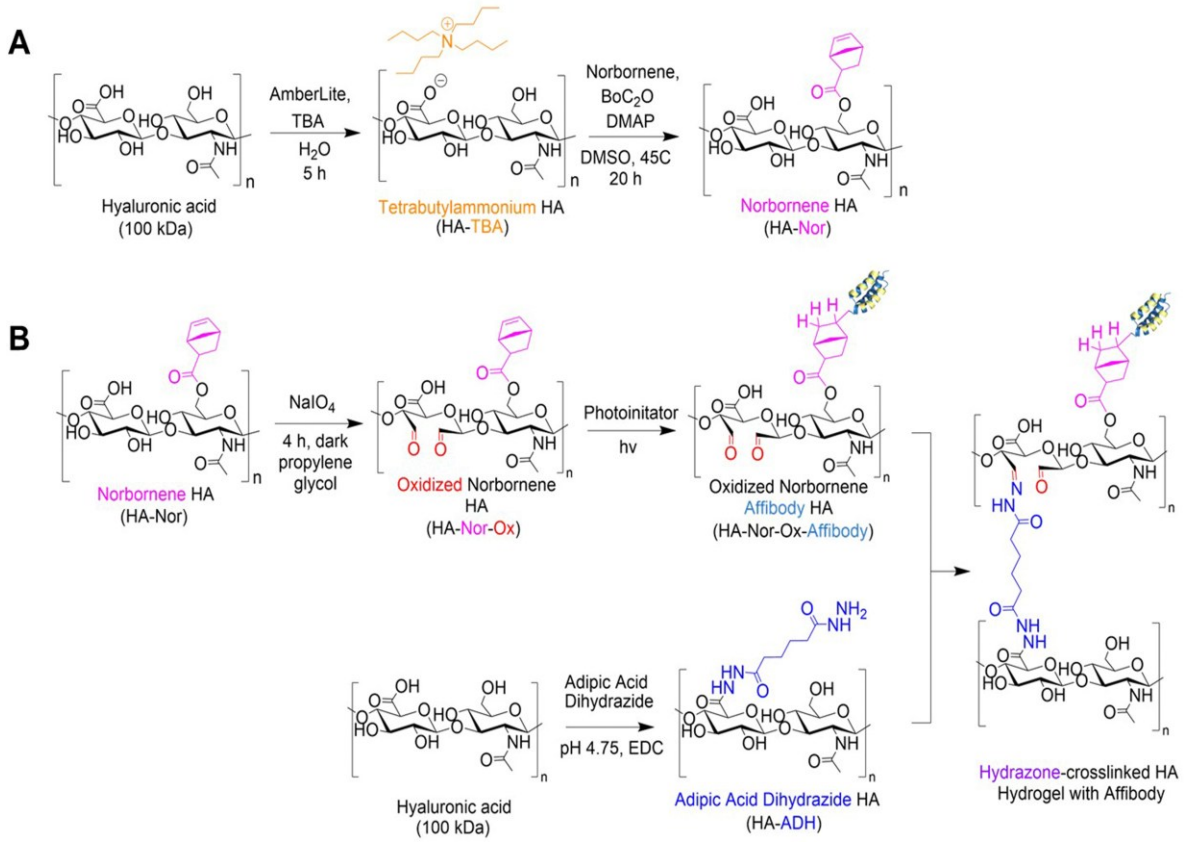

Figure 2.5. Synthesis of HA-Nor, HA-Nor-Ox, and HA-Nor-Ox-Affibody. A) HA was functionalized with a norbornene group through BoC2O activated coupling prior to oxidation resulting in HA-Nor-Ox. B) HA-Nor-Ox was then used to bioconjugate our BMP-2 affibody to the norbornene group through a photoinitiated reaction and thiol–ene click chemistry. The product was then crosslinked with HA-ADH to form a hydrazone-crosslinked hydrogel containing affibodies.

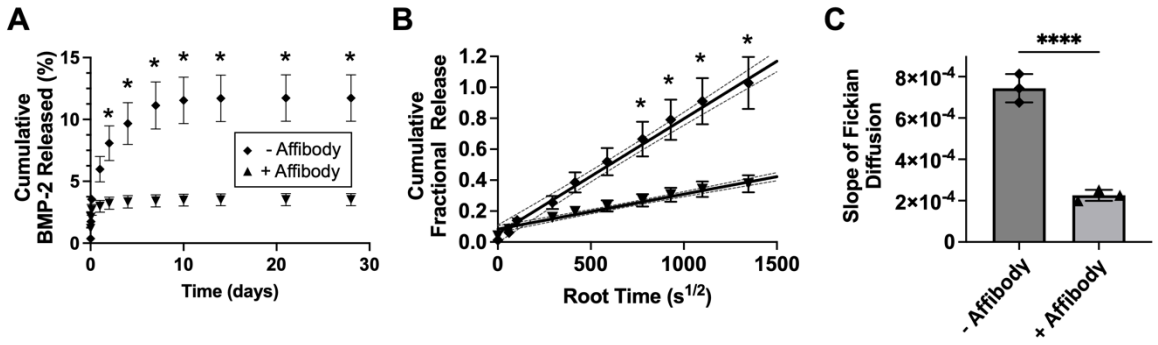

Figure 2.6. Release of BMP-2 from HA hydrogel. A) Cumulative release of BMP-2 from HA hydrogel without affibody (diamond) and with affibody (triangle). Two-way ANOVA, post hoc Dunnett's T3 multiple comparisons. n = 3; * p o 0.05. B) Linearized release of BMP-2 affibody from hydrogels with and without affibody. Two-way ANOVA, post hoc Dunnett's T3 multiple comparisons. n = 3; * p o 0.05. C) Slope of linearized release of BMP-2 from HA hydrogels. One-way ANOVA, post hoc Dunnett's T3 multiple comparisons. n = 3; * p o 0.05, **** p o 0.0001.

2.6 Conclusion

Although hydrazone chemistry is similar in many applications, each hydrogel requires distinct properties for a specific use. Designing an appropriate hydrogel for a biomedical application requires the consideration of many design criteria, such as gelation time, compressive modulus, and stability over time, that can be affected by many factors, including polymer molecular weight and concentration. In this work, we optimized hydrazone-crosslinked HA hydrogels for protein delivery for bone regeneration using DoE to better understand how various input parameters interacted to affect physicochemical properties, while reducing the number of experiments required to obtain this information. We generated models to describe how HA-ADH concentration, HA-Ox concentration, and HA molecular weight affected hydrogel compressive modulus, gelation time, and mass change over time. We identified an optimized hydrogel formulation that simultaneously maximized compressive modulus (62.1 Pa), achieved a target gelation time between 1–10 minutes (3.7 minutes), and was stable over 28 days with minimal mass change. We confirmed the validity of our model by evaluating two pessimal hydrogel formulations that were predicted to provide responses opposite to our optimal formulation. We

also demonstrated that protein release from hydrazone-crosslinked HA hydrogels could be sustained over 28 days by conjugated BMP-2-specific affibodies to the hydrogels to control the release of BMP-2. Ultimately, hydrazone-crosslinked HA hydrogels are a promising platform for protein delivery and DoE is a valuable tool to optimize hydrogels for this application.

2.7 Bridging Paragraph

We successfully developed a statistical model of the physicochemical properties of HA hydrazone crosslinked hydrogels and, as a proof of concept, identified a hydrogel formulation optimal for protein delivery. We can now apply this model to determine HA hydrogel formulations with a desired gelation time, stiffness, and stability for several applications. In the next chapter, we combined HA hydrogels with melt electrowritten scaffolds to produce aligned, HA-coated composite scaffolds and investigated myoblast behavior seeded on top of them for eventual use in volumetric muscle loss tissue repair. In addition, we functionalized of HA hydrogels with fibronectin-derived peptides (RGD) to enhance myoblast attachment, alignment, and differentiation on HA-coated scaffolds. Ultimately, we showed that the addition of HA hydrogels with MEW scaffolds can create a favorable environment for muscle tissue repair.

CHAPTER 3
HYALURONIC ACID-COATED SCAFFOLDS PROMOTE MYOBLAST ATTACHMENT, ALIGNMENT, AND DIFFERENTIATION

From Alycia N. Galindo, Alyssa K. Chi, Ievgenii Liashenko, Kelly L. O'Neill, Chandler L. Asnes, Ruchi Sharma, Jenna D. Khachatourian, Armaan Hajarizadeh, Paul D. Dalton, and Marian H. Hettiaratchi. Hyaluronic Acid-Coated Melt Electrowritten Scaffolds Promote Myoblast Attachment, Alignment, and Differentiation. Cellular and Molecular Bioengineering 18 (5), 501-518 (2025). *This manuscript is under the terms of the Creative Commons Attribution 4.0 International License (CC BY 4.0).*

3.1 Abstract

3.1.1 Purpose

In muscle tissues, anisotropic cell alignment is essential for optimal muscle fiber development and function. Biomaterials for muscle tissue engineering must guide cellular alignment while supporting cell proliferation and myogenic differentiation.

3.1.2 Methods

Here, we describe the fabrication of a tissue-engineered construct consisting of a scaffold of aligned poly(εcaprolactone) (PCL) microfibers coated in a dynamic covalent hydrazone crosslinked hyaluronic acid (HA) hydrogel to support myoblast attachment, myoblast alignment, and myotube formation. Norbornene modification of HA further enabled functionalization with fibronectin-derived arginine-glycine-aspartic acid (RGD) peptide. Scaffolds were fabricated using melt electrowriting (MEW), a three-dimensional (3D)-printing technique that uses stabilization of fluid columns to produce precisely aligned polymeric microfibers. We evaluated C2C12 mouse skeletal myoblasts cultured on non-coated, HA-coated, and HA-RGD-coated MEW scaffolds with fiber diameters of 10, 20, and 30 μm using immunocytochemistry and creatine kinase activity assays. We further evaluated the mechanical properties of 20 μm fiber scaffolds and their effect on myogenic gene expression and alpha-actinin protein expression of C2C12 myoblasts undergoing differentiation.

3.1.3 Results

HA-coated and HA-RGD-coated scaffolds increased attachment of C2C12 myoblasts on all fiber diameters compared to non-coated scaffolds, with HA-RGD-coated scaffolds demonstrating the highest cell attachment. All scaffolds supported cellular alignment along the fibers. Cells differentiated on scaffolds showed anisotropic alignment with increased myotube formation on HA-coated and HA-RGD-coated scaffolds as demonstrated by myosin heavy chain (MHC) staining and by the presence of striations on HA-coated scaffolds visualized with alpha-actinin staining. Increased creatine kinase activity and myogenic gene expression on day 5 further indicated myotube formation on all scaffolds, with HA-coated scaffolds significantly increasing the expression of several key myogenic markers.

3.1.4 Conclusion

This unique combination of tunable biophysical and biochemical cues enables the creation of a biomimetic tissue engineered scaffold, providing a platform for new therapeutic approaches for muscle regeneration.

3.1.5 Keywords

Muscle regeneration · Cellular alignment · Hyaluronic acid · Polycaprolactone · Microfiber scaffold · Melt electrowriting

3.2 Introduction

Volumetric muscle loss (VML), characterized by extensive muscle loss of greater than 20% of its original volume, can be caused by trauma, chronic disease, or surgical resection.[121,122] Such muscle injuries typically have limited regenerative capacity and cannot heal without additional intervention, often leading to fibrosis, fatty tissue infiltration, and impaired function, decreasing a patient's quality of life.[122–124] Muscle tissue has a complex and hierarchical architecture of aligned fascicles enclosed by the epimysium, the outermost layer of muscle.[125,126] Within fascicles are bundles of muscle fibers that are surrounded by the perimysium. Individual muscle fibers within a fascicle are surrounded by endomysium. Muscle fibers, also known as myofibers, are multinucleated muscle cells. Within muscle fibers are myofibrils, which are responsible for muscle contractility and are made from repeating units of sarcomeres that contain thick myosin and thin actin filaments. VML destroys the natural muscle ultrastructure, preventing the muscle from performing essential tasks like contraction and force generation.[124]

Current therapeutic approaches for treating VML often require multiple interventions, including surgical procedures such as autologous muscle transfer,[127] rehabilitation,[128] and long-term management of associated complications.[129,130] However, these approaches often fail to fully restore muscle function due to the difficulty of achieving aligned tissue,[131,132] and restoring this hierarchical structure is considered an important step for the repair of functional muscle tissue following VML.[131,133] Furthermore, the use of muscle autografts and allografts is constrained by the scarcity of available tissue and the potential for donor-site complications, underscoring the urgent need for alternative solutions.[134]

To address the shortcomings of current therapeutic approaches for treating VML, scaffold-based tissue engineering has emerged as a potential therapeutic strategy for stimulating the regeneration of functional, mature muscle tissue after VML. Strategies that combine three-dimensional (3D) scaffolds,[135,136] cell-based therapies,[137] and biochemical cues,[138,139] have shown promise in treating VML. For example, aligned scaffolds have been fabricated using 3D printing of fiber-based scaffolds or hydrogels,[140] injection molding or casting,[141] microfluidics,[142] unidirectional freeze drying or ice templating,[143] and decellularized tissues.[144] Fiber-based scaffolds have been fabricated from synthetic polymers such as polylactic acid (PLA), poly (lactic-co-glycolic acid) (PLGA),[145] and poly(ε-caprolactone) (PCL)[146] with 3D printing techniques such as solution electrospinning and have been used to align myoblasts with a tissue-engineered scaffold and promote their differentiation. These scaffolds may further be tailored to replicate the extracellular matrix (ECM) of native muscle tissue, generating an enhanced microenvironment for myoblast adhesion, migration, and differentiation.[134,147] Scaffolds fabricated from decellularized ECM from native muscle tissue are promising for VML treatment because they retain the biochemical signals and aligned structure of muscle tissue, which can facilitate myoblast alignment and fusion; however, it is often difficult to tune the properties of decellularized ECM scaffolds without losing their bioactivity.[148,149] Similarly, naturally-derived biomaterials such as collagen, gelatin, silk, fibrin, and alginate can be fabricated into aligned materials to promote myoblast alignment and fusion.[150,151] Hydrogels made from type I collagen,[152,153] poly(ethylene glycol) diacrylate (PEG-DA),[139] and gelatin methacryloyl[154] have also shown promise in supporting the development of tissue-engineered muscle constructs, as they mimic the hydrated environment of muscle tissue and have the added benefit of supporting vascularization and innervation within engineered tissues.[139,152–154] However, challenges remain

with synthetic fiber-based approaches that may suffer from ineffective integration with the host tissue and limited biochemical cues to support cell adhesion, proliferation, and differentiation, while hydrogel-based approaches have demonstrated a limited ability to support aligned muscle architecture and long-term tissue stability. Therefore, integrating synthetic fibers with hydrogels could be a promising approach for integrating complementary biochemical and biophysical cues, thereby addressing the weaknesses of each approach when used alone.

Incorporating biochemical cues into scaffolds enhances muscle tissue regeneration by providing essential signals that guide cellular behavior. These cues may include cells, electroconductive materials that improve cell-material interactions, growth factors that stimulate cellular activity, and peptide motifs that facilitate cell attachment.[155–158] By mimicking the body's natural ECM, these scaffolds offer a promising solution to accelerate muscle tissue repair and minimize tissue fibrosis.[159] A variety of ECM-derived peptides, such as fibronectin, laminin, and elastin, have been used in tissue-engineered scaffolds to stimulate myoblast proliferation, highlighting the importance of cell-ECM interactions for driving muscle tissue regeneration.[139,160,161] The fibronectin-derived peptide RGD has been previously shown to support muscle satellite cell survival, attachment, and myogenic differentiation within polyethylene glycol maleimide (PEG-MAL) hydrogels.[162] However, achieving robust muscle tissue formation using bioactive scaffolds is still a challenge, and the ideal combination of biophysical and biochemical cues to create a tissue-engineered scaffold that mimics functional muscle tissue has yet to be determined.

To address these challenges, we have created a composite tissue-engineered scaffold that combines the alignment properties of a synthetic fiber-based scaffold with the cell supportive microenvironment of ECM-derived hydrogels to promote the attachment, alignment, and myogenic differentiation of skeletal myoblasts with a unique combination of biophysical and biochemical cues. We used melt electrowriting (MEW), a 3D-printing technique that uses electrohydrodynamics to precisely deposit multiple layers of microfibers onto a collector, to produce aligned scaffolds.[163,164] To promote C2C12 murine skeletal myoblast attachment, we embedded MEW scaffolds within hydrazone-crosslinked hyaluronic acid (HA) hydrogels that have been previously characterized by our lab and others.[40,42,165] HA can directly interact with myoblasts through the CD44 and RHAMM cell receptors, promoting cell migration, adhesion, and proliferation.[166] We modified HA with norbornene functional groups for the chemical

conjugation of RGD peptide to further promote myoblast attachment and alignment. We seeded C2C12 myoblasts on non-coated, HA-coated, HA RGD-coated PCL microfiber scaffolds and evaluated their attachment to the scaffold, alignment along PCL microfibers, and differentiation into myotubes. We hypothesized that both HA and HA-RGD-coated scaffolds would increase myoblast attachment compared to non-coated MEW scaffolds, and HA-RGD-coated scaffolds would result in the highest cellular attachment and enhanced myogenic differentiation. We evaluated myotube formation through myosin heavy chain staining and creatine kinase activity assays over time. Overall, this HA-coated composite scaffold presents a unique combination of biophysical and biochemical cues that promote myoblast attachment, alignment, and differentiation and has the potential to be used as a tissue engineering scaffold to accelerate functional muscle regeneration.

3.3 Materials and Methods

3.3.1 Oxidized Hyaluronic Acid (HA-Ox)

As previously described, sodium hyaluronate (HA, 100 kDa) (Lifecore Biomedical LLC, Chaska, MN) was oxidized to reveal aldehyde groups.[165] Briefly, 2% w/v HA (1 g, 0.00264 mol) was dissolved in double distilled water (ddH_2O) in a round bottom flask. The flask was covered with foil, and 0.6 molar equivalents of sodium periodate (NaIO4, 338.61 mg, 0.00158 mol) (Sigma Aldrich, St. Louis, MO) were added to the reaction. The reaction was stirred for 4 h in the dark before being quenched with 5 molar equivalents of propylene glycol (VWR Chemicals, Radnor, PA) (1 g, 0.0132 mol). The solution was then dialyzed against ddH_2O for 2 days before being filtered, frozen at −80 °C, and lyophilized.

3.3.2 Hyaluronic Acid-Norbornene (HA-Nor)

HA was functionalized with norbornene as previously described.[51,52,165] An intermediate product, HAtetrabutylammonium (HA-TBA) was first synthesized. 2% w/v HA (1 g, 0.00264 mol) was dissolved in ddH_2O in a round bottom flask. AmberLite MB ion exchange resin (3 g, 0.00962 mol) (Sigma Aldrich) was added to the flask and stirred for 5 h. Vacuum filtration was then used to remove the resin. The solution was collected and titrated with tetrabutylammonium-hydroxide (TBA-OH) (Sigma Aldrich) to pH 7. The solution was then filtered, frozen at −80 °C, and lyophilized. HA-TBA (1 g, 0.00157 mol) was dissolved in anhydrous dimethylsulfoxide (DMSO) (Millipore Sigma, Burlington, MA) at 2% w/v in a round

bottom flask, which was submerged in an oil bath at 45 °C and purged with nitrogen gas. Three molar equivalents of 5-norbornene−2- carboxylic acid (Nor-CHOO, 0.803 g, 0.00581 mol) (Sigma Aldrich) and 1.5 molar equivalents of 4-(dimethylamino) pyridine (DMAP, 0. 287 g, 0.00235 mol) (Sigma Aldrich) were stirred into the flask until completely dissolved. Lastly, 0.4 molar equivalents of di-tert-butyl dicarbonate (Boc2O, 0.137 g, 0.000627 mol) (Sigma Aldrich) were added to the flask, and the reaction was stirred under nitrogen for 20 h. The reaction was quenched with an equal volume of cold ddH_2O and dialyzed against ddH_2O for 3 days. After dialysis, the solution was collected in a beaker and sodium chloride (VWR Chemicals) (1 g/100 mL of solution) was added. Acetone was added to the beaker (1 L/100 mL of solution) to precipitate the product. The precipitate was then collected by centrifugation and redissolved in ddH_2O. The HA-Nor solution was then filtered, frozen, and lyophilized.

3.3.3 Hyaluronic Acid-Norbornene-Adipic Acid Dihydrazide (HA-Nor-ADH)

1% w/v HA-Nor (0.125 g, 0.000240 mol) was dissolved in ddH_2O, and 10 molar equivalents of adipic acid dihydrazide (ADH) Spectrum (Chemical MFG Corp, Gardena, CA) (0.418 g, 0.00240 mol) and a one molar equivalent of hydroxybenzotriazole (HOBt) (Chem Impex, Wood Dale, IL) (0.324 g, 0.000240 mol) were added to the reaction. The pH was adjusted to 4.75 using NaOH/HCl, and one molar equivalent of 1-ethyl-3-(3-dimethylaminopropyl)carbodiimide (EDC) (G Biosciences, St. Louis, MO) (0.0460 g, 0.000240 mol) was added to the solution. The pH was titrated to 4.75 and monitored for 2–4 h until stabilized. The reaction was then stirred for 2 days before being dialyzed against 0.1 M sodium chloride for 2 days followed by ddH_2O for an additional 2 days. The solution was then filtered, frozen at −80 °C, and lyophilized.

3.3.4 Determination of Degree of Modification (DOM)

As previously described, the degree of modification of HANor and HA-Nor-ADH was quantified using proton nuclear magnetic resonance spectroscopy (^{1}H-NMR, 500 Hz, Bruker, USA).[165] The DOM for HA-Nor was calculated by integrating the vinyl peaks on the norbornene functional group from 5.7 to 6.3 ppm and normalizing to the n-acetyl methyl group on HA from 1.8 to 2 ppm (3H).[51] For HANor-ADH, the aliphatic chain peaks from 2.5 to 2.1 ppm and 1.7–1.44 ppm (8H) were integrated and normalized to the n-acetyl methyl group peaks on HA from

1.8 to 2 ppm (3H).[51] A representative ^{1}H-NMR spectrum can be found in the supplemental information (**Figure B1**).

To determine the DOM of HA-Ox, a hydroxylamine hydrochloride titration was performed by dissolving 100 mg of oxidized polymer in 20 mL of 0.25 N hydroxylamine hydrochloride containing 0.05% w/v methyl orange reagent for 2 h.[97,98,165] The pH of the solution was monitored and titrated with 0.1 M NaOH until the pH indicator changed from red to yellow at the end point pH of 4. Equation 1 was used to calculate the DOM or the percentage of HA monomers that contained aldehydes.

Equation 1:

$$\%DOM = (\frac{379.3\ g}{mol} HA \times 0.1M\ NaOH \times \left(\frac{V_f - V_0}{m_{HA-Ox}}\right)) \times 100$$

where 379.3 g/mol is the monomeric molecular weight of HA, 0.1 M is the molarity of NaOH used to adjust the solution pH, Vf is the final volume of NaOH in the burette after titration recorded in liters, V0 is the initial volume of NaOH in the burette before titration recorded in liters, and mHA-Ox is the mass in g of HA-Ox used in the titration.

3.3.5 RGD Conjugation to HA-Nor-ADH (HA-RGD)

2% w/v HA-Nor-ADH (10 mg, 0.0146 mmol) was dissolved in 500 µL of PBS containing 0.05% w/v of Irgacure 2959 (Sigma Aldrich) and 2500 nmol of RGD peptide with a cysteine at the N terminus (CGRGDSG) (GenScript, Piscataway, NJ) with the goal of conjugating 2.5 mM of RGD per 25 µL HA-Nor-ADH-RGD. The solution was exposed to UV light at a wavelength of 365 nm for 1 min to perform a thiolene reaction between HA-Nor-ADH and RGD-cysteine. The solution was dialyzed against ddH_2O for 1 day before being filtered, frozen at −80 °C, and lyophilized. Ellman's reagent (Fisher Scientific, Waltham, MA) was used to detect free thiols and quantify the concentration of RGD conjugated to the HA-Nor-ADH through the disappearance of thiols after the photoinitiated reaction. The Ellman's reagent consisted of 2 mM of 5,5-dithio-bis-(2-nitrobenzoic acid) (DTNB) and 50 mM sodium acetate in 1 M tris(hydroxymethyl)aminomethane (TRIS) buffer. Samples of the reaction before and after UV exposure were diluted to fall within the range of a standard curve of serially diluted RGD-cysteine peptide. 50 µL of each standard and sample were added to a 96-well plate and mixed with 250 µL of Ellman's reagent. The plate was developed at room temperature for 5 min prior to reading absorbance at 412 nm on a microplate reader (BioTek Synergy Neo2).

3.3.6 Fabrication of Melt Electrowritten (MEW) Scaffolds

Three flat scaffold designs were fabricated from medicalgrade PCL (PURAC PC12, Corbion Inc.) using a custombuilt MEW printer.[167] PCL was heated to 75 °C and extruded through an electrically grounded 22 gauge nozzle protruding 1 mm from the printhead. The collector distance was fixed to 3.5 mm, and scaffolds were printed onto 1 mm thick glass microscopy slides resting on a metal collector. Three sets of parameters (including collector voltage, pressure delivered to molten polymer, and translation speed) were optimized to print fibers with nominal diameters of 10, 20, and 30 µm. Printing parameters together with corresponding scaffold designs are detailed in **Table 3.1**.

Square scaffolds (7 × 7 mm) consisting of two sets of perpendicular alternating fibers were printed. The first set of fibers intended for myoblast alignment was spaced 150 µm apart. The second set of fibers intended as reinforcement fibers ran perpendicular to the myoblast alignment fibers and was spaced 500 µm apart. The numbers of alignment fibers and perpendicular reinforcement fibers printed for each design are detailed in **Table 3.1**. The total number of layers for each fiber diameter was selected to provide a consistent scaffold height of approximately 200 µm across the different designs. Scaffolds printed with 10 µm fibers were additionally reinforced on the edges to enable handling through a buckling fiber rim design previously used to improve scaffold handling and printed at 1 mm/min translation speed.[168]

Table 3.1. MEW printing parameters and fiber characteristics for each scaffold design.

	Scaffold design				**Printing conditions**		
Fiber diameter [µm]	Spacing between reinforcing fibers [µm]	Spacing between alignment fibers [µm]	Number of alignment layers printed first	Number of alternating alignment and reinforcing layers printed on top	Voltage [kV]	Pressure [bar]	Translation speed [mm/min]
10	500	150	6	14	5.5	0.17	500
20	500	150	3	7	5.5	0.65	345
30	500	150	2	5	6.2	1.40	345

3.3.7 Etching and Sterilization of MEW Scaffolds

Scaffolds were etched in a biosafety cabinet with 0.1 M NaOH for 30 min before being washed three times with phosphate-buffered saline (PBS). Etched scaffolds were disinfected in 70% v/v ethanol for 15 min before being washed three times with PBS. Scaffolds were stored in 10% v/v fetal bovine serum (FBS) (R&D Biosystems, Minneapolis, MN) in Dulbecco's modified eagle medium (DMEM) (Cytiva, Marlborough, MA) ("high serum medium") at 4 °C overnight before use.

3.3.8 HA Coating of MEW Scaffolds

HA-coated scaffolds were fabricated by adding 25 µL of either HA-Nor-ADH or HA-Nor-ADH-RGD to the bottom of an 8-chamber well slide (Fisher Scientific), followed by the scaffold, and then addition of 25 µL of HA-Ox. Coated scaffolds were agitated, and the polymers were allowed to crosslink for 30 min to create a thin HA hydrogel coating on the MEW scaffold.

3.3.9 Scanning Electron Microscopy (SEM) Imaging and Fiber Measurements of MEW Scaffolds

HA-coated MEW scaffolds were prepared using a freezedrying process for imaging with scanning electron microscopy (SEM). Freshly prepared HA-coated scaffolds were gently placed into a glass vial and suspended by a support on the edges. Samples were frozen at −80 °C for 4 h and then lyophilized overnight. Non-coated and HA-coated samples were then sputter-coated with 7 nm of titanium and imaged with an SEM Everhart–Thornley detector (ETD) (ThermoFisher Apreo 2, USA). Fiber diameter was quantified using ImageJ (FIJI, USA) (**Figure B2**).

3.3.10 C2C12 Myoblast Culture

C2C12 murine skeletal myoblasts (ATCC, Manassas, VA) were seeded at 2500 cells/cm2 in T-75 flasks with high serum medium at 5% CO2 and 37 °C. C2C12 were passaged at 70–80% confluency following standard protocols before use in further experiments.[169]

3.3.11 Myoblast Culture on Scaffolds

To evaluate myoblast attachment and proliferation, C2C12 cells between passages 7–9 were seeded on top of scaffolds at a density of approximately 57,000 cells/cm2 in an 8-chamber slide and allowed to attach to the scaffolds for 2 h in a low volume (100 µL) of high serum medium. The remaining volume (300 µL) of high serum medium was added, and the cells were allowed to proliferate for 24 h. The media were then exchanged to 1% v/v FBS in DMEM ("low

serum medium") for 3 days, after which the cells were fixed with 4% v/v paraformaldehyde (Fisher Scientific) in PBS for immunocytochemistry. To evaluate myotube formation, C2C12 cells between passages 7–9 were seeded on top of scaffolds at a density of approximately 14,000 cells/cm^2 in an 8-chamber well slide and allowed to attach for 2 h in a low volume of high serum medium before the remaining medium was added. The cells were allowed to proliferate for 24 h before the media was exchanged to differentiation media consisting of 2% v/v horse serum (Sigma Aldrich) in DMEM. Cells were differentiated for 7 days. The differentiation media were exchanged every 3 days. Media were collected at 1, 5, or 7 days to evaluate creatine kinase (CK) activity. After 7 days, cells were fixed with 4% v/v paraformaldehyde in PBS for immunocytochemistry.

3.3.12 Immunocytochemistry

All immunocytochemistry steps were performed at room temperature in the dark. For F-actin staining, cells were permeabilized with 0.5% v/v Triton-X 100 (Sigma Aldrich) for 15 min before washing three times with 200 µL of PBS. 200 µL of Alexa Fluor™ 647 phalloidin (5 U/mL) (Biotium, Fremont, CA) were added to the well and incubated for 20 min. The wells were then washed three times with PBS, incubated with 1 mg/mL of 4′,6-diamidino-2-phenylindole (DAPI) (Biotium) for 5 min, and washed three times with PBS again.

For myosin heavy chain staining, cells were permeabilized with 0.5% w/v Triton-X 100 for 15 min at room temperature and washed three times with PBS. Cells were blocked with 1% w/v bovine serum albumin (BSA) (Fisher Scientific), 22.5 mg/mL glycine (TCI Chemicals, Tokyo, Japan), and 0.1% v/v Tween-20 (Acros Organics, Geel, Belgium) in PBS overnight with agitation at 250 rpm at 4 °C. The next day, the cells were washed three times with PBS, anti-fast myosin skeletal heavy chain antibody (ab91506, Abcam, Cambridge, United Kingdom) diluted 1:500 times in 0.1% w/v BSA in PBS was added to the wells, and the cells were incubated overnight with agitation at 250 rpm at 4 °C. The following day, cells were washed with 0.5% v/v Tween-20 in PBS three times for 20 min each with agitation at 250 rpm at 4 °C. After washing, goat anti-rabbit IgG secondary antibody Alexa Fluor™ 488 (Invitrogen, Waltham, MA) diluted 1:200 in 0.1% w/v BSA in PBS was added to the wells and incubated for 1 h with agitation at 250 rpm at 4 °C, then washed three times with PBS. Lastly, 1 mg/mL of DAPI was added to the well for 5 min at room temperature and then washed three times with PBS. Cells were stored in PBS for imaging.

Alpha-actinin staining was performed similarly to myosin heavy chain staining but using anti-alpha-actinin primary antibody (A7732, Sigma Aldrich, 1:67 dilution) and goat anti-mouse IgG secondary antibody Alexa Fluor™ 647 (Invitrogen, 1:1000 dilution) with similar incubation times and washing steps.

3.3.13 Imaging of Scaffolds

C2C12 myoblasts were imaged as z-stacks (0.4 or 2.5 µm slices) using a CSU-W1 SoRa Spinning Disk confocal microscope (Nikon, USA). The average z-stacks were 68 µm for non-coated scaffolds, 110 µm for HA-coated scaffolds, and 129 µm for HA-RGD-coated scaffolds. Images were analyzed using IMARIS imaging software version 9.5. The Rolling Ball Algorithm was applied to each image to correct uneven backgrounds. The following background subtraction of fluorescent signal was applied to each stained channel (DAPI: 3500, Cy5: 3950, FITC: 3300) based on pixel size of the image.

3.3.14 Nuclei Count Analysis

The "surfaces" analysis in IMARIS was used to quantify the number of nuclei per scaffold. The background subtraction width was set to 9 µm to remove any background based on the width of the nuclei. Seed point and surface filters were added to enhance nuclei count accuracy.

3.3.15 Directionality Analysis

The directionality of myosin heavy chain staining was analyzed using the "cells" analysis in IMARIS. In the DAPI channel, the nucleus diameter (15 µm) and the average threshold intensity (327) were set. In the FITC channel, the average cell threshold intensity (173) and split by seed points (10 µm) were analyzed. The angle of the scaffolds was converted to degrees, and then the arctangent of "Cell Ellipsoid Axis X" and "Cell Ellipsoid Axis Y" was calculated and divided by two to get values between −90° and 90°.

The corner points of two scaffold boxes were identified to determine the angle of the scaffold for directionality correction. The absolute value of the arctangent of the difference between the top and the bottom of the scaffold was determined and averaged for each scaffold. If the cell ellipsoid value was less than zero, the scaffold value was added to it. If the cell ellipsoid value was greater than zero, the scaffold value was subtracted from it.

3.3.16 Creatine Kinase (CK) Activity Assay

Creatine kinase (CK) activity was measured using a Colorimetric CK Activity Assay kit (Abcam, Cambridge, United Kingdom) according to the manufacturer's instructions. After Day 1, 5, and 7 of differentiation, cell culture medium was carefully aspirated from the cell culture chambers containing the scaffolds, transferred to sterile 1.5 mL microcentrifuge tubes, and stored at −80 °C. Media samples (10 µL) were thawed and added to 96-well plates followed by the addition of a reaction mixture that included CK assay buffer, CK enzyme, CK developer solution, adenosine triphosphate (ATP), and creatine (CK substrate). The plate was incubated at 37 °C for 40 min, and absorbance at 450 nm was measured using a microplate reader (BioTek Synergy Neo2). CK activity was normalized to protein concentration determined by a bicinchoninic acid (BCA) assay (Fisher Scientific). All samples were processed in technical triplicates. A negative control (cell culture medium from wells without cells) and a positive control (standard provided in the kit) were included in the assay.

3.3.17 Mechanical Properties

The stiffness of non-coated MEW scaffolds was measured using the tension module on the RSA-G2 Solids Analyzer (TA Instruments, New Castle, DE). Scaffolds were attached at the top and bottom along the alignment fibers using tension clamps and allowed to equilibrate for 30 s during a "soak" step. Scaffolds were then stretched at a constant linear rate of 0.005 mm/s, and the slope of the initial linear portion of the stress-strain curve between 1 and 5% strain was calculated to measure stiffness. Tensile testing was performed for 300 s or until 25% strain if the scaffold yielded before 300 s.

3.3.18 Myogenic Gene Expression Analysis via RT-qPCR

Mouse PCR primers for Pax3, Pax7, MyoD, Myf5, MyoG, and GAPDH (Integrated DNA Technology, IDT, Coralville, IA) are summarized in the supplemental information (Table S1). [170,171]Myoblasts were differentiated for 5 days as described above. For RNA extraction, 500 µL of TRIzol™ Reagent (Fisher Scientific) were added to each well and incubated for 5 min at room temperature. The solution was collected in a microcentrifuge tube, and 200 µL of chloroform (Fisher Scientific) were added to each tube. The tube was vortexed and incubated on ice for 10 min before centrifuging at 12,000 rcf for 15 min at 4 °C. After phase separation, the top aqueous phase was carefully collected into a new tube, and 250 µL of ethanol (Decon Labs,

Prussia, PA) were added. The solution was transferred to a Zymo-spin column (Zymo Research, Irvine, CA) to collect the RNA. DNAse I treatment was performed according to the manufacturer's instructions. RNA was then washed and eluted. The RNA quality was assessed using UV-vis spectroscopy at 260/280 nm and 260/230 nm (Implen NanoPhotometer). RNA was transcribed into cDNA using the LunaScript RT SuperMix Kit (New England Biolabs, Ipswich, MA), and controls without reverse transcriptase and the template were included to confirm successful cDNA transcription. Samples were stored at −20 °C before proceeding to quantitative reverse transcription polymerase chain reaction (RTqPCR). Quantabio PerfeCTa® SYBR® Green SuperMix, Low ROX™ (Quantabio, Beverly, MA) was used to perform RT-qPCR in a 10 µL reaction volume following the suggested reaction protocol using the QuantStudio5 RealTime PCR System (ThermoFisher Scientific, Waltham, MA).

3.3.19 Statistical Analysis

Data were analyzed and graphed using GraphPad Prism version 10.1.1 (Boston, MA). Normality and equal variances were checked. Two-way analysis of variance (ANOVA) was used followed by the appropriate post-hoc test. P values less than 0.05 were considered statistically significant.

3.4 Results

3.4.1 Fabrication of HA-coated MEW Scaffolds

HA polymers were modified to enable hydrazone crosslinking as previously described (**Figure 3.1**).[165] 100 kDa HA was oxidized to expose aldehyde groups (HA-Ox). The number of monomers modified with aldehyde groups, which was called the percent degree of modification (%DOM), was determined to be 51.0±10.5%, and the percent yield was 66.0±35.3%. Simultaneously, an ion exchange was performed with 100 kDa HA to form an intermediate product HA-TBA. This intermediate product allowed for HA to become soluble in organic solvents such as DMSO for the modification with norbornene functional groups through Boc2O coupling for peptide conjugation (HA-Nor). The %DOM with norbornene functional groups was determined to be 24.0±2.3% using 1 H-NMR, and the percent yield was determined to be 40.4±5.1%. HA-Nor was then modified with adipic acid dihydrazide (ADH) to form HANor-ADH. The %DOM was determined to be 40.5±2.3% using 1 H-NMR, and the percent yield was determined to be 65.9±9.5%. For hydrogels containing RGD, a photoinitiated thiol-ene click

chemistry reaction was performed between the norbornene functional group on HANor-ADH and the terminal cysteine of the RGD peptide. 55.4±29.3 nmol of RGD were conjugated per mg HA as determined using an Ellman's assay that quantified the disappearance of free thiols. The reaction resulted in approximately 1.1 mM of RGD conjugated per 25 µL of HA-NorADH-RGD, which was less than the desired 2.5 mM of RGD, but still within the range of RGD concentrations that has been previously shown to support cell attachment and survival in hydrogels.[162,172]

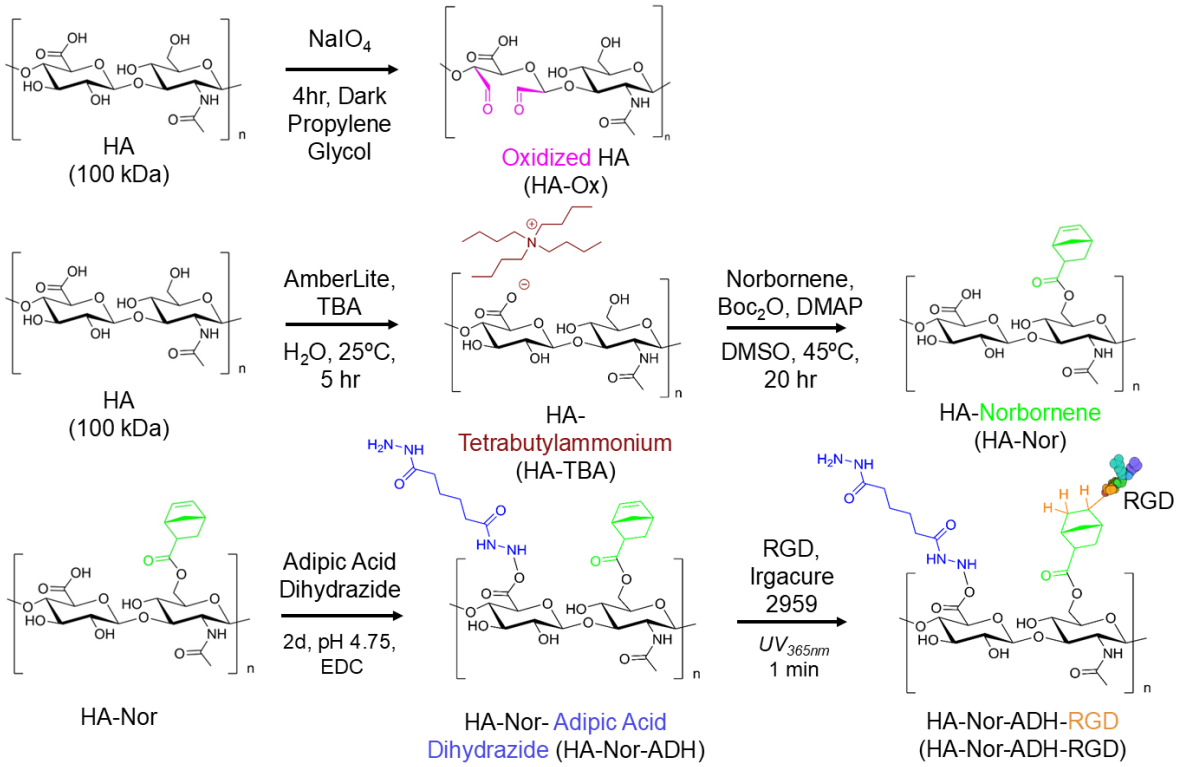

Figure 3.1. Hyaluronic acid (HA) modifications for hydrazone crosslinking. 100 kDa HA was either oxidized to form HA-Ox or modified with norbornene functional groups (HA-Nor). HA-Nor was then modified again with adipic acid dihydrazide functional groups to form HA-Nor-ADH. A thiol-ene click chemistry reaction was then performed with HA-Nor-ADH to form HA-Nor-ADH-RGD.

To coat scaffolds with the HA hydrogel, scaffolds were embedded between equal volumes of 2% w/v HA-Ox and 2% w/v HA-Nor-ADH or HA-Nor-ADH-RGD and allowed to gel for 30 min to create a thin hydrogel coating (**Figure 3.2**). The amine on ADH will

spontaneously react with the aldehyde on HA-Ox through a Schiff base reaction to form hydrazonecrosslinked hydrogels.[40,42,165]

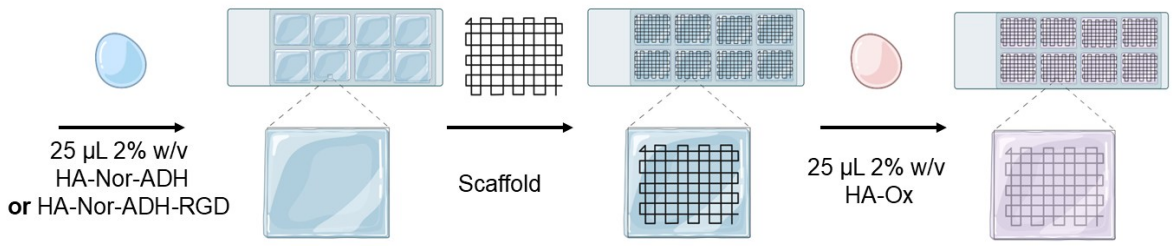

Figure 3.2. Coating of MEW scaffolds with HA. HA-coated scaffolds were fabricated in 8-chamber well plates by crosslinking 25 µL of either 2% w/v HA-Nor-ADH or HA-Nor-ADH-RGD and 25 µL of 2% w/v HA-Ox around MEW scaffolds for 30 min.

3.4.2 Morphology of Non-coated and HA-coated MEW Scaffolds

MEW scaffolds were printed with either 10, 20, or 30 µm diameter PCL fibers to evaluate the effects of fiber diameter on myoblast attachment and differentiation. To create anisotropic cell alignment, myoblast alignment fibers were spaced 150 µm apart in the x-direction, and reinforcement fibers were spaced 500 µm apart in the y-direction to increase the number of fibers in a single direction while remaining within the printing limits of the machine. SEM images of noncoated MEW scaffolds revealed aligned fibers in both the x and y directions with varying fiber diameters (**Figure 3.3A**). All fiber measurements are summarized in **Figure B2**. SEM images of lyophilized HA-coated scaffolds demonstrate coating of the HA hydrogel over the entire MEW scaffold, allowing fibers to remain visible (**Figure 3.3B**).

3.4.3 Myoblast Attachment on MEW Scaffolds

C2C12 myoblasts were seeded on top of non-coated, HAcoated, or HA-RGD-coated MEW scaffolds to assess the impact of different coatings on cell attachment and alignment. Following 24 h of proliferation, the cell culture medium was exchanged to low serum medium for 3 days to initiate the early phase of myogenic differentiation through serum starvation. Cells stained with Alexa Fluor™ 647 phalloidin for F-actin filaments and DAPI for cell nuclei revealed an increased presence of cells on the HA-coated and HA-RGD-coated scaffolds compared to the non-coated scaffolds (**Figure 3.4**).

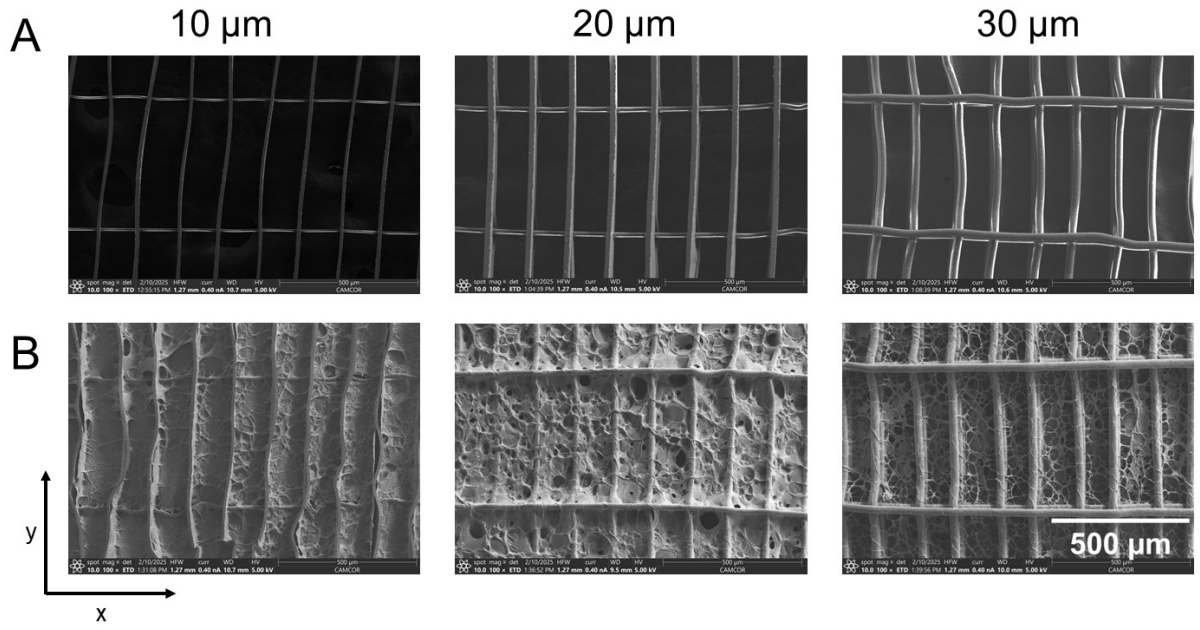

Figure 3.3. SEM images of noncoated and HA-coated MEW scaffolds. A) SEM images of non-coated MEW scaffolds with varying fiber diameters (10, 20, and 30 µm). B) SEM Images of HA-coated MEW scaffolds with varying fiber diameters (10, 20, and 30 µm). Scale bar=500 µm. X and y directions as indicated for fiber measurements.

Cellular attachment was quantified by the number of nuclei, and cell alignment was determined by measuring nuclei directionality. The HA coating significantly increased cell attachment compared to non-coated scaffolds, and the HA-RGD coating further increased cell attachment compared to both HA-coated and non-coated scaffolds for all fiber diameters (**Figure 3.5A**). Interestingly, there was also an effect of fiber diameter on myoblast attachment on HA-RGD-coated scaffolds with scaffolds containing 20 µm fibers having the highest nuclei count compared to scaffolds containing 10 µm and 30 µm fibers. Nuclei did not preferentially align in any direction on the non-coated and HA-coated scaffolds, as indicated by uniform nuclei directionality in all directions ranging from −90° to 90° (**Figure 3.5B–D**). Conversely, nuclei directionality was the highest at 0 degrees along fibers spaced 150 µm apart as intended for anisotropic myoblast alignment on HA-RGD-coated scaffolds containing 10 µm and 30 µm fibers (**Figure 3.5B and D**).

3.4.4 Myotube Formation on MEW Scaffolds

C2C12 myoblasts were differentiated on non-coated, HA-coated, or HA-RGD-coated MEW scaffolds to evaluate the effects of the various coatings on myotube formation. Following 24 h of proliferation, the cell culture medium was exchanged to differentiation medium containing 2% v/v of horse serum for 7 days to promote mature myotube formation through serum starvation. Cells were then fixed and stained for myosin heavy chain (MHC), which is a late myogenic marker for myotubes, and DAPI to visualize the cell nuclei. Confocal imaging revealed an increase in cellular attachment and myotube formation on both HA-coated and HA-RGD-coated scaffolds **(Figure 3.6**).

Similar to results at early time points, nuclei counts revealed increased cell attachment on HA-coated scaffolds compared to non-coated scaffolds for all fiber diameters (**Figure 3.7A**). The HA-RGD coating further increased cellular attachment compared to both non-coated and HA-coated scaffolds for all fiber diameters. HA-RGD-coated scaffolds containing 20 µm fibers demonstrated the highest cellular attachment compared to scaffolds containing 10 µm and 30 µm fibers. Cells cultured on both HA-coated and HA-RGD-coated 10 µm fiber scaffolds also demonstrated increased myotube length compared to non-coated 10 µm fiber scaffolds (**Figure 3.7B**). However, no differences in myotube length were observed between scaffold coatings on 20 µm and 30 µm fiber scaffolds. The directionality of the myotubes in each scaffold was evaluated based on MHC staining. In all cases except non-coated 10 µm fiber scaffolds, increased myotube formation was observed in a single direction along horizontal fibers at 0 degrees regardless of the scaffold coating and fiber diameter (**Figure 3.7C–E**).

Figure 3.4. C2C12 myoblasts attach and align on MEW scaffolds. Immunocytochemistry images of C2C12 myoblasts on MEW scaffolds after four days of attachment. (pink=F-actin, blue=DAPI) Scale bars=250 µm. A) 10 µm non-coated scaffolds, B) 10 µm HA-coated scaffolds, C) 10 µm HA-RGD-coated scaffolds, D) 20 µm non-coated scaffolds, E) 20 µm HA-coated scaffolds, F) 20 µm HA-RGD-coated scaffolds, G 30 µm non-coated scaffolds, H 30 µm HA-coated scaffolds, and I 30 µm HARGD-coated scaffolds.

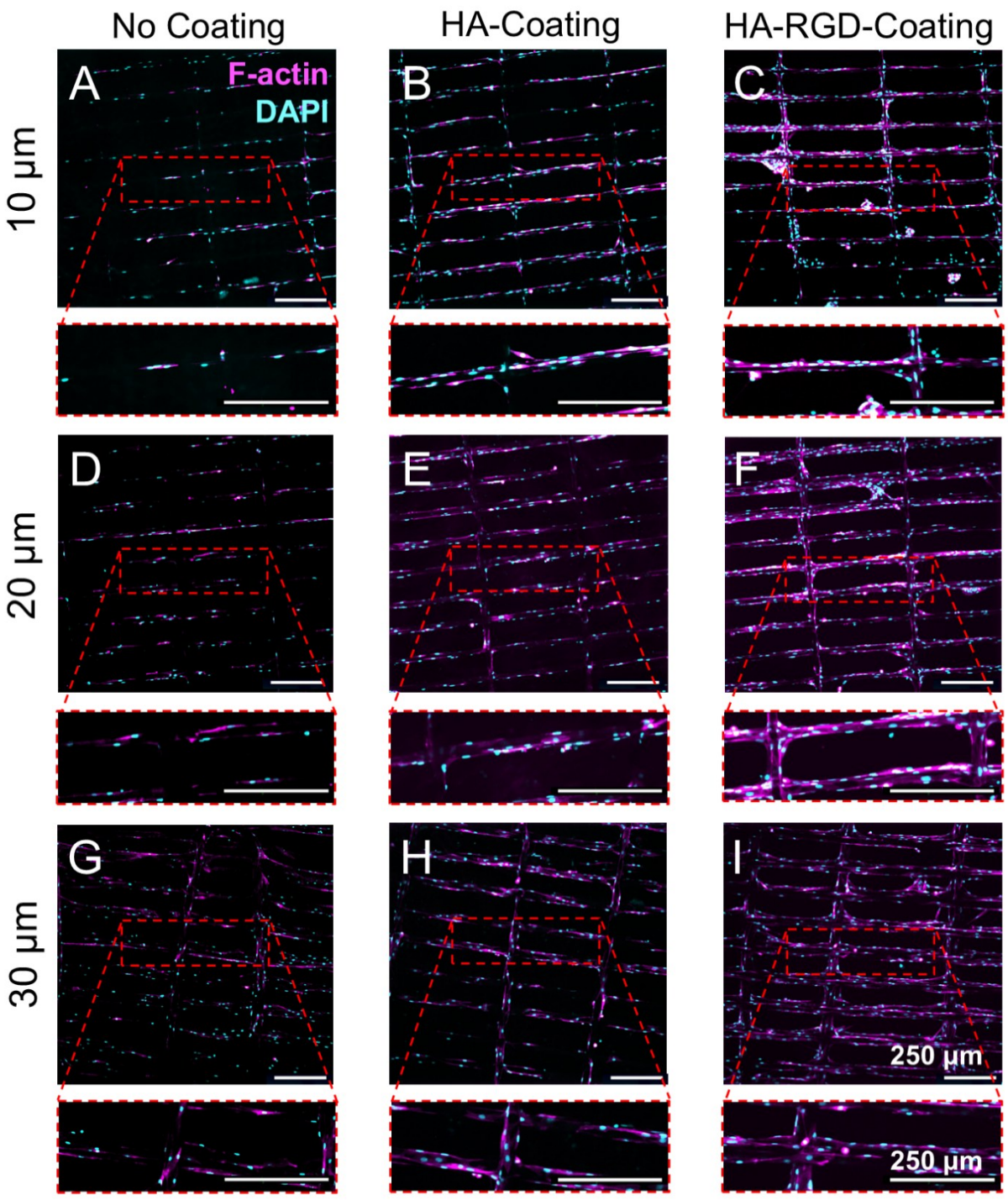
No Coating
HA-Coating
HA-RGD-Coating
10 µm
20 µm
30 µm
A
B
C
D
E
F
G
H
I
F-actin
DAPI
250 µm
250 µm

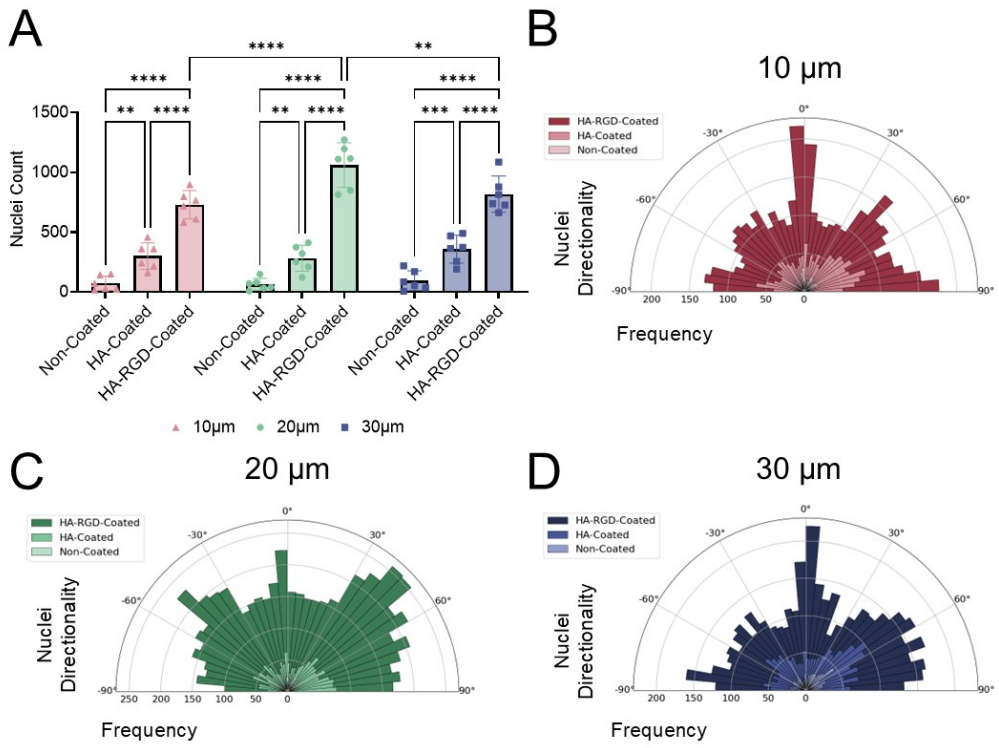

Figure 3.5. HA and HA-RGD-coatings increase myoblast attachment and anisotropic alignment on MEW scaffolds. A) Nuclei count on noncoated, HA-coated, and HA-RGD-coated scaffolds, n=6. (Two-way ANOVA with post-hoc Tukey's multiple comparisons test, *p<0.05, **p<0.01, ****p<0.0001 as indicated) Nuclei directionality on non-coated, HA-coated, and HA-RGD-coated scaffolds with B) 10 µm, C) 20 µm, and D) 30 µm fibers, n=6. For 10 µm fiber scaffolds: non-coated 18-152 nuclei, HA-coated 162-458 nuclei, and HARGD-coated 583-898 nuclei. For 20 µm fiber scaffolds: non-coated 8-150 nuclei, HA-coated 122-412 nuclei, and HA-RGD-coated 815-1273 nuclei. For 30 µm fiber scaffolds: non-coated 8-219 nuclei, HAcoated 193-491 nuclei, and HA-RGD-coated 663-1087 nuclei.

Since HA-RGD-coated scaffolds containing 20 µm fibers displayed higher cellular attachment than 10 and 30 µm scaffolds, we decided to move forward with these scaffolds for further analysis, including scaffold mechanical properties, creatine kinase activity, myogenic gene expression, and alpha-actinin staining to visualize sarcomeres.

3.4.5 Mechanical Properties

Tensile testing was performed on non-coated MEW scaffolds containing 20 µm fibers for comparison to the mechanical properties of native skeletal muscle tissue. Non-coated scaffolds exhibited a stiffness of 0.843 ± 0.219 MPa (**Figure B3**). In comparison, the stiffness of parallel human skeletal muscle fibers has been found to be approximately 0.44 MPa,[173] suggesting that these scaffolds may provide similar mechanical support for myotube formation.

3.4.6 Creatine Kinase Activity

Creatine kinase (CK) is an enzyme that facilitates the reversible transformation of creatine and ATP into phosphocreatine and adenosine diphosphate, which is important for muscle function and regeneration.[174] When myoblasts start differentiating, they stop dividing and enter a final stage of development at which CK levels increase. As myoblasts fuse into myotubes, CK activity reaches its peak, making it a key marker of muscle cell differentiation and maturation.[175,176] CK activity in cell-conditioned media was measured on Day 1, Day 5, and Day 7 of differentiation to assess myogenic differentiation on non-coated, HA-coated, and HA-RGD coated scaffolds, as well as cells cultured on tissue culture plastic (**Figure 3.8**). No differences were observed in CK activity between scaffolds at individual time points. CK activity increased from day 1 to 5 for cells differentiated on HA-RGD coated scaffolds and tissue culture plastic, indicating the formation of myotubes. CK activity then decreased from day 5 to 7 for cells differentiated on HA-coated scaffolds, HA-RGD coated scaffolds, and tissue culture plastic. The subsequent decrease in CK levels may be due to the absence of growth factors that are needed to further promote the survival and maturation of myotubes.[177] Overall, the highest levels of CK activity were observed on day 5. Along with the expression of MHC (**Figure 3.6**), these findings further confirm the formation of myotubes on MEW scaffolds.

Figure 3.6. C2C12 myoblasts form aligned myotubes on MEW scaffolds.

Immunocytochemistry images of C2C12 myoblasts differentiated on MEW scaffolds for 7 days, depicting myosin heavy chain (green) and DAPI (blue). Scale bar=250 µm. A) 10 µm non-coated scaffolds, B) 10 µm HA-coated scaffolds, C) 10 µm HA-RGD-coated scaffolds, D) 20 µm non-coated scaffolds, E) 20 µm HA-coated scaffolds, F 20 µm HA-RGD-coated scaffolds, G 30 µm non-coated scaffolds, H 30 µm HA-coated scaffolds, I 30 µm HA-RGD-coated scaffolds.

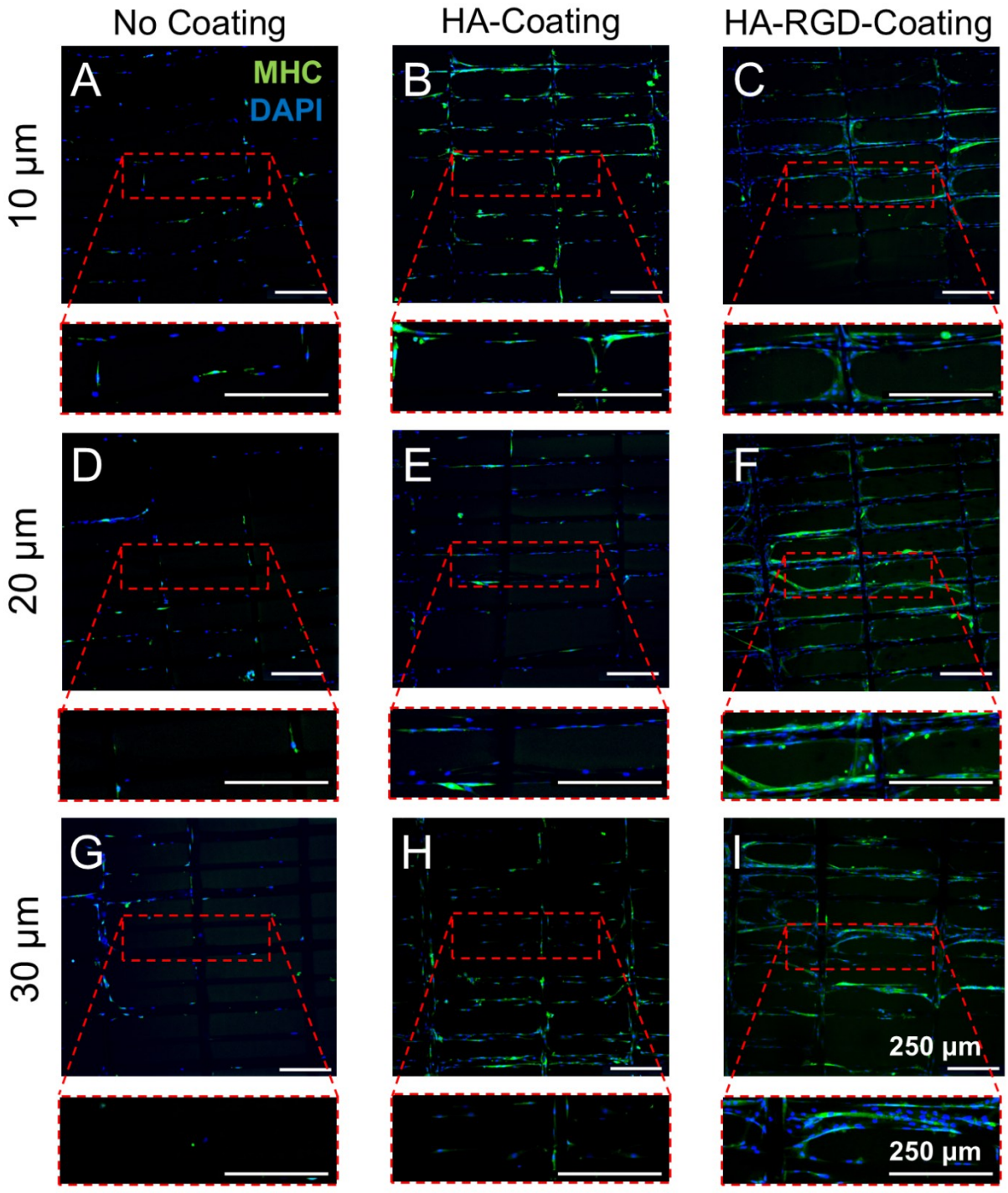
No Coating
HA-Coating
HA-RGD-Coating
10 µm
20 µm
30 µm
A
MHC
DAPI
B
C
D
E
F
G
H
I
250 µm
250 µm

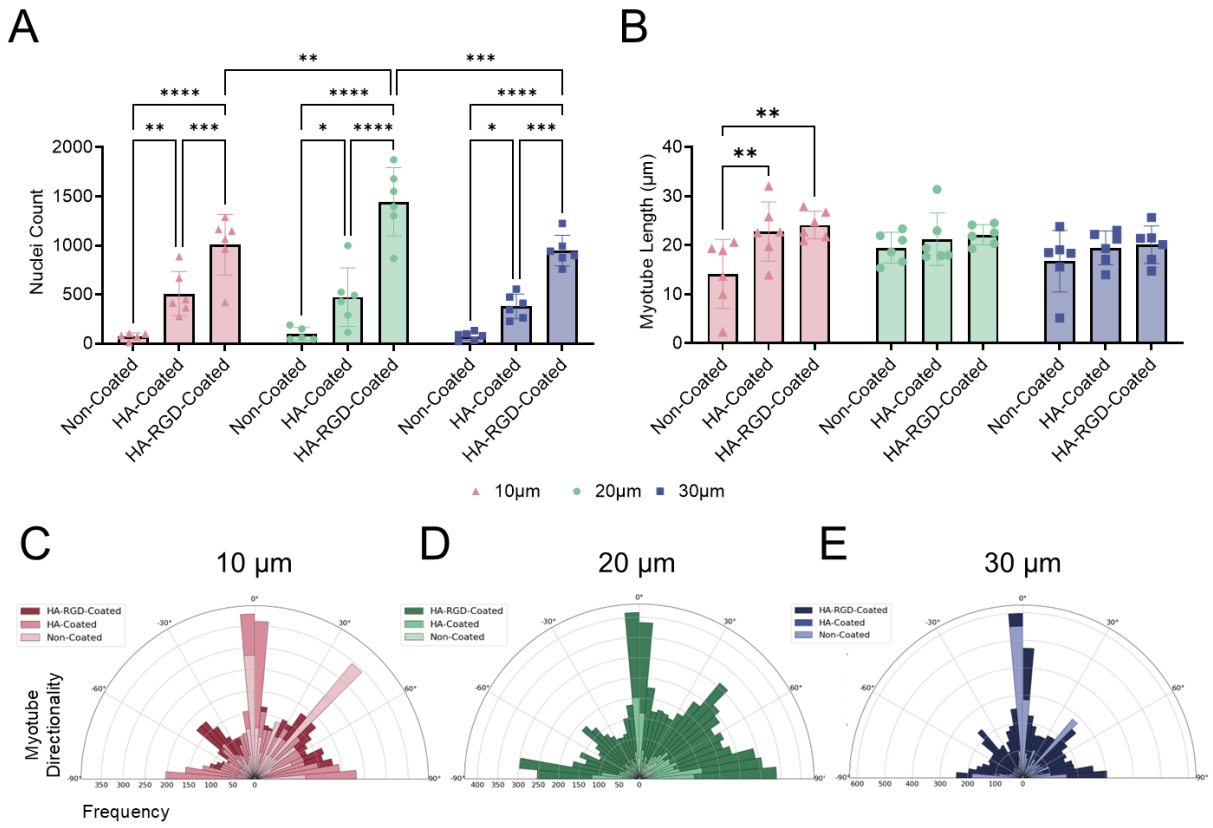

Figure 3.7. MEW scaffolds support anisotropic myotube formation, while HA and HA-RGD coatings increase cellular attachment. A) nuclei count on non-coated, HA-coated, and HA-RGD-coated scaffolds containing 10, 20, and 30 μm diameter fibers, n=6. (Two-way ANOVA with post-hoc Tukey's multiple comparisons test, *p<0.05, **p<0.01, ***p<0.001, ****p<0.0001 as indicated). B) Myotube length on non-coated, HA-coated, and HA-RGD-coated scaffolds containing 10, 20, and 30 μm diameter fibers, n=6. (Two-way ANOVA with post-hoc Tukey's multiple comparisons test, **p<0.01 as indicated) Myotube directionality for non-coated, HA-coated, and HA-RGD-coated scaffolds containing C) 10 μm, D) 20 μm, and E) 30 μm diameter fibers, n=6. For 10 μm fiber scaffolds: non-coated 50-2006 myotubes, HA-coated 301-1933 myotubes, and HA-RGD-coated 470-1386 myotubes. For 20 μm fiber scaffolds: non-coated 107-243 myotubes, HA-coated 194-670 myotubes, and HA-RGD-coated 658-2094 myotubes. For 30 μm fiber scaffolds: non-coated 102-2577 myotubes, HA-coated 179-596 myotubes, and HA-RGD-coated 464-4120 myotubes

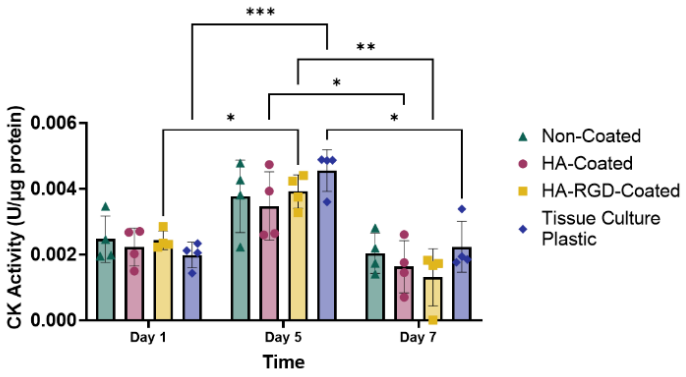

Figure 3.8. Creative kinase (CK) activity of myoblasts during differentiation. CK activity of C2C12 myoblasts differentiated on 20 µm fiber MEW scaffolds and tissue culture plastic after 1, 5, and 7 days of differentiation, n=4. (Two-way ANOVA posthoc Tukey's multiple comparisons test, *p<0.001)

3.4.7 Myogenic Gene Expression

Quantitative reverse transcription polymerase chain reaction (RT-qPCR) was performed on C2C12 myoblasts differentiated for 5 days on non-coated, HA-coated, and HA-RGD coated 20 µm fiber scaffolds as well as tissue culture plastic and compared to undifferentiated myoblasts to determine the effects of substrate and coating on myogenic gene expression (**Figure B4**). Expression of the myogenic genes Pax3, Pax7 MyoD, Myf5, and MyoG was evaluated and compared to GAPDH as the housekeeping gene.[178] The expression of Pax3 suppresses myogenic differentiation;[179] as expected, Pax3 gene expression was decreased in all groups compared to undifferentiated cells (**Figure B4A**). Pax7, MyoD, and Myf5 are myogenic genes that are expressed in the early stages of myoblast differentiation[180,181] and were increased in all groups compared to undifferentiated cells (**Figure B4B–D**). MyoD expression was significantly increased in cells grown on HA-coated scaffolds compared to HA-RGD-coated scaffolds, suggesting that HA-coated scaffolds may further support myotube formation. Interestingly, MyoG, which is typically expressed at later stages of myogenic differentiation,[182] was also increased in all groups compared to undifferentiated myoblasts, with cells grown on HA-coated scaffolds expressing significantly more MyoG than cells grown on non-coated scaffolds, potentially indicating further progression of myogenic differentiation (**Figure B4E**).

3.4.8 Sarcomere Staining

Alpha-actinin staining was performed to visualize sarcomere striations after 7 days of differentiation to characterize the maturity of the myotubes (**Figure 3.9**). While some striations were present in cells grown on the 20 µm HA-coated scaffold (**Figure 3.9B**) and MHC-expressing cells were observed on all scaffolds, the lack of striations in cells grown on both the non-coated (**Figure 3.9A**) and HA-RGD coated scaffolds (**Figure 3.9C**) suggest that these myotubes have not fully matured.

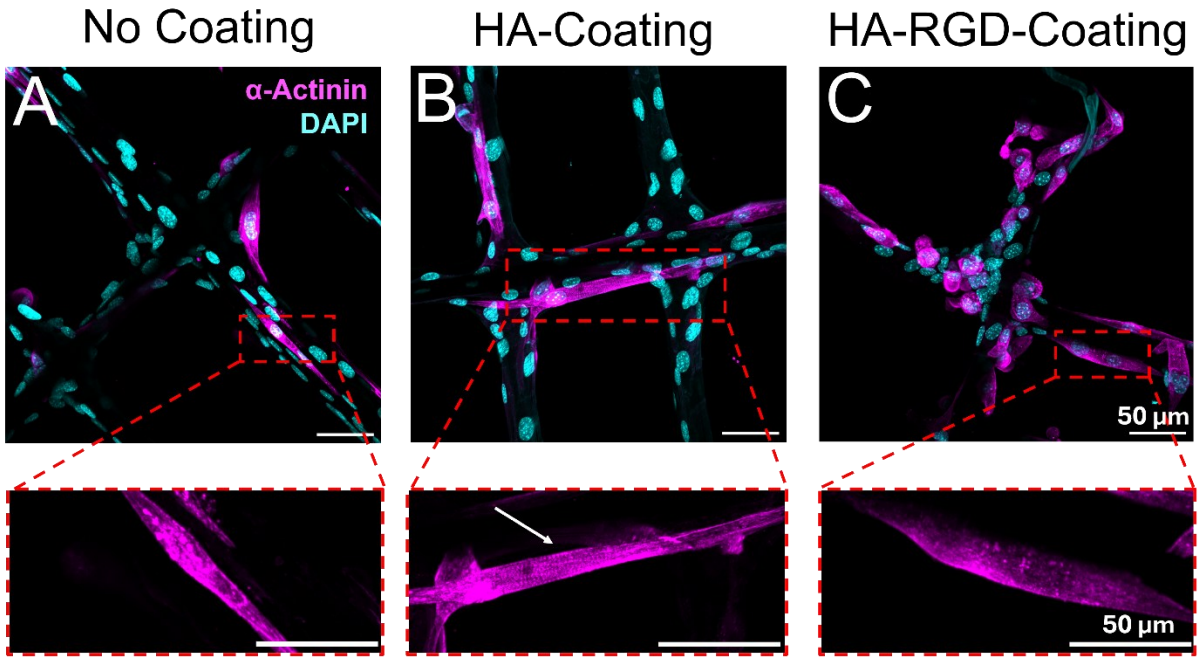

Figure 3.9. Alpha-actinin staining reveals presence of myotubes containing striations on HA-coated MEW scaffolds. Immunocytochemistry images of C2C12 myoblasts differentiated on 20 µm MEW scaffolds for 7 days, depicting alpha-actinin (pink) and DAPI (blue). Scale bar=50 µm. A) non-coated scaffold, B) HA-coated scaffold with white arrow pointing to striations, C) HA-RGD-coated scaffold

3.5 Discussion

Composite materials containing both hydrogels and fiber-based scaffolds provide an opportunity to combine the advantages of the cell-supportive microenvironment of hydrogels with the alignment properties of fiber scaffolds. With their precisely aligned fibers, MEW scaffolds have great potential for directing cellular alignment for the repair of skeletal muscle tissue. Compared to electrospinning, a more commonly studied fiber-based printing technique in

tissue engineering, MEW presents a finely tunable approach for exploring the effects of different fiber thickness and deposition geometries on anisotropic cell alignment.[164] In this study, we harnessed the precision of MEW to fabricate scaffolds containing three different fiber diameters to study the effect of fiber diameter on myoblast alignment and myotube formation. We observed that 20 μm diameter fibers were preferred over 10 and 30 μm fiber diameters, which we hypothesize may be due to the similar size of the 20 μm diameter fibers to C2C12 myotubes, which range from 5 to 25 μm.[183,184] MEW scaffolds made from PCL microfibers without proteins or cell-adhesive peptides have a limited ability to support myoblast attachment and differentiation themselves, revealing the shortcomings of synthetic polymer fiber-based scaffolds for muscle tissue engineering compared to scaffolds derived from natural ECM-based materials. For instance, Tan *et al*. demonstrated that the biophysical cues of an aligned type I collagen scaffold promoted a myogenic response that was dependent on the fibril size, porosity, and stiffness of the scaffold, further emphasizing the importance of considering ECM composition when directing cellular behavior with ECM-based scaffolds.[153] However, while the cellular microenvironment provided by ECM-based scaffolds is amendable to myoblast differentiation, such scaffolds have a limited ability for tuning their physical properties without negatively impacting their biological activity and scaffold integrity. Moreover, it can be challenging to fabricate natural fiber scaffolds with the same precision provided by synthetic fiber scaffolds that can be fabricated using MEW.

We demonstrated that the cell microenvironment created by our MEW scaffolds could be significantly enhanced with the addition of a naturally-derived polymer matrix and ECM-derived cell-adhesive peptide. Our work highlights the value of combining biochemical cues with aligned fiber-based scaffolds to enhance material-cell interactions and provide a more supportive environment for cell growth. In previous work, we have demonstrated that our hydrazone-crosslinked HA hydrogel has a tunable gelation time, low swelling ratio, and stability over 28 days *in vitro*, making it an ideal hydrogel for creating a stable coating on MEW microfiber scaffolds.[165] MEW scaffolds combined with HA and HA-RGD coatings exhibited increased myoblast attachment, myoblast alignment, and myotube formation compared to non-coated scaffolds, likely due to increased interactions between the cells, biopolymer, and cell-adhesive ligands.[166]

Our HA hydrogel has the additional advantage of being functionalized through orthogonal chemistry with norbornene functional groups for the bioconjugation of peptides and proteins. The effects of the HA coating on the MEW scaffolds were further enhanced with the addition of RGD peptides, which increased myoblast attachment and alignment, and accelerated myotube formation. Our findings confirm results from previous studies, in which a similar concentration of RGD increased muscle satellite cell survival and differentiation in PEG-MAL hydrogels compared to the laminin-derived peptides YIGSR and C16.[162] However, in other studies, the laminin-derived peptide IKVAV increased cell attachment and migration in PEG-DA-HA hydrogels compared to RGD.[139] The presence of ECM peptides in HA hydrogels may also be important for myotube formation since the polyanionic surface of crosslinked HA hydrogels has been shown to decrease cell attachment.[139,185] However, in our studies, we did not observe any limitations in cellular attachment on HA-coated scaffolds, which performed better in this regard than non-coated scaffolds. These positive cell attachment results may be due to the physical cues from the PCL fibers guiding cellular alignment and the viscoelastic properties of HA hydrazone-crosslinked hydrogels allowing for cell migration through the biomaterial. Regardless, HA-RGD-coated scaffolds significantly increased myoblast attachment, myoblast alignment, and myotube formation, although there were no differences in myotube length compared to HA-coated scaffolds.

Gene expression analysis revealed increased expression of early (Pax7, MyoD, Myf5) and late (MyoG) myogenic markers in myoblasts differentiated on all scaffolds and on tissue culture plastic, suggesting these cells were at an intermediate stage of differentiation. The presence of MHC staining on all scaffolds further indicated robust myotube formation. However, we only observed some muscle striations on HA-coated scaffolds and not on the other scaffolds, suggesting that the myotubes on our scaffolds were not fully mature. We believe the lack of mature myotubes in our system may be due to the absence of exogenous growth factors, such as insulin-like growth factor 1 (IGF-1), basic fibroblast growth factor (bFGF), and epidermal growth factor (EGF), that may be necessary to promote further myogenic differentiation.[186–189] The controlled release of growth factors, including IGF-1 and bFGF, has shown to promote muscle satellite cell proliferation and differentiation *in vitro* and improve volumetric muscle loss and fibrosis in vivo in a murine VML model.[190]

As MEW technology advances, we will continue to improve the scaffold design to optimize muscle healing outcomes. Minimizing the need for reinforcement fibers and increasing the number of fibers in a single direction will improve anisotropic myotube alignment, potentially enhancing muscle tissue repair. Furthermore, expanding on materials beyond PCL, such as PCL polypyrrole (PPy) or poly(3,4-ethylenedioxythiophene) (PEDOT) composite materials that have electroconductive properties, can further enhance muscle tissue repair, as it has been shown that electroconductive materials can activate cellular signaling related to proliferation and differentiation in electrically active tissues such as muscle [134,191,192]. In addition, it would be motivating to investigate the effects of additional biochemical cues on myoblast attachment, alignment, and differentiation through the conjugation of other peptides and proteins to the HA backbone via the versatile norbornene functional group.[51,52,165]

Although there are limitations in the use of immortalized C2C12 myoblasts compared to primary myoblasts, including their ability to mimic the *in vivo* environment,[193] we were able to use this cell line to investigate preliminary cellular behavior on HA-coated scaffolds, motivating future work to evaluate the effects of HA-coated scaffolds on primary muscle cell culture *in vitro*. In the future, we plan to evaluate HA-coated scaffolds as a muscle tissue repair patch *in vivo* in a rodent model of VML in the quadriceps,[194,195] which will provide further insight into the ability of this scaffold to repair muscle in a complex multicellular environment. Lastly, exploring the impact of the sustained delivery of growth factors, including IGF-1 and bFGF to promote myotube formation and maturation, may further enhance the utility of this scaffold in muscle tissue engineering applications.[165,190]

3.6 Conclusion

Our HA-coated MEW microfiber scaffolds present a unique combination of biophysical and biochemical cues to enhance the attachment, alignment, and differentiation of skeletal myoblasts. The novelty of this work lies in the integration of MEW scaffolds with HA hydrogels, combining the benefits of both fiber-based scaffolds and natural ECM-based hydrogels. MEW scaffolds provide the structural framework for anisotropic cell alignment, while HA-RGD hydrogels offer the biochemical cues necessary for cell adhesion, alignment, and differentiation, allowing for enhanced cell-cell and cell-matrix interactions, which are essential for myogenic differentiation. While fully mature myotubes were not achieved with the use of our composite

biomaterial, the main advantage of HA-coated and HA-RGD-coated MEW scaffolds lies in their ability to dramatically increase myoblast attachment and alignment, paving the way for future incorporation of growth factors and other cues to further enhance mature myotube formation and support eventual applications for functional muscle tissue formation.

3.7 Bridging Paragraph

We developed HA-coated scaffolds that can support myoblast attachment, alignment, and differentiation for muscle tissue repair. Although we observed that these scaffolds can enhance cellular attachment and guide cellular alignment, we found that this platform can benefit from the addition of growth factors or electroconductive materials to better support myotube maturation. The next chapter reviews biomaterials used to modulate neuroinflammation in neural tissue repair, focusing on nanoparticles, hydrogels, implantable scaffolds, and neural probe coatings. Understanding the pathways involved in neuroinflammation and the recent advances in biomaterials approaches is key to their design and development. Because the succeeding chapters will use HA hydrazone crosslinked hydrogels for neural tissue engineering, the next chapter was critical for their inspiration and design.

CHAPTER 4

BIOMATERIAL STRATEGIES FOR REGULATING THE NEUROINFLAMMATORY RESPONSE

From Alycia N. Galindo, David A. Frey Rubio, and Marian H. Hettiaratchi. Biomaterial strategies for regulating the neuroinflammatory response. Materials Advances 5 (10), 4025-4054 (2024). *This manuscript is under the terms of the Creative Commons Attribution-NonCommercial 3.0 Unported License (CC BY-NC 3.0).*

4.1 Abstract

Injury and disease in the central nervous system (CNS) can result in a dysregulated inflammatory environment that inhibits the repair of functional tissue. Biomaterials present a promising approach to tackle this complex inhibitory environment and modulate the mechanisms involved in neuroinflammation to halt the progression of secondary injury and promote the repair of functional tissue. In this review, we will cover recent advances in biomaterial strategies, including nanoparticles, hydrogels, implantable scaffolds, and neural probe coatings, that have been used to modulate the innate immune response to injury and disease within the CNS. The stages of inflammation following CNS injury and the main inflammatory contributors involved in common neurodegenerative diseases will be discussed, as understanding the inflammatory response to injury and disease is critical for identifying therapeutic targets and designing effective biomaterial-based treatment strategies. Biomaterials and novel composites will then be discussed with an emphasis on strategies that deliver immunomodulatory agents or utilize cell–material interactions to modulate inflammation and promote functional tissue repair. We will explore the application of these biomaterial-based strategies in the context of nanoparticle- and hydrogel-mediated delivery of small molecule drugs and therapeutic proteins to inflamed nervous tissue, implantation of hydrogels and scaffolds to modulate immune cell behavior and guide axon elongation, and neural probe coatings to mitigate glial scarring and enhance signaling at the tissue–device interface. Finally, we will present a future outlook on the growing role of biomaterial-based strategies for immunomodulation in regenerative medicine and neuroengineering applications in the CNS.

4.2 Graphical Abstract

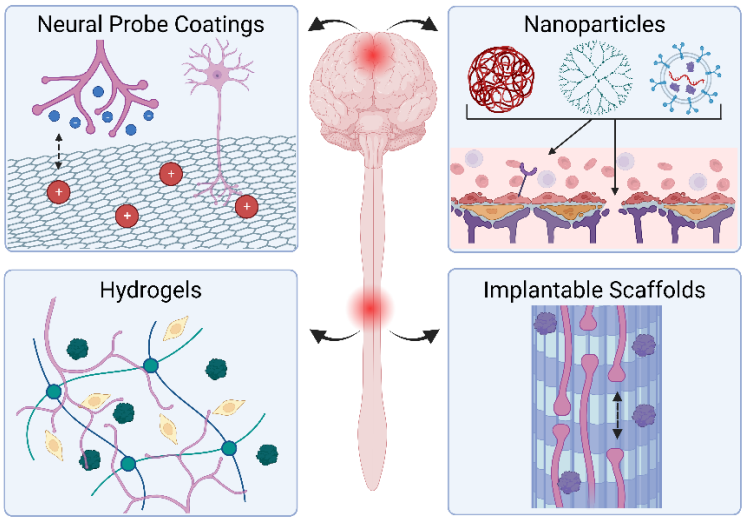

4.3 Introduction

Neuroinflammation is a process through which the central and peripheral nervous systems combat pathogens, remove extracellular debris, and respond to tissue damage to maintain tissue homeostasis. However, if left unresolved, neuroinflammation will negatively affect neuronal health and result in chronic tissue damage and subsequent loss of function. Consequently, dysregulated neuroinflammation has been identified as a hallmark of many neurodegenerative conditions, including traumatic injury and neurodegenerative disorders such as Alzheimer's disease and multiple sclerosis. Injury to the central nervous system (CNS) can occur from motor vehicle accidents, sports, and falls. Globally, there are 27 million individuals who are currently living with a disability following spinal cord injury (SCI) and approximately 50 million individuals who are affected by a traumatic brain injury (TBI) every year.[196–199] Additionally, approximately 15% of the worldwide population is estimated to be currently suffering from some form of neurodegenerative disease with an associated annual cost of approximately $655 billion in the United States alone in 2020.[200,201] With an aging global population on the horizon, the prevalence of neuroinflammatory diseases is expected to increase, requiring more research efforts in these areas than ever before.[202,203]

Since the 1960s, there have been 1200–3000 clinical studies investigating treatments for neuroinflammatory diseases. Combinations of anti-inflammatory drugs,[204–206] antioxidants,[207–209] corticosteroids,[210,211] exercise,[212–214] and tailored diets[215–219] have been implemented with limited

long-term success. While these strategies can help manage disease symptoms, they fail to fully resolve inflammation within the CNS. Our understanding of neuroinflammation is evolving, opening numerous opportunities for new treatment strategies. For example, microglia and astrocytes are critical mediators of neuroinflammation and are the target of many new therapeutics to treat dysregulated immune responses. Biomaterial-based treatment strategies are emerging as a novel approach to address neuroinflammation. Biomaterial-based delivery vehicles such as nanoparticles and hydrogels have shown promise in delivering drugs, proteins, and cells across the intact blood-brain barrier (BBB). Nanoparticles delivered intravenously can extend systemic drug circulation, increasing the likelihood of a therapeutic crossing the BBB and enhancing delivery of therapeutics to target cells in the CNS.[220] Conversely, hydrogels are more commonly delivered directly to the site of interest in the CNS for local drug, protein, or cell delivery.[221–224] Both hydrogels and nanoparticles can be functionalized with targeting ligands to promote localization within specific environments and modulate cell behavior;[225] however, while nanoparticles excel in systemic drug delivery and blood-brain barrier penetration, hydrogels must be locally administered and are thus better suited to treating focal CNS injuries.[221,226] Similarly, bioactive cues can be incorporated into tissue engineered scaffolds to guide neural axon elongation, while various surface coatings have been applied on neural probes to enhance neuron signal recording and stimulation at the tissue–device interface.[227–229] In this review, we will discuss recent advances in the development of biomaterial strategies for addressing neuroinflammation with a focus on nanoparticles, hydrogels, implantable scaffolds, and neural probe coatings.

4.4 Background

4.4.1 Resident Cells of the Central Nervous System

CNS parenchymal tissue is composed of an intricate combination of glycosaminoglycans (e.g., hyaluronic acid), proteoglycans, and glycoproteins (e.g., fibronectin, laminin), but has notably fewer fibrous proteins than muscle or bone (**Figure 4.1**).[230–232] This network of extracellular matrix (ECM) molecules provides latching points for neurons to extend and connect to other cells, modulates neural plasticity, and regulates axon regeneration.[233] Within this matrix lies a diverse population of support cells called glia, including oligodendrocyte progenitor cells, radial glia, ependymal cells, microglia, oligodendrocytes, and astrocytes. Together, these cells

maintain tissue homeostasis by supporting neuron maturation, axon myelination, and nutrient transport, structuring the ECM, and initiating an immune response to foreign bodies such as pathogens, neurotoxins, and implants.[234,235]

Microglia are specialized macrophages that serve as the primary innate immune cell population within the CNS (**Table 4.1**). In healthy tissue, microglia exist in a ‘‘resting’’ state in which their cytoskeletal protrusions interact with other cells and monitor changes to the local environment.[236] Perturbations to parenchymal tissue caused by injury or disease activate microglia, causing alterations in their gene expression and adoption of an amoeboid-like morphology.[237,238] Depending on signals perceived in the surrounding environment, stimulated microglia will transition to either a classically activated (M1) or alternatively activated (M2) state, similar to that of macrophages. While M1/M2 nomenclature is typically used to distinguish between pro- and anti-inflammatory phenotypes, respectively, recent studies have shown this system fails to capture the full spectrum of microglial phenotypes.[239–241] Collectively, microglia resolve homeostatic disturbances by initiating and orchestrating the inflammatory response, phagocytosing cellular debris, and regulating glial cell behavior.

Astrocytes are another type of glial cell that make up a large portion of CNS tissue and work in conjunction with microglia to quickly respond to physiological stimuli and pathological perturbations to maintain tissue homeostasis (**Table 4.1**). Under healthy conditions, astrocytes interact with neurons and other glia via connexin-based gap junctions.[242] These interactions establish large-scale glial networks that regulate neural signal transmission and facilitate nutrient transport. Oligodendrocytes are also included in this network, through which they provide neurotrophic support, deliver metabolites, and myelinate neuronal axons.[243] Furthermore, astrocytes can interact with microvessels in the CNS to help maintain endothelial tight junctions within the BBB and blood-spinal cord barrier (BSCB).[244] When astrocytes are activated, they undergo significant functional and morphological changes and are typically denoted as A1 and A2 astrocytes, mirroring the widely used macrophage/microglia nomenclature system.

4.4.2 The Role of Peripheral Immune Cells in Maintaining Tissue Homeostasis

CNS parenchyma is segregated from the rest of the body by a series of meningeal layers and the BBB/BSCB. The BBB and BSCB are comprised of tightly packed endothelial cells and protect nervous tissue from many circulating pathogens and neurotoxins.[245] Along these tissue borders lie meningeal compartments and perivascular spaces from which bone marrow-derived

immune cells can remain in immunological surveillance. This peripheral niche contains several innate and adaptive immune cell populations such as border-associated macrophages (BAMs), dendritic cells, natural killer cells (NKs), T cells, B cells, and neutrophils.[246] These cell populations communicate with barrier tissue cells through a series of neurotransmitters, neuropeptides, and cytokines.[247] While neurons and glia are the primary residents of CNS parenchyma, recent studies have elaborated on a more active role of peripheral immune cells in maintaining CNS parenchymal homeostasis. Following the onset of injury, the BBB is disrupted, allowing for peripheral immune cell infiltration and inflammatory signaling.[248] Innate immune cells can activate glia and facilitate a local tissue response; however, their prolonged presence can be detrimental and is a hallmark of several neurodegenerative diseases characterized by a dysregulated immune response.[249–252] Preventing further infiltration of immune cells and managing the inflammatory response is critical for preventing irreparable tissue damage.

4.4.3 The Inflammatory Response to Central Nervous System Injury

Trauma to CNS parenchymal tissue by SCI or TBI initiates the death of neurons through apoptosis and necrosis, disrupts the protective BBB/BSCB, and allows peripheral immune cells to infiltrate. Within the damaged tissue environment, local glia and infiltrating immune cells become activated and work together to stabilize the injury site, clear debris, and initiate the healing cascade. While this activity is critical for tissue repair, it can also lead to secondary tissue damage that can prevent timely resolution of neuroinflammation. The inflammatory response to CNS injury is typically broken down into three stages of inflammation, which are each characterized by different time scales, immune cell infiltration rates, protein signaling, and tissue remodeling (**Figure 4.2**). The acute inflammatory phase lasts hours to days after injury, followed by the subacute inflammatory phase which lasts up to weeks after injury, and lastly, the chronic inflammatory phase which can last months to years, depending on the severity of the injury. Understanding the cellular and molecular processes that occur throughout each stage of the inflammatory response to CNS injury is critical for designing effective biomaterial-based interventions.

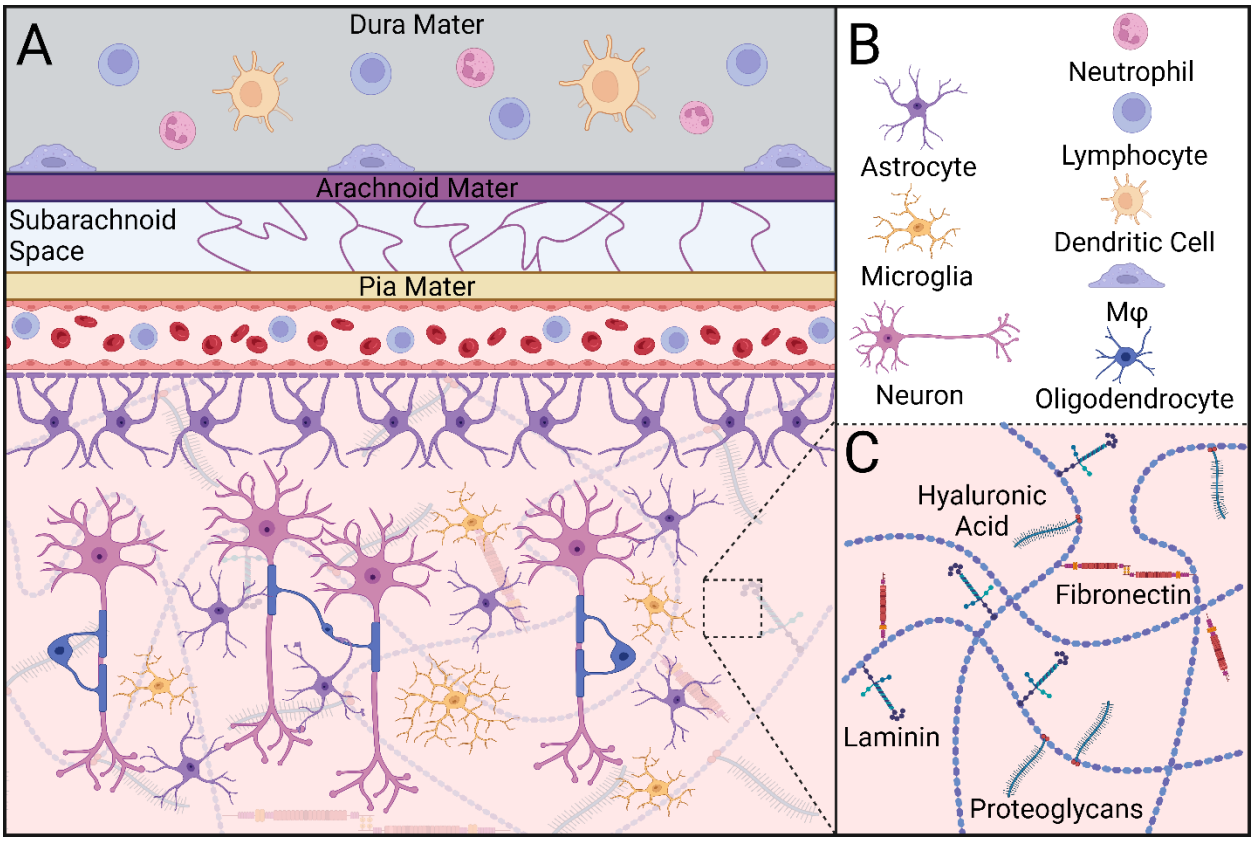

Figure 4.1. Composition of central nervous system parenchymal tissue during homeostasis. A) Peripheral immune cells such as lymphocytes, neutrophils, dendritic cells, and border-associated macrophages (Mφ) reside in the dura mater, contributing to immune surveillance. Astrocytes wrap around neurovasculature, contributing to the integrity and selectivity of the BBB. Astrocytes also facilitate metabolite transport to neighboring glia and neurons. During homeostasis, microglia remain in a branched state, surveying the environment for pathogens, DAMPs, and protein aggregates. Oligodendrocytes myelinate axons and facilitate metabolite transport alongside astrocytes. B) Different cell types present in CNS tissue. C) The extracellular matrix in the CNS primarily consists of hyaluronic acid, fibronectin, laminin, and proteoglycans.

Table 4.1. Role of glial cells in neuroinflammation.

Cell Type	Role in Neuroinflammation
Microglia	• Surveillance for pathogen- and damage-associated molecular patterns • Remove cellular debris and protein aggregates • Facilitate neuronal repair and maturation
M1-like Microglia	• Activate local glia via release of pro-inflammatory cytokines • Release of oxygen and nitrogen reactive species • Facilitate immune cell recruitment through chemokine secretion
M2-like Microglia	• Remove cellular debris and protein aggregates • Neural tissue remodeling • Resolve inflammation • Promote neurogenesis, angiogenesis, and oligodendrogenesis
Astrocyte	• Regulate nutrient transport to neurons • Maintain blood-brain barrier selective permeability • Modulate neuron synapse plasticity • Build the neural extracellular matrix
A1-like Astrocyte	• Produce chondroitin sulfate proteoglycans • Release of oxygen and nitrogen reactive species • Release of pro-inflammatory cytokines
A2-like Astrocyte	• Release of neuroprotective factors • Resolution of inflammation • Produce chondroitin sulfate proteoglycans
Oligodendrocyte	• Myelinate neuronal axons • Regulate nutrient transport to neurons • Antigen presentation & T cell activation • Regulate microglia activation and peripheral immune cell recruitment • Release of neuroprotective factors

4.4.3.1 Acute Inflammation (Hours After Injury)

Immediately after traumatic injury to the brain or spinal cord, several events occur that result in the activation of resident glial cells and a rapid influx of peripheral immune cells. Ischemia, edema, and glutamate excitotoxicity begin within the first few hours after injury and initiate local chemokine production to recruit immune cells to the site of injury.[253] Small endogenous molecules called damage-associated molecular patterns (DAMPs) are released by damaged and dying cells into the extracellular space. DAMPs activate resident glia and recruit peripheral immune cells, contributing to secondary inflammation, additional tissue damage, and the production of cytokines, inducible nitric oxide synthase (iNOS), and matrix metalloproteinases (MMPs). Cytokines such as interleukin-33 (IL-33), IL-1β, and tumor necrosis factor-a (TNF-α) have all been reported to be released within the first 3 hours after injury.[253] IL-33 is an alarmin that is released from damaged oligodendrocytes, causing a cascade of chemokine production from resident astrocytes and microglia that results in the recruitment of neutrophils and monocytes.[254–256] iNOS is an enzyme that is produced by infiltrating and activated immune cells and catalyzes the production of nitric oxide, causing neuronal apoptosis. MMPs are peptidases that are produced by neurons, glia, and endothelial cells and degrade the ECM to foster tissue remodeling and reestablish tissue homeostasis. After injury, excess MMP production can cause damage to blood vessels in the perivascular basement membrane.[213,256–258] The accumulation of reactive oxygen species (ROS) triggers oxidative stress and disturbs tight junction proteins in the BBB/BSCB, providing an avenue for immune cells to infiltrate. While peripheral immune cells from surrounding tissues infiltrate through the disrupted BBB/BSCB, resident cells including oligodendrocytes, microglia, and astrocytes are activated and continuously release inflammatory signals including cytokines, chemokines, secondary messengers, and ROS.[259] Microglia can be activated by cell debris and circulating inflammatory signals to produce inflammatory proteins such as TNF-α, IL-1β, IL-6, and iNOS.[259,260] Elevation of such proteins has been detected 6 to 10 hours after injury and peaks within the first day. These cytokines establish a pro-inflammatory environment, resulting in further apoptosis of neurons and glial cells that peaks approximately 8 and 24 hours after injury, respectively. The overall extent of the injury contributes to the amount of proinflammatory signals released from injured neural cells, dictating the magnitude of the inflammatory response and secondary tissue damage

that occurs. The severity and duration of BBB disruption varies across different pathological conditions and magnitude of trauma. Following injury, defects across the BBB can be large enough to allow entry of circulating serum proteins such as albumin (~67 kDa).[261] During traumatic brain injury, the BBB remains permeable to larger molecular weight proteins (>10 kDa) during the acute phase (<5 hours), while smaller molecules (0.3–10 kDa) may continue to transverse the BBB for several days post-injury.[262] Enhanced BBB permeability is usually localized to the site of injury, allowing for the entry of larger therapeutics within an early time frame following the injury.[262]

The first peripheral immune cells to arrive at the site of injury are neutrophils, which arrive as early as 4 hours and peak 6 to 12 hours after injury.[256] Neutrophils release TNF-α, ROS, antimicrobial peptides (AMPs), elastase, and neutrophil extracellular traps (NETs), which cause neuronal cytotoxicity and vascular leakage.[256] NETs trap and kill bacteria, but also degrade BBB/BSCB tissue, further compromising its integrity and contributing to the infiltration of additional peripheral immune cells.[263] Monocytes are the second and most abundant type of peripheral immune cells that arrive at the site of injury and are first detected within 24 hours after injury.[264] Monocytes begin to differentiate at the site of injury into macrophages. Depending on their phenotype, macrophages can play a dual role in early inflammation. The accumulation of M1 macrophages around the lesion increases the production of iNOS, ROS, pro-inflammatory cytokines, and free radicals, resulting in increased neuronal apoptosis.[256] Conversely, M2 macrophages phagocytose myelin debris, produce growth factors, and release anti-inflammatory cytokines. The timing of macrophage infiltration and the composition of their extracellular environment influence their differentiation to either an M1 or M2 phenotype.[253,256] Microglia can similarly aid in resolving inflammation by expressing anti-inflammatory cytokines such as transforming growth factor-β1 (TGF-β1) and IL-10.[253] Many researchers identify IL-10 as an anti-inflammatory cytokine that can halt the production of TNF-α and IL-6; however, IL-10 can also be considered as a pro-inflammatory cytokine that promotes the production of pro-inflammatory cytokines such as interferon-gamma (IFN-γ) from surrounding cells.[265]

Both astrocytes and microglia are activated within 24 hours after injury and are continuously activated in the first few days following injury. Activated microglia and macrophages are difficult to distinguish because they have similar phenotypes and functions. However, cell surface markers such as ionized calcium binding adaptor molecule 1 ($Iba1^+$),

$CD206^+$, $CD11b^+$, and $CD45^{low/high}$ can be used to distinguish microglia and macrophages; low expression of CD45 is indicative of microglia, while high expression of CD45 is indicative of macrophages.[266,267] Both macrophages and microglia phagocytose cell debris, which is critical for maintaining tissue homeostasis and promoting tissue repair. Astrocytes and endothelial cells have also been reported to participate in phagocytosing cell debris after CNS injury. Myelin debris contains Nogo-A, myelin-associated glycoprotein (MAG), and ephrin B3, which can induce expression of TNF-α and IL-1β; thus, myelin clearance and subsequent removal of these signals is critical for the resolution of neuroinflammation. The prolonged presence of myelin debris can change the phenotype of macrophages to ‘‘foamy’’ or lipid-laden macrophages, leading to immune cell migration and decreased phagocytosis.[256] A1 activated astrocytes are induced by inflammatory signals released from M1 activated microglia, such as TNF-α, IL-1β, and component 1 subcomponent q (C1q).[268] The presence of A1 astrocytes can lead to further secretion of inflammatory signals, such as IL-1β, TNF-α, IL-6, ROS, and lipocalin-2.[269,270] Conversely, A2 activated astrocytes can promote neuronal survival and tissue repair through the secretion of anti-inflammatory cytokines and neuroprotective growth factors, such as brain-derived neurotrophic factor (BDNF), glial-derived neurotrophic factor (GDNF), fibroblast growth factor-2 (FGF-2), and TGF-β.[271–273]

4.4.3.2 Sub-Acute Inflammation (Days to Weeks After Injury)

The sub-acute phase of inflammation in the CNS occurs in the first few days to weeks following injury and, if left unchecked, can result in the extension of tissue damage beyond the initial injury. Expression of the pro-inflammatory cytokines IL-1β, TNF-α, and IL-6 begins to decrease between 2 to 7 days after injury while anti-inflammatory cytokines IL-10 and TGF-β begin to increase 3 to 7 days after injury.[253] In some cases, levels of pro-inflammatory cytokines have been reported to return to baseline around 14 days after injury.[253,260] Within 7 to 10 days after the initial injury, astrocytes proliferate quickly around the lesion to begin forming the glial scar. The glial scar separates the damaged tissue from healthy tissue and protects surrounding neurons from the spread of inflammatory signals. Formation of the glial scar is commonly detected by the presence of glial fibrillary acidic protein (GFAP), which is expressed by astrocytes.[274] Additionally, chondroitin sulfate proteoglycans (CSPGs) are deposited in and around the injury site by activated astrocytes and function as a major growth-inhibitory component of the glial scar.[275] While the glial scar protects neurons from the spread of

inflammatory signals, it also prevents neurons from proliferating and extending axons through the injury site, resulting in limited tissue regeneration.[274,276] Several cell types form the glial scar. This includes reactive astrocytes and microglia that make up the outer barrier, cells such as ependymal cells, fibroblasts, and pericytes line the inner edges of the scar and interact with reactive astrocytes, and macrophages, neutrophils, and stromal cells that fill the core.[199,235,275,277]

Neutrophils continue to be present within the injury site up to 2 to 3 days after injury, while the proliferation of other peripheral immune cells such as monocytes peaks slightly later, at 4 to 7 days after injury.[264] Resident immune cell and astrocyte activation peaks 3 to 7 days after injury.[256] The resolution of inflammation and polarization of macrophages and microglia to M2 phenotypes varies depending on the extent of initial tissue damage and subsequent ischemia. Microglia and macrophages can display both M1 and M2 phenotypic markers throughout the stages of inflammation. Interestingly, in a mouse TBI model, transient M2 microglia first peaked 7 days after injury before differentiating into an M1 phenotype, which peaked 21 to 28 days after injury.[260,278] Microglia and astrocytes typically exhibit a low rate of proliferation in healthy tissue but have been reported to proliferate up to months after injury, with populations starting to gradually decline again approximately two weeks after injury.[260,274,275]

4.4.3.3 Chronic Inflammation (Months to Years After Injury)

A large percentage of individuals who experience a CNS injury develop chronic inflammation that can last several years after injury. In these cases, myelin debris clearance is insufficient after glial scar formation, resulting in the accumulation of ‘‘foamy’’ macrophages and decreased phagocytosis. The accumulation of myelin associated molecules such as Nogo-A and MAG results in neuron retraction and poor axonal regeneration in the tissue adjacent to the injury site. Astrocytes transition into scar-forming astrocytes, and DAMPs remain in the injury environment during the sub-acute and chronic inflammatory phases.[199] The glial scar matures weeks to months after injury, during which tissue remodeling and restoration of the BBB/BSCB occurs. Elevated expression of a variety of proinflammatory cytokines have also been reported in the later stages of inflammation after TBI and SCI. Deposition of collagen I, fibronectin, and additional ECM components by pericytes, resident immune cells, and stromal cells results in the formation of dense fibrotic tissue that may not be functional.[199] The chronic inflammation stage can last years after injury, and the overall mechanisms that result in the secondary progression of neurodegeneration are largely unknown. However, autopsies and positron emission tomography

(PET) scans have been used to characterize the chronic inflammatory response in the brain and spinal cord for individuals who have lived years after severe CNS injury. For instance, activated microglia have been found in individuals affected by TBI multiple years after the initial injury.[260,279] Additionally, SCI and TBI have been associated with progressive neurodegenerative diseases such as Wallerian degeneration and chronic traumatic inflammatory encephalopathy, respectively. TBI has also been linked to dementia, and many patients experience chronic inflammation in the brain after SCI, indicated by elevated TNF-α levels in the brain and accompanied by symptoms similar to TBI.[260,279]

4.4.3.4 Resolution of Inflammation

Although neuroinflammation may be viewed as a negative contributor to injury progression, it is essential for the repair of tissue. The orchestrated infiltration and activation of immune cells and their release of key cytokines are critical to resolving inflammation. The presence of cytokines such as IL-4 or IL-13 can polarize cells including resident glia and peripheral immune cells to their pro-regenerative phenotype. These cells clear cellular debris, protein aggregates, and toxic inflammatory molecules, which is a critical step in the resolution of inflammation. In ideal cases, the increased presence of these immune cells and the release of anti-inflammatory cytokines such as IL-10 and TGF-β can counteract pro-inflammatory molecules to resolve neuroinflammation. An increased presence of proregenerative immune cells is more likely to overcome the inflammatory milieu and return to homeostatic levels of immune cells and cytokines. However, in cases where neuroinflammation does not resolve itself, there is often a shift towards pro-inflammatory cells and molecules, resulting in chronic inflammation that is challenging to resolve. Furthermore, the formation of the glial scar and the production of inhibitory molecules such as CSPGs can inhibit the conversion of immune cells to their pro-regenerative phenotypes, preventing the resolution of inflammation.[280]

4.4.4 Neuroinflammation During Disease

Aggregation of pathological proteins such as amyloid-β and α-synuclein can promote microglial reactivity.[281,282] Prolonged activity of reactive astrocytes and microglia has been identified as a hallmark of several neurodegenerative diseases, including stroke, multiple sclerosis, Alzheimer's disease, and Parkinson's disease.[283] The BBB/BCSB prevents the delivery of numerous therapeutic drugs and biomolecules that could be valuable in treating these conditions. Biomaterials can provide a means to circumvent the BBB/BSCB and deliver therapeutics to the site of injury or disease to modulate neuroinflammation. The underlying mechanisms that are involved in each neuroinflammatory condition are summarized here to understand emerging targets for treating inflammation associated with these diseases.

Figure 4.2. **The stages of the inflammatory response to injury in the central nervous system.** The inflammatory response in the CNS can be broken down into the acute inflammatory phase, which lasts hours to days, the sub-acute inflammatory phase, which lasts days to weeks, and chronic inflammatory stage, which lasts months to years. A) The CNS tissue environment after injury includes an abundance of neurons, glia, and other immune cells as well as a variety of pro- and anti-inflammatory molecules that change throughout the various stages of inflammation. B) Relative abundance of various immune cells during the stages of inflammation. C) Relative abundance of pro- and anti-inflammatory cytokines, growth factors, and other biomolecules during the stages of inflammation. Abbreviations: M1 (classically activated macrophages/microglia), M2 (alternatively activated macrophages/microglia), A1 (activated astrocytes), Glu (glutamate), iNOS (inducible nitric oxide synthase), DAMPs (damage-associated molecular patterns), MMPs (matrix metalloproteinases), IL-6 (interleukin-6), TNF-α (tumor necrosis factor-α), IL-1β (interleukin-1β), IL-4 (interleukin-4), IL-10 (interleukin-10), IL-33 (interleukin-33), transforming growth factor-β (TGF-β), CSPGs (chondroitin sulfate proteoglycans).

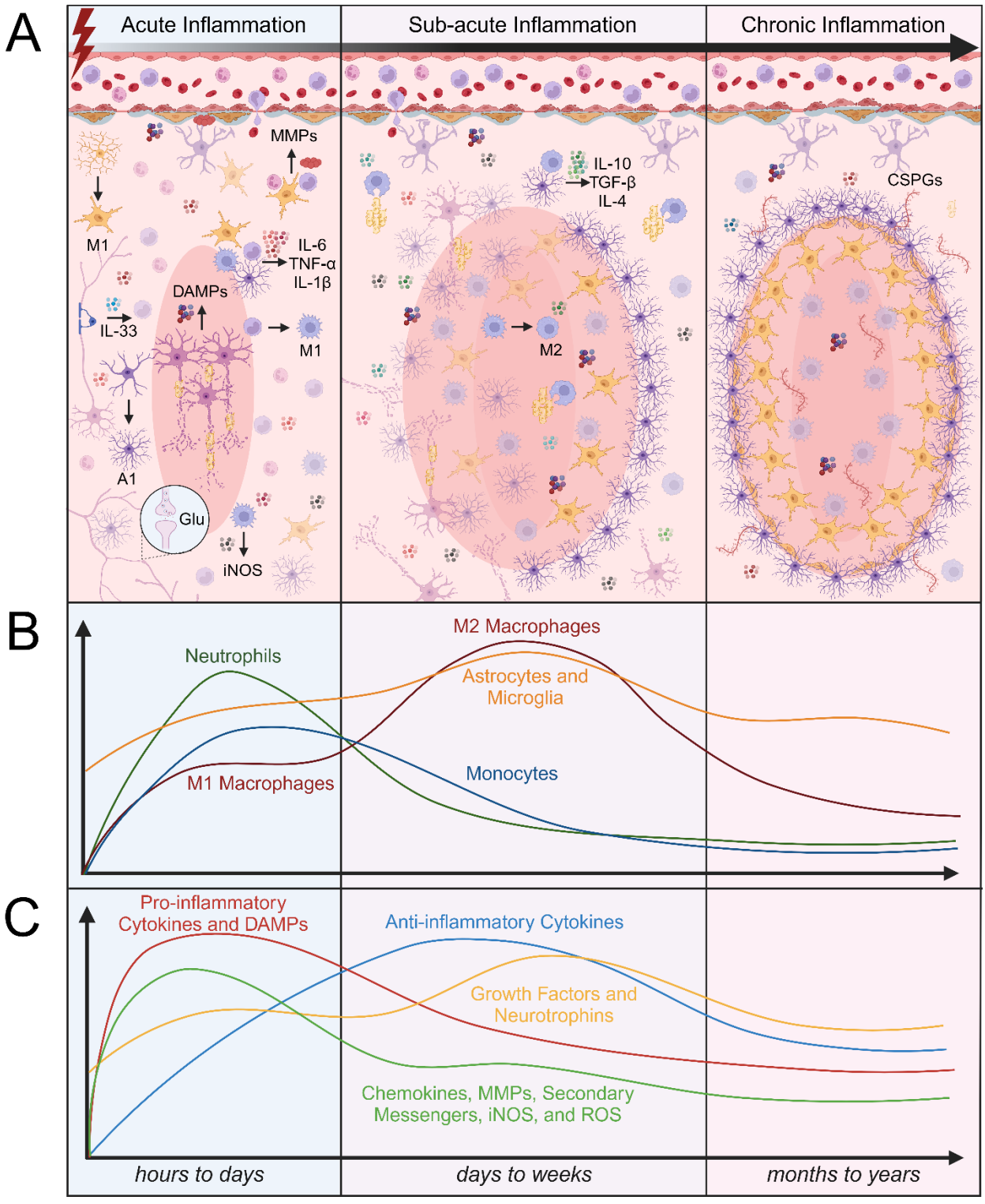
A
Acute Inflammation
Sub-acute Inflammation
Chronic Inflammation
MMPs
M1
IL-6
TNF-α
IL-1β
DAMPs
IL-33
M1
A1
Glu
iNOS
IL-10
TGF-β
IL-4
M2
CSPGs
B
Neutrophils
M2 Macrophages
Astrocytes and Microglia
M1 Macrophages
Monocytes
C
Pro-inflammatory Cytokines and DAMPs
Anti-inflammatory Cytokines
Growth Factors and Neurotrophins
Chemokines, MMPs, Secondary Messengers, iNOS, and ROS
hours to days
days to weeks
months to years

4.4.4.1 Stroke

Stroke is the third leading cause of death worldwide, with the majority of strokes caused by blood vessel occlusion and a subsequent ischemic event.[284] Although stroke is commonly recognized as a disorder of the blood vessels, the interactions between vascular cells and neural cells, such as neurons and glia, are also an important consideration. Following stroke, activated astrocytes and microglia compromise the integrity of the BBB by producing inflammatory molecules such as DAMPs, ROS, iNOS, MMPs, and pro-inflammatory cytokines. These inflammatory molecules damage glia and endothelial cells, increasing BBB permeability.[285,286] MMPs further disrupt the BBB by breaking down tight junction proteins within it. The BBB is a critical barrier that maintains homeostatic levels of immune cells within the CNS tissue, and its disruption facilitates an increase in peripheral immune cell infiltration.[245,287] The extent of BBB damage depends on the severity of injury and magnitude of subsequent inflammatory events.[288] Microglia are localized centrally within the stroke lesion, and astrocytes are located in and around the lesion.[289] Like other cases of neuroinflammation, resident and peripheral immune cells can also resolve inflammation and promote tissue repair by phagocytosing debris, producing anti-inflammatory cytokines, and promoting angiogenesis.[284] The severity of the stroke and the degree of BBB damage significantly contribute to the inflammatory response and secondary tissue damage after stroke. Restoration of the BBB allows for the reduction of infiltrating pro-inflammatory cells, creating a favorable environment for subsequent tissue repair.[290] Therefore, a large focus of stroke treatments includes accelerating the restoration of the BBB and promoting the production of growth factors to repair damaged tissue.

4.4.4.2 Multiple Sclerosis

Multiple sclerosis (MS) is a chronic inflammatory disease that is characterized by demyelination, neurodegeneration, and gliosis in the CNS.[291] Many researchers have considered MS to be an autoimmune disease in which immune cells infiltrate and attack healthy tissue, causing lesions; however, the exact mechanisms of MS remain unknown. The adaptive and innate immune systems synergistically contribute to chronic neuroinflammation in MS. The most common form of MS is relapsing-remitting multiple sclerosis (RRMS), in which inflammatory attacks on neural tissue continually recur. Macrophages typically reside within lesion sites long-term, while microglia populations only increase during the active phases of RRMS.[292] Circulating monocytes infiltrate and differentiate into M1 or M2 macrophage phenotypes.

Identification of macrophage phenotypes is valuable for understanding the mechanisms of MS since different phenotypes progress the disease differently.[292,293] Monocytes release IL-6, IL-10, IL-12, and TNF-α with the highest levels of IL-6 and IL-12 expression found in untreated MS patients.[292] M1 microglia and macrophages express pro-inflammatory cytokines and enhance the adaptive immune response by expressing major histocompatibility complex class II (MHCII), which is a requisite for antigen presentation, ultimately leading to a toxic inflammatory environment.[294] Dying and demyelinated neurons produce large quantities of myelin debris in MS patients.[295] Residual myelin debris increases inflammation and is commonly considered a hurdle in MS treatment. Shifting innate immune cells to their alternatively activated phenotypes to resolve inflammation and promote phagocytosis is necessary for the treatment of MS.

4.4.4.3 Glioblastoma

Gliomas are solid mass tumors arising from the dysregulated activity of glial cells. Glioblastomas are a subtype of highly aggressive gliomas that account for approximately 50% of all malignant tumors in the CNS.[296] The tumor microenvironment consists of an intricate mixture of brain tumor cells, tumor-associated macrophages (TAMs), astrocytes, neurons, T cells, NK cells, and neutrophils.[297] Genetic alterations and metabolic adaptations of the cancer cells promote activation of TAMs, shifting them to an immunosuppressive M2 phenotype described as ‘‘pro-tumor.’’[298,299] The secretion of cytokines such as IL-6, IL-10, and TGF-β inhibits immune effector cells, upregulates immunosuppressive T regulatory cells, and promotes tumor vascularization.[300–302] Ameliorating glioblastoma-associated immunosuppression is necessary for restoring the innate and adaptive immune response. Radiotherapy and chemotherapy are the standard treatment for glioblastoma, but tumor location and off-target side effects pose challenges to this approach.[303,304] Thus, treatment strategies that promote pro-inflammatory, anti-cancer activity in tumor-associated immune cells are currently being explored as an alternative treatment strategy for glioblastoma.

4.4.4.4 Cerebral Palsy

Cerebral palsy is a clinically heterogenous collection of movement disorders arising from neurological dysfunction in the developing brain.[305] Neuroinflammation has been identified as a major contributor to the progression of cerebral palsy. Trauma and/or infection within the uterine environment during fetal development results in a release of DAMPs and alarmins, activating

innate immune cells through the ‘‘Fetal Inflammatory Response Syndrome.’’[306] Excessive inflammatory signaling within the CNS increases glial and immune cell proliferation, the release of proinflammatory cytokines (IL-1β, IL-6, TNF-α, IL-8), and subsequent cell death.[307–309]

4.4.4.5 Parkinson's Disease

Parkinson's disease is characterized by the degeneration of dopaminergic neurons and the appearance of motor abnormalities, such as tremors, bradykinesia, rigidity, and postural instability.[310] M1 activated microglia play a significant role in Parkinson's disease by increasing the expression of pro-inflammatory cytokines including IL-6 and TNF-α, resulting in the death of dopaminergic neurons, prolonged inflammation, and further degeneration of neural tissue. Microglia have also been reported to release exosomes containing aggregated a-synuclein proteins, which act as a potent chemoattractant of additional immune cells and induce neuronal apoptosis.[282] A1 activated astrocyte populations are also elevated in Parkinson's disease, further increasing expression of IL-6 and TNF-α, intercellular adhesion molecule 1 (ICAM1), and ROS in the disease environment. Given the key role of neuroinflammation in Parkinson's disease, therapeutics that reduce the expression of pro-inflammatory cytokines from activated glial cells and work to resolve inflammation are of particular interest.[310]

4.5 Biomaterials for Modulating Neuroinflammation

New insights into the underlying mechanisms of neuroinflammation have prompted the design of novel biomaterials to mitigate the detrimental effects of excessive inflammation and protect surrounding CNS tissue from secondary damage. Recent advances have been made in a variety of biomaterial strategies for modulating neuroinflammation, including nanoparticles with the ability to cross the selectively permeable BBB/ BSCB,[311–313] hydrogels that enable controlled delivery of immunomodulatory therapeutics,[314,315] implantable scaffolds with biophysical cues to enhance cellular alignment and promote a growth-permissive environment for neural regeneration,[316–320] and biomaterial coatings to prolong the lifetime of neural probe implants.[227,321–323]

4.5.1 Nanoparticles

The delivery of small molecules, proteins, lipids, and nucleic acids has been explored for modulating neuroinflammation. These therapeutic agents may be presented to a patient in either a powdered or liquid phase and may be administered through several routes (intravenous,

inhalation, orally, etc.). Once absorbed, these agents pass into systemic circulation until they penetrate a tissue or are cleared by circulating phagocytes.[324] The first challenge arises with determining the optimal dose of the drug. Due to short drug half-lives and rapid clearance by the reticuloendothelial system, systemic delivery of therapeutics often results in a low concentration of the drug reaching the target tissue. To overcome this challenge, higher therapeutic doses are typically used, but often result in cytotoxicity and off-target effects. For systemic delivery of therapeutics to the CNS, nanoparticles must bypass the BBB/BSCB before entering parenchymal tissue. This is considered a major obstacle in the field as the highly selective permeability of these barrier tissues makes entry of drugs very difficult. To address these concerns, nanoparticle-based delivery systems have been developed to extend drug half-life and improve their accumulation in target tissues. Nanoparticles can bypass the BBB/BSCB via transcytosis pathways and gaps in disrupted BBB/BSCB tissue (**Figure 4.3**).[325] Factors such as zeta potential, surface functionalization, and size determine the pathway of a nanoparticle to the CNS, and thus are important to consider when designing nanoscale delivery vehicles.[326,327] Previous studies have shown that particles with a diameter less than 100 nm are more easily transported across the BBB via transcytosis pathways.[328,329] Their nanoscale size (1–100 nm) also enhances tissue penetration as the extracellular space within the brain contains a large range of void spaces (40–700 nm) through which the nanoparticles must transverse before reaching the desired location.[328,330,331] Similarly, microparticles have been used to deliver drugs systemically; however, the larger size of microparticles (2–2000 μm) can reduce their ability to cross the BBB and travel through neural tissue, given the size constraints of the extracellular space.[332] Thus, nanoparticles will be our primary focus for systemic delivery of therapeutics to the CNS.

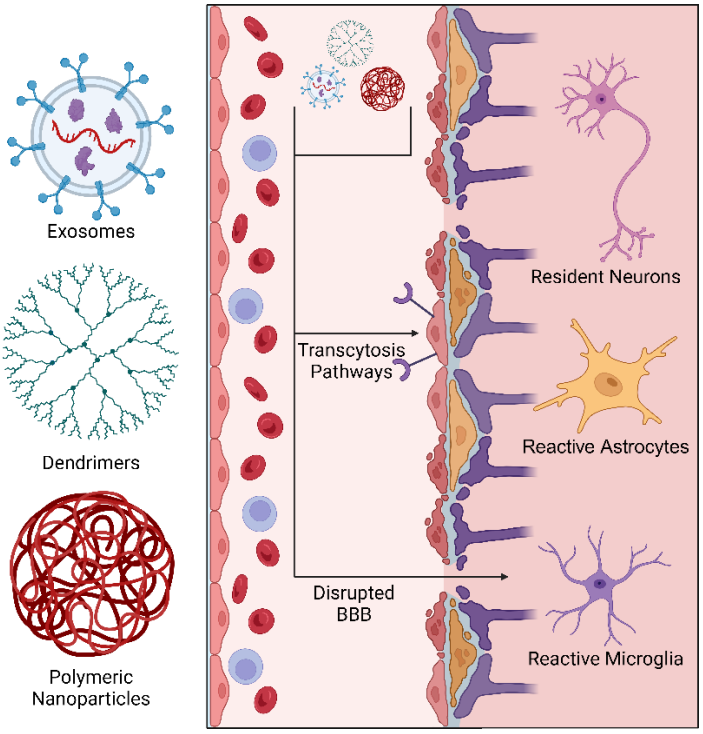

Figure 4.3. Nanoparticle-based delivery vehicles and their transport mechanisms through CNS tissue. Nanoparticle delivery vehicles such as exosomes, dendrimers, and polymeric nanoparticles enhance drug delivery across the blood-brain barrier. Nanoparticles may enter the CNS through gaps in the disrupted BBB or via ‘‘facilitated transport’’ pathways, such as carrier-, adsorptive-, and receptor-mediated transcytosis.

4.5.1.1 Exosomes

Exosomes are nanoscale vesicles released from the outer membrane of cells that facilitate both paracrine and autocrine signaling.[333] The payload within these vehicles consists of a diverse collection of proteins, lipids, and nucleic acids that can alter the recipient cell’s behavior towards therapeutic or pathological outcomes.[334,335] Exosomes have gained traction in recent years as a potential alternative to cell-based therapies as they make it possible to deliver bioactive molecules in a cell-free manner, bypassing concerns related to cell transplantation, including cell viability, potency, and tumorgenicity. Of equal interest are the membrane markers found on these extracellular vesicles. These surface receptors can facilitate vehicle homing to specific cells and tissues, while displaying low immunogenicity, making them ideal candidates for the targeted delivery of therapeutics.[336]

The general process for manufacturing exosomes consists of three steps: (1) culturing exosome-producing cells (days to weeks), (2) harvesting cell-conditioned media, and (3) several rounds filtration and centrifugation to separate exosomes from cells, debris, and microvesicles. Once isolated, exosome pellets can be reconstituted and stored for later use.[318,337–339] The compositions of exosomes are tied to environmental stimuli affecting the secreting cell, which means that exosome composition and release can be primed for specific therapeutic purposes using a variety of conditions. Liu and colleagues demonstrated that culturing bone marrow-derived mesenchymal stem/stromal cells (MSCs) under hypoxic conditions prompted the increased release of exosomes containing a greater quantity of therapeutic microRNAs. Hypoxia-induced MSC-derived exosomes were found to be preferentially uptaken by microglia *in vitro* and shifted microglia polarization towards an M2 phenotype both *in vitro* and in a mouse SCI model.[340] MSCs have also been stimulated with IFNγ to improve the immunomodulatory capabilities of their exosomes. Exosomes derived from IFNγ-stimulated MSCs have been shown to polarize microglia towards an $Iba1^+$ $CD206^+$ M2 phenotype and inhibit expression of proteins associated with pyroptosis, a highly inflammatory form of programmed cell death.[335] IFNγ-stimulated MSC-derived exosomes were systemically delivered in an experimental autoimmune encephalomyelitis mouse model, which mimics the symptoms of MS. Delivered exosomes reduced infiltration of $Iba1^+$ microglia and macrophages and shifted the cells to a branched morphology that is consistent with microglia in a resting state in healthy mice.[341]

While microglia and infiltrating macrophages have been the primary target for many treatment strategies that seek to ameliorate neuroinflammation, astrocytes have been increasingly implicated in the inflammatory response and have been the focus of several recent studies. MSC-derived exosomes delivered intraventricularly in mice reduced TNF-α and IL-1β expression in lipopolysaccharide-stimulated primary hippocampal astrocytes.[338] Exosomes can also be derived from astrocytes themselves. For instance, astrocyte-derived exosomes were found to push microglia towards an M2 state by inhibiting the NF-κB signaling pathway.[334] Combining strategies that target both reactive microglia and astrocytes simultaneously may synergistically work to resolve neuroinflammation by prompting the shift of multiple reactive glial cell types towards M2/A2 phenotypes.[334]

4.5.1.2 Dendrimers

Dendrimers are nanoparticles with branched polymer chains that are radially oriented around a symmetric core. The branched structure of dendrimers results in the creation of internal cavities within the nanoparticles, allowing for non-covalent physical entrapment of hydrophobic drugs and their protection from the external environment until reaching their target destination.[342–345] Dendrimers can also be functionalized with drugs,[346–349] imaging agents,[348,350,351] and targeting moieties[348,352] via covalent attachment, making them effective drug carriers that can be engineered to release their payload in response to target environment stimuli. Dendrimers can both extend drug bioavailability and facilitate the transport of cargo across the disrupted BBB.[353] Generation-4 hydroxyl-terminated polyamidoamine (G4-OH-PAMAM) dendrimers have been studied for resolving neuroinflammation as they preferentially target activated microglia.[354,355] Colocalization of OH-PAMAM dendrimers in reactive microglia is primarily mediated through endocytosis, pinocytosis, caveolae, and aquaporin channels.[356] One such approach focused on inhibiting glutamate carboxypeptidase II (GCPII), a membrane-bound metallopeptidase that is a major contributor to increased extracellular glutamate. Upregulation of GCPII has been observed in activated microglia, contributing to glutamate-mediated excitotoxicity and glial cell dysfunction.[357] GCPII inhibitors show potential for regulating neuroinflammation; however, poor bioavailability and tissue penetration hinder this strategy. To overcome this challenge, Zhang and colleagues conjugated 2-(3-Mercaptopropyl) pentanedioic acid, a GCPII inhibitor, to G4-OH-PAMAM dendrimers. They observed improved therapeutic delivery to damaged brain parenchymal tissue with the use of the dendrimers following intravenous delivery in a rabbit cerebral palsy model. Damage severity was positively correlated with greater therapeutic homing and glial cell uptake, resulting in enhanced TGF-b signaling and transition of activated microglia to a ramified state.[313] Other GCPII inhibitors such as 2-(phosphonomethyl)-pentanedioic acid have also been conjugated to dendrimers and achieved similar results in MS and cerebral palsy models.[312,358]

Dendrimer platforms have been used for the delivery of antiinflammatory drugs. Triamcinolone acetonide is an antiinflammatory agent that has been delivered intravitreally for clinical treatment of diabetic retinopathy; however, this drug can be cytotoxic and expedite cataract formation.[359] Conjugation of triamcinolone acetonide to G4-OH-PAMAM dendrimers resulted in its selective delivery to activated microglia ($CD11b^{+}$, $CD45^{low}$) in the eye and

inhibited the NF-κB pathway.[311] Similarly, G4-OH-PAMAM dendrimers improved the delivery of sinomenine to activated microglia in a rabbit TBI model.[360] Significant changes were observed in the expression of TNF-α, IL-10, and IL-1β; however, sinomenine did not affect the secretion of IL-6, IL-4, and TGF-β1.

Dendrimers can also be engineered to induce anti-tumor behavior in TAMs. Triptolide is a STAT3 inhibitor with promising anti-cancer properties that are overshadowed by its poor aqueous solubility and potential for systemic toxicity. Conjugation of triptolide to G4-OH-PAMAM dendrimers increased its water solubility by 500-fold.[361] Triptolide release was triggered in the glioblastoma microenvironment by the pH- and esterase-sensitive nature of the conjugating linker. This delivery platform not only facilitated targeted delivery of triptolide to TAMs, but also reduced overall off-target activity as indicated by lower levels of markers associated with hepatic toxicity.[361]

Dendrimer size was found to be a major factor contributing to how long the nanoparticles remained in circulation and distributed within tumor tissue.[362] One group found that G6- OH-PAMAM dendrimers exhibited a 10-fold higher accumulation within tumor tissue after 24 hours and 2–3 fold higher tumor specificity compared to a generation-4 dendrimers. These nanoparticles were approximately 6.7 nm in diameter, which is small enough to penetrate the BBB around the tumor (<20 nm) yet large enough to avoid glomerular filtration and subsequent renal clearance (>6 nm).[362] This was further explored by conjugating N-acetyl-L-cysteine to a G6-OH-PAMAM dendrimer.[363] N-Acetyl-L-cysteine is known for its anti-inflammatory and anti-oxidant properties, yet suffers from non-specific binding to circulating plasma proteins and low accumulation in the CNS. For these reasons, systemic delivery of N-acetyl-L-cysteine could greatly benefit from nanoparticle strategies. In this study, dendrimer-mediated delivery of N-acetyl-L-cysteine was localized to M1 microglia and promoted their return to a quiescent state. This decrease in the proinflammatory microglia population improved motor score and survival rate in a rabbit cerebral palsy model. Collectively, these studies highlight dendrimers as versatile platforms capable of enhancing the bioavailability of loaded drugs, diffusing across the extracellular space, and colocalizing with reactive glia.

4.5.1.3 Polymeric nanoparticles

Polymeric nanoparticles can be fabricated from a wide variety of synthetic and natural polymer combinations, such as poly(ethylene glycol) (PEG), poly(lactic-co-glycolic acid)

(PLGA), poly(caprolactone) (PCL), chitosan, and alginate.[364–366] They can be tuned to degrade at different rates, modified with target-specific ligands,[367] and made responsive to environmental stimuli, such as proteases, ROS, and pH.[368–370] Polymeric nanoparticles typically possess a high drug loading capacity and can protect their cargo from the harsh environment of the body until it reaches the site of interest, both increasing drug bioavailability and reducing the dose required to make a drug effective. The ability of polymeric nanoparticles to shield their cargo makes them ideal candidates for transporting therapeutics across the BBB, motivating their growing application towards addressing neuroinflammation.

Nanoparticles that can cross the BBB and accumulate in astrocytes have been synthesized from a biodegradable block copolymer consisting of PLGA and PEG functionalized with a terminal lipophilic triphenylphosphonium cation.[371] These nanoparticles were loaded with antioxidant and anti-inflammatory agents and then delivered intravenously, resulting in a decrease in ROS from reactive astrocytes in a rodent brain injury model. These same nanoparticles were applied in a different study to facilitate the delivery of antiretroviral therapeutics in HIV-infected mice.[372] HIV infection can elicit a neuroinflammatory response from microglia and border-associated immune cells.[373,374] Antiretroviral therapeutics are used to manage viral load, but have a limited ability to cross the BBB when administered freely.[375] In this case, nanoparticle delivery facilitated antiretroviral therapy accumulation in the brain, leading to a decrease in p24, a distinctive HIV antigen. In a different study, epigallocatechin-3-gallate, a potent antioxidant,[376–378] was delivered to a mouse epilepsy model using PEGylated PLGA nanoparticles.[379] Release of the antioxidant agent was facilitated by nanoparticle degradation, while PEGylation masked the nanoparticles from the immune system, effectively increasing the half-life of the nanoparticles. Prolonged release of epigallocatechin-3-gallate from PEGylated PLGA nanoparticles significantly decreased seizure rate and intensity in the mice. Furthermore, immunohistochemical results revealed lower activity by $Iba1^+$ microglia and $GFAP^+$ astrocytes. Polymeric encapsulation of antiepileptic therapeutics has also been reported using naturally-derived polymers such as chitosan.[380]

Polymeric nanoparticles can also be functionalized with targeting ligands. Amphiphilic macromolecule-based nanoparticles have been developed with a tunable binding affinity for CD36, a class B scavenger receptor that mediates microglial activation.[381] Optimization of the alkyl side chain length in the polymer core increased binding of the nanoparticles to CD36,

inhibiting microglial interactions with a-synuclein aggregates, which are known to propagate inflammatory signaling in Parkinson's disease.[282,381] In another study, chitosan nanocarriers were modified with fucoidan,[382] a sulfated amphiphilic polysaccharide that is known to target P-selectin,[383] a cell adhesion molecule used to recruit macrophages to an inflammatory environment.[384,385] Chitosan is particularly responsive to acidic environments, promoting accumulation of chitosan nanoparticles in acidic inflammatory tissue sites.[381]

Semiconducting polymer nanoparticles contain polymers with large p-conjugated rigid backbones. These conjugated polymers can efficiently produce heat or singlet oxygen when exposed to near-infrared light, allowing for activation of heat- and oxygen-responsive therapeutics.[386,387] Semiconducting polymer nanoparticles can leverage the minimally invasive nature of near-infrared irradiation to achieve spatiotemporal control over the delivery and activation of therapeutics. For example, controlled release of the anti-inflammatory agent curcumin has been achieved using these nanoparticles, reducing ROS and intracellular calcium in mouse microglia while also inhibiting amyloid-β aggregation.[388]

4.5.2 Hydrogels

Hydrogels are water-swollen polymeric networks that are promising delivery vehicles for a variety of cells, proteins, and drugs. Hydrogels are preferred for soft tissue applications due to their intrinsically lower mechanical stiffnesses and can come in different sizes including bulk gels, microgels, and nanogels.[389–391] Hydrogels can be surgically implanted, administered intravenously,[389] intranasally,[390,392–394] or injected locally to the site of injury.[395–398] In the CNS, injectable hydrogels are preferable because they can be injected in a minimally invasive manner through the delicate BBB/BBSB with minimal damage, enabling the local delivery of high doses of immunomodulatory therapeutics. Naturally-derived polymers commonly used to fabricate hydrogels for the CNS include hyaluronic acid (HA), alginate, chitosan, gelatin, laminin, fibrin, elastin, and self-assembling peptides.[395,399] Hydrogels can also be made of synthetic polymers such as PEG, PLGA, polyurethane, and poly(N-isopropylacrylamide) (PNIPAAm).[395] A hydrogel that closely matches the mechanical and biochemical properties of the CNS can minimize glial scar formation and facilitate effective tissue repair. For instance, hydrogel stiffnesses should match that of brain and spinal cord tissue, reported to range from 100–2000 Pa.[399,400] Furthermore, the addition of specific peptide sequences or nanoparticles that promote cell–material interactions and respond to pH, temperature, or electromagnetic stimuli can also be

added to a variety of natural and synthetic hydrogels to increase their functionality in the CNS.[395] Here, we will discuss the recent advances in hydrogels that have been used to deliver proteins, cytokines, and anti-inflammatory molecules to modulate the innate inflammatory response after injury or disease in the CNS.

HA is one the most common biopolymers that has been investigated for neural tissue engineering. HA is an abundant ECM molecule in the CNS produced by neurons and astrocytes.[194] HA interacts with several cellular receptors, including the CD44 receptor, receptor for hyaluronan-mediated motility (RHAMM), and toll-like receptors (TLRs) 2 and 4 on neurons and glial cells to promote cell migration, proliferation, and differentiation.[399,401–403] The effects of HA on the inflammatory response in the CNS are dependent on its molecular weight. High molecular weight HA (>1000 kDa) can reduce glial scar formation, hinder astrocyte activation, and decrease the production of pro-inflammatory cytokines, whereas low molecular weight HA (<500 kDa) can elicit pro-inflammatory astrocyte proliferation and cytokine production.[401,404–406] HA is a particularly attractive biopolymer for hydrogels for CNS regeneration, as it can be easily modified to enable tunable crosslinking and incorporate peptides for cell adhesion and material degradation. HA can also be easily modified with different functional groups or peptides to produce hydrogels that can modulate inflammation while simultaneously promoting neuronal regeneration. HA-containing hydrogels have been used to deliver cells, neurotrophins, and other growth factors. Wang *et al*. developed an injectable, dual enzymatically crosslinked HA hydrogel to deliver nerve growth factor (NGF) and bone marrow-derived MSCs to a mouse model of TBI.[407] HA was modified with tyramine to enable dual-enzymatic crosslinking with galactose oxidase and horseradish peroxide. MSCs and NGF were encapsulated within the hydrogel prior to crosslinking.[408] The co-delivery of MSCs and NGF reduced IL-6 production, inhibited neuronal apoptosis, and polarized macrophages and microglia towards an alternatively activated M2 phenotype. It has also been suggested that MSCs can promote neural regeneration by secreting cytokines and proteins that are associated with neural tissue repair.[409]

Hyaluronic acid-methylcellulose (HAMC) hydrogels are frequently used in neural tissue engineering applications for both cell and protein delivery.[225,410–412] This blend of two polymers is physically crosslinked through hydrophobic interactions and is shear-thinning, which enables facile injection through a fine-gauge needle, and inverse thermal gelling, which enables gelation at body temperature.[413] Recently, a HAMC hydrogel was modified with the peptide sequence

KAFAK and the neurotrophic factor BDNF.[225] KAFAK is an immunomodulatory peptide that can suppress the expression of the proinflammatory cytokines IL-6, IL-1β, and TNF-α.[414] BDNF is a potent neurotrophic factor that can enhance the survival of neurons and axonal regeneration. The co-functionalized hydrogel reduced the expression of TNF-α, IL-1β, and IL-6 and promoted functional recovery after SCI (**Figure 4.4A**). This hydrogel also increased the expression of IL-10, which can have anti-inflammatory effects. Interestingly, the HAMC hydrogel alone reduced levels of TNF-α, however less significantly, indicating that the hydrogel itself had an anti-inflammatory effect. One potential mechanism of this effect is that high molecular weight HA (>1000 kDa) can interact with the CD44 cellular receptor on resident and peripheral immune cells to decrease the expression of inflammatory cytokines, leading to a more favorable environment for tissue repair.[401,403] In addition to regulating inflammatory cytokines, this hydrogel was capable of promoting neuronal survival, increasing axonal regeneration, and decreasing glial scar formation.

Other natural biopolymers including alginate, chitosan, gelatin, and combinations of such polymers have also been used to fabricate hydrogels for CNS applications. A fascinating approach is using hydrogels to sequester inflammatory molecules and subsequently halt the progression of downstream inflammatory responses. Cationic polymers such as PAMAM dendrimers can bind to negatively charged DAMPs, reducing the inflammatory response associated with their release and promoting the polarization of macrophages and microglia to an M2 phenotype. A photo-crosslinked gelatin hydrogel was modified with PAMAM dendrimers and loaded with IL-10.[415] This hydrogel effectively sequestered high mobility group box 1 (HMGB1), which is an anionic charged DAMP that triggers TLR-4 activation and stimulates neuroinflammation and cell apoptosis through the NF-κB signaling pathway. The DAMP-scavenging/IL-10-releasing gelatin hydrogel reduced TNF-α and IL-1β levels and glial scar formation, while enhancing neural regeneration and functional recovery in a SCI model (**Figure 4.4B**).

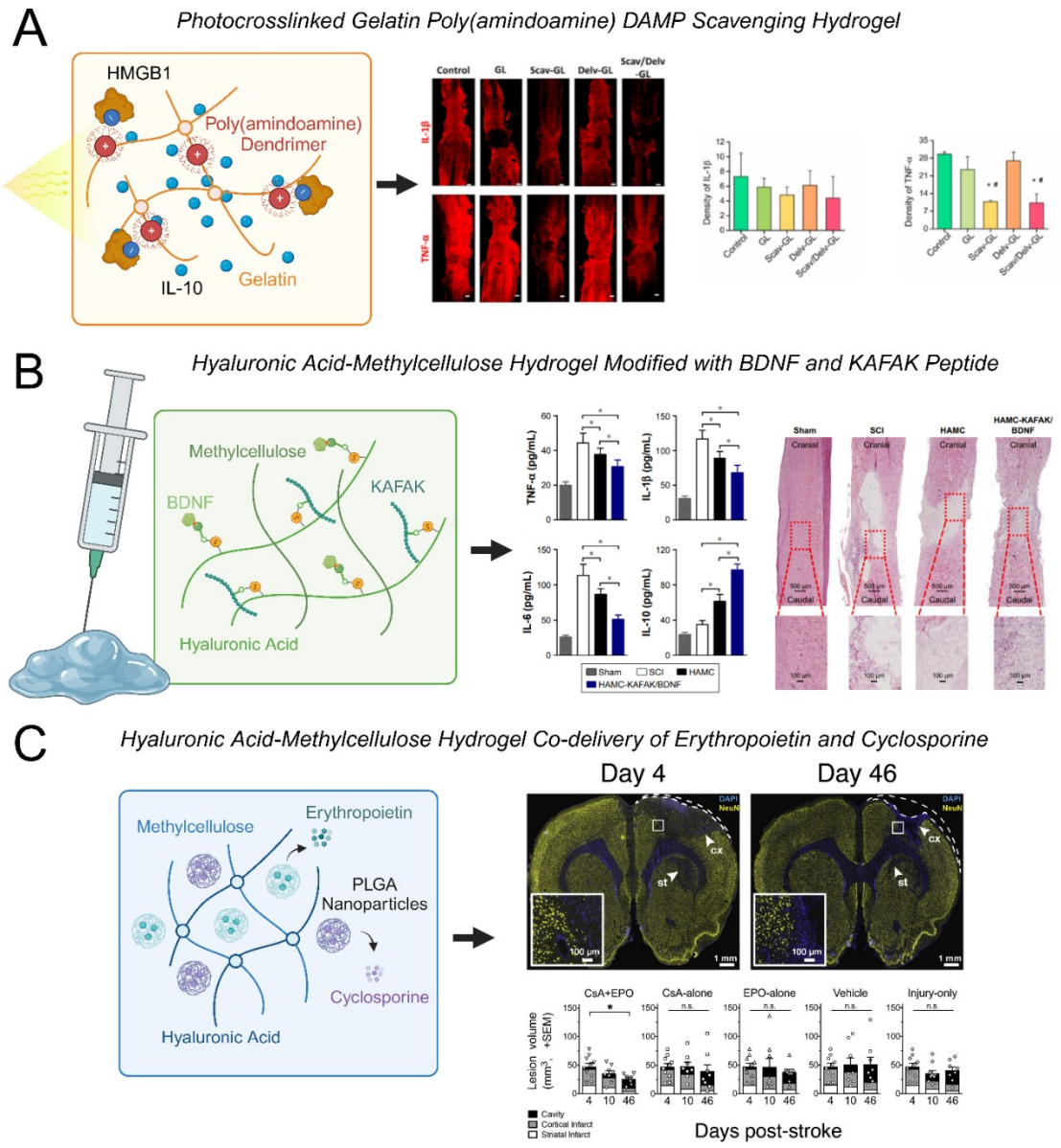

Figure 4.4. **Examples of recent advances in hydrogels to modulate CNS inflammation.** A) A photo-crosslinked gelatin hydrogel modified with cationic charged poly(amindoamine) dendrimers simultaneously scavenged HMGB1 and released IL-10 to reduce expression of TNF-α and IL-1β in spinal cord tissue.[415] B) A hyaluronic acid-methylcellulose (HAMC) hydrogel modified with brain derived growth factor (BDNF) and the immunomodulatory peptide KAFAK reduced expression of TNF-α, IL-1β, and IL-6 and increased expression of IL-10 in spinal cord tissue.[225] C) A HAMC hydrogel loaded with poly(lactic-co-glycolic acid) (PLGA) nanoparticles for the co-delivery of erythropoietin and cyclosporine reduced lesion volume after stroke injury.[416]

Hydrogels made from synthetic polymers such as PLGA, PNIPAAm, polyurethane, and PEG can also be used to treat inflammation in the CNS. A thermosensitive hydrogel made from a triblock copolymer (PLGA–PEG–PLGA) was used to deliver baricitinib, which is an FDA-approved inhibitor of the JAK2/STAT3 pathway that is clinically used to treat autoimmune diseases such as rheumatoid arthritis.[417] The phosphorylation of JAK2 and STAT3 was significantly increased after SCI compared to uninjured tissue, motivating the use of this pathway as a therapeutic target.[417] When delivered in a rat SCI model, the PLGA–PEG–PLGA hydrogel released 80% of the loaded baricitinib within 3 days after injury, during the acute inflammation stage, which is when JAK2/STAT3 expression peaks. Baricitinib successfully inhibited the JAK2/STAT3 signaling pathway *in vivo*, decreasing the levels of iNOS and TNF-α and reducing cell apoptosis. Follow-up *in vitro* studies suggested that baricitinib reduced SCI inflammation by inhibiting the classical activation of microglia.[417] The JAK2/STAT3 pathway is suggested to be upstream of the mTOR signaling pathway involved in microglia and macrophage polarization, making it a promising approach for regulating immune cell polarization.

Hydrogels can also be loaded with peptides to enhance cell– material interactions, nanoparticles that can control the release of anti-inflammatory therapeutics, or nanoparticles that are responsive to specific stimuli. For instance, PLGA nanoparticles have been used for sustained release of anti-inflammatory drugs and growth factors[411,418,419] and are regularly loaded into HAMC hydrogels for the sustained delivery of anti-inflammatory molecules for stroke treatment.[416,419]A HAMC hydrogel loaded with PLGA nanoparticles was used for the codelivery of cyclosporine and erythropoietin to modulate the inflammatory response after stroke.[416] Cyclosporine is an immunosuppressant that is used to treat autoimmune diseases and has the ability to stimulate stem cells in the brain by creating a growth-permissive environment. Erythropoietin can promote neuronal regeneration and increase levels of circulating red blood cells. Cyclosporine and erythropoietin codelivered within the acute phase of inflammation after stroke injury have been shown to synergistically enhance neuroprotection. Sustained co-delivery of cyclosporine and erythropoietin using a HAMC hydrogel containing PLGA nanoparticles successfully enhanced neuronal regeneration, increased neuronal plasticity, and decreased the size of the stroke lesion in the subacute phase of a rat ischemic stroke model (**Figure 4.4C**).

Thus, the delivery of drug-loaded nanoparticles within a HAMC hydrogel presents a viable platform for the sustained co-delivery of multiple therapeutics.

The same composite HAMC hydrogel containing PLGA nanoparticles has also been used to control the release of the neuroprotective peptide pituitary adenylate cyclase-activating poly peptide (PACAP) after stroke.[419] PACAP has immunomodulatory effects and can increase expression of neurotrophins, promote neuronal survival, and polarize microglia towards an M2 phenotype. PLGA nanoparticles were terminated with a carboxylic acid to control their negative surface charge and promote binding to the positively charged PACAP peptide. Tuning the surface charge of the nanoparticles and the pH-responsive carboxylic acid ends on PLGA successfully controlled the release of PACAP. The effect of nanoparticle surface charge on PACAP bioactivity was evaluated by measuring the release of IL-6 from primary astrocytes *in vitro*. Expression of IL6, downstream of PAC1 receptor activation, was inhibited by PACAP and was significantly reduced with PLGA nanoparticles carrying a -24 mV charge at day 10 compared to fresh PACAP. The PLGA-HAMC composite biomaterial successfully sustained the release of PACAP for 10 days in a rat stroke model, providing an avenue for tunable delivery of peptide and protein therapeutics for treating neuroinflammation.

When delivering therapeutics for clinical applications, it is important to consider how the delivery vehicle will affect the pharmacokinetics of the loaded therapeutic. Drug loading is subject to several factors such as drug solubility and size interactions with the delivery vehicle. Nanoparticles can extend drug bioavailability and transport therapeutics across the BBB, yet most nanoparticles suffer from low drug loading (~10% of total vehicle mass).[328,420,421] Renal clearance, circulating monocytes, and complement system protein interactions may limit the circulatory time of nanoparticles and effective therapeutic duration.[422–425] Hydrogels typically have a greater capacity for loading hydrophilic drugs, because the drug can be absorbed into the water-swollen hydrogel network. Delivery of drugs to the target tissue will primarily be dictated by the size of the drug and the size of the hydrogel pores.[426] Most small molecule drugs are much smaller than the pores of a hydrogel, resulting in rapid burst release and clearance from the target tissue.[427,428] Furthermore, hydrogels have a limited ability to deliver hydrophobic drugs that are poorly soluble in aqueous media.[429] Hydrogels are instead ideal for delivering proteins and cells, which can be better entrapped within the polymer network and released in a more sustained manner upon matrix degradation.[222,224,430] The different benefits and drawbacks of nanoparticles

and hydrogels has led to the use of combinations of these two delivery vehicles to leverage the advantages of both delivery platforms.[419]

Hydrogels have been fabricated with the addition of gold nanoparticles to achieve electroconductive characteristics. Specifically, hydrogels that use nanocrosslinkers, such as carbon-based nanomaterials or liposomes, to impart self-healing and responsive properties can be mixed with gold nanoparticles for regenerative medicine applications.[413] A self-healing chitosan derivative hydrogel containing dialdehyde polyurethane nanocrosslinkers and gold nanoparticles was recently evaluated as a treatment for Parkinson's disease.[414] This hydrogel reduced neurodegeneration and improved motor functional recovery in a rat model of Parkinson's disease. The polyurethane nanocrosslinkers and gold nanoparticles were suggested to be responsible for scavenging ROS, a key regulator of inflammation in Parkinson's disease.[414] Polyurethane also exhibited immunomodulatory effects by shifting macrophages from an M1 to M2 phenotype. Altogether, hydrogels are a versatile platform to deliver drugs, cells, and proteins that have the potential to reduce neuroinflammation and improve functional recovery following CNS injury and disease.

4.5.3 Implantable scaffolds

Injuries to the CNS such as stroke, TBI, and SCI can result in the loss of large volumes of functional tissue. In these cases, bulk implantable scaffolds can be advantageous due to their ability to fill cavities formed after injury, provide mechanical support, and guide cell migration and elongation of axons through their pores during neural regeneration. Scaffolds that have mechanical, biophysical, and biochemical characteristics similar to CNS tissue can provide a habitable environment for both transplanted and host cells. Furthermore, scaffolds with electroconductive properties can promote proliferation, differentiation, and regeneration of neuronal cells by transmitting electrical signals to surrounding cells in the brain and spinal cord.[431] In the spinal cord, implantable scaffolds that can provide biophysical cues that guide anisotropic elongation and alignment of axons through the lesion are especially attractive, as they increase the likelihood of promoting robust new synaptic formations and functional recovery.

Implantable scaffolds are produced through numerous methods including templated scaffolds fabricated by casting or injection molding, cryogenic processes such as freeze-drying or ice-templating,[229,432,433] additive manufacturing techniques that extrude fibrous polymers or viscoelastic hydrogels,[434,435] microfluidic devices that can deposit polymeric materials in a

precise structure,[436,437] or by the decellularization of tissues.[438,439] Depending on the method used for producing these scaffolds, scaffolds can exhibit a fibrous, multichannel, or microporous structure that allows for the support of a neural network.[440] Additive manufacturing or deposition of polymeric fibers on a nano- or micro- level can be used to create scaffolds that can have controlled porosity and orientation for guiding cellular alignment. Bioprinting viscoelastic hydrogels provides a convenient method for loading exosomes, cells, nanoparticles, and proteins for implantation directly into the lesion. Freeze-drying polymers can enhance scaffold mechanical strength and provide tunable porosities with appropriate biophysical cues for cell infiltration from surrounding CNS tissue. Implantable scaffolds can be made from a variety of polymers that are commonly used to make hydrogels and can also extend to water-insoluble polymers such as silk fibrin, PCL, and PLGA.

Scaffolds implanted in the spinal cord lesion after injury are commonly used to guide axonal regeneration, bridge synaptic formations, and promote functional recovery. Anisotropic channels can provide biophysical cues to facilitate the migration of transplanted and endogenous cells and elongation of axons through the spinal cord lesion. Aligned collagen scaffolds are popularly used to achieve this goal. Recently, Zou *et al*. used an aligned collagen sponge to promote differentiation and neurite outgrowth of human fetal brain neural stem cells (NSCs) and fetal spinal cord NSCs for the treatment of SCI (**Figure 4.5A**).[316] Both spinal cord and brain NSCs delivered in the collagen scaffolds reduced pro-inflammatory IL-1β and IL-6 secretion and expression of CD68, a cell surface marker for activated microglia/macrophages. However, IL-1β expression levels were significantly lower in the collagen scaffold containing spinal cord-derived NSCs. Furthermore, the collagen scaffold containing spinal cord-derived NSCs induced neurite outgrowth, increased the number of mature neurons, and promoted axonal myelination and synapse formation, demonstrating that spinal cord-derived NSCs were overall more effective than brain-derived NSCs for reducing inflammation and promoting neuronal regeneration after SCI.

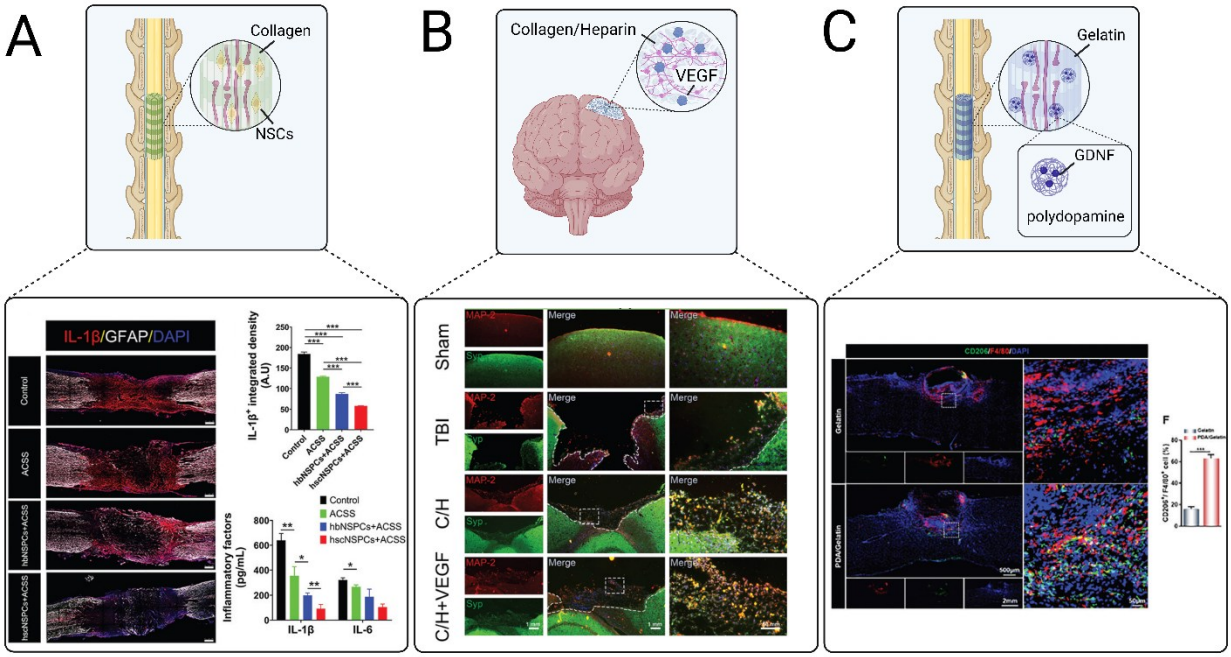

Figure 4.5. Examples of recent advances in implantable scaffolds to modulate CNS inflammation. A) An aligned collagen scaffold loaded with neural stem cells (NSCs) decreased the expression of pro-inflammatory cytokines including IL-1β and IL-6.[316] B) A collagen/heparin scaffold for the repair of brain tissue after TBI promoted synaptic formations as indicated by staining of microtubule associated protein 2 (MAP-2) and synaptophysin (Syn).[441] C) An aligned gelatin scaffold containing glial cell line-derived neurotrophic factor (GDNF)-loaded polydopamine nanoparticles polarized macrophage and microglia to M2 phenotypes after SCI as indicated by CD206 and F40/F80 staining.[442]

Implantable scaffolds fabricated using synthetic polymers present opportunities for investigating the use of cell–material interactions for modulating inflammation, as functional groups can easily be modified in polymer synthesis to tune material properties. The degradation of PLGA produces an acidic environment which increases inflammation; thus, modifying the degradation rate and products of PLGA could modulate the immune response.[443] This idea motivated the evaluation of increasing PLGA content and varying lactic acid and glycolic acid ratios within a polyurethane scaffold with varying soft and hard segments that contain PEG, PCL, PLGA, L-lysine, ethyl ester diisocyanate, and 1,3-propanediol to further adjust the degradation rate of the scaffold, the acidity of its degradation products, and the subsequent

immune response.[444–446] The synthetic water-soluble polymer was fabricated by waterborne polyurethane emulsion, crosslinked using UV light, and freeze-dried. Increasing PLGA content of bulk scaffolds resulted in largely anti-inflammatory effects, including reduced levels of nitric oxide, decreased expression of TNF-α, and increased levels of IL-10 *in vitro*. PLGA containing equal amounts of lactic acid and glycolic acid resulted in the highest expression of anti-inflammatory cytokines. These results also demonstrated the potential of PLGA to polarize microglia to an M2 phenotype.[443] This phenomenon was suggested to be caused by immunomodulatory effects of PLGA in addition to the scaffold's mechanical stiffness and degradation rate, further supporting the use of PLGA for implantable scaffolds.

Exosome-loaded 3D-printed scaffolds offer mechanical support while delivering biochemical cues to modulate neuroinflammation and promote tissue regeneration. A 3D-printed collagen/silk fibroin scaffold loaded with exosomes derived from MSCs pretreated with FGF-2 was used to treat TBI in a canine model.[317] Both FGF-2-pretreated and untreated exosomes reduced lesion size, apoptosis of neurons, and glial scar formation, while also promoting neuronal regeneration, myelination, synapse formation, and angiogenesis. The least neuronal apoptosis was observed with FGF-2-pretreated exosomes. Exosome delivery also reduced IL-6 and TNF-α expression and increased IL-10 expression. Notably, the same research group has evaluated several variations of stimulated stromal cells and exosomes delivered via 3D printed scaffolds. Hypoxic-preconditioned MSCs have been delivered with the same collagen/silk scaffold, while collagen/chitosan 3D-printed scaffolds have been used for the delivery of exosomes derived from insulin-like growth factor (IGF)-1-pretreated NSCs and BDNF-stimulated MSCs for TBI treatment.[319,320,447,448] It will be interesting to compare the overall effectiveness of using exosomes from stimulated MSCs, NSCs, and stromal cells as immunomodulatory treatments in the CNS over the coming years.

Implantable scaffolds have also been used as delivery vehicles for proteins. A freeze-dried collagen/heparin scaffold loaded with vascular endothelial growth factor (VEGF) was delivered to a rat model of TBI (**Figure 4.5B**).[441] This scaffold had been previously evaluated for the treatment of SCI and resulted in significant functional recovery, motivating its use for treating other CNS injuries. The collagen/heparin scaffold provided mechanical support for cells infiltrating from the surrounding brain tissue and successfully sustained the release of VEGF over 27 days. The VEGF-loaded collagen/heparin scaffold promoted angiogenesis, improved

neuronal survival, relieved edema, and reduced lesion size in a rat TBI model. Interestingly, scaffolds with and without VEGF both significantly decreased levels of the inflammatory cytokines IL-1β and IL-6. The success of this scaffold in both the spinal cord and the brain demonstrates its versatility for treating multiple types of CNS injuries. Combination strategies of multiple types of biomaterials have also been explored. Ma *et al.* evaluated a multicomponent gelatin scaffold loaded with polydopamine nanoparticles that released GDNF for the treatment of SCI (**Figure 4.5C**).[442] Polydopamine is used in many regenerative medicine applications for its ability to scavenge ROS, reduce inflammation, and polarize macrophages and microglia towards an M2 phenotype.[449–451] The gelatin scaffold reduced ROS and promoted M2 microglia polarization, as demonstrated by the downregulation of iNOS and increased expression of CD206 *in vitro*. When implanted in a mouse model of SCI, M2 polarization of microglia was significantly increased around the SCI lesion, TNF-α and IL-1β levels were decreased, and IL-10 and TGF-β levels were increased, suggesting an overall positive effect of the scaffold on resolving inflammation. Furthermore, the encapsulation of GDNF into the polydopamine nanoparticles reduced neuronal apoptosis and scar formation and promoted neuronal survival and axonal regeneration. Staining for vGluT1, a synaptic maker, revealed the successful formation of new synapses. Overall, the scaffold provided dynamic biochemical and biophysical cues to successfully promote M2 polarization, modulate cytokine expression, and promote synapse formation, confirming the utility of combinatorial therapeutic strategies to simultaneously modulate the inflammatory response and provide neurotrophic support.

4.5.4 Neural probe coatings

In addition to promoting repair after tissue injury and disease, biomaterials can also aid in the integration of implants for the CNS. Neural probes interface with neural tissue to stimulate and/or record electrical activity on the single-neuron level through changes in the membrane potentials of surrounding neurons. The use of neural probes has enhanced our understanding of neural connectivity, enabled the development of neuro-prosthetics, and advanced treatment of neurological disorders. To measure neural activity with high spatiotemporal resolution, probes are typically inserted directly into parenchymal tissue, compromising the BBB.[452–454] The resulting tissue damage leads to the activation of local glia and initiates a foreign body response.[455,456] Additionally, the brain goes through a range of micromotions during daily activity, which induces mechanical stresses between the implant and surrounding tissue,

resulting in further tissue damage and inflammation.[457,458] Ultimately, probes intended to directly interface with neural tissue are slowly segregated from the CNS as glial scar tissue encapsulates the electrode shank.[459] Thus, regulating neuroinflammatory signaling and glial reactivity to the implant is critical for ensuring the long-term reliability of implanted probes. Two approaches exist in choosing materials for the fabrication of neural probes and their coatings. Materials that support protein and cell adhesion may be used to promote the growth of neurons in direct contact with the neural probes to improve signal detection, or nonfouling materials that resist protein and cell adhesion may be used to try to minimize the foreign body response and shield the probes from damage. Both approaches aim to minimize glial scar formation and maximize the long-term functionality of the neural probes.

Graphene is a popular material for neural probe fabrication as its mechanical flexibility, chemical inertness, and high electrical conductivity allow it to effectively interface with neural tissue (**Figure 4.6A**). Graphene can encourage neuronal adhesion, axonal sprouting, and neural stem cell differentiation.[460,461] Graphene outperforms other materials typically used in electrode interfaces, including parylene-C, polyimide, and diamond, because it results in reduced glial scar formation and limits the retraction of neurons from the area immediately surrounding the implant site. The tissue adjacent to graphene neural probes typically contains higher neuron density, average quantity and length of neurites, and total neural outgrowth than neural probes made from other materials.[227] Application of graphene to silicon probes resulted in a significant decrease of glial cell proliferation, accompanied by a greater number of neural soma and processes around the implant compared to uncoated devices.[227] Despite these advantages, previous studies have raised concerns over graphene's suitability for *in vivo* applications given its susceptibility to enzymatic oxidation by phagocyte-secreted peroxidases.[462–464] This mechanism for degradation poses a challenge for graphene-coated probes, as infiltrating immune cells will cause surface stripping and eventual failure of the device. To prevent potential device failure and particle bioaccumulation, strategies to protect the graphene coating layer of neural probes from degradation will be critical.

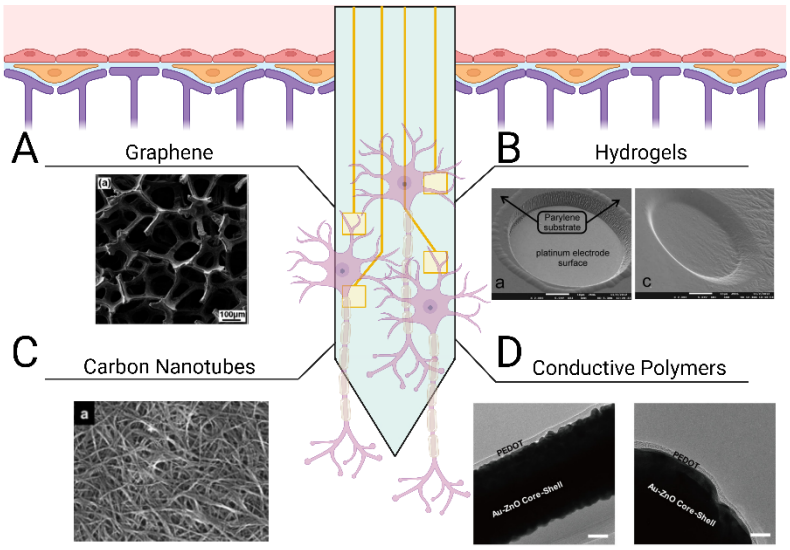

Figure 4.6. **Different types of coatings for improving neural probe integration.** Electrode shanks may be coated with A) graphene monolayers to support neuronal attachment,[465] B) hydrogels with tunable mechanical properties and conjugated ligands for mimicking CNS parenchymal tissue,[228] C) carbon nanotubes for lower electrode impedance and increased charge transfer,[466] and (D) conductive polymers, such as PEDOT, to enhance communication across the tissue–electrode interface.[467]

HA thin films for neural probe coatings are of particular interest, because HA is a primary component of CNS parenchymal ECM.[401] Combining HA thin films with poly-L-lysine (PLL), a positively charged amino acid polymer, improves neural adhesion via electrostatic interactions with the negatively charged cell membrane.[468–470] This thin film composite has been used to coat intracortical electrodes. Following 7 weeks of *in vivo* recording, histological staining revealed a slight decrease in the number of Iba-1$^+$ microglia and GFAP$^+$ astrocytes around the implant site.[321] When deposited on graphene monolayers, the HA/PLL coating improved neuronal adhesion and outgrowth *in vitro* over 14 days. The physical characteristics of the HA/PLL coating on graphene monolayers were also investigated using Raman spectroscopy and atomic force microscopy. The HA/PLL coating was found to adhere to the graphene monolayer without significantly affecting its crystalline quality. Together, this work demonstrates the potential of HA/PLL coatings to facilitate neural probe integration; however, whether HA/PLL coatings can protect graphene from enzymatic oxidation remains to be explored.

Hydrogels are promising materials for coating neural probes because they are cytocompatible, display tunable mechanical properties, and can be easily functionalized with stimuli-responsive crosslinkers or cell-adhesive peptides to enhance probe integration (**Figure 4.6B**). PEG hydrogels are commonly used to shield implants from detection by the immune system due to their resistance to protein and cell adhesion.[471] Spencer *et al.* used PEG-dimethacrylate hydrogel coatings to reduce micromotion-induced stress within implant sites in rats.[472] They evaluated the effect of shank size on the immune response by implanting glass capillaries of varying sizes (150, 200, and 400 μm diameter) and found that increasing the diameter of the shanks increased recruitment of reactive astrocytes and macrophages, increased BBB permeability, and decreased neuronal density within a 100 μm radius of the implant in a rodent brain. Uncoated 150 μm diameter capillaries were then compared to capillaries coated with varying thicknesses (150, 200, 400 μm) of 10% w/v 8000 kDa PEG-dimethacrylate. Hydrogel coatings reduced strain *in vivo* following perpendicular and axial probe displacement, subsequently decreasing trauma at the implant site. Furthermore, reduced GFAP staining confirmed hydrogel coatings ameliorated astrocyte reactivity 8 weeks post implantation. However, swelling of the PEG-dimethacrylate *in vivo* also resulted in a larger implant diameter, increasing BBB permeability, macrophage recruitment, and neuron retreat from the site. While the soft interface of the shanks protected the site from micromotions, reduced neuron density over a 100 μm radius could hinder device efficacy. In another study, a different approach was used, in which a dual-layered microfluidic system consisting of a gelatin methacrylate-PEG hydrogel microchannel encased by a thin, porous polydimethylsiloxane membrane was implanted.[473] The dual-layered system was attached to a metal probe while dry so that it was stable enough to allow implantation without delamination of the coating. Once inserted, the composite hydrogel swelled, releasing encapsulated IL-4 and dexamethasone, which increased M2 macrophages and decreased TNF-α and IL-6 secretion. Platforms such as these present opportunities to explore co-delivery of anti-inflammatory cytokines (IL-13, IL-4), inflammatory cytokine receptor antagonists (IL-1 receptor antagonist), and neurotrophic factors to promote neuronal survival while simultaneously regulating the glial response.

While hydrogel coatings are typically not electroconductive and do not contribute to neuron-electrode communication, hydrogels that contain conductive polymers present the opportunity to improve neural signal detection while also maintaining the advantages of a

mechanically and biochemically tunable coating. Conductive polymer hydrogels can promote neuron differentiation, reduce astrocyte reactivity, and are generally cytocompatible.[474,475] Conductive hydrogels may also help enhance several electrode properties such as electrical conductivity (the ability to conduct current in a given solution), impedance (resistance of the electrode to alternating current, in which low impedance is associated with greater signal quality), cut-off frequency (frequency limit from which signal noise may be removed), and charge storage capacity (the capacity of the device for storing electricity). Cui *et al.* designed a transparent, stretchable hydrogel electrode consisting of PEGylated silk fibroin and the conductive polymer poly(3,4- ethylenedioxythiophene):polystyrene sulfonate (PEDOT:SS).[322] Silk fibroin was first crosslinked using PEG diglycidyl ether, enabling control over the mechanical properties and degradation kinetics of the hydrogel. PEGylated silk fibroin was poured over a thin film of PEDOT:SS prior to the implant interfacing with rat neurovasculature. This conductive polymer hydrogel could both record and stimulate neural activity across the rat cortex. Similarly, PEDOT:SS was used as a conducting polymer within the synthetic copolymer hydrogel, P(DMAA-co-5%MABPco-2,5%SSNa), to enhance the functionality of iridium oxide electrodes.[323] Dimethylacrylamide (DMAA) functions as the polymer backbone of the hydrogel while sodium 4- styrenesulfonate (SSNa) acts as an anion for PEDOT deposition. Methacryloyloxy benzophenone (MABP) is an ultraviolet light-reactive molecule that can form covalent attachments with 4-(3- triethoxysilyl)propoxybenzophenone silane. Photolithographic patterning methods were used to control the covalent attachment of the conductive polymer hydrogel to the electrode surface. Covalent attachment of the conductive polymer hydrogel to iridium oxide electrodes improved charge storage capacity by 2.5-fold, lowered cut-off frequency, and reduced signal impedance. When this material was incubated with the neuroblastoma cell-line SH-SY5Y, no cytotoxic effects or significant changes in material stability were observed. In another study, PEDOT was used to coat a gold-coated, ZnO nanowire microelectrode array (**Figure 4.6D**).[467] ZnO nanowires can help lower the impedance values of the device by increasing the overall effective electrode surface area. The nanowires themselves are flexible, yet ZnO has poor conductivity. Coating the nanowires with gold can improve conductivity, while supplementing with PEDOT can provide a biologically active interface with the neural tissue. Taken together, these studies demonstrate that conductive polymer hydrogels

are a promising class of materials for facilitating tissue–probe integration and enhancing signal sensitivity.

The rigidity of neural probes is a double-edged sword. On one hand, shank stiffness greater than that of neural tissue is necessary for proper insertion. On the other hand, the mechanical mismatch between the probes and the tissue can lead to secondary trauma from the micromotions of the device. Carbon nanotubes are suitable for neural probe fabrication as they are highly elastic yet mechanically strong (**Figure 4.6C**). The structure of carbon nanotubes prevents the release of toxic degradation products, and their innate electrical conductivity allows them to replace commonly used metals as electrodes. When compared to a platinum electrode array, single-walled carbon nanotube electrode arrays did not exhibit appreciable damage and displayed significantly less impedance following 2 months of implantation in rat cortex.[476] Furthermore, long-term implantation of carbon nanotubes did not significantly increase the presence of reactive microglia or astrocytes or change neuron density. In a different application, carbon nanotube fibers were used as a soft cortical electrode compatible with magnetic resonance imaging (MRI) techniques.[477] The carbon nanotube fiber microelectrodes displayed a 9 times lower impedance than the platinum/iridium electrodes used in the study. Two hours post-implantation, the carbon nanotube fiber electrodes recorded precise, single-unit spike activity with a high signal-to-noise ratio. In addition to not interfering with MRI, the carbon nanotube fibers reduced both GFAP and Iba-1 signal around the implant site and maintained higher neuronal density than the platinum/iridium probes. In contrast, the neuron loss zone around the platinum/iridium probes continued to increase in size, indicating progressive neurodegeneration. Carbon nanotube fiber electrodes continued to detect single-neuron recordings for up to 4–5 months, suggesting stable long-term reliability.

4.6 Future Outlook

The successful application of hydrogels in the CNS for the modulation of neuroinflammation has prompted their advancement to clinical trials. Recently, a self-assembled peptide hydrogel based on the short peptide RADA16, which contains four repeating units of the ‘‘RADA’’ peptide sequence, advanced to clinical trials for the treatment of SCI with an expected completion date in 2025.[478] This hydrogel has demonstrated a promising ability to support stem cell viability and promote neural regeneration after SCI in animal models and is currently being

investigated in clinical trials for the delivery of a heterogeneous collection of cells from the stromal vascular fraction of adipose tissue.[478,479] Additionally, intranasal administration of APH-1105 nanoparticles is currently in clinical trials for the treatment of Alzheimer's disease and is expected to be completed in 2024.[480] APH-1105 is a modulator of the enzyme a-secretase, which cleaves pathological amyloid precursor proteins to a soluble product that is easily cleared from the brain and avoids accumulation of amyloid plaques.[394] Intranasal administration of nanoparticles bypasses the BBB and enables transport directly to the brain; this strategy has also been used to deliver other therapeutics such as rivastigmine and insulin.

Several recent advances have been made in hydrogel research that we expect will translate into valuable therapeutic strategies for managing neuroinflammation in the coming years. Hydrogels that can scavenge pro-inflammatory molecules are emerging as a novel strategy to reduce inflammation in many tissues. The addition of a variety of functional groups, peptides, and charged polymers to hydrogels can confer the ability to scavenge and remove pro-inflammatory molecules. For example, material modifications using gallic acid, polyurethane, PAMAM dendrimers, and polyethylenimine have been recently used to scavenge pro-inflammatory molecules, such as ROS and DAMPs.[314,415,481] Nanocrosslinked hydrogels, which are made from nanoclays, nanoparticles, or liposomes, are a novel class of hydrogels that combine the injectability and self-healing properties of dynamic covalent crosslinked hydrogels with the versatility of nanoscale materials. By changing the crosslinkers employed, these hydrogels can be engineered to degrade in response to a variety of stimuli, including light, heat, pH, and electromagnetism. Some recent examples of this class of materials include dialdehyde polyurethane nanocrosslinkers and graphene oxide, which has been used to modulate microglia polarization and promote angiogenesis and tissue regeneration after SCI.[482]

Emerging developments to enhance temporal control over biomaterial structure and the delivery of proteins and other biomolecules may also have applications in mitigating neuroinflammation, which is an innately time-dependent process. Photodynamic hydrogels, which use light to trigger changes in material structure or the release of cargo, present a versatile approach to enable spatiotemporal control over biomaterial behavior. Current methods for fabricating photodynamic hydrogels are limited to the use of high-energy ultraviolet light (<400 nm), which exhibits low tissue penetration.[483–486] A recent investigation by Rapp and DeForest reports the use of three photolabile crosslinkers, expanding the compatibility of photocleavable

crosslinkers to a greater spectrum of visible and infrared light.289 PEG-based hydrogels showcased rapid, orthogonal degradation in response to red (617 nm), green (530 nm), and blue (405 nm) light. The multiplexed degradation of hydrogel constructs creates new opportunities for triggered, spatiotemporal release of multiple bioactive agents from a single hydrogel. This approach could also potentially be reversed for finer control in biofabrication processes, paving the way for light-mediated gelation of deep tissue implants or gradient patterning of cell-supporting peptides or conjugated therapeutics, as well as differential photocrosslinking of various polymers into a single platform. As the selection of wavelength-selective crosslinkers grows, we can expect to see more complex hydrogel-based platforms for studying pathophysiological phenomena and controlling the release of bioactive agents. This approach may have utility in SCI specifically, in which the staggered delivery of multiple therapeutics has been shown to improve tissue repair and functional recovery.[487]

Novel strategies are also being employed to improve the ability of implantable scaffolds to align axons within damaged neural tissue, including the implantation of prevascularized and conductive scaffolds. Aligned, prevascularized scaffolds can recruit neural cells to the site of injury and promote vascular infiltration, aiding in tissue regeneration.[488–490] Additionally, several aligned collagen sponge scaffolds are now making their way into clinical trials for axonal alignment and spinal cord tissue repair after SCI. These include a study completed in 2021 that evaluated an aligned collagen sponge scaffold for the treatment of acute SCI, a study that assessed the effectiveness of an aligned collagen sponge combined with epidural electrical stimulation, and a third study that evaluated the NeuroRegen Scaffold™ loaded with bone marrow mononuclear cells compared to traditional intradural decompression and adhesiolysis treatment.[491–493] Lastly, an aligned scaffold fabricated from PLGA-b-PLL called Neuro-Spinal Scaffold™ is currently in clinical trials for treating anatomically complete SCI with an expected completion date of 2028.[494]

Enhancing the tissue-electrode interface and mitigating the foreign body response to neural probes is a major priority in the neuroelectronic field. Biohybrid neural interfaces, also known as ‘‘living electrodes,’’ are an emerging concept in which neural probes contain engineered networks of neurons or materials that encourage host neurons to grow into the implant to facilitate a seamless tissue–electrode interface and improve signal recording. A study by Cullen et al. reported the design of hydrogel microconduits for supporting neuron outgrowth

and unidirectional axon elongation.[495] While the motivation of the work was originally to reconnect damaged neural tracts, these microtissue constructs could also be used to stimulate target neurons. This proof-of-concept was later reported by Adewole *et al*., in a study where engineered neuronal networks were implanted into the male rat cortex.[301] The self-contained nature of these living electrodes facilitated synaptogenesis with target neurons, as indicated by sustained neuronal activity and signal detection over a 5-week period. This work suggests that living electrodes could be used to overcome the challenge of diminishing functionality observed with inorganic neural probes; however, longitudinal studies are still needed to confirm long-term construct integration.

4.7 Conclusion

A dysregulated neuroinflammatory response is a hallmark of traumatic injury and several neurodegenerative diseases. While injury and disease onset in the CNS may result from a myriad of causes, unresolved neuroinflammation from any of these causes can result in secondary injury, worsening tissue damage. Biomaterials are emerging as a promising therapeutic approach for resolving dysregulated inflammatory responses. Ultimately, we expect that the recent advances in a variety of biomaterials described within this review will lead to viable strategies for treating injury and disease in the CNS. As the population affected by CNS injury and disease grows in the future, it will be critical to continue expanding our understanding of the pathological mechanisms of neuroinflammation to be able to use these new insights to design better biomaterials for regenerative medicine and neuroengineering applications in the CNS.

4.8 Bridging Paragraph

Now that we have a thorough understanding of the field of biomaterial strategies for modulating neuroinflammation and key design criteria for developing hydrogels in neural tissue repair, we will investigate the generation and maturation of V2a interneurons in HA-alginate (HA-Alg) hydrazone-crosslinked hydrogels. Alginate is emerging in neural tissue engineering as biomaterials made from alginate may provide neuroprotection and promote an environment favorable for tissue repair. V2a interneurons are a highly relevant cell type in neural tissue repair, as their transplantation has been identified as a promising therapeutic approach for spinal cord injury. We functionalized HA with fibronectin- and laminin-derived peptides (RGD and IKVAV, respectively) and evaluated their effects on the generation of viable V2a interneuron and their

maturation. Overall, we identified a promising hydrogel formulation that provides the adhesion cues necessary for neuronal maturation and is suitable for neural tissue engineering applications.

CHAPTER 5

HYALURONIC ACID-ALGINATE HYDRAZONE CROSSLINKED HYDROGELS SUPPORT THE GENERATION AND MATURATION OF V2A INTERNEURONS

From Alycia N. Galindo, Madison E. McLaren, Alyssa K. Chi, Jenna D. Khachatourian, Jessica C. Butts, Marian H. Hettiaratchi. Hyaluronic Acid-Alginate Hydrazone Crosslinked Hydrogels Support the Generation and Maturation of V2a Interneurons. bioRxiv 2026–06 (2026) and currently under review for the Journal of Materials Chemistry B. This manuscript is currently under the terms of the Creative Commons Attribution-NonCommercial-NoDerivatives 4.0 License (CC BY-NC-ND 3.0).

5.1 Abstract

Injury to the central nervous system (CNS) causes inflammation, cell death, and glial scar formation that inhibits tissue repair. Injectable hydrogels modified with extracellular matrix (ECM)-derived peptides can provide biochemical cues to promote neural tissue repair and serve as a vehicle to deliver therapeutics across the blood-spinal/blood-brain barrier in a minimally invasive manner. We developed an injectable hydrazone crosslinked hyaluronic acid-alginate (HA-Alg) hydrogel for neural tissue repair. We fabricated hydrogels with a range of polymer concentrations and evaluated their physicochemical properties to identify formulations that mimic the stiffness and viscoelastic properties of the CNS tissue environment. Hyaluronic acid was further modified with ECM-derived, cell-adhesive peptides (RGD and IKVAV) to enhance neuronal adhesion and viability. To evaluate the therapeutic potential of our hydrogel platform, we embedded mouse embryonic stem cell aggregates and differentiated them toward mature V2a interneurons. These interneurons are critical for relaying motor signals and represent a promising therapeutic cell population for treating spinal cord injuries. We demonstrated successful enrichment for V2a interneurons in HA-Alg hydrogels containing ECM-derived peptides. Interestingly, both our newly described HA-Alg and established crosslinked HA-HA hydrogels containing IKVAV peptides demonstrated significantly increased neurite length in interneuron enriched cultures compared to hydrogels without peptides. This study demonstrates that the

addition of ECM-derived peptides is essential to support the neuronal adhesion and viability required for functional CNS tissue repair.

5.2 Graphical Abstract

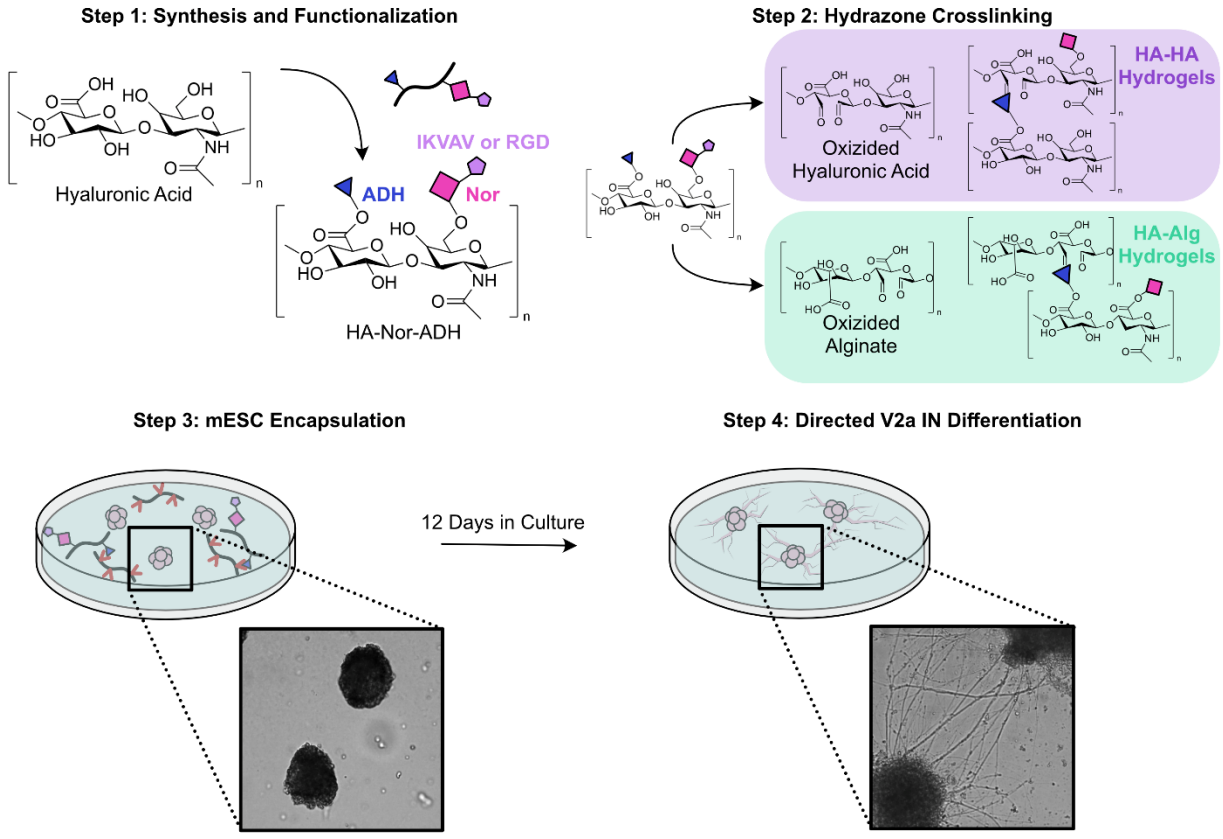

5.3 Introduction

The spinal cord transmits sensory information to the brain while relaying motor commands back to the peripheral nervous system.[496] Spinal cord injury (SCI) is characterized by degeneration of neurons that can result in motor, sensory and autonomic dysfunction.[497] Following injury, the rapid invasion of immune cells and activation of radial glia create an inflammatory environment that causes secondary tissue damage, a cavity of lost tissue, and the formation of a glial scar that physically and biochemically inhibits tissue regeneration.[498] Various therapeutic approaches have been developed to attempt to restore neural tissue function after SCI. These approaches include targeting the neuroinflammatory environment, reconstituting damaged tissue by delivering cells that support neural tissue repair,[316,499] removing biomolecules from the injury environment that

inhibit tissue repair,[500] and delivering neurotrophic factors to promote neuronal growth and remyelination.[501,502] While some of these approaches have had success in promoting neural tissue regeneration in rodent models, these successes rarely translate into meaningful motor or sensory gains in human clinical trials. This translational failure likely stems from the different anatomical scales, the heterogeneity of clinical injuries,[503] and the development of multi-centimeter cystic cavities that create growth barriers that are magnitudes more severe than those modeled in typical rodent contusions.[503,504] Biomaterials such as hydrogels, nanoparticles, and aligned scaffolds have the potential to overcome these hurdles, because they can be engineered to support the local delivery of viable cells, sustained release of bioactive proteins, and presentation of other biomolecules that modify the injury environment to support axonal regeneration. Biomaterials can be specifically tailored to treating SCI such that they can be injected through the blood-spinal cord/blood-brain barrier, provide directional topographical cues that guide axons across the lesion, and act as reservoirs that protect therapeutic molecules from rapid degradation *in vivo*.[505]

Hydrogels that mimic mechanical properties of CNS extracellular matrix (ECM), including its stiffness that ranges from 100-1000 Pa[400,506–508], cell adhesion, and viscoelastic properties, can support cell proliferation and differentiation and guide axonal extension.[399,509] Hydrogels made from modified ECM molecules, such as hyaluronic acid (HA), collagen, and gelatin, are particularly attractive biomaterials for treating SCI because they can also mimic the biochemical composition of neural tissue,[510] providing neuroprotection and stabilizing neuronal networks.[511] HA, which is the most abundant ECM molecule in the CNS, maintains neural tissue homeostasis by enhancing migration, proliferation, and differentiation of neural progenitor cells and oligodendrocyte progenitor cells to help drive repair after injury.[396,512] HA can be modified with functional groups such as aldehydes, maleimides, methacrylates, or hydrazides that allow it to be crosslinked into a hydrogel. For these reasons, HA hydrogels have been used extensively in pre-clinical models to deliver cells proteins, and enzymes to the CNS and are a favored biomaterial for CNS tissue engineering applications.[509,513,514]

Alginate, a naturally occurring polysaccharide derived from brown seaweed, is emerging in CNS applications for its antioxidant, anti-inflammatory, and neuroprotective properties.[515,516] Although not a native component of the brain ECM, alginate hydrogels can be fabricated to match CNS tissue stiffness and viscoelasticity.[517] Alginate's high carboxylic acid content allows it to sequester divalent cations, potentially mitigating the oxidative stress triggered by the release of

redox-active ions during hemorrhage.[518] Alginate hydrogels physically crosslinked with calcium ions have facilitated neurite outgrowth and neural stem cell transplantation.[519,520] However, calcium-crosslinked alginate hydrogels are limited in CNS applications because they can undergo calcium ion exchange, resulting in an inflammatory response,[521,522] and tend to swell or stiffen in the highly ionic CNS environments.[523] Alternatively, modifying alginate with functional groups, such as aldehydes, ester linkages, or amide bonds,[524] can enable chemical crosslinking schemes that do not require the use of calcium ions.

Because functional tissue restoration after SCI depends on the directed regeneration of specific neuronal subpopulations to their natural target regions, we sought to investigate the development of a hydrogel to support the growth and viability of a specific subpopulation of neurons. V2a interneurons are prime candidates for this application, as they are excitatory cells that span the hindbrain and spinal cord, serving as a critical bridge for relaying sensorimotor information between intersegmental regions and contributing to the coordination of sympathetic and parasympathetic functions.[525–527] Within the spinal cord, these neurons coordinate excitatory inputs that are critical for autonomic and voluntary motor function.[528] V2a interneurons also play a role in spinal respiratory networks and facilitate the plasticity of neuronal networks in respiratory muscles as observed in models of amyotrophic lateral sclerosis and cervical SCI.[529,530] The ablation of V2a interneurons in mice disrupts breathing patterns, forelimb reaching tasks, and left-right hindlimb coordination.[527] The Sakiyama-Elbert lab pioneered initial protocols for V2a interneuron differentiation from mouse embryonic stem cells (mESCs) in 2014.[531,532] Since then, V2a interneurons have been successfully differentiated from human pluripotent stem cells,[527,528] and their transplantation in SCI has been identified as a promising therapeutic approach.[533] V2a interneurons transplanted into cervical SCI rat models functionally integrate with the host spinal cord, improving electrophysical signaling and restoring diaphragm activity.[526,530,534,535] However, the survival and engraftment of transplanted neurons *in vivo* can be a challenge in larger injuries, as chronic inflammation, the growth-inhibitory environment of the glial scar, and the lack of cell-adhesive substrates can all contribute to cell death.[536] While HA hydrogels containing astrocyte-derived ECM have been successfully used for the transplantation of V2a interneurons,[535] neuronal staining showed that neuronal processes in the lesion area was not significantly enhanced in this system compared to HA hydrogels alone, which may be due to the fact that HA inherently lacks neuronal adhesion cues necessary to support neuron attachment and proliferation.[502] Thus, there is

a need to develop hydrogels with cell-adhesive cues to support the viability and engraftment of transplanted neurons.

To address these challenges, here we describe a dual polymer, hyaluronic acid-alginate (HA-Alg) hydrazone crosslinked hydrogel to support V2a interneuron differentiation, maturation and survival for neural tissue repair. We hypothesized that a hydrogel that combines the properties of both HA and alginate through dynamic covalent crosslinking could more closely mimic the biomechanical properties of CNS tissue and eliminate the need for calcium-based crosslinkers. HA was functionalized with adipic acid dihydrazide for crosslinking with oxidized alginate to form reversible hydrazone bonds. This dynamic covalent crosslinking enables the fabrication of injectable hydrogels with shear-thinning and self-healing properties that are ideal for CNS tissue repair as they can be easily injected through the blood-spinal/blood-brain barrier in a minimally invasive manner to fill the cavity of lost tissue.[537–539] However, despite successfully mimicking the physical properties of CNS tissue, current hydrogels often fail to provide the cell-adhesive cues essential for the long-term survival and maturation of transplanted cells. Thus, we also hypothesized that chemically conjugating ECM-derived peptides, such as fibronectin-derived (RGD) and laminin-derived peptides (IKVAV), to HA could provide an adhesive substrate with the appropriate biochemical cues to support the culture of V2a interneurons.

We evaluated the physicochemical properties of hydrogels fabricated using a range of polymer concentrations to identify a hydrogel formulation that could support neuronal culture. We targeted a hydrogel with a gelation time between 1 and 5 minutes to facilitate cell dispersion throughout the hydrogel, stiffness of ~100 Pa to mimic CNS tissue, and minimal degradation (±25%) over 28 days to support long-term cell culture. We then investigated whether HA-Alg hydrogels modified with ECM-derived peptides could provide support the differentiation of mESCs into viable, mature V2a interneurons. HA-Alg hydrogels were compared to similar, previously developed HA-HA hydrazone-crosslinked hydrogels to evaluate the use of alginate in a biomaterial for V2a interneuron transplantation. The differentiation and maturity of V2a interneurons were assessed via cell viability, neurite outgrowth and gene expression. We determined that alginate can be combined with HA to form stable hydrogels that meet our criteria for a cell transplantation vehicle and that HA-Alg hydrogels modified with IKVAV can support

V2a interneuron viability and maturation. Overall, we developed an HA-Alg hydrogel platform that can be used for future applications in neural tissue repair.

5.4 Materials and Methods

5.4.1 Synthesis of Norbornene-Hyaluronic Acid (HA-Nor)

HA-Nor was synthesized as previously described.[18,53] Briefly, an initial intermediate product, tetrabutylammonium-hyaluronic acid (HA-TBA) was created through an ion exchange. HA-TBA was made by dissolving sodium hyaluronic acid (Lifecore Biomedical LLC, Chaska, MN) (1 g, 2.64 mmol) for 20 minutes in 20 mL of double distilled water (ddH_2O) at 2% w/v. Dowex (Amberlight™ MB) (Sigma Aldrich, Saint Louis, MO) was weighted at a 3:1 mass ratio and added to a flask for ion exchange for 5 hours followed by vacuum filtration. The pH of the filtrate was then adjusted to pH 7 using tetrabutylammonium hydroxide 30-hydrate (Millipore Sigma, Milwaukee, WI). The product was then frozen at -80°C prior to being lyophilized.

HA-TBA (1 g, 1.61 mmol) was dissolved in dimethyl sulfoxide (DMSO) (Fisher Scientific, Waltham, Massachusetts) at 2% w/v for 20 minutes followed by a purge with N_2 and the addition of 5-norbornene-2-carboxylic acid (Millipore Sigma) at 0.5 molar equivalences (0.11 g, 0.81 mmol), 4-(Dimethylamino)pyridine (DMAP) (Millipore Sigma) Millipore Sigma) at 0.25 molar equivalences (0.05 g,0.40 mmol), and Di-tert-butyl dicarbonate (Boc_2O) (Millipore Sigma) at 0.07 molar equivalence (0.03 g, 0.11 mmol). The reaction was stirred at 45°C for 20 hours, solution was quenched with equal volume cold water and dialyzed for 3 days against ddH_2O. Following 3 days, the product was precipitated out with the addition of NaCl (1 g of per 100 mL of solution) and cold acetone (1 L per 100 mL solution). Precipitate was then redissolved in ddH_2O, frozen, and lyophilized.

5.4.2 Synthesis of Adipic Acid Dihydrazide Norbornene Hyaluronic Acid (HA-Nor-ADH)

HA-Nor (0.13 g, 0.24 mmol) was then modified a second time with an adipic acid dihydrazide (ADH) group for crosslinking. HA-Nor was dissolved in ddH_2O at 2% w/v followed by the addition of ADH (Spectrum Chemical Mfg. Corp., Gardena, CA) at 10 molar equivalences (0.418 g, 2.40 mmol) and hydroxybenzotriazole hydrate (Chem-Impex, Wood Dale, IL) at 1 molar equivalence (0.03 g, 0.24 mmol). The pH was adjusted to 4.75, then 1- 1-Ethyl-3-[3-dimethylaminopropyl] carbodiimide hydrochloride (EDC) (G-Biosciences, St. Louis, MO) EDC was added at 1 molar equivalence (0.05 g, 0.24 mmol). pH was monitored at 4.75 for

2 hours. The reaction stirred for 48 hours, then dialyzed against 0.1 M NaCl for 2 days followed by dialysis against ddH_2O for an additional 2 days prior to being frozen and lyophilized.

5.4.3 Synthesis of Oxidized Alginate (Alg-Ox)

Sodium alginate (low viscosity <20mPa*s and molecular weight <75 kDa) purchased from NovaMatrix (Sandvika, Norway) (1 g, 2.51 mmol) was dissolved at 2% w/v in ddH_2O. Sodium periodate (NaIO4) (Millipore Sigma) was dissolved in ddH_2O at 3% w/v at 0.6 molar equivalence (0.32 g, 1.51 mmol) and then added to alginate in a round bottom flask covered with aluminum foil to protect from light. After letting the solution react for 4 hours, the reaction was quenched with 5 molar excess propylene glycol (Avantor, Center, PA) (0.96 g, 12.56 mmol) and rotated for 2 hours. The solution was then dialyzed against ddH_2O for 2 days, frozen, then lyophilized.[97] HA was oxidized similarly, as previously described.[53]

5.4.4 Peptide Conjugation and Quantification

A 1% w/v solution containing HA-Nor-ADH (10 mg, 0.01 mmol, 0.0016 mmol norbornene), 2 molar excess of RGD (CGRGDSG) (GenScript, Piscataway, NJ) (2 mg, 0.0032 mmol) or IKVAV (CGKIKVAVG) (GenScript) (2.8 mg, 0.0032 mmol) to 1 mol of norbornene, 0.05% w/v Irgacure 2959 Advanced Biomatrix (Carlsbad, California), and PBS was made. A thiol-ene reaction between HA-Nor-ADH and the terminal cysteine was performed by exposing the solution to UV light at a wavelength of 365 nm at 5 mW/cm2 for 5 minutes. The solution was dialyzed against ddH_2O for 1 day before being sterile-filtered, frozen at -80°C, and lyophilized.

The disappearance of thiols after the photoinitiated reaction was detected using Ellman's reagent as previously described.[53] The Ellman's reagent (Fisher Scientific) consisted of 2 mM of 5,5-dithio-bis-(2-nitrobenzoic acid) (DTNB) and 50 mM sodium acetate in 1 M tris(hydroxymethyl)aminomethane (TRIS) buffer. Samples of the reaction before and after UV exposure were diluted to fall within the range of a standard curve of serially diluted peptides. 50 µL of each standard and sample were added to a 96-well plate and mixed with 250 µL of Ellman's reagent. The plate was developed at room temperature for 5 minutes prior to reading absorbance at 412 nm on a microplate reader (BioTek Synergy Neo2).

5.4.5 Degree of Modification (DOM) Determination

Proton nuclear magnetic resonance spectroscopy (^1H NMR, 500Hz, BrukerUSA) was used to quantify the degree of modification of both HA-Nor and HA-Nor-ADH as previously

described.[18,53] A representative spectrum of HA-Nor-ADH can be found in supplementary information (**Figure C1**).

A hydroxylamine hydrochloride titration was performed to quantify the degree of modification of Alg-Ox. The volume of NaOH used in the titration was used in **equation 1** to equate the degree of modification.

Equation 5.1. Hydroxylamine hydrochloride titration equation for oxidation degree of modification

$$\%DOM_{Alg-Ox} = (\frac{198\ g}{mol}\ Alginate * 0.1\ M\ NaOH * \left(\frac{V_f - V_0}{m_{Alg-Ox}}\right)) * 100$$

where 198 g/mol is the monomeric molecular weight of alginate, 0.1 M is the molarity of NaOH used to adjust the solution pH, V_f is the final volume of NaOH in the burette after titration recorded in liters, V_0 is the initial volume of NaOH in the burette before titration recorded in liters, and $m_{Alg\text{-}Ox}$ is the mass in g of Alg-Ox used in the titration.

5.4.6 Preparation of Hyaluronic Acid Alginate (HA-Alg) Hydrogels

To form HA-Alg hydrogels to evaluate the gelation time, compressive modulus, and mass change, 50 µL of HA-Nor-ADH and 50 µL Alg-Ox at varying concentrations (1-3% w/v) were mixed **(Table 5.1)**. Hydrogels used for mass change and gelation time optimization experiments were prepared in 2 mL microcentrifuge tubes. Hydrogels for compression testing were prepared in cylindrical silicon molds with an 8 mm diameter and depth of 4 mm.

5.4.7 Physiochemical Characterization of Hydrogels

5.4.7.1 Gelation Time

The gelation time of the hydrogels were quantified using the inverted tube test.[18] 50µL of HA-Nor-ADH and 50 µL of Alg-Ox at desired concentrations were added to a 2 mL tube, mixed, and inverted once every minute to assess viscosity until gelation. Determination of gelation time began at initial mixing of the two solutions and the time there were no visual signs of fluid flow was recorded.

Table 5.1. Table of hydrogel formulations for physicochemical characterization.

HA-Nor-ADH (% w/v)	Alg-Ox (% w/v)	Hydrogel Polymer Total (% w/v)
1.0	1.0	1.0
1.0	2.0	1.5
1.0	3.0	2.0
2.0	1.0	1.5
2.0	2.0	2.0
2.0	3.0	2.5
3.0	1.0	2.0
3.0	2.0	2.5
3.0	3.0	3.0

5.4.7.2 Compressive Modulus

Hydrogel compression modulus was evaluated using a Discovery Hybrid Rheometer-2 (DHR-2; TA Instruments, New Castle, DE, USA). 100 µL HA-Alg hydrogels were created in cylindrical molds and placed on a Peltier plate maintained at 37°C. Hydrogels were compressed at a constant linear rate of 10 µm/s to 15% of their original heights using an 8 mm aluminum parallel plate.

5.4.7.3 Mass Change

We determined the mass change of the hydrogels over 28 days in PBS and artificial cerebrospinal fluid (aCSF) (NaCl (149 mM), KCl (3 mM), $MgCl_2 * 6H_2O$ (0.8 mM), $CaCl_2 * 2H_2O$ (1.4 mM), $Na_2HPO_4 * 7H_2O$ (1.5 mM), and NaH_2PO_4 (0.2 mM)). 100 µL hydrogels were formed in 2 mL tubes and allowed to crosslink for 24 hours. Initial crosslinked hydrogels were weighed before the addition of 500µL of 0.05% sodium azide in PBS or 500 µL of aCSF in their respective tubes. At 0 hours, 24 hours, 7, 14, 21, and 28 days, the solution was carefully removed from the tubes, and the hydrogel was weighed. The mass change compared to the initial hydrogel mass was calculated at each time point as a percentage using **equation 2**.

Equation 5.2. Percent mass change.

$$Mass\ Change\ (\%) = \frac{(m_{time} - m_{tube\ weight}) - (m_{initial\ crosslinked\ weight} - m_{tube\ weight})}{(m_{initial\ crosslinked\ weight} - m_{tube\ weight})} \times 100$$

5.4.8 Ab2.2 Mouse Embryonic Stem Cell Culture

Mouse embryonic stem cells (mESCs) derived from Ab2.2 mice were cultured on gelatin-coated T-25 flasks. The complete culture medium consisted of high-glucose Dulbecco's Modified Eagle's Medium (DMEM; Gibco) supplemented with 10% newborn calf serum (NBCS; Gibco), 10% fetal bovine serum (FBS; GeminiBio), 1X nucleosides (Sigma-Aldrich), 1000 U/mL leukemia inhibitory factor (LIF; Millipore), and 100 µM beta-mercaptoethanol (BME; Gibco). Cells were passaged every 2 days and seeded at a density of 1.75 x 10^6 cells per flask in fresh complete medium.

5.4.9 Preparing Embryoid Bodies (EBs)

Polydimethylsiloxane (PDMS) microwell inserts (400 x 400 µm inverted pyramids) were used to form 3D embryoid body (EB) aggregates of mESCs. Inserts were sterilized by sonicating twice in 100% isopropyl alcohol, placed in fresh 24-well plates, washed again with 100% isopropyl alcohol, then rinsed three times in excess 1X Dulbecco's phosphate-buffered saline (dPBS) followed by UV sterilization for 30 minutes.

Prior to seeding cells, 500 µL of DFK5 medium was added to each insert and centrifuged at 2000 x g for 5 minutes to remove bubbles. DFK5 consisted of a DMEM/F12 base supplemented with 5% Knockout Serum Replacement (KSR; Gibco), 50 µM non-essential amino acids (NEAA; Gibco), 100 µM BME, 1:100 100X Insulin-Transferrin-Selenium (ITS; Gibco), 1:200 1X Nucleosides. 160,000 cells were seeded into each microwell insert then centrifuged at 200 x g for 5 minutes to achieve approximately 130 cells per EB. EBs were allowed to form undisturbed for 2 days.

5.4.10 Embedding Embryoid Bodies (EBs) into Hydrogels

Solutions of HA-Nor-ADH, HA-IKVAV, and HA-RGD were dissolved at 3% (w/v) in 1X dPBS, while HA-Ox and Alg-Ox were dissolved at 6% (w/v) in dPBS. In a 48-well plate, 250 µL of gelatin were added to control wells and 100 µL of HA-Nor-ADH, HA-IKVAV, or HA-RGD were added to their respective wells.

For each plate, 2 mL of EB suspension was collected from microwells, centrifuged at 200 x g for 5 minutes, and resuspended in 400 µL of DFK5 medium. Next, 50 µL of EBs were gently mixed with HA hydrogels. Finally, 50 µL of the HA-Ox or Alg-Ox were gently mixed into their respective wells, resulting in a final hydrogel volume of 200 µL at a 3% (w/v) concentration. To avoid EB breakage, P200 pipette tips were trimmed using a sterile blade to increase the bore diameter. The hydrogels were allowed to crosslink for 30 minutes before adding 400 µL of DFK5 medium supplemented with 10 nM retinoic acid (RA; Sigma-Aldrich) and 1 µM purmorphamine (Pur; Millipore). The embedded EBs were then cultured for 2 days.

5.4.11 Differentiation and Maturation of V2a Interneurons

Cells were enriched for V2a interneurons following previously established protocols in mESCs.[528,531,532] 2 days of culture, the medium was replaced with DFK5 medium supplemented with 10 nM RA, 1 µM Pur, and 5 µM *N*-[N-(3,5-difluorophenacetyl)-l-alanyl]-S-phenylglycine t-butyl ester (DAPT). DAPT was included to inhibit the Notch signaling pathway and initiate differentiation to V2a interneruons. The EBs were cultured for an additional 2 days.

On Day 6 of the protocol, the cells cultured on gelatin were trypsinized for 5 minutes at 37°C using 0.25% trypsin-EDTA and transferred to laminin-coated wells. To prepare these wells, 150 µL of 0.01% (v/v) poly-L-ornithine solution was added to each well and incubated at 37°C for 1 hour. The poly-L-ornithine was aspirated, and the wells were washed five times with 250 µL Tris-buffered-saline (TBS). 100 µL of 0.01 mg/mL laminin diluted in HEPES buffered saline was added to each well and incubated overnight at 4°C. Prior to plating cells, the laminin solution was aspirated and washed once with HEPES buffered saline.

Approximately 175,000 V2a interneurons were plated in maturation medium (DFK5NB) in each laminin-coated well. DFK5NB consisted of a 1:1 ratio of DFK5 and neurobasal media (Gibco), supplemented with 1X B-27 (Gibco), and 1X GultaMAX (Gibco). The differentiation medium in the hydrogel-containing wells was similarly exchanged for 400 µL of DFK5NB maturation medium on Day 6. All cultures were then maintained until Day 12 of the protocol, with replacement of 50% of the medium performed every 2 days between Day 6 and Day 12 to yield mature V2 interneurons.

5.4.12 Live/Dead Assay

Live/dead assays were performed per manufacturer's instructions. Briefly, 1 µM of Calcein AM and 4 µM of Ethidium Homodimer-1 (EthD-1) were mixed in 1X dPBS, 300 µL of solution were added to each well and incubated at 37°C for 1 hour protected from light. Cells were then imaged using the Zeiss AxioObserver.

5.4.13 RNA Extraction and Purification

Cells were collected for RNA extraction by adding 500 µL of TRIzol reagent (ThermoFisher) to each well and incubating at room temperature for 5 minutes. Following incubation, 200 µL of chloroform were added, and tubes were vortexed for 15 seconds. The tubes were incubated on ice for 10 minutes followed by centrifugation at 12,000 x g for 15 minutes at 4°C to induce phase separation. 150 µL of the upper aqueous phase were collected, mixed with 250 µL of 70% ethanol, and purified using the RNeasy Mini Kit (Qiagen) according to the manufacturer's instructions. To elute the RNA, 30 µL of RNase-free water was added directly to the column membrane and centrifuged for 1 minute at 23,000 x g. To maximize RNA yield, the eluate was pipetted back onto the spin column and centrifuged for additional minute.

5.4.14 cDNA Synthesis

The purified RNA samples underwent cDNA conversion using the High-Capacity RNA-to-cDNA kit (Applied Biosystems). Briefly, 10 µL of RT Buffer and 1 µL of RT Enzyme Mix were added to an 8-tube PCR strip. For each sample, 80 ng of RNA was added, and the final reaction volume was brought up to 20 µL using Ultrapure DNase/RNase free water (Invitrogen). The reverse transcription reaction was performed in a thermocycler with an incubation at 37°C for 60 minutes, followed by enzyme inactivation at 95°C for 5 minutes.

5.4.15 Quantitative Real-Time PCR (qPCR)

For qPCR, a master mix was prepared for each target gene (*Chx10*, *Slc17a6*, *Mapt, Ppia*) by adding 5 µL of PowerTrack SYBR Green Master Mix (Applied Biosystems), 1 µL of a 100 µM primer mix **(Table 5.2)**, and 3 µL of ultrapure RNase/DNase free water per reaction. Next, 9 µL of the respective master mix and 1 µL of cDNA were added to the wells of an optical 96-well reaction plate (Applied Biosystems). The plates were sealed, vortexed, and centrifuged to remove bubbles. qPCR was performed using the BioRad CFX96 Real-Time PCR Detection System with the following thermal cycling conditions: an initial denaturation step at 95°C for 2

minutes, followed by 40 cycles of denaturation at 95°C for 15 seconds and annealing/extension at 60°C for 1 minute. Following amplification, a continuous melt curve analysis was performed (95°C for 15 seconds, 60°C for 1 minute, followed by a temperature ramp to 95°C) to verify product specificity.

Relative gene expression was calculated by using the comparative cycle threshold ($2^{-\Delta\Delta Cq}$) method. Target gene expression was normalized to *Ppia* as the housekeeping gene, and final gene expression levels were reported as $\log_2$ fold change relative to the control group (laminin).

Table 5.2. Table of primer pairs for qPCR listed 5' to 3'.

Target Gene	Forward Primer	Reverse Primer
Ppia	CATACAGGTCCTGGCATCTTGTC	AGACCACATGCTTGCCATCCAG
Chx10	GGCATAATGGATTCCTGTGC	TACAGTCCCCAGAACCTTGG
Slc17a6	CCTATGCTGGAGCAGTCATTGC	GGCTCTCATAAGACACCAGAAGC
Mapt	CCTGAGCAAAGTGACCTCCAAG	CAAGGAGCCAATCTTCGACTGG

5.4.16 Immunocytochemistry

After 12 days of culture, cells were washed with 250 µL of 1X dPBS and fixed with 200 µL 4% (w/v) paraformaldehyde for 30 minutes at room temperature. The wells were then washed three times with 250 µL of 1X dPBS. To permeabilize cells, 200 µL of 0.1% (v/v) Triton X-100 in 1X PBS was added to each well and incubated at room temperature for 15 minutes. The wells were washed three times with 200 µL of washing buffer (0.1% (v/v) Tween-20 in 1X PBS).

To prevent non-specific binding, 200 µL of blocking buffer, consisting of 1% (w/v) bovine serum albumin (BSA), 22.5 mg/mL glycine, 5% (v/v) normal goat serum (NGS) and 0.1% (v/v) Tween-20 in PBS, were added to each well. The plates were incubated overnight at 4°C with shaking at 150 rpm.

The following day, wells were washed three times for 15 minutes each with 200 µL of washing buffer. Cells were then incubated with 200 µL of primary antibody solution, consisting of rabbit anti-βIII-tubulin (1:1000; BioLegend) in 1% (w/v) BSA and 2% (v/v) NGS in 1X PBS overnight at 4°C with shaking at 150 rpm.

After primary antibody incubation, the wells were washed three times for 15 minutes each with 200 µL of washing buffer. Next, 200 µL of secondary antibody solution containing goat anti-rabbit 555 (1:500; Invitrogen) and DAPI (1:1000; Invitrogen) in 1% (w/v) BSA and 2% (v/v) NGS in 1X PBS were added to each well. Plates were incubated overnight at 4°C with shaking at 150 rpm.

Following the secondary antibody incubation, the wells were washed three times with washing buffer with gentle agitation at 20 rpm for 30 minutes at room temperature. Finally, 200 µL of 1X PBS were added to each well, and the cells were imaged using the Zeiss Observer microscope. A summary of antibodies used for immunocytochemistry is found in **Table 5.3**.

Table 5.3. Table of antibodies used for immunostaining.

Antibody	Species	Dilution	Catalog No.
Anti-βTubbIII	Rabbit	1:1000	Biolegend 802001
Anti-Rabbit 555	Goat	1:500	Invitrogen A-21428

5.4.17 Live/Dead Image Analysis

All image analysis was performed with ImageJ. Images were converted to 8-bit image type, and z stacks were projected. Channels were split for Calcein AM (green) and EthD-1 (red). The background was subtracted using a rolling ball radius of 600 pixels, and image contrast was enhanced for saturated pixels of 0.35%. An Ostu threshold was performed and adjusted to include aggregates. Binary images were then cleaned by filling holes, and open commands were used to remove debris. The area and integrated density were measured, and particles larger than 100 µm^2 were analyzed. The percentage viability was calculated using **Equation 5.3**. Brightness and contrast were adjusted using the set display range and applied to all images. The display range for the green channel was 501-63888, and the display range for the red channel was 230-17722.

Equation 5.3. Percent viability.

$$Viability\ (\%) = \frac{Total\ Area\ of\ Green}{Total\ Area\ of\ Green + Total\ Area\ of\ Red} * 100\%$$

5.4.18 Neurite Length Analysis

Image brightness and contrast were adjusted using the set display range and applied to all images. The display range for the blue channel was 16-40, and the display range for the red channel was 50-86. Neurite lengths from the aggregate were manually measured using the neuroanatomy plug in and the simple neurite tracer software in ImageJ.

5.5 Results

5.5.1 Polymer Modifications for the Synthesis of Hydrazone Crosslinked HA-Alg Hydrogels

To form hydrazone-crosslinked HA-Alg hydrogels (**Figure 5.1**), alginate was oxidized resulting in a ring break, exposing aldehydes for crosslinking (Alg-Ox). A hydroxylamine hydrochloride titration was performed to calculate average percent degree of modification (%DOM) or the percentage of aldehydes per chain of alginate, which was 61.26 ± 8.82% with an average percent yield of 72.65 ± 10.93%. HA was then modified with norbornene functional groups as previously described and optimized for a low degree of modification to favor the downstream peptide conjugation.[53,55] The average %DOM or the number of norbornene functional groups per chain of hyaluronic acid was 4.75 ± 2.21% with an average percent yield of 42.77 ± 1.93%. HA-Nor was then functionalized with adipic acid dihydrazide (HA-Nor-ADH) for crosslinking with Alg-Ox. An average %DOM of adipic acid dihydrazide groups per chain of HA determined by 1H NMR was 37.50 ± 5.71% with an average percent yield of 65.19 ± 5.29 %. HA-Nor ADH was then used to conjugate cysteine terminal peptides, IKVAV and RGD using a photoinitiated thiol-ene click chemistry reaction (HA-IKVAV or HA-RGD). The average concentration of peptides conjugated to the backbone of HA was determined to detect using an Ellman's assay which detects the disappearance of free thiol groups before and after UV exposure and conjugation. The average concentration of IKVAV on the polymer was determined to be 12.69 ± 6.10 nmol/mg HA, and the average concentration of RGD on the polymer was determined to be 14.27 ± 7.55 nmol/mg HA. A summary of polymer modifications quantifications can be found in **Tabel C1**.

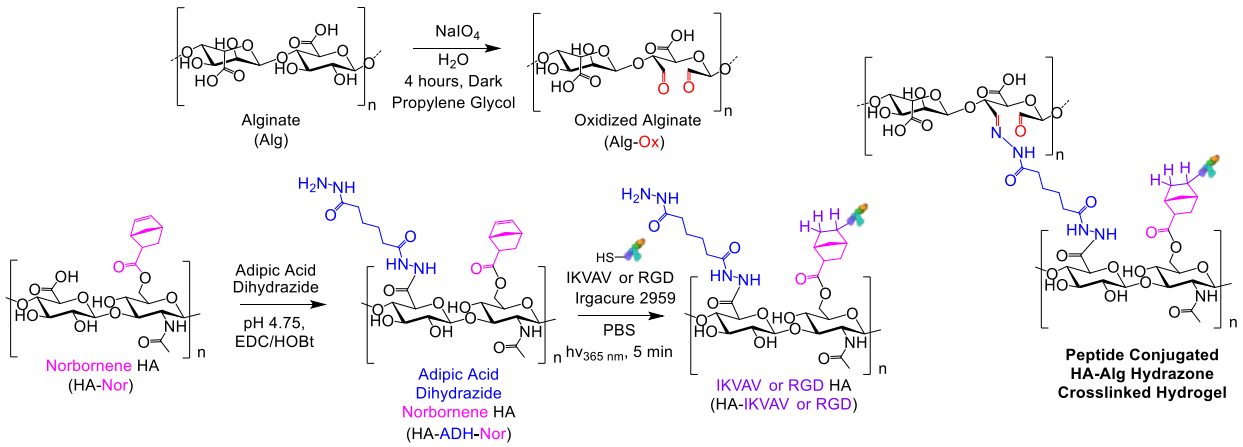

Figure 5.1. Polymer modifications for the fabrication of HA-Alg hydrogels. Alginate was oxidized to reveal aldehyde groups for crosslinking (Alg-OX). An EDC/HoBt coupling reaction was performed with HA-Nor to form HA functionalized with adipic acid dihydrazide and norbornene (HA-Nor-ADH). A photoinitiated reaction between HA-Nor-ADH and the terminal cysteine on the IKVAV or RGD peptide was then performed with UV light at a wavelength of 365 nm. The terminal products of these reactions, HA-Nor-ADH and Alg-Ox, were mixed at different polymer concentrations to produce hydrazone crosslinked hyaluronic acid-alginate (HA-Alg) hydrogels.

5.5.2 HA-Alg Hydrogels Exhibit a Range of Physicochemical Properties

HA and alginate were mixed at different polymer concentrations (1-3% (w/v)) to form hydrogels. We confirmed hydrogel injectability by passing through a needle and the physiochemical properties of the HA-Alg hydrogels were evaluated to determine the optimal hydrogel formulation for neuronal culture. Our target gelation time was between 1 to 5 minutes to produce a workable hydrogel for embedding mESCs for V2a interneuron differentiation and maturation. Increasing the polymer concentrations of the hydrogel decreased the gelation time, likely due to the increase of functional groups available for crosslinking. All hydrogels gelled within 5 minutes except for the $HA_{1.0}Alg_{1.0}$, $HA_{1.0}Alg_{2.0}$, and $HA_{2.0}Alg_{1.0}$ hydrogels with lower polymer concentrations (**Figure 5.2A**). We targeted a hydrogel stiffness that would match the stiffness of CNS tissue (100-1000 Pa). We observed an overall increase in compressive modulus with increasing polymer concentrations (**Figure 5.2B**). The $HA_{3.0}Alg_{3.0}$ hydrogel was the only hydrogel to display a compressive modulus above 100 Pa. Lastly, we measured the mass change

of the hydrogels in both PBS and aCSF over 28 days to observe swelling and degradation over time (**Figure 5.2C-D**). We targeted a stable hydrogel, defined as a mass change of no more than ± 25% of its original mass, over 28 days to enable long-term neuronal culture. Hydrogel stability in both PBS and aCSF decreased as polymer concentrations deviated from a 1:1 stoichiometric ratio. Additionally, hydrogel formulations with higher alginate concentrations were less stable in aCSF compared to PBS due the increased concentration of ions in the solution.

We determined that the hydrogel formulation $HA_{3.0}Alg_{3.0}$ displayed physicochemical properties that best aligned with our desired properties for neural cell culture. This hydrogel exhibited an average gelation time of 1.2 ± 0.3 minutes and compressive modulus of 130.3 ± 9.6 Pa. Although the $HA_{3.0}Alg_{3.0}$ lost more than 25% of its original volume in the first 14 days in both PBS and aCSF, the hydrogel stabilized within 25% of its original mass by day 28. Conjugating IKVAV and RGD peptides to HA-Nor-ADH to form peptide-containing hydrogels resulted in approximately 0.38 ± 0.18 mM of IKVAV per hydrogel and 0.43 ± 0.23 mM of RGD per hydrogel which falls within the concentration needed for neural cell adhesion.[540,541]

5.5.3 HA-Alg Hydrogels Support V2a Interneuron Viability

To evaluate the ability of the HA-Alg hydrogels to support neuronal culture, V2a interneurons were differentiated from mESCs and cultured over 12 days in HA-Alg hydrogels and compared to cells cultured in previously established HA-HA hydrogels and 2D gelatin/laminin-coated control wells.[528,531,532] Following 2 days of forced aggregation, EBs were mixed with either unmodified or peptide-modified HA-ADH, either HA-Ox or Alg-Ox was added, and the hydrogels were crosslinked for 30 minutes. After 12 days of culture, quantitative live/dead analysis demonstrated that the incorporation of the laminin-derived IKVAV peptide was essential for sustaining 3D cell viability at levels comparable to standard 2D laminin controls (**Figure 5.3A and B**). While viability did not differ between any of the hydrogels themselves, cells embedded in the unmodified HA+Alg hydrogels (54.9 ± 2.6%) and RGD-modified HA-RGD+HA and HA-RGD+Alg hydrogels (50.0 ± 7.7% and 52.7 ± 1.4%, respectively) exhibited significantly lower viability than cells in the 2D laminin control (91.4 ± 6.0%). In contrast, IKVAV-modified HA-IKVAV+HA and HA-IKVAV+Alg hydrogels supported cell survival, yielding viabilities (77.1 ± 7.2% and 72.4 ± 20.9%) that were comparable to the 2D laminin control.

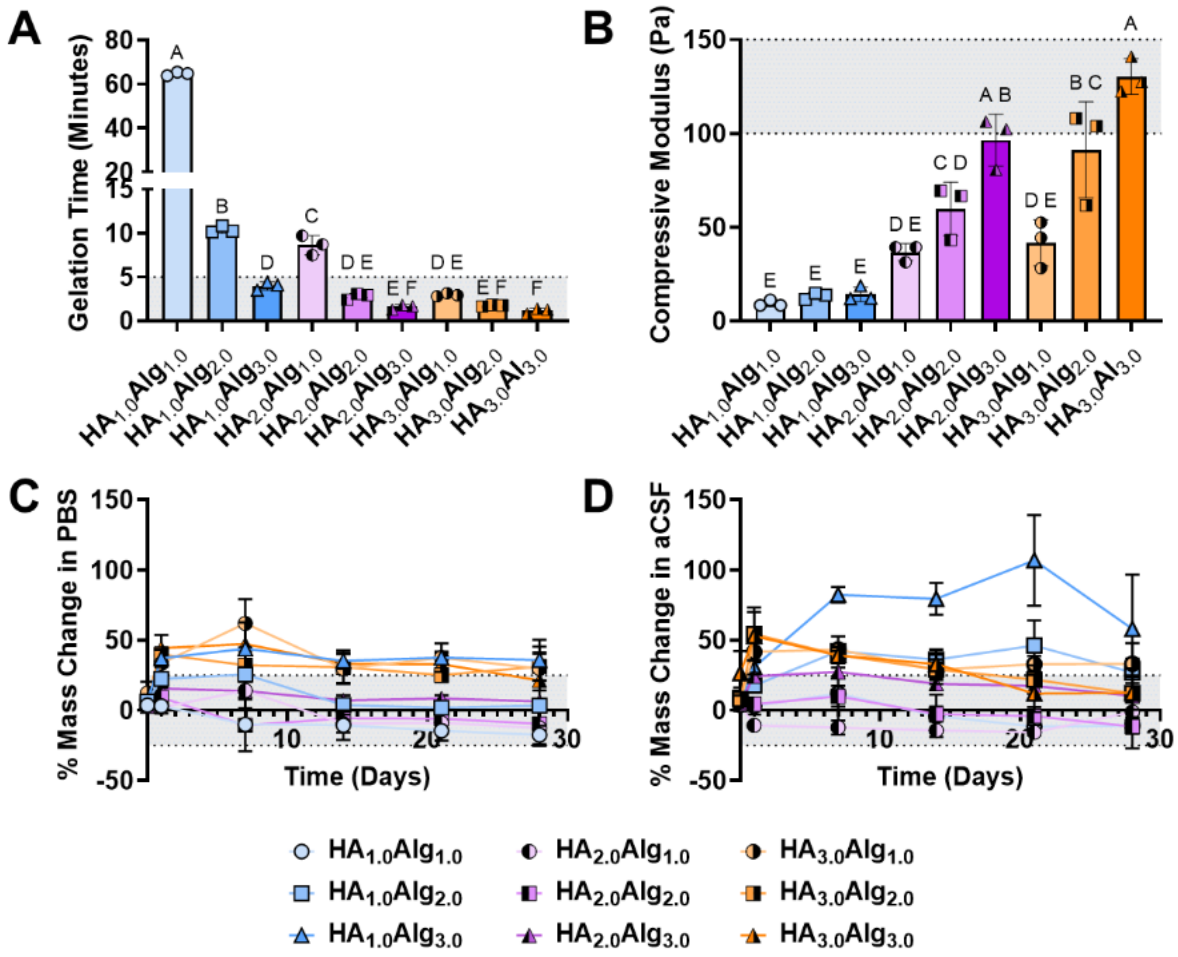

Figure 5.2. **Physiochemical properties of HA-Alg hydrogels**. HA-Alg hydrogels with various polymer concentrations of HA and alginate denoted by subscripts ($HA_{\%\ w/v}Alg_{\%\ w/v}$). Shaded regions indicate desired hydrogel properties. A) The gelation time of HA-Alg hydrogels decreased with increasing polymer concentration. B) The compressive modulus of HA-Alg hydrogels increased with increasing polymer concentration. C) Mass change of HA-Alg hydrogels in phosphate-buffered saline (PBS) over 28 days. D) Mass change of HA-Alg hydrogels in artificial cerebrospinal fluid (aCSF) over 28 days. One-way ANOVA, post hoc Tukey's multiple comparisons was performed for individual replicates. Statistics are summarized using the Compact Letter Display, where differing letters (A, B) represent groups that are statistically different ($p < 0.05$) and the same letter represents groups with no statistical differences ($p > 0.05$) for three technical replicates (n=3).

5.5.4 Evaluation of V2a Interneuron Differentiation in HA-Alg Hydrogels

To assess if the culture had been successfully enriched for V2a interneurons after 12 days, quantitative real-time PCR (qPCR) was performed. Gene expression profiles of cells embedded in all hydrogel formulations were compared to those of cells cultured on standard 2D laminin coatings (**Figure 5.3C**). Primer specificity and reaction efficiencies were confirmed via melt curve analysis and amplification plots (**Figure C3 and 4**), and the stable expression of the endogenous control gene *Ppia* was verified across all samples.

Overall, embedding cells within the hydrogels promoted upregulation of V2a interneuron markers (*Chx10*) and general neuronal maturation markers (*Mapt* and *Slc17a6*) compared to the 2D laminin control (**Figure 5.3C**). Expression of *Chx10*, a transcription factor expressed in V2a interneurons, was upregulated across all hydrogel formulations. Interestingly, despite their restricted morphological development, unmodified hydrogel formulations demonstrated some of the highest relative expression levels of *Chx10*. To assess the maturation of the differentiated neurons, the expression of *Mapt,* a general marker of mature neurons, and *Slc17a6*, the gene that encodes for VGlut2, a marker of excitatory glutamatergic neurons, were evaluated. Similar to the *Chx10* profiles, *Mapt* and *Slc17a6* exhibited positive fold changes across most of the hydrogel conditions compared to laminin.

Importantly, all hydrogel formulations supported comparable expression of *Chx10 and Slc17a6* compared to 2D laminin controls, confirming successful enrichment of V2a interneurons. The comparable gene expression profiles observed across the different hydrogel formulations indicate that the small molecules driving differentiation were efficiently diffusing through the 3D polymer networks, regardless of the polymer type, crosslinking chemistry, and peptide modification. These transcriptional profiles further suggest that early lineage specification was primarily driven by soluble media cues rather than matrix-bound adhesive signals.

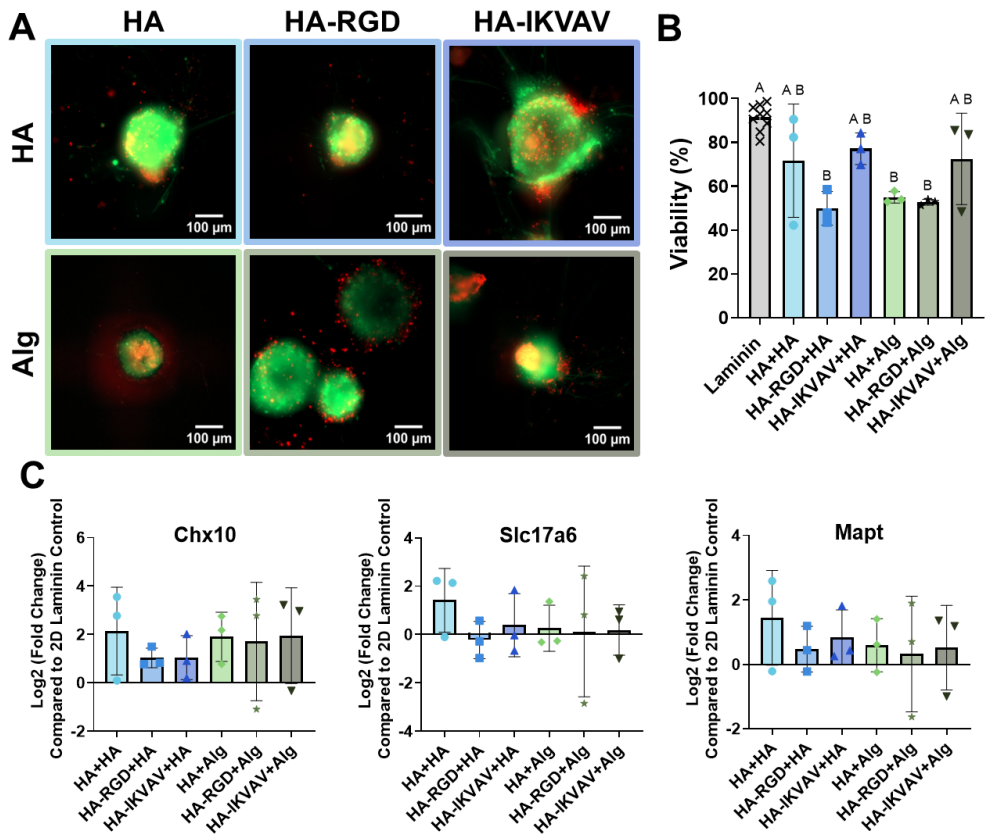

Figure 5.3. V2a interneurons remain viable and express neural marker expression in HA-Alg and HA-HA hydrogels. A.) Representative live/dead fluorescent images of cells encapsulated within hydrogels after 12 days in culture. Live cells are stained green (Calcein-AM), and dead cells are stained red (EthD-1). Scale bars = 100 µm. B.) Quantification of cell viability expressed as the percentage of live cells over total cells. Data are presented as mean ± standard deviation. One-way ANOVA, post hoc Tukey's multiple comparisons was performed for individual biological replicates (N = 3). Statistics are summarized using the Compact Letter Display, where differing letters (A, B) represent groups which are statistically different ($p < 0.05$) and the same letter represents groups with no statistical differences ($p > 0.05$). C.) Relative gene expression (Log2 Fold Change) of neural differentiation markers *Chx10*, *Mapt*, and *Slc17a6* quantified via RT-qPCR. Bars represent the mean Log2 fold change relative to the 2D laminin control, and error bars represent the standard error of the mean (SEM). Individual datapoints represent independent biological replicates (N = 3). No statistically significant differences were found between hydrogel formulations ($p > 0.05$) using a one-way ANOVA with Tukey's post-hoc test.

5.5.5 IKVAV-modified HA-Alg Hydrogels Enhance V2a Interneuron Neurite Outgrowth

The surrounding hydrogel network heavily influenced the morphology and structural maturation of the cells in 3D. To characterize this development, we evaluated EB morphology alongside immunostaining for the neuron-specific microtubule marker βIII-Tubulin (TUBB3) after 12 days of culture. As expected, cells cultured on 2D laminin controls exhibited characteristic planar cellular adhesion and dispersed TUBB3 positive neurite networks (**Figure C5**). In 3D cultures, the biochemical makeup of the microenvironment dictated the structural fate of the V2a interneurons (**Figure 5.4A, C5**). EBs encapsulated within the unmodified hydrogels (HA+HA and HA+Alg) formed dense, DAPI-positive spheroids that maintained tightly restricted morphologies. These structures were characterized by distinct smooth borders and an absence of outward neurite extension. Interestingly, modifying hydrogels with the fibronectin-derived RGD peptide (HA-RGD+HA and HA-RGD+Alg) failed to overcome this physical confinement. TUBB3 staining indicated a lack of macroscopic cytoskeletal extensions with minimal expression restricted to the EB surface. While a small fraction of EBs within these unmodified and RGD functionalized environments occasionally exhibited small projections, overall structural development was negligible.

Conversely, functionalization with the laminin-derived-peptide IKVAV (HA-IKVAV+HA and HA-IKVAV+Alg) established a permissive microenvironment that facilitated extensive structural development. EBs within IKVAV-modified hydrogels demonstrated clear morphological maturation, marked by TUBB3 positive neurites projecting radially into the surrounding 3D hydrogel space. These robust microtubule networks demonstrate that IKVAV not only permits physical cell spreading but actively supports the cytoskeletal assembly required for mature neuronal process extension. While the presence and length of extending neurites naturally exhibited some heterogeneity within samples, outgrowth within the IKVAV-containing hydrogels was overwhelmingly consistent.

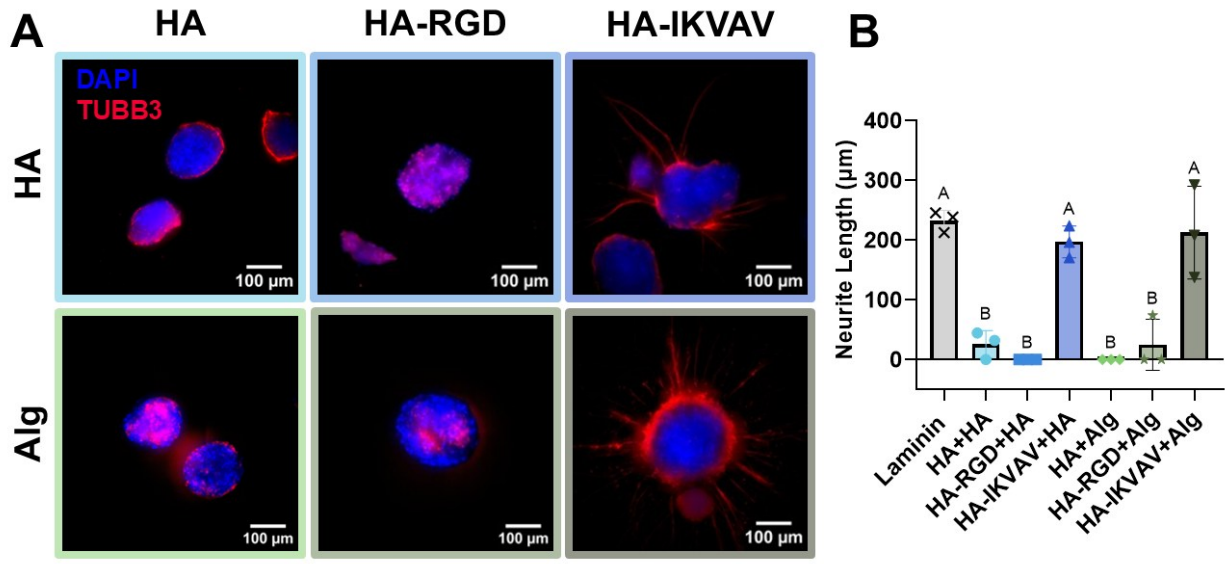

Figure 5.4. Immunostaining assessing V2a interneuron maturation and neurite length. A.) Representative maximum intensity projections of V2a interneurons cultured for 12 days in HA-HA and HA-Alg crosslinked hydrogels (unmodified, RGD, and IKVAV). Cells were immunostained for the neuronal microtubule marker *β*III-Tubulin (TUBB3, red) and nuclei (DAPI, blue). Scale bars = 100 µm. B.) Quantification of average neurite length (µm) extending from the embryoid bodies in various hydrogel formulations and the 2D laminin control. One-way ANOVA, post hoc Tukey's multiple comparisons was performed for individual biological replicates with three technical replicates (N = 3, n=3). Error bars represent the standard error of the mean (SEM). Statistics are summarized using the Compact Letter Display, where differing letters (A, B) represent groups which are statistically different ($p < 0.05$) and the same letter represents groups with no statistical differences ($p > 0.05$).

Quantitative analysis of neurite length corroborated these visual observations (**Figure 5.4B**). IKVAV-modified hydrogels supported substantial neurite outgrowth, averaging approximately 197.2 ± 53.5 µm for HA-IKVAV+HA and 212.4 ± 75.2 µm for HA-IKVAV+Alg hydrogels that was comparable standard 2D laminin controls (232.3 ± 25.6 µm) where robust neurite extension would be expected. Conversely, the unmodified and RGD-modified hydrogels yielded negligible extensions. This morphological divergence demonstrates that incorporating targeted laminin-derived peptides like IKVAV effectively breaks the physical restrictions around

the EBs and drives the maturation and neurite outgrowth of V2a interneurons in 3D. Taken together with the gene expression profiles, while chemical differentiation proceeded efficiently across all groups, the physical architecture and biochemical cues provided for the IKVAV-modified hydrogels was critical for structural maturation.

5.6 Discussion

The successful maturation of neurons within defined 3D hydrogel microenvironments is a critical step toward developing effective cell-based regenerative therapies for SCI. In this study, we developed hydrazone crosslinked HA-Alg hydrogels modified with fibronectin- and laminin-derived peptides (RGD and IKVAV, respectively) and evaluated their capacity to support the viability, lineage specification, and morphological development of mESC-derived V2a interneurons.

A primary challenge in neural tissue engineering is designing scaffolds that mimic the environment of the CNS without sacrificing 3D architecture. By optimizing the polymer concentration to the $HA_{3.0}Alg_{3.0}$ formulation we achieved a compressive modulus of 130.3 ± 9.6, aligning directly with the properties of native CNS tissue (100-1000 Pa). Previous literature has demonstrated that excessive stiffness drives neural progenitor cells toward glial lineage and exacerbate astrogliosis, whereas compliant matrices are permissive to neurogenesis and robust neurite outgrowth.[542] In addition to matching target stiffness, the gelation kinetics of our HA-Alg system were optimized to address the practical challenges of embedding cells in 3D. Slower-gelling systems frequently suffer from gravity-induced cell sedimentation before crosslinking is complete, leading to heterogeneous cell distributions, localized nutrient deprivation, and inconsistent cell-matrix interactions. We observed that the $HA_{3.0}Alg_{3.0}$ formulation gels within 1. 2 ± 0.3 minutes, rapid enough to ensure uniform 3D suspension.[86]

The most significant physicochemical advantage of our system is its long-term stability in physiological fluids. Conventional alginate hydrogels rely on transient ionic crosslinks, which rapidly dissociate in sodium-rich or chelator-containing media due to ion exchange.[543] This premature dissolution limits their utility in neural cultures, as neurons require extended timelines for functional maturation. By using covalent hydrazone bonds between oxidized alginate and ADH-modified HA, our hydrogels overcame this limitation, stabilizing within 25% of their original mass over 28 days in ion-rich aCSF.

We compared HA-Alg hydrogels to a previously established HA-HA hydrogel to specifically evaluate the effects of alginate on cell viability and maturation. While HA is a ubiquitous component of the neural ECM, our results demonstrated that an HA-Alg hybrid system is equally cytocompatible compared to HA-HA hydrogels. This finding is significant as it validates the use of alginate as a tunable and clinically relevant copolymer for neural cell culture that does not compromise the ability of the scaffold to support neural differentiation and neurite outgrowth.

Our findings reveal a notable divergence between differentiation and morphological maturation within these 3D environments. While V2a interneuron differentiation was efficiently driven by soluble cues across hydrogel conditions, we observed that structural maturation and neurite outgrowth required specific ECM-derived peptides **(Figure 5.4A**). Specifically, our findings highlight that, while both the HA-Alg and HA-HA backbones provided a stable structural system for supporting cell viability, the presence of laminin-derived IKVAV was the essential driver for neurite extension, thereby dictating functional cellular behavior.

Gene expression profiling revealed that embedding within both peptide-modified and unmodified hydrogels supported the upregulation of the V2a interneuron transcription factor *Chx10* and mature neuronal markers (*Mapt*, *Slc17a6*) (**Figure 5.3C**). The success of this differentiation across all hydrogel formulations indicates that the small molecules added for differentiation were equally effective across the different hydrogel networks and were not hindered by the crosslinking chemistry or presence of peptides. The successful upregulation of *Chx10* is a critical benchmark for V2a interneuron differentiation, as $Chx10^{+}$ V2a interneurons play an integral role in driving the excitatory pathways of motor neurons and are essential for locomotor initiation. In fact, recent studies have demonstrated that V2a interneurons are explicitly required for the recovery of critical motor functions following cervical SCI, making them a primary therapeutic target for regenerative medicine.[525,530,544,545]

Interestingly, the morphology of V2a interneurons varied drastically across hydrogel formulations. While unmodified hydrogels and hydrogels modified with RGD exhibited tightly confined EB morphology and lacked meaningful neurite projections, IKVAV-modified hydrogels facilitated radial neurite extension (**Figure 5.4A, C5**). Furthermore, immunostaining for TUBB3 revealed dense, radially aligned microtubule networks (**Figure 5.4A, C5**). This structural divergence highlights that, while the basic physical properties of the hydrogels may

permit cell survival, tissue-specific biochemical cues were required to drive structural maturation. Universal cell-adhesive motifs like RGD have been shown to successfully support neural differentiation and neurite extension in specific defined 3D microenvironments, including HA and polyethylene glycol-based hydrogels.[546,547] However, although few V2a interneurons exhibited spontaneous neurite extension in RGD-modified hydrogels similar to unmodified HA hydrogels, the morphological maturation within RGD networks proved highly variable and less robust than IKVAV-functionalized hydrogels. These findings reflect established *in vitro* standards, as laminin is often used in neural differentiation protocols. Furthermore, laminin plays a central role in the native CNS ECM, targeting specific integrin pathways that are essential for neural maturation. By integrating the IKVAV peptide into our 3D scaffold, we successfully recapitulated the biochemical cues traditionally provided by 2D laminin coatings, thereby better mimicking the native CNS environment.

Notably, our peptide conjugation strategy yielded relatively low peptide concentrations compared to conventional hydrogels, resulting in approximately 0.38 ± 0.18 mM IKVAV and 0.43 ± 0.23 mM RGD per hydrogel compared to 2-6 mM observed in literature.[548–550] This quantification offers a compelling explanation for the divergent morphological outcomes, which are likely driven by a combination of the low viability observed in RGD-modified hydrogels and the context-dependent biphasic influence of generic integrin-binding peptides. For example, one study demonstrated that low densities of RGD may provide baseline traction required for growth, but higher ligand densities can rapidly establish excessively rigid focal adhesions.[551] These strong adhesions can anchor the growth cone to the matrix and restrict motility, preventing neurite outgrowth. Consequently, minor batch-to-batch variations in macroscopic hydrogel properties or localized peptide presentation can shift an RGD matrix from a permissive state to a restrictive one. However, given that our peptide conjugation yielded relatively low concentrations, it is more likely that our RGD hydrogels lacked the ligand density required to reach the critical threshold for neural adhesion. This aligns with findings from neurospheres seeded on top of similar HA-RGD-modified hydrogels, which showed that neurite density is dependent on precise RGD concentration.[547] In contrast, IKVAV mimics the native laminin-rich ECM of the central nervous system, engaging neural specific receptors to promote true microtubule assembly, possibly requiring a lower concentration of conjugated peptide for a robust morphological response. While fibronectin-binding integrins are expressed in early stages

of stem/progenitor cell neuronal differentiation, they are reported to be downregulated as neurons mature,[552] and late-stage neurons predominantly express laminin-binding integrins (α1β1 and α6β1).[553] These differences in integrin expression further support the hypothesis that higher concentrations of RGD are needed to activate cell adhesion while lower concentrations of IKVAV may be needed to elicit similar responses.

Native brain and spinal cord ECM heavily rely on complex proteoglycans and structural proteins to regulate the adhesion of neurons and drive subsequent neurite extension.[554] Our results align with recent studies demonstrating that polymers such as alginate or HA lack the requisite motifs to engage neural integrins, thereby acting as physical barriers rather than permissive scaffolds unless modified. For instance, alginate hydrogels functionalized with laminin and gelatin significantly enhanced the neurite outgrowth and migration of human induced pluripotent stem cell derived neurospheres, suggesting that ligand-receptor interactions are required to trigger the cytoskeletal remodeling necessary for axonal extension.[555] Similarly, hydrogels containing alginate and collagen supported robust neural network formation.[556] The success of these hybrid systems is largely attributed to the fact that gelatin and collagen naturally present a high density of cell-adhesive sequences, including RGD, which provide the necessary biochemical anchors for neural attachment. However, when these general motifs support broad neural network formation, V2a interneurons appear to require more specialized signaling for functional development. Specifically, one study found that the incorporation of astrocyte-derived protoplasmic ECM into HA hydrogels promoted V2a interneuron process extension, with the ECM abundant in fibronectin, collagen, perlecan, and laminin.[535,557] In another study, laminin was required to support the viability of V2a interneurons embedded in HA hydrogels and treated with neurotrophin-3.[502] These findings supporting our observation that V2a interneurons are highly sensitive to their microenvironment and require laminin-derived ECM recognition cues for their maturation.

Our use of precise peptide conjugation offers a defined approach to engaging the cell's mechanotransducive machinery. By utilizing IKVAV peptides, we successfully bypassed the restrictive physical boundaries of the hydrogel, allowing mESC-derived interneurons to achieve maturation. The heterogeneity in neurite length observed within these functionalized groups likely reflects the variability of mESC differentiation kinetics and intra-EB spatial positioning,

which could be further optimized in future studies by tuning the peptide density or the degradation rate of the polymer network.

5.7 Conclusion

We successfully engineered an injectable, hydrazone-crosslinked HA-Alg hydrogel designed to meet the complex physicochemical and biochemical requirements of neuronal cell culture with eventual applications in CNS tissue repair. We discovered a fundamental decoupling of biochemical differentiation and morphological maturation of V2a interneurons within 3D microenvironments. While small molecule for neuronal differentiation efficiently permeated all hydrogel formulations to drive the robust transcriptional differentiation of *Chx10*$^{+}$ V2a interneurons, structural maturation required biochemical cell-adhesive cues. Modification of the hydrogels with the laminin-derived IKVAV peptide transformed the matrix into a highly permissive scaffold that maintained cell viability and drove extensive neurite growth. Furthermore, the HA-Alg composite hydrogel outperformed the similarly crosslinked HA-HA network in facilitating this structural maturation, highlighting the advantages of using blended polymer systems. Ultimately, the HA-IKVAV+Alg hydrogel represents a highly tunable, biomimetic platform capable of overcoming the physical restrictions of encapsulating stem cell aggregates in hydrogels. By successfully supporting the survival, differentiation, and structural maturation of therapeutically critical V2a interneurons, this injectable biomaterial offers a promising, minimally invasive strategy to transplant cells to promote functional regeneration following SCI in the future.

5.8 Bridging Paragraph

We investigated the effects of HA-Alg hydrazone-crosslinked hydrogels on the generation, and maturation of V2a interneurons embedded in hydrogels. Functionalizing HA with laminin-derived peptides (IKVAV) showed to be superior in supporting both viable and mature neurons observed by neurite outgrowth from V2a interneurons embedded in hydrogels. We showed that HA and HA-Alg hydrazone-crosslinked hydrogels can provide an environment suitable for neural tissue engineering applications. Therefore, in the next chapter, we used HA hydrogels to deliver glial cell line-derived neurotrophic factor (GDNF) via functionalization with GDNF affibodies. Since GDNF is known to contribute to glioblastoma migration and therapeutic resistance, we combined this platform with aligned melt eletcrowritten (MEW) scaffolds to

engineer *in vitro* models of the glioblastoma microenvironment. Using HA hydrogels to engineer 3D *in vitro* models is an exciting approach to expanding their use in several tissue engineering applications.

CHAPTER 6

CONTROLLED RELEASE OF GLIAL CELL LINE-DERIVED NEUROTROPHIC FACTOR PROMOTES GLIOBLASTOMA MIGRATION ON ALIGNED MELT ELECTROWRITTEN MICROFIBER SCAFFOLDS

This chapter contains unpublished work currently in preparation from Alycia N. Galindo, Maya Kasteleiner, Andy J. Huang, Alyssa K. Chi, Jenna D. Khachatourian, Gabriella CJ. Lindberg, Paul D. Dalton, and Marian H. Hettiaratchi. Controlled Release of Glial Cell Line-Derived Neurotrophic Factor Promotes Glioblastoma Migration on Aligned Melt Electrowritten Microfiber Scaffolds.

6.1 Abstract

Neurotrophic factors play an essential role in regulating neural tissue homeostasis; however, excess amounts of neurotrophic factors can be detrimental in a tumor environment. Specifically, glial cell line-derived neurotrophic factor (GDNF) can contribute to tumor migration and therapeutic resistance in glioblastoma. Glioblastoma is largely a clinical challenge due to accelerated tumor progression and low survival rates following diagnosis. The development of three-dimensional (3D) *in vitro* models of glioblastoma is needed to advance effective therapeutics to the clinic; however, recapitulating the complexity of the tumor microenvironment remains a challenge. We developed hyaluronic acid (HA) hydrogels with controlled GDNF delivery. We combined them with aligned, 3D-printed, melt-electrowritten (MEW) scaffolds to produce a composite scaffold that mimics the biochemical and biophysical cues of the brain involved in glioblastoma progression. Affibodies with low affinity for GDNF were used to enable controlled release from HA hydrogels over 7 days, and the resulting hydrogels were then combined with MEW scaffolds to evaluate the effects of GDNF delivery in a mimetic 3D tumor microenvironment. We observed that GDNF delivery increases cellular migration from glioblastoma spheroids along MEW fibers and may be used to further investigate the glioblastoma microenvironment. The development of this platform can elucidate the roles

involved in tumor progression and may inform the development of effective therapies to improve the long-term survival of glioblastoma patients.

6.2 Introduction

Neurotrophic factors are key signaling proteins that support the growth, survival, and differentiation of neurons and glial cells and have been widely investigated for their use in central nervous system (CNS) tissue repair. Glial cell line-derived neurotrophic factor (GDNF) is produced by neurons and glial cells and acts as a chemoattractant to direct axonal growth and promotes neuronal survival. GDNF signals primarily through the Rearranged During Transfection (RET)-dependent pathway, forming a complex with glycosyl-phosphatidylinositol-anchored GDNF family receptor alpha-1 (GFRα1) and RET that activates the RAS/MAPK, p38MAPK, and PI3K/AKT pathways, which promote cell survival, differentiation, and neurite outgrowth.[558] GDNF is also known to signal through several RET-independent pathways, including a GDNF/GFRα1/neural cell adhesion molecule-1 (NACAM1) signaling pathway that activates the FAK, SRC, and MAPK1/3 pathways to promote cytoskeleton remodeling, neurite outgrowth, and cell migration.[558–560] Exogenous delivery of GDNF to the brain and spinal cord has been shown to promote the survival of both motor and sensory neurons, reduce the area of lost tissue after injury, repair disrupted blood-brain or blood-spinal cord barriers, and decrease the production of inflammatory signals following injury or disease.[430,561–563]

While GDNF is a potent neurotrophic factor for neural tissue repair, high concentrations of GDNF can also contribute to glioblastoma progression and therapeutic resistance. Specifically, GDNF has been reported to increase glioblastoma cell migration and resistance to radio- and chemotherapy.[564,565] Glioblastoma is a highly aggressive cancer with limited treatment options that solely rely on surgical approaches and radio- and chemotherapy.[566] After diagnosis, the median survival rarely exceeded 12 months, even with current treatment options.[567] There is a clear need to develop effective therapies for glioblastoma; however, current therapeutic assessment is limited to 2D models and *in vivo* systems, such as transgenic animal models generated by gene delivery and knockout designs, which often fail to fully recapitulate the complexity of the tumor.[568] Recent efforts have focused on engineering 3D glioblastoma models to study the microenvironment and cellular-extracellular matrix interactions that promote tumor growth. 3D models comprising glioblastoma cell spheroids are often used to investigate cell proliferation and have been grown in

hydrogels and other three-dimensional scaffolds to study tumor invasion and interactions with the tumor microenvironment that may influence tumor progression. For instance, scaffolds made from dynamic polyethylene glycol hydrogels were used to study the influence of viscoelasticity on glioblastoma invasiveness and drug sensitivity.[569] Furthermore, fibrous scaffolds have been used to mimic the white matter tracts and blood vessels in the brain.[570] Although advances in biomaterials that mimic the glioblastoma microenvironment are promising, incorporating biochemical cues, such as GDNF, which influences tumor migration and radio- and chemotherapy responses, can help researchers investigate the cell signaling cascades involved in tumor progression and therapeutic resistance, thereby developing effective treatments for glioblastoma.

Current methods for neurotrophic factor delivery have limited ability to precisely control the release of the protein payload, making it difficult to maintain a therapeutic dosage locally for extended periods.[571,572] Affinity-mediated protein delivery uses affinity interactions between a protein and a material to control the release rate of target proteins.[104,573–576] Traditional affinity-mediated delivery methods use heparin-modified biomaterials to achieve sustained delivery of heparin-binding neurotrophic factors such as GDNF;[441,572,577] however, heparin-based materials lack specificity and tunability to deliver specific proteins at tunable rates, requiring the need for affinity-based molecules with higher specificity. Affibodies are small, highly stable proteins folded into α-helical secondary structure with 17 variable amino acids on the binding interface that can be mutated to confer a desired specificity and affinity to a target protein.[578,579] Affibodies can be modified to contain a terminal cysteine residue for site-specific covalent conjugation to polymers, producing biomaterials for tunable protein delivery. Affibodies have previously been used to control the delivery of several growth factors, including bone morphogenetic protein-2 (BMP-2), platelet-derived growth factor, vascular endothelial growth factor (VEGF), and fibroblast growth factor-2, from hydrogels, in which the affibody affinity and hydrogel properties can be tuned to achieve the desired temporal release of the proteins.[18,573,580]

Hydrogels fabricated from HA are preferred in neural tissue engineering because HA is the most abundant extracellular matrix molecule in the CNS and can be readily modified to mimic CNS mechanical properties, including stiffness and viscoelasticity.[396,581] HA hydrogels are often used to generate 3D glioblastoma models, as HA is overexpressed in malignant glioma cells.[582] Furthermore, glioma stem-like cells express high levels of CD44, which is primarily activated by binding to HA, to activate downstream signaling pathways that promote tumor cell invasion and

proliferation.[583–585] In addition to HA hydrogels, nano- and microfibrous scaffolds have previously been used in glioblastoma models to provide topographical cues resembling white matter tracts and blood vessels in the brain.[570,586–588] However, current methods for producing scaffolds for glioblastoma models often fail to mimic the highly organized alignment the brain's extracellular matrix. Anisotropically aligned scaffolds can resemble the brain's native architecture and serve as a platform for investigating tumor migration.[588,589] Melt electrowriting (MEW) is an additive manufacturing method that uses the extrusion of molten polymers, such as poly (ε-caprolactone) (PCL), under an electric field to create nano- and microfibrous scaffolds that can guide cellular alignment.[587] By fine-tuning the extrusion and voltage parameters, MEW fibers can be precisely placed onto a moving collector to form highly aligned scaffolds that may be difficult to achieve using other 3D printing techniques.

Here, we fabricated HA hydrogels with affinity-mediated GDNF delivery that provide biochemical cues to reflect the cell signaling pathways involved in tumor migration and therapeutic resistance. We then combined this hydrogel platform with anisotropic scaffolds to engineer 3D models that further provide biophysical cues to investigate how the brain's extracellular matrix influences glioblastoma tumor invasion and progression. Affibodies specific to GDNF were identified using sequential rounds of magnetic- and fluorescence-activated cell sorting of a yeast surface display library of affibody variants. Affibodies specific to GDNF were synthesized by solid-phase peptide synthesis and conjugated to a dynamic hydrazone-crosslinked HA hydrogel to enable controlled release of GDNF. Glioblastoma spheroids were then seeded on MEW scaffolds embedded in HA hydrogels to evaluate cell migration. Nuclei staining was used to quantify glioblastoma cell migration along scaffolds. The development of this platform is valuable for investigating the roles of HA and GDNF in tumor progression and therapeutic resistance in a microenvironment with topographical cues that mimic the brain's extracellular matrix, ultimately serving as a high-throughput screening platform for novel therapeutics to treat glioblastoma and to further elucidate the role of GDNF in therapeutic resistance.

6.3 Materials and Methods

6.3.1 Isolation of GDNF Specific Affibodies from a Yeast Surface Display Library

6.3.1.1 Yeast Induction Check

S. cerevisiae EBY100 yeast containing a pCT surface display vector for galactose-induced protein expression of $4x10^8$ diverse affibody variants was used as the starting library.[573,580] Yeast were grown in selective growth media (16.8 g sodium citrate dihydrate, 3.9 g citric acid, 20.0 g dextrose, 6.7 g yeast nitrogen base, 5.0 g casamino acids, 1 mg ciprofloxacin and 100 mg ampicillin in 1 L double distilled water (ddH_2O) at 30°C in an incubator (Innova) with orbital shaking at 250 rpm until a final concentration of 10^7 cells/mL. 15x the yeast diversity was then pelleted and resuspended in selective induction media (10.2 g sodium phosphate dibasic heptahydrate, 8.6 g sodium phosphate monobasic monohydrate, 19.0 g galactose, 1.0 g dextrose, 6.7 g yeast nitrogen base, 5.0 g casamino acids, 1 mg ciprofloxacin and 100 mg ampicillin in 1 L ddH_2O) and incubated at 30°C with orbital shaking at 250 rpm for approximately 20 hours.

Terminal c-myc tags were included within the yeast plasmid reading frame to identify the expression of affibodies on the surface of yeast. Induction of affibody expression was confirmed using flow cytometry prior to proceeding with magnetic activated cell sorting using an Accuri C6 Plus flow cytometer (Becton Dickinson). Controls with unstained cells and cells stained only with secondary antibodies were used to determine gating boundaries. 10^6 cells were pelleted and washed with 1mL of 0.1% w/v BSA in phosphate-buffered saline (PBSA) before being pelleted and resuspended in 50 µL of PBSA. Cells were then incubated with primary mouse α c-myc (9E10; BioLegend) antibody for 20 minutes rotating at 4°C to confirm affibody expression. After, cells were washed and pelleted in 50 µL of PBSA and a fluorescent secondary antibody, goat α mouse-Alexa flour 488 (Thermo Fisher) was incubated for 15 minutes rotating at 4°C. Cells were then washed and resuspended in 200 µL and transferred to a 96-well plate for flow cytometry analysis. Flow cytometry was used to determine the percentage of yeast expressing the affibody and to confirm successful induction before proceeding with magnetic-activated cell sorting.

6.3.1.2 Magnetic Activated Cell Sorting

Carboxylic acid magnetic beads (Invitrogen Dynabeads M-270 Carboxylic Acid) were conjugated with tris(hydroxymethyl)aminomethane) (TRIS), bovine serum albumin (BSA), and GDNF (PeproTech) using carbodiimide chemistry as previously described.[573] Magnetic beads conjugated with TRIS and BSA were used as negative sorts prior to sorting with magnetic beads conjugated with 33 pmol of GDNF to remove non-specific binders. Briefly, 15x the affibody diversity was washed and reconstituted in BSA-conjugated magnetic beads for 2 hours rotating at 4°C. The solution was then exposed to a magnet, and the unbound yeast was removed and transferred to TRIS-conjugated magnetic beads for 2 hours at 4 °C while rotating. The solution was exposed to a magnetic field, and the unbound yeast was then transferred to GDNF-conjugated magnetic beads for an additional 2 hours, with rotation at 4°C. The solution was exposed to the magnet, and the bound yeast was collected. Yeast bound to the magnetic beads for the BSA-, TRIS-, and GDNF-conjugated magnetic beads were then diluted 100x and 2000x in PBSA before plating 10 µL of the solution on selective growth plates (16.8 g sodium citrate dihydrate, 3.9 g citric acid, 16 g bacto agar, 20 g dextrose, 6.7 g yeast nitrogen base, 5 g casamino acids, ddH_2O water) and incubated for 36 hours at 30 °C. The remaining bound yeast on GDNF-conjugated magnetic beads was placed in selective growth media to expand for another round. Colonies that grew on the selection plates were used to calculate the diversity of the new yeast library and the ratio of positive-to-negative affibody binders. The yeast library was enriched over 4 rounds of MACS before binders were isolated by FACS.

6.3.1.3 Fluorescence Activated Cell Sorting

For FACS, GDNF was biotinylated using an EZ-Link Sulfo-NHS-Biotin Kit (Thermo Fisher Scientific), and the biotinylation of GDNF was confirmed (~2 biotin/mol GDNF) using the HABA/Avidin Biotinylation Quantification Kit (Thermo Fisher Scientific) per manufacturer's instructions. 10^6 cells from the final magnetic-activated cell sort were pelleted and used as controls, including unstained cells and cells stained only with secondary antibodies, to determine gating boundaries. For the cell sorting, 40 x 10^6 cells were resuspended in 50 µL of PBSA with 1 µM biotinylated GDNF and 2.5 µL of α c-myc antibody and incubated for 1 hour rotating at 4 °C. Yeast were then washed and resuspended in 50 µL of a solution containing 10.4 µL of 333 nm goat anti-mouse IgG AlexaFluor 647 and 3.25 µL of AlexaFluor 488 streptavidin conjugate, 187 µL PBSA (secondary solution), and incubated for 30 minutes rotating at 4 °C.

Cells were then washed and resuspended in 1 mL of PBSA and sorted using a SH800 Cell Sorter. Yeast exhibiting binding to GDNF were collected and grown to a density of 10^7 cells/mL for a second sort. Following the second sort, yeast was plated on selective growth plates and incubated for 36 hours at 30°C.

6.3.2 Gene Sequencing of GDNF-Specific Affibodies

Monoclonal yeast isolated from agar plates post-FACS were grown in selective growth medium to a density of 10^7 cells/mL. Yeast plasmids were collected using Zymo Research Corporation Zymoprep™ Yeast Plasmid Miniprep II Kit per manufacturer's instructions. Affibody sequences were amplified by polymerase chain reaction (PCR) in an Applied Biosystems Thermocycler (Fisher Scientific) using HiFi PCR Premix (CloneAmp), forward primer (5′-CCCTCAACAACTAGCAAAGG-3′), and reverse primer (3′-ATGTGTAAAGTTGGTAACGGAACG-5′) for 35 cycles and purified using a DNA Clean and Concentrator Kit (ZymoGen). Purified products were sequenced using Sanger sequencing by Genewiz.

6.3.3 GDNF-Affibody Yeast-Bound Specificity and Affinity

Flow cytometry was used to confirm GDNF binding to affibodies as previously described.[573,580] Briefly, 10^6 induced monoclonal GDNF-specific yeast were incubated in 50 µL of PBSA with biotinylated GDNF, 1.25 µL of α c-myc antibody, and incubated for 1 hour rotating at 4 °C. Yeast were then washed and resuspended in 50 µL of a secondary solution and incubated for 30 minutes rotating at 4 °C. Cells were then washed and resuspended in 200 µL of PBSA and transferred to a 96-well plate for flow cytometry analysis using an Accuri C6 Plus flow cytometer. We successfully identified 6 unique affibodies that showed binding to GDNF. The affibody, which showed the highest percentage of yeast bound to 1 µM GDNF, was then used to calculate its affinity across a range of GDNF concentrations (0.5-6 µM). The ratio of yeast-bound to GDNF to unbound yeast was plotted against the concentration of GDNF to determine the yeast-bound equilibrium dissociation constant (K_D).

6.3.4 Solid Phase Peptide Synthesis

The GDNF affibody was synthesized using Fmoc SPPS as previously described. Affibodies containing penultimate cysteine and C-terminal glycine were synthesized using a Liberty Blue 2.0 microwave peptide synthesizer (CEM Corporation). Briefly, F-moc amino acids

were dissolved in dimethylformamide (DMF) at 0.5 M. 8% v/v of pyrrolidine (Sigma Aldrich) was used as a deprotection reagent and 0.26 M of Oxyma (CEM Corporation) and 0.75 M of DIC (Oakwood Chemical) in DMF were used as activation reagents. Fmoc-Gly-Wang (CEM Corporation) resin at a loading of 0.602 mmol/g was weighed and allowed to swell in DMF at least 10 minutes before synthesis.

After synthesis, resin-bound affibodies were washed with dichloromethane twice and resuspended in a solution containing a 1:1:1:1:36 ratio of ddH_2O, triisopropyl silane (Oakwood Chemical), 2,2'-(ethylenedioxy)diethanethiol (Tokyo Chemical Industry), thioanisole (Oakwood Chemical), and trifluoroacetic acid (Oakwood Chemical) for 1-2 hours at 42 °C for cleavage from the resin. The solution was vacuum-filtered, and the filtrate was precipitated and washed using cold diethyl ether three times. The precipitated affibody was then resuspended in 10% acetic acid and sonicated for 2 hours before freezing and lyophilizing. The expected molecular weight was confirmed using matrix-assisted laser desorption/ionization time of flight (MALDI-TOF) Smart LS system (Bruker).

Crude affibody products were then purified using high performance liquid chromatography (CEM Prodigy). Affibody products were dissolved in 3% v/v acetonitrile and 0.1% v/v trifluoroacetic acid in ddH_2O, and the sample was run through a 19 x 150 mm C18 Waters column with a gradient of 3 to 65% v/v acetonitrile and 0.1% v/v trifluoroacetic acid in ddH_2O. Affibodies were eluted from the column at 50- 55% v/v acetonitrile in ddH_2O. The purity of the affibody was confirmed through MALDI-TOF.

6.3.5 GDNF-Affibody Characterization

6.3.5.1 Circular Dichroism

A circular dichroism spectropolarimeter (Jasco J-815) was used to characterize the secondary protein structure of the affibody. Purified affibody was reconstituted in 5 nM TRIS buffer at a pH of 8 at 0.3 mg/mL, and 200 µL was loaded into a quartz cuvette (Starna Cells, Inc.) with a 1 mm path length. Circular dichroism spectra were obtained between 190-250 nm and the molar ellipticity was calculated using the affibody molecular weight and concentration.

6.3.5.2 Biolayer Interferometry

Affibody binding kinetics were calculated using biolayer interferometry (Gator Bio). 50 nM of biotinylated GDNF was loaded onto streptavidin-coated probes in PBS. 1500 nM of

affibody was then loaded onto the probe for 600 seconds before dissociating in PBS for 600 seconds. Background subtraction of a reference well and non-specific reference were used. The dissociation constant (K_D), the association constant (k_{on}) and the dissociation constant (k_{off}) were then calculated using the association then dissociation nonlinear fit in GraphPad Prism.

6.3.6 Hyaluronic Acid Hydrogel Fabrication

HA hydrogels were fabricated as previously described.[18,53,592] Briefly, HA was first modified with a norbornene functional group using Boc_2O-activated coupling for affibody conjugation (HA-Nor). HA-Nor was then modified with an adipic acid dihydrazide functional group (HA-Nor-ADH) via carbodiimide chemistry to crosslink with oxidized hyaluronic acid (HA-Ox).

6.3.6 Conjugation of GDNF-Affibodies for Controlled Delivery of Glial Cell Line-Derived Neurotrophic Factor

5 mg of HA-Nor-ADH was dissolved at 20 mg/mL, and 250 µL of 20 mg/mL of affibody in PBS was added. 0.015% w/v Irgacure 2959 was added to the solution, which was then exposed to UV at 365 nm at 5 mW/cm2 for 10 minutes. The solution was then dialyzed against ddH_2O for 1 day. The solution was then filtered, frozen at -80 °C, and lyophilized.

The Pierce 660 protein quantification assay was used to determine the affibody concentration per mg of HA-Nor-ADH, as previously described.[18] Briefly, 2 mg of polymer was dissolved at 1% w/v in PBS, and 10 µL of affibody-conjugated polymer was added to a 96-well plate. An affibody ladder ranging from 0.1 to 2 mg/mL in PBS was used to create a protein standard curve. 150 µL of the Pierce 660 reagent was then added to each well containing the sample and standard, and the plate was incubated at room temperature for 5 minutes before reading at 660 nm (BioTek Synergy Neo2).

6.3.7 Controlled Release of GDNF

Affibody-conjugated polymer was dissolved at 2% w/v and diluted with unconjugated polymer dissolved at 2% w/v to achieve a 500 times molar excess of affibody (1.65 nmol/mg of HA) to 100 ng of GDNF. 50 µL of affibody-conjugated HA-Nor-ADH, 40 µL of 2.5% w/v oxidized hyaluronic acid, and 10 µL of 0.01 µg/µl GDNF in PBS were then added to a flat-bottom 2 mL tube to form affibody-conjugated hydrogels. Hydrogels were crosslinked for 4 hours at 37 °C, then washed with 200 µL of DMEM containing 10% FBS; the media were

collected to calculate encapsulation efficiency. 900 µL of media was then added, and the tubes were incubated at 37 °C. 200 µL aliquots were then collected and replaced at 4 hours and 1, 3, 5, and 7 days. A GDNF ELISA kit (R&D Systems) was then used to determine the amount of GDNF released at each time point. The initial wash was diluted 30x while all other points were diluted 40x. The initial encapsulation efficiency and cumulative release of GDNF over 7 days were then calculated.

6.3.8 U-87 Glioblastoma Cell Culture

U-87 MG glioblastoma cells (ATCC) were thawed from liquid nitrogen storage and expanded in Dulbecco's Modified Eagle Medium (DMEM, Gibco) containing 10% v/v fetal bovine serum (FBS) and 1% v/v penicillin-streptomycin in a T75 flask until the culture reached 70-80% confluency. 3 mL of trypsin was then added to the flask, and the flask was incubated for 5 minutes at 37 °C to detach the cells. 7 mL of expansion media was added to the flask, and cells were transferred to a 15 mL Falcon tube for centrifugation at 125 g for 5 minutes. The supernatant was removed and resuspended in 1 mL for a cell count using a hemocytometer.

6.3.9 U-87 Glioblastoma Spheroid Formation

8,000 cells per well were added to a 96 V-bottom plate, and media was added to a total of 200 µL. Cells were then centrifuged at 1640 g for 5 minutes, then incubated for 7 days at 37°C. Partial media changes were performed every two days.

6.3.10 Aligned Melt-Electrowritten Scaffold Fabrication

Poly(ε-caprolactone) (PCL) scaffolds were fabricated using a custom melt electrowriting (MEW) setup equipped with a 22 G stainless steel nozzle (6 mm length) protruding approximately 1 mm from the printhead. PCL was heated to 64°C and extruded at a pressure of 0.38 bar. Fibers were deposited onto a 2.4-mm-thick glass slide positioned at a nozzle-to-collector distance of 1.5 mm. An accelerating voltage of 4.0 kV and a collector translation speed of 500 mm min^{-1} were used for scaffold fabrication. A dwell time of 0.3 s was incorporated at each change in printing direction to ensure stable fiber deposition and accurate fiber placement. To improve scaffold handling and mechanical stability, a reinforcing ring was printed around the scaffold perimeter following deposition of the main scaffold. The reinforcement ring was fabricated using the same temperature, voltage, and collector distance conditions as described

above, but with an increased extrusion pressure of 4.0 bar and a reduced collector speed of 20 mm min^{-1}. Single reinforcement rings were used for all experiments unless otherwise specified.

Melt electrowritten scaffolds were etched in 1 M NaOH for 15 min and washed with PBS. Scaffolds were subsequently sterilized in 70% ethanol for 1 h, then exposed to UV for 30 min.

6.3.11 Soluble Glial Cell Line-Derived Neurotrophic Factor Delivery to Glioblastoma Spheroids

To seed GBM spheroids in HA-MEW composite scaffolds, 150 µL of 1% or 2% w/v HA-Nor-ADH was added to a 24-well plate, and MEW scaffolds were then added to their respective well. A single GMB spheroid in 50 µL of expansion medium was then gently seeded onto MEW scaffolds and allowed to attach for 30 minutes, after which 100 µL of 1.5% or 2.5% w/v HA-Ox was added. Hydrogels were allowed to crosslink for 4 hours, incubated at 37°C, then 500 µL of expansion media containing 50 ng/ml GDNF was added, and cells were incubated for 7 days at 37 °C. Partial media changes were performed every 2 days with expansion media containing 50 ng/mL GDNF.

6.3.12 Controlled Glial Cell Line-Derived Neurotrophic Factor Delivery to Glioblastoma Spheroids

150 µL of a 2% w/v HA-Nor-ADH-Affibody solution containing 100 ng of GDNF was added to a 24-well plate, and MEW scaffolds were then added to their respective well. A single GMB spheroid in 50 µL expansion media was then gently placed on top of MEW scaffolds and allowed to attach for 30 minutes before adding 100 µL of 2.5% w/v HA-Ox. Hydrogels were allowed to crosslink for 4 hours and incubated at 37°C before adding 500 µL of expansion media. Partial media changes using expansion media were then performed every 2 days.

6.3.13 Immunocytochemistry and Image Analysis

Samples were fixed in 4% paraformaldehyde, washed with PBS three times, and then blocked and permeabilized for 30 min in 2% w/v bovine serum albumin (BSA) containing 0.1% v/v Triton X-100. F-actin was stained using rhodamine phalloidin 594 for 1 h. 50 minutes into the incubation, nuclei were stained with DAPI (1:1000) for an additional 10 minutes. Samples were stored in PBS at 4°C.

Fluorescently stained samples were imaged using a 10x objective on a SoRa spinning disk confocal microscope (Nikon, Tokyo, Japan) equipped with a 405 nm laser for DAPI

excitation and a 561 nm laser for rhodamine phalloidin 594 excitation. Z-stack images were processed in FIJI (ImageJ). Single-cell migration distances were subsequently quantified using a custom Python script.

6.4 Results

6.4.1 Discovery and Isolation of GDNF Affibodies

A library of yeast displaying $4x10^8$ unique affibodies on their surface was subjected to MACS to enrich the library for affibodies with affinity for GDNF. (**Figure 6.1A**). After each sort, yeast bound to both the negative and positive beads was collected and grown out on agar plates to calculate the new total yeast diversity (number of colonies on positive plates) and the positive-to-negative ratio of binding yeast (number of colonies on positive plates divided by the number of colonies on negative plates) (**Figure 6.1B**). Following the 4th sort, the positive-to-negative ratio increased, indicating enrichment of the yeast library for GDNF specificity, with approximately 47% of the yeast library displaying affinity for GDNF. Furthermore, the resulting yeast library decreased by more than 2500 times after MACS. FACS was then performed on the enriched population to isolate affibodies with affinity for GDNF (**Figure 6.1C**). While only 33% of the population showed affibody expression following MACS, 0.91% showed both affibody expression and binding to GDNF. This population was collected and grown out for another round of FACS (FACS 1); the resulting population showed increased affibody expression and GDNF binding, with a total double-positive population of 1.52%. This process was repeated, and the new population was then placed on agar plates to isolate monoclonal yeast for sequencing. Yeast plasmids were extracted, and the affibody sequence was amplified using PCR for sequencing. Sequencing confirmed 6 unique affibody sequences, and single colonies were evaluated for GDNF binding using flow cytometry with 1 μM of GDNF. Through this process, we moved forward with one GDNF affibody.

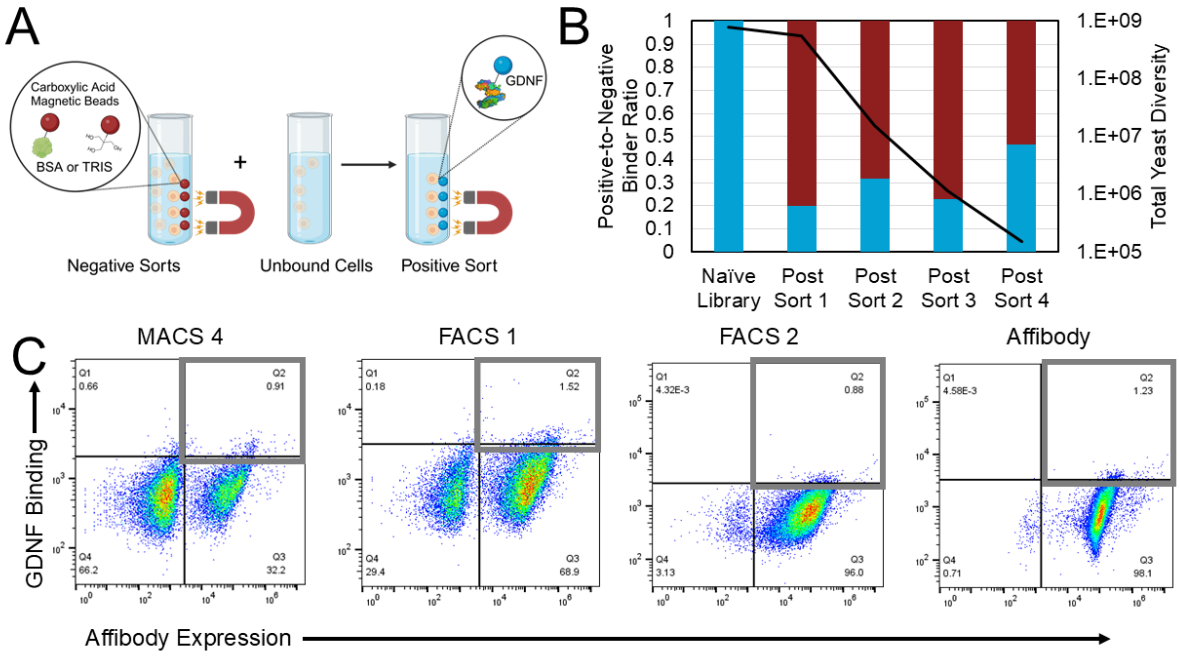

Figure 6.1. Sorting of an affibody-displaying yeast surface display library identified one GDNF affibody. A) MACS was performed using TRIS or BSA-conjugated beads as negative sorts. Unbound yeast cells were then collected and used for a positive sort with GDNF-conjugated beads. B) The positive-to-negative ratio of GDNF-binding yeast following each round of MACS and the total diversity of the yeast library at each sorting step. C) Two rounds of FACS were performed on the MACS-enriched yeast library, leading to the discovery of a GDNF affibody. Boxes indicate the double-positive yeast population for GDNF that was isolated by FACS for subsequent sorting steps.

6.4.2 Characterization of GDNF Affibody

The affibody was then synthesized using Fmoc SPPS and purified using HPLC. Affibody purity was evaluated using sodium dodecyl sulfate-polyacrylamide gel electrophoresis (SDS-PAGE) and MALDI (**Figure 6.2A and B**). A single band or peak at the expected affibody molecular weight confirms affibody purity. Circular dichroism was then used to assess proper protein folding of the purified affibody, which confirmed the characteristic α-helical affibody secondary protein structure by a peak in molar ellipticity at 195 nm and minima at 208 and 222 nm (**Figure 6.2C**).

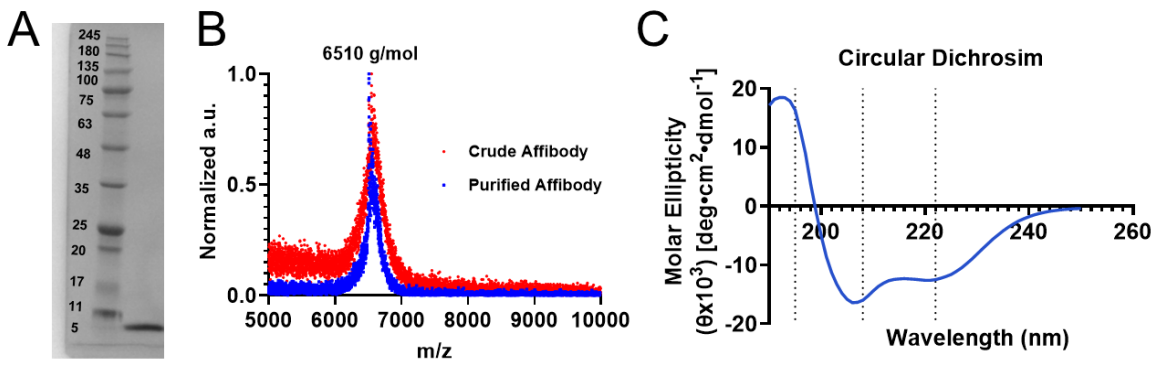

Figure 6.2. Synthesis of affibody and characterization of secondary structure. A) Sodium dodecyl sulfate-polyacrylamide gel electrophoresis (SDS-PAGE) confirmed affibody purity by the presence of a single band at the expected molecular weight. B) Crude (red) and purified (blue) MALDI peaks of affibody displayed a definite peak at the expected molecular weight. B) Circular dichroism on the synthesized and purified affibody confirmed the α-helical affibody secondary protein structure by a peak in the molar ellipticity at 195 nm and a minimum at wavelengths 208 and 222 nm.

The equilibrium dissociation constant for GDNF binding to the GDNF-specific affibody displayed on monoclonal yeast was calculated by measuring the fraction of yeast bound to GDNF across a range of GDNF concentrations using flow cytometry (**Figure 5.3A).** The inflection point was determined using a nonlinear Boltzmann sigmoidal fit, and the K_D was calculated to be 2.9 μM, which is considered relatively low based on previous work.[579,593,594] Biolayer interferometry of the purified affibody was used to determine the association and dissociation rates and confirm the purified affibody K_D (**Figure 6.3B**). The association constant (k_{on}) was 778.3 M–1 s–1, and the dissociation constant (koff) was 0.0017696 s^{-1}. The equilibrium dissociation constant from biolayer interferometry was calculated to be 2.3 μM, which closely agreed with the K_D observed by flow cytometry.

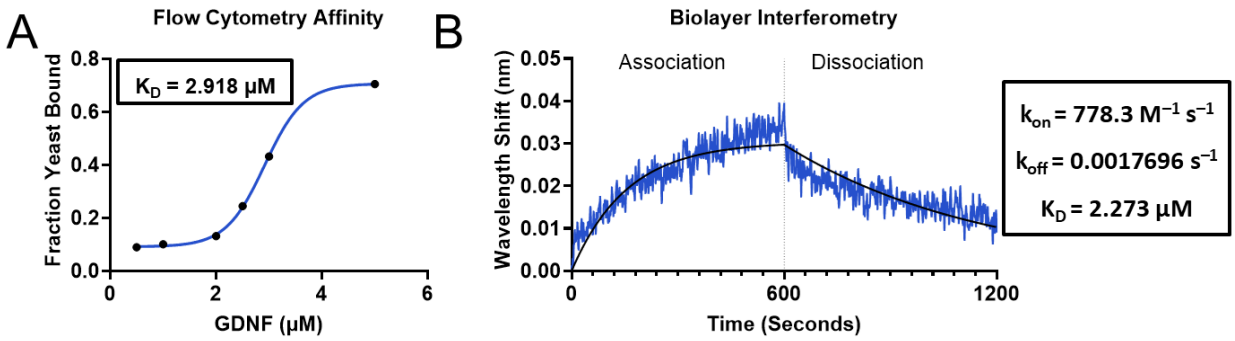

Figure 6.3. Affinity characterization of GDNF affibody. A) Affibody dissociation constant (K_D) was determined using a range of GDNF concentrations. The fraction of yeast bound was plotted against GDNF concentration, and a Boltzmann sigmoidal fit was used to determine the K_D. B) Biolayer interferometry of affibody associating then dissociating to GDNF-loaded probes to determine the association (k_{on}) and dissociation (k_{off}) constants and K_D.

The predicted binding interface of the affibody and GDNF with respect to GFRα1 receptor was then inspected using AlphaFold 3 and PyMOL (**Figure 6.4**). Interestingly, the predicted binding interface of the affibody with GDNF was not in the same interface as the GFRα1 receptor. Previously discovered yeast display affibodies have often been predicted and shown to overlap with the receptor.[573] However, more recently, interleukin-4-specific affibodies have shown binding that differs from the receptor binding interface.[595] From this prediction, we further hypothesized that GDNF would remain available to interact with GFRα1 in its bound state, localizing the protein within a hydrogel and allowing the activation of downstream signaling pathways.

6.4.3 Affibody Conjugated HA Hydrogels Sustain GDNF Release

HA was modified with norbornene functional groups for affibody conjugation and adipic acid dihydrazide functional groups (HA-Nor-ADH) for crosslinking with oxidized hyaluronic acid (HA-Ox). Affibodies were then conjugated to the norbornene functional group on HA-Nor-ADH using a thiol-ene photoinitiated reaction. 100 ng of GDNF was added to each hydrogel, with varying molar excesses of affibodies, then the hydrogels were crosslinked with HA-Ox and submerged in media. The amount of GDNF encapsulated in hydrogels with and without

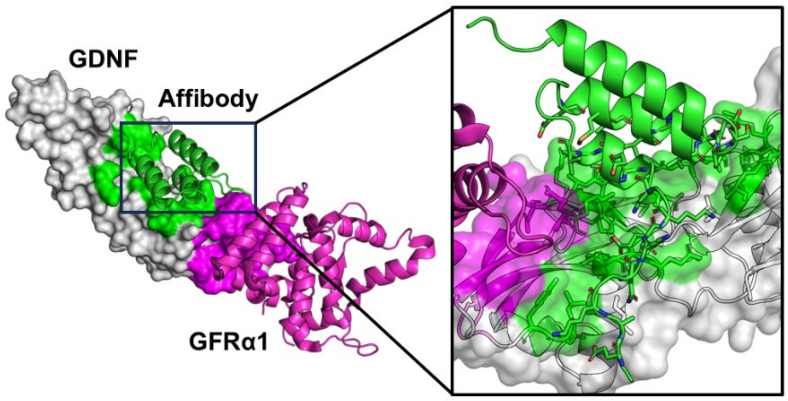

Figure 6.4. Computational binding interface of Affibody and GDNF with respect to GFRα1 receptor. AlphaFold 3 was used to model a complex between GDNF (white), affibody (green), and the GFRα1 receptor (pink), and the model was visualized in PyMOL. The affibody and affibody-GDNF binding interface is shown in green, while the GFRα1 receptor and GFRα1-GDNF binding interface are shown in magenta.

affibodies was calculated, where all hydrogels, regardless of affibody concentration, showed high encapsulation efficiencies above 95% (**Figure 6.5A**). The cumulative release at 4 hours, 1, 3, 5, and 7 days was calculated for hydrogels with and without affibodies (**Figure 6.5B**). Consistent with previous studies, we observed that the GDNF release profile can be modified by tuning the affibody molar excess in hydrogels.[595] By day 5, hydrogels containing 500x molar excess affibodies were the only group showing a statistically significantly slower release than GDNF released from hydrogels with no affibodies. On day 7, approximately 64.75 ± 5.72% of GDNF was released from hydrogels with no affibodies, and 35.47 ± 2.05% was released from hydrogels with affibodies at a 500x molar excess.

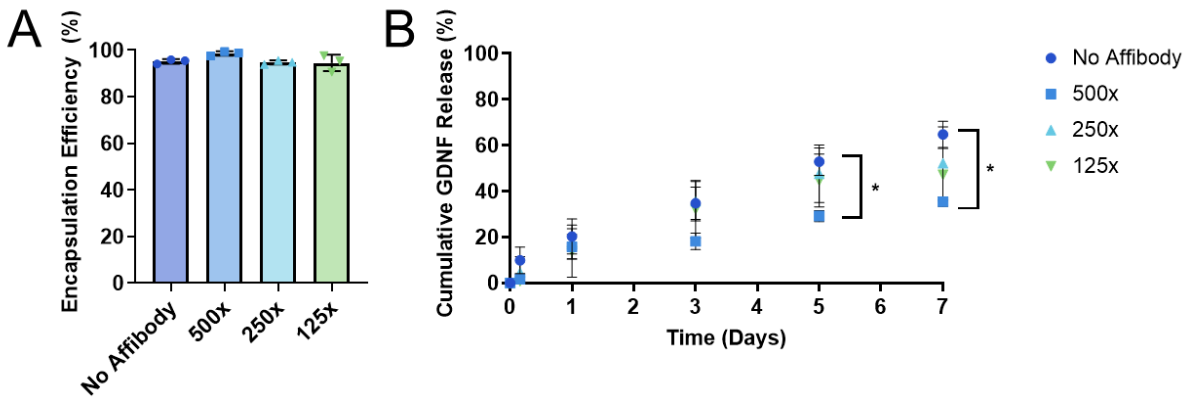

Figure 6.5. Controlled release of GDNF from affibody-conjugated HA hydrogels. A) The encapsulation efficiency of 100 ng of GDNF loaded into HA hydrogels with no affibody and 500, 250, and 125 times molar excess affibodies. B) Cumulative release of GDNF from HA hydrogels with no affibody and 500, 250, and 125 times molar excess at time points 4 hours, 1, 3, 5, and 7 days. Two-way ANOVA and Tukey's post hoc test (n = 3, * $p < 0.05$ between the no affibody and 500 times molar excess groups).

6.4.4 Localized GDNF Delivery Enhances Glioblastoma Migration Along Aligned Fibers

To investigate the effects of GDNF on glioblastoma migration in the presence of fibrous topographical cues that mimic the brain's extracellular matrix, we embedded aligned MEW scaffolds in HA hydrogels to fabricate composite scaffolds (**Figure 6.6**). We first evaluated soluble GDNF delivery to spheroids on composite scaffolds with 1% and 2% w/v hydrogels to assess the effects of migration in hydrogels with differing HA content and stiffness. 150 µL of either 1% or 2% HA-Nor-ADH was added to the well before MEW scaffolds were added. A single spheroid in 50 µL of media was then placed on the center of the scaffold and allowed to attach for 30 minutes, after which 100 µL of either 1.5% or 2.5% HA-Ox was added. The two solutions were crosslinked for 4 hours at 37 °C to form hydrogels. Media, with or without 50 ng/mL soluble GDNF, were then added to the well.

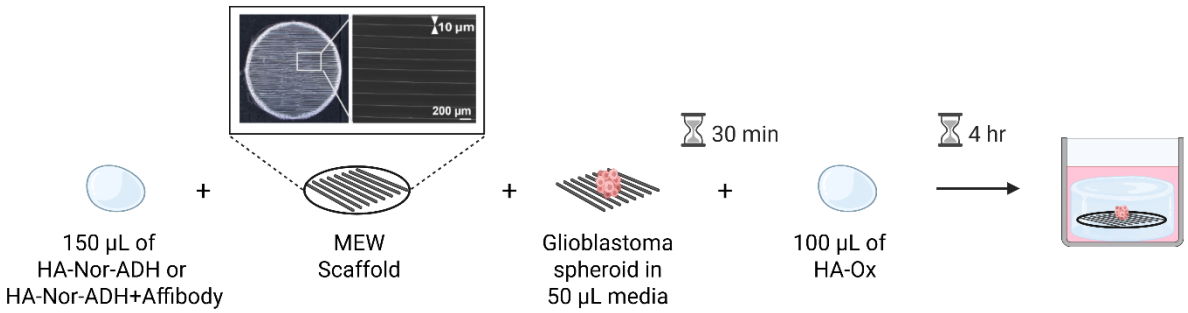

Figure 6.6. Fabrication of HA MEW 3D glioblastoma model.

Soluble GDNF was delivered for 7 days to glioblastoma spheroids on composite scaffolds, then stained for DAPI (nuclei) to quantify cellular migration (**Figure 6**). We observed spheroid migration in both 1% and 2% w/v hydrogels. On initial observation, we observed the formation of smaller cell aggregates in samples with soluble GDNF compared with those without GDNF (**Figure 6.7A**). After quantifying cellular migration along fibers, we observed increased migration in samples treated with soluble GDNF. Preliminary results show no statistical differences for 1% w/v hydrogels. However, further experiments are needed to determine whether any statistical differences exist for 2% w/v hydrogels. In addition, we will perform experiments with soluble GDNF bound to affibodies to investigate the predicted GDNF-affibody binding interface. Previous studies have shown that protein-affibody complexes have prevented downstream cell signaling pathways *in vitro*.[573] Similarly, we will deliver soluble GDNF and GDNF-affibody complexes to assess whether GDNF-mediated migration is present. Lastly, migration experiments using controlled delivery of GDNF from hydrogels containing affibodies will be performed.

6.5 Discussion

Developing 3D *in vitro* models of glioblastoma is necessary for the translation of novel therapeutics that can slow tumor progression and minimize the resistance to radio- and chemotherapy. Advancements in tissue engineering technologies, including 3D printing and controlled protein delivery, can enable the creation of 3D environments that mimic the biochemical and topographical cues of the tumor microenvironment.

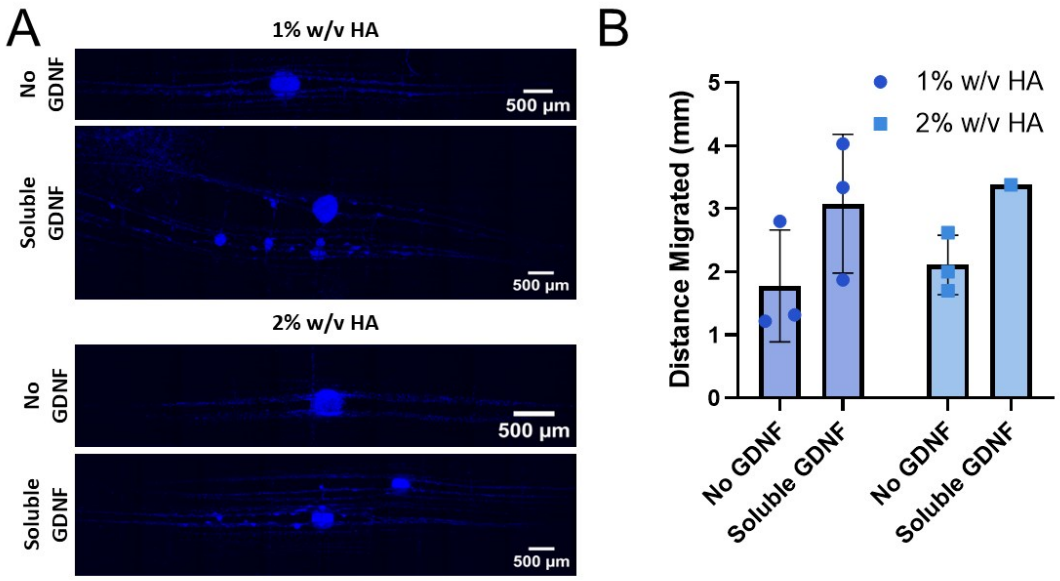

Figure 6.7. Migration of glioblastoma cells on scaffolds with soluble GDNF. A) Representative fluorescent images of glioblastoma spheroids seeded on scaffolds embedded in both 1% and 2% w/v HA hydrogels with and without soluble GDNF (50 ng/mL) (Scale bar = 500 µm). B) The distance of cells migrated from the spheroid in both 1% and 2% w/v HA hydrogels with and without soluble GDNF.

We developed novel composite scaffolds by combining HA hydrogels with controlled GDNF delivery and aligned MEW scaffolds to model the glioblastoma tumor microenvironment. Both HA and GDNF play pivotal roles in glioblastoma invasion and are highly expressed in the tumor microenvironment.[564,582,583] GDNF is additionally known to contribute to therapeutic resistance in glioblastoma.[565,596,597] The addition of GDNF to a glioblastoma model can facilitate further investigation of its role in therapeutic resistance, thereby enabling the development of effective therapies. Affibodies within an HA hydrogel can control GDNF delivery and further mimic the biochemical cues of the extracellular brain matrix. However, HA hydrogels alone cannot provide the topographical cues present in the brain; therefore, we added aligned MEW scaffolds to our system to further mimic the native architecture of the brain's white matter tracts and blood vessels.

We successfully identified a low-affinity GDNF affibody that can control GDNF delivery from HA hydrogels over 7 days. Lower excesses of affibody conjugated to HA-Nor-

ADH did not show significant controlled release. Interestingly, this release profile closely aligns with a previously discovered high-affinity VEGF affibody with a K_D of 0.0583 μM, conjugated to polyethylene glycol hydrogels at a similar molar excess.[593] This could be due to the use of an HA hydrogel platform, since HA is an anionic polymer; these inherent properties may slow the release of proteins from affibody-conjugated hydrogels. Moderate-affinity BMP-2 affibodies conjugated to HA hydrogels showed much lower release profiles, with less than 5% of BMP-2 released over 28 days.[18] For this model, having a low-affinity GDNF affibody and a faster release profile is preferred, as many *in vitro* glioblastoma models are cultured for 2 weeks or less.[598]

Because our affibody was predicted to bind at a site different from the receptor-binding interface, we sought to explore whether GDNF-affibody complexes prevent downstream signaling pathways. Two previously discovered BMP-2 affibodies were predicted to bind to both a different location and the same location as the receptor binding interface.[573] Interestingly, both BMP-2-affibody complexes muted the downstream signaling pathways, reducing alkaline phosphatase activity. It will be interesting to determine whether GDNF affibodies can be used to modulate the signaling pathways involved in glioblastoma migration, thereby enabling investigation of the signaling pathways underlying tumor migration and therapeutic resistance in a model of the tumor microenvironment.

The hydrogel platform used in this model is advantageous because it can exhibit a range of physicochemical properties by varying the polymer concentration.[18] Although we investigated only two hydrogels with differing weight percentages and stiffnesses that have been previously characterized, future work should further examine how fine-tuning the physicochemical properties might influence tumor migration. Previous studies have shown that HA content, molecular weight, and hydrogel stiffness and viscoelasticity can greatly modulate glioblastoma invasiveness.[599,600] Because hydrazone-crosslinked HA hydrogels can be fine-tuned by varying the polymer molecular weight and concentrations, they can serve as a promising platform for fabricating 3D glioblastoma models. In addition, modifying HA with norbornene groups enables conjugation of peptides and small proteins, such as affibodies. In addition to affibodies, previous studies have shown that adding peptides to HA hydrogels, such as fibronectin-derived peptides and matrix metalloprotease-degradable peptides, can influence tumor invasiveness.[600,601] Due to the tunable physicochemical properties and functional groups of HA hydrazone crosslinked

hydrogels, it would be possible to easily investigate the influence of several biochemical cues involved in glioblastoma progression.

Combining HA hydrazone crosslinked hydrogels with fibrous MEW scaffolds can mimic the topographical cues of the brain's extracellular matrix. It has been reported that white matter tracts and blood vessels in brain tissue can facilitate tumor invasion.[587,589] Therefore, the addition of HA hydrogels with MEW scaffolds can provide both the biochemical and biophysical cues present in glioblastoma tumors. Taken together, this multilayered approach can better recapitulate tumor complexity. The development of this platform will be advantageous for investigating cellular signaling pathways associated with tumor migration and therapeutic resistance, as well as cellular-extracellular matrix interactions that can contribute to glioblastoma progression. Investigation of these individual roles can lead to the development of effective therapeutics that may extend survival rates for patients with glioblastoma.

6.6 Conclusion

We successfully fabricated 3D *in vitro* models of glioblastoma that recapitulate tumor complexity by presenting both biochemical and biophysical cues reported to underlie glioblastoma migration and therapeutic resistance. GDNF affibodies with low affinity were discovered through sequential rounds of cell sorting of a yeast surface display library. Affibodies were then conjugated to HA-Nor-ADH for crosslinking with HA-Ox to form hydrogels to determine cumulative release profiles of GDNF from hydrogels with varying molar excesses. We observed that hydrogels with a 500x molar excess of affibody exhibited a statistically significant reduction in GDNF delivery by day 5, making them suitable for fabricating glioblastoma models. We then combined HA hydrogels with aligned MEW scaffolds to investigate the effects of cellular behavior in the presence of topographical cues and soluble GDNF delivery. The bioactivity of the GDNF-affibody complexes will be investigated to evaluate the predicted binding interface of GDNF and affibody. Lastly, localized, controlled delivery of GDNF within HA hydrogels will be evaluated for its effects on cellular migration along MEW fibers. This platform can be used to investigate the cell-signaling pathways and cellular interactions within a tumor-mimetic microenvironment that drives tumor progression. While elucidating the roles of the tumor microenvironment, this platform can additionally be used for the high-throughput screening of novel therapeutics for glioblastoma.

CHAPTER 7
CONCLUSIONS AND FUTURE DIRECTIONS

7.1 Conclusions

7.1.1 Statistical Optimization of HA Hydrogels

We developed HA hydrazone-crosslinked hydrogels for tissue repair and evaluated their use in several tissue-engineering applications. Hydrazone crosslinking chemistry was used to form biocompatible hydrogels with self-healing, viscoelastic, and injectable characteristics, as well as a range of physicochemical properties. Because these hydrogels exhibited a wide range of characteristics, this platform was an ideal candidate for building a statistical optimization model using design of experiments. This model was used to determine an optimal hydrogel formulation for controlled protein delivery of BMP-2. Using a design of experiments approach, interactions among multiple input variables were evaluated, which often cannot be captured with a one-variable-at-a-time approach. In addition, building statistical models can reduce the number of experiments required for determining optimal biomaterial properties for the given application. This methodology has been advantageous for determining hydrogel formulations with specific physicochemical or biological properties for several applications. For example, this approach has been used to optimize hydrogel properties for cervical cancer models to maximize cell invasion and endothelial microvessel length,[602] and for neural progenitor cells derived induced pluripotent stem cells survival.[603]

7.1.2 HA-Coated Scaffolds Promote Myoblast Attachment, Alignment, and Differentiation

We then combined HA hydrogels with aligned MEW scaffolds to investigate myoblast alignment and differentiation. Muscle tissue has a highly ordered and aligned architecture. In large muscle injuries, volumetric muscle loss creates a cavity of lost tissue and greatly reduces biochemical cues required for tissue repair, ultimately leading to fibrosis and loss of function. Engineering aligned scaffolds can guide cellular alignment to promote muscle tissue repair and serve as a platform for therapeutic delivery. HA was additionally functionalized with fibronectin-derived peptides (RGD) to increase myoblast attachment to scaffolds. By combining HA hydrogels, which provide a cell-supportive microenvironment, with the alignment properties of fiber scaffolds, we were able to guide cellular attachment, alignment, and differentiation. We

additionally evaluated the effects of PCL fiber diameter on myoblast behavior and determined that 20 μm fibers best supported cellular attachment. While both HA- and HA RGD-coated scaffolds supported myoblast differentiation and the formation of myotubes, these scaffolds did not support the maturation of myotubes, as seen from the absence of α-actinin striations. Expanding this work to develop HA-coated scaffolds that support myotube maturation would be key for its use in volumetric muscle tissue repair.

7.1.3 HA Hydrogels for the Generation and Maturation of V2a Interneurons

We evaluated HA-Alg hydrogels functionalized with fibronectin- and laminin-derived peptides (RGD and IKVAV, respectively) for neural tissue engineering. We compared this hydrogel with our previously established HA hydrogel to evaluate alginate as a potential biomaterial for neural tissue engineering applications. We investigated the use of these hydrogels to support the generation and maturation of V2a interneurons, a clinically relevant, highly specific neuronal type that has been identified as a therapeutic approach for treating spinal cord injuries. We found that all hydrogels supported the generation of viable V2a interneurons; however, only IKVAV-functionalized hydrogels provided the appropriate adhesion cues for their maturation, as exhibited by neurite extensions. The development of these hydrogels is an important step toward translating cell transplantation as a therapeutic approach for treating spinal cord injuries. Next steps for this work would include evaluating this platform for V2a interneuron transplantation *in vivo* in a rat model of cervical spinal cord injury and assessing interneuron integration and functional outcomes.[530,535]

7.1.4 Controlled GDNF Delivery from HA Hydrogels

Injectable HA hydrogels can serve as a drug delivery system for minimally invasive delivery to the central nervous system. GDNF is a potent neurotrophic factor for neural tissue repair; however, it can also contribute to glioblastoma migration and therapeutic resistance. We investigated GDNF-controlled delivery in an engineering 3D model of the glioblastoma tumor microenvironment to assess cellular migration. Affibodies specific to GDNF were discovered through sequential rounds of cell sorting. Affibodies were then synthesized and functionalized to HA hydrogels to evaluate GDNF release profiles. We showed controlled delivery of GDNF from HA hydrogels over 7 days. Aligned MEW scaffolds were then embedded in HA hydrogels to model the glioblastoma microenvironment. This platform provided both biochemical and

biophysical cues that contribute to tumor progression. The development of this novel platform is critical for investigating cellular signaling and cell-extracellular matrix interactions that may lead to the development of effective therapeutics to treat glioblastoma.

7.2 Future Directions

7.2.1 HA-Coated Scaffolds for Muscle Tissue Repair

Promoting the maturation of myotubes on tissue engineered scaffolds is important for their translation as a therapeutic approach for muscle tissue repair. Using HA hydrogels for growth factor delivery is a promising approach to drive myotube maturation. For instance, the controlled delivery of basic fibroblast growth factor (FGF), followed by insulin-like growth factor-1 (IGF-1), resulted in improved muscle tissue repair and reduced fibrosis in a mouse model of volumetric muscle loss.[604] It would be interesting to combine this idea with HA-coated scaffolds using affibodies to engineer implantable scaffolds that can restore muscle tissue function following volumetric muscle loss. Affibodies have successfully been used to sequentially deliver multiple growth factors from a hydrogel.[593] Using a similar approach, affibodies with varying affinities could be used to achieve distinct growth factor release profiles, which can be easily combined with aligned MEW scaffolds to promote mature myotube formation and muscle tissue repair.

In addition to growth factor delivery, another interesting approach to promoting muscle tissue repair using HA hydrogels would be to functionalize them with electroconductive molecules. Previous work has used polyaniline (PANI)-grafted HA to adipic acid dihydrazide-modified HA to form HA hydrazone-crosslinked hydrogels with electroconductive properties for muscle tissue repair.[605] These hydrogels were evaluated in a rat model of volumetric muscle injury and showed significantly improved muscle tissue repair compared to HA hydrogels without PANI. Combining a similar electroconductive HA hydrogel with MEW scaffolds would be advantageous to further enhance tissue repair following volumetric muscle loss.

7.2.2 Central Nervous System Tissue Repair following Injury and Disease

7.2.2.1 GDNF Delivery for Parkinson's Disease

While GDNF can contribute to glioblastoma migration and therapeutic resistance, it has also been used to repair tissue following central nervous system injury and disease.[559,562,563,606,607] Of particular interest, several ongoing clinical trials are evaluating viral and recombinant

delivery of GDNF for the treatment of Parkinson's disease, as GDNF is a potent neurotrophic factor for the survival and regeneration of dopaminergic neurons. However, a major challenge in translating GDNF into clinical use is the need for sustained, minimally invasive delivery methods.[608] HA hydrogels functionalized with GDNF affibodies can be used to overcome these challenges, as this platform can be easily injected past the blood-brain barrier. Affibodies can also be tuned to achieve long-term delivery of GDNF from an HA hydrogel, as previous studies have shown that BMP-2 affibodies can sustain BMP-2 delivery for over 28 days.[18] We have also shown that HA hydrogels can support neuronal survival and maturation *in vitro*, providing a suitable platform for neural tissue repair for Parkinson's Disease. HA hydrogels can additionally provide a supportive matrix for tissue repair, which has not been used in current infusion and viral delivery methods. HA hydrogels can be further modified with peptides or electroconductive molecules to improve neural tissue repair or to serve as a drug-delivery platform for cells and therapeutics, to enhance the effects of GDNF delivery. For instance, a recent hypothesis for why GDNF delivery fails in clinical trials for Parkinson's disease is that downregulation of nuclear receptor-related protein 1 (Nurr1), a transcription factor that protects dopaminergic neurons, could interfere with downstream GDNF signaling.[609] Perhaps controlled delivery of GDNF with Nurr1 agonists could improve the therapeutic effects of GDNF for the treatment of Parkinson's Disease. Nurr1 agonists could certainly be delivered in HA hydrogels with controlled delivery of GDNF to further investigate this hypothesis and be used as a therapeutic approach for Parkinson's Disease.

7.2.2.2 Multiple Neurotrophic Factor Delivery for CNS Tissue Repair

In addition to controlled GDNF delivery, affibodies towards multiple neurotrophic factors can be used to inform the ideal delivery and combination of neurotrophic factors for neural tissue repair after injury or disease. While individual neurotrophic factor delivery is promising for neural tissue repair, the temporal and combinatorial delivery of multiple neurotrophic factors remains underexplored.[571,591] For instance, both brain-derived neurotrophic factor (BDNF) and GDNF can protect dopaminergic neurons in Parkinson's disease; however, the synergistic effects of viral vector delivery of BDNF and GDNF did not improve behavioral impairments in a rat model of Parkinson's Disease.[610] This is likely due to the need to precisely control the presentation and concentration of neurotrophic factors within the system. Affibodies could be used to overcome these challenges by tuning the release profiles of neurotrophic factors

to inform their optimal temporal release for tissue repair. The controlled, temporal delivery of multiple neurotrophic factors within injectable HA hydrogels is advantageous for developing therapeutics for CNS injury and disease.

7.2.2.3 Aligned Composite Scaffolds for Spinal Cord Injury

Given the spinal cord's inherent anisotropic architecture,[611–613] combining HA hydrogels with controlled neurotrophic factor delivery with aligned MEW scaffolds could be a promising approach to guiding axonal elongation and synaptic formation for functional tissue repair. Previously, GDNF has been delivered from polydopamine nanoparticles on anisotropic gelatin scaffolds, promoting functional recovery in a mouse spinal cord injury model.[563] Evaluating an aligned HA hydrogel composite scaffold with controlled GDNF delivery would be an attractive approach to fill the cavity left by SCI and promote tissue function. MEW scaffolds can guide axonal elongation and the formation of new synapses, while HA hydrogels serve as a delivery platform and provide a supportive environment for tissue repair.

Furthermore, it would also be fascinating to evaluate a spatial gradient of GDNF affibody conjugated to HA along an aligned MEW scaffold. Because GDNF can act as a chemoattractant for neurons, gradients in GDNF concentration along fibers could better guide neuronal migration, thereby further promoting the alignment and elongation of axons during tissue repair. Gradients of GDNF have been previously achieved using heparin-modified polyethylene glycol nanoparticles,[614] and lentiviral vectors to investigate Schwann cell axonal trapping, maturation, and myelination.[615] Using norbornene thiol-ene click chemistry, a gradient of GDNF affibody concentration conjugated to HA hydrogels along MEW fibers could be used for spatiotemporal delivery of GDNF along MEW fibers, since the release profile of GDNF can be tuned by varying the affibody concentration in hydrogels. Thiol-ene norbornene click chemistry has previously been used to photopattern multiple peptides and dyes into hydrogels.[52,616] Similarly, a gradient of affibodies could be achieved by varying light exposure and intensity, photoinitiator concentration, and affibody concentration. Overall, it would be interesting to evaluate the cellular behavior of neurons in response to both the chemoattractant effects of GDNF and the topographical cues of MEW fibers.

7.2.3 Neuromuscular Junctions

At the intersection of HA hydrogels for muscle and neural tissue repair, it would be exciting to investigate this platform for treating neuromuscular diseases or for developing models of neuromuscular junctions. Neuromuscular junctions are chemical synapses where motor neurons communicate with skeletal muscle, initiating muscle contraction. HA hydrogels with neurotrophic factor delivery can be used as a therapeutic approach to promote neuromuscular junction formation in neuromuscular diseases. Specifically, the delivery of GDNF and GDNF in combination with VEGF from mesenchymal stem cells has been investigated for the treatment of amyotrophic lateral sclerosis.[617] HA hydrogels with controlled neurotrophic factor delivery could be an interesting approach for treating neuromuscular diseases.

In addition, models of neuromuscular junctions have been used to study several neuromuscular diseases, including spinal muscular atrophy, amyotrophic lateral sclerosis, and myasthenia gravis.[618] Investigating neuromuscular junctions by co-culturing muscle and neurons on aligned scaffolds would be an interesting approach to developing a tissue-engineered model to guide therapeutic development. For instance, several approaches have been developed to generate and co-culture appropriate combinations of muscle and neuronal cells. Recently, promising results have been reported using assembled or self-organized cells derived from human pluripotent stem cells to model neuromuscular junctions.[618–620] However, a current limitation is the difficulty of forming mature neuromuscular junctions. The addition of electrical stimulation, glial cells, or vascularization could promote the formation of mature neuromuscular junctions.[621] MEW scaffolds provide an opportunity to engineer complex tissue models by guiding cellular interactions in co-cultures through variations in fiber diameter and pattern.[622] Combining hydrogels with scaffolds could be further used to fabricate such complex models. Varying HA hydrogel properties, including stiffness and biochemical cue functionalization, can also be used to modulate cellular behavior. Both HA hydrogels and HA hydrogel composite scaffolds would be highly impactful for both developing models and therapeutics for neuromuscular junction diseases.

APPENDICES

APPENDIX A: STATISTICAL OPTIMIZATION OF HYDRAZONE-CROSSLINKED HYALURONIC ACID HYDROGELS FOR PROTEIN DELIVERY

Degree of Modification

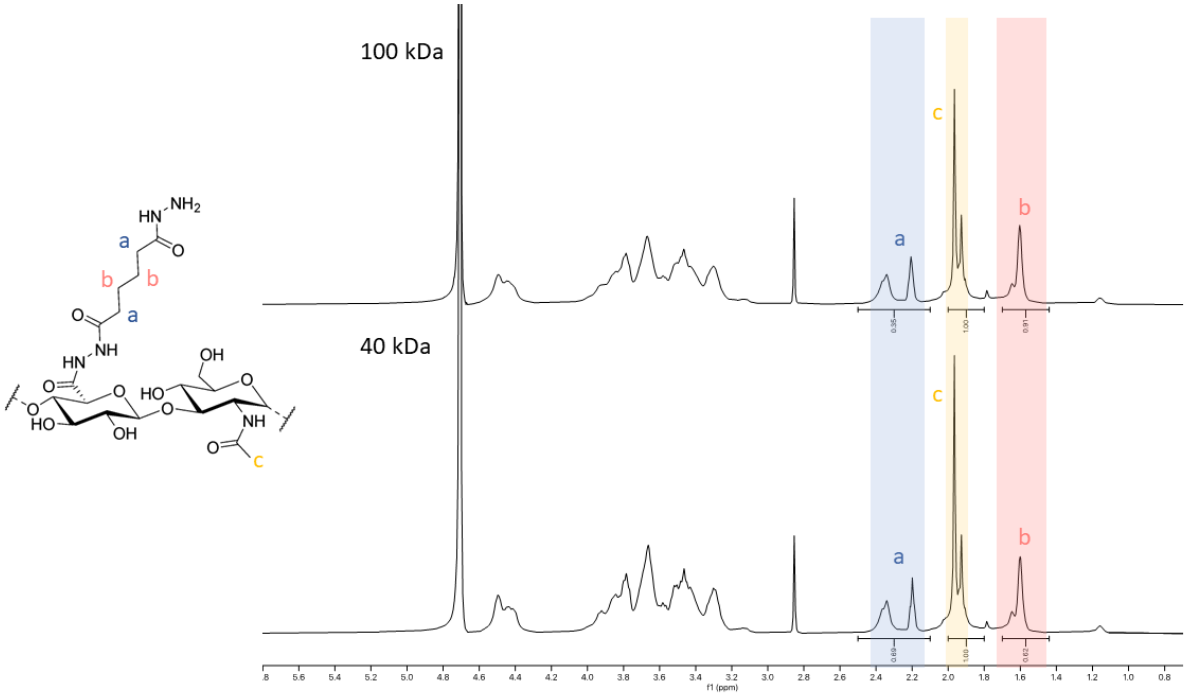

Figure A1. ^{1}H NMR of 40 kDa and 100 kDa HA-ADH. HA-ADH functionalization was confirmed by ^{1}H NMR. The percentage of ADH functional groups per polymer chain was calculated by integrating the hydrogen peaks from the aliphatic chain on ADH (8H, a-b) and normalizing by the hydrogen peaks from the on the n-actyl group on HA (3H, c).

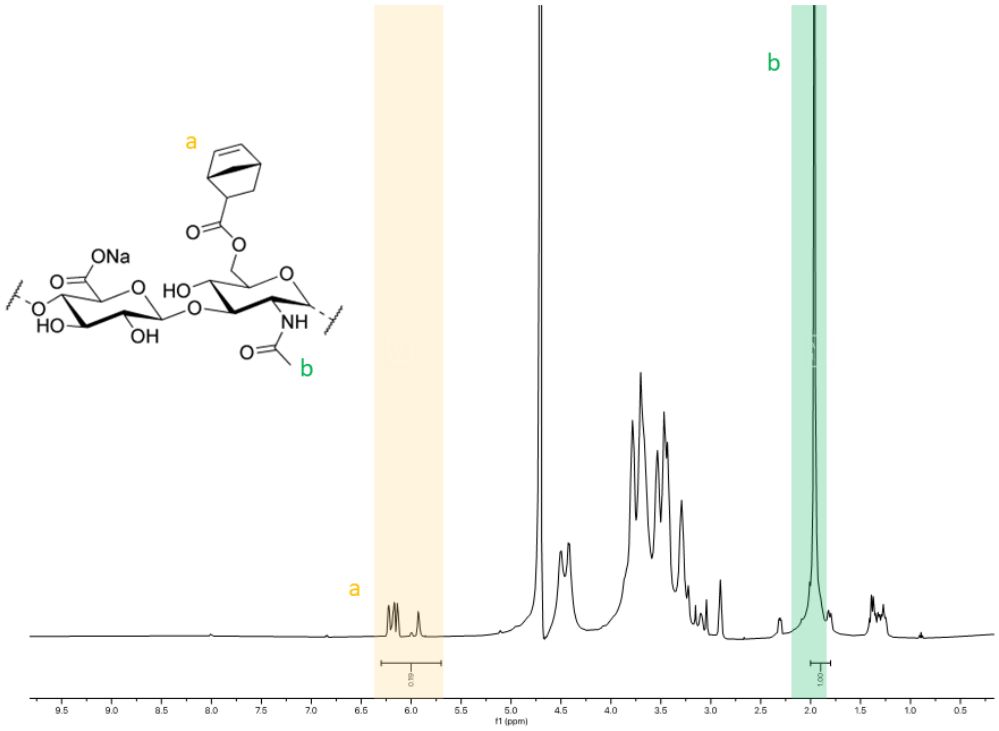

Figure A2. ^{1}H NMR of HA-Nor. The functionalization of HA-Nor was confirmed by 1H NMR. The degree of modification or the percentage of norbornene groups per HA polymer chain was calculated by integrating the vinyl hydrogen peaks on the norbornene functional group (2H, a) and normalizing to the hydrogen peaks from the on the n-acetyl group on HA (3H, b).

Table A1. Degree of Modification and Yield for Functionalized HA Polymers. A summary of the average degrees of modification and average yields for each functionalized HA polymer, including HA-Ox, HA-ADH, and HA-Nor.

	%Degree of Modification		**%Yield**	
Modification	**40 kDa**	**100 kDa**	**40 kDa**	**100 kDa**
HA-Ox	22.5%	56.0%	42.0%	68.3%
	25.9%	35.5%	21.8%	89.2%
	34.0%	32.6%	27.6%	83.4%
	27.5 ± 5.9%	**41.4 ± 12.8%**	**30.5 ± 10.4%**	**80.3 ± 10.8%**
HA-ADH	69.3%	45.1%	45.1%	44.9%
	67.5%	52.7%	52.7%	46.4%
	66.8%	40.6%	40.6%	49.5%
	66.9%	63.7%	52.8%	46.6%
	67.6 ± 1.2%	**50.6 ± 10.1%**	**47.8 ± 6.0%**	**46.8 ± 1.9%**
HA-Nor	-	30.0%	-	34.0%
	-	27.0%	-	54.0%
	-	33.3%	-	31.0%
	-	**30.1 ± 3.2%**	**-**	**38.7 ± 12.5%**

Molecular Weight of Unmodified and Modified HA

Table A2. HA polymer molecular weight. Molecular weight of unmodified and modified HA determined by gel permeation chromatography. N=3.

	Number Molecular Weight, M_n (Da)		**Average Molecular Weight, M_w (Da)**		**Polydispersity Index (PDI)**	
Modification	**40 kDa**	**100 kDa**	**40 kDa**	**100 kDa**	**40 kDa**	**100 kDa**
HA	34,912	76,797	62,776	131,134	1.798	1.708
	37,549	72,300	62,123	128,996	1.654	1.784
	36,438	78,179	61,823	132,258	1.697	1.692
	36,300 ± 1,081	**75,759 ± 2,510**	**62,241 ± 398**	**130,796 ± 1,353**	**1.716 ± 0.060**	**1.728 ± 0.040**
HA-Ox	19,284	46,061	31,778	85,120	1.648	1.848
	18,922	47,872	31,907	85,328	1.686	1.782
	20,029	43,046	31,853	80,005	1.590	1.859
	19,412 ± 461	**45,660 ± 1,991**	**31,846 ± 53**	**83,484 ± 2,462**	**1.641 ± 0.039**	**1.830 ± 0.034**
HA-ADH	112,437	113,363	376,002	267,904	1.9878	2.1431
	111,212	123,308	381,266	290,938	2.0184	2.3186
	107,304	109,823	343,204	283,265	2.0553	2.0860
	110,318 ± 2,189	**115,498 ± 5,708**	**366,824 ± 16,840**	**280,702 ± 9,577**	**2.0205 ± 0.0276**	**2.1826 ± 0.0990**

Statistical Analysis of Gelation Time

Table A3. Summary of significance for 40 kDa HA gelation times and 100 kDa HA gelation time. A summary of significance for the gelation times for both 40 kDa and 100 kDa is listed, a one-way ANOVA post-hoc Dunnett's T3 multiple comparisons was performed. n = 3; * p < 0.05, ** < p 0.01, *** p < 0.001, **** p < 0.0001.

Gelation Time Significance		
Dunnett's T3 multiple comparisons test	Summary	Adjusted P Value
HA-ADH$_{1.00}$HA-Ox$_{1.00\ (40\ kDa)}$ vs. HA-ADH$_{3.00}$HA-Ox$_{1.00\ (40\ kDa)}$	****	<0.0001
HA-ADH$_{1.00}$HA-Ox$_{1.00\ (40\ kDa)}$ vs. HA-ADH$_{1.00}$HA-Ox$_{3.00\ (40\ kDa)}$	***	0.0005
HA-ADH$_{1.00}$HA-Ox$_{1.00\ (40\ kDa)}$ vs. HA-ADH$_{3.00}$HA-Ox$_{3.00\ (40\ kDa)}$	****	<0.0001
HA-ADH$_{1.00}$HA-Ox$_{1.00\ (40\ kDa)}$ vs. HA-ADH$_{1.67}$HA-Ox$_{1.00\ (40\ kDa)}$	**	0.0043
HA-ADH$_{1.00}$HA-Ox$_{1.00\ (40\ kDa)}$ vs. HA-ADH$_{2.00}$HA-Ox$_{2.00\ (40\ kDa)}$	**	0.0026
HA-ADH$_{1.00}$HA-Ox$_{1.00\ (40\ kDa)}$ vs. HA-ADH$_{1.00}$HA-Ox$_{1.00\ (100\ kDa)}$	****	<0.0001
HA-ADH$_{1.00}$HA-Ox$_{1.00\ (40\ kDa)}$ vs. HA-ADH$_{3.00}$HA-Ox$_{1.00\ (100\ kDa)}$	****	<0.0001
HA-ADH$_{1.00}$HA-Ox$_{1.00\ (40\ kDa)}$ vs. HA-ADH$_{1.00}$HA-Ox$_{3.00\ (100\ kDa)}$	***	0.0002
HA-ADH$_{1.00}$HA-Ox$_{1.00\ (40\ kDa)}$ vs. HA-ADH$_{3.00}$HA-Ox$_{3.00\ (100\ kDa)}$	****	<0.0001
HA-ADH$_{1.00}$HA-Ox$_{1.00\ (40\ kDa)}$ vs. HA-ADH$_{1.00}$HA-Ox$_{1.67\ (100\ kDa)}$	****	<0.0001
HA-ADH$_{1.00}$HA-Ox$_{1.00\ (40\ kDa)}$ vs. HA-ADH$_{3.00}$HA-Ox$_{2.33\ (100\ kDa)}$	****	<0.0001
HA-ADH$_{1.00}$HA-Ox$_{1.00\ (40\ kDa)}$ vs. HA-ADH$_{2.33}$HA-Ox$_{1.00\ (100\ kDa)}$	***	0.0005
HA-ADH$_{1.00}$HA-Ox$_{1.00\ (40\ kDa)}$ vs. HA-ADH$_{1.67}$HA-Ox$_{3.00\ (100\ kDa)}$	***	0.0005
HA-ADH$_{1.00}$HA-Ox$_{1.00\ (40\ kDa)}$ vs. HA-ADH$_{2.00}$HA-Ox$_{2.00\ (100\ kDa)}$	****	<0.0001
HA-ADH$_{3.00}$HA-Ox$_{1.00\ (40\ kDa)}$ vs. HA-ADH$_{1.00}$HA-Ox$_{3.00\ (40\ kDa)}$	ns	0.3702
HA-ADH$_{3.00}$HA-Ox$_{1.00\ (40\ kDa)}$ vs. HA-ADH$_{3.00}$HA-Ox$_{3.00\ (40\ kDa)}$	***	0.0002
HA-ADH$_{3.00}$HA-Ox$_{1.00\ (40\ kDa)}$ vs. HA-ADH$_{1.67}$HA-Ox$_{1.00\ (40\ kDa)}$	**	0.0048
HA-ADH$_{3.00}$HA-Ox$_{1.00\ (40\ kDa)}$ vs. HA-ADH$_{2.00}$HA-Ox$_{2.00\ (40\ kDa)}$	ns	0.0888
HA-ADH$_{3.00}$HA-Ox$_{1.00\ (40\ kDa)}$ vs. HA-ADH$_{1.00}$HA-Ox$_{1.00\ (100\ kDa)}$	***	0.0004
HA-ADH$_{3.00}$HA-Ox$_{1.00\ (40\ kDa)}$ vs. HA-ADH$_{3.00}$HA-Ox$_{1.00\ (100\ kDa)}$	**	0.0021
HA-ADH$_{3.00}$HA-Ox$_{1.00\ (40\ kDa)}$ vs. HA-ADH$_{1.00}$HA-Ox$_{3.00\ (100\ kDa)}$	**	0.0027
HA-ADH$_{3.00}$HA-Ox$_{1.00\ (40\ kDa)}$ vs. HA-ADH$_{3.00}$HA-Ox$_{3.00\ (100\ kDa)}$	**	0.0018
HA-ADH$_{3.00}$HA-Ox$_{1.00\ (40\ kDa)}$ vs. HA-ADH$_{1.00}$HA-Ox$_{1.67\ (100\ kDa)}$	ns	>0.9999
HA-ADH$_{3.00}$HA-Ox$_{1.00\ (40\ kDa)}$ vs. HA-ADH$_{3.00}$HA-Ox$_{2.33\ (100\ kDa)}$	***	0.0002
HA-ADH$_{3.00}$HA-Ox$_{1.00\ (40\ kDa)}$ vs. HA-ADH$_{2.33}$HA-Ox$_{1.00\ (100\ kDa)}$	*	0.0335
HA-ADH$_{3.00}$HA-Ox$_{1.00\ (40\ kDa)}$ vs. HA-ADH$_{1.67}$HA-Ox$_{3.00\ (100\ kDa)}$	*	0.0427

HA-ADH$_{3.00}$HA-Ox$_{1.00\ (40\ kDa)}$ vs. HA-ADH$_{2.00}$HA-Ox$_{2.00\ (100\ kDa)}$	****	<0.0001
HA-ADH$_{1.00}$HA-Ox$_{3.00\ (40\ kDa)}$ vs. HA-ADH$_{3.00}$HA-Ox$_{3.00\ (40\ kDa)}$	*	0.0246
HA-ADH$_{1.00}$HA-Ox$_{3.00\ (40\ kDa)}$ vs. HA-ADH$_{1.67}$HA-Ox$_{1.00\ (40\ kDa)}$	****	<0.0001
HA-ADH$_{1.00}$HA-Ox$_{3.00\ (40\ kDa)}$ vs. HA-ADH$_{2.00}$HA-Ox$_{2.00\ (40\ kDa)}$	*	0.0269
HA-ADH$_{1.00}$HA-Ox$_{3.00\ (40\ kDa)}$ vs. HA-ADH$_{1.00}$HA-Ox$_{1.00\ (100\ kDa)}$	*	0.0359
HA-ADH$_{1.00}$HA-Ox$_{3.00\ (40\ kDa)}$ vs. HA-ADH$_{3.00}$HA-Ox$_{1.00\ (100\ kDa)}$	*	0.0252
HA-ADH$_{1.00}$HA-Ox$_{3.00\ (40\ kDa)}$ vs. HA-ADH$_{1.00}$HA-Ox$_{3.00\ (100\ kDa)}$	*	0.0305
HA-ADH$_{1.00}$HA-Ox$_{3.00\ (40\ kDa)}$ vs. HA-ADH$_{3.00}$HA-Ox$_{3.00\ (100\ kDa)}$	*	0.0206
HA-ADH$_{1.00}$HA-Ox$_{3.00\ (40\ kDa)}$ vs. HA-ADH$_{1.00}$HA-Ox$_{1.67\ (100\ kDa)}$	ns	0.3194
HA-ADH$_{1.00}$HA-Ox$_{3.00\ (40\ kDa)}$ vs. HA-ADH$_{3.00}$HA-Ox$_{2.33\ (100\ kDa)}$	*	0.0243
HA-ADH$_{1.00}$HA-Ox$_{3.00\ (40\ kDa)}$ vs. HA-ADH$_{2.33}$HA-Ox$_{1.00\ (100\ kDa)}$	*	0.0204
HA-ADH$_{1.00}$HA-Ox$_{3.00\ (40\ kDa)}$ vs. HA-ADH$_{1.67}$HA-Ox$_{3.00\ (100\ kDa)}$	*	0.0327
HA-ADH$_{1.00}$HA-Ox$_{3.00\ (40\ kDa)}$ vs. HA-ADH$_{2.00}$HA-Ox$_{2.00\ (100\ kDa)}$	*	0.0465
HA-ADH$_{3.00}$HA-Ox$_{3.00\ (40\ kDa)}$ vs. HA-ADH$_{1.67}$HA-Ox$_{1.00\ (40\ kDa)}$	**	0.0024
HA-ADH$_{3.00}$HA-Ox$_{3.00\ (40\ kDa)}$ vs. HA-ADH$_{2.00}$HA-Ox$_{2.00\ (40\ kDa)}$	*	0.0173
HA-ADH$_{3.00}$HA-Ox$_{3.00\ (40\ kDa)}$ vs. HA-ADH$_{1.00}$HA-Ox$_{1.00\ (100\ kDa)}$	****	<0.0001
HA-ADH$_{3.00}$HA-Ox$_{3.00\ (40\ kDa)}$ vs. HA-ADH$_{3.00}$HA-Ox$_{1.00\ (100\ kDa)}$	ns	0.8765
HA-ADH$_{3.00}$HA-Ox$_{3.00\ (40\ kDa)}$ vs. HA-ADH$_{1.00}$HA-Ox$_{3.00\ (100\ kDa)}$	ns	0.0698
HA-ADH$_{3.00}$HA-Ox$_{3.00\ (40\ kDa)}$ vs. HA-ADH$_{3.00}$HA-Ox$_{3.00\ (100\ kDa)}$	*	0.0367
HA-ADH$_{3.00}$HA-Ox$_{3.00\ (40\ kDa)}$ vs. HA-ADH$_{1.00}$HA-Ox$_{1.67\ (100\ kDa)}$	****	<0.0001
HA-ADH$_{3.00}$HA-Ox$_{3.00\ (40\ kDa)}$ vs. HA-ADH$_{3.00}$HA-Ox$_{2.33\ (100\ kDa)}$	ns	>0.9999
HA-ADH$_{3.00}$HA-Ox$_{3.00\ (40\ kDa)}$ vs. HA-ADH$_{2.33}$HA-Ox$_{1.00\ (100\ kDa)}$	ns	0.2687
HA-ADH$_{3.00}$HA-Ox$_{3.00\ (40\ kDa)}$ vs. HA-ADH$_{1.67}$HA-Ox$_{3.00\ (100\ kDa)}$	ns	0.2078
HA-ADH$_{3.00}$HA-Ox$_{3.00\ (40\ kDa)}$ vs. HA-ADH$_{2.00}$HA-Ox$_{2.00\ (100\ kDa)}$	****	<0.0001
HA-ADH$_{1.67}$HA-Ox$_{1.00\ (40\ kDa)}$ vs. HA-ADH$_{2.00}$HA-Ox$_{2.00\ (40\ kDa)}$	**	0.0013
HA-ADH$_{1.67}$HA-Ox$_{1.00\ (40\ kDa)}$ vs. HA-ADH$_{1.00}$HA-Ox$_{1.00\ (100\ kDa)}$	**	0.0072
HA-ADH$_{1.67}$HA-Ox$_{1.00\ (40\ kDa)}$ vs. HA-ADH$_{3.00}$HA-Ox$_{1.00\ (100\ kDa)}$	**	0.0024
HA-ADH$_{1.67}$HA-Ox$_{1.00\ (40\ kDa)}$ vs. HA-ADH$_{1.00}$HA-Ox$_{3.00\ (100\ kDa)}$	***	0.0003
HA-ADH$_{1.67}$HA-Ox$_{1.00\ (40\ kDa)}$ vs. HA-ADH$_{3.00}$HA-Ox$_{3.00\ (100\ kDa)}$	**	0.0023
HA-ADH$_{1.67}$HA-Ox$_{1.00\ (40\ kDa)}$ vs. HA-ADH$_{1.00}$HA-Ox$_{1.67\ (100\ kDa)}$	**	0.0047
HA-ADH$_{1.67}$HA-Ox$_{1.00\ (40\ kDa)}$ vs. HA-ADH$_{3.00}$HA-Ox$_{2.33\ (100\ kDa)}$	**	0.0024
HA-ADH$_{1.67}$HA-Ox$_{1.00\ (40\ kDa)}$ vs. HA-ADH$_{2.33}$HA-Ox$_{1.00\ (100\ kDa)}$	****	<0.0001
HA-ADH$_{1.67}$HA-Ox$_{1.00\ (40\ kDa)}$ vs. HA-ADH$_{1.67}$HA-Ox$_{3.00\ (100\ kDa)}$	****	<0.0001

HA-ADH$_{1.67}$HA-Ox$_{1.00\ (40\ kDa)}$ vs. HA-ADH$_{2.00}$HA-Ox$_{2.00\ (100\ kDa)}$	**	0.0033
HA-ADH$_{2.00}$HA-Ox$_{2.00\ (40\ kDa)}$ vs. HA-ADH$_{1.00}$HA-Ox$_{1.00\ (100\ kDa)}$	ns	0.4885
HA-ADH$_{2.00}$HA-Ox$_{2.00\ (40\ kDa)}$ vs. HA-ADH$_{3.00}$HA-Ox$_{1.00\ (100\ kDa)}$	*	0.0176
HA-ADH$_{2.00}$HA-Ox$_{2.00\ (40\ kDa)}$ vs. HA-ADH$_{1.00}$HA-Ox$_{3.00\ (100\ kDa)}$	*	0.027
HA-ADH$_{2.00}$HA-Ox$_{2.00\ (40\ kDa)}$ vs. HA-ADH$_{3.00}$HA-Ox$_{3.00\ (100\ kDa)}$	*	0.016
HA-ADH$_{2.00}$HA-Ox$_{2.00\ (40\ kDa)}$ vs. HA-ADH$_{1.00}$HA-Ox$_{1.67\ (100\ kDa)}$	ns	0.0889
HA-ADH$_{2.00}$HA-Ox$_{2.00\ (40\ kDa)}$ vs. HA-ADH$_{3.00}$HA-Ox$_{2.33\ (100\ kDa)}$	*	0.0172
HA-ADH$_{2.00}$HA-Ox$_{2.00\ (40\ kDa)}$ vs. HA-ADH$_{2.33}$HA-Ox$_{1.00\ (100\ kDa)}$	**	0.0074
HA-ADH$_{2.00}$HA-Ox$_{2.00\ (40\ kDa)}$ vs. HA-ADH$_{1.67}$HA-Ox$_{3.00\ (100\ kDa)}$	**	0.0086
HA-ADH$_{2.00}$HA-Ox$_{2.00\ (40\ kDa)}$ vs. HA-ADH$_{2.00}$HA-Ox$_{2.00\ (100\ kDa)}$	*	0.0297
HA-ADH$_{1.00}$HA-Ox$_{1.00\ (100\ kDa)}$ vs. HA-ADH$_{3.00}$HA-Ox$_{1.00\ (100\ kDa)}$	***	0.0008
HA-ADH$_{1.00}$HA-Ox$_{1.00\ (100\ kDa)}$ vs. HA-ADH$_{1.00}$HA-Ox$_{3.00\ (100\ kDa)}$	***	0.0005
HA-ADH$_{1.00}$HA-Ox$_{1.00\ (100\ kDa)}$ vs. HA-ADH$_{3.00}$HA-Ox$_{3.00\ (100\ kDa)}$	***	0.0007
HA-ADH$_{1.00}$HA-Ox$_{1.00\ (100\ kDa)}$ vs. HA-ADH$_{1.00}$HA-Ox$_{1.67\ (100\ kDa)}$	**	0.0012
HA-ADH$_{1.00}$HA-Ox$_{1.00\ (100\ kDa)}$ vs. HA-ADH$_{3.00}$HA-Ox$_{2.33\ (100\ kDa)}$	****	<0.0001
HA-ADH$_{1.00}$HA-Ox$_{1.00\ (100\ kDa)}$ vs. HA-ADH$_{2.33}$HA-Ox$_{1.00\ (100\ kDa)}$	*	0.0122
HA-ADH$_{1.00}$HA-Ox$_{1.00\ (100\ kDa)}$ vs. HA-ADH$_{1.67}$HA-Ox$_{3.00\ (100\ kDa)}$	*	0.0147
HA-ADH$_{1.00}$HA-Ox$_{1.00\ (100\ kDa)}$ vs. HA-ADH$_{2.00}$HA-Ox$_{2.00\ (100\ kDa)}$	****	<0.0001
HA-ADH$_{3.00}$HA-Ox$_{1.00\ (100\ kDa)}$ vs. HA-ADH$_{1.00}$HA-Ox$_{3.00\ (100\ kDa)}$	ns	0.0748
HA-ADH$_{3.00}$HA-Ox$_{1.00\ (100\ kDa)}$ vs. HA-ADH$_{3.00}$HA-Ox$_{3.00\ (100\ kDa)}$	**	0.0023
HA-ADH$_{3.00}$HA-Ox$_{1.00\ (100\ kDa)}$ vs. HA-ADH$_{1.00}$HA-Ox$_{1.67\ (100\ kDa)}$	****	<0.0001
HA-ADH$_{3.00}$HA-Ox$_{1.00\ (100\ kDa)}$ vs. HA-ADH$_{3.00}$HA-Ox$_{2.33\ (100\ kDa)}$	ns	0.657
HA-ADH$_{3.00}$HA-Ox$_{1.00\ (100\ kDa)}$ vs. HA-ADH$_{2.33}$HA-Ox$_{1.00\ (100\ kDa)}$	ns	0.2964
HA-ADH$_{3.00}$HA-Ox$_{1.00\ (100\ kDa)}$ vs. HA-ADH$_{1.67}$HA-Ox$_{3.00\ (100\ kDa)}$	ns	0.2257
HA-ADH$_{3.00}$HA-Ox$_{1.00\ (100\ kDa)}$ vs. HA-ADH$_{2.00}$HA-Ox$_{2.00\ (100\ kDa)}$	****	<0.0001
HA-ADH$_{1.00}$HA-Ox$_{3.00\ (100\ kDa)}$ vs. HA-ADH$_{3.00}$HA-Ox$_{3.00\ (100\ kDa)}$	*	0.0446
HA-ADH$_{1.00}$HA-Ox$_{3.00\ (100\ kDa)}$ vs. HA-ADH$_{1.00}$HA-Ox$_{1.67\ (100\ kDa)}$	*	0.0121
HA-ADH$_{1.00}$HA-Ox$_{3.00\ (100\ kDa)}$ vs. HA-ADH$_{3.00}$HA-Ox$_{2.33\ (100\ kDa)}$	ns	0.0674
HA-ADH$_{1.00}$HA-Ox$_{3.00\ (100\ kDa)}$ vs. HA-ADH$_{2.33}$HA-Ox$_{1.00\ (100\ kDa)}$	ns	0.9998
HA-ADH$_{1.00}$HA-Ox$_{3.00\ (100\ kDa)}$ vs. HA-ADH$_{1.67}$HA-Ox$_{3.00\ (100\ kDa)}$	ns	>0.9999
HA-ADH$_{1.00}$HA-Ox$_{3.00\ (100\ kDa)}$ vs. HA-ADH$_{2.00}$HA-Ox$_{2.00\ (100\ kDa)}$	ns	0.5425
HA-ADH$_{3.00}$HA-Ox$_{3.00\ (100\ kDa)}$ vs. HA-ADH$_{1.00}$HA-Ox$_{1.67\ (100\ kDa)}$	****	<0.0001
HA-ADH$_{3.00}$HA-Ox$_{3.00\ (100\ kDa)}$ vs. HA-ADH$_{3.00}$HA-Ox$_{2.33\ (100\ kDa)}$	*	0.0417

HA-ADH$_{3.00}$HA-Ox$_{3.00\ (100\ kDa)}$ vs. HA-ADH$_{2.33}$HA-Ox$_{1.00\ (100\ kDa)}$	ns	0.1714
HA-ADH$_{3.00}$HA-Ox$_{3.00\ (100\ kDa)}$ vs. HA-ADH$_{1.67}$HA-Ox$_{3.00\ (100\ kDa)}$	ns	0.141
HA-ADH$_{3.00}$HA-Ox$_{3.00\ (100\ kDa)}$ vs. HA-ADH$_{2.00}$HA-Ox$_{2.00\ (100\ kDa)}$	****	<0.0001
HA-ADH$_{1.00}$HA-Ox$_{1.67\ (100\ kDa)}$ vs. HA-ADH$_{3.00}$HA-Ox$_{2.33\ (100\ kDa)}$	****	<0.0001
HA-ADH$_{1.00}$HA-Ox$_{1.67\ (100\ kDa)}$ vs. HA-ADH$_{2.33}$HA-Ox$_{1.00\ (100\ kDa)}$	*	0.0303
HA-ADH$_{1.00}$HA-Ox$_{1.67\ (100\ kDa)}$ vs. HA-ADH$_{1.67}$HA-Ox$_{3.00\ (100\ kDa)}$	*	0.0389
HA-ADH$_{1.00}$HA-Ox$_{1.67\ (100\ kDa)}$ vs. HA-ADH$_{2.00}$HA-Ox$_{2.00\ (100\ kDa)}$	****	<0.0001
HA-ADH$_{3.00}$HA-Ox$_{2.33\ (100\ kDa)}$ vs. HA-ADH$_{2.33}$HA-Ox$_{1.00\ (100\ kDa)}$	ns	0.2597
HA-ADH$_{3.00}$HA-Ox$_{2.33\ (100\ kDa)}$ vs. HA-ADH$_{1.67}$HA-Ox$_{3.00\ (100\ kDa)}$	ns	0.2018
HA-ADH$_{3.00}$HA-Ox$_{2.33\ (100\ kDa)}$ vs. HA-ADH$_{2.00}$HA-Ox$_{2.00\ (100\ kDa)}$	****	<0.0001
HA-ADH$_{2.33}$HA-Ox$_{1.00\ (100\ kDa)}$ vs. HA-ADH$_{1.67}$HA-Ox$_{3.00\ (100\ kDa)}$	ns	>0.9999
HA-ADH$_{2.33}$HA-Ox$_{1.00\ (100\ kDa)}$ vs. HA-ADH$_{2.00}$HA-Ox$_{2.00\ (100\ kDa)}$	ns	0.5742
HA-ADH$_{1.67}$HA-Ox$_{3.00\ (100\ kDa)}$ vs. HA-ADH$_{2.00}$HA-Ox$_{2.00\ (100\ kDa)}$	ns	0.9285

Statistical Analysis of Compressive Modulus

Table A4. Summary of significance for 40 kDa HA compressive modulus and 100 kDa HA compressive modulus. A summary of significance for the compressive modulus for both 40 kDa and 100 kDa is listed, a one-way ANOVA post-hoc Dunnett's T3 multiple comparisons was performed. n = 3; * $p < 0.05$, ** < p 0.01, *** $p < 0.001$, **** $p < 0.0001$.

Compressive Modulus Significance		
Dunnett's T3 multiple comparisons test	Summary	Adjusted P Value
HA-$ADH_{1.00}$HA-$Ox_{1.00\ (40\ kDa)}$ vs. HA-$ADH_{3.00}$HA-$Ox_{1.00\ (40\ kDa)}$	ns	0.9591
HA-$ADH_{1.00}$HA-$Ox_{1.00\ (40\ kDa)}$ vs. HA-$ADH_{1.00}$HA-$Ox_{3.00\ (40\ kDa)}$	ns	>0.9999
HA-$ADH_{1.00}$HA-$Ox_{1.00\ (40\ kDa)}$ vs. HA-$ADH_{3.00}$HA-$Ox_{3.00\ (40\ kDa)}$	ns	0.4543
HA-$ADH_{1.00}$HA-$Ox_{1.00\ (40\ kDa)}$ vs. HA-$ADH_{1.67}$HA-$Ox_{1.00\ (40\ kDa)}$	ns	0.5122
HA-$ADH_{1.00}$HA-$Ox_{1.00\ (40\ kDa)}$ vs. HA-$ADH_{2.00}$HA-$Ox_{2.00\ (40\ kDa)}$	ns	0.8766
HA-$ADH_{1.00}$HA-$Ox_{1.00\ (40\ kDa)}$ vs. HA-$ADH_{1.00}$HA-$Ox_{1.00\ (100\ kDa)}$	*	0.0297
HA-$ADH_{1.00}$HA-$Ox_{1.00\ (40\ kDa)}$ vs. HA-$ADH_{3.00}$HA-$Ox_{1.00\ (100\ kDa)}$	ns	0.3815
HA-$ADH_{1.00}$HA-$Ox_{1.00\ (40\ kDa)}$ vs. HA-$ADH_{1.00}$HA-$Ox_{3.00\ (100\ kDa)}$	ns	0.5412
HA-$ADH_{1.00}$HA-$Ox_{1.00\ (40\ kDa)}$ vs. HA-$ADH_{3.00}$HA-$Ox_{3.00\ (100\ kDa)}$	ns	0.1398
HA-$ADH_{1.00}$HA-$Ox_{1.00\ (40\ kDa)}$ vs. HA-$ADH_{1.00}$HA-$Ox_{1.67\ (100\ kDa)}$	ns	0.2201
HA-$ADH_{1.00}$HA-$Ox_{1.00\ (40\ kDa)}$ vs. HA-$ADH_{3.00}$HA-$Ox_{2.33\ (100\ kDa)}$	**	0.0065
HA-$ADH_{1.00}$HA-$Ox_{1.00\ (40\ kDa)}$ vs. HA-$ADH_{2.33}$HA-$Ox_{1.00\ (100\ kDa)}$	*	0.0296
HA-$ADH_{1.00}$HA-$Ox_{1.00\ (40\ kDa)}$ vs. HA-$ADH_{1.67}$HA-$Ox_{3.00\ (100\ kDa)}$	ns	0.1101
HA-$ADH_{1.00}$HA-$Ox_{1.00\ (40\ kDa)}$ vs. HA-$ADH_{2.00}$HA-$Ox_{2.00\ (100\ kDa)}$	***	0.0001
HA-$ADH_{3.00}$HA-$Ox_{1.00\ (40\ kDa)}$ vs. HA-$ADH_{1.00}$HA-$Ox_{3.00\ (40\ kDa)}$	ns	0.9702
HA-$ADH_{3.00}$HA-$Ox_{1.00\ (40\ kDa)}$ vs. HA-$ADH_{3.00}$HA-$Ox_{3.00\ (40\ kDa)}$	ns	0.5643
HA-$ADH_{3.00}$HA-$Ox_{1.00\ (40\ kDa)}$ vs. HA-$ADH_{1.67}$HA-$Ox_{1.00\ (40\ kDa)}$	ns	0.9999
HA-$ADH_{3.00}$HA-$Ox_{1.00\ (40\ kDa)}$ vs. HA-$ADH_{2.00}$HA-$Ox_{2.00\ (40\ kDa)}$	ns	0.9989
HA-$ADH_{3.00}$HA-$Ox_{1.00\ (40\ kDa)}$ vs. HA-$ADH_{1.00}$HA-$Ox_{1.00\ (100\ kDa)}$	ns	0.144
HA-$ADH_{3.00}$HA-$Ox_{1.00\ (40\ kDa)}$ vs. HA-$ADH_{3.00}$HA-$Ox_{1.00\ (100\ kDa)}$	ns	0.431
HA-$ADH_{3.00}$HA-$Ox_{1.00\ (40\ kDa)}$ vs. HA-$ADH_{1.00}$HA-$Ox_{3.00\ (100\ kDa)}$	ns	0.6178
HA-$ADH_{3.00}$HA-$Ox_{1.00\ (40\ kDa)}$ vs. HA-$ADH_{3.00}$HA-$Ox_{3.00\ (100\ kDa)}$	ns	0.1057
HA-$ADH_{3.00}$HA-$Ox_{1.00\ (40\ kDa)}$ vs. HA-$ADH_{1.00}$HA-$Ox_{1.67\ (100\ kDa)}$	ns	0.2891
HA-$ADH_{3.00}$HA-$Ox_{1.00\ (40\ kDa)}$ vs. HA-$ADH_{3.00}$HA-$Ox_{2.33\ (100\ kDa)}$	**	0.0036
HA-$ADH_{3.00}$HA-$Ox_{1.00\ (40\ kDa)}$ vs. HA-$ADH_{2.33}$HA-$Ox_{1.00\ (100\ kDa)}$	*	0.0491
HA-$ADH_{3.00}$HA-$Ox_{1.00\ (40\ kDa)}$ vs. HA-$ADH_{1.67}$HA-$Ox_{3.00\ (100\ kDa)}$	ns	0.0833

HA-ADH$_{3.00}$HA-Ox$_{1.00\ (40\ kDa)}$ vs. HA-ADH$_{2.00}$HA-Ox$_{2.00\ (100\ kDa)}$	***	0.0002
HA-ADH$_{1.00}$HA-Ox$_{3.00\ (40\ kDa)}$ vs. HA-ADH$_{3.00}$HA-Ox$_{3.00\ (40\ kDa)}$	ns	0.4708
HA-ADH$_{1.00}$HA-Ox$_{3.00\ (40\ kDa)}$ vs. HA-ADH$_{1.67}$HA-Ox$_{1.00\ (40\ kDa)}$	ns	0.5468
HA-ADH$_{1.00}$HA-Ox$_{3.00\ (40\ kDa)}$ vs. HA-ADH$_{2.00}$HA-Ox$_{2.00\ (40\ kDa)}$	ns	0.9131
HA-ADH$_{1.00}$HA-Ox$_{3.00\ (40\ kDa)}$ vs. HA-ADH$_{1.00}$HA-Ox$_{1.00\ (100\ kDa)}$	*	0.0434
HA-ADH$_{1.00}$HA-Ox$_{3.00\ (40\ kDa)}$ vs. HA-ADH$_{3.00}$HA-Ox$_{1.00\ (100\ kDa)}$	ns	0.3904
HA-ADH$_{1.00}$HA-Ox$_{3.00\ (40\ kDa)}$ vs. HA-ADH$_{1.00}$HA-Ox$_{3.00\ (100\ kDa)}$	ns	0.5559
HA-ADH$_{1.00}$HA-Ox$_{3.00\ (40\ kDa)}$ vs. HA-ADH$_{3.00}$HA-Ox$_{3.00\ (100\ kDa)}$	ns	0.1407
HA-ADH$_{1.00}$HA-Ox$_{3.00\ (40\ kDa)}$ vs. HA-ADH$_{1.00}$HA-Ox$_{1.67\ (100\ kDa)}$	ns	0.2246
HA-ADH$_{1.00}$HA-Ox$_{3.00\ (40\ kDa)}$ vs. HA-ADH$_{3.00}$HA-Ox$_{2.33\ (100\ kDa)}$	*	0.0243
HA-ADH$_{1.00}$HA-Ox$_{3.00\ (40\ kDa)}$ vs. HA-ADH$_{2.33}$HA-Ox$_{1.00\ (100\ kDa)}$	ns	0.0734
HA-ADH$_{1.00}$HA-Ox$_{3.00\ (40\ kDa)}$ vs. HA-ADH$_{1.67}$HA-Ox$_{3.00\ (100\ kDa)}$	ns	0.1083
HA-ADH$_{1.00}$HA-Ox$_{3.00\ (40\ kDa)}$ vs. HA-ADH$_{2.00}$HA-Ox$_{2.00\ (100\ kDa)}$	***	0.0003
HA-ADH$_{3.00}$HA-Ox$_{3.00\ (40\ kDa)}$ vs. HA-ADH$_{1.67}$HA-Ox$_{1.00\ (40\ kDa)}$	ns	0.638
HA-ADH$_{3.00}$HA-Ox$_{3.00\ (40\ kDa)}$ vs. HA-ADH$_{2.00}$HA-Ox$_{2.00\ (40\ kDa)}$	ns	0.8503
HA-ADH$_{3.00}$HA-Ox$_{3.00\ (40\ kDa)}$ vs. HA-ADH$_{1.00}$HA-Ox$_{1.00\ (100\ kDa)}$	ns	0.9537
HA-ADH$_{3.00}$HA-Ox$_{3.00\ (40\ kDa)}$ vs. HA-ADH$_{3.00}$HA-Ox$_{1.00\ (100\ kDa)}$	ns	0.9545
HA-ADH$_{3.00}$HA-Ox$_{3.00\ (40\ kDa)}$ vs. HA-ADH$_{1.00}$HA-Ox$_{3.00\ (100\ kDa)}$	ns	>0.9999
HA-ADH$_{3.00}$HA-Ox$_{3.00\ (40\ kDa)}$ vs. HA-ADH$_{3.00}$HA-Ox$_{3.00\ (100\ kDa)}$	ns	0.9992
HA-ADH$_{3.00}$HA-Ox$_{3.00\ (40\ kDa)}$ vs. HA-ADH$_{1.00}$HA-Ox$_{1.67\ (100\ kDa)}$	ns	>0.9999
HA-ADH$_{3.00}$HA-Ox$_{3.00\ (40\ kDa)}$ vs. HA-ADH$_{3.00}$HA-Ox$_{2.33\ (100\ kDa)}$	ns	0.7687
HA-ADH$_{3.00}$HA-Ox$_{3.00\ (40\ kDa)}$ vs. HA-ADH$_{2.33}$HA-Ox$_{1.00\ (100\ kDa)}$	ns	0.9996
HA-ADH$_{3.00}$HA-Ox$_{3.00\ (40\ kDa)}$ vs. HA-ADH$_{1.67}$HA-Ox$_{3.00\ (100\ kDa)}$	ns	>0.9999
HA-ADH$_{3.00}$HA-Ox$_{3.00\ (40\ kDa)}$ vs. HA-ADH$_{2.00}$HA-Ox$_{2.00\ (100\ kDa)}$	ns	0.2458
HA-ADH$_{1.67}$HA-Ox$_{1.00\ (40\ kDa)}$ vs. HA-ADH$_{2.00}$HA-Ox$_{2.00\ (40\ kDa)}$	ns	>0.9999
HA-ADH$_{1.67}$HA-Ox$_{1.00\ (40\ kDa)}$ vs. HA-ADH$_{1.00}$HA-Ox$_{1.00\ (100\ kDa)}$	ns	0.2323
HA-ADH$_{1.67}$HA-Ox$_{1.00\ (40\ kDa)}$ vs. HA-ADH$_{3.00}$HA-Ox$_{1.00\ (100\ kDa)}$	ns	0.4638
HA-ADH$_{1.67}$HA-Ox$_{1.00\ (40\ kDa)}$ vs. HA-ADH$_{1.00}$HA-Ox$_{3.00\ (100\ kDa)}$	ns	0.6686
HA-ADH$_{1.67}$HA-Ox$_{1.00\ (40\ kDa)}$ vs. HA-ADH$_{3.00}$HA-Ox$_{3.00\ (100\ kDa)}$	ns	0.203
HA-ADH$_{1.67}$HA-Ox$_{1.00\ (40\ kDa)}$ vs. HA-ADH$_{1.00}$HA-Ox$_{1.67\ (100\ kDa)}$	ns	0.3314
HA-ADH$_{1.67}$HA-Ox$_{1.00\ (40\ kDa)}$ vs. HA-ADH$_{3.00}$HA-Ox$_{2.33\ (100\ kDa)}$	**	0.0039
HA-ADH$_{1.67}$HA-Ox$_{1.00\ (40\ kDa)}$ vs. HA-ADH$_{2.33}$HA-Ox$_{1.00\ (100\ kDa)}$	ns	0.057
HA-ADH$_{1.67}$HA-Ox$_{1.00\ (40\ kDa)}$ vs. HA-ADH$_{1.67}$HA-Ox$_{3.00\ (100\ kDa)}$	ns	0.0997

HA-ADH$_{1.67}$HA-Ox$_{1.00\ (40\ kDa)}$ vs. HA-ADH$_{2.00}$HA-Ox$_{2.00\ (100\ kDa)}$	***	0.0003
HA-ADH$_{2.00}$HA-Ox$_{2.00\ (40\ kDa)}$ vs. HA-ADH$_{1.00}$HA-Ox$_{1.00\ (100\ kDa)}$	ns	0.9845
HA-ADH$_{2.00}$HA-Ox$_{2.00\ (40\ kDa)}$ vs. HA-ADH$_{3.00}$HA-Ox$_{1.00\ (100\ kDa)}$	ns	0.5079
HA-ADH$_{2.00}$HA-Ox$_{2.00\ (40\ kDa)}$ vs. HA-ADH$_{1.00}$HA-Ox$_{3.00\ (100\ kDa)}$	ns	0.7857
HA-ADH$_{2.00}$HA-Ox$_{2.00\ (40\ kDa)}$ vs. HA-ADH$_{3.00}$HA-Ox$_{3.00\ (100\ kDa)}$	ns	0.2589
HA-ADH$_{2.00}$HA-Ox$_{2.00\ (40\ kDa)}$ vs. HA-ADH$_{1.00}$HA-Ox$_{1.67\ (100\ kDa)}$	ns	0.5083
HA-ADH$_{2.00}$HA-Ox$_{2.00\ (40\ kDa)}$ vs. HA-ADH$_{3.00}$HA-Ox$_{2.33\ (100\ kDa)}$	ns	0.0877
HA-ADH$_{2.00}$HA-Ox$_{2.00\ (40\ kDa)}$ vs. HA-ADH$_{2.33}$HA-Ox$_{1.00\ (100\ kDa)}$	ns	0.1852
HA-ADH$_{2.00}$HA-Ox$_{2.00\ (40\ kDa)}$ vs. HA-ADH$_{1.67}$HA-Ox$_{3.00\ (100\ kDa)}$	ns	0.2961
HA-ADH$_{2.00}$HA-Ox$_{2.00\ (40\ kDa)}$ vs. HA-ADH$_{2.00}$HA-Ox$_{2.00\ (100\ kDa)}$	**	0.0047
HA-ADH$_{1.00}$HA-Ox$_{1.00\ (100\ kDa)}$ vs. HA-ADH$_{3.00}$HA-Ox$_{1.00\ (100\ kDa)}$	ns	0.6264
HA-ADH$_{1.00}$HA-Ox$_{1.00\ (100\ kDa)}$ vs. HA-ADH$_{1.00}$HA-Ox$_{3.00\ (100\ kDa)}$	ns	0.8819
HA-ADH$_{1.00}$HA-Ox$_{1.00\ (100\ kDa)}$ vs. HA-ADH$_{3.00}$HA-Ox$_{3.00\ (100\ kDa)}$	ns	0.3723
HA-ADH$_{1.00}$HA-Ox$_{1.00\ (100\ kDa)}$ vs. HA-ADH$_{1.00}$HA-Ox$_{1.67\ (100\ kDa)}$	ns	0.6428
HA-ADH$_{1.00}$HA-Ox$_{1.00\ (100\ kDa)}$ vs. HA-ADH$_{3.00}$HA-Ox$_{2.33\ (100\ kDa)}$	*	0.0263
HA-ADH$_{1.00}$HA-Ox$_{1.00\ (100\ kDa)}$ vs. HA-ADH$_{2.33}$HA-Ox$_{1.00\ (100\ kDa)}$	ns	0.1541
HA-ADH$_{1.00}$HA-Ox$_{1.00\ (100\ kDa)}$ vs. HA-ADH$_{1.67}$HA-Ox$_{3.00\ (100\ kDa)}$	ns	0.2902
HA-ADH$_{1.00}$HA-Ox$_{1.00\ (100\ kDa)}$ vs. HA-ADH$_{2.00}$HA-Ox$_{2.00\ (100\ kDa)}$	***	0.001
HA-ADH$_{3.00}$HA-Ox$_{1.00\ (100\ kDa)}$ vs. HA-ADH$_{1.00}$HA-Ox$_{3.00\ (100\ kDa)}$	ns	>0.9999
HA-ADH$_{3.00}$HA-Ox$_{1.00\ (100\ kDa)}$ vs. HA-ADH$_{3.00}$HA-Ox$_{3.00\ (100\ kDa)}$	ns	0.9991
HA-ADH$_{3.00}$HA-Ox$_{1.00\ (100\ kDa)}$ vs. HA-ADH$_{1.00}$HA-Ox$_{1.67\ (100\ kDa)}$	ns	0.9743
HA-ADH$_{3.00}$HA-Ox$_{1.00\ (100\ kDa)}$ vs. HA-ADH$_{3.00}$HA-Ox$_{2.33\ (100\ kDa)}$	ns	>0.9999
HA-ADH$_{3.00}$HA-Ox$_{1.00\ (100\ kDa)}$ vs. HA-ADH$_{2.33}$HA-Ox$_{1.00\ (100\ kDa)}$	ns	0.9915
HA-ADH$_{3.00}$HA-Ox$_{1.00\ (100\ kDa)}$ vs. HA-ADH$_{1.67}$HA-Ox$_{3.00\ (100\ kDa)}$	ns	0.9682
HA-ADH$_{3.00}$HA-Ox$_{1.00\ (100\ kDa)}$ vs. HA-ADH$_{2.00}$HA-Ox$_{2.00\ (100\ kDa)}$	ns	0.9996
HA-ADH$_{1.00}$HA-Ox$_{3.00\ (100\ kDa)}$ vs. HA-ADH$_{3.00}$HA-Ox$_{3.00\ (100\ kDa)}$	ns	>0.9999
HA-ADH$_{1.00}$HA-Ox$_{3.00\ (100\ kDa)}$ vs. HA-ADH$_{1.00}$HA-Ox$_{1.67\ (100\ kDa)}$	ns	>0.9999
HA-ADH$_{1.00}$HA-Ox$_{3.00\ (100\ kDa)}$ vs. HA-ADH$_{3.00}$HA-Ox$_{2.33\ (100\ kDa)}$	ns	>0.9999
HA-ADH$_{1.00}$HA-Ox$_{3.00\ (100\ kDa)}$ vs. HA-ADH$_{2.33}$HA-Ox$_{1.00\ (100\ kDa)}$	ns	>0.9999
HA-ADH$_{1.00}$HA-Ox$_{3.00\ (100\ kDa)}$ vs. HA-ADH$_{1.67}$HA-Ox$_{3.00\ (100\ kDa)}$	ns	>0.9999
HA-ADH$_{1.00}$HA-Ox$_{3.00\ (100\ kDa)}$ vs. HA-ADH$_{2.00}$HA-Ox$_{2.00\ (100\ kDa)}$	ns	0.8547
HA-ADH$_{3.00}$HA-Ox$_{3.00\ (100\ kDa)}$ vs. HA-ADH$_{1.00}$HA-Ox$_{1.67\ (100\ kDa)}$	ns	>0.9999
HA-ADH$_{3.00}$HA-Ox$_{3.00\ (100\ kDa)}$ vs. HA-ADH$_{3.00}$HA-Ox$_{2.33\ (100\ kDa)}$	ns	0.9655

HA-ADH$_{3.00}$HA-Ox$_{3.00\ (100\ kDa)}$ vs. HA-ADH$_{2.33}$HA-Ox$_{1.00\ (100\ kDa)}$	ns	>0.9999
HA-ADH$_{3.00}$HA-Ox$_{3.00\ (100\ kDa)}$ vs. HA-ADH$_{1.67}$HA-Ox$_{3.00\ (100\ kDa)}$	ns	>0.9999
HA-ADH$_{3.00}$HA-Ox$_{3.00\ (100\ kDa)}$ vs. HA-ADH$_{2.00}$HA-Ox$_{2.00\ (100\ kDa)}$	ns	0.1859
HA-ADH$_{1.00}$HA-Ox$_{1.67\ (100\ kDa)}$ vs. HA-ADH$_{3.00}$HA-Ox$_{2.33\ (100\ kDa)}$	ns	0.6977
HA-ADH$_{1.00}$HA-Ox$_{1.67\ (100\ kDa)}$ vs. HA-ADH$_{2.33}$HA-Ox$_{1.00\ (100\ kDa)}$	ns	>0.9999
HA-ADH$_{1.00}$HA-Ox$_{1.67\ (100\ kDa)}$ vs. HA-ADH$_{1.67}$HA-Ox$_{3.00\ (100\ kDa)}$	ns	>0.9999
HA-ADH$_{1.00}$HA-Ox$_{1.67\ (100\ kDa)}$ vs. HA-ADH$_{2.00}$HA-Ox$_{2.00\ (100\ kDa)}$	ns	0.1135
HA-ADH$_{3.00}$HA-Ox$_{2.33\ (100\ kDa)}$ vs. HA-ADH$_{2.33}$HA-Ox$_{1.00\ (100\ kDa)}$	ns	0.7478
HA-ADH$_{3.00}$HA-Ox$_{2.33\ (100\ kDa)}$ vs. HA-ADH$_{1.67}$HA-Ox$_{3.00\ (100\ kDa)}$	ns	0.5603
HA-ADH$_{3.00}$HA-Ox$_{2.33\ (100\ kDa)}$ vs. HA-ADH$_{2.00}$HA-Ox$_{2.00\ (100\ kDa)}$	ns	0.2718
HA-ADH$_{2.33}$HA-Ox$_{1.00\ (100\ kDa)}$ vs. HA-ADH$_{1.67}$HA-Ox$_{3.00\ (100\ kDa)}$	ns	>0.9999
HA-ADH$_{2.33}$HA-Ox$_{1.00\ (100\ kDa)}$ vs. HA-ADH$_{2.00}$HA-Ox$_{2.00\ (100\ kDa)}$	ns	0.0538
HA-ADH$_{1.67}$HA-Ox$_{3.00\ (100\ kDa)}$ vs. HA-ADH$_{2.00}$HA-Ox$_{2.00\ (100\ kDa)}$	*	0.044

Statistical Analysis of Mass Change

Table A5. Summary of significance for 40 kDa HA mass change and 100 kDa HA mass change. A summary of significance for the mass change for both 40 kDa and 100 kDa is listed, a two-way ANOVA post-hoc Tukey's multiple comparisons was performed. n = 3; * $p < 0.05$, ** < p 0.01, *** $p < 0.001$, **** $p < 0.0001$.

Mass Change Significance		
Tukey's multiple comparisons test	Summary	Adjusted P Value
Day 1		
HA-$ADH_{3.00}$HA-$Ox_{3.00\ (40\ kDa)}$ vs. HA-$ADH_{3.00}$HA-$Ox_{1.00\ (40\ kDa)}$	ns	0.484
HA-$ADH_{3.00}$HA-$Ox_{3.00\ (40\ kDa)}$ vs. HA-$ADH_{2.00}$HA-$Ox_{2.00\ (40\ kDa)}$	ns	0.5557
HA-$ADH_{3.00}$HA-$Ox_{3.00\ (40\ kDa)}$ vs. HA-$ADH_{1.67}$HA-$Ox_{1.00\ (40\ kDa)}$	ns	0.6338
HA-$ADH_{3.00}$HA-$Ox_{3.00\ (40\ kDa)}$ vs. HA-$ADH_{1.00}$HA-$Ox_{3.00\ (40\ kDa)}$	ns	0.9969
HA-$ADH_{3.00}$HA-$Ox_{3.00\ (40\ kDa)}$ vs. HA-$ADH_{1.00}$HA-$Ox_{1.00\ (40\ kDa)}$	ns	0.3629
HA-$ADH_{3.00}$HA-$Ox_{3.00\ (40\ kDa)}$ vs. HA-$ADH_{3.00}$HA-$Ox_{3.00\ (100\ kDa)}$	ns	0.1086
HA-$ADH_{3.00}$HA-$Ox_{3.00\ (40\ kDa)}$ vs. HA-$ADH_{3.00}$HA-$Ox_{2.33\ (100\ kDa)}$	ns	0.7109
HA-$ADH_{3.00}$HA-$Ox_{3.00\ (40\ kDa)}$ vs. HA-$ADH_{3.00}$HA-$Ox_{1.00\ (100\ kDa)}$	ns	>0.9999
HA-$ADH_{3.00}$HA-$Ox_{3.00\ (40\ kDa)}$ vs. HA-$ADH_{2.33}$HA-$Ox_{1.00\ (100\ kDa)}$	ns	0.9294
HA-$ADH_{3.00}$HA-$Ox_{3.00\ (40\ kDa)}$ vs. HA-$ADH_{2.00}$HA-$Ox_{2.00\ (100\ kDa)}$	ns	0.7845
HA-$ADH_{3.00}$HA-$Ox_{3.00\ (40\ kDa)}$ vs. HA-$ADH_{1.67}$HA-$Ox_{3.00\ (100\ kDa)}$	ns	>0.9999
HA-$ADH_{3.00}$HA-$Ox_{3.00\ (40\ kDa)}$ vs. HA-$ADH_{1.00}$HA-$Ox_{3.00\ (100\ kDa)}$	ns	0.683
HA-$ADH_{3.00}$HA-$Ox_{3.00\ (40\ kDa)}$ vs. HA-$ADH_{1.00}$HA-$Ox_{1.67\ (100\ kDa)}$	ns	>0.9999
HA-$ADH_{3.00}$HA-$Ox_{3.00\ (40\ kDa)}$ vs. HA-$ADH_{1.00}$HA-$Ox_{1.00\ (100\ kDa)}$	ns	0.3514
HA-$ADH_{3.00}$HA-$Ox_{1.00\ (40\ kDa)}$ vs. HA-$ADH_{2.00}$HA-$Ox_{2.00\ (40\ kDa)}$	ns	0.7532
HA-$ADH_{3.00}$HA-$Ox_{1.00\ (40\ kDa)}$ vs. HA-$ADH_{1.67}$HA-$Ox_{1.00\ (40\ kDa)}$	ns	0.7932
HA-$ADH_{3.00}$HA-$Ox_{1.00\ (40\ kDa)}$ vs. HA-$ADH_{1.00}$HA-$Ox_{3.00\ (40\ kDa)}$	ns	>0.9999
HA-$ADH_{3.00}$HA-$Ox_{1.00\ (40\ kDa)}$ vs. HA-$ADH_{1.00}$HA-$Ox_{1.00\ (40\ kDa)}$	ns	>0.9999
HA-$ADH_{3.00}$HA-$Ox_{1.00\ (40\ kDa)}$ vs. HA-$ADH_{3.00}$HA-$Ox_{3.00\ (100\ kDa)}$	ns	0.1164
HA-$ADH_{3.00}$HA-$Ox_{1.00\ (40\ kDa)}$ vs. HA-$ADH_{3.00}$HA-$Ox_{2.33\ (100\ kDa)}$	ns	0.2618
HA-$ADH_{3.00}$HA-$Ox_{1.00\ (40\ kDa)}$ vs. HA-$ADH_{3.00}$HA-$Ox_{1.00\ (100\ kDa)}$	ns	0.5469
HA-$ADH_{3.00}$HA-$Ox_{1.00\ (40\ kDa)}$ vs. HA-$ADH_{2.33}$HA-$Ox_{1.00\ (100\ kDa)}$	ns	0.3309
HA-$ADH_{3.00}$HA-$Ox_{1.00\ (40\ kDa)}$ vs. HA-$ADH_{2.00}$HA-$Ox_{2.00\ (100\ kDa)}$	ns	0.2637
HA-$ADH_{3.00}$HA-$Ox_{1.00\ (40\ kDa)}$ vs. HA-$ADH_{1.67}$HA-$Ox_{3.00\ (100\ kDa)}$	ns	0.855

HA-ADH$_{3.00}$HA-Ox$_{1.00\ (40\ kDa)}$ vs. HA-ADH$_{1.00}$HA-Ox$_{3.00\ (100\ kDa)}$	ns	>0.9999
HA-ADH$_{3.00}$HA-Ox$_{1.00\ (40\ kDa)}$ vs. HA-ADH$_{1.00}$HA-Ox$_{1.67\ (100\ kDa)}$	ns	0.8929
HA-ADH$_{3.00}$HA-Ox$_{1.00\ (40\ kDa)}$ vs. HA-ADH$_{1.00}$HA-Ox$_{1.00\ (100\ kDa)}$	ns	0.2722
HA-ADH$_{2.00}$HA-Ox$_{2.00\ (40\ kDa)}$ vs. HA-ADH$_{1.67}$HA-Ox$_{1.00\ (40\ kDa)}$	ns	>0.9999
HA-ADH$_{2.00}$HA-Ox$_{2.00\ (40\ kDa)}$ vs. HA-ADH$_{1.00}$HA-Ox$_{3.00\ (40\ kDa)}$	ns	0.9999
HA-ADH$_{2.00}$HA-Ox$_{2.00\ (40\ kDa)}$ vs. HA-ADH$_{1.00}$HA-Ox$_{1.00\ (40\ kDa)}$	ns	0.7066
HA-ADH$_{2.00}$HA-Ox$_{2.00\ (40\ kDa)}$ vs. HA-ADH$_{3.00}$HA-Ox$_{3.00\ (100\ kDa)}$	ns	0.0524
HA-ADH$_{2.00}$HA-Ox$_{2.00\ (40\ kDa)}$ vs. HA-ADH$_{3.00}$HA-Ox$_{2.33\ (100\ kDa)}$	ns	0.302
HA-ADH$_{2.00}$HA-Ox$_{2.00\ (40\ kDa)}$ vs. HA-ADH$_{3.00}$HA-Ox$_{1.00\ (100\ kDa)}$	ns	0.9163
HA-ADH$_{2.00}$HA-Ox$_{2.00\ (40\ kDa)}$ vs. HA-ADH$_{2.33}$HA-Ox$_{1.00\ (100\ kDa)}$	ns	0.424
HA-ADH$_{2.00}$HA-Ox$_{2.00\ (40\ kDa)}$ vs. HA-ADH$_{2.00}$HA-Ox$_{2.00\ (100\ kDa)}$	ns	0.489
HA-ADH$_{2.00}$HA-Ox$_{2.00\ (40\ kDa)}$ vs. HA-ADH$_{1.67}$HA-Ox$_{3.00\ (100\ kDa)}$	ns	>0.9999
HA-ADH$_{2.00}$HA-Ox$_{2.00\ (40\ kDa)}$ vs. HA-ADH$_{1.00}$HA-Ox$_{3.00\ (100\ kDa)}$	ns	0.9259
HA-ADH$_{2.00}$HA-Ox$_{2.00\ (40\ kDa)}$ vs. HA-ADH$_{1.00}$HA-Ox$_{1.67\ (100\ kDa)}$	ns	>0.9999
HA-ADH$_{2.00}$HA-Ox$_{2.00\ (40\ kDa)}$ vs. HA-ADH$_{1.00}$HA-Ox$_{1.00\ (100\ kDa)}$	ns	0.068
HA-ADH$_{1.67}$HA-Ox$_{1.00\ (40\ kDa)}$ vs. HA-ADH$_{1.00}$HA-Ox$_{3.00\ (40\ kDa)}$	ns	>0.9999
HA-ADH$_{1.67}$HA-Ox$_{1.00\ (40\ kDa)}$ vs. HA-ADH$_{1.00}$HA-Ox$_{1.00\ (40\ kDa)}$	ns	0.773
HA-ADH$_{1.67}$HA-Ox$_{1.00\ (40\ kDa)}$ vs. HA-ADH$_{3.00}$HA-Ox$_{3.00\ (100\ kDa)}$	*	0.0444
HA-ADH$_{1.67}$HA-Ox$_{1.00\ (40\ kDa)}$ vs. HA-ADH$_{3.00}$HA-Ox$_{2.33\ (100\ kDa)}$	ns	0.2954
HA-ADH$_{1.67}$HA-Ox$_{1.00\ (40\ kDa)}$ vs. HA-ADH$_{3.00}$HA-Ox$_{1.00\ (100\ kDa)}$	ns	0.9206
HA-ADH$_{1.67}$HA-Ox$_{1.00\ (40\ kDa)}$ vs. HA-ADH$_{2.33}$HA-Ox$_{1.00\ (100\ kDa)}$	ns	0.4266
HA-ADH$_{1.67}$HA-Ox$_{1.00\ (40\ kDa)}$ vs. HA-ADH$_{2.00}$HA-Ox$_{2.00\ (100\ kDa)}$	ns	0.4784
HA-ADH$_{1.67}$HA-Ox$_{1.00\ (40\ kDa)}$ vs. HA-ADH$_{1.67}$HA-Ox$_{3.00\ (100\ kDa)}$	ns	>0.9999
HA-ADH$_{1.67}$HA-Ox$_{1.00\ (40\ kDa)}$ vs. HA-ADH$_{1.00}$HA-Ox$_{3.00\ (100\ kDa)}$	ns	0.9473
HA-ADH$_{1.67}$HA-Ox$_{1.00\ (40\ kDa)}$ vs. HA-ADH$_{1.00}$HA-Ox$_{1.67\ (100\ kDa)}$	ns	>0.9999
HA-ADH$_{1.67}$HA-Ox$_{1.00\ (40\ kDa)}$ vs. HA-ADH$_{1.00}$HA-Ox$_{1.00\ (100\ kDa)}$	ns	0.1043
HA-ADH$_{1.00}$HA-Ox$_{3.00\ (40\ kDa)}$ vs. HA-ADH$_{1.00}$HA-Ox$_{1.00\ (40\ kDa)}$	ns	>0.9999
HA-ADH$_{1.00}$HA-Ox$_{3.00\ (40\ kDa)}$ vs. HA-ADH$_{3.00}$HA-Ox$_{3.00\ (100\ kDa)}$	ns	0.8693
HA-ADH$_{1.00}$HA-Ox$_{3.00\ (40\ kDa)}$ vs. HA-ADH$_{3.00}$HA-Ox$_{2.33\ (100\ kDa)}$	ns	0.9709
HA-ADH$_{1.00}$HA-Ox$_{3.00\ (40\ kDa)}$ vs. HA-ADH$_{3.00}$HA-Ox$_{1.00\ (100\ kDa)}$	ns	0.998
HA-ADH$_{1.00}$HA-Ox$_{3.00\ (40\ kDa)}$ vs. HA-ADH$_{2.33}$HA-Ox$_{1.00\ (100\ kDa)}$	ns	0.9846
HA-ADH$_{1.00}$HA-Ox$_{3.00\ (40\ kDa)}$ vs. HA-ADH$_{2.00}$HA-Ox$_{2.00\ (100\ kDa)}$	ns	0.9557
HA-ADH$_{1.00}$HA-Ox$_{3.00\ (40\ kDa)}$ vs. HA-ADH$_{1.67}$HA-Ox$_{3.00\ (100\ kDa)}$	ns	0.9997

HA-ADH$_{1.00}$HA-Ox$_{3.00\ (40\ kDa)}$ vs. HA-ADH$_{1.00}$HA-Ox$_{3.00\ (100\ kDa)}$	ns	>0.9999
HA-ADH$_{1.00}$HA-Ox$_{3.00\ (40\ kDa)}$ vs. HA-ADH$_{1.00}$HA-Ox$_{1.67\ (100\ kDa)}$	ns	0.9997
HA-ADH$_{1.00}$HA-Ox$_{3.00\ (40\ kDa)}$ vs. HA-ADH$_{1.00}$HA-Ox$_{1.00\ (100\ kDa)}$	ns	0.9713
HA-ADH$_{1.00}$HA-Ox$_{1.00\ (40\ kDa)}$ vs. HA-ADH$_{3.00}$HA-Ox$_{3.00\ (100\ kDa)}$	*	0.0491
HA-ADH$_{1.00}$HA-Ox$_{1.00\ (40\ kDa)}$ vs. HA-ADH$_{3.00}$HA-Ox$_{2.33\ (100\ kDa)}$	ns	0.1617
HA-ADH$_{1.00}$HA-Ox$_{1.00\ (40\ kDa)}$ vs. HA-ADH$_{3.00}$HA-Ox$_{1.00\ (100\ kDa)}$	ns	0.4526
HA-ADH$_{1.00}$HA-Ox$_{1.00\ (40\ kDa)}$ vs. HA-ADH$_{2.33}$HA-Ox$_{1.00\ (100\ kDa)}$	ns	0.2208
HA-ADH$_{1.00}$HA-Ox$_{1.00\ (40\ kDa)}$ vs. HA-ADH$_{2.00}$HA-Ox$_{2.00\ (100\ kDa)}$	ns	0.2375
HA-ADH$_{1.00}$HA-Ox$_{1.00\ (40\ kDa)}$ vs. HA-ADH$_{1.67}$HA-Ox$_{3.00\ (100\ kDa)}$	ns	0.8852
HA-ADH$_{1.00}$HA-Ox$_{1.00\ (40\ kDa)}$ vs. HA-ADH$_{1.00}$HA-Ox$_{3.00\ (100\ kDa)}$	ns	>0.9999
HA-ADH$_{1.00}$HA-Ox$_{1.00\ (40\ kDa)}$ vs. HA-ADH$_{1.00}$HA-Ox$_{1.67\ (100\ kDa)}$	ns	0.9225
HA-ADH$_{1.00}$HA-Ox$_{1.00\ (40\ kDa)}$ vs. HA-ADH$_{1.00}$HA-Ox$_{1.00\ (100\ kDa)}$	ns	0.1607
HA-ADH$_{3.00}$HA-Ox$_{3.00\ (100\ kDa)}$ vs. HA-ADH$_{3.00}$HA-Ox$_{2.33\ (100\ kDa)}$	ns	0.6167
HA-ADH$_{3.00}$HA-Ox$_{3.00\ (100\ kDa)}$ vs. HA-ADH$_{3.00}$HA-Ox$_{1.00\ (100\ kDa)}$	ns	0.1228
HA-ADH$_{3.00}$HA-Ox$_{3.00\ (100\ kDa)}$ vs. HA-ADH$_{2.33}$HA-Ox$_{1.00\ (100\ kDa)}$	ns	0.3806
HA-ADH$_{3.00}$HA-Ox$_{3.00\ (100\ kDa)}$ vs. HA-ADH$_{2.00}$HA-Ox$_{2.00\ (100\ kDa)}$	ns	0.9736
HA-ADH$_{3.00}$HA-Ox$_{3.00\ (100\ kDa)}$ vs. HA-ADH$_{1.67}$HA-Ox$_{3.00\ (100\ kDa)}$	ns	0.3941
HA-ADH$_{3.00}$HA-Ox$_{3.00\ (100\ kDa)}$ vs. HA-ADH$_{1.00}$HA-Ox$_{3.00\ (100\ kDa)}$	ns	0.1959
HA-ADH$_{3.00}$HA-Ox$_{3.00\ (100\ kDa)}$ vs. HA-ADH$_{1.00}$HA-Ox$_{1.67\ (100\ kDa)}$	ns	0.457
HA-ADH$_{3.00}$HA-Ox$_{3.00\ (100\ kDa)}$ vs. HA-ADH$_{1.00}$HA-Ox$_{1.00\ (100\ kDa)}$	ns	0.3744
HA-ADH$_{3.00}$HA-Ox$_{2.33\ (100\ kDa)}$ vs. HA-ADH$_{3.00}$HA-Ox$_{1.00\ (100\ kDa)}$	ns	0.7645
HA-ADH$_{3.00}$HA-Ox$_{2.33\ (100\ kDa)}$ vs. HA-ADH$_{2.33}$HA-Ox$_{1.00\ (100\ kDa)}$	ns	>0.9999
HA-ADH$_{3.00}$HA-Ox$_{2.33\ (100\ kDa)}$ vs. HA-ADH$_{2.00}$HA-Ox$_{2.00\ (100\ kDa)}$	ns	>0.9999
HA-ADH$_{3.00}$HA-Ox$_{2.33\ (100\ kDa)}$ vs. HA-ADH$_{1.67}$HA-Ox$_{3.00\ (100\ kDa)}$	ns	0.8888
HA-ADH$_{3.00}$HA-Ox$_{2.33\ (100\ kDa)}$ vs. HA-ADH$_{1.00}$HA-Ox$_{3.00\ (100\ kDa)}$	ns	0.4145
HA-ADH$_{3.00}$HA-Ox$_{2.33\ (100\ kDa)}$ vs. HA-ADH$_{1.00}$HA-Ox$_{1.67\ (100\ kDa)}$	ns	0.9128
HA-ADH$_{3.00}$HA-Ox$_{2.33\ (100\ kDa)}$ vs. HA-ADH$_{1.00}$HA-Ox$_{1.00\ (100\ kDa)}$	ns	>0.9999
HA-ADH$_{3.00}$HA-Ox$_{1.00\ (100\ kDa)}$ vs. HA-ADH$_{2.33}$HA-Ox$_{1.00\ (100\ kDa)}$	ns	0.9491
HA-ADH$_{3.00}$HA-Ox$_{1.00\ (100\ kDa)}$ vs. HA-ADH$_{2.00}$HA-Ox$_{2.00\ (100\ kDa)}$	ns	0.7916
HA-ADH$_{3.00}$HA-Ox$_{1.00\ (100\ kDa)}$ vs. HA-ADH$_{1.67}$HA-Ox$_{3.00\ (100\ kDa)}$	ns	>0.9999
HA-ADH$_{3.00}$HA-Ox$_{1.00\ (100\ kDa)}$ vs. HA-ADH$_{1.00}$HA-Ox$_{3.00\ (100\ kDa)}$	ns	0.7551
HA-ADH$_{3.00}$HA-Ox$_{1.00\ (100\ kDa)}$ vs. HA-ADH$_{1.00}$HA-Ox$_{1.67\ (100\ kDa)}$	ns	>0.9999
HA-ADH$_{3.00}$HA-Ox$_{1.00\ (100\ kDa)}$ vs. HA-ADH$_{1.00}$HA-Ox$_{1.00\ (100\ kDa)}$	ns	0.5763

HA-ADH$_{2.33}$HA-Ox$_{1.00\ (100\ kDa)}$ vs. HA-ADH$_{2.00}$HA-Ox$_{2.00\ (100\ kDa)}$	ns	0.9963
HA-ADH$_{2.33}$HA-Ox$_{1.00\ (100\ kDa)}$ vs. HA-ADH$_{1.67}$HA-Ox$_{3.00\ (100\ kDa)}$	ns	0.9713
HA-ADH$_{2.33}$HA-Ox$_{1.00\ (100\ kDa)}$ vs. HA-ADH$_{1.00}$HA-Ox$_{3.00\ (100\ kDa)}$	ns	0.5067
HA-ADH$_{2.33}$HA-Ox$_{1.00\ (100\ kDa)}$ vs. HA-ADH$_{1.00}$HA-Ox$_{1.67\ (100\ kDa)}$	ns	0.9785
HA-ADH$_{2.33}$HA-Ox$_{1.00\ (100\ kDa)}$ vs. HA-ADH$_{1.00}$HA-Ox$_{1.00\ (100\ kDa)}$	ns	0.9998
HA-ADH$_{2.00}$HA-Ox$_{2.00\ (100\ kDa)}$ vs. HA-ADH$_{1.67}$HA-Ox$_{3.00\ (100\ kDa)}$	ns	0.8588
HA-ADH$_{2.00}$HA-Ox$_{2.00\ (100\ kDa)}$ vs. HA-ADH$_{1.00}$HA-Ox$_{3.00\ (100\ kDa)}$	ns	0.3959
HA-ADH$_{2.00}$HA-Ox$_{2.00\ (100\ kDa)}$ vs. HA-ADH$_{1.00}$HA-Ox$_{1.67\ (100\ kDa)}$	ns	0.8818
HA-ADH$_{2.00}$HA-Ox$_{2.00\ (100\ kDa)}$ vs. HA-ADH$_{1.00}$HA-Ox$_{1.00\ (100\ kDa)}$	ns	0.9999
HA-ADH$_{1.67}$HA-Ox$_{3.00\ (100\ kDa)}$ vs. HA-ADH$_{1.00}$HA-Ox$_{3.00\ (100\ kDa)}$	ns	0.9574
HA-ADH$_{1.67}$HA-Ox$_{3.00\ (100\ kDa)}$ vs. HA-ADH$_{1.00}$HA-Ox$_{1.67\ (100\ kDa)}$	ns	>0.9999
HA-ADH$_{1.67}$HA-Ox$_{3.00\ (100\ kDa)}$ vs. HA-ADH$_{1.00}$HA-Ox$_{1.00\ (100\ kDa)}$	ns	0.8511
HA-ADH$_{1.00}$HA-Ox$_{3.00\ (100\ kDa)}$ vs. HA-ADH$_{1.00}$HA-Ox$_{1.67\ (100\ kDa)}$	ns	0.9718
HA-ADH$_{1.00}$HA-Ox$_{3.00\ (100\ kDa)}$ vs. HA-ADH$_{1.00}$HA-Ox$_{1.00\ (100\ kDa)}$	ns	0.4109
HA-ADH$_{1.00}$HA-Ox$_{1.67\ (100\ kDa)}$ vs. HA-ADH$_{1.00}$HA-Ox$_{1.00\ (100\ kDa)}$	ns	0.886
Day 7		
HA-ADH$_{3.00}$HA-Ox$_{3.00\ (40\ kDa)}$ vs. HA-ADH$_{3.00}$HA-Ox$_{1.00\ (40\ kDa)}$	ns	>0.9999
HA-ADH$_{3.00}$HA-Ox$_{3.00\ (40\ kDa)}$ vs. HA-ADH$_{2.00}$HA-Ox$_{2.00\ (40\ kDa)}$	ns	>0.9999
HA-ADH$_{3.00}$HA-Ox$_{3.00\ (40\ kDa)}$ vs. HA-ADH$_{1.67}$HA-Ox$_{1.00\ (40\ kDa)}$	ns	>0.9999
HA-ADH$_{3.00}$HA-Ox$_{3.00\ (40\ kDa)}$ vs. HA-ADH$_{1.00}$HA-Ox$_{3.00\ (40\ kDa)}$	ns	0.988
HA-ADH$_{3.00}$HA-Ox$_{3.00\ (40\ kDa)}$ vs. HA-ADH$_{1.00}$HA-Ox$_{1.00\ (40\ kDa)}$	ns	0.1866
HA-ADH$_{3.00}$HA-Ox$_{3.00\ (40\ kDa)}$ vs. HA-ADH$_{3.00}$HA-Ox$_{3.00\ (100\ kDa)}$	ns	0.6369
HA-ADH$_{3.00}$HA-Ox$_{3.00\ (40\ kDa)}$ vs. HA-ADH$_{3.00}$HA-Ox$_{2.33\ (100\ kDa)}$	ns	0.9882
HA-ADH$_{3.00}$HA-Ox$_{3.00\ (40\ kDa)}$ vs. HA-ADH$_{3.00}$HA-Ox$_{1.00\ (100\ kDa)}$	ns	0.925
HA-ADH$_{3.00}$HA-Ox$_{3.00\ (40\ kDa)}$ vs. HA-ADH$_{2.33}$HA-Ox$_{1.00\ (100\ kDa)}$	ns	0.8254
HA-ADH$_{3.00}$HA-Ox$_{3.00\ (40\ kDa)}$ vs. HA-ADH$_{2.00}$HA-Ox$_{2.00\ (100\ kDa)}$	ns	0.6777
HA-ADH$_{3.00}$HA-Ox$_{3.00\ (40\ kDa)}$ vs. HA-ADH$_{1.67}$HA-Ox$_{3.00\ (100\ kDa)}$	ns	0.7135
HA-ADH$_{3.00}$HA-Ox$_{3.00\ (40\ kDa)}$ vs. HA-ADH$_{1.00}$HA-Ox$_{3.00\ (100\ kDa)}$	ns	0.6983
HA-ADH$_{3.00}$HA-Ox$_{3.00\ (40\ kDa)}$ vs. HA-ADH$_{1.00}$HA-Ox$_{1.67\ (100\ kDa)}$	ns	>0.9999
HA-ADH$_{3.00}$HA-Ox$_{3.00\ (40\ kDa)}$ vs. HA-ADH$_{1.00}$HA-Ox$_{1.00\ (100\ kDa)}$	ns	0.9999
HA-ADH$_{3.00}$HA-Ox$_{1.00\ (40\ kDa)}$ vs. HA-ADH$_{2.00}$HA-Ox$_{2.00\ (40\ kDa)}$	ns	>0.9999
HA-ADH$_{3.00}$HA-Ox$_{1.00\ (40\ kDa)}$ vs. HA-ADH$_{1.67}$HA-Ox$_{1.00\ (40\ kDa)}$	ns	>0.9999
HA-ADH$_{3.00}$HA-Ox$_{1.00\ (40\ kDa)}$ vs. HA-ADH$_{1.00}$HA-Ox$_{3.00\ (40\ kDa)}$	ns	>0.9999

HA-ADH$_{3.00}$HA-Ox$_{1.00\ (40\ kDa)}$ vs. HA-ADH$_{1.00}$HA-Ox$_{1.00\ (40\ kDa)}$	ns	0.9675
HA-ADH$_{3.00}$HA-Ox$_{1.00\ (40\ kDa)}$ vs. HA-ADH$_{3.00}$HA-Ox$_{3.00\ (100\ kDa)}$	ns	0.9998
HA-ADH$_{3.00}$HA-Ox$_{1.00\ (40\ kDa)}$ vs. HA-ADH$_{3.00}$HA-Ox$_{2.33\ (100\ kDa)}$	ns	>0.9999
HA-ADH$_{3.00}$HA-Ox$_{1.00\ (40\ kDa)}$ vs. HA-ADH$_{3.00}$HA-Ox$_{1.00\ (100\ kDa)}$	ns	>0.9999
HA-ADH$_{3.00}$HA-Ox$_{1.00\ (40\ kDa)}$ vs. HA-ADH$_{2.33}$HA-Ox$_{1.00\ (100\ kDa)}$	ns	>0.9999
HA-ADH$_{3.00}$HA-Ox$_{1.00\ (40\ kDa)}$ vs. HA-ADH$_{2.00}$HA-Ox$_{2.00\ (100\ kDa)}$	ns	>0.9999
HA-ADH$_{3.00}$HA-Ox$_{1.00\ (40\ kDa)}$ vs. HA-ADH$_{1.67}$HA-Ox$_{3.00\ (100\ kDa)}$	ns	0.9995
HA-ADH$_{3.00}$HA-Ox$_{1.00\ (40\ kDa)}$ vs. HA-ADH$_{1.00}$HA-Ox$_{3.00\ (100\ kDa)}$	ns	0.9984
HA-ADH$_{3.00}$HA-Ox$_{1.00\ (40\ kDa)}$ vs. HA-ADH$_{1.00}$HA-Ox$_{1.67\ (100\ kDa)}$	ns	>0.9999
HA-ADH$_{3.00}$HA-Ox$_{1.00\ (40\ kDa)}$ vs. HA-ADH$_{1.00}$HA-Ox$_{1.00\ (100\ kDa)}$	ns	>0.9999
HA-ADH$_{2.00}$HA-Ox$_{2.00\ (40\ kDa)}$ vs. HA-ADH$_{1.67}$HA-Ox$_{1.00\ (40\ kDa)}$	ns	>0.9999
HA-ADH$_{2.00}$HA-Ox$_{2.00\ (40\ kDa)}$ vs. HA-ADH$_{1.00}$HA-Ox$_{3.00\ (40\ kDa)}$	ns	>0.9999
HA-ADH$_{2.00}$HA-Ox$_{2.00\ (40\ kDa)}$ vs. HA-ADH$_{1.00}$HA-Ox$_{1.00\ (40\ kDa)}$	ns	0.5016
HA-ADH$_{2.00}$HA-Ox$_{2.00\ (40\ kDa)}$ vs. HA-ADH$_{3.00}$HA-Ox$_{3.00\ (100\ kDa)}$	ns	0.9642
HA-ADH$_{2.00}$HA-Ox$_{2.00\ (40\ kDa)}$ vs. HA-ADH$_{3.00}$HA-Ox$_{2.33\ (100\ kDa)}$	ns	>0.9999
HA-ADH$_{2.00}$HA-Ox$_{2.00\ (40\ kDa)}$ vs. HA-ADH$_{3.00}$HA-Ox$_{1.00\ (100\ kDa)}$	ns	>0.9999
HA-ADH$_{2.00}$HA-Ox$_{2.00\ (40\ kDa)}$ vs. HA-ADH$_{2.33}$HA-Ox$_{1.00\ (100\ kDa)}$	ns	0.9982
HA-ADH$_{2.00}$HA-Ox$_{2.00\ (40\ kDa)}$ vs. HA-ADH$_{2.00}$HA-Ox$_{2.00\ (100\ kDa)}$	ns	0.9838
HA-ADH$_{2.00}$HA-Ox$_{2.00\ (40\ kDa)}$ vs. HA-ADH$_{1.67}$HA-Ox$_{3.00\ (100\ kDa)}$	ns	0.9643
HA-ADH$_{2.00}$HA-Ox$_{2.00\ (40\ kDa)}$ vs. HA-ADH$_{1.00}$HA-Ox$_{3.00\ (100\ kDa)}$	ns	0.9371
HA-ADH$_{2.00}$HA-Ox$_{2.00\ (40\ kDa)}$ vs. HA-ADH$_{1.00}$HA-Ox$_{1.67\ (100\ kDa)}$	ns	>0.9999
HA-ADH$_{2.00}$HA-Ox$_{2.00\ (40\ kDa)}$ vs. HA-ADH$_{1.00}$HA-Ox$_{1.00\ (100\ kDa)}$	ns	>0.9999
HA-ADH$_{1.67}$HA-Ox$_{1.00\ (40\ kDa)}$ vs. HA-ADH$_{1.00}$HA-Ox$_{3.00\ (40\ kDa)}$	ns	0.9815
HA-ADH$_{1.67}$HA-Ox$_{1.00\ (40\ kDa)}$ vs. HA-ADH$_{1.00}$HA-Ox$_{1.00\ (40\ kDa)}$	ns	0.2282
HA-ADH$_{1.67}$HA-Ox$_{1.00\ (40\ kDa)}$ vs. HA-ADH$_{3.00}$HA-Ox$_{3.00\ (100\ kDa)}$	ns	0.6514
HA-ADH$_{1.67}$HA-Ox$_{1.00\ (40\ kDa)}$ vs. HA-ADH$_{3.00}$HA-Ox$_{2.33\ (100\ kDa)}$	ns	0.9773
HA-ADH$_{1.67}$HA-Ox$_{1.00\ (40\ kDa)}$ vs. HA-ADH$_{3.00}$HA-Ox$_{1.00\ (100\ kDa)}$	ns	0.9105
HA-ADH$_{1.67}$HA-Ox$_{1.00\ (40\ kDa)}$ vs. HA-ADH$_{2.33}$HA-Ox$_{1.00\ (100\ kDa)}$	ns	0.8193
HA-ADH$_{1.67}$HA-Ox$_{1.00\ (40\ kDa)}$ vs. HA-ADH$_{2.00}$HA-Ox$_{2.00\ (100\ kDa)}$	ns	0.6974
HA-ADH$_{1.67}$HA-Ox$_{1.00\ (40\ kDa)}$ vs. HA-ADH$_{1.67}$HA-Ox$_{3.00\ (100\ kDa)}$	ns	0.7032
HA-ADH$_{1.67}$HA-Ox$_{1.00\ (40\ kDa)}$ vs. HA-ADH$_{1.00}$HA-Ox$_{3.00\ (100\ kDa)}$	ns	0.6834
HA-ADH$_{1.67}$HA-Ox$_{1.00\ (40\ kDa)}$ vs. HA-ADH$_{1.00}$HA-Ox$_{1.67\ (100\ kDa)}$	ns	>0.9999
HA-ADH$_{1.67}$HA-Ox$_{1.00\ (40\ kDa)}$ vs. HA-ADH$_{1.00}$HA-Ox$_{1.00\ (100\ kDa)}$	ns	0.9988

HA-ADH$_{1.00}$HA-Ox$_{3.00\ (40\ kDa)}$ vs. HA-ADH$_{1.00}$HA-Ox$_{1.00\ (40\ kDa)}$	ns	0.9026
HA-ADH$_{1.00}$HA-Ox$_{3.00\ (40\ kDa)}$ vs. HA-ADH$_{3.00}$HA-Ox$_{3.00\ (100\ kDa)}$	ns	>0.9999
HA-ADH$_{1.00}$HA-Ox$_{3.00\ (40\ kDa)}$ vs. HA-ADH$_{3.00}$HA-Ox$_{2.33\ (100\ kDa)}$	ns	>0.9999
HA-ADH$_{1.00}$HA-Ox$_{3.00\ (40\ kDa)}$ vs. HA-ADH$_{3.00}$HA-Ox$_{1.00\ (100\ kDa)}$	ns	>0.9999
HA-ADH$_{1.00}$HA-Ox$_{3.00\ (40\ kDa)}$ vs. HA-ADH$_{2.33}$HA-Ox$_{1.00\ (100\ kDa)}$	ns	>0.9999
HA-ADH$_{1.00}$HA-Ox$_{3.00\ (40\ kDa)}$ vs. HA-ADH$_{2.00}$HA-Ox$_{2.00\ (100\ kDa)}$	ns	>0.9999
HA-ADH$_{1.00}$HA-Ox$_{3.00\ (40\ kDa)}$ vs. HA-ADH$_{1.67}$HA-Ox$_{3.00\ (100\ kDa)}$	ns	>0.9999
HA-ADH$_{1.00}$HA-Ox$_{3.00\ (40\ kDa)}$ vs. HA-ADH$_{1.00}$HA-Ox$_{3.00\ (100\ kDa)}$	ns	0.9999
HA-ADH$_{1.00}$HA-Ox$_{3.00\ (40\ kDa)}$ vs. HA-ADH$_{1.00}$HA-Ox$_{1.67\ (100\ kDa)}$	ns	0.9997
HA-ADH$_{1.00}$HA-Ox$_{3.00\ (40\ kDa)}$ vs. HA-ADH$_{1.00}$HA-Ox$_{1.00\ (100\ kDa)}$	ns	0.9974
HA-ADH$_{1.00}$HA-Ox$_{1.00\ (40\ kDa)}$ vs. HA-ADH$_{3.00}$HA-Ox$_{3.00\ (100\ kDa)}$	ns	0.5108
HA-ADH$_{1.00}$HA-Ox$_{1.00\ (40\ kDa)}$ vs. HA-ADH$_{3.00}$HA-Ox$_{2.33\ (100\ kDa)}$	ns	0.1558
HA-ADH$_{1.00}$HA-Ox$_{1.00\ (40\ kDa)}$ vs. HA-ADH$_{3.00}$HA-Ox$_{1.00\ (100\ kDa)}$	ns	0.1621
HA-ADH$_{1.00}$HA-Ox$_{1.00\ (40\ kDa)}$ vs. HA-ADH$_{2.33}$HA-Ox$_{1.00\ (100\ kDa)}$	ns	0.2364
HA-ADH$_{1.00}$HA-Ox$_{1.00\ (40\ kDa)}$ vs. HA-ADH$_{2.00}$HA-Ox$_{2.00\ (100\ kDa)}$	ns	0.2819
HA-ADH$_{1.00}$HA-Ox$_{1.00\ (40\ kDa)}$ vs. HA-ADH$_{1.67}$HA-Ox$_{3.00\ (100\ kDa)}$	ns	0.9047
HA-ADH$_{1.00}$HA-Ox$_{1.00\ (40\ kDa)}$ vs. HA-ADH$_{1.00}$HA-Ox$_{3.00\ (100\ kDa)}$	ns	0.9944
HA-ADH$_{1.00}$HA-Ox$_{1.00\ (40\ kDa)}$ vs. HA-ADH$_{1.00}$HA-Ox$_{1.67\ (100\ kDa)}$	ns	0.3217
HA-ADH$_{1.00}$HA-Ox$_{1.00\ (40\ kDa)}$ vs. HA-ADH$_{1.00}$HA-Ox$_{1.00\ (100\ kDa)}$	ns	0.0907
HA-ADH$_{3.00}$HA-Ox$_{3.00\ (100\ kDa)}$ vs. HA-ADH$_{3.00}$HA-Ox$_{2.33\ (100\ kDa)}$	ns	0.8528
HA-ADH$_{3.00}$HA-Ox$_{3.00\ (100\ kDa)}$ vs. HA-ADH$_{3.00}$HA-Ox$_{1.00\ (100\ kDa)}$	ns	0.8863
HA-ADH$_{3.00}$HA-Ox$_{3.00\ (100\ kDa)}$ vs. HA-ADH$_{2.33}$HA-Ox$_{1.00\ (100\ kDa)}$	ns	0.9957
HA-ADH$_{3.00}$HA-Ox$_{3.00\ (100\ kDa)}$ vs. HA-ADH$_{2.00}$HA-Ox$_{2.00\ (100\ kDa)}$	ns	0.9992
HA-ADH$_{3.00}$HA-Ox$_{3.00\ (100\ kDa)}$ vs. HA-ADH$_{1.67}$HA-Ox$_{3.00\ (100\ kDa)}$	ns	>0.9999
HA-ADH$_{3.00}$HA-Ox$_{3.00\ (100\ kDa)}$ vs. HA-ADH$_{1.00}$HA-Ox$_{3.00\ (100\ kDa)}$	ns	0.9998
HA-ADH$_{3.00}$HA-Ox$_{3.00\ (100\ kDa)}$ vs. HA-ADH$_{1.00}$HA-Ox$_{1.67\ (100\ kDa)}$	ns	0.8928
HA-ADH$_{3.00}$HA-Ox$_{3.00\ (100\ kDa)}$ vs. HA-ADH$_{1.00}$HA-Ox$_{1.00\ (100\ kDa)}$	ns	0.5199
HA-ADH$_{3.00}$HA-Ox$_{2.33\ (100\ kDa)}$ vs. HA-ADH$_{3.00}$HA-Ox$_{1.00\ (100\ kDa)}$	ns	>0.9999
HA-ADH$_{3.00}$HA-Ox$_{2.33\ (100\ kDa)}$ vs. HA-ADH$_{2.33}$HA-Ox$_{1.00\ (100\ kDa)}$	ns	0.9949
HA-ADH$_{3.00}$HA-Ox$_{2.33\ (100\ kDa)}$ vs. HA-ADH$_{2.00}$HA-Ox$_{2.00\ (100\ kDa)}$	ns	0.8492
HA-ADH$_{3.00}$HA-Ox$_{2.33\ (100\ kDa)}$ vs. HA-ADH$_{1.67}$HA-Ox$_{3.00\ (100\ kDa)}$	ns	0.9104
HA-ADH$_{3.00}$HA-Ox$_{2.33\ (100\ kDa)}$ vs. HA-ADH$_{1.00}$HA-Ox$_{3.00\ (100\ kDa)}$	ns	0.8787
HA-ADH$_{3.00}$HA-Ox$_{2.33\ (100\ kDa)}$ vs. HA-ADH$_{1.00}$HA-Ox$_{1.67\ (100\ kDa)}$	ns	>0.9999

HA-ADH$_{3.00}$HA-Ox$_{2.33\ (100\ kDa)}$ vs. HA-ADH$_{1.00}$HA-Ox$_{1.00\ (100\ kDa)}$	ns	0.9996
HA-ADH$_{3.00}$HA-Ox$_{1.00\ (100\ kDa)}$ vs. HA-ADH$_{2.33}$HA-Ox$_{1.00\ (100\ kDa)}$	ns	0.9997
HA-ADH$_{3.00}$HA-Ox$_{1.00\ (100\ kDa)}$ vs. HA-ADH$_{2.00}$HA-Ox$_{2.00\ (100\ kDa)}$	ns	0.8427
HA-ADH$_{3.00}$HA-Ox$_{1.00\ (100\ kDa)}$ vs. HA-ADH$_{1.67}$HA-Ox$_{3.00\ (100\ kDa)}$	ns	0.9397
HA-ADH$_{3.00}$HA-Ox$_{1.00\ (100\ kDa)}$ vs. HA-ADH$_{1.00}$HA-Ox$_{3.00\ (100\ kDa)}$	ns	0.9102
HA-ADH$_{3.00}$HA-Ox$_{1.00\ (100\ kDa)}$ vs. HA-ADH$_{1.00}$HA-Ox$_{1.67\ (100\ kDa)}$	ns	0.9995
HA-ADH$_{3.00}$HA-Ox$_{1.00\ (100\ kDa)}$ vs. HA-ADH$_{1.00}$HA-Ox$_{1.00\ (100\ kDa)}$	ns	0.9477
HA-ADH$_{2.33}$HA-Ox$_{1.00\ (100\ kDa)}$ vs. HA-ADH$_{2.00}$HA-Ox$_{2.00\ (100\ kDa)}$	ns	0.9999
HA-ADH$_{2.33}$HA-Ox$_{1.00\ (100\ kDa)}$ vs. HA-ADH$_{1.67}$HA-Ox$_{3.00\ (100\ kDa)}$	ns	0.9929
HA-ADH$_{2.33}$HA-Ox$_{1.00\ (100\ kDa)}$ vs. HA-ADH$_{1.00}$HA-Ox$_{3.00\ (100\ kDa)}$	ns	0.9743
HA-ADH$_{2.33}$HA-Ox$_{1.00\ (100\ kDa)}$ vs. HA-ADH$_{1.00}$HA-Ox$_{1.67\ (100\ kDa)}$	ns	0.9875
HA-ADH$_{2.33}$HA-Ox$_{1.00\ (100\ kDa)}$ vs. HA-ADH$_{1.00}$HA-Ox$_{1.00\ (100\ kDa)}$	ns	0.7805
HA-ADH$_{2.00}$HA-Ox$_{2.00\ (100\ kDa)}$ vs. HA-ADH$_{1.67}$HA-Ox$_{3.00\ (100\ kDa)}$	ns	0.998
HA-ADH$_{2.00}$HA-Ox$_{2.00\ (100\ kDa)}$ vs. HA-ADH$_{1.00}$HA-Ox$_{3.00\ (100\ kDa)}$	ns	0.9868
HA-ADH$_{2.00}$HA-Ox$_{2.00\ (100\ kDa)}$ vs. HA-ADH$_{1.00}$HA-Ox$_{1.67\ (100\ kDa)}$	ns	0.9256
HA-ADH$_{2.00}$HA-Ox$_{2.00\ (100\ kDa)}$ vs. HA-ADH$_{1.00}$HA-Ox$_{1.00\ (100\ kDa)}$	ns	0.4203
HA-ADH$_{1.67}$HA-Ox$_{3.00\ (100\ kDa)}$ vs. HA-ADH$_{1.00}$HA-Ox$_{3.00\ (100\ kDa)}$	ns	>0.9999
HA-ADH$_{1.67}$HA-Ox$_{3.00\ (100\ kDa)}$ vs. HA-ADH$_{1.00}$HA-Ox$_{1.67\ (100\ kDa)}$	ns	0.9126
HA-ADH$_{1.67}$HA-Ox$_{3.00\ (100\ kDa)}$ vs. HA-ADH$_{1.00}$HA-Ox$_{1.00\ (100\ kDa)}$	ns	0.7366
HA-ADH$_{1.00}$HA-Ox$_{3.00\ (100\ kDa)}$ vs. HA-ADH$_{1.00}$HA-Ox$_{1.67\ (100\ kDa)}$	ns	0.8762
HA-ADH$_{1.00}$HA-Ox$_{3.00\ (100\ kDa)}$ vs. HA-ADH$_{1.00}$HA-Ox$_{1.00\ (100\ kDa)}$	ns	0.7393
HA-ADH$_{1.00}$HA-Ox$_{1.67\ (100\ kDa)}$ vs. HA-ADH$_{1.00}$HA-Ox$_{1.00\ (100\ kDa)}$	ns	>0.9999
Day 14		
HA-ADH$_{3.00}$HA-Ox$_{3.00\ (40\ kDa)}$ vs. HA-ADH$_{3.00}$HA-Ox$_{1.00\ (40\ kDa)}$	ns	0.4582
HA-ADH$_{3.00}$HA-Ox$_{3.00\ (40\ kDa)}$ vs. HA-ADH$_{2.00}$HA-Ox$_{2.00\ (40\ kDa)}$	ns	>0.9999
HA-ADH$_{3.00}$HA-Ox$_{3.00\ (40\ kDa)}$ vs. HA-ADH$_{1.67}$HA-Ox$_{1.00\ (40\ kDa)}$	ns	0.8718
HA-ADH$_{3.00}$HA-Ox$_{3.00\ (40\ kDa)}$ vs. HA-ADH$_{1.00}$HA-Ox$_{3.00\ (40\ kDa)}$	ns	0.1187
HA-ADH$_{3.00}$HA-Ox$_{3.00\ (40\ kDa)}$ vs. HA-ADH$_{1.00}$HA-Ox$_{1.00\ (40\ kDa)}$	ns	0.1181
HA-ADH$_{3.00}$HA-Ox$_{3.00\ (40\ kDa)}$ vs. HA-ADH$_{3.00}$HA-Ox$_{3.00\ (100\ kDa)}$	ns	0.5724
HA-ADH$_{3.00}$HA-Ox$_{3.00\ (40\ kDa)}$ vs. HA-ADH$_{3.00}$HA-Ox$_{2.33\ (100\ kDa)}$	ns	0.9227
HA-ADH$_{3.00}$HA-Ox$_{3.00\ (40\ kDa)}$ vs. HA-ADH$_{3.00}$HA-Ox$_{1.00\ (100\ kDa)}$	ns	0.991
HA-ADH$_{3.00}$HA-Ox$_{3.00\ (40\ kDa)}$ vs. HA-ADH$_{2.33}$HA-Ox$_{1.00\ (100\ kDa)}$	ns	0.9455
HA-ADH$_{3.00}$HA-Ox$_{3.00\ (40\ kDa)}$ vs. HA-ADH$_{2.00}$HA-Ox$_{2.00\ (100\ kDa)}$	ns	0.5572

HA-ADH$_{3.00}$HA-Ox$_{3.00\ (40\ kDa)}$ vs. HA-ADH$_{1.67}$HA-Ox$_{3.00\ (100\ kDa)}$	ns	0.6568
HA-ADH$_{3.00}$HA-Ox$_{3.00\ (40\ kDa)}$ vs. HA-ADH$_{1.00}$HA-Ox$_{3.00\ (100\ kDa)}$	ns	0.2582
HA-ADH$_{3.00}$HA-Ox$_{3.00\ (40\ kDa)}$ vs. HA-ADH$_{1.00}$HA-Ox$_{1.67\ (100\ kDa)}$	ns	0.5764
HA-ADH$_{3.00}$HA-Ox$_{3.00\ (40\ kDa)}$ vs. HA-ADH$_{1.00}$HA-Ox$_{1.00\ (100\ kDa)}$	ns	0.737
HA-ADH$_{3.00}$HA-Ox$_{1.00\ (40\ kDa)}$ vs. HA-ADH$_{2.00}$HA-Ox$_{2.00\ (40\ kDa)}$	ns	0.3856
HA-ADH$_{3.00}$HA-Ox$_{1.00\ (40\ kDa)}$ vs. HA-ADH$_{1.67}$HA-Ox$_{1.00\ (40\ kDa)}$	ns	0.7673
HA-ADH$_{3.00}$HA-Ox$_{1.00\ (40\ kDa)}$ vs. HA-ADH$_{1.00}$HA-Ox$_{3.00\ (40\ kDa)}$	ns	0.0613
HA-ADH$_{3.00}$HA-Ox$_{1.00\ (40\ kDa)}$ vs. HA-ADH$_{1.00}$HA-Ox$_{1.00\ (40\ kDa)}$	ns	0.0607
HA-ADH$_{3.00}$HA-Ox$_{1.00\ (40\ kDa)}$ vs. HA-ADH$_{3.00}$HA-Ox$_{3.00\ (100\ kDa)}$	ns	0.1396
HA-ADH$_{3.00}$HA-Ox$_{1.00\ (40\ kDa)}$ vs. HA-ADH$_{3.00}$HA-Ox$_{2.33\ (100\ kDa)}$	ns	0.2126
HA-ADH$_{3.00}$HA-Ox$_{1.00\ (40\ kDa)}$ vs. HA-ADH$_{3.00}$HA-Ox$_{1.00\ (100\ kDa)}$	ns	0.2473
HA-ADH$_{3.00}$HA-Ox$_{1.00\ (40\ kDa)}$ vs. HA-ADH$_{2.33}$HA-Ox$_{1.00\ (100\ kDa)}$	ns	0.1941
HA-ADH$_{3.00}$HA-Ox$_{1.00\ (40\ kDa)}$ vs. HA-ADH$_{2.00}$HA-Ox$_{2.00\ (100\ kDa)}$	ns	0.1354
HA-ADH$_{3.00}$HA-Ox$_{1.00\ (40\ kDa)}$ vs. HA-ADH$_{1.67}$HA-Ox$_{3.00\ (100\ kDa)}$	ns	0.1381
HA-ADH$_{3.00}$HA-Ox$_{1.00\ (40\ kDa)}$ vs. HA-ADH$_{1.00}$HA-Ox$_{3.00\ (100\ kDa)}$	ns	0.0589
HA-ADH$_{3.00}$HA-Ox$_{1.00\ (40\ kDa)}$ vs. HA-ADH$_{1.00}$HA-Ox$_{1.67\ (100\ kDa)}$	ns	0.0993
HA-ADH$_{3.00}$HA-Ox$_{1.00\ (40\ kDa)}$ vs. HA-ADH$_{1.00}$HA-Ox$_{1.00\ (100\ kDa)}$	ns	0.1289
HA-ADH$_{2.00}$HA-Ox$_{2.00\ (40\ kDa)}$ vs. HA-ADH$_{1.67}$HA-Ox$_{1.00\ (40\ kDa)}$	ns	0.641
HA-ADH$_{2.00}$HA-Ox$_{2.00\ (40\ kDa)}$ vs. HA-ADH$_{1.00}$HA-Ox$_{3.00\ (40\ kDa)}$	*	0.031
HA-ADH$_{2.00}$HA-Ox$_{2.00\ (40\ kDa)}$ vs. HA-ADH$_{1.00}$HA-Ox$_{1.00\ (40\ kDa)}$	*	0.0291
HA-ADH$_{2.00}$HA-Ox$_{2.00\ (40\ kDa)}$ vs. HA-ADH$_{3.00}$HA-Ox$_{3.00\ (100\ kDa)}$	ns	0.1527
HA-ADH$_{2.00}$HA-Ox$_{2.00\ (40\ kDa)}$ vs. HA-ADH$_{3.00}$HA-Ox$_{2.33\ (100\ kDa)}$	ns	0.4779
HA-ADH$_{2.00}$HA-Ox$_{2.00\ (40\ kDa)}$ vs. HA-ADH$_{3.00}$HA-Ox$_{1.00\ (100\ kDa)}$	ns	0.7365
HA-ADH$_{2.00}$HA-Ox$_{2.00\ (40\ kDa)}$ vs. HA-ADH$_{2.33}$HA-Ox$_{1.00\ (100\ kDa)}$	ns	0.5914
HA-ADH$_{2.00}$HA-Ox$_{2.00\ (40\ kDa)}$ vs. HA-ADH$_{2.00}$HA-Ox$_{2.00\ (100\ kDa)}$	ns	0.1439
HA-ADH$_{2.00}$HA-Ox$_{2.00\ (40\ kDa)}$ vs. HA-ADH$_{1.67}$HA-Ox$_{3.00\ (100\ kDa)}$	ns	0.208
HA-ADH$_{2.00}$HA-Ox$_{2.00\ (40\ kDa)}$ vs. HA-ADH$_{1.00}$HA-Ox$_{3.00\ (100\ kDa)}$	ns	0.0852
HA-ADH$_{2.00}$HA-Ox$_{2.00\ (40\ kDa)}$ vs. HA-ADH$_{1.00}$HA-Ox$_{1.67\ (100\ kDa)}$	ns	0.2629
HA-ADH$_{2.00}$HA-Ox$_{2.00\ (40\ kDa)}$ vs. HA-ADH$_{1.00}$HA-Ox$_{1.00\ (100\ kDa)}$	ns	0.3485
HA-ADH$_{1.67}$HA-Ox$_{1.00\ (40\ kDa)}$ vs. HA-ADH$_{1.00}$HA-Ox$_{3.00\ (40\ kDa)}$	*	0.0156
HA-ADH$_{1.67}$HA-Ox$_{1.00\ (40\ kDa)}$ vs. HA-ADH$_{1.00}$HA-Ox$_{1.00\ (40\ kDa)}$	*	0.0141
HA-ADH$_{1.67}$HA-Ox$_{1.00\ (40\ kDa)}$ vs. HA-ADH$_{3.00}$HA-Ox$_{3.00\ (100\ kDa)}$	*	0.0325
HA-ADH$_{1.67}$HA-Ox$_{1.00\ (40\ kDa)}$ vs. HA-ADH$_{3.00}$HA-Ox$_{2.33\ (100\ kDa)}$	ns	0.0959

HA-ADH$_{1.67}$HA-Ox$_{1.00\ (40\ kDa)}$ vs. HA-ADH$_{3.00}$HA-Ox$_{1.00\ (100\ kDa)}$	ns	0.1362
HA-ADH$_{1.67}$HA-Ox$_{1.00\ (40\ kDa)}$ vs. HA-ADH$_{2.33}$HA-Ox$_{1.00\ (100\ kDa)}$	ns	0.0983
HA-ADH$_{1.67}$HA-Ox$_{1.00\ (40\ kDa)}$ vs. HA-ADH$_{2.00}$HA-Ox$_{2.00\ (100\ kDa)}$	*	0.03
HA-ADH$_{1.67}$HA-Ox$_{1.00\ (40\ kDa)}$ vs. HA-ADH$_{1.67}$HA-Ox$_{3.00\ (100\ kDa)}$	*	0.0385
HA-ADH$_{1.67}$HA-Ox$_{1.00\ (40\ kDa)}$ vs. HA-ADH$_{1.00}$HA-Ox$_{3.00\ (100\ kDa)}$	*	0.0326
HA-ADH$_{1.67}$HA-Ox$_{1.00\ (40\ kDa)}$ vs. HA-ADH$_{1.00}$HA-Ox$_{1.67\ (100\ kDa)}$	ns	0.083
HA-ADH$_{1.67}$HA-Ox$_{1.00\ (40\ kDa)}$ vs. HA-ADH$_{1.00}$HA-Ox$_{1.00\ (100\ kDa)}$	ns	0.0859
HA-ADH$_{1.00}$HA-Ox$_{3.00\ (40\ kDa)}$ vs. HA-ADH$_{1.00}$HA-Ox$_{1.00\ (40\ kDa)}$	ns	>0.9999
HA-ADH$_{1.00}$HA-Ox$_{3.00\ (40\ kDa)}$ vs. HA-ADH$_{3.00}$HA-Ox$_{3.00\ (100\ kDa)}$	*	0.0231
HA-ADH$_{1.00}$HA-Ox$_{3.00\ (40\ kDa)}$ vs. HA-ADH$_{3.00}$HA-Ox$_{2.33\ (100\ kDa)}$	**	0.0054
HA-ADH$_{1.00}$HA-Ox$_{3.00\ (40\ kDa)}$ vs. HA-ADH$_{3.00}$HA-Ox$_{1.00\ (100\ kDa)}$	**	0.0057
HA-ADH$_{1.00}$HA-Ox$_{3.00\ (40\ kDa)}$ vs. HA-ADH$_{2.33}$HA-Ox$_{1.00\ (100\ kDa)}$	*	0.0362
HA-ADH$_{1.00}$HA-Ox$_{3.00\ (40\ kDa)}$ vs. HA-ADH$_{2.00}$HA-Ox$_{2.00\ (100\ kDa)}$	*	0.0282
HA-ADH$_{1.00}$HA-Ox$_{3.00\ (40\ kDa)}$ vs. HA-ADH$_{1.67}$HA-Ox$_{3.00\ (100\ kDa)}$	*	0.0481
HA-ADH$_{1.00}$HA-Ox$_{3.00\ (40\ kDa)}$ vs. HA-ADH$_{1.00}$HA-Ox$_{3.00\ (100\ kDa)}$	ns	0.362
HA-ADH$_{1.00}$HA-Ox$_{3.00\ (40\ kDa)}$ vs. HA-ADH$_{1.00}$HA-Ox$_{1.67\ (100\ kDa)}$	ns	0.1778
HA-ADH$_{1.00}$HA-Ox$_{3.00\ (40\ kDa)}$ vs. HA-ADH$_{1.00}$HA-Ox$_{1.00\ (100\ kDa)}$	ns	0.1041
HA-ADH$_{1.00}$HA-Ox$_{1.00\ (40\ kDa)}$ vs. HA-ADH$_{3.00}$HA-Ox$_{3.00\ (100\ kDa)}$	*	0.0188
HA-ADH$_{1.00}$HA-Ox$_{1.00\ (40\ kDa)}$ vs. HA-ADH$_{3.00}$HA-Ox$_{2.33\ (100\ kDa)}$	**	0.0027
HA-ADH$_{1.00}$HA-Ox$_{1.00\ (40\ kDa)}$ vs. HA-ADH$_{3.00}$HA-Ox$_{1.00\ (100\ kDa)}$	**	0.0031
HA-ADH$_{1.00}$HA-Ox$_{1.00\ (40\ kDa)}$ vs. HA-ADH$_{2.33}$HA-Ox$_{1.00\ (100\ kDa)}$	*	0.0333
HA-ADH$_{1.00}$HA-Ox$_{1.00\ (40\ kDa)}$ vs. HA-ADH$_{2.00}$HA-Ox$_{2.00\ (100\ kDa)}$	*	0.0237
HA-ADH$_{1.00}$HA-Ox$_{1.00\ (40\ kDa)}$ vs. HA-ADH$_{1.67}$HA-Ox$_{3.00\ (100\ kDa)}$	*	0.0444
HA-ADH$_{1.00}$HA-Ox$_{1.00\ (40\ kDa)}$ vs. HA-ADH$_{1.00}$HA-Ox$_{3.00\ (100\ kDa)}$	ns	0.3645
HA-ADH$_{1.00}$HA-Ox$_{1.00\ (40\ kDa)}$ vs. HA-ADH$_{1.00}$HA-Ox$_{1.67\ (100\ kDa)}$	ns	0.1769
HA-ADH$_{1.00}$HA-Ox$_{1.00\ (40\ kDa)}$ vs. HA-ADH$_{1.00}$HA-Ox$_{1.00\ (100\ kDa)}$	ns	0.1021
HA-ADH$_{3.00}$HA-Ox$_{3.00\ (100\ kDa)}$ vs. HA-ADH$_{3.00}$HA-Ox$_{2.33\ (100\ kDa)}$	ns	0.3062
HA-ADH$_{3.00}$HA-Ox$_{3.00\ (100\ kDa)}$ vs. HA-ADH$_{3.00}$HA-Ox$_{1.00\ (100\ kDa)}$	ns	0.1386
HA-ADH$_{3.00}$HA-Ox$_{3.00\ (100\ kDa)}$ vs. HA-ADH$_{2.33}$HA-Ox$_{1.00\ (100\ kDa)}$	ns	0.6462
HA-ADH$_{3.00}$HA-Ox$_{3.00\ (100\ kDa)}$ vs. HA-ADH$_{2.00}$HA-Ox$_{2.00\ (100\ kDa)}$	ns	>0.9999
HA-ADH$_{3.00}$HA-Ox$_{3.00\ (100\ kDa)}$ vs. HA-ADH$_{1.67}$HA-Ox$_{3.00\ (100\ kDa)}$	ns	>0.9999
HA-ADH$_{3.00}$HA-Ox$_{3.00\ (100\ kDa)}$ vs. HA-ADH$_{1.00}$HA-Ox$_{3.00\ (100\ kDa)}$	ns	0.6112
HA-ADH$_{3.00}$HA-Ox$_{3.00\ (100\ kDa)}$ vs. HA-ADH$_{1.00}$HA-Ox$_{1.67\ (100\ kDa)}$	ns	>0.9999

HA-ADH$_{3.00}$HA-Ox$_{3.00\ (100\ kDa)}$ vs. HA-ADH$_{1.00}$HA-Ox$_{1.00\ (100\ kDa)}$	ns	>0.9999
HA-ADH$_{3.00}$HA-Ox$_{2.33\ (100\ kDa)}$ vs. HA-ADH$_{3.00}$HA-Ox$_{1.00\ (100\ kDa)}$	ns	0.9148
HA-ADH$_{3.00}$HA-Ox$_{2.33\ (100\ kDa)}$ vs. HA-ADH$_{2.33}$HA-Ox$_{1.00\ (100\ kDa)}$	ns	>0.9999
HA-ADH$_{3.00}$HA-Ox$_{2.33\ (100\ kDa)}$ vs. HA-ADH$_{2.00}$HA-Ox$_{2.00\ (100\ kDa)}$	ns	0.3058
HA-ADH$_{3.00}$HA-Ox$_{2.33\ (100\ kDa)}$ vs. HA-ADH$_{1.67}$HA-Ox$_{3.00\ (100\ kDa)}$	ns	0.6844
HA-ADH$_{3.00}$HA-Ox$_{2.33\ (100\ kDa)}$ vs. HA-ADH$_{1.00}$HA-Ox$_{3.00\ (100\ kDa)}$	ns	0.2558
HA-ADH$_{3.00}$HA-Ox$_{2.33\ (100\ kDa)}$ vs. HA-ADH$_{1.00}$HA-Ox$_{1.67\ (100\ kDa)}$	ns	0.7057
HA-ADH$_{3.00}$HA-Ox$_{2.33\ (100\ kDa)}$ vs. HA-ADH$_{1.00}$HA-Ox$_{1.00\ (100\ kDa)}$	ns	0.9137
HA-ADH$_{3.00}$HA-Ox$_{1.00\ (100\ kDa)}$ vs. HA-ADH$_{2.33}$HA-Ox$_{1.00\ (100\ kDa)}$	ns	0.9914
HA-ADH$_{3.00}$HA-Ox$_{1.00\ (100\ kDa)}$ vs. HA-ADH$_{2.00}$HA-Ox$_{2.00\ (100\ kDa)}$	ns	0.145
HA-ADH$_{3.00}$HA-Ox$_{1.00\ (100\ kDa)}$ vs. HA-ADH$_{1.67}$HA-Ox$_{3.00\ (100\ kDa)}$	ns	0.3953
HA-ADH$_{3.00}$HA-Ox$_{1.00\ (100\ kDa)}$ vs. HA-ADH$_{1.00}$HA-Ox$_{3.00\ (100\ kDa)}$	ns	0.1926
HA-ADH$_{3.00}$HA-Ox$_{1.00\ (100\ kDa)}$ vs. HA-ADH$_{1.00}$HA-Ox$_{1.67\ (100\ kDa)}$	ns	0.5219
HA-ADH$_{3.00}$HA-Ox$_{1.00\ (100\ kDa)}$ vs. HA-ADH$_{1.00}$HA-Ox$_{1.00\ (100\ kDa)}$	ns	0.6955
HA-ADH$_{2.33}$HA-Ox$_{1.00\ (100\ kDa)}$ vs. HA-ADH$_{2.00}$HA-Ox$_{2.00\ (100\ kDa)}$	ns	0.6174
HA-ADH$_{2.33}$HA-Ox$_{1.00\ (100\ kDa)}$ vs. HA-ADH$_{1.67}$HA-Ox$_{3.00\ (100\ kDa)}$	ns	0.8849
HA-ADH$_{2.33}$HA-Ox$_{1.00\ (100\ kDa)}$ vs. HA-ADH$_{1.00}$HA-Ox$_{3.00\ (100\ kDa)}$	ns	0.2652
HA-ADH$_{2.33}$HA-Ox$_{1.00\ (100\ kDa)}$ vs. HA-ADH$_{1.00}$HA-Ox$_{1.67\ (100\ kDa)}$	ns	0.8038
HA-ADH$_{2.33}$HA-Ox$_{1.00\ (100\ kDa)}$ vs. HA-ADH$_{1.00}$HA-Ox$_{1.00\ (100\ kDa)}$	ns	0.974
HA-ADH$_{2.00}$HA-Ox$_{2.00\ (100\ kDa)}$ vs. HA-ADH$_{1.67}$HA-Ox$_{3.00\ (100\ kDa)}$	ns	>0.9999
HA-ADH$_{2.00}$HA-Ox$_{2.00\ (100\ kDa)}$ vs. HA-ADH$_{1.00}$HA-Ox$_{3.00\ (100\ kDa)}$	ns	0.6462
HA-ADH$_{2.00}$HA-Ox$_{2.00\ (100\ kDa)}$ vs. HA-ADH$_{1.00}$HA-Ox$_{1.67\ (100\ kDa)}$	ns	>0.9999
HA-ADH$_{2.00}$HA-Ox$_{2.00\ (100\ kDa)}$ vs. HA-ADH$_{1.00}$HA-Ox$_{1.00\ (100\ kDa)}$	ns	>0.9999
HA-ADH$_{1.67}$HA-Ox$_{3.00\ (100\ kDa)}$ vs. HA-ADH$_{1.00}$HA-Ox$_{3.00\ (100\ kDa)}$	ns	0.5666
HA-ADH$_{1.67}$HA-Ox$_{3.00\ (100\ kDa)}$ vs. HA-ADH$_{1.00}$HA-Ox$_{1.67\ (100\ kDa)}$	ns	0.9997
HA-ADH$_{1.67}$HA-Ox$_{3.00\ (100\ kDa)}$ vs. HA-ADH$_{1.00}$HA-Ox$_{1.00\ (100\ kDa)}$	ns	>0.9999
HA-ADH$_{1.00}$HA-Ox$_{3.00\ (100\ kDa)}$ vs. HA-ADH$_{1.00}$HA-Ox$_{1.67\ (100\ kDa)}$	ns	0.928
HA-ADH$_{1.00}$HA-Ox$_{3.00\ (100\ kDa)}$ vs. HA-ADH$_{1.00}$HA-Ox$_{1.00\ (100\ kDa)}$	ns	0.6496
HA-ADH$_{1.00}$HA-Ox$_{1.67\ (100\ kDa)}$ vs. HA-ADH$_{1.00}$HA-Ox$_{1.00\ (100\ kDa)}$	ns	0.9998
Day 21		
HA-ADH$_{3.00}$HA-Ox$_{3.00\ (40\ kDa)}$ vs. HA-ADH$_{3.00}$HA-Ox$_{1.00\ (40\ kDa)}$	ns	0.2215
HA-ADH$_{3.00}$HA-Ox$_{3.00\ (40\ kDa)}$ vs. HA-ADH$_{2.00}$HA-Ox$_{2.00\ (40\ kDa)}$	ns	>0.9999
HA-ADH$_{3.00}$HA-Ox$_{3.00\ (40\ kDa)}$ vs. HA-ADH$_{1.67}$HA-Ox$_{1.00\ (40\ kDa)}$	ns	0.8054

HA-ADH$_{3.00}$HA-Ox$_{3.00\ (40\ kDa)}$ vs. HA-ADH$_{1.00}$HA-Ox$_{3.00\ (40\ kDa)}$	ns	0.0537
HA-ADH$_{3.00}$HA-Ox$_{3.00\ (40\ kDa)}$ vs. HA-ADH$_{1.00}$HA-Ox$_{1.00\ (40\ kDa)}$	ns	0.052
HA-ADH$_{3.00}$HA-Ox$_{3.00\ (40\ kDa)}$ vs. HA-ADH$_{3.00}$HA-Ox$_{3.00\ (100\ kDa)}$	ns	0.2209
HA-ADH$_{3.00}$HA-Ox$_{3.00\ (40\ kDa)}$ vs. HA-ADH$_{3.00}$HA-Ox$_{2.33\ (100\ kDa)}$	ns	0.4186
HA-ADH$_{3.00}$HA-Ox$_{3.00\ (40\ kDa)}$ vs. HA-ADH$_{3.00}$HA-Ox$_{1.00\ (100\ kDa)}$	ns	0.8093
HA-ADH$_{3.00}$HA-Ox$_{3.00\ (40\ kDa)}$ vs. HA-ADH$_{2.33}$HA-Ox$_{1.00\ (100\ kDa)}$	ns	0.5724
HA-ADH$_{3.00}$HA-Ox$_{3.00\ (40\ kDa)}$ vs. HA-ADH$_{2.00}$HA-Ox$_{2.00\ (100\ kDa)}$	ns	0.3462
HA-ADH$_{3.00}$HA-Ox$_{3.00\ (40\ kDa)}$ vs. HA-ADH$_{1.67}$HA-Ox$_{3.00\ (100\ kDa)}$	ns	0.6414
HA-ADH$_{3.00}$HA-Ox$_{3.00\ (40\ kDa)}$ vs. HA-ADH$_{1.00}$HA-Ox$_{3.00\ (100\ kDa)}$	*	0.05
HA-ADH$_{3.00}$HA-Ox$_{3.00\ (40\ kDa)}$ vs. HA-ADH$_{1.00}$HA-Ox$_{1.67\ (100\ kDa)}$	ns	0.8314
HA-ADH$_{3.00}$HA-Ox$_{3.00\ (40\ kDa)}$ vs. HA-ADH$_{1.00}$HA-Ox$_{1.00\ (100\ kDa)}$	ns	0.4346
HA-ADH$_{3.00}$HA-Ox$_{1.00\ (40\ kDa)}$ vs. HA-ADH$_{2.00}$HA-Ox$_{2.00\ (40\ kDa)}$	ns	0.2288
HA-ADH$_{3.00}$HA-Ox$_{1.00\ (40\ kDa)}$ vs. HA-ADH$_{1.67}$HA-Ox$_{1.00\ (40\ kDa)}$	ns	0.4165
HA-ADH$_{3.00}$HA-Ox$_{1.00\ (40\ kDa)}$ vs. HA-ADH$_{1.00}$HA-Ox$_{3.00\ (40\ kDa)}$	ns	0.0523
HA-ADH$_{3.00}$HA-Ox$_{1.00\ (40\ kDa)}$ vs. HA-ADH$_{1.00}$HA-Ox$_{1.00\ (40\ kDa)}$	ns	0.0517
HA-ADH$_{3.00}$HA-Ox$_{1.00\ (40\ kDa)}$ vs. HA-ADH$_{3.00}$HA-Ox$_{3.00\ (100\ kDa)}$	ns	0.0994
HA-ADH$_{3.00}$HA-Ox$_{1.00\ (40\ kDa)}$ vs. HA-ADH$_{3.00}$HA-Ox$_{2.33\ (100\ kDa)}$	ns	0.0962
HA-ADH$_{3.00}$HA-Ox$_{1.00\ (40\ kDa)}$ vs. HA-ADH$_{3.00}$HA-Ox$_{1.00\ (100\ kDa)}$	ns	0.133
HA-ADH$_{3.00}$HA-Ox$_{1.00\ (40\ kDa)}$ vs. HA-ADH$_{2.33}$HA-Ox$_{1.00\ (100\ kDa)}$	ns	0.132
HA-ADH$_{3.00}$HA-Ox$_{1.00\ (40\ kDa)}$ vs. HA-ADH$_{2.00}$HA-Ox$_{2.00\ (100\ kDa)}$	ns	0.0968
HA-ADH$_{3.00}$HA-Ox$_{1.00\ (40\ kDa)}$ vs. HA-ADH$_{1.67}$HA-Ox$_{3.00\ (100\ kDa)}$	ns	0.1098
HA-ADH$_{3.00}$HA-Ox$_{1.00\ (40\ kDa)}$ vs. HA-ADH$_{1.00}$HA-Ox$_{3.00\ (100\ kDa)}$	*	0.0495
HA-ADH$_{3.00}$HA-Ox$_{1.00\ (40\ kDa)}$ vs. HA-ADH$_{1.00}$HA-Ox$_{1.67\ (100\ kDa)}$	ns	0.1034
HA-ADH$_{3.00}$HA-Ox$_{1.00\ (40\ kDa)}$ vs. HA-ADH$_{1.00}$HA-Ox$_{1.00\ (100\ kDa)}$	ns	0.0965
HA-ADH$_{2.00}$HA-Ox$_{2.00\ (40\ kDa)}$ vs. HA-ADH$_{1.67}$HA-Ox$_{1.00\ (40\ kDa)}$	ns	0.5479
HA-ADH$_{2.00}$HA-Ox$_{2.00\ (40\ kDa)}$ vs. HA-ADH$_{1.00}$HA-Ox$_{3.00\ (40\ kDa)}$	*	0.0148
HA-ADH$_{2.00}$HA-Ox$_{2.00\ (40\ kDa)}$ vs. HA-ADH$_{1.00}$HA-Ox$_{1.00\ (40\ kDa)}$	*	0.013
HA-ADH$_{2.00}$HA-Ox$_{2.00\ (40\ kDa)}$ vs. HA-ADH$_{3.00}$HA-Ox$_{3.00\ (100\ kDa)}$	*	0.0415
HA-ADH$_{2.00}$HA-Ox$_{2.00\ (40\ kDa)}$ vs. HA-ADH$_{3.00}$HA-Ox$_{2.33\ (100\ kDa)}$	ns	0.2038
HA-ADH$_{2.00}$HA-Ox$_{2.00\ (40\ kDa)}$ vs. HA-ADH$_{3.00}$HA-Ox$_{1.00\ (100\ kDa)}$	ns	0.5384
HA-ADH$_{2.00}$HA-Ox$_{2.00\ (40\ kDa)}$ vs. HA-ADH$_{2.33}$HA-Ox$_{1.00\ (100\ kDa)}$	ns	0.2089
HA-ADH$_{2.00}$HA-Ox$_{2.00\ (40\ kDa)}$ vs. HA-ADH$_{2.00}$HA-Ox$_{2.00\ (100\ kDa)}$	ns	0.1285
HA-ADH$_{2.00}$HA-Ox$_{2.00\ (40\ kDa)}$ vs. HA-ADH$_{1.67}$HA-Ox$_{3.00\ (100\ kDa)}$	ns	0.397

HA-ADH$_{2.00}$HA-Ox$_{2.00\ (40\ kDa)}$ vs. HA-ADH$_{1.00}$HA-Ox$_{3.00\ (100\ kDa)}$	**	0.0085
HA-ADH$_{2.00}$HA-Ox$_{2.00\ (40\ kDa)}$ vs. HA-ADH$_{1.00}$HA-Ox$_{1.67\ (100\ kDa)}$	ns	0.7396
HA-ADH$_{2.00}$HA-Ox$_{2.00\ (40\ kDa)}$ vs. HA-ADH$_{1.00}$HA-Ox$_{1.00\ (100\ kDa)}$	ns	0.2194
HA-ADH$_{1.67}$HA-Ox$_{1.00\ (40\ kDa)}$ vs. HA-ADH$_{1.00}$HA-Ox$_{3.00\ (40\ kDa)}$	*	0.0173
HA-ADH$_{1.67}$HA-Ox$_{1.00\ (40\ kDa)}$ vs. HA-ADH$_{1.00}$HA-Ox$_{1.00\ (40\ kDa)}$	*	0.0161
HA-ADH$_{1.67}$HA-Ox$_{1.00\ (40\ kDa)}$ vs. HA-ADH$_{3.00}$HA-Ox$_{3.00\ (100\ kDa)}$	*	0.0362
HA-ADH$_{1.67}$HA-Ox$_{1.00\ (40\ kDa)}$ vs. HA-ADH$_{3.00}$HA-Ox$_{2.33\ (100\ kDa)}$	ns	0.0602
HA-ADH$_{1.67}$HA-Ox$_{1.00\ (40\ kDa)}$ vs. HA-ADH$_{3.00}$HA-Ox$_{1.00\ (100\ kDa)}$	ns	0.1296
HA-ADH$_{1.67}$HA-Ox$_{1.00\ (40\ kDa)}$ vs. HA-ADH$_{2.33}$HA-Ox$_{1.00\ (100\ kDa)}$	ns	0.0746
HA-ADH$_{1.67}$HA-Ox$_{1.00\ (40\ kDa)}$ vs. HA-ADH$_{2.00}$HA-Ox$_{2.00\ (100\ kDa)}$	*	0.0433
HA-ADH$_{1.67}$HA-Ox$_{1.00\ (40\ kDa)}$ vs. HA-ADH$_{1.67}$HA-Ox$_{3.00\ (100\ kDa)}$	ns	0.1067
HA-ADH$_{1.67}$HA-Ox$_{1.00\ (40\ kDa)}$ vs. HA-ADH$_{1.00}$HA-Ox$_{3.00\ (100\ kDa)}$	**	0.0062
HA-ADH$_{1.67}$HA-Ox$_{1.00\ (40\ kDa)}$ vs. HA-ADH$_{1.00}$HA-Ox$_{1.67\ (100\ kDa)}$	ns	0.3496
HA-ADH$_{1.67}$HA-Ox$_{1.00\ (40\ kDa)}$ vs. HA-ADH$_{1.00}$HA-Ox$_{1.00\ (100\ kDa)}$	ns	0.064
HA-ADH$_{1.00}$HA-Ox$_{3.00\ (40\ kDa)}$ vs. HA-ADH$_{1.00}$HA-Ox$_{1.00\ (40\ kDa)}$	ns	>0.9999
HA-ADH$_{1.00}$HA-Ox$_{3.00\ (40\ kDa)}$ vs. HA-ADH$_{3.00}$HA-Ox$_{3.00\ (100\ kDa)}$	*	0.0145
HA-ADH$_{1.00}$HA-Ox$_{3.00\ (40\ kDa)}$ vs. HA-ADH$_{3.00}$HA-Ox$_{2.33\ (100\ kDa)}$	ns	0.065
HA-ADH$_{1.00}$HA-Ox$_{3.00\ (40\ kDa)}$ vs. HA-ADH$_{3.00}$HA-Ox$_{1.00\ (100\ kDa)}$	*	0.0391
HA-ADH$_{1.00}$HA-Ox$_{3.00\ (40\ kDa)}$ vs. HA-ADH$_{2.33}$HA-Ox$_{1.00\ (100\ kDa)}$	*	0.0171
HA-ADH$_{1.00}$HA-Ox$_{3.00\ (40\ kDa)}$ vs. HA-ADH$_{2.00}$HA-Ox$_{2.00\ (100\ kDa)}$	ns	0.0531
HA-ADH$_{1.00}$HA-Ox$_{3.00\ (40\ kDa)}$ vs. HA-ADH$_{1.67}$HA-Ox$_{3.00\ (100\ kDa)}$	ns	0.0611
HA-ADH$_{1.00}$HA-Ox$_{3.00\ (40\ kDa)}$ vs. HA-ADH$_{1.00}$HA-Ox$_{3.00\ (100\ kDa)}$	ns	0.2976
HA-ADH$_{1.00}$HA-Ox$_{3.00\ (40\ kDa)}$ vs. HA-ADH$_{1.00}$HA-Ox$_{1.67\ (100\ kDa)}$	ns	0.2014
HA-ADH$_{1.00}$HA-Ox$_{3.00\ (40\ kDa)}$ vs. HA-ADH$_{1.00}$HA-Ox$_{1.00\ (100\ kDa)}$	ns	0.0664
HA-ADH$_{1.00}$HA-Ox$_{1.00\ (40\ kDa)}$ vs. HA-ADH$_{3.00}$HA-Ox$_{3.00\ (100\ kDa)}$	*	0.0104
HA-ADH$_{1.00}$HA-Ox$_{1.00\ (40\ kDa)}$ vs. HA-ADH$_{3.00}$HA-Ox$_{2.33\ (100\ kDa)}$	ns	0.0618
HA-ADH$_{1.00}$HA-Ox$_{1.00\ (40\ kDa)}$ vs. HA-ADH$_{3.00}$HA-Ox$_{1.00\ (100\ kDa)}$	*	0.0367
HA-ADH$_{1.00}$HA-Ox$_{1.00\ (40\ kDa)}$ vs. HA-ADH$_{2.33}$HA-Ox$_{1.00\ (100\ kDa)}$	*	0.0143
HA-ADH$_{1.00}$HA-Ox$_{1.00\ (40\ kDa)}$ vs. HA-ADH$_{2.00}$HA-Ox$_{2.00\ (100\ kDa)}$	*	0.0497
HA-ADH$_{1.00}$HA-Ox$_{1.00\ (40\ kDa)}$ vs. HA-ADH$_{1.67}$HA-Ox$_{3.00\ (100\ kDa)}$	ns	0.0584
HA-ADH$_{1.00}$HA-Ox$_{1.00\ (40\ kDa)}$ vs. HA-ADH$_{1.00}$HA-Ox$_{3.00\ (100\ kDa)}$	ns	0.2844
HA-ADH$_{1.00}$HA-Ox$_{1.00\ (40\ kDa)}$ vs. HA-ADH$_{1.00}$HA-Ox$_{1.67\ (100\ kDa)}$	ns	0.1981
HA-ADH$_{1.00}$HA-Ox$_{1.00\ (40\ kDa)}$ vs. HA-ADH$_{1.00}$HA-Ox$_{1.00\ (100\ kDa)}$	ns	0.0633

HA-ADH$_{3.00}$HA-Ox$_{3.00\ (100\ kDa)}$ vs. HA-ADH$_{3.00}$HA-Ox$_{2.33\ (100\ kDa)}$	ns	0.9289
HA-ADH$_{3.00}$HA-Ox$_{3.00\ (100\ kDa)}$ vs. HA-ADH$_{3.00}$HA-Ox$_{1.00\ (100\ kDa)}$	ns	0.3451
HA-ADH$_{3.00}$HA-Ox$_{3.00\ (100\ kDa)}$ vs. HA-ADH$_{2.33}$HA-Ox$_{1.00\ (100\ kDa)}$	ns	0.2547
HA-ADH$_{3.00}$HA-Ox$_{3.00\ (100\ kDa)}$ vs. HA-ADH$_{2.00}$HA-Ox$_{2.00\ (100\ kDa)}$	ns	0.9641
HA-ADH$_{3.00}$HA-Ox$_{3.00\ (100\ kDa)}$ vs. HA-ADH$_{1.67}$HA-Ox$_{3.00\ (100\ kDa)}$	ns	0.6719
HA-ADH$_{3.00}$HA-Ox$_{3.00\ (100\ kDa)}$ vs. HA-ADH$_{1.00}$HA-Ox$_{3.00\ (100\ kDa)}$	ns	0.1406
HA-ADH$_{3.00}$HA-Ox$_{3.00\ (100\ kDa)}$ vs. HA-ADH$_{1.00}$HA-Ox$_{1.67\ (100\ kDa)}$	ns	0.9736
HA-ADH$_{3.00}$HA-Ox$_{3.00\ (100\ kDa)}$ vs. HA-ADH$_{1.00}$HA-Ox$_{1.00\ (100\ kDa)}$	ns	0.9185
HA-ADH$_{3.00}$HA-Ox$_{2.33\ (100\ kDa)}$ vs. HA-ADH$_{3.00}$HA-Ox$_{1.00\ (100\ kDa)}$	ns	0.9381
HA-ADH$_{3.00}$HA-Ox$_{2.33\ (100\ kDa)}$ vs. HA-ADH$_{2.33}$HA-Ox$_{1.00\ (100\ kDa)}$	ns	0.9901
HA-ADH$_{3.00}$HA-Ox$_{2.33\ (100\ kDa)}$ vs. HA-ADH$_{2.00}$HA-Ox$_{2.00\ (100\ kDa)}$	ns	>0.9999
HA-ADH$_{3.00}$HA-Ox$_{2.33\ (100\ kDa)}$ vs. HA-ADH$_{1.67}$HA-Ox$_{3.00\ (100\ kDa)}$	ns	0.9997
HA-ADH$_{3.00}$HA-Ox$_{2.33\ (100\ kDa)}$ vs. HA-ADH$_{1.00}$HA-Ox$_{3.00\ (100\ kDa)}$	ns	0.1191
HA-ADH$_{3.00}$HA-Ox$_{2.33\ (100\ kDa)}$ vs. HA-ADH$_{1.00}$HA-Ox$_{1.67\ (100\ kDa)}$	ns	>0.9999
HA-ADH$_{3.00}$HA-Ox$_{2.33\ (100\ kDa)}$ vs. HA-ADH$_{1.00}$HA-Ox$_{1.00\ (100\ kDa)}$	ns	>0.9999
HA-ADH$_{3.00}$HA-Ox$_{1.00\ (100\ kDa)}$ vs. HA-ADH$_{2.33}$HA-Ox$_{1.00\ (100\ kDa)}$	ns	0.9998
HA-ADH$_{3.00}$HA-Ox$_{1.00\ (100\ kDa)}$ vs. HA-ADH$_{2.00}$HA-Ox$_{2.00\ (100\ kDa)}$	ns	0.8315
HA-ADH$_{3.00}$HA-Ox$_{1.00\ (100\ kDa)}$ vs. HA-ADH$_{1.67}$HA-Ox$_{3.00\ (100\ kDa)}$	ns	0.9999
HA-ADH$_{3.00}$HA-Ox$_{1.00\ (100\ kDa)}$ vs. HA-ADH$_{1.00}$HA-Ox$_{3.00\ (100\ kDa)}$	*	0.0408
HA-ADH$_{3.00}$HA-Ox$_{1.00\ (100\ kDa)}$ vs. HA-ADH$_{1.00}$HA-Ox$_{1.67\ (100\ kDa)}$	ns	>0.9999
HA-ADH$_{3.00}$HA-Ox$_{1.00\ (100\ kDa)}$ vs. HA-ADH$_{1.00}$HA-Ox$_{1.00\ (100\ kDa)}$	ns	0.9517
HA-ADH$_{2.33}$HA-Ox$_{1.00\ (100\ kDa)}$ vs. HA-ADH$_{2.00}$HA-Ox$_{2.00\ (100\ kDa)}$	ns	0.9314
HA-ADH$_{2.33}$HA-Ox$_{1.00\ (100\ kDa)}$ vs. HA-ADH$_{1.67}$HA-Ox$_{3.00\ (100\ kDa)}$	ns	>0.9999
HA-ADH$_{2.33}$HA-Ox$_{1.00\ (100\ kDa)}$ vs. HA-ADH$_{1.00}$HA-Ox$_{3.00\ (100\ kDa)}$	*	0.0341
HA-ADH$_{2.33}$HA-Ox$_{1.00\ (100\ kDa)}$ vs. HA-ADH$_{1.00}$HA-Ox$_{1.67\ (100\ kDa)}$	ns	>0.9999
HA-ADH$_{2.33}$HA-Ox$_{1.00\ (100\ kDa)}$ vs. HA-ADH$_{1.00}$HA-Ox$_{1.00\ (100\ kDa)}$	ns	0.9941
HA-ADH$_{2.00}$HA-Ox$_{2.00\ (100\ kDa)}$ vs. HA-ADH$_{1.67}$HA-Ox$_{3.00\ (100\ kDa)}$	ns	0.9946
HA-ADH$_{2.00}$HA-Ox$_{2.00\ (100\ kDa)}$ vs. HA-ADH$_{1.00}$HA-Ox$_{3.00\ (100\ kDa)}$	ns	0.1065
HA-ADH$_{2.00}$HA-Ox$_{2.00\ (100\ kDa)}$ vs. HA-ADH$_{1.00}$HA-Ox$_{1.67\ (100\ kDa)}$	ns	>0.9999
HA-ADH$_{2.00}$HA-Ox$_{2.00\ (100\ kDa)}$ vs. HA-ADH$_{1.00}$HA-Ox$_{1.00\ (100\ kDa)}$	ns	>0.9999
HA-ADH$_{1.67}$HA-Ox$_{3.00\ (100\ kDa)}$ vs. HA-ADH$_{1.00}$HA-Ox$_{3.00\ (100\ kDa)}$	ns	0.0881
HA-ADH$_{1.67}$HA-Ox$_{3.00\ (100\ kDa)}$ vs. HA-ADH$_{1.00}$HA-Ox$_{1.67\ (100\ kDa)}$	ns	>0.9999
HA-ADH$_{1.67}$HA-Ox$_{3.00\ (100\ kDa)}$ vs. HA-ADH$_{1.00}$HA-Ox$_{1.00\ (100\ kDa)}$	ns	0.9999

HA-$ADH_{1.00}$HA-$Ox_{3.00\ (100\ kDa)}$ vs. HA-$ADH_{1.00}$HA-$Ox_{1.67\ (100\ kDa)}$	ns	0.3893
HA-$ADH_{1.00}$HA-$Ox_{3.00\ (100\ kDa)}$ vs. HA-$ADH_{1.00}$HA-$Ox_{1.00\ (100\ kDa)}$	ns	0.1199
HA-$ADH_{1.00}$HA-$Ox_{1.67\ (100\ kDa)}$ vs. HA-$ADH_{1.00}$HA-$Ox_{1.00\ (100\ kDa)}$	ns	>0.9999
Day 28		
HA-$ADH_{3.00}$HA-$Ox_{3.00\ (40\ kDa)}$ vs. HA-$ADH_{3.00}$HA-$Ox_{1.00\ (40\ kDa)}$	ns	0.0887
HA-$ADH_{3.00}$HA-$Ox_{3.00\ (40\ kDa)}$ vs. HA-$ADH_{2.00}$HA-$Ox_{2.00\ (40\ kDa)}$	ns	0.8973
HA-$ADH_{3.00}$HA-$Ox_{3.00\ (40\ kDa)}$ vs. HA-$ADH_{1.67}$HA-$Ox_{1.00\ (40\ kDa)}$	ns	0.4655
HA-$ADH_{3.00}$HA-$Ox_{3.00\ (40\ kDa)}$ vs. HA-$ADH_{1.00}$HA-$Ox_{3.00\ (40\ kDa)}$	**	0.0025
HA-$ADH_{3.00}$HA-$Ox_{3.00\ (40\ kDa)}$ vs. HA-$ADH_{1.00}$HA-$Ox_{1.00\ (40\ kDa)}$	**	0.0015
HA-$ADH_{3.00}$HA-$Ox_{3.00\ (40\ kDa)}$ vs. HA-$ADH_{3.00}$HA-$Ox_{3.00\ (100\ kDa)}$	*	0.0108
HA-$ADH_{3.00}$HA-$Ox_{3.00\ (40\ kDa)}$ vs. HA-$ADH_{3.00}$HA-$Ox_{2.33\ (100\ kDa)}$	*	0.013
HA-$ADH_{3.00}$HA-$Ox_{3.00\ (40\ kDa)}$ vs. HA-$ADH_{3.00}$HA-$Ox_{1.00\ (100\ kDa)}$	ns	0.9982
HA-$ADH_{3.00}$HA-$Ox_{3.00\ (40\ kDa)}$ vs. HA-$ADH_{2.33}$HA-$Ox_{1.00\ (100\ kDa)}$	ns	0.2129
HA-$ADH_{3.00}$HA-$Ox_{3.00\ (40\ kDa)}$ vs. HA-$ADH_{2.00}$HA-$Ox_{2.00\ (100\ kDa)}$	ns	0.2207
HA-$ADH_{3.00}$HA-$Ox_{3.00\ (40\ kDa)}$ vs. HA-$ADH_{1.67}$HA-$Ox_{3.00\ (100\ kDa)}$	**	0.0032
HA-$ADH_{3.00}$HA-$Ox_{3.00\ (40\ kDa)}$ vs. HA-$ADH_{1.00}$HA-$Ox_{3.00\ (100\ kDa)}$	*	0.0127
HA-$ADH_{3.00}$HA-$Ox_{3.00\ (40\ kDa)}$ vs. HA-$ADH_{1.00}$HA-$Ox_{1.67\ (100\ kDa)}$	ns	0.1384
HA-$ADH_{3.00}$HA-$Ox_{3.00\ (40\ kDa)}$ vs. HA-$ADH_{1.00}$HA-$Ox_{1.00\ (100\ kDa)}$	ns	0.2095
HA-$ADH_{3.00}$HA-$Ox_{1.00\ (40\ kDa)}$ vs. HA-$ADH_{2.00}$HA-$Ox_{2.00\ (40\ kDa)}$	ns	0.2687
HA-$ADH_{3.00}$HA-$Ox_{1.00\ (40\ kDa)}$ vs. HA-$ADH_{1.67}$HA-$Ox_{1.00\ (40\ kDa)}$	ns	0.2282
HA-$ADH_{3.00}$HA-$Ox_{1.00\ (40\ kDa)}$ vs. HA-$ADH_{1.00}$HA-$Ox_{3.00\ (40\ kDa)}$	*	0.018
HA-$ADH_{3.00}$HA-$Ox_{1.00\ (40\ kDa)}$ vs. HA-$ADH_{1.00}$HA-$Ox_{1.00\ (40\ kDa)}$	*	0.0173
HA-$ADH_{3.00}$HA-$Ox_{1.00\ (40\ kDa)}$ vs. HA-$ADH_{3.00}$HA-$Ox_{3.00\ (100\ kDa)}$	*	0.0224
HA-$ADH_{3.00}$HA-$Ox_{1.00\ (40\ kDa)}$ vs. HA-$ADH_{3.00}$HA-$Ox_{2.33\ (100\ kDa)}$	*	0.0442
HA-$ADH_{3.00}$HA-$Ox_{1.00\ (40\ kDa)}$ vs. HA-$ADH_{3.00}$HA-$Ox_{1.00\ (100\ kDa)}$	ns	0.0557
HA-$ADH_{3.00}$HA-$Ox_{1.00\ (40\ kDa)}$ vs. HA-$ADH_{2.33}$HA-$Ox_{1.00\ (100\ kDa)}$	*	0.0148
HA-$ADH_{3.00}$HA-$Ox_{1.00\ (40\ kDa)}$ vs. HA-$ADH_{2.00}$HA-$Ox_{2.00\ (100\ kDa)}$	*	0.0164
HA-$ADH_{3.00}$HA-$Ox_{1.00\ (40\ kDa)}$ vs. HA-$ADH_{1.67}$HA-$Ox_{3.00\ (100\ kDa)}$	*	0.025
HA-$ADH_{3.00}$HA-$Ox_{1.00\ (40\ kDa)}$ vs. HA-$ADH_{1.00}$HA-$Ox_{3.00\ (100\ kDa)}$	**	0.0064
HA-$ADH_{3.00}$HA-$Ox_{1.00\ (40\ kDa)}$ vs. HA-$ADH_{1.00}$HA-$Ox_{1.67\ (100\ kDa)}$	**	0.0096
HA-$ADH_{3.00}$HA-$Ox_{1.00\ (40\ kDa)}$ vs. HA-$ADH_{1.00}$HA-$Ox_{1.00\ (100\ kDa)}$	*	0.0133
HA-$ADH_{2.00}$HA-$Ox_{2.00\ (40\ kDa)}$ vs. HA-$ADH_{1.67}$HA-$Ox_{1.00\ (40\ kDa)}$	ns	>0.9999
HA-$ADH_{2.00}$HA-$Ox_{2.00\ (40\ kDa)}$ vs. HA-$ADH_{1.00}$HA-$Ox_{3.00\ (40\ kDa)}$	ns	0.061

HA-$ADH_{2.00}$HA-$Ox_{2.00\ (40\ kDa)}$ vs. HA-$ADH_{1.00}$HA-$Ox_{1.00\ (40\ kDa)}$	ns	0.0601
HA-$ADH_{2.00}$HA-$Ox_{2.00\ (40\ kDa)}$ vs. HA-$ADH_{3.00}$HA-$Ox_{3.00\ (100\ kDa)}$	ns	0.1631
HA-$ADH_{2.00}$HA-$Ox_{2.00\ (40\ kDa)}$ vs. HA-$ADH_{3.00}$HA-$Ox_{2.33\ (100\ kDa)}$	ns	0.2372
HA-$ADH_{2.00}$HA-$Ox_{2.00\ (40\ kDa)}$ vs. HA-$ADH_{3.00}$HA-$Ox_{1.00\ (100\ kDa)}$	ns	0.8603
HA-$ADH_{2.00}$HA-$Ox_{2.00\ (40\ kDa)}$ vs. HA-$ADH_{2.33}$HA-$Ox_{1.00\ (100\ kDa)}$	ns	0.224
HA-$ADH_{2.00}$HA-$Ox_{2.00\ (40\ kDa)}$ vs. HA-$ADH_{2.00}$HA-$Ox_{2.00\ (100\ kDa)}$	ns	0.2533
HA-$ADH_{2.00}$HA-$Ox_{2.00\ (40\ kDa)}$ vs. HA-$ADH_{1.67}$HA-$Ox_{3.00\ (100\ kDa)}$	ns	0.1493
HA-$ADH_{2.00}$HA-$Ox_{2.00\ (40\ kDa)}$ vs. HA-$ADH_{1.00}$HA-$Ox_{3.00\ (100\ kDa)}$	ns	0.052
HA-$ADH_{2.00}$HA-$Ox_{2.00\ (40\ kDa)}$ vs. HA-$ADH_{1.00}$HA-$Ox_{1.67\ (100\ kDa)}$	ns	0.0979
HA-$ADH_{2.00}$HA-$Ox_{2.00\ (40\ kDa)}$ vs. HA-$ADH_{1.00}$HA-$Ox_{1.00\ (100\ kDa)}$	ns	0.1733
HA-$ADH_{1.67}$HA-$Ox_{1.00\ (40\ kDa)}$ vs. HA-$ADH_{1.00}$HA-$Ox_{3.00\ (40\ kDa)}$	*	0.0253
HA-$ADH_{1.67}$HA-$Ox_{1.00\ (40\ kDa)}$ vs. HA-$ADH_{1.00}$HA-$Ox_{1.00\ (40\ kDa)}$	*	0.0242
HA-$ADH_{1.67}$HA-$Ox_{1.00\ (40\ kDa)}$ vs. HA-$ADH_{3.00}$HA-$Ox_{3.00\ (100\ kDa)}$	*	0.0452
HA-$ADH_{1.67}$HA-$Ox_{1.00\ (40\ kDa)}$ vs. HA-$ADH_{3.00}$HA-$Ox_{2.33\ (100\ kDa)}$	ns	0.0936
HA-$ADH_{1.67}$HA-$Ox_{1.00\ (40\ kDa)}$ vs. HA-$ADH_{3.00}$HA-$Ox_{1.00\ (100\ kDa)}$	ns	0.5128
HA-$ADH_{1.67}$HA-$Ox_{1.00\ (40\ kDa)}$ vs. HA-$ADH_{2.33}$HA-$Ox_{1.00\ (100\ kDa)}$	ns	0.0679
HA-$ADH_{1.67}$HA-$Ox_{1.00\ (40\ kDa)}$ vs. HA-$ADH_{2.00}$HA-$Ox_{2.00\ (100\ kDa)}$	ns	0.0741
HA-$ADH_{1.67}$HA-$Ox_{1.00\ (40\ kDa)}$ vs. HA-$ADH_{1.67}$HA-$Ox_{3.00\ (100\ kDa)}$	*	0.0459
HA-$ADH_{1.67}$HA-$Ox_{1.00\ (40\ kDa)}$ vs. HA-$ADH_{1.00}$HA-$Ox_{3.00\ (100\ kDa)}$	**	0.0095
HA-$ADH_{1.67}$HA-$Ox_{1.00\ (40\ kDa)}$ vs. HA-$ADH_{1.00}$HA-$Ox_{1.67\ (100\ kDa)}$	*	0.0396
HA-$ADH_{1.67}$HA-$Ox_{1.00\ (40\ kDa)}$ vs. HA-$ADH_{1.00}$HA-$Ox_{1.00\ (100\ kDa)}$	ns	0.0633
HA-$ADH_{1.00}$HA-$Ox_{3.00\ (40\ kDa)}$ vs. HA-$ADH_{1.00}$HA-$Ox_{1.00\ (40\ kDa)}$	ns	>0.9999
HA-$ADH_{1.00}$HA-$Ox_{3.00\ (40\ kDa)}$ vs. HA-$ADH_{3.00}$HA-$Ox_{3.00\ (100\ kDa)}$	*	0.0301
HA-$ADH_{1.00}$HA-$Ox_{3.00\ (40\ kDa)}$ vs. HA-$ADH_{3.00}$HA-$Ox_{2.33\ (100\ kDa)}$	****	<0.0001
HA-$ADH_{1.00}$HA-$Ox_{3.00\ (40\ kDa)}$ vs. HA-$ADH_{3.00}$HA-$Ox_{1.00\ (100\ kDa)}$	ns	0.0639
HA-$ADH_{1.00}$HA-$Ox_{3.00\ (40\ kDa)}$ vs. HA-$ADH_{2.33}$HA-$Ox_{1.00\ (100\ kDa)}$	ns	0.0914
HA-$ADH_{1.00}$HA-$Ox_{3.00\ (40\ kDa)}$ vs. HA-$ADH_{2.00}$HA-$Ox_{2.00\ (100\ kDa)}$	ns	0.0732
HA-$ADH_{1.00}$HA-$Ox_{3.00\ (40\ kDa)}$ vs. HA-$ADH_{1.67}$HA-$Ox_{3.00\ (100\ kDa)}$	*	0.0216
HA-$ADH_{1.00}$HA-$Ox_{3.00\ (40\ kDa)}$ vs. HA-$ADH_{1.00}$HA-$Ox_{3.00\ (100\ kDa)}$	ns	0.4367
HA-$ADH_{1.00}$HA-$Ox_{3.00\ (40\ kDa)}$ vs. HA-$ADH_{1.00}$HA-$Ox_{1.67\ (100\ kDa)}$	ns	0.3021
HA-$ADH_{1.00}$HA-$Ox_{3.00\ (40\ kDa)}$ vs. HA-$ADH_{1.00}$HA-$Ox_{1.00\ (100\ kDa)}$	ns	0.1566
HA-$ADH_{1.00}$HA-$Ox_{1.00\ (40\ kDa)}$ vs. HA-$ADH_{3.00}$HA-$Ox_{3.00\ (100\ kDa)}$	*	0.0248
HA-$ADH_{1.00}$HA-$Ox_{1.00\ (40\ kDa)}$ vs. HA-$ADH_{3.00}$HA-$Ox_{2.33\ (100\ kDa)}$	****	<0.0001

HA-ADH$_{1.00}$HA-Ox$_{1.00\ (40\ kDa)}$ vs. HA-ADH$_{3.00}$HA-Ox$_{1.00\ (100\ kDa)}$	ns	0.0625
HA-ADH$_{1.00}$HA-Ox$_{1.00\ (40\ kDa)}$ vs. HA-ADH$_{2.33}$HA-Ox$_{1.00\ (100\ kDa)}$	ns	0.0891
HA-ADH$_{1.00}$HA-Ox$_{1.00\ (40\ kDa)}$ vs. HA-ADH$_{2.00}$HA-Ox$_{2.00\ (100\ kDa)}$	ns	0.0707
HA-ADH$_{1.00}$HA-Ox$_{1.00\ (40\ kDa)}$ vs. HA-ADH$_{1.67}$HA-Ox$_{3.00\ (100\ kDa)}$	*	0.0156
HA-ADH$_{1.00}$HA-Ox$_{1.00\ (40\ kDa)}$ vs. HA-ADH$_{1.00}$HA-Ox$_{3.00\ (100\ kDa)}$	ns	0.4361
HA-ADH$_{1.00}$HA-Ox$_{1.00\ (40\ kDa)}$ vs. HA-ADH$_{1.00}$HA-Ox$_{1.67\ (100\ kDa)}$	ns	0.3009
HA-ADH$_{1.00}$HA-Ox$_{1.00\ (40\ kDa)}$ vs. HA-ADH$_{1.00}$HA-Ox$_{1.00\ (100\ kDa)}$	ns	0.1547
HA-ADH$_{3.00}$HA-Ox$_{3.00\ (100\ kDa)}$ vs. HA-ADH$_{3.00}$HA-Ox$_{2.33\ (100\ kDa)}$	ns	0.6017
HA-ADH$_{3.00}$HA-Ox$_{3.00\ (100\ kDa)}$ vs. HA-ADH$_{3.00}$HA-Ox$_{1.00\ (100\ kDa)}$	ns	0.2775
HA-ADH$_{3.00}$HA-Ox$_{3.00\ (100\ kDa)}$ vs. HA-ADH$_{2.33}$HA-Ox$_{1.00\ (100\ kDa)}$	ns	0.9758
HA-ADH$_{3.00}$HA-Ox$_{3.00\ (100\ kDa)}$ vs. HA-ADH$_{2.00}$HA-Ox$_{2.00\ (100\ kDa)}$	ns	0.8782
HA-ADH$_{3.00}$HA-Ox$_{3.00\ (100\ kDa)}$ vs. HA-ADH$_{1.67}$HA-Ox$_{3.00\ (100\ kDa)}$	ns	0.9973
HA-ADH$_{3.00}$HA-Ox$_{3.00\ (100\ kDa)}$ vs. HA-ADH$_{1.00}$HA-Ox$_{3.00\ (100\ kDa)}$	ns	0.1094
HA-ADH$_{3.00}$HA-Ox$_{3.00\ (100\ kDa)}$ vs. HA-ADH$_{1.00}$HA-Ox$_{1.67\ (100\ kDa)}$	ns	0.9713
HA-ADH$_{3.00}$HA-Ox$_{3.00\ (100\ kDa)}$ vs. HA-ADH$_{1.00}$HA-Ox$_{1.00\ (100\ kDa)}$	ns	>0.9999
HA-ADH$_{3.00}$HA-Ox$_{2.33\ (100\ kDa)}$ vs. HA-ADH$_{3.00}$HA-Ox$_{1.00\ (100\ kDa)}$	ns	0.4403
HA-ADH$_{3.00}$HA-Ox$_{2.33\ (100\ kDa)}$ vs. HA-ADH$_{2.33}$HA-Ox$_{1.00\ (100\ kDa)}$	ns	>0.9999
HA-ADH$_{3.00}$HA-Ox$_{2.33\ (100\ kDa)}$ vs. HA-ADH$_{2.00}$HA-Ox$_{2.00\ (100\ kDa)}$	ns	>0.9999
HA-ADH$_{3.00}$HA-Ox$_{2.33\ (100\ kDa)}$ vs. HA-ADH$_{1.67}$HA-Ox$_{3.00\ (100\ kDa)}$	ns	0.23
HA-ADH$_{3.00}$HA-Ox$_{2.33\ (100\ kDa)}$ vs. HA-ADH$_{1.00}$HA-Ox$_{3.00\ (100\ kDa)}$	ns	0.0885
HA-ADH$_{3.00}$HA-Ox$_{2.33\ (100\ kDa)}$ vs. HA-ADH$_{1.00}$HA-Ox$_{1.67\ (100\ kDa)}$	ns	0.6834
HA-ADH$_{3.00}$HA-Ox$_{2.33\ (100\ kDa)}$ vs. HA-ADH$_{1.00}$HA-Ox$_{1.00\ (100\ kDa)}$	ns	0.998
HA-ADH$_{3.00}$HA-Ox$_{1.00\ (100\ kDa)}$ vs. HA-ADH$_{2.33}$HA-Ox$_{1.00\ (100\ kDa)}$	ns	0.5763
HA-ADH$_{3.00}$HA-Ox$_{1.00\ (100\ kDa)}$ vs. HA-ADH$_{2.00}$HA-Ox$_{2.00\ (100\ kDa)}$	ns	0.6545
HA-ADH$_{3.00}$HA-Ox$_{1.00\ (100\ kDa)}$ vs. HA-ADH$_{1.67}$HA-Ox$_{3.00\ (100\ kDa)}$	ns	0.2314
HA-ADH$_{3.00}$HA-Ox$_{1.00\ (100\ kDa)}$ vs. HA-ADH$_{1.00}$HA-Ox$_{3.00\ (100\ kDa)}$	ns	0.0562
HA-ADH$_{3.00}$HA-Ox$_{1.00\ (100\ kDa)}$ vs. HA-ADH$_{1.00}$HA-Ox$_{1.67\ (100\ kDa)}$	ns	0.2151
HA-ADH$_{3.00}$HA-Ox$_{1.00\ (100\ kDa)}$ vs. HA-ADH$_{1.00}$HA-Ox$_{1.00\ (100\ kDa)}$	ns	0.4379
HA-ADH$_{2.33}$HA-Ox$_{1.00\ (100\ kDa)}$ vs. HA-ADH$_{2.00}$HA-Ox$_{2.00\ (100\ kDa)}$	ns	>0.9999
HA-ADH$_{2.33}$HA-Ox$_{1.00\ (100\ kDa)}$ vs. HA-ADH$_{1.67}$HA-Ox$_{3.00\ (100\ kDa)}$	ns	0.8422
HA-ADH$_{2.33}$HA-Ox$_{1.00\ (100\ kDa)}$ vs. HA-ADH$_{1.00}$HA-Ox$_{3.00\ (100\ kDa)}$	ns	0.1372
HA-ADH$_{2.33}$HA-Ox$_{1.00\ (100\ kDa)}$ vs. HA-ADH$_{1.00}$HA-Ox$_{1.67\ (100\ kDa)}$	ns	0.8311
HA-ADH$_{2.33}$HA-Ox$_{1.00\ (100\ kDa)}$ vs. HA-ADH$_{1.00}$HA-Ox$_{1.00\ (100\ kDa)}$	ns	>0.9999

HA-ADH$_{2.00}$HA-Ox$_{2.00\ (100\ kDa)}$ vs. HA-ADH$_{1.67}$HA-Ox$_{3.00\ (100\ kDa)}$	ns	0.6715
HA-ADH$_{2.00}$HA-Ox$_{2.00\ (100\ kDa)}$ vs. HA-ADH$_{1.00}$HA-Ox$_{3.00\ (100\ kDa)}$	ns	0.0946
HA-ADH$_{2.00}$HA-Ox$_{2.00\ (100\ kDa)}$ vs. HA-ADH$_{1.00}$HA-Ox$_{1.67\ (100\ kDa)}$	ns	0.7148
HA-ADH$_{2.00}$HA-Ox$_{2.00\ (100\ kDa)}$ vs. HA-ADH$_{1.00}$HA-Ox$_{1.00\ (100\ kDa)}$	ns	0.9969
HA-ADH$_{1.67}$HA-Ox$_{3.00\ (100\ kDa)}$ vs. HA-ADH$_{1.00}$HA-Ox$_{3.00\ (100\ kDa)}$	ns	0.1566
HA-ADH$_{1.67}$HA-Ox$_{3.00\ (100\ kDa)}$ vs. HA-ADH$_{1.00}$HA-Ox$_{1.67\ (100\ kDa)}$	ns	0.998
HA-ADH$_{1.67}$HA-Ox$_{3.00\ (100\ kDa)}$ vs. HA-ADH$_{1.00}$HA-Ox$_{1.00\ (100\ kDa)}$	ns	0.9992
HA-ADH$_{1.00}$HA-Ox$_{3.00\ (100\ kDa)}$ vs. HA-ADH$_{1.00}$HA-Ox$_{1.67\ (100\ kDa)}$	ns	0.7591
HA-ADH$_{1.00}$HA-Ox$_{3.00\ (100\ kDa)}$ vs. HA-ADH$_{1.00}$HA-Ox$_{1.00\ (100\ kDa)}$	ns	0.3106
HA-ADH$_{1.00}$HA-Ox$_{1.67\ (100\ kDa)}$ vs. HA-ADH$_{1.00}$HA-Ox$_{1.00\ (100\ kDa)}$	ns	0.9872

Effect of Hydrogel Size on Gelation Time

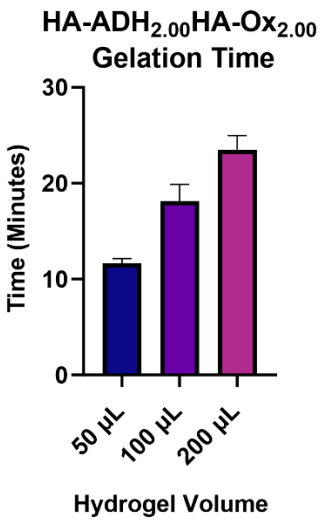

Figure A3. Gelation time of HA-ADH$_{2.00}$HA-Ox$_{2.00}$ hydrogels of different volumes. Gelation times of HA-ADH$_{2.00}$HA-Ox$_{2.00}$ hydrogels were evaluated at 50, 100, and 200 µL to determine the effect of hydrogel size on gelation time. As the hydrogel volume increased, the gelation time increased.

Compressive Modulus

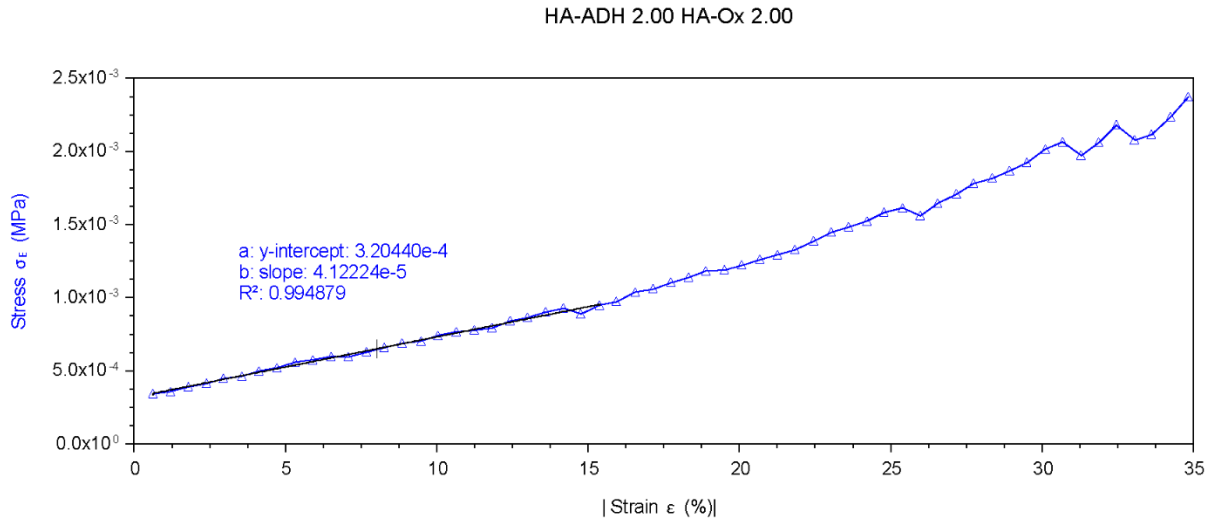

Figure A4. Stress-strain curves of HA hydrogels. Representative stress-strain curve of the centrally repeated HA hydrogel formulation HA-ADH$_{2.00}$HA-Ox$_{2.00}$. The slope of stress-stain curves at 15% strain was used to determine the compressive moduli of the HA hydrogels.

Hydrogel Morphology

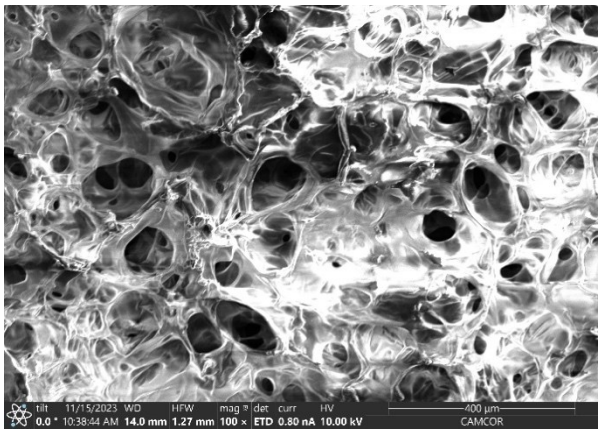

Figure A5. Scanning electron microscopy images of optimal hydrogel. Representative image of optimal hydrogel formulation, HA-ADH$_{3.00}$HA-Ox$_{2.33}$, depicting the porous morphology of the hydrazone-crosslinked HA hydrogel. Scale bar = 400 µm.

Affibody Bioconjugation

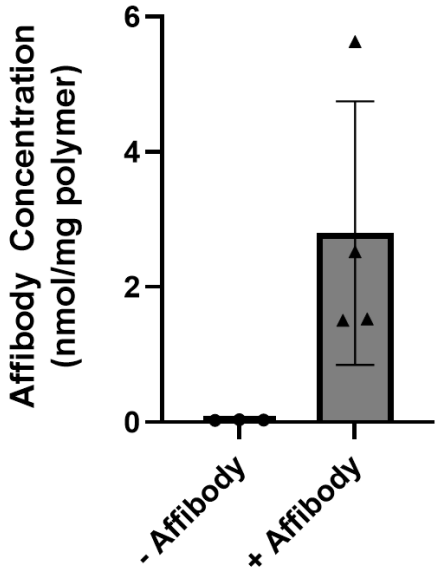

Figure A6. Quantification of affibody conjugation on HA-Nor-Ox-Affibody polymer. Pierce 660 Protein Assay was used to measure the amount of affibody conjugated per mg of HA-Nor-Ox-Affibody polymer and compared to HA-Nor-Ox polymer without conjugated affibodies as a control.

APPENDIX B: HYALURONIC ACID-COATED SCAFFOLDS PROMOTE MYOBLAST ATTACHMENT, ALIGNMENT, AND DIFFERENTIATION

Degree of Modification

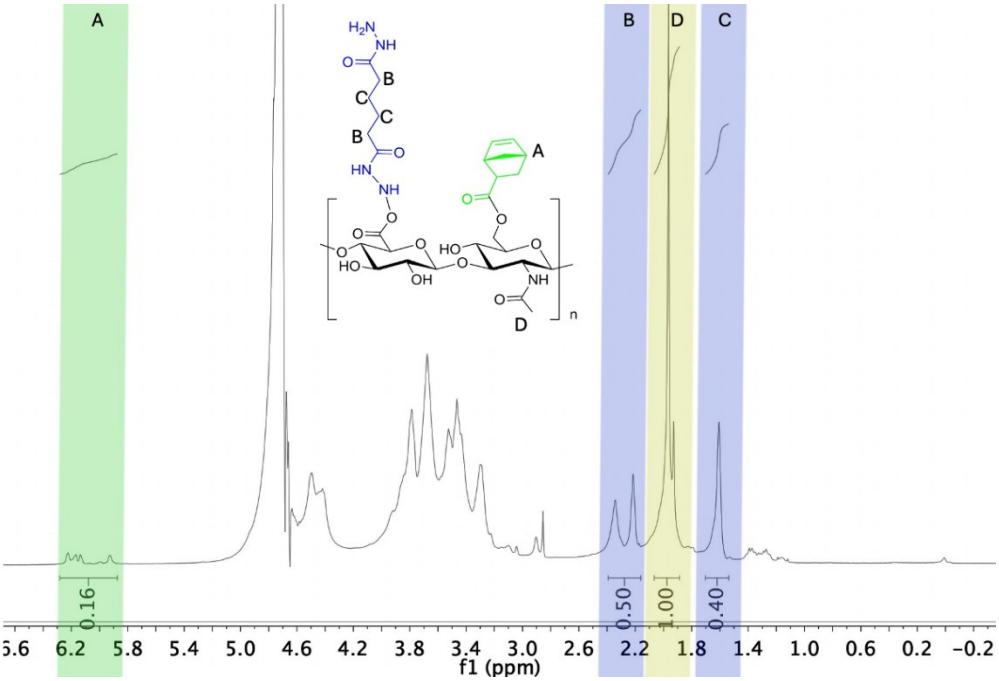

Figure B1. Representative ^{1}H-NMR spectrum confirming modification of HA with norbornene and adipic acid dihydrazide functional groups.

MEW Fiber Diameter

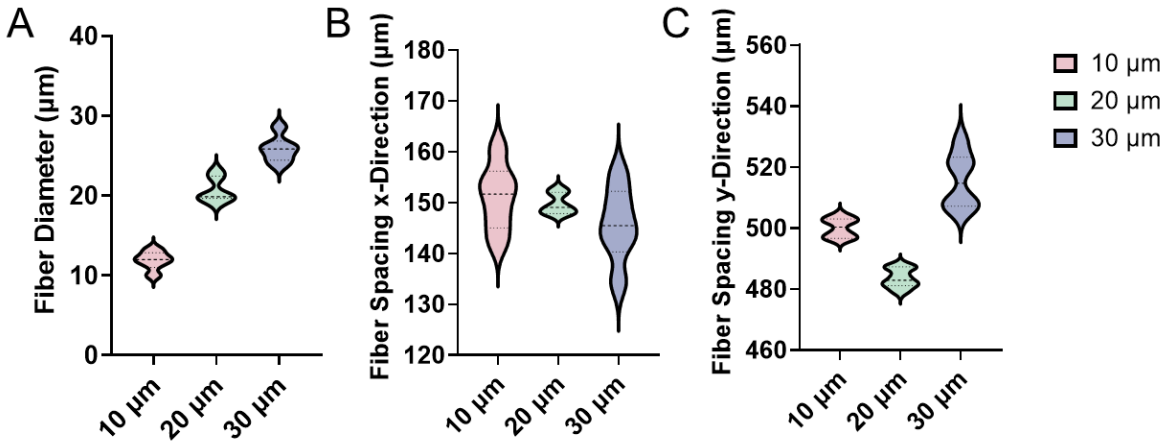

Figure B2. Measurements of MEW scaffold fiber diameters and fiber spacing using SEM images.

Compressive Modulus

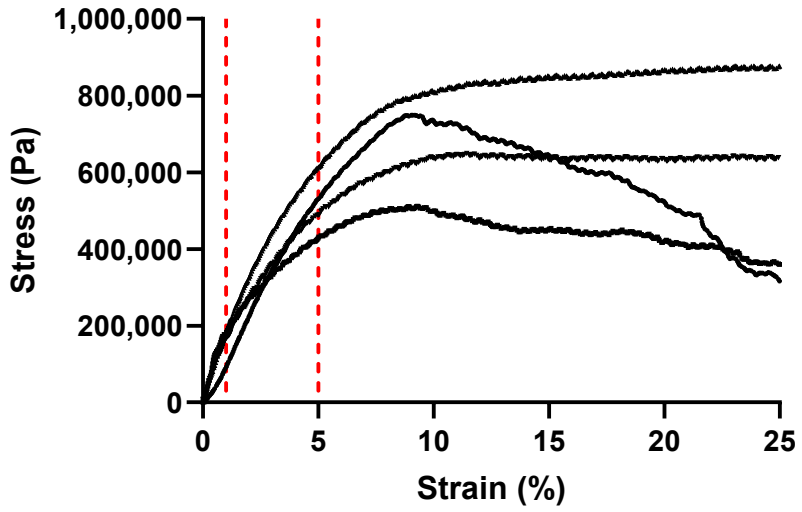

Figure. B3 Stress-strain curves for determining the stiffness of 20 µm non-coated scaffolds. The slope of the linear region between 1-5% strain, indicated by dashed red lines, was used to determine the stiffness of the scaffolds.

Myogenic Gene Expression

Table B1. Summary of Primer Sequences

	Forward Sequence (3'-5')	Reverse Sequence (3'-5')
Pax3	GCG TCT CTA AGA TCC TGT GCA G	GAT TTC CCA GCT AAA CAT GCC CG
Pax7	GAG TTC GAT TAG CCG AGT GC	CGG GTT CTG ATT CCA CAT CT
Myf5	AAC CAG AGA CTC AAG GT	GCT GGA CAA GCA ATC CAA GC
MyoD	AGT GAA TGA GGC CTT CGA GA	GCA TCT GAG TCG CCA CTG TA
MyoG	GAA GAA AAG GGA CTG GGG AC	GCG CAG GAT CTC CAC TTT AG
GAPDH	TCA ACG ACC CCT TCA TTG AC	ATG CAG GGA TGA TGT TCT GG

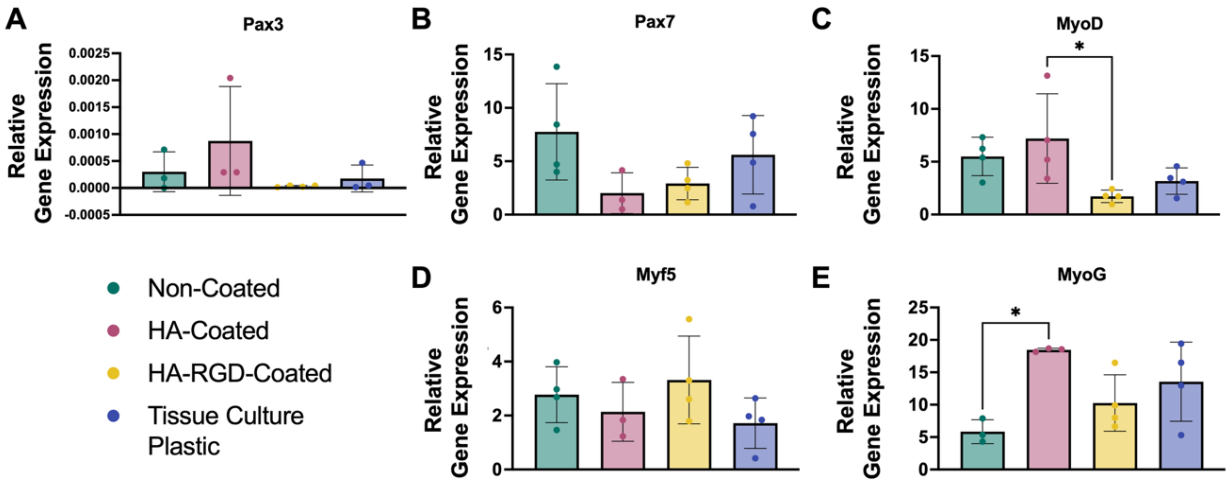

Figure. B4 Myogenic gene expression of C2C12 myoblasts differentiated on non-coated, HA-coated, and HA-RGD-coated 20 µm fiber scaffolds or tissue culture plastic for 5 days. RT-qPCR was performed on differentiated cells and compared to undifferentiated cells and a GAPDH housekeeping gene to assess Pax3, Pax7, MyoD, Myf5, and MyoG gene expression, n=3-4. (One-way ANOVA with post-hoc Tukey's multiple comparisons test, * $p < 0.05$ as indicated).

APPENDIX C: HYALURONIC ACID-ALGINATE HYDRAZONE CROSSLINKED HYDROGELS SUPPORT THE GENERATION AND MATURATION OF V2A INTERNEURONS

Degree of Modification

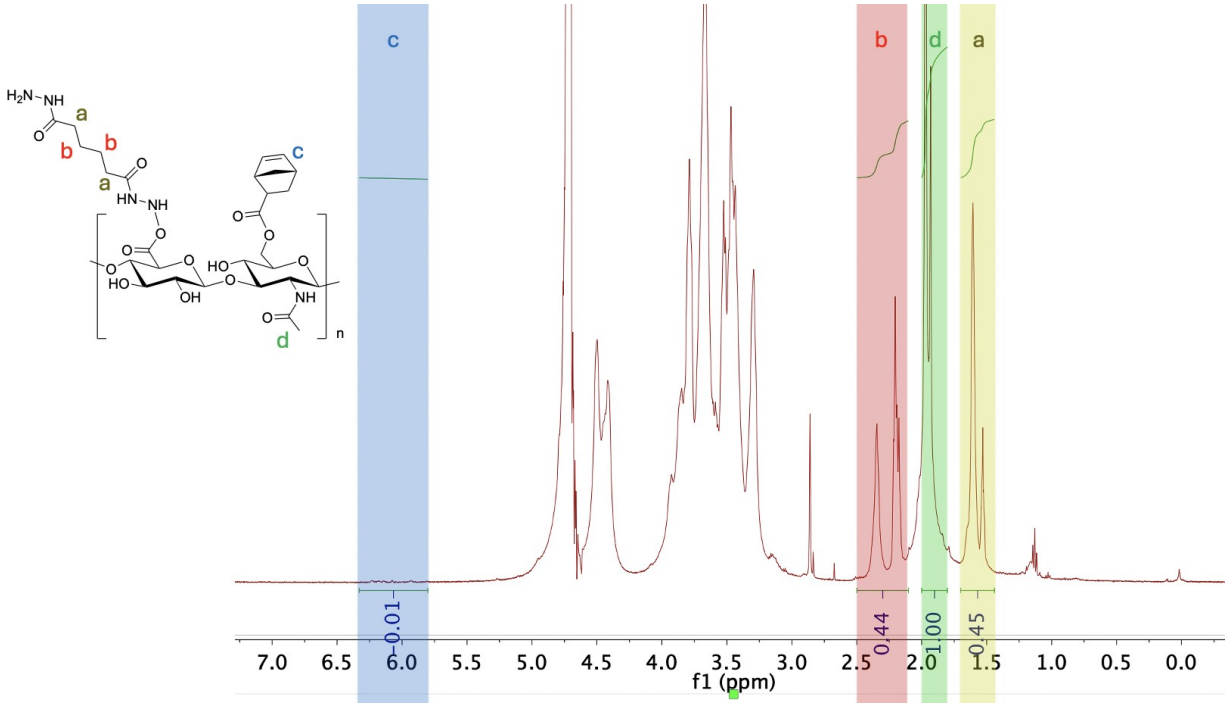

Figure C1. ^{1}H-NMR spectra of HA-Nor-ADH. Norbornene (HA-Nor) and adipic acid dihyrazide (HA-Nor-ADH) modifications of hyaluronic acid were confirmed by ^{1}H-NMR spectroscopy. Degree of modification of ADH was determined by peaks found at 1.44- 1.7 ppm (a) and 2.1-2.5 ppm (b) (8H). Degree of modification of norbornene was determined by peaks found at 5.7 -6.3ppm (2H). Both peaks were normalized to the n-acetyl group on HA found at 1.8-2 ppm (3H, d).

Table C1. Summary of polymer modification quantification.

	Degree of Modification (%)	Percent Yield
Alg-Ox	61.26 ± 8.82	72.65 ± 10.93
HA-Nor	4.75 ± 2.21	42.77 ± 1.93
HA-Nor-ADH	37.50 ± 5.71	65.19 ± 5.29
	Peptide Concentration (nmol/mg HA)	
HA-RGD	14.27 ± 7.55	-
HA-IKVAV	12.69 ± 6.10	-

Viability Analysis

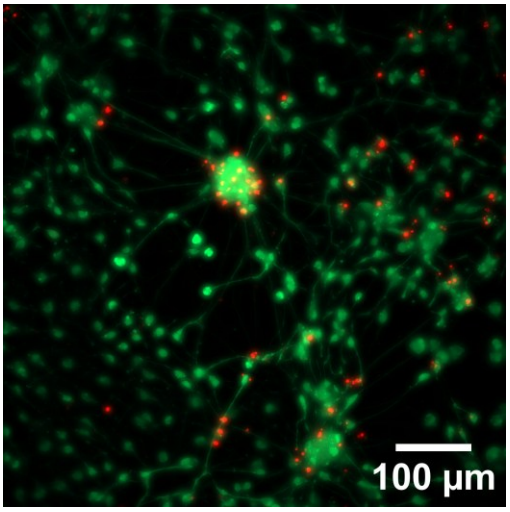

Figure C2. Represent live/dead staining of cells cultured on 2D laminin coating. Live cells are stained green (Calcein-AM), and dead cells are stained red (EthD-1). Scale bar = 100 µm.

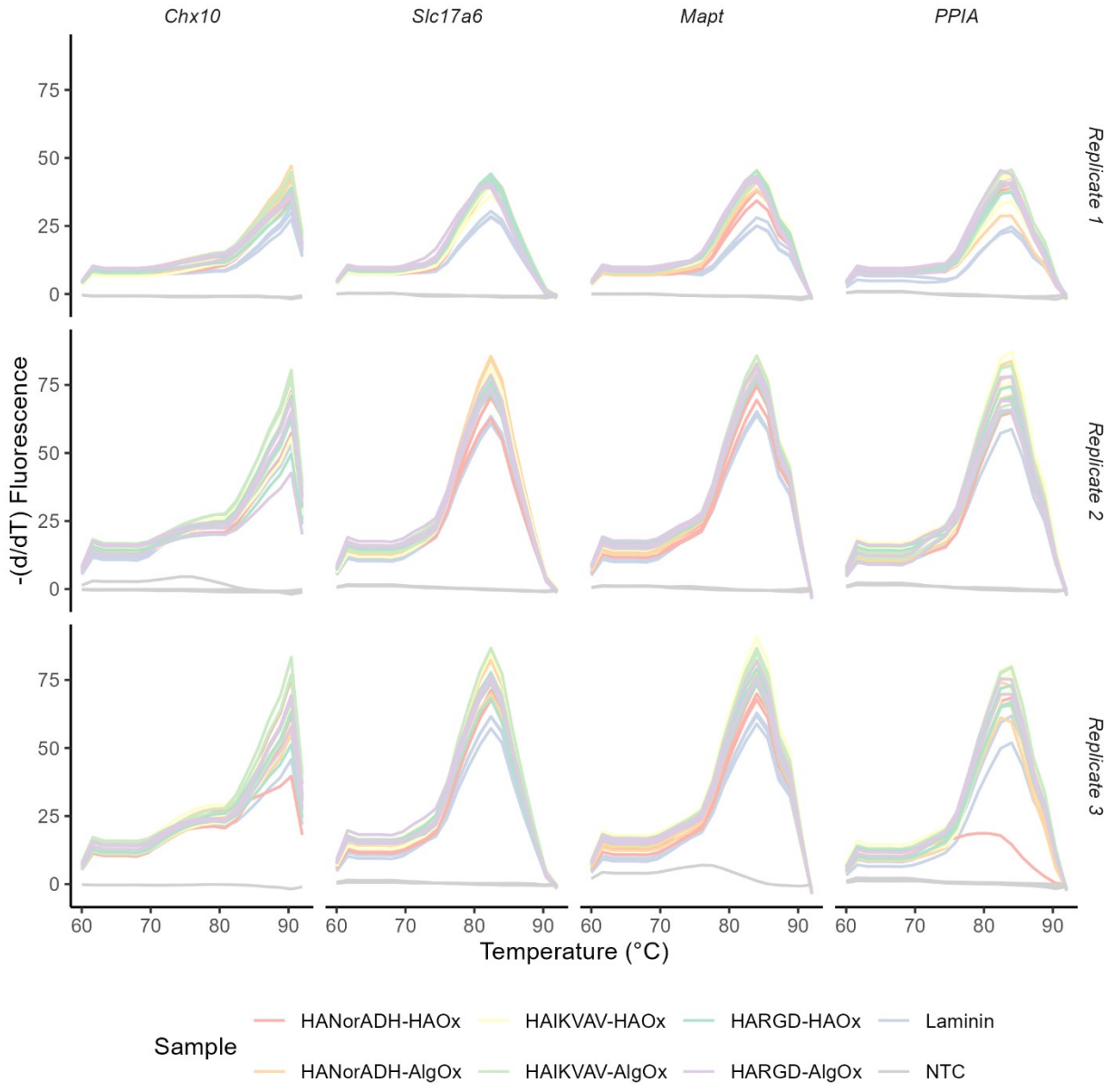

Figure C3. Melt curve analysis for qPCR. Melt curves represented as the negative derivative of fluorescence with respect to temperature for target genes. The presence of a single peak for each gene confirms primer specificity and absence of non-specific amplification. Columns correspond to a specific gene target, and rows represent independent biological replicates.

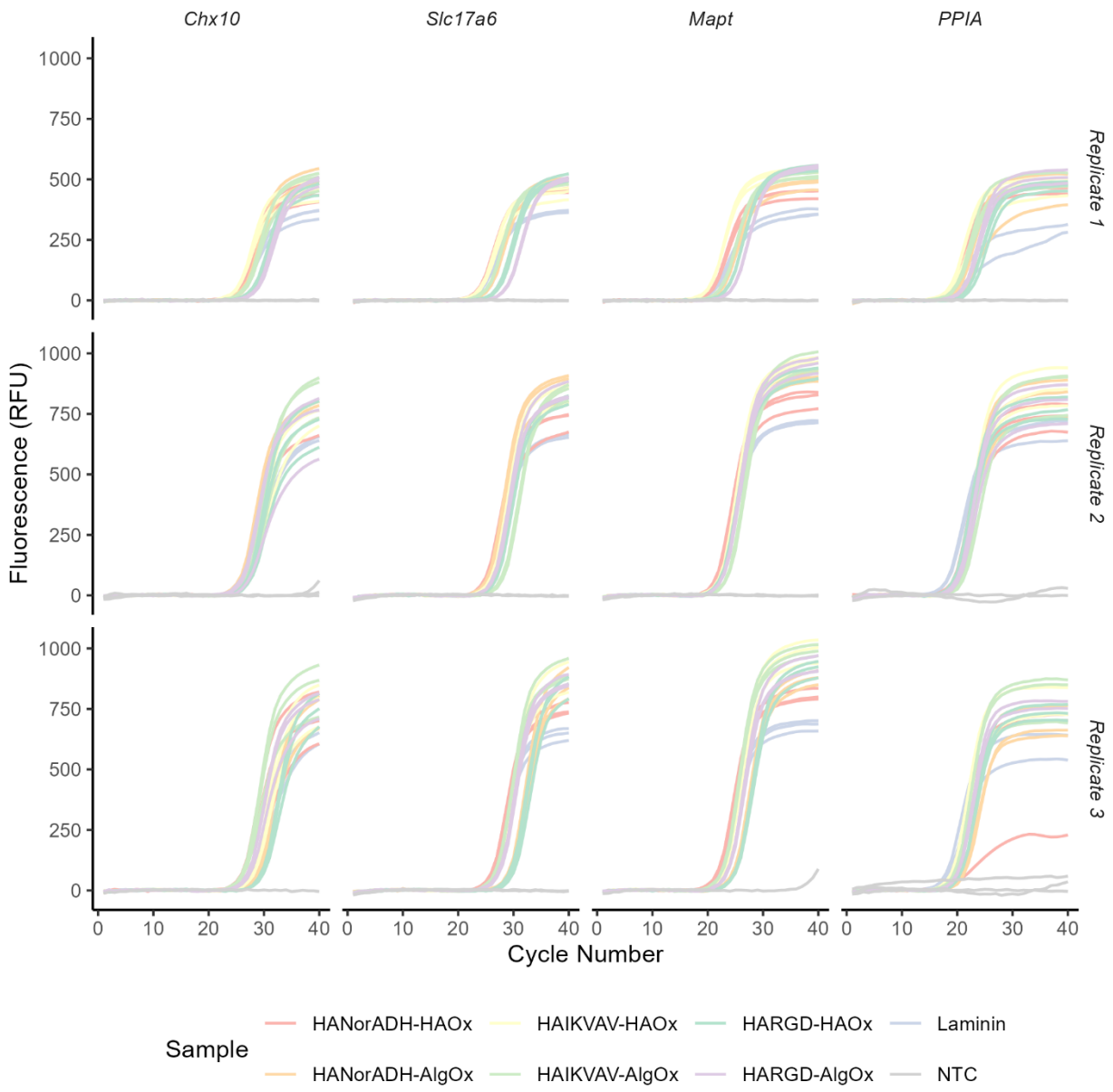

Figure C4. Amplification profiles for qPCR. Real-time amplification curves for target genes (*Chx10*, *Slc17a6*, *Mapt*, *Ppia*) exhibit characteristic sigmoidal profiles across hydrogel conditions and laminin controls. Flat profiles for non-template controls confirm the absence of genomic DNA contamination or primer-dimer artifacts. Columns correspond to a specific gene target, and rows represent independent biological replicates.

Immunostaining

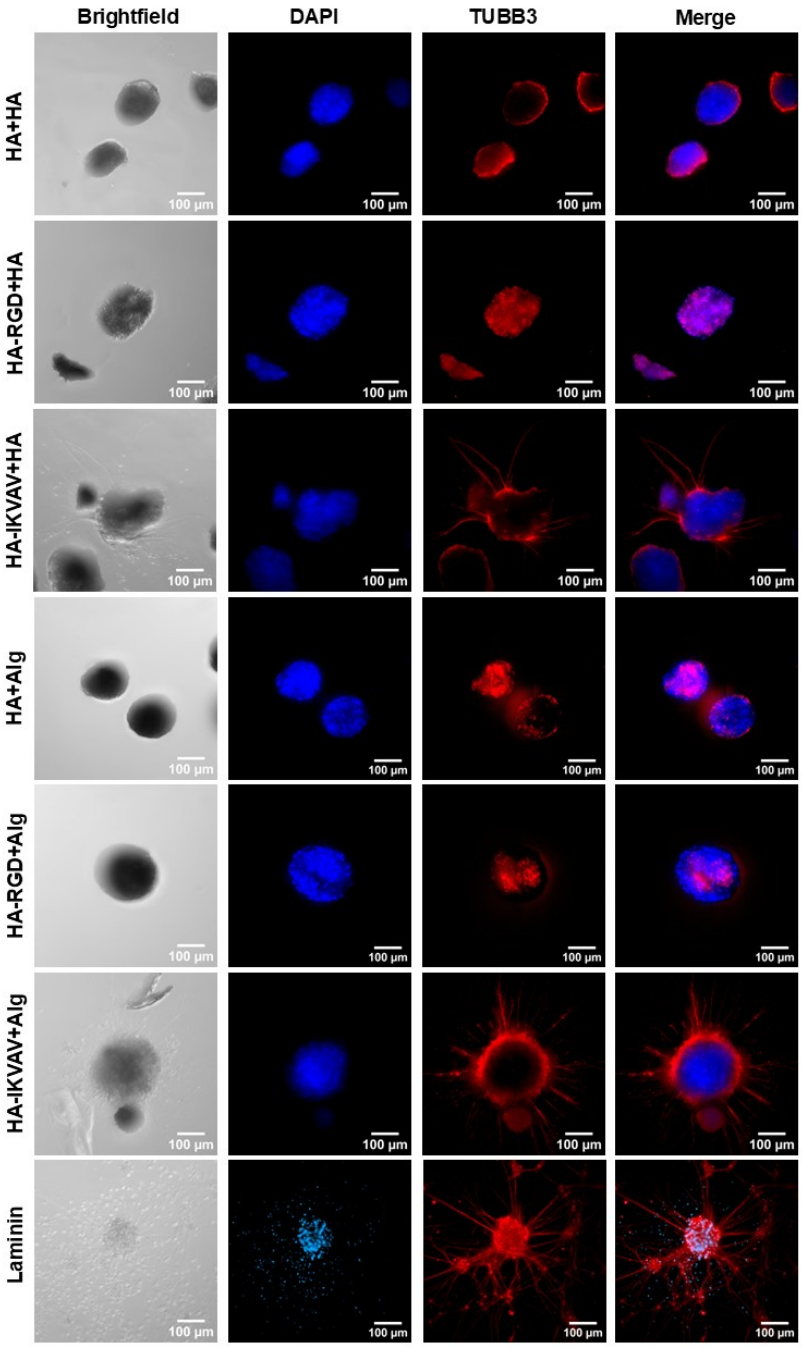

Figure C5. Immunostaining of V2a interneurons. Individual channels for immunostaining of V2a interneurons embedded in hydrogels and cultured on the 2D laminin control. Cells were immunostained for the neuronal microtubule marker βIII-Tubulin (TUBB3, red) and nuclei (DAPI, blue). Scale bars = 100 µm.

REFERENCES CITED

(1) A History of Biomaterials. In *Biomaterials Science*; Academic Press, 2020; pp 21–34. https://doi.org/10.1016/B978-0-12-816137-1.00002-7.

(2) Todros, S.; Todesco, M.; Bagno, A. Biomaterials and Their Biomedical Applications: From Replacement to Regeneration. *Processes* **2021**, *9* (11), 1949. https://doi.org/10.3390/pr9111949.

(3) Lim, K. S.; Mishra, A. Sir Harold Ridley as the Pioneer of Intraocular Lenses: His Inspiration Drawn From World War II Pilots. *Cureus 16* (9), e68722. https://doi.org/10.7759/cureus.68722.

(4) Velema, J.; Kaplan, D. Biopolymer-Based Biomaterials as Scaffolds for Tissue Engineering. In *Tissue Engineering I*; Lee, K., Kaplan, D., Eds.; Springer: Berlin, Heidelberg, 2006; pp 187–238. https://doi.org/10.1007/10_013.

(5) Fournier, E.; Passirani, C.; Montero-Menei, C. N.; Benoit, J. P. Biocompatibility of Implantable Synthetic Polymeric Drug Carriers: Focus on Brain Biocompatibility. *Biomaterials* **2003**, *24* (19), 3311–3331. https://doi.org/10.1016/S0142-9612(03)00161-3.

(6) Reddy, M. S. B.; Ponnamma, D.; Choudhary, R.; Sadasivuni, K. K. A Comparative Review of Natural and Synthetic Biopolymer Composite Scaffolds. *Polymers* **2021**, *13* (7), 1105. https://doi.org/10.3390/polym13071105.

(7) Muir, V. G.; Burdick, J. A. Chemically Modified Biopolymers for the Formation of Biomedical Hydrogels. *Chem. Rev.* **2021**, *121* (18), 10908–10949. https://doi.org/10.1021/acs.chemrev.0c00923.

(8) Ho, T.-C.; Chang, C.-C.; Chan, H.-P.; Chung, T.-W.; Shu, C.-W.; Chuang, K.-P.; Duh, T.-H.; Yang, M.-H.; Tyan, Y.-C. Hydrogels: Properties and Applications in Biomedicine. *Molecules* **2022**, *27* (9), 2902. https://doi.org/10.3390/molecules27092902.

(9) Wichterle, O.; Lím, D. Hydrophilic Gels for Biological Use. *Nature* **1960**, *185* (4706), 117–118. https://doi.org/10.1038/185117a0.

(10) Sockett, K. A.; Jiang, N.-C.; Ungolan, P.; Niu, J.; Grinstaff, M. W. Advancements in Hyaluronic Acid Synthetic Methodologies and Their Translational Relevance. *Chem. Rev.* **2026**, *126* (5), 3224–3286. https://doi.org/10.1021/acs.chemrev.5c00790.

(11) *CDMO Services FAQ – Expert Pharmaceutical Manufacturing Support*. CDMO | Sodium Hyaluronate Producer | Sterile Injectable CDMO | Lifecore. https://www.lifecore.com/faq/ (accessed 2026-06-03).

(12) Cowman, M. K.; Lee, H.-G.; Schwertfeger, K. L.; McCarthy, J. B.; Turley, E. A. The Content and Size of Hyaluronan in Biological Fluids and Tissues. *Front Immunol* **2015**, *6*, 261. https://doi.org/10.3389/fimmu.2015.00261.

(13) NOBLE, P. W.; LIANG, J.; JIANG, D. Hyaluronan as an Immune Regulator in Human Diseases. *Physiol Rev* **2011**, *91* (1), 221–264. https://doi.org/10.1152/physrev.00052.2009.

(14) Lee, B. M.; Park, S. J.; Noh, I.; Kim, C.-H. The Effects of the Molecular Weights of Hyaluronic Acid on the Immune Responses. *Biomater Res* **2021**, *25*, 27. https://doi.org/10.1186/s40824-021-00228-4.

(15) Petit, N.; Chang, Y. J.; Lobianco, F. A.; Hodgkinson, T.; Browne, S. Hyaluronic Acid as a Versatile Building Block for the Development of Biofunctional Hydrogels: In Vitro Models and Preclinical Innovations. *Mater Today Bio* **2025**, *31*, 101596. https://doi.org/10.1016/j.mtbio.2025.101596.

(16) Luo, Z.; Wang, Y.; Xu, Y.; Wang, J.; Yu, Y. Modification and Crosslinking Strategies for Hyaluronic Acid-based Hydrogel Biomaterials. *Smart Med* **2023**, *2* (4), e20230029. https://doi.org/10.1002/SMMD.20230029.

(17) Wang, L. L.; Highley, C. B.; Yeh, Y.-C.; Galarraga, J. H.; Uman, S.; Burdick, J. A. 3D Extrusion Bioprinting of Single- and Double-Network Hydrogels Containing Dynamic Covalent Crosslinks. *J Biomed Mater Res A* **2018**, *106* (4), 865–875. https://doi.org/10.1002/jbm.a.36323.

(18) Mozipo, E. A.; Galindo, A. N.; Khachatourian, J. D.; Harris, C. G.; Dorogin, J.; Spaulding, V. R.; Ford, M. R.; Singhal, M.; Fogg, K. C.; Hettiaratchi, M. H. Statistical Optimization of Hydrazone-Crosslinked Hyaluronic Acid Hydrogels for Protein Delivery. *J. Mater. Chem. B* **2024**, *12* (10), 2523–2536. https://doi.org/10.1039/D3TB01588B.

(19) Khunmanee, S.; Jeong, Y.; Park, H. Crosslinking Method of Hyaluronic-Based Hydrogel for Biomedical Applications. *J Tissue Eng* **2017**, *8*, 2041731417726464. https://doi.org/10.1177/2041731417726464.

(20) Wang, S.; Tavakoli, S.; Parvathaneni, R. P.; Nawale, G. N.; Oommen, O. P.; Hilborn, J.; Varghese, O. P. Dynamic Covalent Crosslinked Hyaluronic Acid Hydrogels and Nanomaterials for Biomedical Applications. *Biomater. Sci.* **2022**, *10* (22), 6399–6412. https://doi.org/10.1039/D2BM01154A.

(21) Wang, X.; Zhu, K.; Liu, W.; Deng, G.; Peng, Y.; Lu, H.; Wang, Q. Chitosan-Hyaluronic Acid Composite Hydrogel with Slow-Release Hydrogen Sulfide and Cerium Oxide for Multifunctional Synergy to Promote Healing of Infected Wounds. *Int J Nanomedicine* **2026**, *21*, 538774. https://doi.org/10.2147/IJN.S538774.

(22) Antoniuk, I.; Plazzotta, B.; Wintgens, V.; Volet, G.; Nielsen, T. T.; Pedersen, J. S.; Amiel, C. Host–Guest Interaction and Structural Ordering in Polymeric Nanoassemblies: Influence of Molecular Design. *International Journal of Pharmaceutics* **2017**, *531* (2), 433–443. https://doi.org/10.1016/j.ijpharm.2017.02.061.

(23) Rodell, C. B.; Kaminski, A.; Burdick, J. A. Rational Design of Network Properties in Guest-Host Assembled and Shear-Thinning Hyaluronic Acid Hydrogels.

Biomacromolecules **2013**, *14* (11), 10.1021/bm401280z. https://doi.org/10.1021/bm401280z.

(24) Nejati, S.; Mongeau, L. Injectable, Pore-Forming, Self-Healing, and Adhesive Hyaluronan Hydrogels for Soft Tissue Engineering Applications. *Sci Rep* **2023**, *13*, 14303. https://doi.org/10.1038/s41598-023-41468-9.

(25) Hinsenkamp, A.; Ézsiás, B.; Pál, É.; Hricisák, L.; Fülöp, Á.; Besztercei, B.; Somkuti, J.; Smeller, L.; Pinke, B.; Kardos, D.; Simon, M.; Lacza, Z.; Hornyák, I. Crosslinked Hyaluronic Acid Gels with Blood-Derived Protein Components for Soft Tissue Regeneration. *Tissue Eng Part A* **2021**, *27* (11–12), 806–820. https://doi.org/10.1089/ten.TEA.2020.0197.

(26) Morani, D. O.; Patil, P. O. Formulation and Evaluation of Hyaluronic Acid and Adipic Acid Dihydrazide Modified Graphene Quantum Dot-Based Nanotherapeutics for Paclitaxel-Targeted Delivery in Breast Cancer. *Futur J Pharm Sci* **2025**, *11* (1), 7. https://doi.org/10.1186/s43094-024-00754-7.

(27) Obata, H.; Yamazaki, Y.; Matsunaga, T.; Sato, T. Synthesis and Evaluation of Hyaluronic Acid Hydrogels Modified with Various Crosslinkers as Biodegradable Polymers. *Journal of Applied Polymer Science* **2017**, *134* (43), 45453. https://doi.org/10.1002/app.45453.

(28) Lu, J.; Gao, Z.; He, W.; Lu, Y. Harnessing the Potential of Hyaluronic Acid Methacrylate (HAMA) Hydrogel for Clinical Applications in Orthopaedic Diseases. *Journal of Orthopaedic Translation* **2025**, *50*, 111–128. https://doi.org/10.1016/j.jot.2024.11.004.

(29) Lagneau, N.; Tournier, P.; Halgand, B.; Loll, F.; Maugars, Y.; Guicheux, J.; Le Visage, C.; Delplace, V. Click and Bioorthogonal Hyaluronic Acid Hydrogels as an Ultra-Tunable Platform for the Investigation of Cell-Material Interactions. *Bioact Mater* **2023**, *24*, 438–449. https://doi.org/10.1016/j.bioactmat.2022.12.022.

(30) Lo Re, A.; Fan, Y.; Pitarresi, G.; Palumbo, F. S.; Biscari, G.; Malkoch, M.; Fiorica, C. Thiol–Yne Crosslinked Nanocomposite Hyaluronic Acid Hydrogels as In Situ-Forming Bone Grafts for the Treatment of Irregular Bone Defects. *Chem. Mater.* **2025**, *37* (23), 9440–9450. https://doi.org/10.1021/acs.chemmater.5c01899.

(31) Chung, T.-W.; Chen, W.-P.; Tai, P.-W.; Lo, H.-Y.; Wu, T.-Y. Roles of Silk Fibroin on Characteristics of Hyaluronic Acid/Silk Fibroin Hydrogels for Tissue Engineering of Nucleus Pulposus. *Materials* **2020**, *13* (12), 2750. https://doi.org/10.3390/ma13122750.

(32) Wang, L.; Li, J.; Zhang, D.; Ma, S.; Zhang, J.; Gao, F.; Guan, F.; Yao, M. Dual-Enzymatically Crosslinked and Injectable Hyaluronic Acid Hydrogels for Potential Application in Tissue Engineering. *RSC Adv.* **2020**, *10* (5), 2870–2876. https://doi.org/10.1039/C9RA09531D.

(33) Raia, N. R.; Partlow, B. P.; McGill, M.; Kimmerling, E. P.; Ghezzi, C. E.; Kaplan, D. L. Enzymatically Crosslinked Silk-Hyaluronic Acid Hydrogels. *Biomaterials* **2017**, *131*, 58–67. https://doi.org/10.1016/j.biomaterials.2017.03.046.

(34) Gultian, K. A.; Gandhi, R.; Kim, T. W. B.; Vega, S. L. Self-Forming Norbornene-Tetrazine Hydrogels with Independently Tunable Properties. *Macromol Biosci* **2023**, *23* (3), e2200425. https://doi.org/10.1002/mabi.202200425.

(35) Oommen, O. P.; Wang, S.; Kisiel, M.; Sloff, M.; Hilborn, J.; Varghese, O. P. Smart Design of Stable Extracellular Matrix Mimetic Hydrogel: Synthesis, Characterization, and In Vitro and In Vivo Evaluation for Tissue Engineering. *Advanced Functional Materials* **2013**, *23* (10), 1273–1280. https://doi.org/10.1002/adfm.201201698.

(36) Shu, X. Z.; Liu, Y.; Luo, Y.; Roberts, M. C.; Prestwich, G. D. Disulfide Cross-Linked Hyaluronan Hydrogels. *Biomacromolecules* **2002**, *3* (6), 1304–1311. https://doi.org/10.1021/bm025603c.

(37) Shi, L.; Wang, F.; Zhu, W.; Xu, Z.; Fuchs, S.; Hilborn, J.; Zhu, L.; Ma, Q.; Wang, Y.; Weng, X.; Ossipov, D. A. Self-Healing Silk Fibroin-Based Hydrogel for Bone Regeneration: Dynamic Metal-Ligand Self-Assembly Approach. *Advanced Functional Materials* **2017**, *27* (37), 1700591. https://doi.org/10.1002/adfm.201700591.

(38) Paidikondala, M.; Wang, S.; Hilborn, J.; Larsson, S.; Varghese, O. P. Impact of Hydrogel Cross-Linking Chemistry on the in Vitro and in Vivo Bioactivity of Recombinant Human Bone Morphogenetic Protein-2. *ACS Appl. Bio Mater.* **2019**, *2* (5), 2006–2012. https://doi.org/10.1021/acsabm.9b00060.

(39) Figueiredo, T.; Cosenza, V.; Ogawa, Y.; Jeacomine, I.; Vallet, A.; Ortega, S.; Michel, R.; Olsson, J. D. M.; Gerfaud, T.; Boiteau, J.-G.; Jing, J.; Harris, C.; Auzély-Velty, R. Boronic Acid and Diol-Containing Polymers: How to Choose the Correct Couple to Form "Strong" Hydrogels at Physiological pH. *Soft Matter* **2020**, *16* (15), 3628–3641. https://doi.org/10.1039/d0sm00178c.

(40) Su, W.-Y.; Chen, K.-H.; Chen, Y.-C.; Lee, Y.-H.; Tseng, C.-L.; Lin, F.-H. An Injectable Oxidated Hyaluronic Acid/Adipic Acid Dihydrazide Hydrogel as a Vitreous Substitute. *Journal of Biomaterials Science -- Polymer Edition* **2011**, *22* (13), 1777–1797. https://doi.org/10.1163/092050610X522729.

(41) Hu, M. H.; Yang, K. C.; Sun, Y. H.; Chen, Y. C.; Yang, S. H.; Lin, F. H. In Situ Forming Oxidised Hyaluronic Acid/Adipic Acid Dihydrazide Hydrogel for Prevention of Epidural Fibrosis after Laminectomy. *Eur Cell Mater* **2017**, *34*, 307–320. https://doi.org/10.22203/eCM.v034a19.

(42) França, C. G.; Villalva, D. G.; Santana, M. H. A. Oxi-HA/ADH Hydrogels: A Novel Approach in Tissue Engineering and Regenerative Medicine. *Polysaccharides* **2021**, *2* (2), 477–496. https://doi.org/10.3390/polysaccharides2020029.

(43) França, C. G.; Sacomani, D. P.; Villalva, D. G.; Nascimento, V. F.; Dávila, J. L.; Santana, M. H. A. Structural Changes and Crosslinking Modulated Functional Properties of Oxi-HA/ADH Hydrogels Useful for Regenerative Purposes. *European Polymer Journal* **2019**, *121*, 109288. https://doi.org/10.1016/j.eurpolymj.2019.109288.

(44) Martínez-Sanz, E.; Ossipov, D. A.; Hilborn, J.; Larsson, S.; Jonsson, K. B.; Varghese, O. P. Bone Reservoir: Injectable Hyaluronic Acid Hydrogel for Minimal Invasive Bone Augmentation. *J Control Release* **2011**, *152* (2), 232–240. https://doi.org/10.1016/j.jconrel.2011.02.003.

(45) Johnson, I. D. DESIGN AND CYTOCOMPATIBILITY OF HYALURONIC ACID HYDROGELS FOR BONE REGENERATION.

(46) França, C. G.; Leme, K. C.; Luzo, Â. C. M.; Hernandez-Montelongo, J.; Santana, M. H. A. Oxidized Hyaluronic Acid/Adipic Acid Dihydrazide Hydrogel as Cell Microcarriers for Tissue Regeneration Applications. *e-Polymers* **2022**, *22* (1), 949–958. https://doi.org/10.1515/epoly-2022-0086.

(47) Su, W.-Y.; Chen, Y.-C.; Lin, F.-H. Injectable Oxidized Hyaluronic Acid/Adipic Acid Dihydrazide Hydrogel for Nucleus Pulposus Regeneration. *Acta Biomater* **2010**, *6* (8), 3044–3055. https://doi.org/10.1016/j.actbio.2010.02.037.

(48) Liao, C.-H.; Chen, C. S.; Chen, Y.-C.; Jiang, N.-E.; Farn, C. J.; Shen, Y.-S.; Hsu, M.-L.; Chang, C.-H. Vancomycin-Loaded Oxidized Hyaluronic Acid and Adipic Acid Dihydrazide Hydrogel: Bio-Compatibility, Drug Release, Antimicrobial Activity, and Biofilm Model. *Journal of Microbiology, Immunology and Infection* **2020**, *53* (4), 525–531. https://doi.org/10.1016/j.jmii.2019.08.008.

(49) Sayed, M.; Pal, H. An Overview from Simple Host–Guest Systems to Progressively Complex Supramolecular Assemblies. *Phys. Chem. Chem. Phys.* **2021**, *23* (46), 26085–26107. https://doi.org/10.1039/d1cp03556h.

(50) Alešković, M.; Šekutor, M. Overcoming Barriers with Non-Covalent Interactions: Supramolecular Recognition of Adamantyl Cucurbit[n]Uril Assemblies for Medical Applications. *RSC Med. Chem.* **2024**, *15* (2), 433–471. https://doi.org/10.1039/d3md00596h.

(51) Davidson, M. D.; Ban, E.; Schoonen, A. C. M.; Lee, M.-H.; D'Este, M.; Shenoy, V. B.; Burdick, J. A. Mechanochemical Adhesion and Plasticity in Multifiber Hydrogel Networks. *Advanced Materials* **2020**, *32* (8), 1905719. https://doi.org/10.1002/adma.201905719.

(52) Gramlich, W. M.; Kim, I. L.; Burdick, J. A. Synthesis and Orthogonal Photopatterning of Hyaluronic Acid Hydrogels with Thiol-Norbornene Chemistry. *Biomaterials* **2013**, *34* (38), 10.1016/j.biomaterials.2013.08.089. https://doi.org/10.1016/j.biomaterials.2013.08.089.

(53) Galindo, A. N.; Chi, A. K.; Liashenko, I.; O'Neill, K. L.; Asnes, C. L.; Sharma, R.; Khachatourian, J. D.; Hajarizadeh, A.; Dalton, P. D.; Hettiaratchi, M. H. Hyaluronic Acid-Coated Melt Electrowritten Scaffolds Promote Myoblast Attachment, Alignment, and Differentiation. *Cel. Mol. Bioeng.* **2025**. https://doi.org/10.1007/s12195-025-00865-y.

(54) Kruczkowska, W.; Gałęziewska, J.; Grabowska, K. H.; Gromek, P.; Czajkowska, K.; Rybicki, M.; Kciuk, M.; Kłosiński, K. K. From Molecules to Mind: The Critical Role of Chitosan, Collagen, Alginate, and Other Biopolymers in Neuroprotection and Neurodegeneration. *Molecules* **2025**, *30* (5), 1017. https://doi.org/10.3390/molecules30051017.

(55) Gentry, J. L.; Caliari, S. R. Norbornene Homopolymerization Limits Cell Spreading in Thiol-Ene Photoclick Hydrogels. *Adv Healthc Mater* **2025**, *14* (32), e02172. https://doi.org/10.1002/adhm.202502172.

(56) Gomez, C. G.; Rinaudo, M.; Villar, M. A. Oxidation of Sodium Alginate and Characterization of the Oxidized Derivatives. *Carbohydrate Polymers* **2007**, *67* (3), 296–304. https://doi.org/10.1016/j.carbpol.2006.05.025.

(57) Liu, X.; Peng, W.; Wang, Y.; Zhu, M.; Sun, T.; Peng, Q.; Zeng, Y.; Feng, B.; Lu, X.; Weng, J.; Wang, J. Synthesis of an RGD-Grafted Oxidized Sodium Alginate–N-Succinyl Chitosan Hydrogel and an in Vitro Study of Endothelial and Osteogenic Differentiation. *J. Mater. Chem. B* **2013**, *1* (35), 4484–4492. https://doi.org/10.1039/C3TB20552E.

(58) Dorogin, J.; Townsend, J. M.; Hettiaratchi, M. H. Biomaterials for Protein Delivery for Complex Tissue Healing Responses. *Biomater. Sci.* **2021**, *9* (7), 2339–2361. https://doi.org/10.1039/D0BM01804J.

(59) James, A. W.; LaChaud, G.; Shen, J.; Asatrian, G.; Nguyen, V.; Zhang, X.; Ting, K.; Soo, C. A Review of the Clinical Side Effects of Bone Morphogenetic Protein-2. *Tissue Eng Part B Rev* **2016**, *22* (4), 284–297. https://doi.org/10.1089/ten.teb.2015.0357.

(60) Bartnikowski, M.; Wellard, R. M.; Woodruff, M.; Klein, T. Tailoring Hydrogel Viscoelasticity with Physical and Chemical Crosslinking. *Polymers* **2015**, *7* (12), 2650–2669. https://doi.org/10.3390/polym7121539.

(61) Vermonden, T.; Censi, R.; Hennink, W. E. Hydrogels for Protein Delivery. *Chem. Rev.* **2012**, *112* (5), 2853–2888. https://doi.org/10.1021/cr200157d.

(62) Naahidi, S.; Jafari, M.; Logan, M.; Wang, Y.; Yuan, Y.; Bae, H.; Dixon, B.; Chen, P. Biocompatibility of Hydrogel-Based Scaffolds for Tissue Engineering Applications. *Biotechnol Adv* **2017**, *35* (5), 530–544. https://doi.org/10.1016/j.biotechadv.2017.05.006.

(63) Darnell, M.; Mooney, D. J. Leveraging Advances in Biology to Design Biomaterials. *Nature Mater* **2017**, *16* (12), 1178–1185. https://doi.org/10.1038/nmat4991.

(64) Telford, J. A Brief Introduction to Design of Experiments. *TELFORD JOhns hOpKins ApL TEchnicAL DigEsT* **2007**, *27*.

(65) Lam, J.; Carmichael, S. T.; Lowry, W. E.; Segura, T. Hydrogel Design of Experiments Methodology to Optimize Hydrogel for iPSC-NPC Culture. *Advanced Healthcare Materials* **2015**, *4* (4), 534–539. https://doi.org/10.1002/adhm.201400410.

(66) Ahmed, A. Sh.; Mandal, U. K.; Taher, M.; Susanti, D.; Jaffri, J. Md. PVA-PEG Physically Cross-Linked Hydrogel Film as a Wound Dressing: Experimental Design and Optimization. *Pharmaceutical Development & Technology* **2018**, *23* (8), 751–760. https://doi.org/10.1080/10837450.2017.1295067.

(67) Nih, L. R.; Moshayedi, P.; Llorente, I. L.; Berg, A. R.; Cinkornpumin, J.; Lowry, W. E.; Segura, T.; Carmichael, S. T. Engineered HA Hydrogel for Stem Cell Transplantation in the Brain: Biocompatibility Data Using a Design of Experiment Approach. *Data Brief* **2016**, *10*, 202–209. https://doi.org/10.1016/j.dib.2016.11.069.

(68) Cadena, I. A.; Buchanan, M. R.; Harris, C. G.; Jenne, M. A.; Rochefort, W. E.; Nelson, D.; Fogg, K. C. Engineering High Throughput Screening Platforms of Cervical Cancer. *J Biomedical Materials Res* **2023**, *111* (6), 747–764. https://doi.org/10.1002/jbm.a.37522.

(69) Arafa, M. G.; Ayoub, B. M. DOE Optimization of Nano-Based Carrier of Pregabalin as Hydrogel: New Therapeutic & Chemometric Approaches for Controlled Drug Delivery Systems. *Sci Rep* **2017**, *7* (1), 41503. https://doi.org/10.1038/srep41503.

(70) Nastruzzi, A.; Pitingolo, G.; Luca, G.; Nastruzzi, C. DoE Analysis of Approaches for Hydrogel Microbeads' Preparation by Millifluidic Methods. *Micromachines (Basel)* **2020**, *11* (11), 1007. https://doi.org/10.3390/mi11111007.

(71) Pakulska, M. M.; Vulic, K.; Tam, R. Y.; Shoichet, M. S. Hybrid Crosslinked Methylcellulose Hydrogel: A Predictable and Tunable Platform for Local Drug Delivery. *Advanced Materials* **2015**, *27* (34), 5002–5008. https://doi.org/10.1002/adma.201502767.

(72) Yousefi, A.-M.; Liu, J.; Sheppard, R.; Koo, S.; Silverstein, J.; Zhang, J.; James, P. F. I-Optimal Design of Hierarchical 3D Scaffolds Produced by Combining Additive Manufacturing and Thermally Induced Phase Separation. *ACS Appl Bio Mater* **2019**, *2* (2), 685–696. https://doi.org/10.1021/acsabm.8b00534.

(73) Asadi-Eydivand, M.; Solati-Hashjin, M.; Fathi, A.; Padashi, M.; Abu Osman, N. A. Optimal Design of a 3D-Printed Scaffold Using Intelligent Evolutionary Algorithms. *Applied Soft Computing* **2016**, *39*, 36–47. https://doi.org/10.1016/j.asoc.2015.11.011.

(74) Kuterbekov, M.; Machillot, P.; Baillet, F.; Jonas, A. M.; Glinel, K.; Picart, C. Design of Experiments to Assess the Effect of Culture Parameters on the Osteogenic Differentiation of Human Adipose Stromal Cells. *Stem Cell Research & Therapy* **2019**, *10* (1), 256. https://doi.org/10.1186/s13287-019-1333-7.

(75) Graça, M. F. P.; Miguel, S. P.; Cabral, C. S. D.; Correia, I. J. Hyaluronic Acid-Based Wound Dressings: A Review. *Carbohydr Polym* **2020**, *241*, 116364. https://doi.org/10.1016/j.carbpol.2020.116364.

(76) Necas, J.; Bartosikova, L.; Brauner, P.; Kolar, J. Hyaluronic Acid (Hyaluronan): A Review. *Veterinární medicína* **2008**, *53* (8), 397–411. https://doi.org/10.17221/1930-VETMED.

(77) Dovedytis, M.; Liu, Z. J.; Bartlett, S. Hyaluronic Acid and Its Biomedical Applications: A Review. *Engineered Regeneration* **2020**, *1*, 102–113. https://doi.org/10.1016/j.engreg.2020.10.001.

(78) Cowman, M. K.; Lee, H.-G.; Schwertfeger, K. L.; McCarthy, J. B.; Turley, E. A. The Content and Size of Hyaluronan in Biological Fluids and Tissues. *Frontiers in Immunology* **2015**, *6*.

(79) Tavianatou, A. G.; Caon, I.; Franchi, M.; Piperigkou, Z.; Galesso, D.; Karamanos, N. K. Hyaluronan: Molecular Size-Dependent Signaling and Biological Functions in Inflammation and Cancer. *The FEBS Journal* **2019**, *286* (15), 2883–2908. https://doi.org/10.1111/febs.14777.

(80) Yang, J.; Hsu, C.-C.; Cao, T.-T.; Ye, H.; Chen, J.; Li, Y.-Q. A Hyaluronic Acid Granular Hydrogel Nerve Guidance Conduit Promotes Regeneration and Functional Recovery of Injured Sciatic Nerves in Rats. *Neural Regeneration Research* **2023**, *18* (3), 657. https://doi.org/10.4103/1673-5374.350212.

(81) Halperin-Sternfeld, M.; Pokhojaev, A.; Ghosh, M.; Rachmiel, D.; Kannan, R.; Grinberg, I.; Asher, M.; Aviv, M.; Ma, P. X.; Binderman, I.; Sarig, R.; Adler-Abramovich, L. Immunomodulatory Fibrous Hyaluronic Acid-Fmoc-Diphenylalanine-Based Hydrogel Induces Bone Regeneration. *Journal of Clinical Periodontology* **2023**, *50* (2), 200–219. https://doi.org/10.1111/jcpe.13725.

(82) Yoon, S. J.; Fang, Y. H.; Lim, C. H.; Kim, B. S.; Son, H. S.; Park, Y.; Sun, K. Regeneration of Ischemic Heart Using Hyaluronic Acid-Based Injectable Hydrogel. *Journal of Biomedical Materials Research Part B: Applied Biomaterials* **2009**, *91B* (1), 163–171. https://doi.org/10.1002/jbm.b.31386.

(83) Engler, A. J.; Sen, S.; Sweeney, H. L.; Discher, D. E. Matrix Elasticity Directs Stem Cell Lineage Specification. *Cell* **2006**, *126* (4), 677–689. https://doi.org/10.1016/j.cell.2006.06.044.

(84) Young, D. A.; Choi, Y. S.; Engler, A. J.; Christman, K. L. Stimulation of Adipogenesis of Adult Adipose-Derived Stem Cells Using Substrates That Mimic the Stiffness of Adipose Tissue. *Biomaterials* **2013**, *34* (34), 8581–8588. https://doi.org/10.1016/j.biomaterials.2013.07.103.

(85) Xue, X.; Liang, K.; Huang, W.; Yang, H.; Jiang, L.; Jiang, Q.; Jiang, T.; Lin, B.; Chen, Y.; Jiang, B.; Komarneni, S. Molecular Engineering of Injectable, Fast Self-Repairing Hydrogels with Tunable Gelation Time: Characterization by Diffusing Wave Spectroscopy. *Macromolecules* **2022**, *55* (15), 6474–6486. https://doi.org/10.1021/acs.macromol.2c00899.

(86) Delplace, V.; Nickerson, P. E. B.; Ortin-Martinez, A.; Baker, A. E. G.; Wallace, V. A.; Shoichet, M. S. Nonswelling, Ultralow Content Inverse Electron-Demand Diels–Alder Hyaluronan Hydrogels with Tunable Gelation Time: Synthesis and In Vitro Evaluation. *Advanced Functional Materials* **2020**, *30* (14), 1903978. https://doi.org/10.1002/adfm.201903978.

(87) Park, H.; Guo, X.; Temenoff, J. S.; Tabata, Y.; Caplan, A. I.; Kasper, F. K.; Mikos, A. G. Effect of Swelling Ratio of Injectable Hydrogel Composites on Chondrogenic Differentiation of Encapsulated Rabbit Marrow Mesenchymal Stem Cells In Vitro. *Biomacromolecules* **2009**, *10* (3), 541–546. https://doi.org/10.1021/bm801197m.

(88) Mubarok, W.; Elvitigala, K. C. M. L.; Nakahata, M.; Kojima, M.; Sakai, S. Modulation of Cell-Cycle Progression by Hydrogen Peroxide-Mediated Cross-Linking and Degradation of Cell-Adhesive Hydrogels. *Cells* **2022**, *11* (5), 881. https://doi.org/10.3390/cells11050881.

(89) Wang, C.; Tong, X.; Jiang, X.; Yang, F. Effect of Matrix Metalloproteinase-Mediated Matrix Degradation on Glioblastoma Cell Behavior in 3D PEG-Based Hydrogels. *J Biomed Mater Res A* **2017**, *105* (3), 770–778. https://doi.org/10.1002/jbm.a.35947.

(90) Vítková, L.; Musilová, L.; Achbergerová, E.; Kolařík, R.; Mrlík, M.; Korpasová, K.; Mahelová, L.; Capáková, Z.; Mráček, A. Formulation of Magneto-Responsive Hydrogels from Dually Cross-Linked Polysaccharides: Synthesis, Tuning and Evaluation of Rheological Properties. *Int J Mol Sci* **2022**, *23* (17), 9633. https://doi.org/10.3390/ijms23179633.

(91) Jia, X.; Colombo, G.; Padera, R.; Langer, R.; Kohane, D. S. Prolongation of Sciatic Nerve Blockade by in Situ Cross-Linked Hyaluronic Acid. *Biomaterials* **2004**, *25* (19), 4797–4804. https://doi.org/10.1016/j.biomaterials.2003.12.012.

(92) Yeo, Y.; Highley, C. B.; Bellas, E.; Ito, T.; Marini, R.; Langer, R.; Kohane, D. S. In Situ Cross-Linkable Hyaluronic Acid Hydrogels Prevent Post-Operative Abdominal Adhesions in a Rabbit Model. *Biomaterials* **2006**, *27* (27), 4698–4705. https://doi.org/10.1016/j.biomaterials.2006.04.043.

(93) de Paiva Narciso, N.; Navarro, R. S.; Gilchrist, A. E.; Trigo, M. L. M.; Aviles Rodriguez, G.; Heilshorn, S. C. Design Parameters for Injectable Biopolymeric Hydrogels with Dynamic Covalent Chemistry Crosslinks. *Advanced Healthcare Materials* **2023**, *12* (27), 2301265. https://doi.org/10.1002/adhm.202301265.

(94) Department of Orthopaedics, National Taiwan University College of Medicine and National Taiwan University Hospital, No.1, Sec. 1, JenAi Road, Taipei 100, Taiwan; Hu, M.; Yang, K.; Sun, Y.; Chen, Y.; Yang, S.; Lin, F. In Situ Forming Oxidised Hyaluronic Acid/Adipic Acid Dihydrazide Hydrogel for Prevention of Epidural Fibrosis after Laminectomy. *eCM* **2017**, 307–320. https://doi.org/10.22203/eCM.v034a19.

(95) Dorogin, J.; Hochstatter, H. B.; Shepherd, S. O.; Svendsen, J. E.; Benz, M. A.; Powers, A. C.; Fear, K. M.; Townsend, J. M.; Prell, J. S.; Hosseinzadeh, P.; Hettiaratchi, M. H. Moderate-Affinity Affibodies Modulate the Delivery and Bioactivity of Bone Morphogenetic Protein-2. *Advanced Healthcare Materials n/a* (n/a), 2300793. https://doi.org/10.1002/adhm.202300793.

(96) Davidson, M. D.; Ban, E.; Schoonen, A. C. M.; Lee, M.-H.; D'Este, M.; Shenoy, V. B.; Burdick, J. A. Mechanochemical Adhesion and Plasticity in Multifiber Hydrogel Networks. *Advanced Materials* **2020**, *32* (8), 1905719. https://doi.org/10.1002/adma.201905719.

(97) Zhao, H.; Heindel, N. D. Determination of Degree of Substitution of Formyl Groups in Polyaldehyde Dextran by the Hydroxylamine Hydrochloride Method. *Pharm Res* **1991**, *8* (3), 400–402. https://doi.org/10.1023/A:1015866104055.

(98) Wang, Q.; Wang, Z.; Zhang, D.; Gu, J.; Ma, Y.; Zhang, Y.; Chen, J. Circular Patterns of Dynamic Covalent Hydrogels with Gradient Stiffness for Screening of the Stem Cell Microenvironment. *ACS Appl. Mater. Interfaces* **2022**, *14* (42), 47461–47471. https://doi.org/10.1021/acsami.2c14924.

(99) *Injectable Hydrogels: From Laboratory to Industrialization - PMC*. https://www.ncbi.nlm.nih.gov/pmc/articles/PMC7926321/ (accessed 2023-07-03).

(100) Raia, N. R.; Partlow, B. P.; McGill, M.; Kimmerling, E. P.; Ghezzi, C. E.; Kaplan, D. L. Enzymatically Crosslinked Silk-Hyaluronic Acid Hydrogels. *Biomaterials* **2017**, *131*, 58–67. https://doi.org/10.1016/j.biomaterials.2017.03.046.

(101) Rosaming, P.; Jirayupapong, J.; Thamnium, S.; Win, Y. Y.; Limprasutr, V.; Rodsiri, R.; Pavasant, P.; Luckanagul, J. A. Interpenetrating Low-Molecular Weight Hyaluronic Acid in Hyaluronic Acid-Based In Situ Hydrogel Scaffold for Periodontal and Oral Wound Applications. *Polymers* **2022**, *14* (22), 4986. https://doi.org/10.3390/polym14224986.

(102) Muir, V. G.; Weintraub, S.; Dhand, A. P.; Fallahi, H.; Han, L.; Burdick, J. A. Influence of Microgel and Interstitial Matrix Compositions on Granular Hydrogel Composite Properties. *Advanced Science* **2023**, *10* (10), 2206117. https://doi.org/10.1002/advs.202206117.

(103) Ritger, P. L.; Peppas, N. A. A Simple Equation for Description of Solute Release I. Fickian and Non-Fickian Release from Non-Swellable Devices in the Form of Slabs, Spheres, Cylinders or Discs. *Journal of Controlled Release* **1987**, *5* (1), 23–36. https://doi.org/10.1016/0168-3659(87)90034-4.

(104) Pakulska, M. M.; Vulic, K.; Shoichet, M. S. Affinity-Based Release of Chondroitinase ABC from a Modified Methylcellulose Hydrogel. *J Control Release* **2013**, *171* (1), 11–16. https://doi.org/10.1016/j.jconrel.2013.06.029.

(105) Bruns, R. E.; Scarminio, I. S.; Neto, B. de B. *Statistical Design - Chemometrics*, 1st edition.; Elsevier Science: Amsterdam ; Boston, 2006.

(106) *MODDE® 12 User Guide*, June 21, 2017.; Sartorius Stedim Data Analytics AB.

(107) França, C. G.; Sacomani, D. P.; Villalva, D. G.; Nascimento, V. F.; Dávila, J. L.; Santana, M. H. A. Structural Changes and Crosslinking Modulated Functional Properties of Oxi-HA/ADH Hydrogels Useful for Regenerative Purposes. *European Polymer Journal* **2019**, *121*, 109288. https://doi.org/10.1016/j.eurpolymj.2019.109288.

(108) Su, W.-Y.; Chen, K.-H.; Chen, Y.-C.; Lee, Y.-H.; Tseng, C.-L.; Lin, F.-H. An Injectable Oxidated Hyaluronic Acid/Adipic Acid Dihydrazide Hydrogel as a Vitreous Substitute. *Journal of Biomaterials Science -- Polymer Edition* **2011**, *22* (13), 1777–1797. https://doi.org/10.1163/092050610X522729.

(109) Uman, S.; Wang, L. L.; Thorn, S. L.; Liu, Z.; Duncan, J. S.; Sinusas, A. J.; Burdick, J. A. Imaging of Injectable Hydrogels Delivered into Myocardium with SPECT/CT. *Adv Healthc Mater* **2020**, *9* (14), e2000294. https://doi.org/10.1002/adhm.202000294.

(110) Wang, Y.; Chen, Y.; Zheng, J.; Liu, L.; Zhang, Q. Three-Dimensional Printing Self-Healing Dynamic/Photocrosslinking Gelatin-Hyaluronic Acid Double-Network Hydrogel for Tissue Engineering. *ACS Omega* **2022**, *7* (14), 12076–12088. https://doi.org/10.1021/acsomega.2c00335.

(111) Kadi, S.; Cui, D.; Bayma, E.; Boudou, T.; Nicolas, C.; Glinel, K.; Picart, C.; Auzély-Velty, R. Alkylamino Hydrazide Derivatives of Hyaluronic Acid: Synthesis, Characterization in Semidilute Aqueous Solutions, and Assembly into Thin Multilayer Films. *Biomacromolecules* **2009**, *10* (10), 2875–2884. https://doi.org/10.1021/bm900701m.

(112) Lagneau, N.; Tournier, P.; Halgand, B.; Loll, F.; Maugars, Y.; Guicheux, J.; Le Visage, C.; Delplace, V. Click and Bioorthogonal Hyaluronic Acid Hydrogels as an Ultra-Tunable Platform for the Investigation of Cell-Material Interactions. *Bioactive Materials* **2023**, *24*, 438–449. https://doi.org/10.1016/j.bioactmat.2022.12.022.

(113) Richbourg, N. R.; Wancura, M.; Gilchrist, A. E.; Toubbeh, S.; Harley, B. A. C.; Cosgriff-Hernandez, E.; Peppas, N. A. Precise Control of Synthetic Hydrogel Network Structure via Linear, Independent Synthesis-Swelling Relationships. *Science Advances* **2021**, *7* (7), eabe3245. https://doi.org/10.1126/sciadv.abe3245.

(114) Alonso, J. M.; Andrade Del Olmo, J.; Perez Gonzalez, R.; Saez-Martinez, V. Injectable Hydrogels: From Laboratory to Industrialization. *Polymers (Basel)* **2021**, *13* (4), 650. https://doi.org/10.3390/polym13040650.

(115) Löfblom, J.; Feldwisch, J.; Tolmachev, V.; Carlsson, J.; Ståhl, S.; Frejd, F. Y. Affibody Molecules: Engineered Proteins for Therapeutic, Diagnostic and Biotechnological Applications. *FEBS Lett* **2010**, *584* (12), 2670–2680. https://doi.org/10.1016/j.febslet.2010.04.014.

(116) Ståhl, S.; Gräslund, T.; Eriksson Karlström, A.; Frejd, F. Y.; Nygren, P.-Å.; Löfblom, J. Affibody Molecules in Biotechnological and Medical Applications. *Trends in Biotechnology* **2017**, *35* (8), 691–712. https://doi.org/10.1016/j.tibtech.2017.04.007.

(117) Teal, C. J.; Hettiaratchi, M. H.; Ho, M. T.; Ortin-Martinez, A.; Ganesh, A. N.; Pickering, A. J.; Golinski, A. W.; Hackel, B. J.; Wallace, V. A.; Shoichet, M. S. Directed Evolution Enables Simultaneous Controlled Release of Multiple Therapeutic Proteins from Biopolymer-Based Hydrogels. *Advanced Materials* **2022**, *34* (34), 2202612. https://doi.org/10.1002/adma.202202612.

(118) Bostock, C.; Teal, C. J.; Dang, M.; Golinski, A. W.; Hackel, B. J.; Shoichet, M. S. Affibody-Mediated Controlled Release of Fibroblast Growth Factor 2. *Journal of Controlled Release* **2022**, *350*, 815–828. https://doi.org/10.1016/j.jconrel.2022.09.004.

(119) Hettiaratchi, M. H.; Krishnan, L.; Rouse, T.; Chou, C.; McDevitt, T. C.; Guldberg, R. E. Heparin-Mediated Delivery of Bone Morphogenetic Protein-2 Improves Spatial Localization of Bone Regeneration. *Sci Adv* **2020**, *6* (1), eaay1240. https://doi.org/10.1126/sciadv.aay1240.

(120) Dorogin, J.; Hochstatter, H. B.; Shepherd, S. O.; Svendsen, J. E.; Benz, M. A.; Powers, A. C.; Fear, K. M.; Townsend, J. M.; Prell, J. S.; Hosseinzadeh, P.; Hettiaratchi, M. H. Moderate-Affinity Affibodies Modulate the Delivery and Bioactivity of Bone Morphogenetic Protein-2. *Advanced Healthcare Materials* **2023**, *12* (26), 2300793. https://doi.org/10.1002/adhm.202300793.

(121) Eugenis, I.; Wu, D.; Rando, T. A. Cells, Scaffolds, and Bioactive Factors: Engineering Strategies for Improving Regeneration Following Volumetric Muscle Loss. *Biomaterials* **2021**, *278*, 121173. https://doi.org/10.1016/j.biomaterials.2021.121173.

(122) Kim, J. T.; Kasukonis, B.; Brown, L.; Washington, T.; Wolchok, J. C. Recovery from Volumetric Muscle Loss Injury: A Comparison Between Young and Aged Rats. *Exp Gerontol* **2016**, *83*, 37–46. https://doi.org/10.1016/j.exger.2016.07.008.

(123) Volpi, M.; Paradiso, A.; Costantini, M.; Święszkowski, W. Hydrogel-Based Fiber Biofabrication Techniques for Skeletal Muscle Tissue Engineering. *ACS Biomater Sci Eng* **2022**, *8* (2), 379–405. https://doi.org/10.1021/acsbiomaterials.1c01145.

(124) Gilbert-Honick, J.; Grayson, W. Vascularized and Innervated Skeletal Muscle Tissue Engineering. *Adv Healthc Mater* **2020**, *9* (1), e1900626. https://doi.org/10.1002/adhm.201900626.

(125) Purslow, P. P. The Structure and Role of Intramuscular Connective Tissue in Muscle Function. *Front. Physiol.* **2020**, *11*. https://doi.org/10.3389/fphys.2020.00495.

(126) Zhang, W.; Liu, Y.; Zhang, H. Extracellular Matrix: An Important Regulator of Cell Functions and Skeletal Muscle Development. *Cell & Bioscience* **2021**, *11* (1), 65. https://doi.org/10.1186/s13578-021-00579-4.

(127) Ward, C. L.; Ji, L.; Corona, B. T. An Autologous Muscle Tissue Expansion Approach for the Treatment of Volumetric Muscle Loss. *Biores Open Access* **2015**, *4* (1), 198–208. https://doi.org/10.1089/biores.2015.0009.

(128) Greising, S. M.; Warren, G. L.; Southern, W. M.; Nichenko, A. S.; Qualls, A. E.; Corona, B. T.; Call, J. A. Early Rehabilitation for Volumetric Muscle Loss Injury Augments Endogenous Regenerative Aspects of Muscle Strength and Oxidative Capacity. *BMC Musculoskelet Disord* **2018**, *19*, 173. https://doi.org/10.1186/s12891-018-2095-6.

(129) Mintz, E. L.; Passipieri, J. A.; Franklin, I. R.; Toscano, V. M.; Afferton, E. C.; Sharma, P. R.; Christ, G. J. Long-Term Evaluation of Functional Outcomes Following Rat Volumetric Muscle Loss Injury and Repair. *Tissue Eng Part A* **2020**, *26* (3–4), 140–156. https://doi.org/10.1089/ten.TEA.2019.0126.

(130) Dolan, C. P.; Motherwell, J. M.; Franco, S. R.; Janakiram, N. B.; Valerio, M. S.; Goldman, S. M.; Dearth, C. L. Evaluating the Potential Use of Functional Fibrosis to Facilitate Improved Outcomes Following Volumetric Muscle Loss Injury. *Acta Biomaterialia* **2022**, *140*, 379–388. https://doi.org/10.1016/j.actbio.2021.11.032.

(131) Carnes, M. E.; Pins, G. D. Skeletal Muscle Tissue Engineering: Biomaterials-Based Strategies for the Treatment of Volumetric Muscle Loss. *Bioengineering* **2020**, *7* (3), 85. https://doi.org/10.3390/bioengineering7030085.

(132) Hu, C.; Chiang, G.; Chan, A. H.-P.; Alcazar, C.; Nakayama, K. H.; Quarta, M.; Rando, T. A.; Huang, N. F. A Mouse Model of Volumetric Muscle Loss and Therapeutic Scaffold Implantation. *Nat Protoc* **2024**. https://doi.org/10.1038/s41596-024-01059-y.

(133) Niknezhad, S. V.; Mehrali, M.; Khorasgani, F. R.; Heidari, R.; Kadumudi, F. B.; Golafshan, N.; Castilho, M.; Pennisi, C. P.; Hasany, M.; Jahanshahi, M.; Mehrali, M.; Ghasemi, Y.; Azarpira, N.; Andresen, T. L.; Dolatshahi-Pirouz, A. Enhancing Volumetric Muscle Loss (VML) Recovery in a Rat Model Using Super Durable Hydrogels Derived from Bacteria. *Bioactive Materials* **2024**, *38*, 540–558. https://doi.org/10.1016/j.bioactmat.2024.04.006.

(134) Browe, D.; Freeman, J. Optimizing C2C12 Myoblast Differentiation Using Polycaprolactone-Polypyrrole Copolymer Scaffolds. *J Biomed Mater Res A* **2019**, *107* (1), 220–231. https://doi.org/10.1002/jbm.a.36556.

(135) Carnes, M. E.; Pins, G. D. Skeletal Muscle Tissue Engineering: Biomaterials-Based Strategies for the Treatment of Volumetric Muscle Loss. *Bioengineering (Basel)* **2020**, *7* (3), 85. https://doi.org/10.3390/bioengineering7030085.

(136) Zhu, C.; Sklyar, K.; Karvar, M.; Endo, Y.; Sinha, I. Scaffold Tissue Engineering Strategies for Volumetric Muscle Loss. *par* **2023**, *10* (0), N/A-N/A. https://doi.org/10.20517/2347-9264.2022.89.

(137) Bian, W.; Juhas, M.; Pfeiler, T. W.; Bursac, N. Local Tissue Geometry Determines Contractile Force Generation of Engineered Muscle Networks. *Tissue Eng Part A* **2012**, *18* (9–10), 957–967. https://doi.org/10.1089/ten.TEA.2011.0313.

(138) Narayanan, N.; Jia, Z.; Kim, K. H.; Kuang, L.; Lengemann, P.; Shafer, G.; Bernal-Crespo, V.; Kuang, S.; Deng, M. Biomimetic Glycosaminoglycan-Based Scaffolds Improve Skeletal Muscle Regeneration in a Murine Volumetric Muscle Loss Model. *Bioactive Materials* **2021**, *6* (4), 1201–1213. https://doi.org/10.1016/j.bioactmat.2020.10.012.

(139) Silva Garcia, J. M.; Panitch, A.; Calve, S. Functionalization of Hyaluronic Acid Hydrogels with ECM-Derived Peptides to Control Myoblast Behavior. *Acta Biomater* **2019**, *84*, 169–179. https://doi.org/10.1016/j.actbio.2018.11.030.

(140) Hwangbo, H.; Lee, H.; Jin, E.-J.; Lee, J.; Jo, Y.; Ryu, D.; Kim, G. Bio-Printing of Aligned GelMa-Based Cell-Laden Structure for Muscle Tissue Regeneration. *Bioactive Materials* **2022**, *8*, 57–70. https://doi.org/10.1016/j.bioactmat.2021.06.031.

(141) Wang, L.; Wu, Y.; Guo, B.; Ma, P. X. Nanofiber Yarn/Hydrogel Core–Shell Scaffolds Mimicking Native Skeletal Muscle Tissue for Guiding 3D Myoblast Alignment, Elongation, and Differentiation. *ACS Nano* **2015**, *9* (9), 9167–9179. https://doi.org/10.1021/acsnano.5b03644.

(142) Abdalkader, R.; Konishi, S.; Fujita, T. The Development of Biomimetic Aligned Skeletal Muscles in a Fully 3D Printed Microfluidic Device. *Biomimetics (Basel)* **2021**, *7* (1), 2. https://doi.org/10.3390/biomimetics7010002.

(143) Hu, T.; Shi, M.; Zhao, X.; Liang, Y.; Bi, L.; Zhang, Z.; Liu, S.; Chen, B.; Duan, X.; Guo, B. Biomimetic 3D Aligned Conductive Tubular Cryogel Scaffolds with Mechanical Anisotropy for 3D Cell Alignment, Differentiation and *in Vivo* Skeletal Muscle Regeneration. *Chemical Engineering Journal* **2022**, *428*, 131017. https://doi.org/10.1016/j.cej.2021.131017.

(144) Cheng, Y.-W.; Shiwarski, D. J.; Ball, R. L.; Whitehead, K. A.; Feinberg, A. W. Engineering Aligned Skeletal Muscle Tissue Using Decellularized Plant-Derived Scaffolds. *ACS Biomater Sci Eng* **2020**, *6* (5), 3046–3054. https://doi.org/10.1021/acsbiomaterials.0c00058.

(145) Chen, H.; Zhong, J.; Wang, J.; Huang, R.; Qiao, X.; Wang, H.; Tan, Z. Enhanced Growth and Differentiation of Myoblast Cells Grown on E-Jet 3D Printed Platforms. *Int J Nanomedicine* **2019**, *14*, 937–950. https://doi.org/10.2147/IJN.S193624.

(146) Pacilio, S.; Costa, R.; Papa, V.; Rodia, M. T.; Gotti, C.; Pagnotta, G.; Cenacchi, G.; Focarete, M. L. Electrospun Poly(L-Lactide-Co-ε-Caprolactone) Scaffold Potentiates C2C12 Myoblast Bioactivity and Acts as a Stimulus for Cell Commitment in Skeletal Muscle Myogenesis. *Bioengineering* **2023**, *10* (2), 239. https://doi.org/10.3390/bioengineering10020239.

(147) Nakayama, K. H.; Shayan, M.; Huang, N. F. Engineering Biomimetic Materials for Skeletal Muscle Repair and Regeneration. *Adv Healthc Mater* **2019**, *8* (5), e1801168. https://doi.org/10.1002/adhm.201801168.

(148) Zhang, S.; Guo, Y.; Lu, Y.; Liu, F.; Heng, B. C.; Deng, X. The Considerations on Selecting the Appropriate Decellularized ECM for Specific Regeneration Demands. *Mater Today Bio* **2024**, *29*, 101301. https://doi.org/10.1016/j.mtbio.2024.101301.

(149) Chaturvedi, V.; Dye, D. E.; Kinnear, B. F.; van Kuppevelt, T. H.; Grounds, M. D.; Coombe, D. R. Interactions between Skeletal Muscle Myoblasts and Their Extracellular Matrix Revealed by a Serum Free Culture System. *PLoS One* **2015**, *10* (6), e0127675. https://doi.org/10.1371/journal.pone.0127675.

(150) Kozan, N. G.; Joshi, M.; Sicherer, S. T.; Grasman, J. M. Porous Biomaterial Scaffolds for Skeletal Muscle Tissue Engineering. *Front Bioeng Biotechnol* **2023**, *11*, 1245897. https://doi.org/10.3389/fbioe.2023.1245897.

(151) Colin, C.; Akpo, E.; Perrin, A.; Cornu, D.; Cambedouzou, J. Encapsulation in Alginates Hydrogels and Controlled Release: An Overview. *Molecules* **2024**, *29* (11), 2515. https://doi.org/10.3390/molecules29112515.

(152) Kozan, N. G.; Caswell, S.; Patel, M.; Grasman, J. M. Aligned Collagen Sponges with Tunable Pore Size for Skeletal Muscle Tissue Regeneration. *J Funct Biomater* **2023**, *14* (11), 533. https://doi.org/10.3390/jfb14110533.

(153) Tan, Y. H.; Habing, K. M.; Riesterer, J. L.; Stempinski, E. S.; Lewis, S. H.; Pfeifer, C. S.; Malhotra, S. V.; Nakayama, K. H. Engineered Nanofibrillar Collagen with Tunable Biophysical Properties for Myogenic, Endothelial, and Osteogenic Cell Guidance. *Acta Biomater* **2024**, *186*, 95–107. https://doi.org/10.1016/j.actbio.2024.08.002.

(154) Yang, G. H.; Kim, W.; Kim, J.; Kim, G. A Skeleton Muscle Model Using GelMA-Based Cell-Aligned Bioink Processed with an Electric-Field Assisted 3D/4D Bioprinting. *Theranostics* **2021**, *11* (1), 48–63. https://doi.org/10.7150/thno.50794.

(155) Borselli, C.; Cezar, C. A.; Shvartsman, D.; Vandenburgh, H. H.; Mooney, D. J. The Role of Multifunctional Delivery Scaffold in the Ability of Cultured Myoblasts to Promote

Muscle Regeneration. *Biomaterials* **2011**, *32* (34), 8905–8914. https://doi.org/10.1016/j.biomaterials.2011.08.019.

(156) Panayi, A. C.; Smit, L.; Hays, N.; Udeh, K.; Endo, Y.; Li, B.; Sakthivel, D.; Tamayol, A.; Neppl, R. L.; Orgill, D. P.; Nuutila, K.; Sinha, I. A Porous Collagen-GAG Scaffold Promotes Muscle Regeneration Following Volumetric Muscle Loss Injury. *Wound Repair Regen* **2020**, *28* (1), 61–74. https://doi.org/10.1111/wrr.12768.

(157) Hu, C.; Ayan, B.; Chiang, G.; Chan, A. H. P.; Rando, T. A.; Huang, N. F. Comparative Effects of Basic Fibroblast Growth Factor Delivery or Voluntary Exercise on Muscle Regeneration after Volumetric Muscle Loss. *Bioengineering* **2022**, *9* (1), 37. https://doi.org/10.3390/bioengineering9010037.

(158) Saveh-Shemshaki, N.; Barajaa, M. A.; Otsuka, T.; Mirdamadi, E. S.; Nair, L. S.; Laurencin, C. T. Electroconductivity, a Regenerative Engineering Approach to Reverse Rotator Cuff Muscle Degeneration. *Regen Biomater* **2023**, *10*, rbad099. https://doi.org/10.1093/rb/rbad099.

(159) Wang, L.; Cao, L.; Shansky, J.; Wang, Z.; Mooney, D.; Vandenburgh, H. Minimally Invasive Approach to the Repair of Injured Skeletal Muscle with a Shape-Memory Scaffold. *Mol Ther* **2014**, *22* (8), 1441–1449. https://doi.org/10.1038/mt.2014.78.

(160) Ibáñez-Fonseca, A.; Santiago Maniega, S.; Gorbenko del Blanco, D.; Catalán Bernardos, B.; Vega Castrillo, A.; Álvarez Barcia, Á. J.; Alonso, M.; Aguado, H. J.; Rodríguez-Cabello, J. C. Elastin-Like Recombinamer Hydrogels for Improved Skeletal Muscle Healing Through Modulation of Macrophage Polarization. *Front Bioeng Biotechnol* **2020**, *8*, 413. https://doi.org/10.3389/fbioe.2020.00413.

(161) Csapo, R.; Gumpenberger, M.; Wessner, B. Skeletal Muscle Extracellular Matrix – What Do We Know About Its Composition, Regulation, and Physiological Roles? A Narrative Review. *Front Physiol* **2020**, *11*, 253. https://doi.org/10.3389/fphys.2020.00253.

(162) Han, W. M.; Anderson, S. E.; Mohiuddin, M.; Barros, D.; Nakhai, S. A.; Shin, E.; Amaral, I. F.; Pêgo, A. P.; García, A. J.; Jang, Y. C. Synthetic Matrix Enhances Transplanted Satellite Cell Engraftment in Dystrophic and Aged Skeletal Muscle with Comorbid Trauma. *Sci Adv* **2018**, *4* (8), eaar4008. https://doi.org/10.1126/sciadv.aar4008.

(163) Brown, T. D.; Dalton, P. D.; Hutmacher, D. W. Direct Writing by Way of Melt Electrospinning. *Adv Mater* **2011**, *23* (47), 5651–5657. https://doi.org/10.1002/adma.201103482.

(164) Calero-Castro, F. J.; Perez-Puyana, V. M.; Laga, I.; Padillo Ruiz, J.; Romero, A.; de la Portilla de Juan, F. Mechanical Stimulation and Aligned Poly(ε-Caprolactone)–Gelatin Electrospun Scaffolds Promote Skeletal Muscle Regeneration. *ACS Appl. Bio Mater.* **2024**, *7* (10), 6430–6440. https://doi.org/10.1021/acsabm.4c00559.

(165) Mozipo, E. A.; Galindo, A. N.; Khachatourian, J. D.; Harris, C. G.; Dorogin, J.; Spaulding, V. R.; Ford, M. R.; Singhal, M.; Fogg, K. C.; Hettiaratchi, M. H. Statistical Optimization of Hydrazone-Crosslinked Hyaluronic Acid Hydrogels for Protein Delivery. *J. Mater. Chem. B* **2024**, *12* (10), 2523–2536. https://doi.org/10.1039/D3TB01588B.

(166) Leng, Y.; Abdullah, A.; Wendt, M. K.; Calve, S. Hyaluronic Acid, CD44 and RHAMM Regulate Myoblast Behavior during Embryogenesis. *Matrix Biol* **2019**, *78–79*, 236–254. https://doi.org/10.1016/j.matbio.2018.08.008.

(167) Dalton, P. D.; Polites, M. *Visualizing fiber path and generating G-code for melt electrowriting of tubular scaffolds using Grasshopper software*.

(168) Hrynevich, A.; Achenbach, P.; Jungst, T.; Brook, G. A.; Dalton, P. D. Design of Suspended Melt Electrowritten Fiber Arrays for Schwann Cell Migration and Neurite Outgrowth. *Macromol Biosci* **2021**, *21* (7), e2000439. https://doi.org/10.1002/mabi.202000439.

(169) Hettiaratchi, M. H.; Miller, T.; Temenoff, J. S.; Guldberg, R. E.; McDevitt, T. C. Heparin Microparticle Effects on Presentation and Bioactivity of Bone Morphogenetic Protein-2. *Biomaterials* **2014**, *35* (25), 7228–7238. https://doi.org/10.1016/j.biomaterials.2014.05.011.

(170) Kim, H.-J.; Lee, J.-H.; Kim, S.-W.; Lee, S.-H.; Jung, D.-W.; Williams, D. R. Investigation of Niclosamide as a Repurposing Agent for Skeletal Muscle Atrophy. *PLoS One* **2021**, *16* (5), e0252135. https://doi.org/10.1371/journal.pone.0252135.

(171) Wang, H.; Lööf, S.; Borg, P.; Nader, G. A.; Blau, H. M.; Simon, A. Turning Terminally Differentiated Skeletal Muscle Cells into Regenerative Progenitors. *Nat Commun* **2015**, *6* (1), 7916. https://doi.org/10.1038/ncomms8916.

(172) Burdick, J. A.; Anseth, K. S. Photoencapsulation of Osteoblasts in Injectable RGD-Modified PEG Hydrogels for Bone Tissue Engineering. *Biomaterials* **2002**, *23* (22), 4315–4323. https://doi.org/10.1016/S0142-9612(02)00176-X.

(173) Kuthe, C. D.; Uddanwadiker, R. V.; Ramteke, A. Experimental Evaluation of Fiber Orientation Based Material Properties of Skeletal Muscle in Tension. *Mol Cell Biomech* **2014**, *11* (2), 113–128.

(174) Tai, P. W.; Fisher-Aylor, K. I.; Himeda, C. L.; Smith, C. L.; MacKenzie, A. P.; Helterline, D. L.; Angello, J. C.; Welikson, R. E.; Wold, B. J.; Hauschka, S. D. Differentiation and Fiber Type-Specific Activity of a Muscle Creatine Kinase Intronic Enhancer. *Skeletal Muscle* **2011**, *1* (1), 25. https://doi.org/10.1186/2044-5040-1-25.

(175) Diel, P.; Baadners, D.; Schlüpmann, K.; Velders, M.; Schwarz, J. P. C2C12 Myoblastoma Cell Differentiation and Proliferation Is Stimulated by Androgens and Associated with a Modulation of Myostatin and Pax7 Expression. *J Mol Endocrinol* **2008**, *40* (5), 231–241. https://doi.org/10.1677/JME-07-0175.

(176) Jang, M.; Scheffold, J.; Røst, L. M.; Cheon, H.; Bruheim, P. Serum-Free Cultures of C2C12 Cells Show Different Muscle Phenotypes Which Can Be Estimated by Metabolic Profiling. *Sci Rep* **2022**, *12* (1), 827. https://doi.org/10.1038/s41598-022-04804-z.

(177) Cai, A.; Hardt, M.; Schneider, P.; Schmid, R.; Lange, C.; Dippold, D.; Schubert, D. W.; Boos, A. M.; Weigand, A.; Arkudas, A.; Horch, R. E.; Beier, J. P. Myogenic Differentiation of Primary Myoblasts and Mesenchymal Stromal Cells under Serum-Free Conditions on PCL-Collagen I-Nanoscaffolds. *BMC Biotechnol* **2018**, *18* (1), 75. https://doi.org/10.1186/s12896-018-0482-6.

(178) Ma, J.; Chen, J.; Gan, M.; Chen, L.; Zhao, Y.; Niu, L.; Zhu, Y.; Zhang, S.; Li, X.; Guo, Z.; Wang, J.; Zhu, L.; Shen, L. Comparison of Reference Gene Expression Stability in Mouse Skeletal Muscle via Five Algorithms. *PeerJ* **2022**, *10*, e14221. https://doi.org/10.7717/peerj.14221.

(179) Azhar, M.; Wardhani, B. W. K.; Renesteen, E. The Regenerative Potential of Pax3/Pax7 on Skeletal Muscle Injury. *Journal of Genetic Engineering and Biotechnology* **2022**, *20* (1), 143. https://doi.org/10.1186/s43141-022-00429-x.

(180) Yamamoto, M.; Legendre, N. P.; Biswas, A. A.; Lawton, A.; Yamamoto, S.; Tajbakhsh, S.; Kardon, G.; Goldhamer, D. J. Loss of MyoD and Myf5 in Skeletal Muscle Stem Cells Results in Altered Myogenic Programming and Failed Regeneration. *Stem Cell Reports* **2018**, *10* (3), 956–969. https://doi.org/10.1016/j.stemcr.2018.01.027.

(181) Zammit, P. S.; Relaix, F.; Nagata, Y.; Ruiz, A. P.; Collins, C. A.; Partridge, T. A.; Beauchamp, J. R. Pax7 and Myogenic Progression in Skeletal Muscle Satellite Cells. *Journal of Cell Science* **2006**, *119* (9), 1824–1832. https://doi.org/10.1242/jcs.02908.

(182) Ganassi, M.; Badodi, S.; Wanders, K.; Zammit, P. S.; Hughes, S. M. Myogenin Is an Essential Regulator of Adult Myofibre Growth and Muscle Stem Cell Homeostasis. *eLife* **2020**, *9*, e60445. https://doi.org/10.7554/eLife.60445.

(183) *C2C12 cells: biophysical, biochemical, and immunocytochemical properties - PubMed*. https://pubmed.ncbi.nlm.nih.gov/8023908/ (accessed 2025-07-14).

(184) Nolan, A.; Heaton, R. A.; Adamova, P.; Cole, P.; Turton, N.; Gillham, S. H.; Owens, D. J.; Sexton, D. W. Fluorescent Characterization of Differentiated Myotubes Using Flow Cytometry. *Cytometry A* **2024**, *105* (5), 332–344. https://doi.org/10.1002/cyto.a.24822.

(185) Shu, X. Z.; Ghosh, K.; Liu, Y.; Palumbo, F. S.; Luo, Y.; Clark, R. A.; Prestwich, G. D. Attachment and Spreading of Fibroblasts on an RGD Peptide–Modified Injectable Hyaluronan Hydrogel. *Journal of Biomedical Materials Research Part A* **2004**, *68A* (2), 365–375. https://doi.org/10.1002/jbm.a.20002.

(186) Alcazar, C. A.; Hu, C.; Rando, T. A.; Huang, N. F.; Nakayama, K. H. Transplantation of Insulin-like Growth Factor-1 Laden Scaffolds Combined with Exercise Promotes

Neuroregeneration and Angiogenesis in a Preclinical Muscle Injury Model. *Biomater. Sci.* **2020**, *8* (19), 5376–5389. https://doi.org/10.1039/D0BM00990C.

(187) Dreher, S. I.; Grubba, P.; Von Toerne, C.; Moruzzi, A.; Maurer, J.; Goj, T.; Birkenfeld, A. L.; Peter, A.; Loskill, P.; Hauck, S. M.; Weigert, C. IGF1 Promotes Human Myotube Differentiation toward a Mature Metabolic and Contractile Phenotype. *American Journal of Physiology-Cell Physiology* **2024**, *326* (5), C1462–C1481. https://doi.org/10.1152/ajpcell.00654.2023.

(188) Pawlikowski, B.; Vogler, T. O.; Gadek, K.; Olwin, B. B. Regulation of Skeletal Muscle Stem Cells by Fibroblast Growth Factors. *Developmental Dynamics* **2017**, *246* (5), 359–367. https://doi.org/10.1002/dvdy.24495.

(189) Wroblewski, O. M.; Vega-Soto, E. E.; Nguyen, M. H.; Cederna, P. S.; Larkin, L. M. Impact of Human Epidermal Growth Factor on Tissue-Engineered Skeletal Muscle Structure and Function. *Tissue Engineering Part A* **2021**, *27* (17–18), 1151–1159. https://doi.org/10.1089/ten.tea.2020.0255.

(190) Wu, D.; Eugenis, I.; Hu, C.; Kim, S.; Kanugovi, A.; Yue, S.; Wheeler, J. R.; Fathali, I.; Feeley, S.; Shrager, J. B.; Huang, N. F.; Rando, T. A. Bioinstructive Scaffolds Enhance Stem Cell Engraftment for Functional Tissue Regeneration. *Nat. Mater.* **2025**, 1–11. https://doi.org/10.1038/s41563-025-02212-y.

(191) Hao, L.; Yu, D.; Hou, X.; Zhao, Y. Advances in Polypyrrole Nanofiber Composites: Design, Synthesis, and Performance in Tissue Engineering. *Materials (Basel)* **2025**, *18* (13), 2965. https://doi.org/10.3390/ma18132965.

(192) Dong, R.; Ma, P. X.; Guo, B. Conductive Biomaterials for Muscle Tissue Engineering. *Biomaterials* **2020**, *229*, 119584. https://doi.org/10.1016/j.biomaterials.2019.119584.

(193) Taye, N.; Stanley, S.; Hubmacher, D. Stable Knockdown of Genes Encoding Extracellular Matrix Proteins in the C2C12 Myoblast Cell Line Using Small-Hairpin (Sh)RNA. *J Vis Exp* **2020**, No. 156, 10.3791/60824. https://doi.org/10.3791/60824.

(194) Willett, N. J.; Krishnan, L.; Li, M. T. A.; Guldberg, R. E.; Warren, G. L. Guidelines for Models of Skeletal Muscle Injury and Therapeutic Assessment. *Cells Tissues Organs* **2016**, *202* (3–4), 214–226. https://doi.org/10.1159/000445345.

(195) Anderson, S. E.; Han, W. M.; Srinivasa, V.; Mohiuddin, M.; Ruehle, M. A.; Moon, J. Y.; Shin, E.; San Emeterio, C. L.; Ogle, M. E.; Botchwey, E. A.; Willett, N. J.; Jang, Y. C. Determination of a Critical Size Threshold for Volumetric Muscle Loss in the Mouse Quadriceps. *Tissue Engineering Part C: Methods* **2019**, *25* (2), 59–70. https://doi.org/10.1089/ten.tec.2018.0324.

(196) Sandean, D. Management of Acute Spinal Cord Injury: A Summary of the Evidence Pertaining to the Acute Management, Operative and Non-Operative Management. *World J Orthop* **2020**, *11* (12), 573–583. https://doi.org/10.5312/wjo.v11.i12.573.

(197) *Report to Congress: Traumatic Brain Injury in the United States | Concussion | Traumatic Brain Injury | CDC Injury Center*. https://www.cdc.gov/traumaticbraininjury/pubs/tbi_report_to_congress.html (accessed 2023-09-10).

(198) *TBI Data | Concussion | Traumatic Brain Injury | CDC Injury Center*. https://www.cdc.gov/traumaticbraininjury/data/index.html (accessed 2023-09-10).

(199) Bradbury, E. J.; Burnside, E. R. Moving beyond the Glial Scar for Spinal Cord Repair. *Nat Commun* **2019**, *10* (1), 3879. https://doi.org/10.1038/s41467-019-11707-7.

(200) Thorpe, K. E.; Levey, A. I.; Thomas, J. OF NEURODEGENERATIVE DISEASE.

(201) Van Schependom, J.; D'haeseleer, M. Advances in Neurodegenerative Diseases. *J Clin Med* **2023**, *12* (5), 1709. https://doi.org/10.3390/jcm12051709.

(202) Zheng, J. C.; Chen, S. Translational Neurodegeneration in the Era of Fast Growing International Brain Research. *Transl Neurodegener* **2022**, *11* (1), 1, s40035-021-00276–00279. https://doi.org/10.1186/s40035-021-00276-9.

(203) Hou, Y.; Dan, X.; Babbar, M.; Wei, Y.; Hasselbalch, S. G.; Croteau, D. L.; Bohr, V. A. Ageing as a Risk Factor for Neurodegenerative Disease. *Nat Rev Neurol* **2019**, *15* (10), 565–581. https://doi.org/10.1038/s41582-019-0244-7.

(204) Margetts, G.; Kleidonas, S.; Zaibi, N. S.; Zaibi, M. S.; Edwards, K. D. Evidence for Anti-Inflammatory Effects and Modulation of Neurotransmitter Metabolism by Salvia Officinalis L. *BMC Complement Med Ther* **2022**, *22*, 131. https://doi.org/10.1186/s12906-022-03605-1.

(205) Park, J.-E.; Leem, Y.-H.; Park, J.-S.; Kim, D.-Y.; Kang, J. L.; Kim, H.-S. Anti-Inflammatory and Neuroprotective Mechanisms of GTS-21, an A7 Nicotinic Acetylcholine Receptor Agonist, in Neuroinflammation and Parkinson's Disease Mouse Models. *Int J Mol Sci* **2022**, *23* (8), 4420. https://doi.org/10.3390/ijms23084420.

(206) Rom, S.; Zuluaga-Ramirez, V.; Reichenbach, N. L.; Erickson, M. A.; Winfield, M.; Gajghate, S.; Christofidou-Solomidou, M.; Jordan-Sciutto, K. L.; Persidsky, Y. Secoisolariciresinol Diglucoside Is a Blood-Brain Barrier Protective and Anti-Inflammatory Agent: Implications for Neuroinflammation. *J Neuroinflammation* **2018**, *15* (1), 25. https://doi.org/10.1186/s12974-018-1065-0.

(207) Zhao, Y.; Zhang, J.; Zheng, Y.; Zhang, Y.; Zhang, X. J.; Wang, H.; Du, Y.; Guan, J.; Wang, X.; Fu, J. NAD+ Improves Cognitive Function and Reduces Neuroinflammation by Ameliorating Mitochondrial Damage and Decreasing ROS Production in Chronic Cerebral Hypoperfusion Models through Sirt1/PGC-1α Pathway. *J Neuroinflammation* **2021**, *18*, 207. https://doi.org/10.1186/s12974-021-02250-8.

(208) Zhang, D.; Jing, B.; Chen, Z.-N.; Li, X.; Shi, H.-M.; Zheng, Y.-C.; Chang, S.-Q.; Gao, L.; Zhao, G.-P. Ferulic Acid Alleviates Sciatica by Inhibiting Neuroinflammation and Promoting Nerve Repair via the TLR4/NF-κB Pathway. *CNS Neurosci Ther* **2023**, *29* (4), 1000–1011. https://doi.org/10.1111/cns.14060.

(209) Mani, S.; Dubey, R.; Lai, I.-C.; Babu, M. A.; Tyagi, S.; Swargiary, G.; Mody, D.; Singh, M.; Agarwal, S.; Iqbal, D.; Kumar, S.; Hamed, M.; Sachdeva, P.; Almutary, A. G.; Albadrani, H. M.; Ojha, S.; Singh, S. K.; Jha, N. K. Oxidative Stress and Natural Antioxidants: Back and Forth in the Neurological Mechanisms of Alzheimer's Disease. *J Alzheimers Dis* **2023**, *96* (3), 877–912. https://doi.org/10.3233/JAD-220700.

(210) Takahashi, Y.; Morimoto, N.; Takamiya, M.; Morimoto, M.; Mino, S.; Kuramoto, S.; Kawauchi, M.; Yokota, K.; Abe, K. Successful Treatment with Corticosteroids for Refractory Deterioration of Cryptococcal Meningitis with an Increasing Cryptococcal Antigen Titer. *J Clin Neurosci* **2020**, *72*, 455–457. https://doi.org/10.1016/j.jocn.2020.01.028.

(211) Alkabie, S.; Budhram, A. Prolonged Corticosteroids Without Maintenance Immunotherapy for Treatment of Anti-LGI1 Encephalitis: Analysis of Outcomes and Relapse Rate. *Neurol Neuroimmunol Neuroinflamm* **2023**, *10* (3), e200115. https://doi.org/10.1212/NXI.0000000000200115.

(212) Wang, M.; Zhang, H.; Liang, J.; Huang, J.; Chen, N. Exercise Suppresses Neuroinflammation for Alleviating Alzheimer's Disease. *J Neuroinflammation* **2023**, *20*, 76. https://doi.org/10.1186/s12974-023-02753-6.

(213) Zhang, Y.; Zhang, P.; Shen, X.; Tian, S.; Wu, Y.; Zhu, Y.; Jia, J.; Wu, J.; Hu, Y. Early Exercise Protects the Blood-Brain Barrier from Ischemic Brain Injury via the Regulation of MMP-9 and Occludin in Rats. *International Journal of Molecular Sciences* **2013**, *14* (6), 11096–11112. https://doi.org/10.3390/ijms140611096.

(214) Jacob, A.; Nina Peralta, L.; Pegues, D.; Okamura, K.; Chang, A.; McSkimming, D.; Alexander, J. Exercise Alleviates Symptoms of CNS Lupus. *Brain Res* **2021**, *1765*, 147478. https://doi.org/10.1016/j.brainres.2021.147478.

(215) Tao, Y.; Leng, S. X.; Zhang, H. Ketogenic Diet: An Effective Treatment Approach for Neurodegenerative Diseases. *Curr Neuropharmacol* **2022**, *20* (12), 2303–2319. https://doi.org/10.2174/1570159X20666220830102628.

(216) Jiang, Z.; Yin, X.; Wang, M.; Chen, T.; Wang, Y.; Gao, Z.; Wang, Z. Effects of Ketogenic Diet on Neuroinflammation in Neurodegenerative Diseases. *Aging Dis* **2022**, *13* (4), 1146–1165. https://doi.org/10.14336/AD.2021.1217.

(217) Xu, Y.; Jiang, C.; Wu, J.; Liu, P.; Deng, X.; Zhang, Y.; Peng, B.; Zhu, Y. Ketogenic Diet Ameliorates Cognitive Impairment and Neuroinflammation in a Mouse Model of Alzheimer's Disease. *CNS Neurosci Ther* **2022**, *28* (4), 580–592. https://doi.org/10.1111/cns.13779.

(218) Jiang, J.; Pan, H.; Shen, F.; Tan, Y.; Chen, S. Ketogenic Diet Alleviates Cognitive Dysfunction and Neuroinflammation in APP/PS1 Mice via the Nrf2/HO-1 and NF-κB Signaling Pathways. *Neural Regen Res* **2023**, *18* (12), 2767–2772. https://doi.org/10.4103/1673-5374.373715.

(219) Li, C.; Pan, J.; Sun, P.; Wang, S.; Wang, S.; Feng, W.; Chen, S.; Chai, X.; Zhao, S.; Zhu, X. Ketogenic Diet Alleviates Hypoglycemia-Induced Neuroinflammation via Modulation the Gut Microbiota in Mice. *Mol Nutr Food Res* **2023**, *67* (11), e2200711. https://doi.org/10.1002/mnfr.202200711.

(220) Moscariello, P.; Ng, D. Y. W.; Jansen, M.; Weil, T.; Luhmann, H. J.; Hedrich, J. Brain Delivery of Multifunctional Dendrimer Protein Bioconjugates. *Adv Sci (Weinh)* **2018**, *5* (5), 1700897. https://doi.org/10.1002/advs.201700897.

(221) Bellotti, E.; Schilling, A. L.; Little, S. R.; Decuzzi, P. Injectable Thermoresponsive Hydrogels as Drug Delivery System for the Treatment of Central Nervous System Disorders: A Review. *J Control Release* **2021**, *329*, 16–35. https://doi.org/10.1016/j.jconrel.2020.11.049.

(222) Wei, Z.; Zhao, J.; Chen, Y. M.; Zhang, P.; Zhang, Q. Self-Healing Polysaccharide-Based Hydrogels as Injectable Carriers for Neural Stem Cells. *Sci Rep* **2016**, *6* (1), 37841. https://doi.org/10.1038/srep37841.

(223) Khaing, Z. Z.; Agrawal, N. K.; Park, J. H.; Xin, S.; Plumton, G. C.; Lee, K. H.; Huang, Y.-J.; Niemerski, A. L.; Schmidt, C. E.; Grau, J. W. Localized and Sustained Release of Brain-Derived Neurotrophic Factor from Injectable Hydrogel/Microparticle Composites Fosters Spinal Learning after Spinal Cord Injury. *J Mater Chem B* **2016**, *4* (47), 7560–7571. https://doi.org/10.1039/c6tb01602b.

(224) Piantino, J.; Burdick, J. A.; Goldberg, D.; Langer, R.; Benowitz, L. I. An Injectable, Biodegradable Hydrogel for Trophic Factor Delivery Enhances Axonal Rewiring and Improves Performance after Spinal Cord Injury. *Exp Neurol* **2006**, *201* (2), 359–367. https://doi.org/10.1016/j.expneurol.2006.04.020.

(225) He, Z.; Zang, H.; Zhu, L.; Huang, K.; Yi, T.; Zhang, S.; Cheng, S. An Anti-Inflammatory Peptide and Brain-Derived Neurotrophic Factor-Modified Hyaluronan-Methylcellulose Hydrogel Promotes Nerve Regeneration in Rats with Spinal Cord Injury. *Int J Nanomedicine* **2019**, *14*, 721–732. https://doi.org/10.2147/IJN.S187854.

(226) Shultz, R. B.; Zhong, Y. Hydrogel-Based Local Drug Delivery Strategies for Spinal Cord Repair. *Neural Regen Res* **2020**, *16* (2), 247–253. https://doi.org/10.4103/1673-5374.290882.

(227) Bourrier, A.; Shkorbatova, P.; Bonizzato, M.; Rey, E.; Barraud, Q.; Courtine, G.; Othmen, R.; Reita, V.; Bouchiat, V.; Delacour, C. Monolayer Graphene Coating of Intracortical Probes for Long-Lasting Neural Activity Monitoring. *Advanced Healthcare Materials* **2019**, *8* (18), 1801331. https://doi.org/10.1002/adhm.201801331.

(228) Lee, C. D.; Hara, S. A.; Yu, L.; Kuo, J. T. W.; Kim, B. J.; Hoang, T.; Pikov, V.; Meng, E. Matrigel Coatings for Parylene Sheath Neural Probes. *J Biomed Mater Res B Appl Biomater* **2016**, *104* (2), 357–368. https://doi.org/10.1002/jbm.b.33390.

(229) Francis, N. L.; Hunger, P. M.; Donius, A. E.; Riblett, B. W.; Zavaliangos, A.; Wegst, U. G. K.; Wheatley, M. A. An Ice-Templated, Linearly Aligned Chitosan-Alginate Scaffold for Neural Tissue Engineering. *J Biomed Mater Res A* **2013**, *101* (12), 3493–3503. https://doi.org/10.1002/jbm.a.34668.

(230) Dityatev, A.; Schachner, M.; Sonderegger, P. The Dual Role of the Extracellular Matrix in Synaptic Plasticity and Homeostasis. *Nat Rev Neurosci* **2010**, *11* (11), 735–746. https://doi.org/10.1038/nrn2898.

(231) Song, I.; Dityatev, A. Crosstalk between Glia, Extracellular Matrix and Neurons. *Brain Research Bulletin* **2018**, *136*, 101–108. https://doi.org/10.1016/j.brainresbull.2017.03.003.

(232) Burnside, E. R.; Bradbury, E. J. Review: Manipulating the Extracellular Matrix and Its Role in Brain and Spinal Cord Plasticity and Repair. *Neuropathology and Applied Neurobiology* **2014**, *40* (1), 26–59. https://doi.org/10.1111/nan.12114.

(233) Lam, D.; Enright, H. A.; Cadena, J.; Peters, S. K. G.; Sales, A. P.; Osburn, J. J.; Soscia, D. A.; Kulp, K. S.; Wheeler, E. K.; Fischer, N. O. Tissue-Specific Extracellular Matrix Accelerates the Formation of Neural Networks and Communities in a Neuron-Glia Co-Culture on a Multi-Electrode Array. *Sci Rep* **2019**, *9* (1), 4159. https://doi.org/10.1038/s41598-019-40128-1.

(234) Allen, N. J.; Lyons, D. A. Glia as Architects of Central Nervous System Formation and Function. *Science* **2018**, *362* (6411), 181–185. https://doi.org/10.1126/science.aat0473.

(235) Deng, S.; Gan, L.; Liu, C.; Xu, T.; Zhou, S.; Guo, Y.; Zhang, Z.; Yang, G.-Y.; Tian, H.; Tang, Y. Roles of Ependymal Cells in the Physiology and Pathology of the Central Nervous System. *Aging Dis* **2023**, *14* (2), 468–483. https://doi.org/10.14336/AD.2022.0826-1.

(236) Nimmerjahn, A.; Kirchhoff, F.; Helmchen, F. Resting Microglial Cells Are Highly Dynamic Surveillants of Brain Parenchyma in Vivo. *Science* **2005**, *308* (5726), 1314–1318. https://doi.org/10.1126/science.1110647.

(237) Green, T. R. F.; Murphy, S. M.; Moreno-Montano, M. P.; Audinat, E.; Rowe, R. K. Reactive Morphology of Dividing Microglia Following Kainic Acid Administration. *Front Neurosci* **2022**, *16*, 972138. https://doi.org/10.3389/fnins.2022.972138.

(238) Fujita, Y.; Yamashita, T. Alterations in Chromatin Structure and Function in the Microglia. *Front Cell Dev Biol* **2021**, *8*, 626541. https://doi.org/10.3389/fcell.2020.626541.

(239) Tan, Y.-L.; Yuan, Y.; Tian, L. Microglial Regional Heterogeneity and Its Role in the Brain. *Mol Psychiatry* **2020**, *25* (2), 351–367. https://doi.org/10.1038/s41380-019-0609-8.

(240) Ransohoff, R. M. A Polarizing Question: Do M1 and M2 Microglia Exist? *Nat Neurosci* **2016**, *19* (8), 987–991. https://doi.org/10.1038/nn.4338.

(241) Kim, C. C.; Nakamura, M. C.; Hsieh, C. L. Brain Trauma Elicits Non-Canonical Macrophage Activation States. *J Neuroinflammation* **2016**, *13* (1), 117. https://doi.org/10.1186/s12974-016-0581-z.

(242) Peng, H.-R.; Zhang, Y.-K.; Zhou, J.-W. The Structure and Function of Glial Networks: Beyond the Neuronal Connections. *Neurosci. Bull.* **2023**, *39* (3), 531–540. https://doi.org/10.1007/s12264-022-00992-w.

(243) Molina-Gonzalez, I.; Holloway, R. K.; Jiwaji, Z.; Dando, O.; Kent, S. A.; Emelianova, K.; Lloyd, A. F.; Forbes, L. H.; Mahmood, A.; Skripuletz, T.; Gudi, V.; Febery, J. A.; Johnson, J. A.; Fowler, J. H.; Kuhlmann, T.; Williams, A.; Chandran, S.; Stangel, M.; Howden, A. J. M.; Hardingham, G. E.; Miron, V. E. Astrocyte-Oligodendrocyte Interaction Regulates Central Nervous System Regeneration. *Nat Commun* **2023**, *14* (1), 3372. https://doi.org/10.1038/s41467-023-39046-8.

(244) Heithoff, B. P.; George, K. K.; Phares, A. N.; Zuidhoek, I. A.; Munoz-Ballester, C.; Robel, S. Astrocytes Are Necessary for Blood-Brain Barrier Maintenance in the Adult Mouse Brain. *Glia* **2021**, *69* (2), 436–472. https://doi.org/10.1002/glia.23908.

(245) Kadry, H.; Noorani, B.; Cucullo, L. A Blood–Brain Barrier Overview on Structure, Function, Impairment, and Biomarkers of Integrity. *Fluids Barriers CNS* **2020**, *17*, 69. https://doi.org/10.1186/s12987-020-00230-3.

(246) Castellani, G.; Croese, T.; Peralta Ramos, J. M.; Schwartz, M. Transforming the Understanding of Brain Immunity. *Science* **2023**, *380* (6640), eabo7649. https://doi.org/10.1126/science.abo7649.

(247) Rustenhoven, J.; Drieu, A.; Mamuladze, T.; de Lima, K. A.; Dykstra, T.; Wall, M.; Papadopoulos, Z.; Kanamori, M.; Salvador, A. F.; Baker, W.; Lemieux, M.; Da Mesquita, S.; Cugurra, A.; Fitzpatrick, J.; Sviben, S.; Kossina, R.; Bayguinov, P.; Townsend, R. R.; Zhang, Q.; Erdmann-Gilmore, P.; Smirnov, I.; Lopes, M.-B.; Herz, J.; Kipnis, J. Functional Characterization of the Dural Sinuses as a Neuroimmune Interface. *Cell* **2021**, *184* (4), 1000-1016.e27. https://doi.org/10.1016/j.cell.2020.12.040.

(248) Huang, Y.; Chen, S.; Luo, Y.; Han, Z. Crosstalk between Inflammation and the BBB in Stroke. *Curr Neuropharmacol* **2020**, *18* (12), 1227–1236. https://doi.org/10.2174/1570159X18666200620230321.

(249) Garofalo, S.; Cocozza, G.; Bernardini, G.; Savage, J.; Raspa, M.; Aronica, E.; Tremblay, M.-E.; Ransohoff, R. M.; Santoni, A.; Limatola, C. Blocking Immune Cell Infiltration of the Central Nervous System to Tame Neuroinflammation in Amyotrophic Lateral

Sclerosis. *Brain, Behavior, and Immunity* **2022**, *105*, 1–14. https://doi.org/10.1016/j.bbi.2022.06.004.

(250) Williams, G. P.; Schonhoff, A. M.; Jurkuvenaite, A.; Gallups, N. J.; Standaert, D. G.; Harms, A. S. CD4 T Cells Mediate Brain Inflammation and Neurodegeneration in a Mouse Model of Parkinson's Disease. *Brain* **2021**, *144* (7), 2047–2059. https://doi.org/10.1093/brain/awab103.

(251) Gate, D.; Saligrama, N.; Leventhal, O.; Yang, A. C.; Unger, M. S.; Middeldorp, J.; Chen, K.; Lehallier, B.; Channappa, D.; De Los Santos, M. B.; McBride, A.; Pluvinage, J.; Elahi, F.; Tam, G. K.-Y.; Kim, Y.; Greicius, M.; Wagner, A. D.; Aigner, L.; Galasko, D. R.; Davis, M. M.; Wyss-Coray, T. Clonally Expanded CD8 T Cells Patrol the Cerebrospinal Fluid in Alzheimer's Disease. *Nature* **2020**, *577* (7790), 399–404. https://doi.org/10.1038/s41586-019-1895-7.

(252) Khanh Vu, T. H.; Chen, H.; Pan, L.; Cho, K.-S.; Doesburg, D.; Thee, E. F.; Wu, N.; Arlotti, E.; Jager, M. J.; Chen, D. F. CD4+ T-Cell Responses Mediate Progressive Neurodegeneration in Experimental Ischemic Retinopathy. *Am J Pathol* **2020**, *190* (8), 1723–1734. https://doi.org/10.1016/j.ajpath.2020.04.011.

(253) Hellenbrand, D. J.; Quinn, C. M.; Piper, Z. J.; Morehouse, C. N.; Fixel, J. A.; Hanna, A. S. Inflammation after Spinal Cord Injury: A Review of the Critical Timeline of Signaling Cues and Cellular Infiltration. *Journal of Neuroinflammation* **2021**, *18* (1), 284. https://doi.org/10.1186/s12974-021-02337-2.

(254) Gadani, S. P.; Walsh, J. T.; Smirnov, I.; Zheng, J.; Kipnis, J. The Glia-Derived Alarmin IL-33 Orchestrates the Immune Response and Promotes Recovery Following CNS Injury. *Neuron* **2015**, *85* (4), 703–709. https://doi.org/10.1016/j.neuron.2015.01.013.

(255) Pomeshchik, Y.; Kidin, I.; Korhonen, P.; Savchenko, E.; Jaronen, M.; Lehtonen, S.; Wojciechowski, S.; Kanninen, K.; Koistinaho, J.; Malm, T. Interleukin-33 Treatment Reduces Secondary Injury and Improves Functional Recovery after Contusion Spinal Cord Injury. *Brain Behav Immun* **2015**, *44*, 68–81. https://doi.org/10.1016/j.bbi.2014.08.002.

(256) Salvador, A. F. M.; Kipnis, J. Immune Response after Central Nervous System Injury. *Seminars in Immunology* **2022**, *59*, 101629. https://doi.org/10.1016/j.smim.2022.101629.

(257) Chaturvedi, M.; Kaczmarek, L. MMP-9 Inhibition: A Therapeutic Strategy in Ischemic Stroke. *Mol Neurobiol* **2014**, *49* (1), 563–573. https://doi.org/10.1007/s12035-013-8538-z.

(258) Lee, J. Y.; Choi, H. Y.; Ahn, H.-J.; Ju, B. G.; Yune, T. Y. Matrix Metalloproteinase-3 Promotes Early Blood–Spinal Cord Barrier Disruption and Hemorrhage and Impairs Long-Term Neurological Recovery after Spinal Cord Injury. *The American Journal of Pathology* **2014**, *184* (11), 2985–3000. https://doi.org/10.1016/j.ajpath.2014.07.016.

(259) DiSabato, D.; Quan, N.; Godbout, J. P. Neuroinflammation: The Devil Is in the Details. *J Neurochem* **2016**, *139* (Suppl 2), 136–153. https://doi.org/10.1111/jnc.13607.

(260) Simon, D. W.; McGeachy, M. J.; Bayır, H.; Clark, R. S. B.; Loane, D. J.; Kochanek, P. M. The Far-Reaching Scope of Neuroinflammation after Traumatic Brain Injury. *Nat Rev Neurol* **2017**, *13* (3), 171–191. https://doi.org/10.1038/nrneurol.2017.13.

(261) LeVine, S. M. Albumin and Multiple Sclerosis. *BMC Neurol* **2016**, *16*, 47. https://doi.org/10.1186/s12883-016-0564-9.

(262) Habgood, M. D.; Bye, N.; Dziegielewska, K. M.; Ek, C. J.; Lane, M. A.; Potter, A.; Morganti-Kossmann, C.; Saunders, N. R. Changes in Blood-Brain Barrier Permeability to Large and Small Molecules Following Traumatic Brain Injury in Mice. *Eur J Neurosci* **2007**, *25* (1), 231–238. https://doi.org/10.1111/j.1460-9568.2006.05275.x.

(263) Shafqat, A.; Noor Eddin, A.; Adi, G.; Al-Rimawi, M.; Abdul Rab, S.; Abu-Shaar, M.; Adi, K.; Alkattan, K.; Yaqinuddin, A. Neutrophil Extracellular Traps in Central Nervous System Pathologies: A Mini Review. *Front Med (Lausanne)* **2023**, *10*, 1083242. https://doi.org/10.3389/fmed.2023.1083242.

(264) Javdani, M.; Barzegar-Bafrouei, A. The Key Role of Macrophages and Monocytes in Spinal Cord Injury: Development of Novel Therapeutic Approaches. *The Neuroscience Journal of Shefaye Khatam* **2020**, *8* (4), 90–102. https://doi.org/10.29252/shefa.8.4.90.

(265) Saxton, R. A.; Tsutsumi, N.; Su, L. L.; Abhiraman, G. C.; Mohan, K.; Henneberg, L. T.; Aduri, N. G.; Gati, C.; Garcia, K. C. Structure-Based Decoupling of the pro- and Anti-Inflammatory Functions of Interleukin-10. *Science* **2021**, *371* (6535), eabc8433. https://doi.org/10.1126/science.abc8433.

(266) Jurga, A. M.; Paleczna, M.; Kuter, K. Z. Overview of General and Discriminating Markers of Differential Microglia Phenotypes. *Front Cell Neurosci* **2020**, *14*, 198. https://doi.org/10.3389/fncel.2020.00198.

(267) Ohsawa, K.; Imai, Y.; Sasaki, Y.; Kohsaka, S. Microglia/Macrophage-Specific Protein Iba1 Binds to Fimbrin and Enhances Its Actin-Bundling Activity. *J Neurochem* **2004**, *88* (4), 844–856. https://doi.org/10.1046/j.1471-4159.2003.02213.x.

(268) Liddelow, S. A.; Guttenplan, K. A.; Clarke, L. E.; Bennett, F. C.; Bohlen, C. J.; Schirmer, L.; Bennett, M. L.; Münch, A. E.; Chung, W.-S.; Peterson, T. C.; Wilton, D. K.; Frouin, A.; Napier, B. A.; Panicker, N.; Kumar, M.; Buckwalter, M. S.; Rowitch, D. H.; Dawson, V. L.; Dawson, T. M.; Stevens, B.; Barres, B. A. Neurotoxic Reactive Astrocytes Are Induced by Activated Microglia. *Nature* **2017**, *541* (7638), 481–487. https://doi.org/10.1038/nature21029.

(269) Ng, W.; Ng, S.-Y. Remodeling of Astrocyte Secretome in Amyotrophic Lateral Sclerosis: Uncovering Novel Targets to Combat Astrocyte-Mediated Toxicity. *Translational Neurodegeneration* **2022**, *11* (1), 54. https://doi.org/10.1186/s40035-022-00332-y.

(270) Bi, F.; Huang, C.; Tong, J.; Qiu, G.; Huang, B.; Wu, Q.; Li, F.; Xu, Z.; Bowser, R.; Xia, X.-G.; Zhou, H. Reactive Astrocytes Secrete Lcn2 to Promote Neuron Death. *Proc Natl Acad Sci U S A* **2013**, *110* (10), 4069–4074. https://doi.org/10.1073/pnas.1218497110.

(271) Becerra-Calixto, A.; Cardona-Gómez, G. P. The Role of Astrocytes in Neuroprotection after Brain Stroke: Potential in Cell Therapy. *Frontiers in Molecular Neuroscience* **2017**, *10*.

(272) Diniz, L. P.; Tortelli, V.; Matias, I.; Morgado, J.; Araujo, A. P. B.; Melo, H. M.; Silva, G. S. S. da; Alves-Leon, S. V.; Souza, J. M. de; Ferreira, S. T.; Felice, F. G. D.; Gomes, F. C. A. Astrocyte Transforming Growth Factor Beta 1 Protects Synapses against Aβ Oligomers in Alzheimer's Disease Model. *J. Neurosci.* **2017**, *37* (28), 6797–6809. https://doi.org/10.1523/JNEUROSCI.3351-16.2017.

(273) Cekanaviciute, E.; Dietrich, H. K.; Axtell, R. C.; Williams, A. M.; Egusquiza, R.; Wai, K. M.; Koshy, A. A.; Buckwalter, M. S. Astrocytic TGF-β Signaling Limits Inflammation and Reduces Neuronal Damage during Central Nervous System Toxoplasma Infection. *The Journal of Immunology* **2014**, *193* (1), 139–149. https://doi.org/10.4049/jimmunol.1303284.

(274) Zhou, Y.; Shao, A.; Yao, Y.; Tu, S.; Deng, Y.; Zhang, J. Dual Roles of Astrocytes in Plasticity and Reconstruction after Traumatic Brain Injury. *Cell Communication and Signaling* **2020**, *18* (1), 62. https://doi.org/10.1186/s12964-020-00549-2.

(275) Yang, T.; Dai, Y.; Chen, G.; Cui, S. Dissecting the Dual Role of the Glial Scar and Scar-Forming Astrocytes in Spinal Cord Injury. *Front Cell Neurosci* **2020**, *14*, 78. https://doi.org/10.3389/fncel.2020.00078.

(276) He, X.; Li, Y.; Deng, B.; Lin, A.; Zhang, G.; Ma, M.; Wang, Y.; Yang, Y.; Kang, X. The PI3K/AKT Signalling Pathway in Inflammation, Cell Death and Glial Scar Formation after Traumatic Spinal Cord Injury: Mechanisms and Therapeutic Opportunities. *Cell Proliferation* **2022**, *55* (9), e13275. https://doi.org/10.1111/cpr.13275.

(277) Adams, K. L.; Gallo, V. The Diversity and Disparity of the Glial Scar. *Nat Neurosci* **2018**, *21* (1), 9–15. https://doi.org/10.1038/s41593-017-0033-9.

(278) Wang, G.; Zhang, J.; Hu, X.; Zhang, L.; Mao, L.; Jiang, X.; Liou, A. K.-F.; Leak, R. K.; Gao, Y.; Chen, J. Microglia/Macrophage Polarization Dynamics in White Matter after Traumatic Brain Injury. *J Cereb Blood Flow Metab* **2013**, *33* (12), 1864–1874. https://doi.org/10.1038/jcbfm.2013.146.

(279) Faden, A. I.; Wu, J.; Stoica, B. A.; Loane, D. J. Progressive Inflammation-Mediated Neurodegeneration after Traumatic Brain or Spinal Cord Injury. *British Journal of Pharmacology* **2016**, *173* (4), 681–691. https://doi.org/10.1111/bph.13179.

(280) *Chondroitin sulfate proteoglycans prevent immune cell phenotypic conversion and inflammation resolution via TLR4 in rodent models of spinal cord injury | Nature*

Communications. https://www.nature.com/articles/s41467-022-30467-5 (accessed 2024-02-12).

(281) Heurtaux, T.; Michelucci, A.; Losciuto, S.; Gallotti, C.; Felten, P.; Dorban, G.; Grandbarbe, L.; Morga, E.; Heuschling, P. Microglial Activation Depends on Beta-Amyloid Conformation: Role of the Formylpeptide Receptor 2. *J Neurochem* **2010**, *114* (2), 576–586. https://doi.org/10.1111/j.1471-4159.2010.06783.x.

(282) Su, X.; Maguire-Zeiss, K. A.; Giuliano, R.; Prifti, L.; Venkatesh, K.; Federoff, H. J. Synuclein Activates Microglia in a Model of Parkinson's Disease. *Neurobiol Aging* **2008**, *29* (11), 1690–1701. https://doi.org/10.1016/j.neurobiolaging.2007.04.006.

(283) Hickman, S.; Izzy, S.; Sen, P.; Morsett, L.; El Khoury, J. Microglia in Neurodegeneration. *Nat Neurosci* **2018**, *21* (10), 1359–1369. https://doi.org/10.1038/s41593-018-0242-x.

(284) Jayaraj, R. L.; Azimullah, S.; Beiram, R.; Jalal, F. Y.; Rosenberg, G. A. Neuroinflammation: Friend and Foe for Ischemic Stroke. *J Neuroinflammation* **2019**, *16* (1), 142. https://doi.org/10.1186/s12974-019-1516-2.

(285) Guo, Y.; Dong, L.; Gong, A.; Zhang, J.; Jing, L.; Ding, T.; Li, P.-A. A.; Zhang, J.-Z. Damage to the Blood-Brain Barrier and Activation of Neuroinflammation by Focal Cerebral Ischemia under Hyperglycemic Condition. *Int J Mol Med* **2021**, *48* (1), 142. https://doi.org/10.3892/ijmm.2021.4975.

(286) Hu, X.; De Silva, T. M.; Chen, J.; Faraci, F. M. Cerebral Vascular Disease and Neurovascular Injury in Ischemic Stroke. *Circ Res* **2017**, *120* (3), 449–471. https://doi.org/10.1161/CIRCRESAHA.116.308427.

(287) Marchetti, L.; Engelhardt, B. Immune Cell Trafficking across the Blood-Brain Barrier in the Absence and Presence of Neuroinflammation. *Vasc Biol* **2020**, *2* (1), H1–H18. https://doi.org/10.1530/VB-19-0033.

(288) Bernardo-Castro, S.; Sousa, J. A.; Brás, A.; Cecília, C.; Rodrigues, B.; Almendra, L.; Machado, C.; Santo, G.; Silva, F.; Ferreira, L.; Santana, I.; Sargento-Freitas, J. Pathophysiology of Blood–Brain Barrier Permeability Throughout the Different Stages of Ischemic Stroke and Its Implication on Hemorrhagic Transformation and Recovery. *Front Neurol* **2020**, *11*, 594672. https://doi.org/10.3389/fneur.2020.594672.

(289) Fang, M.; Zhong, L.; Jin, X.; Cui, R.; Yang, W.; Gao, S.; Lv, J.; Li, B.; Liu, T. Effect of Inflammation on the Process of Stroke Rehabilitation and Poststroke Depression. *Front Psychiatry* **2019**, *10*, 184. https://doi.org/10.3389/fpsyt.2019.00184.

(290) Audebert, H. J.; Rott, M. M.; Eck, T.; Haberl, R. L. Systemic Inflammatory Response Depends on Initial Stroke Severity but Is Attenuated by Successful Thrombolysis. *Stroke* **2004**, *35* (9), 2128–2133. https://doi.org/10.1161/01.STR.0000137607.61697.77.

(291) Hauser, S. L.; Cree, B. A. C. Treatment of Multiple Sclerosis: A Review. *The American Journal of Medicine* **2020**, *133* (12), 1380-1390.e2. https://doi.org/10.1016/j.amjmed.2020.05.049.

(292) Haase, S.; Linker, R. A. Inflammation in Multiple Sclerosis. *Ther Adv Neurol Disord* **2021**, *14*, 17562864211007687. https://doi.org/10.1177/17562864211007687.

(293) Carstensen, M.; Christensen, T.; Stilund, M.; Møller, H. J.; Petersen, E. L.; Petersen, T. Activated Monocytes and Markers of Inflammation in Newly Diagnosed Multiple Sclerosis. *Immunol Cell Biol* **2020**, *98* (7), 549–562. https://doi.org/10.1111/imcb.12337.

(294) O'Loughlin, E.; Madore, C.; Lassmann, H.; Butovsky, O. Microglial Phenotypes and Functions in Multiple Sclerosis. *Cold Spring Harb Perspect Med* **2018**, *8* (2), a028993. https://doi.org/10.1101/cshperspect.a028993.

(295) Cignarella, F.; Filipello, F.; Bollman, B.; Cantoni, C.; Locca, A.; Mikesell, R.; Manis, M.; Ibrahim, A.; Deng, L.; Benitez, B. A.; Cruchaga, C.; Licastro, D.; Mihindukulasuriya, K.; Harari, O.; Buckland, M.; Holtzman, D. M.; Rosenthal, A.; Schwabe, T.; Tassi, I.; Piccio, L. TREM2 Activation on Microglia Promotes Myelin Debris Clearance and Remyelination in a Model of Multiple Sclerosis. *Acta Neuropathol* **2020**, *140* (4), 513–534. https://doi.org/10.1007/s00401-020-02193-z.

(296) Ostrom, Q. T.; Price, M.; Neff, C.; Cioffi, G.; Waite, K. A.; Kruchko, C.; Barnholtz-Sloan, J. S. CBTRUS Statistical Report: Primary Brain and Other Central Nervous System Tumors Diagnosed in the United States in 2015-2019. *Neuro Oncol* **2022**, *24* (Suppl 5), v1–v95. https://doi.org/10.1093/neuonc/noac202.

(297) Gabrusiewicz, K.; Rodriguez, B.; Wei, J.; Hashimoto, Y.; Healy, L. M.; Maiti, S. N.; Thomas, G.; Zhou, S.; Wang, Q.; Elakkad, A.; Liebelt, B. D.; Yaghi, N. K.; Ezhilarasan, R.; Huang, N.; Weinberg, J. S.; Prabhu, S. S.; Rao, G.; Sawaya, R.; Langford, L. A.; Bruner, J. M.; Fuller, G. N.; Bar-Or, A.; Li, W.; Colen, R. R.; Curran, M. A.; Bhat, K. P.; Antel, J. P.; Cooper, L. J.; Sulman, E. P.; Heimberger, A. B. Glioblastoma-Infiltrated Innate Immune Cells Resemble M0 Macrophage Phenotype. *JCI Insight* **2016**, *1* (2), e85841, 85841. https://doi.org/10.1172/jci.insight.85841.

(298) Ma, X.; Zhu, H.; Cheng, L.; Chen, X.; Shu, K.; Zhang, S. Targeting FGL2 in Glioma Immunosuppression and Malignant Progression. *Front Oncol* **2022**, *12*, 1004700. https://doi.org/10.3389/fonc.2022.1004700.

(299) Chen, A. X.; Gartrell, R. D.; Zhao, J.; Upadhyayula, P. S.; Zhao, W.; Yuan, J.; Minns, H. E.; Dovas, A.; Bruce, J. N.; Lasorella, A.; Iavarone, A.; Canoll, P.; Sims, P. A.; Rabadan, R. Single-Cell Characterization of Macrophages in Glioblastoma Reveals MARCO as a Mesenchymal pro-Tumor Marker. *Genome Med* **2021**, *13*, 88. https://doi.org/10.1186/s13073-021-00906-x.

(300) Peng, P.; Zhu, H.; Liu, D.; Chen, Z.; Zhang, X.; Guo, Z.; Dong, M.; Wan, L.; Zhang, P.; Liu, G.; Zhang, S.; Dong, F.; Hu, F.; Cheng, F.; Huang, S.; Guo, D.; Zhang, B.; Yu, X.;

Wan, F. TGFBI Secreted by Tumor-Associated Macrophages Promotes Glioblastoma Stem Cell-Driven Tumor Growth via Integrin Avβ5-Src-Stat3 Signaling. *Theranostics* **2022**, *12* (9), 4221–4236. https://doi.org/10.7150/thno.69605.

(301) Liu, Q.; Li, G.; Li, R.; Shen, J.; He, Q.; Deng, L.; Zhang, C.; Zhang, J. IL-6 Promotion of Glioblastoma Cell Invasion and Angiogenesis in U251 and T98G Cell Lines. *J Neurooncol* **2010**, *100* (2), 165–176. https://doi.org/10.1007/s11060-010-0158-0.

(302) Ravi, V. M.; Neidert, N.; Will, P.; Joseph, K.; Maier, J. P.; Kückelhaus, J.; Vollmer, L.; Goeldner, J. M.; Behringer, S. P.; Scherer, F.; Boerries, M.; Follo, M.; Weiss, T.; Delev, D.; Kernbach, J.; Franco, P.; Schallner, N.; Dierks, C.; Carro, M. S.; Hofmann, U. G.; Fung, C.; Sankowski, R.; Prinz, M.; Beck, J.; Salié, H.; Bengsch, B.; Schnell, O.; Heiland, D. H. T-Cell Dysfunction in the Glioblastoma Microenvironment Is Mediated by Myeloid Cells Releasing Interleukin-10. *Nat Commun* **2022**, *13* (1), 925. https://doi.org/10.1038/s41467-022-28523-1.

(303) Sulman, E. P.; Ismaila, N.; Armstrong, T. S.; Tsien, C.; Batchelor, T. T.; Cloughesy, T.; Galanis, E.; Gilbert, M.; Gondi, V.; Lovely, M.; Mehta, M.; Mumber, M. P.; Sloan, A.; Chang, S. M. Radiation Therapy for Glioblastoma: American Society of Clinical Oncology Clinical Practice Guideline Endorsement of the American Society for Radiation Oncology Guideline. *J Clin Oncol* **2017**, *35* (3), 361–369. https://doi.org/10.1200/JCO.2016.70.7562.

(304) Manrique-Guzmán, S.; Herrada-Pineda, T.; Revilla-Pacheco, F. Surgical Management of Glioblastoma. In *Glioblastoma*; De Vleeschouwer, S., Ed.; Codon Publications: Brisbane (AU), 2017.

(305) Vitrikas, K.; Dalton, H.; Breish, D. Cerebral Palsy:An Overview. *CEREBRAL PALSY* **2020**, *101* (4).

(306) Jung, E.; Romero, R.; Yeo, L.; Diaz-Primera, R.; Marin-Concha, J.; Para, R.; Lopez, A. M.; Pacora, P.; Gomez-Lopez, N.; Yoon, B. H.; Kim, C. J.; Berry, S. M.; Hsu, C.-D. The Fetal Inflammatory Response Syndrome: The Origins of a Concept, Pathophysiology, Diagnosis, and Obstetrical Implications. *Semin Fetal Neonatal Med* **2020**, *25* (4), 101146. https://doi.org/10.1016/j.siny.2020.101146.

(307) Kölliker-Frers, R.; Udovin, L.; Otero-Losada, M.; Kobiec, T.; Herrera, M. I.; Palacios, J.; Razzitte, G.; Capani, F. Neuroinflammation: An Integrating Overview of Reactive-Neuroimmune Cell Interactions in Health and Disease. *Mediators Inflamm* **2021**, *2021*, 9999146. https://doi.org/10.1155/2021/9999146.

(308) Kim, G. H.; Kim, J. E.; Rhie, S. J.; Yoon, S. The Role of Oxidative Stress in Neurodegenerative Diseases. *Exp Neurobiol* **2015**, *24* (4), 325–340. https://doi.org/10.5607/en.2015.24.4.325.

(309) Liy, P. M.; Puzi, N. N. A.; Jose, S.; Vidyadaran, S. Nitric Oxide Modulation in Neuroinflammation and the Role of Mesenchymal Stem Cells. *Exp Biol Med (Maywood)* **2021**, *246* (22), 2399–2406. https://doi.org/10.1177/1535370221997052.

(310) Pajares, M.; I. Rojo, A.; Manda, G.; Boscá, L.; Cuadrado, A. Inflammation in Parkinson's Disease: Mechanisms and Therapeutic Implications. *Cells* **2020**, *9* (7), 1687. https://doi.org/10.3390/cells9071687.

(311) Cho, H.; Kambhampati, S. P.; Lai, M. J.; Zhou, L.; Lee, G.; Xie, Y.; Hui, Q.; Kannan, R. M.; Duh, E. J. Dendrimer-Triamcinolone Acetonide Reduces Neuroinflammation, Pathological Angiogenesis, and Neuroretinal Dysfunction in Ischemic Retinopathy. *Adv Ther (Weinh)* **2021**, *4* (2), 2000181. https://doi.org/10.1002/adtp.202000181.

(312) Hollinger, K. R.; Sharma, A.; Tallon, C.; Lovell, L.; Thomas, A. G.; Zhu, X.; Wiseman, R.; Wu, Y.; Kambhampati, S. P.; Liaw, K.; Sharma, R.; Rojas, C.; Rais, R.; Kannan, S.; Kannan, R. M.; Slusher, B. S. Dendrimer-2PMPA Selectively Blocks Upregulated Microglial GCPII Activity and Improves Cognition in a Mouse Model of Multiple Sclerosis. *Nanotheranostics* **2022**, *6* (2), 126–142. https://doi.org/10.7150/ntno.63158.

(313) Zhang, F.; Zhang, Z.; Alt, J.; Kambhampati, S. P.; Sharma, A.; Singh, S.; Nance, E.; Thomas, A. G.; Rojas, C.; Rais, R.; Slusher, B. S.; Kannan, R. M.; Kannan, S. Dendrimer-Enabled Targeted Delivery Attenuates Glutamate Excitotoxicity and Improves Motor Function in a Rabbit Model of Cerebral Palsy. *Journal of Controlled Release* **2023**, *358*, 27–42. https://doi.org/10.1016/j.jconrel.2023.04.017.

(314) Zhang, D.; Ren, Y.; He, Y.; Chang, R.; Guo, S.; Ma, S.; Guan, F.; Yao, M. In Situ Forming and Biocompatible Hyaluronic Acid Hydrogel with Reactive Oxygen Species-Scavenging Activity to Improve Traumatic Brain Injury Repair by Suppressing Oxidative Stress and Neuroinflammation. *Materials Today Bio* **2022**, *15*, 100278. https://doi.org/10.1016/j.mtbio.2022.100278.

(315) Albashari, A.; He, Y.; Zhang, Y.; Ali, J.; Lin, F.; Zheng, Z.; Zhang, K.; Cao, Y.; Xu, C.; Luo, L.; Wang, J.; Ye, Q. Thermosensitive bFGF-Modified Hydrogel with Dental Pulp Stem Cells on Neuroinflammation of Spinal Cord Injury. *ACS Omega* **2020**, *5* (26), 16064–16075. https://doi.org/10.1021/acsomega.0c01379.

(316) Zou, Y.; Ma, D.; Shen, H.; Zhao, Y.; Xu, B.; Fan, Y.; Sun, Z.; Chen, B.; Xue, W.; Shi, Y.; Xiao, Z.; Gu, R.; Dai, J. Aligned Collagen Scaffold Combination with Human Spinal Cord-Derived Neural Stem Cells to Improve Spinal Cord Injury Repair. *Biomater. Sci.* **2020**, *8* (18), 5145–5156. https://doi.org/10.1039/D0BM00431F.

(317) Liu, X.; Zhang, G.; Wei, P.; Hao, L.; Zhong, L.; Zhong, K.; Liu, C.; Liu, P.; Feng, Q.; Wang, S.; Zhang, J.; Tian, R.; Zhou, L. 3D-Printed Collagen/Silk Fibroin/Secretome Derived from bFGF-Pretreated HUCMSCs Scaffolds Enhanced Therapeutic Ability in Canines Traumatic Brain Injury Model. *Front Bioeng Biotechnol* **2022**, *10*, 995099. https://doi.org/10.3389/fbioe.2022.995099.

(318) Liu, X.; Wang, J.; Wang, P.; Zhong, L.; Wang, S.; Feng, Q.; Wei, X.; Zhou, L. Hypoxia-Pretreated Mesenchymal Stem Cell-Derived Exosomes-Loaded Low-Temperature Extrusion 3D-Printed Implants for Neural Regeneration after Traumatic Brain Injury in Canines. *Frontiers in Bioengineering and Biotechnology* **2022**, *10*.

(319) Liu, X.-Y.; Feng, Y.-H.; Feng, Q.-B.; Zhang, J.-Y.; Zhong, L.; Liu, P.; Wang, S.; Huang, Y.-R.; Chen, X.-Y.; Zhou, L.-X. Low-Temperature 3D-Printed Collagen/Chitosan Scaffolds Loaded with Exosomes Derived from Neural Stem Cells Pretreated with Insulin Growth Factor-1 Enhance Neural Regeneration after Traumatic Brain Injury. *Neural Regen Res* **2023**, *18* (9), 1990–1998. https://doi.org/10.4103/1673-5374.366497.

(320) Liu, X.; Zhang, J.; Cheng, X.; Liu, P.; Feng, Q.; Wang, S.; Li, Y.; Gu, H.; Zhong, L.; Chen, M.; Zhou, L. Integrated Printed BDNF-Stimulated HUCMSCs-Derived Exosomes/Collagen/Chitosan Biological Scaffolds with 3D Printing Technology Promoted the Remodelling of Neural Networks after Traumatic Brain Injury. *Regenerative Biomaterials* **2023**, *10*, rbac085. https://doi.org/10.1093/rb/rbac085.

(321) Bourrier, A.; Szarpak-Jankowska, A.; Veliev, F.; Olarte-Hernandez, R.; Shkorbatova, P.; Bonizzato, M.; Rey, E.; Barraud, Q.; Briançon-Marjollet, A.; Auzely, R.; Courtine, G.; Bouchiat, V.; Delacour, C. Introducing a Biomimetic Coating for Graphene Neuroelectronics: Towardin-Vivoapplications. *Biomed Phys Eng Express* **2020**, *7* (1). https://doi.org/10.1088/2057-1976/ab42d6.

(322) Cui, Y.; Zhang, F.; Chen, G.; Yao, L.; Zhang, N.; Liu, Z.; Li, Q.; Zhang, F.; Cui, Z.; Zhang, K.; Li, P.; Cheng, Y.; Zhang, S.; Chen, X. A Stretchable and Transparent Electrode Based on PEGylated Silk Fibroin for In Vivo Dual-Modal Neural-Vascular Activity Probing. *Adv Mater* **2021**, *33* (34), e2100221. https://doi.org/10.1002/adma.202100221.

(323) Kleber, C.; Bruns, M.; Lienkamp, K.; Rühe, J.; Asplund, M. An Interpenetrating, Microstructurable and Covalently Attached Conducting Polymer Hydrogel for Neural Interfaces. *Acta Biomater* **2017**, *58*, 365–375. https://doi.org/10.1016/j.actbio.2017.05.056.

(324) Dobrovolskaia, M. A.; Aggarwal, P.; Hall, J. B.; McNeil, S. E. Preclinical Studies To Understand Nanoparticle Interaction with the Immune System and Its Potential Effects on Nanoparticle Biodistribution. *Mol. Pharmaceutics* **2008**, *5* (4), 487–495. https://doi.org/10.1021/mp800032f.

(325) Zhou, Y.; Peng, Z.; Seven, E. S.; Leblanc, R. M. Crossing the Blood-Brain Barrier with Nanoparticles. *J Control Release* **2018**, *270*, 290–303. https://doi.org/10.1016/j.jconrel.2017.12.015.

(326) Honary, S.; Zahir, F. Effect of Zeta Potential on the Properties of Nano-Drug Delivery Systems - A Review (Part 1). *Tropical Journal of Pharmaceutical Research* **2013**, *12* (2), 255–264. https://doi.org/10.4314/tjpr.v12i2.19.

(327) Ma, N.; Ma, C.; Li, C.; Wang, T.; Tang, Y.; Wang, H.; Moul, X.; Chen, Z.; Hel, N. Influence of Nanoparticle Shape, Size, and Surface Functionalization on Cellular Uptake. *J Nanosci Nanotechnol* **2013**, *13* (10), 6485–6498. https://doi.org/10.1166/jnn.2013.7525.

(328) Lombardo, S. M.; Schneider, M.; Türeli, A. E.; Günday Türeli, N. Key for Crossing the BBB with Nanoparticles: The Rational Design. *Beilstein J Nanotechnol* **2020**, *11*, 866–883. https://doi.org/10.3762/bjnano.11.72.

(329) Zhang, S.; Li, J.; Lykotrafitis, G.; Bao, G.; Suresh, S. Size-Dependent Endocytosis of Nanoparticles. *Adv Mater* **2009**, *21*, 419–424. https://doi.org/10.1002/adma.200801393.

(330) Godin, A. G.; Varela, J. A.; Gao, Z.; Danné, N.; Dupuis, J. P.; Lounis, B.; Groc, L.; Cognet, L. Single-Nanotube Tracking Reveals the Nanoscale Organization of the Extracellular Space in the Live Brain. *Nat Nanotechnol* **2017**, *12* (3), 238–243. https://doi.org/10.1038/nnano.2016.248.

(331) Nicholson, C.; Hrabětová, S. Brain Extracellular Space: The Final Frontier of Neuroscience. *Biophys J* **2017**, *113* (10), 2133–2142. https://doi.org/10.1016/j.bpj.2017.06.052.

(332) Singh, M. N.; Hemant, K. S. Y.; Ram, M.; Shivakumar, H. G. Microencapsulation: A Promising Technique for Controlled Drug Delivery. *Res Pharm Sci* **2010**, *5* (2), 65–77.

(333) Weng, S.; Lai, Q.-L.; Wang, J.; Zhuang, L.; Cheng, L.; Mo, Y.; Liu, L.; Zhao, Z.; Zhang, Y.; Qiao, S. The Role of Exosomes as Mediators of Neuroinflammation in the Pathogenesis and Treatment of Alzheimer's Disease. *Front Aging Neurosci* **2022**, *14*, 899944. https://doi.org/10.3389/fnagi.2022.899944.

(334) Long, X.; Yao, X.; Jiang, Q.; Yang, Y.; He, X.; Tian, W.; Zhao, K.; Zhang, H. Astrocyte-Derived Exosomes Enriched with miR-873a-5p Inhibit Neuroinflammation via Microglia Phenotype Modulation after Traumatic Brain Injury. *J Neuroinflammation* **2020**, *17* (1), 89. https://doi.org/10.1186/s12974-020-01761-0.

(335) Liu, X.; Zhang, M.; Liu, H.; Zhu, R.; He, H.; Zhou, Y.; Zhang, Y.; Li, C.; Liang, D.; Zeng, Q.; Huang, G. Bone Marrow Mesenchymal Stem Cell-Derived Exosomes Attenuate Cerebral Ischemia-Reperfusion Injury-Induced Neuroinflammation and Pyroptosis by Modulating Microglia M1/M2 Phenotypes. *Experimental Neurology* **2021**, *341*, 113700. https://doi.org/10.1016/j.expneurol.2021.113700.

(336) Ekström, K.; Crescitelli, R.; Pétursson, H. I.; Johansson, J.; Lässer, C.; Olofsson Bagge, R. Characterization of Surface Markers on Extracellular Vesicles Isolated from Lymphatic Exudate from Patients with Breast Cancer. *BMC Cancer* **2022**, *22* (1), 50. https://doi.org/10.1186/s12885-021-08870-w.

(337) Riazifar, M.; Mohammadi, M. R.; Pone, E. J.; Yeri, A.; Lässer, C.; Segaliny, A. I.; McIntyre, L. L.; Shelke, G. V.; Hutchins, E.; Hamamoto, A.; Calle, E. N.; Crescitelli, R.; Liao, W.; Pham, V.; Yin, Y.; Jayaraman, J.; Lakey, J. R. T.; Walsh, C. M.; Van Keuren-

Jensen, K.; Lotvall, J.; Zhao, W. Stem Cell-Derived Exosomes as Nanotherapeutics for Autoimmune and Neurodegenerative Disorders. *ACS Nano* **2019**, *13* (6), 6670–6688. https://doi.org/10.1021/acsnano.9b01004.

(338) Xian, P.; Hei, Y.; Wang, R.; Wang, T.; Yang, J.; Li, J.; Di, Z.; Liu, Z.; Baskys, A.; Liu, W.; Wu, S.; Long, Q. Mesenchymal Stem Cell-Derived Exosomes as a Nanotherapeutic Agent for Amelioration of Inflammation-Induced Astrocyte Alterations in Mice. *Theranostics* **2019**, *9* (20), 5956–5975. https://doi.org/10.7150/thno.33872.

(339) Long, X.; Yao, X.; Jiang, Q.; Yang, Y.; He, X.; Tian, W.; Zhao, K.; Zhang, H. Astrocyte-Derived Exosomes Enriched with miR-873a-5p Inhibit Neuroinflammation via Microglia Phenotype Modulation after Traumatic Brain Injury. *J Neuroinflammation* **2020**, *17*, 89. https://doi.org/10.1186/s12974-020-01761-0.

(340) Liu, W.; Rong, Y.; Wang, J.; Zhou, Z.; Ge, X.; Ji, C.; Jiang, D.; Gong, F.; Li, L.; Chen, J.; Zhao, S.; Kong, F.; Gu, C.; Fan, J.; Cai, W. Exosome-Shuttled miR-216a-5p from Hypoxic Preconditioned Mesenchymal Stem Cells Repair Traumatic Spinal Cord Injury by Shifting Microglial M1/M2 Polarization. *J Neuroinflammation* **2020**, *17* (1), 47. https://doi.org/10.1186/s12974-020-1726-7.

(341) Riazifar, M.; Mohammadi, M. R.; Pone, E. J.; Yeri, A.; Lässer, C.; Segaliny, A. I.; McIntyre, L. L.; Shelke, G. V.; Hutchins, E.; Hamamoto, A.; Calle, E. N.; Crescitelli, R.; Liao, W.; Pham, V.; Yin, Y.; Jayaraman, J.; Lakey, J. R. T.; Walsh, C. M.; Van Keuren-Jensen, K.; Lotvall, J.; Zhao, W. Stem Cell-Derived Exosomes as Nanotherapeutics for Autoimmune and Neurodegenerative Disorders. *ACS Nano* **2019**, *13* (6), 6670–6688. https://doi.org/10.1021/acsnano.9b01004.

(342) Cheng, Y.; Xu, Z.; Ma, M.; Xu, T. Dendrimers as Drug Carriers: Applications in Different Routes of Drug Administration. *J Pharm Sci* **2008**, *97* (1), 123–143. https://doi.org/10.1002/jps.21079.

(343) Choudhary, S.; Gupta, L.; Rani, S.; Dave, K.; Gupta, U. Impact of Dendrimers on Solubility of Hydrophobic Drug Molecules. *Front Pharmacol* **2017**, *8*, 261. https://doi.org/10.3389/fphar.2017.00261.

(344) Najafi, F.; Salami-Kalajahi, M.; Roghani-Mamaqani, H.; Kahaie-Khosrowshahi, A. A Comparative Study on Solubility Improvement of Tetracycline and Dexamethasone by Poly(Propylene Imine) and Polyamidoamine Dendrimers: An Insight into Cytotoxicity and Cell Proliferation. *J Biomed Mater Res A* **2020**, *108* (3), 485–495. https://doi.org/10.1002/jbm.a.36830.

(345) Namazi, H.; Adeli, M. Dendrimers of Citric Acid and Poly (Ethylene Glycol) as the New Drug-Delivery Agents. *Biomaterials* **2005**, *26* (10), 1175–1183. https://doi.org/10.1016/j.biomaterials.2004.04.014.

(346) Navath, R. S.; Kurtoglu, Y. E.; Wang, B.; Kannan, S.; Romero, R.; Kannan, R. M. Dendrimer-Drug Conjugates for Tailored Intracellular Drug Release Based on Glutathione Levels. *Bioconjug Chem* **2008**, *19* (12), 2446–2455. https://doi.org/10.1021/bc800342d.

(347) Kurtoglu, Y. E.; Mishra, M. K.; Kannan, S.; Kannan, R. M. Drug Release Characteristics of PAMAM Dendrimer-Drug Conjugates with Different Linkers. *Int J Pharm* **2010**, *384* (1–2), 189–194. https://doi.org/10.1016/j.ijpharm.2009.10.017.

(348) Majoros, I. J.; Myc, A.; Thomas, T.; Mehta, C. B.; Baker, J. R. PAMAM Dendrimer-Based Multifunctional Conjugate for Cancer Therapy: Synthesis, Characterization, and Functionality. *Biomacromolecules* **2006**, *7* (2), 572–579. https://doi.org/10.1021/bm0506142.

(349) Kuruvilla, S. P.; Tiruchinapally, G.; Crouch, A. C.; ElSayed, M. E. H.; Greve, J. M. Dendrimer-Doxorubicin Conjugates Exhibit Improved Anticancer Activity and Reduce Doxorubicin-Induced Cardiotoxicity in a Murine Hepatocellular Carcinoma Model. *PLoS One* **2017**, *12* (8), e0181944. https://doi.org/10.1371/journal.pone.0181944.

(350) McMahon, M. T.; Bulte, J. W. M. Two Decades of Dendrimers as Versatile MRI Agents: A Tale with and without Metals. *Wiley Interdiscip Rev Nanomed Nanobiotechnol* **2018**, *10* (3), e1496. https://doi.org/10.1002/wnan.1496.

(351) Zhao, L.; Zhu, J.; Cheng, Y.; Xiong, Z.; Tang, Y.; Guo, L.; Shi, X.; Zhao, J. Chlorotoxin-Conjugated Multifunctional Dendrimers Labeled with Radionuclide 131I for Single Photon Emission Computed Tomography Imaging and Radiotherapy of Gliomas. *ACS Appl Mater Interfaces* **2015**, *7* (35), 19798–19808. https://doi.org/10.1021/acsami.5b05836.

(352) Sharma, R.; Liaw, K.; Sharma, A.; Jimenez, A.; Chang, M.; Salazar, S.; Amlani, I.; Kannan, S.; Kannan, R. M. Glycosylation of PAMAM Dendrimers Significantly Improves Tumor Macrophage Targeting and Specificity in Glioblastoma. *J Control Release* **2021**, *337*, 179–192. https://doi.org/10.1016/j.jconrel.2021.07.018.

(353) Chauhan, A.; Anton, B.; Singh, M. K. 3 - Dendrimers for Drug Solubilization, Dissolution and Bioavailability. In *Pharmaceutical Applications of Dendrimers*; Chauhan, A., Kulhari, H., Eds.; Micro and Nano Technologies; Elsevier, 2020; pp 59–92. https://doi.org/10.1016/B978-0-12-814527-2.00003-2.

(354) Shi, A.; Khoury, E.; Sah, N.; Fowler, A.; Liaw, K.; Sharma, A.; Kannan, R.; Kannan, S. Characterization of Microglial Phagocytosis and Dendrimer Nanoparticle Uptake in a Neonatal Rabbit Model of Cerebral Palsy. *Precision Nanomedicine* **2021**, *4*. https://doi.org/10.33218/001c.29729.

(355) Dai, H.; Navath, R. S.; Balakrishnan, B.; Guru, B. R.; Mishra, M. K.; Romero, R.; Kannan, R. M.; Kannan, S. Intrinsic Targeting of Inflammatory Cells in the Brain by Polyamidoamine Dendrimers upon Subarachnoid Administration. *Nanomedicine (Lond)* **2010**, *5* (9), 1317–1329. https://doi.org/10.2217/nnm.10.89.

(356) Alnasser, Y.; Kambhampati, S. P.; Nance, E.; Rajbhandari, L.; Shrestha, S.; Venkatesan, A.; Kannan, R. M.; Kannan, S. Preferential and Increased Uptake of Hydroxyl-Terminated PAMAM Dendrimers by Activated Microglia in Rabbit Brain Mixed Glial Culture. *Molecules* **2018**, *23* (5), 1025. https://doi.org/10.3390/molecules23051025.

(357) Yang, S.; Datta, D.; Elizabeth Woo; Duque, A.; Morozov, Y. M.; Arellano, J.; Slusher, B. S.; Wang, M.; Arnsten, A. F. T. Inhibition of Glutamate-Carboxypeptidase-II in Dorsolateral Prefrontal Cortex: Potential Therapeutic Target for Neuroinflammatory Cognitive Disorders. *Mol Psychiatry* **2022**, *27* (10), 4252–4263. https://doi.org/10.1038/s41380-022-01656-x.

(358) Sah, N.; Zhang, Z.; Chime, A.; Fowler, A.; Mendez-Trendler, A.; Sharma, A.; Rangaramanujam, K.; Slusher, B.; Kannan, S. Dendrimer Conjugated Glutamate Carboxypeptidase II Inhibitor Restores Microglial Changes in a Rabbit Model of Cerebral Palsy. *Dev Neurosci* **2023**. https://doi.org/10.1159/000530389.

(359) Cekiç, O.; Chang, S.; Tseng, J. J.; Akar, Y.; Barile, G. R.; Schiff, W. M. Cataract Progression after Intravitreal Triamcinolone Injection. *Am J Ophthalmol* **2005**, *139* (6), 993–998. https://doi.org/10.1016/j.ajo.2005.01.022.

(360) Sharma, R.; Kambhampati, S. P.; Zhang, Z.; Sharma, A.; Chen, S.; Duh, E. I.; Kannan, S.; Tso, M. O. M.; Kannan, R. M. Dendrimer Mediated Targeted Delivery of Sinomenine for the Treatment of Acute Neuroinflammation in Traumatic Brain Injury. *J Control Release* **2020**, *323*, 361–375. https://doi.org/10.1016/j.jconrel.2020.04.036.

(361) Liaw, K.; Sharma, R.; Sharma, A.; Salazar, S.; Appiani La Rosa, S.; Kannan, R. M. Systemic Dendrimer Delivery of Triptolide to Tumor-Associated Macrophages Improves Anti-Tumor Efficacy and Reduces Systemic Toxicity in Glioblastoma. *J Control Release* **2021**, *329*, 434–444. https://doi.org/10.1016/j.jconrel.2020.12.003.

(362) Liaw, K.; Zhang, F.; Mangraviti, A.; Kannan, S.; Tyler, B.; Kannan, R. M. Dendrimer Size Effects on the Selective Brain Tumor Targeting in Orthotopic Tumor Models upon Systemic Administration. *Bioeng Transl Med* **2020**, *5* (2), e10160. https://doi.org/10.1002/btm2.10160.

(363) Zhang, Z.; Lin, Y.-A.; Kim, S.-Y.; Su, L.; Liu, J.; Kannan, R. M.; Kannan, S. Systemic Dendrimer-Drug Nanomedicines for Long-Term Treatment of Mild-Moderate Cerebral Palsy in a Rabbit Model. *J Neuroinflammation* **2020**, *17*, 319. https://doi.org/10.1186/s12974-020-01984-1.

(364) Fan, S.; Zheng, Y.; Liu, X.; Fang, W.; Chen, X.; Liao, W.; Jing, X.; Lei, M.; Tao, E.; Ma, Q.; Zhang, X.; Guo, R.; Liu, J. Curcumin-Loaded PLGA-PEG Nanoparticles Conjugated with B6 Peptide for Potential Use in Alzheimer's Disease. *Drug Deliv* **2018**, *25* (1), 1091–1102. https://doi.org/10.1080/10717544.2018.1461955.

(365) Schlachet, I.; Moshe Halamish, H.; Sosnik, A. Mixed Amphiphilic Polymeric Nanoparticles of Chitosan, Poly(Vinyl Alcohol) and Poly(Methyl Methacrylate) for

Intranasal Drug Delivery: A Preliminary In Vivo Study. *Molecules* **2020**, *25* (19), 4496. https://doi.org/10.3390/molecules25194496.

(366) Grillo, R.; de Melo, N. F. S.; de Araújo, D. R.; de Paula, E.; Rosa, A. H.; Fraceto, L. F. Polymeric Alginate Nanoparticles Containing the Local Anesthetic Bupivacaine. *J Drug Target* **2010**, *18* (9), 688–699. https://doi.org/10.3109/10611861003649738.

(367) Hu, C.-M. J.; Zhang, L.; Aryal, S.; Cheung, C.; Fang, R. H.; Zhang, L. Erythrocyte Membrane-Camouflaged Polymeric Nanoparticles as a Biomimetic Delivery Platform. *Proc Natl Acad Sci U S A* **2011**, *108* (27), 10980–10985. https://doi.org/10.1073/pnas.1106634108.

(368) Fang, F.; Ni, Y.; Yu, H.; Yin, H.; Yang, F.; Li, C.; Sun, D.; Pei, T.; Ma, J.; Deng, L.; Zhang, H.; Wang, G.; Li, S.; Shen, Y.; Liu, X. Inflammatory Endothelium-Targeted and Cathepsin Responsive Nanoparticles Are Effective against Atherosclerosis. *Theranostics* **2022**, *12* (9), 4200–4220. https://doi.org/10.7150/thno.70896.

(369) Palanikumar, L.; Al-Hosani, S.; Kalmouni, M.; Nguyen, V. P.; Ali, L.; Pasricha, R.; Barrera, F. N.; Magzoub, M. pH-Responsive High Stability Polymeric Nanoparticles for Targeted Delivery of Anticancer Therapeutics. *Commun Biol* **2020**, *3* (1), 1–17. https://doi.org/10.1038/s42003-020-0817-4.

(370) Xu, L.; Zhao, M.; Gao, W.; Yang, Y.; Zhang, J.; Pu, Y.; He, B. Polymeric Nanoparticles Responsive to Intracellular ROS for Anticancer Drug Delivery. *Colloids Surf B Biointerfaces* **2019**, *181*, 252–260. https://doi.org/10.1016/j.colsurfb.2019.05.064.

(371) Surnar, B.; Basu, U.; Banik, B.; Ahmad, A.; Marples, B.; Kolishetti, N.; Dhar, S. Nanotechnology-Mediated Crossing of Two Impermeable Membranes to Modulate the Stars of the Neurovascular Unit for Neuroprotection. *Proc Natl Acad Sci U S A* **2018**, *115* (52), E12333–E12342. https://doi.org/10.1073/pnas.1816429115.

(372) Surnar, B.; Shah, A. S.; Park, M.; Kalathil, A. A.; Kamran, M. Z.; Jaime, R. R.; Toborek, M.; Nair, M.; Kolishetti, N.; Dhar, S. Brain-Accumulating Nanoparticles for Assisting Astrocytes to Reduce Human Immunodeficiency Virus and Drug Abuse-Induced Neuroinflammation and Oxidative Stress. *ACS Nano* **2021**, *15* (10), 15741–15753. https://doi.org/10.1021/acsnano.0c09553.

(373) Akiyama, H.; Jalloh, S.; Park, S.; Lei, M.; Mostoslavsky, G.; Gummuluru, S. Expression of HIV-1 Intron-Containing RNA in Microglia Induces Inflammatory Responses. *J Virol* **2021**, *95* (5), e01386-20, JVI.01386-20. https://doi.org/10.1128/JVI.01386-20.

(374) Peng, H.; Sun, L.; Jia, B.; Lan, X.; Zhu, B.; Wu, Y.; Zheng, J. HIV-1-Infected and Immune-Activated Macrophages Induce Astrocytic Differentiation of Human Cortical Neural Progenitor Cells via the STAT3 Pathway. *PLoS One* **2011**, *6* (5), e19439. https://doi.org/10.1371/journal.pone.0019439.

(375) Hoenigl, M.; Chaillon, A.; Moore, D. J.; Morris, S. R.; Mehta, S. R.; Gianella, S.; Amico, K. R.; Little, S. J. Rapid HIV Viral Load Suppression in Those Initiating Antiretroviral Therapy at First Visit after HIV Diagnosis. *Sci Rep* **2016**, *6*, 32947. https://doi.org/10.1038/srep32947.

(376) Kim, H.-S.; Quon, M. J.; Kim, J.-A. New Insights into the Mechanisms of Polyphenols beyond Antioxidant Properties; Lessons from the Green Tea Polyphenol, Epigallocatechin 3-Gallate. *Redox Biol* **2014**, *2*, 187–195. https://doi.org/10.1016/j.redox.2013.12.022.

(377) Chowdhury, A.; Sarkar, J.; Chakraborti, T.; Pramanik, P. K.; Chakraborti, S. Protective Role of Epigallocatechin-3-Gallate in Health and Disease: A Perspective. *Biomed Pharmacother* **2016**, *78*, 50–59. https://doi.org/10.1016/j.biopha.2015.12.013.

(378) de la Torre, R.; de Sola, S.; Hernandez, G.; Farré, M.; Pujol, J.; Rodriguez, J.; Espadaler, J. M.; Langohr, K.; Cuenca-Royo, A.; Principe, A.; Xicota, L.; Janel, N.; Catuara-Solarz, S.; Sanchez-Benavides, G.; Bléhaut, H.; Dueñas-Espín, I.; Del Hoyo, L.; Benejam, B.; Blanco-Hinojo, L.; Videla, S.; Fitó, M.; Delabar, J. M.; Dierssen, M.; TESDAD study group. Safety and Efficacy of Cognitive Training plus Epigallocatechin-3-Gallate in Young Adults with Down's Syndrome (TESDAD): A Double-Blind, Randomised, Placebo-Controlled, Phase 2 Trial. *Lancet Neurol* **2016**, *15* (8), 801–810. https://doi.org/10.1016/S1474-4422(16)30034-5.

(379) Cano, A.; Ettcheto, M.; Espina, M.; Auladell, C.; Calpena, A. C.; Folch, J.; Barenys, M.; Sánchez-López, E.; Camins, A.; García, M. L. Epigallocatechin-3-Gallate Loaded PEGylated-PLGA Nanoparticles: A New Anti-Seizure Strategy for Temporal Lobe Epilepsy. *Nanomedicine* **2018**, *14* (4), 1073–1085. https://doi.org/10.1016/j.nano.2018.01.019.

(380) Firdous, A.; Sarwar, S.; Shah, F. A.; Tabasum, S.; Zeb, A.; Nadeem, H.; Alamro, A.; Alghamdi, A. A.; Alvi, A. M.; Naeem, K.; Khalid, M. S. Contribution of Attenuation of TNF-α and NF-κB in the Anti-Epileptic, Anti-Apoptotic and Neuroprotective Potential of Rosa Webbiana Fruit and Its Chitosan Encapsulation. *Molecules* **2021**, *26* (8), 2347. https://doi.org/10.3390/molecules26082347.

(381) Zhao, N.; Francis, N. L.; Song, S.; Kholodovych, V.; Calvelli, H. R.; Hoop, C. L.; Pang, Z. P.; Baum, J.; Uhrich, K. E.; Moghe, P. V. CD36-Binding Amphiphilic Nanoparticles for Attenuation of Alpha Synuclein-Induced Microglial Activation. *Adv Nanobiomed Res* **2022**, *2* (6), 2100120. https://doi.org/10.1002/anbr.202100120.

(382) Don, T.-M.; Chang, W.-J.; Jheng, P.-R.; Huang, Y.-C.; Chuang, E.-Y. Curcumin-Laden Dual-Targeting Fucoidan/Chitosan Nanocarriers for Inhibiting Brain Inflammation via Intranasal Delivery. *Int J Biol Macromol* **2021**, *181*, 835–846. https://doi.org/10.1016/j.ijbiomac.2021.04.045.

(383) Jafari, M.; Sriram, V.; Xu, Z.; Harris, G. M.; Lee, J.-Y. Fucoidan-Doxorubicin Nanoparticles Targeting P-Selectin for Effective Breast Cancer Therapy. *Carbohydr Polym* **2020**, *249*, 116837. https://doi.org/10.1016/j.carbpol.2020.116837.

(384) Yeini, E.; Ofek, P.; Pozzi, S.; Albeck, N.; Ben-Shushan, D.; Tiram, G.; Golan, S.; Kleiner, R.; Sheinin, R.; Israeli Dangoor, S.; Reich-Zeliger, S.; Grossman, R.; Ram, Z.; Brem, H.; Hyde, T. M.; Magod, P.; Friedmann-Morvinski, D.; Madi, A.; Satchi-Fainaro, R. P-Selectin Axis Plays a Key Role in Microglia Immunophenotype and Glioblastoma Progression. *Nat Commun* **2021**, *12* (1), 1912. https://doi.org/10.1038/s41467-021-22186-0.

(385) Chandrasekharan, U. M.; Siemionow, M.; Unsal, M.; Yang, L.; Poptic, E.; Bohn, J.; Ozer, K.; Zhou, Z.; Howe, P. H.; Penn, M.; DiCorleto, P. E. Tumor Necrosis Factor α (TNF-α) Receptor-II Is Required for TNF-α–Induced Leukocyte-Endothelial Interaction in Vivo. *Blood* **2007**, *109* (5), 1938–1944. https://doi.org/10.1182/blood-2006-05-020875.

(386) Li, J.; Pu, K. Semiconducting Polymer Nanomaterials as Near-Infrared Photoactivatable Protherapeutics for Cancer. *Acc Chem Res* **2020**, *53* (4), 752–762. https://doi.org/10.1021/acs.accounts.9b00569.

(387) Rejinold, N. S.; Choi, G.; Choy, J.-H. Recent Developments on Semiconducting Polymer Nanoparticles as Smart Photo-Therapeutic Agents for Cancer Treatments—A Review. *Polymers (Basel)* **2021**, *13* (6), 981. https://doi.org/10.3390/polym13060981.

(388) Li, B.; Li, N.; Chen, L.; Ren, S.; Gao, D.; Geng, H.; Fu, J.; Zhou, M.; Xing, C. Alleviating Neuroinflammation through Photothermal Conjugated Polymer Nanoparticles by Regulating Reactive Oxygen Species and Ca2+ Signaling. *ACS Appl Mater Interfaces* **2022**, *14* (43), 48416–48425. https://doi.org/10.1021/acsami.2c13322.

(389) Li, X.; Xu, X.; Xu, M.; Geng, Z.; Ji, P.; Liu, Y. Hydrogel Systems for Targeted Cancer Therapy. *Front Bioeng Biotechnol* **2023**, *11*, 1140436. https://doi.org/10.3389/fbioe.2023.1140436.

(390) Zhang, Y.; Zou, Z.; Liu, S.; Miao, S.; Liu, H. Nanogels as Novel Nanocarrier Systems for Efficient Delivery of CNS Therapeutics. *Frontiers in Bioengineering and Biotechnology* **2022**, *10*.

(391) de Lima, C. S. A.; Balogh, T. S.; Varca, J. P. R. O.; Varca, G. H. C.; Lugão, A. B.; A. Camacho-Cruz, L.; Bucio, E.; Kadlubowski, S. S. An Updated Review of Macro, Micro, and Nanostructured Hydrogels for Biomedical and Pharmaceutical Applications. *Pharmaceutics* **2020**, *12* (10), 970. https://doi.org/10.3390/pharmaceutics12100970.

(392) Al Harthi, S.; Alavi, S. E.; Radwan, M. A.; El Khatib, M. M.; AlSarra, I. A. Nasal Delivery of Donepezil HCl-Loaded Hydrogels for the Treatment of Alzheimer's Disease. *Sci Rep* **2019**, *9* (1), 9563. https://doi.org/10.1038/s41598-019-46032-y.

(393) Wang, Q.-S.; Li, K.; Gao, L.-N.; Zhang, Y.; Lin, K.-M.; Cui, Y.-L. Intranasal Delivery of Berberine via in Situ Thermoresponsive Hydrogels with Non-Invasive Therapy Exhibits Better Antidepressant-like Effects. *Biomater. Sci.* **2020**, *8* (10), 2853–2865. https://doi.org/10.1039/C9BM02006C.

(394) Taléns-Visconti, R.; de Julián-Ortiz, J. V.; Vila-Busó, O.; Diez-Sales, O.; Nácher, A. Intranasal Drug Administration in Alzheimer-Type Dementia: Towards Clinical Applications. *Pharmaceutics* **2023**, *15* (5), 1399. https://doi.org/10.3390/pharmaceutics15051399.

(395) Hasanzadeh, E.; Seifalian, A.; Mellati, A.; Saremi, J.; Asadpour, S.; Enderami, S. E.; Nekounam, H.; Mahmoodi, N. Injectable Hydrogels in Central Nervous System: Unique and Novel Platforms for Promoting Extracellular Matrix Remodeling and Tissue Engineering. *Materials Today Bio* **2023**, *20*, 100614. https://doi.org/10.1016/j.mtbio.2023.100614.

(396) Jensen, G.; Holloway, J. L.; Stabenfeldt, S. E. Hyaluronic Acid Biomaterials for Central Nervous System Regenerative Medicine. *Cells* **2020**, *9* (9), E2113. https://doi.org/10.3390/cells9092113.

(397) Bellotti, E.; Schilling, A. L.; Little, S. R.; Decuzzi, P. Injectable Thermoresponsive Hydrogels as Drug Delivery System for the Treatment of Central Nervous System Disorders: A Review. *Journal of Controlled Release* **2021**, *329*, 16–35. https://doi.org/10.1016/j.jconrel.2020.11.049.

(398) Li, Q.; Shao, X.; Dai, X.; Guo, Q.; Yuan, B.; Liu, Y.; Jiang, W. Recent Trends in the Development of Hydrogel Therapeutics for the Treatment of Central Nervous System Disorders. *NPG Asia Mater* **2022**, *14* (1), 1–14. https://doi.org/10.1038/s41427-022-00362-y.

(399) Nelson, D. W.; Gilbert, R. J. Extracellular Matrix-Mimetic Hydrogels for Treating Neural Tissue Injury: A Focus on Fibrin, Hyaluronic Acid, and Elastin-Like Polypeptide Hydrogels. *Adv Healthc Mater* **2021**, *10* (22), e2101329. https://doi.org/10.1002/adhm.202101329.

(400) Hen Lin, P.; Dong, Q.; Yian Chew, S. Injectable Hydrogels in Stroke and Spinal Cord Injury Treatment: A Review on Hydrogel Materials, Cell–Matrix Interactions and Glial Involvement. *Materials Advances* **2021**, *2* (8), 2561–2583. https://doi.org/10.1039/D0MA00732C.

(401) Jensen, G.; Holloway, J. L.; Stabenfeldt, S. E. Hyaluronic Acid Biomaterials for Central Nervous System Regenerative Medicine. *Cells* **2020**, *9* (9), 2113. https://doi.org/10.3390/cells9092113.

(402) Casini, P.; Nardi, I.; Ori, M. RHAMM mRNA Expression in Proliferating and Migrating Cells of the Developing Central Nervous System. *Gene Expression Patterns* **2010**, *10* (2), 93–97. https://doi.org/10.1016/j.gep.2009.12.003.

(403) Khaing, Z. Z.; Seidlits, S. K. Hyaluronic Acid and Neural Stem Cells: Implications for Biomaterial Design. *J. Mater. Chem. B* **2015**, *3* (40), 7850–7866. https://doi.org/10.1039/C5TB00974J.

(404) Chistyakov, D. V.; Astakhova, A. A.; Azbukina, N. V.; Goriainov, S. V.; Chistyakov, V. V.; Sergeeva, M. G. High and Low Molecular Weight Hyaluronic Acid Differentially Influences Oxylipins Synthesis in Course of Neuroinflammation. *International Journal of Molecular Sciences* **2019**, *20* (16), 3894. https://doi.org/10.3390/ijms20163894.

(405) Khaing, Z. Z.; Milman, B. D.; Vanscoy, J. E.; Seidlits, S. K.; Grill, R. J.; Schmidt, C. E. High Molecular Weight Hyaluronic Acid Limits Astrocyte Activation and Scar Formation after Spinal Cord Injury. *J. Neural Eng.* **2011**, *8* (4), 046033. https://doi.org/10.1088/1741-2560/8/4/046033.

(406) Salathia, S.; Gigliobianco, M. R.; Casadidio, C.; Di Martino, P.; Censi, R. Hyaluronic Acid-Based Nanosystems for CD44 Mediated Anti-Inflammatory and Antinociceptive Activity. *International Journal of Molecular Sciences* **2023**, *24* (8), 7286. https://doi.org/10.3390/ijms24087286.

(407) Wang, L.; Li, J.; Zhang, D.; Ma, S.; Zhang, J.; Gao, F.; Guan, F.; Yao, M. Dual-Enzymatically Crosslinked and Injectable Hyaluronic Acid Hydrogels for Potential Application in Tissue Engineering. *RSC Adv.* **2020**, *10* (5), 2870–2876. https://doi.org/10.1039/C9RA09531D.

(408) Wang, L.; Zhang, D.; Ren, Y.; Guo, S.; Li, J.; Ma, S.; Yao, M.; Guan, F. Injectable Hyaluronic Acid Hydrogel Loaded with BMSC and NGF for Traumatic Brain Injury Treatment. *Materials Today Bio* **2022**, *13*, 100201. https://doi.org/10.1016/j.mtbio.2021.100201.

(409) Zeng, C.-W. Multipotent Mesenchymal Stem Cell-Based Therapies for Spinal Cord Injury: Current Progress and Future Prospects. *Biology* **2023**, *12* (5), 653. https://doi.org/10.3390/biology12050653.

(410) Delplace, V.; Pickering, A. J.; Hettiaratchi, M. H.; Zhao, S.; Kivijärvi, T.; Shoichet, M. S. Inverse Electron-Demand Diels–Alder Methylcellulose Hydrogels Enable the Co-Delivery of Chondroitinase ABC and Neural Progenitor Cells. *Biomacromolecules* **2020**, *21* (6), 2421–2431.

(411) Ho, M. T.; Teal, C. J.; Shoichet, M. S. A Hyaluronan/Methylcellulose-Based Hydrogel for Local Cell and Biomolecule Delivery to the Central Nervous System. *Brain Research Bulletin* **2019**, *148*, 46–54. https://doi.org/10.1016/j.brainresbull.2019.03.005.

(412) Pakulska, M. M.; Vulic, K.; Shoichet, M. S. Affinity-Based Release of Chondroitinase ABC from a Modified Methylcellulose Hydrogel. *Journal of Controlled Release* **2013**, *171* (1), 11–16. https://doi.org/10.1016/j.jconrel.2013.06.029.

(413) Tam, R. Y.; Cooke, M. J.; Shoichet, M. S. A Covalently Modified Hydrogel Blend of Hyaluronan–Methyl Cellulose with Peptides and Growth Factors Influences Neural Stem/Progenitor Cell Fate. *J. Mater. Chem.* **2012**, *22* (37), 19402–19411. https://doi.org/10.1039/C2JM33680D.

(414) Bartlett, R. L.; Sharma, S.; Panitch, A. Cell-Penetrating Peptides Released from Thermosensitive Nanoparticles Suppress pro-Inflammatory Cytokine Response by Specifically Targeting Inflamed Cartilage Explants. *Nanomedicine* **2013**, *9* (3), 419–427. https://doi.org/10.1016/j.nano.2012.09.003.

(415) Shen, H.; Xu, B.; Yang, C.; Xue, W.; You, Z.; Wu, X.; Ma, D.; Shao, D.; Leong, K.; Dai, J. A DAMP-Scavenging, IL-10-Releasing Hydrogel Promotes Neural Regeneration and Motor Function Recovery after Spinal Cord Injury. *Biomaterials* **2022**, *280*, 121279.

(416) Tuladhar, A.; Obermeyer, J. M.; Payne, S. L.; Siu, R. C. W.; Zand, S.; Morshead, C. M.; Shoichet, M. S. Injectable Hydrogel Enables Local and Sustained Co-Delivery to the Brain: Two Clinically Approved Biomolecules, Cyclosporine and Erythropoietin, Accelerate Functional Recovery in Rat Model of Stroke. *Biomaterials* **2020**, *235*, 119794. https://doi.org/10.1016/j.biomaterials.2020.119794.

(417) Zheng, X.-Q.; Huang, J.-F.; Lin, J.-L.; Zhu, Y.-X.; Wang, M.-Q.; Guo, M.-L.; Zan, X.-J.; Wu, A.-M. Controlled Release of Baricitinib from a Thermos-Responsive Hydrogel System Inhibits Inflammation by Suppressing JAK2/STAT3 Pathway in Acute Spinal Cord Injury. *Colloids Surf B Biointerfaces* **2021**, *199*, 111532. https://doi.org/10.1016/j.colsurfb.2020.111532.

(418) Cunha, A.; Gaubert, A.; Latxague, L.; Dehay, B. PLGA-Based Nanoparticles for Neuroprotective Drug Delivery in Neurodegenerative Diseases. *Pharmaceutics* **2021**, *13* (7), 1042. https://doi.org/10.3390/pharmaceutics13071042.

(419) Ho, E.; Deng, Y.; Akbar, D.; Da, K.; Létourneau, M.; Morshead, C. M.; Chatenet, D.; Shoichet, M. S. Tunable Surface Charge Enables the Electrostatic Adsorption-Controlled Release of Neuroprotective Peptides from a Hydrogel–Nanoparticle Drug Delivery System. *ACS Appl. Mater. Interfaces* **2023**, *15* (1), 91–105. https://doi.org/10.1021/acsami.2c17631.

(420) Liu, Y.; Yang, G.; Jin, S.; Xu, L.; Zhao, C.-X. Development of High-Drug-Loading Nanoparticles. *Chempluschem* **2020**, *85* (9), 2143–2157. https://doi.org/10.1002/cplu.202000496.

(421) Shen, S.; Wu, Y.; Liu, Y.; Wu, D. High Drug-Loading Nanomedicines: Progress, Current Status, and Prospects. *Int J Nanomedicine* **2017**, *12*, 4085–4109. https://doi.org/10.2147/IJN.S132780.

(422) Choi, H. S.; Liu, W.; Misra, P.; Tanaka, E.; Zimmer, J. P.; Ipe, B. I.; Bawendi, M. G.; Frangioni, J. V. Renal Clearance of Nanoparticles. *Nat Biotechnol* **2007**, *25* (10), 1165–1170. https://doi.org/10.1038/nbt1340.

(423) Settles, M.; Etzrodt, M.; Kosanke, K.; Schiemann, M.; Zimmermann, A.; Meier, R.; Braren, R.; Huber, A.; Rummeny, E. J.; Weissleder, R.; Swirski, F. K.; Wildgruber, M. Different Capacity of Monocyte Subsets to Phagocytose Iron-Oxide Nanoparticles. *PLoS One* **2011**, *6* (10), e25197. https://doi.org/10.1371/journal.pone.0025197.

(424) Zolnik, B. S.; González-Fernández, Á.; Sadrieh, N.; Dobrovolskaia, M. A. Nanoparticles and the Immune System. *Endocrinology* **2010**, *151* (2), 458–465. https://doi.org/10.1210/en.2009-1082.

(425) Wang, Z.; Hood, E. D.; Nong, J.; Ding, J.; Marcos-Contreras, O. A.; Glassman, P. M.; Rubey, K. M.; Zaleski, M.; Espy, C. L.; Gullipali, D.; Miwa, T.; Muzykantov, V. R.; Song, W.-C.; Myerson, J. W.; Brenner, J. S. Combating Complement's Deleterious Effects on Nanomedicine by Conjugating Complement Regulatory Proteins to Nanoparticles. *Adv Mater* **2022**, *34* (8), e2107070. https://doi.org/10.1002/adma.202107070.

(426) Li, J.; Mooney, D. J. Designing Hydrogels for Controlled Drug Delivery. *Nat Rev Mater* **2016**, *1* (12), 16071. https://doi.org/10.1038/natrevmats.2016.71.

(427) Huang, X.; Brazel, C. S. On the Importance and Mechanisms of Burst Release in Matrix-Controlled Drug Delivery Systems. *J Control Release* **2001**, *73* (2–3), 121–136. https://doi.org/10.1016/s0168-3659(01)00248-6.

(428) Chehreghanianzabi, Y.; Barua, R.; Shi, T.; Yurgelevic, S.; Auner, G.; Markel, D. C.; Ren, W. Comparing the Release of Erythromycin and Vancomycin from Calcium Polyphosphate Hydrogel Using Different Drug Loading Methods. *J Biomed Mater Res B Appl Biomater* **2020**, *108* (2), 475–483. https://doi.org/10.1002/jbm.b.34404.

(429) McKenzie, M.; Betts, D.; Suh, A.; Bui, K.; Kim, L. D.; Cho, H. Hydrogel-Based Drug Delivery Systems for Poorly Water-Soluble Drugs. *Molecules* **2015**, *20* (11), 20397–20408. https://doi.org/10.3390/molecules201119705.

(430) Ansorena, E.; De Berdt, P.; Ucakar, B.; Simón-Yarza, T.; Jacobs, D.; Schakman, O.; Jankovski, A.; Deumens, R.; Blanco-Prieto, M. J.; Préat, V.; Rieux, A. des. Injectable Alginate Hydrogel Loaded with GDNF Promotes Functional Recovery in a Hemisection Model of Spinal Cord Injury. *International Journal of Pharmaceutics* **2013**, *455* (1), 148–158. https://doi.org/10.1016/j.ijpharm.2013.07.045.

(431) Xue, F.; Liu, T.; Liu, X.; Chen, K.; Duan, L.; Gao, G. Electroconductive and Porous Graphene-Xanthan Gum Gel Scaffold for Spinal Cord Regeneration. *European Polymer Journal* **2022**, *173*, 111225. https://doi.org/10.1016/j.eurpolymj.2022.111225.

(432) Dryg, I. Modulating Neuroinflammation with Porous Templated Scaffolds. PhD Thesis, 2019.

(433) *Ice-Templated Scaffolds with Microridged Pores Direct DRG Neurite Growth - Riblett - 2012 - Advanced Functional Materials - Wiley Online Library*. https://onlinelibrary.wiley.com/doi/10.1002/adfm.201201323 (accessed 2024-02-09).

(434) Tran, K. A.; DeOre, B. J.; Ikejiani, D.; Means, K.; Paone, L. S.; De Marchi, L.; Suprewicz, Ł.; Koziol, K.; Bouyer, J.; Byfield, F. J.; Jin, Y.; Georges, P.; Fischer, I.; Janmey, P. A.; Galie, P. A. Matching Mechanical Heterogeneity of the Native Spinal Cord Augments

Axon Infiltration in 3D-Printed Scaffolds. *Biomaterials* **2023**, *295*, 122061. https://doi.org/10.1016/j.biomaterials.2023.122061.

(435) Moncal, K. K.; Tigli Aydın, R. S.; Godzik, K. P.; Acri, T. M.; Heo, D. N.; Rizk, E.; Wee, H.; Lewis, G. S.; Salem, A. K.; Ozbolat, I. T. Controlled Co-Delivery of pPDGF-B and pBMP-2 from Intraoperatively Bioprinted Bone Constructs Improves the Repair of Calvarial Defects in Rats. *Biomaterials* **2022**, *281*, 121333. https://doi.org/10.1016/j.biomaterials.2021.121333.

(436) Zhuge, W.; Liu, H.; Wang, W.; Wang, J. Microfluidic Bioscaffolds for Regenerative Engineering. *Engineered Regeneration* **2022**, *3* (1), 110–120. https://doi.org/10.1016/j.engreg.2021.12.003.

(437) Zhao, M.; Liu, H.; Zhang, X.; Wang, H.; Tao, T.; Qin, J. A Flexible Microfluidic Strategy to Generate Grooved Microfibers for Guiding Cell Alignment. *Biomater. Sci.* **2021**, *9* (14), 4880–4890. https://doi.org/10.1039/D1BM00549A.

(438) Ma, Y.-H.; Shi, H.-J.; Wei, Q.-S.; Deng, Q.-W.; Sun, J.-H.; Liu, Z.; Lai, B.-Q.; Li, G.; Ding, Y.; Niu, W.-T.; Zeng, Y.-S.; Zeng, X. Developing a Mechanically Matched Decellularized Spinal Cord Scaffold for the in Situ Matrix-Based Neural Repair of Spinal Cord Injury. *Biomaterials* **2021**, *279*, 121192. https://doi.org/10.1016/j.biomaterials.2021.121192.

(439) *A novel decellularization method to produce brain scaffolds - PubMed*. https://pubmed.ncbi.nlm.nih.gov/32866727/ (accessed 2023-03-14).

(440) *Anisotropic 3D scaffolds for spinal cord guided repair: Current concepts | Elsevier Enhanced Reader*. https://doi.org/10.1016/j.bioadv.2023.213353.

(441) Zhang, J.; Liu, X.; Ma, K.; Chen, M.; Xu, H.; Niu, X.; Gu, H.; Wang, R.; Chen, X.; Sun, H. Collagen/Heparin Scaffold Combined with Vascular Endothelial Growth Factor Promotes the Repair of Neurological Function in Rats with Traumatic Brain Injury. *Biomater. Sci.* **2021**, *9* (3), 745–764. https://doi.org/10.1039/C9BM01446B.

(442) Ma, J.; Li, J.; Wang, X.; Li, M.; Teng, W.; Tao, Z.; Xie, J.; Ma, Y.; Shi, Q.; Li, B.; Saijilafu. GDNF-Loaded Polydopamine Nanoparticles-Based Anisotropic Scaffolds Promote Spinal Cord Repair by Modulating Inhibitory Microenvironment. *Advanced Healthcare Materials* **2023**, *12* (8), 2202377. https://doi.org/10.1002/adhm.202202377.

(443) Ma, S.; Feng, X.; Liu, F.; Wang, B.; Zhang, H.; Niu, X. The Pro-Inflammatory Response of Macrophages Regulated by Acid Degradation Products of Poly(Lactide-Co-Glycolide) Nanoparticles. *Engineering in Life Sciences* **2021**, *21* (10), 709–720. https://doi.org/10.1002/elsc.202100040.

(444) Zhang, G.; Zhen, A.; Chen, J.; Du, B.; Luo, F.; Li, J.; Tan, H. In Vitro Effects of Waterborne Polyurethane 3D Scaffolds Containing Poly(Lactic-Co-Glycolic Acid)s of

Different Lactic Acid/Glycolic Acid Ratios on the Inflammatory Response. *Polymers (Basel)* **2023**, *15* (7), 1786. https://doi.org/10.3390/polym15071786.

(445) Du, B.; Yin, H.; Chen, Y.; Lin, W.; Wang, Y.; Zhao, D.; Wang, G.; He, X.; Li, J.; Li, Z.; Luo, F.; Tan, H.; Fu, Q. A Waterborne Polyurethane 3D Scaffold Containing PLGA with a Controllable Degradation Rate and an Anti-Inflammatory Effect for Potential Applications in Neural Tissue Repair. *J. Mater. Chem. B* **2020**, *8* (20), 4434–4446. https://doi.org/10.1039/D0TB00656D.

(446) Hao, H.; Shao, J.; Deng, Y.; He, S.; Luo, F.; Wu, Y.; Li, J.; Tan, H.; Li, J.; Fu, Q. Synthesis and Characterization of Biodegradable Lysine-Based Waterborne Polyurethane for Soft Tissue Engineering Applications. *Biomater. Sci.* **2016**, *4* (11), 1682–1690. https://doi.org/10.1039/C6BM00588H.

(447) Liu, X.; Wang, J.; Wang, P.; Zhong, L.; Wang, S.; Feng, Q.; Wei, X.; Zhou, L. Hypoxia-Pretreated Mesenchymal Stem Cell-Derived Exosomes-Loaded Low-Temperature Extrusion 3D-Printed Implants for Neural Regeneration after Traumatic Brain Injury in Canines. *Front Bioeng Biotechnol* **2022**, *10*, 1025138. https://doi.org/10.3389/fbioe.2022.1025138.

(448) Liu, X.; Zhang, G.; Wei, P.; Zhong, L.; Chen, Y.; Zhang, J.; Chen, X.; Zhou, L. Three-Dimensional-Printed Collagen/Chitosan/Secretome Derived from HUCMSCs Scaffolds for Efficient Neural Network Reconstruction in Canines with Traumatic Brain Injury. *Regenerative Biomaterials* **2022**, *9*, rbac043. https://doi.org/10.1093/rb/rbac043.

(449) Li, Y.; Yang, L.; Hou, Y.; Zhang, Z.; Chen, M.; Wang, M.; Liu, J.; Wang, J.; Zhao, Z.; Xie, C.; Lu, X. Polydopamine-Mediated Graphene Oxide and Nanohydroxyapatite-Incorporated Conductive Scaffold with an Immunomodulatory Ability Accelerates Periodontal Bone Regeneration in Diabetes. *Bioact Mater* **2022**, *18*, 213–227. https://doi.org/10.1016/j.bioactmat.2022.03.021.

(450) Liu, Z.; Deng, Q.; Qin, G.; Yang, J.; Zhang, H.; Ren, J.; Qu, X. Biomarker-Activated Multifunctional Lysosome-Targeting Chimeras Mediated Selective Degradation of Extracellular Amyloid Fibrils. *Chem* **2023**, *9* (7), 2016–2038. https://doi.org/10.1016/j.chempr.2023.06.003.

(451) Zhu, T.; Wang, H.; Gu, H.; Ju, L.; Wu, X.; Pan, W.; Zhao, M.; Yang, J.; Liu, P. Melanin-like Polydopamine Nanoparticles Mediating Anti-Inflammatory and Rescuing Synaptic Loss for Inflammatory Depression Therapy. *Journal of Nanobiotechnology* **2023**, *21* (1), 52. https://doi.org/10.1186/s12951-023-01807-4.

(452) Vetter, R. J.; Williams, J. C.; Hetke, J. F.; Nunamaker, E. A.; Kipke, D. R. Chronic Neural Recording Using Silicon-Substrate Microelectrode Arrays Implanted in Cerebral Cortex. *IEEE Trans Biomed Eng* **2004**, *51* (6), 896–904. https://doi.org/10.1109/TBME.2004.826680.

(453) Schjetnan, A. G. P.; Luczak, A. Recording Large-Scale Neuronal Ensembles with Silicon Probes in the Anesthetized Rat. *J Vis Exp* **2011**, No. 56, 3282. https://doi.org/10.3791/3282.

(454) Barz, F.; Trouillet, V.; Paul, O.; Ruther, P. CMOS-Compatible, Flexible, Intracortical Neural Probes. *IEEE Transactions on Biomedical Engineering* **2020**, *67* (5), 1366–1376. https://doi.org/10.1109/TBME.2019.2936740.

(455) Joseph, K.; Kirsch, M.; Johnston, M.; Münkel, C.; Stieglitz, T.; Haas, C. A.; Hofmann, U. G. Transcriptional Characterization of the Glial Response Due to Chronic Neural Implantation of Flexible Microprobes. *Biomaterials* **2021**, *279*, 121230. https://doi.org/10.1016/j.biomaterials.2021.121230.

(456) Lee, H. C.; Gaire, J.; Currlin, S. W.; McDermott, M. D.; Park, K.; Otto, K. J. Foreign Body Response to Intracortical Microelectrodes Is Not Altered with Dip-Coating of Polyethylene Glycol (PEG). *Front Neurosci* **2017**, *11*, 513. https://doi.org/10.3389/fnins.2017.00513.

(457) Sharafkhani, N.; Kouzani, A. Z.; Adams, S. D.; Long, J. M.; Lissorgues, G.; Rousseau, L.; Orwa, J. O. Neural Tissue-Microelectrode Interaction: Brain Micromotion, Electrical Impedance, and Flexible Microelectrode Insertion. *Journal of Neuroscience Methods* **2022**, *365*, 109388. https://doi.org/10.1016/j.jneumeth.2021.109388.

(458) Duncan, J.; Sridharan, A.; Kumar, S. S.; Iradukunda, D.; Muthuswamy, J. Biomechanical Micromotion at the Neural Interface Modulates Intracellular Membrane Potentialsin Vivo. *J Neural Eng* **2021**, *18* (4). https://doi.org/10.1088/1741-2552/ac0a56.

(459) Song, S.; Druschel, L. N.; Chan, E. R.; Capadona, J. R. Differential Expression of Genes Involved in the Chronic Response to Intracortical Microelectrodes. *Acta Biomaterialia* **2023**, *169*, 348–362. https://doi.org/10.1016/j.actbio.2023.07.038.

(460) Akhavan, O.; Ghaderi, E. The Use of Graphene in the Self-Organized Differentiation of Human Neural Stem Cells into Neurons under Pulsed Laser Stimulation. *J Mater Chem B* **2014**, *2* (34), 5602–5611. https://doi.org/10.1039/c4tb00668b.

(461) Pampaloni, N. P.; Lottner, M.; Giugliano, M.; Matruglio, A.; D'Amico, F.; Prato, M.; Garrido, J. A.; Ballerini, L.; Scaini, D. Single-Layer Graphene Modulates Neuronal Communication and Augments Membrane Ion Currents. *Nat Nanotechnol* **2018**, *13* (8), 755–764. https://doi.org/10.1038/s41565-018-0163-6.

(462) Girish, C. M.; Sasidharan, A.; Gowd, G. S.; Nair, S.; Koyakutty, M. Confocal Raman Imaging Study Showing Macrophage Mediated Biodegradation of Graphene in Vivo. *Adv Healthc Mater* **2013**, *2* (11), 1489–1500. https://doi.org/10.1002/adhm.201200489.

(463) Kurapati, R.; Martìn, C.; Palermo, V.; Nishina, Y.; Bianco, A. Biodegradation of Graphene Materials Catalyzed by Human Eosinophil Peroxidase. *Faraday Discuss* **2021**, *227*, 189–203. https://doi.org/10.1039/c9fd00094a.

(464) Kurapati, R.; Russier, J.; Squillaci, M. A.; Treossi, E.; Ménard-Moyon, C.; Del Rio-Castillo, A. E.; Vazquez, E.; Samorì, P.; Palermo, V.; Bianco, A. Dispersibility-Dependent Biodegradation of Graphene Oxide by Myeloperoxidase. *Small* **2015**, *11* (32), 3985–3994. https://doi.org/10.1002/smll.201500038.

(465) Dong, X.; Ma, Y.; Zhu, G.; Huang, Y.; Wang, J.; Chan-Park, M. B.; Wang, L.; Huang, W.; Chen, P. Synthesis of Graphene–Carbon Nanotube Hybrid Foam and Its Use as a Novel Three-Dimensional Electrode for Electrochemical Sensing. *J. Mater. Chem.* **2012**, *22* (33), 17044. https://doi.org/10.1039/c2jm33286h.

(466) Wallace, G. G.; Chen, J.; Li, D.; Moulton, S. E.; Razal, J. M. Nanostructured Carbon Electrodes. *J. Mater. Chem.* **2010**, *20* (18), 3553. https://doi.org/10.1039/b918672g.

(467) Ryu, M.; Yang, J. H.; Ahn, Y.; Sim, M.; Lee, K. H.; Kim, K.; Lee, T.; Yoo, S.-J.; Kim, S. Y.; Moon, C.; Je, M.; Choi, J.-W.; Lee, Y.; Jang, J. E. Enhancement of Interface Characteristics of Neural Probe Based on Graphene, ZnO Nanowires, and Conducting Polymer PEDOT. *ACS Appl Mater Interfaces* **2017**, *9* (12), 10577–10586. https://doi.org/10.1021/acsami.7b02975.

(468) Khademhosseini, A.; Suh, K. Y.; Yang, J. M.; Eng, G.; Yeh, J.; Levenberg, S.; Langer, R. Layer-by-Layer Deposition of Hyaluronic Acid and Poly-L-Lysine for Patterned Cell Co-Cultures. *Biomaterials* **2004**, *25* (17), 3583–3592. https://doi.org/10.1016/j.biomaterials.2003.10.033.

(469) Adhesion of Cells to Surfaces Coated with Polylysine. Applications to Electron Microscopy. *J Cell Biol* **1975**, *66* (1), 198–200.

(470) Faussner, A.; Deininger, M. M.; Weber, C.; Steffens, S. Direct Addition of Poly-Lysine or Poly-Ethylenimine to the Medium: A Simple Alternative to Plate Pre-Coating. *PLoS One* **2022**, *17* (7), e0260173. https://doi.org/10.1371/journal.pone.0260173.

(471) Gökaltun, A.; Kang, Y. B. (Abraham); Yarmush, M. L.; Usta, O. B.; Asatekin, A. Simple Surface Modification of Poly(Dimethylsiloxane) via Surface Segregating Smart Polymers for Biomicrofluidics. *Sci Rep* **2019**, *9* (1), 7377. https://doi.org/10.1038/s41598-019-43625-5.

(472) Spencer, K. C.; Sy, J. C.; Ramadi, K. B.; Graybiel, A. M.; Langer, R.; Cima, M. J. Characterization of Mechanically Matched Hydrogel Coatings to Improve the Biocompatibility of Neural Implants. *Sci Rep* **2017**, *7* (1), 1952. https://doi.org/10.1038/s41598-017-02107-2.

(473) Frey, L.; Bandaru, P.; Zhang, Y. S.; O'Kelly, K.; Khademhosseini, A.; Shin, S. R. A Dual-Layered Microfluidic System for Long-Term Controlled In Situ Delivery of Multiple Anti-Inflammatory Factors for Chronic Neural Applications. *Adv Funct Mater* **2018**, *28* (12), 1702009. https://doi.org/10.1002/adfm.201702009.

(474) Stewart, E.; Kobayashi, N. R.; Higgins, M. J.; Quigley, A. F.; Jamali, S.; Moulton, S. E.; Kapsa, R. M. I.; Wallace, G. G.; Crook, J. M. Electrical Stimulation Using Conductive Polymer Polypyrrole Promotes Differentiation of Human Neural Stem Cells: A Biocompatible Platform for Translational Neural Tissue Engineering. *Tissue Eng Part C Methods* **2015**, *21* (4), 385–393. https://doi.org/10.1089/ten.TEC.2014.0338.

(475) Sun, K.-H.; Liu, Z.; Liu, C.; Yu, T.; Shang, T.; Huang, C.; Zhou, M.; Liu, C.; Ran, F.; Li, Y.; Shi, Y.; Pan, L. Evaluation of in Vitro and in Vivo Biocompatibility of a Myo-Inositol Hexakisphosphate Gelated Polyaniline Hydrogel in a Rat Model. *Sci Rep* **2016**, *6*, 23931. https://doi.org/10.1038/srep23931.

(476) Pavone, L.; Moyanova, S.; Mastroiacovo, F.; Fazi, L.; Busceti, C.; Gaglione, A.; Martinello, K.; Fucile, S.; Bucci, D.; Prioriello, A.; Nicoletti, F.; Fornai, F.; Morales, P.; Senesi, R. Chronic Neural Interfacing with Cerebral Cortex Using Single-Walled Carbon Nanotube-Polymer Grids. *J Neural Eng* **2020**, *17* (3), 036032. https://doi.org/10.1088/1741-2552/ab98db.

(477) Lu, L.; Fu, X.; Liew, Y.; Zhang, Y.; Zhao, S.; Xu, Z.; Zhao, J.; Li, D.; Li, Q.; Stanley, G. B.; Duan, X. Soft and MRI Compatible Neural Electrodes from Carbon Nanotube Fibers. *Nano Lett.* **2019**, *19* (3), 1577–1586. https://doi.org/10.1021/acs.nanolett.8b04456.

(478) Zhu, H. *Safety and Feasibility of Stromal Vascular Fraction (SVF) Combined With Functional Self-Assembling Peptide Nanofiber Hydrogels in the Treatment of Spinal Cord Injury*; Clinical trial registration NCT05967325; clinicaltrials.gov, 2023. https://clinicaltrials.gov/study/NCT05967325 (accessed 2023-09-01).

(479) Zhai, H.; Zhou, J.; Xu, J.; Sun, X.; Xu, Y.; Qiu, X.; Zhang, C.; Wu, Z.; Long, H.; Bai, Y.; Quan, D. Mechanically Strengthened Hybrid Peptide-Polyester Hydrogel and Potential Applications in Spinal Cord Injury Repair. *Biomed Mater* **2020**, *15* (5), 055031. https://doi.org/10.1088/1748-605X/ab9e45.

(480) Aphios. *Safety, Tolerability and Efficacy Assessment of Intranasal Nanoparticles of APH-1105, A Novel Alpha Secretase Modulator For Mild to Moderate Cognitive Impairment Due to Alzheimer's Disease(AD)*; Clinical trial registration NCT03806478; clinicaltrials.gov, 2021. https://clinicaltrials.gov/study/NCT03806478 (accessed 2023-09-12).

(481) Huang, X.; He, D.; Pan, Z.; Luo, G.; Deng, J. Reactive-Oxygen-Species-Scavenging Nanomaterials for Resolving Inflammation. *Materials Today Bio* **2021**, *11*, 100124. https://doi.org/10.1016/j.mtbio.2021.100124.

(482) Agarwal, G.; Roy, A.; Kumar, H.; Srivastava, A. Graphene-Collagen Cryogel Controls Neuroinflammation and Fosters Accelerated Axonal Regeneration in Spinal Cord Injury. *Biomaterials Advances* **2022**, *139*, 212971.

(483) Rapp, T. L.; DeForest, C. A. Visible Light-Responsive Dynamic Biomaterials: Going Deeper and Triggering More. *Adv Healthc Mater* **2020**, *9* (7), e1901553. https://doi.org/10.1002/adhm.201901553.

(484) Rapp, T. L.; DeForest, C. A. Tricolor Visible Wavelength-Selective Photodegradable Hydrogel Biomaterials. *Nat Commun* **2023**, *14* (1), 5250. https://doi.org/10.1038/s41467-023-40805-w.

(485) Clement, M.; Daniel, G.; Trelles, M. Optimising the Design of a Broad-Band Light Source for the Treatment of Skin. *J Cosmet Laser Ther* **2005**, *7* (3–4), 177–189. https://doi.org/10.1080/14764170500344575.

(486) Ash, C.; Dubec, M.; Donne, K.; Bashford, T. Effect of Wavelength and Beam Width on Penetration in Light-Tissue Interaction Using Computational Methods. *Lasers Med Sci* **2017**, *32* (8), 1909–1918. https://doi.org/10.1007/s10103-017-2317-4.

(487) Anderson, M. A.; O'Shea, T. M.; Burda, J. E.; Ao, Y.; Barlatey, S. L.; Bernstein, A. M.; Kim, J. H.; James, N. D.; Rogers, A.; Kato, B.; Wollenberg, A. L.; Kawaguchi, R.; Coppola, G.; Wang, C.; Deming, T. J.; He, Z.; Courtine, G.; Sofroniew, M. V. Required Growth Facilitators Propel Axon Regeneration across Complete Spinal Cord Injury. *Nature* **2018**, *561* (7723), 396–400. https://doi.org/10.1038/s41586-018-0467-6.

(488) Zhong, J.; Xu, J.; Lu, S.; Wang, Z.; Zheng, Y.; Tang, Q.; Zhu, J.; Zhu, T. A Prevascularization Strategy Using Novel Fibrous Porous Silk Scaffolds for Tissue Regeneration in Mice with Spinal Cord Injury. *Stem Cells and Development* **2020**, *29* (9), 615–624. https://doi.org/10.1089/scd.2019.0199.

(489) Guo, S.; Redenski, I.; Landau, S.; Szklanny, A.; Merdler, U.; Levenberg, S. Prevascularized Scaffolds Bearing Human Dental Pulp Stem Cells for Treating Complete Spinal Cord Injury. *Adv Healthc Mater* **2020**, *9* (20), e2000974. https://doi.org/10.1002/adhm.202000974.

(490) Tran, K. A.; Partyka, P. P.; Jin, Y.; Bouyer, J.; Fischer, I.; Galie, P. A. Vascularization of Self-Assembled Peptide Scaffolds for Spinal Cord Injury Repair. *Acta Biomater* **2020**, *104*, 76–84. https://doi.org/10.1016/j.actbio.2019.12.033.

(491) Dai, J. *Safety and Efficacy of Functional Neural Regeneration Collagen Scaffold Transplantation in Complete (AISA) Acute Spinal Cord Injury Patients*; Clinical trial registration NCT02510365; clinicaltrials.gov, 2020. https://clinicaltrials.gov/study/NCT02510365 (accessed 2023-09-01).

(492) Dai, J. *Safety and Efficacy of Functional Neural Regeneration Collagen Scaffold Transplantation Combined With Epidural Electrical Stimulation for Spinal Cord Injury Repair*; Clinical trial registration NCT03966794; clinicaltrials.gov, 2019. https://clinicaltrials.gov/study/NCT03966794 (accessed 2023-09-01).

(493) Dai, J. *NeuroRegen Scaffold™ With Bone Marrow Mononuclear Cells Transplantation vs. Intradural Decompression and Adhesiolysis in Patients With Chronic Spinal Cord Injury*; Clinical trial registration NCT02688062; clinicaltrials.gov, 2020. https://clinicaltrials.gov/study/NCT02688062 (accessed 2023-09-01).

(494) InVivo Therapeutics. *Randomized, Controlled, Single-Blind Study of Probable Benefit of the Neuro-Spinal Scaffold™ for Safety and Neurologic Recovery in Subjects With Complete Thoracic AIS A Spinal Cord Injury as Compared to Standard of Care*; Clinical trial registration NCT03762655; clinicaltrials.gov, 2022. https://clinicaltrials.gov/study/NCT03762655 (accessed 2023-09-01).

(495) Cullen, D. K.; Tang-Schomer, M. D.; Struzyna, L. A.; Patel, A. R.; Johnson, V. E.; Wolf, J. A.; Smith, D. H. Microtissue Engineered Constructs with Living Axons for Targeted Nervous System Reconstruction. *Tissue Eng Part A* **2012**, *18* (21–22), 2280–2289. https://doi.org/10.1089/ten.tea.2011.0534.

(496) Thau, L.; Reddy, V.; Singh, P. Anatomy, Central Nervous System. In *StatPearls*; StatPearls Publishing: Treasure Island (FL), 2024.

(497) Margetis, K.; Das, J. M.; Emmady, P. D. Spinal Cord Injuries. In *StatPearls*; StatPearls Publishing: Treasure Island (FL), 2026.

(498) Moeendarbary, E.; Weber, I. P.; Sheridan, G. K.; Koser, D. E.; Soleman, S.; Haenzi, B.; Bradbury, E. J.; Fawcett, J.; Franze, K. The Soft Mechanical Signature of Glial Scars in the Central Nervous System. *Nat Commun* **2017**, *8* (1), 14787. https://doi.org/10.1038/ncomms14787.

(499) Monje, P. V.; Deng, L.; Xu, X.-M. Human Schwann Cell Transplantation for Spinal Cord Injury: Prospects and Challenges in Translational Medicine. *Frontiers in Cellular Neuroscience* **2021**, *15*.

(500) Hettiaratchi, M. H.; O'Meara, M. J.; Teal, C. J.; Payne, S. L.; Pickering, A. J.; Shoichet, M. S. Local Delivery of Stabilized Chondroitinase ABC Degrades Chondroitin Sulfate Proteoglycans in Stroke-Injured Rat Brains. *J Control Release* **2019**, *297*, 14–25. https://doi.org/10.1016/j.jconrel.2019.01.033.

(501) Sandoval-Castellanos, A. M.; Claeyssens, F.; Haycock, J. W. Biomimetic Surface Delivery of NGF and BDNF to Enhance Neurite Outgrowth. *Biotechnology and Bioengineering* **2020**, *117* (10), 3124–3135. https://doi.org/10.1002/bit.27466.

(502) Ramos Ferrer, P.; Vardhan, S.; Sakiyama-Elbert, S. Sustained Neurotrophin-3 Delivery from Hyaluronic Acid Hydrogels for Neural Tissue Regeneration. *J Biomed Mater Res A* **2024**, *112* (8), 1188–1199. https://doi.org/10.1002/jbm.a.37596.

(503) Ahuja, C. S.; Wilson, J. R.; Nori, S.; Kotter, M. R. N.; Druschel, C.; Curt, A.; Fehlings, M. G. Traumatic Spinal Cord Injury. *Nat Rev Dis Primers* **2017**, *3* (1), 17018. https://doi.org/10.1038/nrdp.2017.18.

(504) Cheriyan, T.; Ryan, D. J.; Weinreb, J. H.; Cheriyan, J.; Paul, J. C.; Lafage, V.; Kirsch, T.; Errico, T. J. Spinal Cord Injury Models: A Review. *Spinal Cord* **2014**, *52* (8), 588–595. https://doi.org/10.1038/sc.2014.91.

(505) Koffler, J.; Zhu, W.; Qu, X.; Platoshyn, O.; Dulin, J. N.; Brock, J.; Graham, L.; Lu, P.; Sakamoto, J.; Marsala, M.; Chen, S.; Tuszynski, M. H. Biomimetic 3D-Printed Scaffolds for Spinal Cord Injury Repair. *Nat Med* **2019**, *25* (2), 263–269. https://doi.org/10.1038/s41591-018-0296-z.

(506) Galindo, A. N.; Frey Rubio, D. A.; Hettiaratchi, M. H. Biomaterial Strategies for Regulating the Neuroinflammatory Response. *Mater. Adv.* **2024**, *5* (10), 4025–4054. https://doi.org/10.1039/D3MA00736G.

(507) Karimi, A.; Shojaei, A.; Tehrani, P. Mechanical Properties of the Human Spinal Cord under the Compressive Loading. *J Chem Neuroanat* **2017**, *86*, 15–18. https://doi.org/10.1016/j.jchemneu.2017.07.004.

(508) Stanners, M.; O'Riordan, M.; Theodosiou, E.; Souppez, J.-B. R. G.; Gardner, A. The Mechanical Properties of the Spinal Cord: A Systematic Review. *The Spine Journal* **2024**, *24* (7), 1302–1312. https://doi.org/10.1016/j.spinee.2024.02.022.

(509) Roth, J. G.; Huang, M. S.; Navarro, R. S.; Akram, J. T.; LeSavage, B. L.; Heilshorn, S. C. Tunable Hydrogel Viscoelasticity Modulates Human Neural Maturation. *Sci. Adv.* **2023**, *9* (42), eadh8313. https://doi.org/10.1126/sciadv.adh8313.

(510) Walczak, P. A.; Perez-Esteban, P.; Bassett, D. C.; Hill, E. J. Modelling the Central Nervous System: Tissue Engineering of the Cellular Microenvironment. *Emerging Topics in Life Sciences* **2021**, *5* (4), 507–517. https://doi.org/10.1042/ETLS20210245.

(511) Mohammed Butt, A.; Rupareliya, V.; Hariharan, A.; Kumar, H. Building a Pathway to Recovery: Targeting ECM Remodeling in CNS Injuries. *Brain Research* **2023**, *1819*, 148533. https://doi.org/10.1016/j.brainres.2023.148533.

(512) Peters, A.; Sherman, L. S. Diverse Roles for Hyaluronan and Hyaluronan Receptors in the Developing and Adult Nervous System. *International Journal of Molecular Sciences* **2020**, *21* (17), 5988. https://doi.org/10.3390/ijms21175988.

(513) Ho, M. T.; Teal, C. J.; Shoichet, M. S. A Hyaluronan/Methylcellulose-Based Hydrogel for Local Cell and Biomolecule Delivery to the Central Nervous System. *Brain Research Bulletin* **2019**, *148*, 46–54. https://doi.org/10.1016/j.brainresbull.2019.03.005.

(514) Murenu, N.; Tuerker, E.; Wiessler, A.-L.; Faber, J.; Liashenko, I.; Weigelt, J.; Tessmar, J.; Dalton, P. D.; Jablonka, S.; Andrade Mier, M. S.; Villmann, C.; Budday, S.; Schaefer, N. Purpose-Adaptable Reinforced 3D Hyaluronic-Acid Based Platform to Study Pathomechanisms of the Central Nervous System. *Adv Healthc Mater* **2026**, e05946. https://doi.org/10.1002/adhm.202505946.

(515) Lee, K. Y.; Mooney, D. J. Alginate: Properties and Biomedical Applications. *Progress in Polymer Science* **2012**, *37* (1), 106–126. https://doi.org/10.1016/j.progpolymsci.2011.06.003.

(516) Kruczkowska, W.; Gałęziewska, J.; Grabowska, K. H.; Gromek, P.; Czajkowska, K.; Rybicki, M.; Kciuk, M.; Kłosiński, K. K. From Molecules to Mind: The Critical Role of Chitosan, Collagen, Alginate, and Other Biopolymers in Neuroprotection and Neurodegeneration. *Molecules* **2025**, *30* (5), 1017. https://doi.org/10.3390/molecules30051017.

(517) Jarrah, R.; Sammak, S. E.; Onyedimma, C.; Ghaith, A. K.; Moinuddin, F. M.; Bhandarkar, A. R.; Siddiqui, A.; Madigan, N.; Bydon, M. The Role of Alginate Hydrogels as a Potential Treatment Modality for Spinal Cord Injury: A Comprehensive Review of the Literature. *Neurospine* **2022**, *19* (2), 272–280. https://doi.org/10.14245/ns.2244186.093.

(518) Agulhon, P.; Markova, V.; Robitzer, M.; Quignard, F.; Mineva, T. Structure of Alginate Gels: Interaction of Diuronate Units with Divalent Cations from Density Functional Calculations. *Biomacromolecules* **2012**, *13* (6), 1899–1907. https://doi.org/10.1021/bm300420z.

(519) Matyash, M.; Despang, F.; Mandal, R.; Fiore, D.; Gelinsky, M.; Ikonomidou, C. Novel Soft Alginate Hydrogel Strongly Supports Neurite Growth and Protects Neurons against Oxidative Stress. *Tissue Eng Part A* **2012**, *18* (1–2), 55–66. https://doi.org/10.1089/ten.TEA.2011.0097.

(520) Zhou, J.; Wu, Y.; Tang, Z.; Zou, K.; Chen, J.; Lei, Z.; Wan, X.; Liu, Y.; Zhang, H.; Wang, Y.; Blesch, A.; Lei, T.; Liu, S. Alginate Hydrogel Cross-Linked by Ca2+ to Promote Spinal Cord Neural Stem/Progenitor Cell Differentiation and Functional Recovery after a Spinal Cord Injuryhh. *Regen Biomater* **2022**, *9*, rbac057. https://doi.org/10.1093/rb/rbac057.

(521) Sattler, R.; Tymianski, M. Molecular Mechanisms of Calcium-Dependent Excitotoxicity. *J Mol Med (Berl)* **2000**, *78* (1), 3–13. https://doi.org/10.1007/s001090000077.

(522) Chan, G.; Mooney, D. J. Ca2+ Released from Calcium Alginate Gels Can Promote Inflammatory Responses in Vitro and in Vivo. *Acta Biomater* **2013**, *9* (12), 10.1016/j.actbio.2013.08.002. https://doi.org/10.1016/j.actbio.2013.08.002.

(523) Matyash, M.; Despang, F.; Ikonomidou, C.; Gelinsky, M. Swelling and Mechanical Properties of Alginate Hydrogels with Respect to Promotion of Neural Growth. *Tissue Engineering Part C: Methods* **2014**, *20* (5), 401–411. https://doi.org/10.1089/ten.tec.2013.0252.

(524) Wang, W.; Huang, Y.; Pan, Y.; Dabbour, M.; Dai, C.; Zhou, M.; He, R. Sodium Alginate Modifications: A Critical Review of Current Strategies and Emerging Applications. *Foods* **2025**, *14* (22), 3931. https://doi.org/10.3390/foods14223931.

(525) Zavvarian, M.-M.; Hong, J.; Fehlings, M. G. The Functional Role of Spinal Interneurons Following Traumatic Spinal Cord Injury. *Front Cell Neurosci* **2020**, *14*, 127. https://doi.org/10.3389/fncel.2020.00127.

(526) Zholudeva, L. V.; Abraira, V. E.; Satkunendrarajah, K.; McDevitt, T. C.; Goulding, M. D.; Magnuson, D. S. K.; Lane, M. A. Spinal Interneurons as Gatekeepers to Neuroplasticity after Injury or Disease. *J Neurosci* **2021**, *41* (5), 845–854. https://doi.org/10.1523/JNEUROSCI.1654-20.2020.

(527) Butts, J. C.; McCreedy, D. A.; Martinez-Vargas, J. A.; Mendoza-Camacho, F. N.; Hookway, T. A.; Gifford, C. A.; Taneja, P.; Noble-Haeusslein, L.; McDevitt, T. C. Differentiation of V2a Interneurons from Human Pluripotent Stem Cells. *Proc Natl Acad Sci U S A* **2017**, *114* (19), 4969–4974. https://doi.org/10.1073/pnas.1608254114.

(528) Butts, J. C.; Iyer, N.; White, N.; Thompson, R.; Sakiyama-Elbert, S.; McDevitt, T. C. V2a Interneuron Differentiation from Mouse and Human Pluripotent Stem Cells. *Nat Protoc* **2019**, *14* (11), 3033–3058. https://doi.org/10.1038/s41596-019-0203-1.

(529) Jensen, V. N.; Huffman, E. E.; Jalufka, F. L.; Pritchard, A. L.; Baumgartner, S.; Walling, I.; C. Gibbs, H.; McCreedy, D. A.; Alilain, W. J.; Crone, S. A. V2a Neurons Restore Diaphragm Function in Mice Following Spinal Cord Injury. *Proceedings of the National Academy of Sciences* **2024**, *121* (11), e2313594121. https://doi.org/10.1073/pnas.2313594121.

(530) Zholudeva, L. V.; Iyer, N.; Qiang, L.; Spruance, V. M.; Randelman, M. L.; White, N. W.; Bezdudnaya, T.; Fischer, I.; Sakiyama-Elbert, S. E.; Lane, M. A. Transplantation of Neural Progenitors and V2a Interneurons after Spinal Cord Injury. *J Neurotrauma* **2018**, *35* (24), 2883–2903. https://doi.org/10.1089/neu.2017.5439.

(531) Iyer, N. R.; Huettner, J. E.; Butts, J. C.; Brown, C. R.; Sakiyama-Elbert, S. E. Generation of Highly Enriched V2a Interneurons from Mouse Embryonic Stem Cells. *Experimental Neurology* **2016**, *277*, 305–316. https://doi.org/10.1016/j.expneurol.2016.01.011.

(532) Brown, C. R.; Butts, J. C.; McCreedy, D. A.; Sakiyama-Elbert, S. E. Generation of V2a Interneurons from Mouse Embryonic Stem Cells. *Stem Cells and Development* **2014**, *23* (15), 1765–1776. https://doi.org/10.1089/scd.2013.0628.

(533) Squair, J. W.; Milano, M.; de Coucy, A.; Gautier, M.; Skinnider, M. A.; James, N. D.; Cho, N.; Lasne, A.; Kathe, C.; Hutson, T. H.; Ceto, S.; Baud, L.; Galan, K.; Aureli, V.; Laskaratos, A.; Barraud, Q.; Deming, T. J.; Kohman, R. E.; Schneider, B. L.; He, Z.; Bloch, J.; Sofroniew, M. V.; Courtine, G.; Anderson, M. A. Recovery of Walking after Paralysis by Regenerating Characterized Neurons to Their Natural Target Region. *Science* **2023**, *381* (6664), 1338–1345. https://doi.org/10.1126/science.adi6412.

(534) Zholudeva, L. V.; Fortino, T.; Agrawal, A.; Vila, O. F.; Williams, M.; McDevitt, T.; Lane, M. A.; Srivastava, D. Human Spinal Interneurons Repair the Injured Spinal Cord through

Synaptic Integration. *bioRxiv* **2024**, 2024.01.11.575264. https://doi.org/10.1101/2024.01.11.575264.

(535) Thompson, R. E.; Pardieck, J.; Smith, L.; Kenny, P.; Crawford, L.; Shoichet, M.; Sakiyama-Elbert, S. Effect of Hyaluronic Acid Hydrogels Containing Astrocyte-Derived Extracellular Matrix and/or V2a Interneurons on Histologic Outcomes Following Spinal Cord Injury. *Biomaterials* **2018**, *162*, 208–223. https://doi.org/10.1016/j.biomaterials.2018.02.013.

(536) Hettiaratchi, M. H.; Führmann, T.; Shoichet, M. S. Recent Advances in Regenerative Medicine Approaches for Spinal Cord Injuries. *Current Opinion in Biomedical Engineering* **2017**, *4*, 40–49. https://doi.org/10.1016/j.cobme.2017.08.002.

(537) Ballios, B. G.; Cooke, M. J.; Donaldson, L.; Coles, B. L. K.; Morshead, C. M.; der Kooy, D. van; Shoichet, M. S. A Hyaluronan-Based Injectable Hydrogel Improves the Survival and Integration of Stem Cell Progeny Following Transplantation. *Stem Cell Reports* **2015**, *4* (6), 1031–1045. https://doi.org/10.1016/j.stemcr.2015.04.008.

(538) Mothe, A. J.; Tam, R. Y.; Zahir, T.; Tator, C. H.; Shoichet, M. S. Repair of the Injured Spinal Cord by Transplantation of Neural Stem Cells in a Hyaluronan-Based Hydrogel. *Biomaterials* **2013**, *34* (15), 3775–3783. https://doi.org/10.1016/j.biomaterials.2013.02.002.

(539) Ho, M. T.; Teal, C. J.; Shoichet, M. S. A Hyaluronan/Methylcellulose-Based Hydrogel for Local Cell and Biomolecule Delivery to the Central Nervous System. *Brain Research Bulletin* **2019**, *148*, 46–54. https://doi.org/10.1016/j.brainresbull.2019.03.005.

(540) Yang, Y.-H.; Khan, Z.; Ma, C.; Lim, H. J.; Smith Callahan, L. A. Optimization of Adhesive Conditions for Neural Differentiation of Murine Embryonic Stem Cells Using Hydrogels Functionalized with Continuous Ile-Lys-Val-Ala-Val Concentration Gradients. *Acta Biomaterialia* **2015**, *21*, 55–62. https://doi.org/10.1016/j.actbio.2015.04.031.

(541) Glotzbach, K.; Stamm, N.; Weberskirch, R.; Faissner, A. Hydrogels Derivatized With Cationic Moieties or Functional Peptides as Efficient Supports for Neural Stem Cells. *Front. Neurosci.* **2020**, *14*. https://doi.org/10.3389/fnins.2020.00475.

(542) Saha, K.; Keung, A. J.; Irwin, E. F.; Li, Y.; Little, L.; Schaffer, D. V.; Healy, K. E. Substrate Modulus Directs Neural Stem Cell Behavior. *Biophysical Journal* **2008**, *95* (9), 4426–4438. https://doi.org/10.1529/biophysj.108.132217.

(543) Lee, K. Y.; Mooney, D. J. Alginate: Properties and Biomedical Applications. *Progress in Polymer Science* **2012**, *37* (1), 106–126. https://doi.org/10.1016/j.progpolymsci.2011.06.003.

(544) Zholudeva, L. V.; Karliner, J. S.; Dougherty, K. J.; Lane, M. A. Anatomical Recruitment of Spinal V2a Interneurons into Phrenic Motor Circuitry after High Cervical Spinal Cord

Injury. *Journal of Neurotrauma* **2017**, *34* (21), 3058–3065. https://doi.org/10.1089/neu.2017.5045.

(545) Salamatina, A.; Yang, J. H.; Brenner-Morton, S.; Bikoff, J. B.; Fang, L.; Kintner, C. R.; Jessell, T. M.; Sweeney, L. B. Differential Loss of Spinal Interneurons in a Mouse Model of ALS. *Neuroscience* **2020**, *450*, 81–95. https://doi.org/10.1016/j.neuroscience.2020.08.011.

(546) *Functional Self-Assembling Peptide Nanofiber Hydrogels Designed for Nerve Degeneration | ACS Applied Materials & Interfaces*. https://pubs.acs.org/doi/10.1021/acsami.5b11473 (accessed 2026-05-31).

(547) Tarus, D.; Hamard, L.; Caraguel, F.; Wion, D.; Szarpak-Jankowska, A.; van der Sanden, B.; Auzély-Velty, R. Design of Hyaluronic Acid Hydrogels to Promote Neurite Outgrowth in Three Dimensions. *ACS Appl. Mater. Interfaces* **2016**, *8* (38), 25051–25059. https://doi.org/10.1021/acsami.6b06446.

(548) Alderfer, L.; Saha, S.; Fan, F.; Wu, J.; Littlepage, L. E.; Hanjaya-Putra, D. Multi-Parameter Tunable Synthetic Matrix for Engineering Lymphatic Vessels. *Commun Biol* **2024**, *7* (1), 1262. https://doi.org/10.1038/s42003-024-06935-7.

(549) Maynard, S. A.; Gelmi, A.; Skaalure, S. C.; Pence, I. J.; Lee-Reeves, C.; Sero, J. E.; Whittaker, T. E.; Stevens, M. M. Nanoscale Molecular Quantification of Stem Cell–Hydrogel Interactions. *ACS Nano* **2020**, *14* (12), 17321–17332. https://doi.org/10.1021/acsnano.0c07428.

(550) Le, N. N. T.; Liu, T. L.; Johnston, J.; Krutty, J. D.; Templeton, K. M.; Harms, V.; Dias, A.; Le, H.; Gopalan, P.; Murphy, W. L. Customized Hydrogel Substrates for Serum-Free Expansion of Functional hMSCs. *Biomater Sci* **2020**, *8* (14), 3819–3829. https://doi.org/10.1039/d0bm00540a.

(551) Schense, J. C.; Bloch, J.; Aebischer, P.; Hubbell, J. A. Enzymatic Incorporation of Bioactive Peptides into Fibrin Matrices Enhances Neurite Extension. *Nat Biotechnol* **2000**, *18* (4), 415–419. https://doi.org/10.1038/74473.

(552) Meland, M. N.; Herndon, M. E.; Stipp, C. S. Expression of Alpha5 Integrin Rescues Fibronectin Responsiveness in NT2N CNS Neuronal Cells. *J Neurosci Res* **2010**, *88* (1), 222–232. https://doi.org/10.1002/jnr.22171.

(553) Flanagan, L. A.; Rebaza, L. M.; Derzic, S.; Schwartz, P. H.; Monuki, E. S. Regulation of Human Neural Precursor Cells by Laminin and Integrins. *J Neurosci Res* **2006**, *83* (5), 845–856. https://doi.org/10.1002/jnr.20778.

(554) Beller, J. A.; Snow, D. M. Proteoglycans: Road Signs for Neurite Outgrowth. *Neural Regen Res* **2014**, *9* (4), 343–355. https://doi.org/10.4103/1673-5374.128235.

(555) Distler, T.; Lauria, I.; Detsch, R.; Sauter, C. M.; Bendt, F.; Kapr, J.; Rütten, S.; Boccaccini, A. R.; Fritsche, E. Neuronal Differentiation from Induced Pluripotent Stem Cell-Derived Neurospheres by the Application of Oxidized Alginate-Gelatin-Laminin Hydrogels. *Biomedicines* **2021**, *9* (3), 261. https://doi.org/10.3390/biomedicines9030261.

(556) Moxon, S. R.; Corbett, N. J.; Fisher, K.; Potjewyd, G.; Domingos, M.; Hooper, N. M. Blended Alginate/Collagen Hydrogels Promote Neurogenesis and Neuronal Maturation. *Mater Sci Eng C Mater Biol Appl* **2019**, *104*, 109904. https://doi.org/10.1016/j.msec.2019.109904.

(557) Thompson, R. E.; Lake, A.; Kenny, P.; Saunders, M. N.; Sakers, K.; Iyer, N. R.; Dougherty, J. D.; Sakiyama-Elbert, S. E. Different Mixed Astrocyte Populations Derived from Embryonic Stem Cells Have Variable Neuronal Growth Support Capacities. *Stem Cells Dev* **2017**, *26* (22), 1597–1611. https://doi.org/10.1089/scd.2017.0121.

(558) Takahashi, M. The GDNF/RET Signaling Pathway and Human Diseases. *Cytokine Growth Factor Rev* **2001**, *12* (4), 361–373. https://doi.org/10.1016/s1359-6101(01)00012-0.

(559) Ortmann, S. D.; Hellenbrand, D. J. Glial Cell Line-Derived Neurotrophic Factor as a Treatment after Spinal Cord Injury. *Neural Regen Res* **2018**, *13* (10), 1733–1734. https://doi.org/10.4103/1673-5374.238610.

(560) Rosich, K.; Hanna, B. F.; Ibrahim, R. K.; Hellenbrand, D. J.; Hanna, A. The Effects of Glial Cell Line-Derived Neurotrophic Factor after Spinal Cord Injury. *Journal of Neurotrauma* **2017**, *34* (24), 3311–3325. https://doi.org/10.1089/neu.2017.5175.

(561) Baloh, R. H.; Johnson, J. P.; Avalos, P.; Allred, P.; Svendsen, S.; Gowing, G.; Roxas, K.; Wu, A.; Donahue, B.; Osborne, S.; Lawless, G.; Shelley, B.; Wheeler, K.; Prina, C.; Fine, D.; Kendra-Romito, T.; Stokes, H.; Manoukian, V.; Muthukumaran, A.; Garcia, L.; Bañuelos, M. G.; Godoy, M.; Bresee, C.; Yu, H.; Drazin, D.; Ross, L.; Naruse, R.; Babu, H.; Macklin, E. A.; Vo, A.; Elsayegh, A.; Tourtellotte, W.; Maya, M.; Burford, M.; Diaz, F.; Patil, C. G.; Lewis, R. A.; Svendsen, C. N. Transplantation of Human Neural Progenitor Cells Secreting GDNF into the Spinal Cord of Patients with ALS: A Phase 1/2a Trial. *Nat Med* **2022**, *28* (9), 1813–1822. https://doi.org/10.1038/s41591-022-01956-3.

(562) Moriarty, N.; Cabré, S.; Alamilla, V.; Pandit, A.; Dowd, E. Encapsulation of Young Donor Age Dopaminergic Grafts in a GDNF-Loaded Collagen Hydrogel Further Increases Their Survival, Reinnervation, and Functional Efficacy after Intrastriatal Transplantation in Hemi-Parkinsonian Rats. *Eur J Neurosci* **2019**, *49* (4), 487–496. https://doi.org/10.1111/ejn.14090.

(563) Ma, J.; Li, J.; Wang, X.; Li, M.; Teng, W.; Tao, Z.; Xie, J.; Ma, Y.; Shi, Q.; Li, B.; Saijilafu. GDNF-Loaded Polydopamine Nanoparticles-Based Anisotropic Scaffolds Promote Spinal Cord Repair by Modulating Inhibitory Microenvironment. *Advanced Healthcare Materials* **2023**, *12* (8), 2202377. https://doi.org/10.1002/adhm.202202377.

(564) Guo, X.; Zhou, H.; Liu, Y.; Xu, W.; Kanwore, K.; Zhang, L. Glial-Cell-Line-Derived Neurotrophic Factor Promotes Glioblastoma Cell Migration and Invasion via the SMAD2/3-SERPINE1-Signaling Axis. *Int J Mol Sci* **2024**, *25* (18), 10229. https://doi.org/10.3390/ijms251810229.

(565) Avenel, I. C. N.; Ewald, J. D.; Ariey-Bonnet, J.; Kristensen, I. H.; Petterson, S. A.; Thesbjerg, M. N.; Burton, M.; Thomassen, M.; Wennerberg, K.; Michaelsen, S. R.; Kristensen, B. W. GDNF/GFRA1 Signaling Contributes to Chemo- and Radioresistance in Glioblastoma. *Sci Rep* **2024**, *14* (1), 17639. https://doi.org/10.1038/s41598-024-68626-x.

(566) *Glioblastoma - Survival rates - Mayo Clinic*. https://www.mayoclinic.org/diseases-conditions/glioblastoma/survival-rates/gnc-20596050 (accessed 2026-06-24).

(567) Jaoude, D. A.; Moore, J. A.; Moore, M. B.; Twumasi-Ankrah, P.; Ablah, E.; Moore, D. F. Glioblastoma and Increased Survival with Longer Chemotherapy Duration. *Kans J Med* **2019**, *12* (3), 65–69.

(568) Pasupuleti, V.; Vora, L.; Prasad, R.; Nandakumar, D. N.; Khatri, D. K. Glioblastoma Preclinical Models: Strengths and Weaknesses. *Biochimica et Biophysica Acta (BBA) - Reviews on Cancer* **2024**, *1879* (1), 189059. https://doi.org/10.1016/j.bbcan.2023.189059.

(569) *Dynamically Crosslinked Poly(ethylene-glycol) Hydrogels Reveal a Critical Role of Viscoelasticity in Modulating Glioblastoma Fates and Drug Responses in 3D - PubMed*. https://pubmed.ncbi.nlm.nih.gov/36239185/ (accessed 2026-06-25).

(570) Unal, S.; Arslan, S.; Yilmaz, B. K.; Oktar, F. N.; Ficai, D.; Ficai, A.; Gunduz, O. Polycaprolactone/Gelatin/Hyaluronic Acid Electrospun Scaffolds to Mimic Glioblastoma Extracellular Matrix. *Materials (Basel)* **2020**, *13* (11), 2661. https://doi.org/10.3390/ma13112661.

(571) Muheremu, A.; Shu, L.; Liang, J.; Aili, A.; Jiang, K. Sustained Delivery of Neurotrophic Factors to Treat Spinal Cord Injury. *Translational Neuroscience* **2021**, *12* (1), 494–511. https://doi.org/10.1515/tnsci-2020-0200.

(572) Ramos Ferrer, P.; Vardhan, S.; Sakiyama-Elbert, S. Sustained Neurotrophin-3 Delivery from Hyaluronic Acid Hydrogels for Neural Tissue Regeneration. *Journal of Biomedical Materials Research Part A* **2024**, *112* (8), 1188–1199. https://doi.org/10.1002/jbm.a.37596.

(573) Dorogin, J.; Hochstatter, H. B.; Shepherd, S. O.; Svendsen, J. E.; Benz, M. A.; Powers, A. C.; Fear, K. M.; Townsend, J. M.; Prell, J. S.; Hosseinzadeh, P.; Hettiaratchi, M. H. Moderate-Affinity Affibodies Modulate the Delivery and Bioactivity of Bone Morphogenetic Protein-2. *Adv Healthc Mater* **2023**, e2300793. https://doi.org/10.1002/adhm.202300793.

(574) Abune, L.; Wang, Y. Affinity Hydrogels for Protein Delivery. *Trends Pharmacol Sci* **2021**, *42* (4), 300–312. https://doi.org/10.1016/j.tips.2021.01.005.

(575) Teal, C. J.; Lu, S. P.; Shoichet, M. S. Engineering Hydrogels for Affinity-Based Release of Therapeutic Proteins. *Chem. Mater.* **2024**. https://doi.org/10.1021/acs.chemmater.3c02242.

(576) Butterfield, K. C.; Conovaloff, A. W.; Panitch, A. Development of Affinity-Based Delivery of NGF from a Chondroitin Sulfate Biomaterial. *Biomatter* **2011**, *1* (2), 174–181. https://doi.org/10.4161/biom.18791.

(577) Wood, M. D.; Moore, A. M.; Hunter, D. A.; Tuffaha, S.; Borschel, G. H.; Mackinnon, S. E.; Sakiyama-Elbert, S. E. Affinity-Based Release of Glial-Derived Neurotrophic Factor from Fibrin Matrices Enhances Sciatic Nerve Regeneration. *Acta Biomater* **2009**, *5* (4), 959–968. https://doi.org/10.1016/j.actbio.2008.11.008.

(578) Barozzi, A.; Lavoie, R. A.; Day, K. N.; Prodromou, R.; Menegatti, S. Affibody-Binding Ligands. *IJMS* **2020**, *21* (11), 3769. https://doi.org/10.3390/ijms21113769.

(579) Bostock, C.; Teal, C. J.; Dang, M.; Golinski, A. W.; Hackel, B. J.; Shoichet, M. S. Affibody-Mediated Controlled Release of Fibroblast Growth Factor 2. *Journal of Controlled Release* **2022**, *350*, 815–828. https://doi.org/10.1016/j.jconrel.2022.09.004.

(580) Svendsen, J. E.; Ford, M. R.; Asnes, C. L.; Oh, S. C.; Dorogin, J.; Fear, K. M.; O'Hara-Smith, J. R.; Chisholm, L. O.; Phillips, S. R.; Harms, M. J.; Hosseinzadeh, P.; Hettiaratchi, M. H. Applying Computational Protein Design to Engineer Affibodies for Affinity-Controlled Delivery of Vascular Endothelial Growth Factor and Platelet-Derived Growth Factor. *Biomacromolecules* **2025**. https://doi.org/10.1021/acs.biomac.5c00097.

(581) Khaing, Z. Z.; Seidlits, S. K. Hyaluronic Acid and Neural Stem Cells: Implications for Biomaterial Design. *J. Mater. Chem. B* **2015**, *3* (40), 7850–7866. https://doi.org/10.1039/C5TB00974J.

(582) Park, J. B.; Kwak, H.-J.; Lee, S.-H. Role of Hyaluronan in Glioma Invasion. *Cell Adh Migr* **2008**, *2* (3), 202–207. https://doi.org/10.4161/cam.2.3.6320.

(583) Inoue, A.; Ohnishi, T.; Nishikawa, M.; Ohtsuka, Y.; Kusakabe, K.; Yano, H.; Tanaka, J.; Kunieda, T. A Narrative Review on CD44's Role in Glioblastoma Invasion, Proliferation, and Tumor Recurrence. *Cancers (Basel)* **2023**, *15* (19), 4898. https://doi.org/10.3390/cancers15194898.

(584) Lubanska, D.; Alrashed, S.; Mason, G. T.; Nadeem, F.; Awada, A.; DiPasquale, M.; Sorge, A.; Malik, A.; Kojic, M.; Soliman, M. A. R.; deCarvalho, A. C.; Shamisa, A.; Kulkarni, S.; Marquardt, D.; Porter, L. A.; Rondeau-Gagné, S. Impairing Proliferation of Glioblastoma Multiforme with CD44+ Selective Conjugated Polymer Nanoparticles. *Sci Rep* **2022**, *12* (1), 12078. https://doi.org/10.1038/s41598-022-15244-0.

(585) Pietras, A.; Katz, A. M.; Ekström, E. J.; Wee, B.; Halliday, J. J.; Pitter, K. L.; Werbeck, J. L.; Amankulor, N. M.; Huse, J. T.; Holland, E. C. Osteopontin-CD44 Signaling in the Glioma Perivascular Niche Enhances Cancer Stem Cell Phenotypes and Promotes

Aggressive Tumor Growth. *Cell Stem Cell* **2014**, *14* (3), 357–369. https://doi.org/10.1016/j.stem.2014.01.005.

(586) Akasov, R. A.; Trifanova, E. M.; Khvorostina, M. A.; Sochilina, A. V.; Pavlova, S. A.; Alekseeva, A. I.; Pavlova, G. V.; Khaydukov, E. V.; Popov, V. K. Electrospun and 3D Printed Scaffolds Based on Biocompatible Polymers for 3D Cultivation of Glioblastoma Cells *in Vitro*. *Annals of 3D Printed Medicine* **2024**, *15*, 100161. https://doi.org/10.1016/j.stlm.2024.100161.

(587) Bakirci, E.; Schaefer, N.; Dahri, O.; Hrynevich, A.; Strissel, P.; Strick, R.; Dalton, P. D.; Villmann, C. Melt Electrowritten In Vitro Radial Device to Study Cell Growth and Migration. *Advanced Biosystems* **2020**, *4* (10), 2000077. https://doi.org/10.1002/adbi.202000077.

(588) Erickson, A.; Sun, J.; Levengood, S. K. L.; Zhang, M. Hyaluronic Acid-Coated Aligned Nanofibers for the Promotion of Glioblastoma Migration. *ACS Appl. Bio Mater.* **2019**, *2* (3), 1088–1097. https://doi.org/10.1021/acsabm.8b00704.

(589) Swan, A.; Hillen, T.; Bowman, J. C.; Murtha, A. D. A Patient-Specific Anisotropic Diffusion Model for Brain Tumour Spread. *Bull Math Biol* **2018**, *80* (5), 1259–1291. https://doi.org/10.1007/s11538-017-0271-8.

(590) Harvey, A. R.; Lovett, S. J.; Majda, B. T.; Yoon, J. H.; Wheeler, L. P. G.; Hodgetts, S. I. Neurotrophic Factors for Spinal Cord Repair: Which, Where, How and When to Apply, and for What Period of Time? *Brain Research* **2015**, *1619*, 36–71. https://doi.org/10.1016/j.brainres.2014.10.049.

(591) Bahlakeh, G.; Rahbarghazi, R.; Mohammadnejad, D.; Abedelahi, A.; Karimipour, M. Current Knowledge and Challenges Associated with Targeted Delivery of Neurotrophic Factors into the Central Nervous System: Focus on Available Approaches. *Cell & Bioscience* **2021**, *11* (1), 181. https://doi.org/10.1186/s13578-021-00694-2.

(592) Galindo, A.; McLaren, M. E.; Chi, A. K.; Khachatourian, J. D.; Butts, J. C.; Hettiaratchi, M. H. Hyaluronic Acid-Alginate Hydrazone Crosslinked Hydrogels Support the Generation and Maturation of V2a Interneurons. *bioRxiv* **2026**, 2026–06.

(593) Svendsen, J. E.; Asnes, C. L.; Nightheart, S. R.; Ford, M. R.; Hajarizadeh, A.; Oh, S. C.; Hochstatter, H. B.; O'Hara-Smith, J. R.; Guldberg, R. E.; Hettiaratchi, M. H. Phased Affinity-Controlled Delivery of Vascular Endothelial Growth Factor, Fibroblast Growth Factor-2, and Platelet Derived Growth Factor Enhances in Vitro Angiogenesis. bioRxiv July 5, 2025, p 2025.07.01.662647. https://doi.org/10.1101/2025.07.01.662647.

(594) Boder, E. T.; Wittrup, K. D. [25] Yeast Surface Display for Directed Evolution of Protein Expression, Affinity, and Stability. In *Applications of Chimeric Genes and Hybrid Proteins - Part C: Protein-Protein Interactions and Genomics*; Thorner, J., Emr, S. D., Abelson, J. N., Eds.; Methods in Enzymology; Academic Press, 2000; Vol. 328, pp 430–444. https://doi.org/10.1016/S0076-6879(00)28410-3.

(595) Dorogin, J.; Lamichhane, A.; Huang, A. J.; Svendsen, J. E.; Benz, M. A.; Raghavan, S. A.; Hettiaratchi, M. H. Discovery and Characterization of Interleukin-4-Specific Affibodies for Affinity-Controlled Protein Release and Macrophage Polarization. bioRxiv: The Preprint Server for Biology May 12, 2026. https://doi.org/10.64898/2026.05.07.723637.

(596) Ayanlaja, A. A.; Zhang, B.; Ji, G.; Gao, Y.; Wang, J.; Kanwore, K.; Gao, D. The Reversible Effects of Glial Cell Line-Derived Neurotrophic Factor (GDNF) in the Human Brain. *Semin Cancer Biol* **2018**, *53*, 212–222. https://doi.org/10.1016/j.semcancer.2018.07.005.

(597) Ewald, J. D.; Knudsen, A. M.; Wohlleben, H.; Christiansen, L.; Michaelsen, S. R.; Anand, A.; Kristensen, B. W. Expression of Glial Cell Line-Derived Neurotrophic Factor and Its Receptors in Glioblastoma. *J Histochem Cytochem* **2025**, *73* (9–10), 393–414. https://doi.org/10.1369/00221554251374108.

(598) Oraiopoulou, M.-E.; Tampakaki, M.; Tzamali, E.; Tamiolakis, T.; Makatounakis, V.; Vakis, A. F.; Zacharakis, G.; Sakkalis, V.; Papamatheakis, J. A 3D Tumor Spheroid Model for the T98G Glioblastoma Cell Line Phenotypic Characterization. *Tissue Cell* **2019**, *59*, 39–43. https://doi.org/10.1016/j.tice.2019.05.007.

(599) Chen, J.-W. E.; Pedron, S.; Harley, B. A. C. The Combined Influence of Hydrogel Stiffness and Matrix-Bound Hyaluronic Acid Content on Glioblastoma Invasion. *Macromol Biosci* **2017**, *17* (8), 10.1002/mabi.201700018. https://doi.org/10.1002/mabi.201700018.

(600) Carvalho, E. M.; Ding, E. A.; Saha, A.; Garcia, D. C.; Weldy, A.; Zushin, P.-J. H.; Stahl, A.; Aghi, M. K.; Kumar, S. Viscoelastic High-Molecular-Weight Hyaluronic Acid Hydrogels Support Rapid Glioblastoma Cell Invasion with Leader–Follower Dynamics. *Advanced Materials* **2024**, *36* (50), 2404885. https://doi.org/10.1002/adma.202404885.

(601) Smith, L. J.; Skirzynska, A.; Chin, A. A.; Arnold, A. E.; Kushida, M.; Dirks, P. B.; Shoichet, M. S. Engineered In Vitro Tumor Model Recapitulates Molecular Signatures of Invasion in Glioblastoma. *ACS Mater Au* **2023**, *3* (5), 514–527. https://doi.org/10.1021/acsmaterialsau.3c00029.

(602) Cadena, I. A.; Buchanan, M. R.; Harris, C. G.; Jenne, M. A.; Rochefort, W. E.; Nelson, D.; Fogg, K. C. Engineering High Throughput Screening Platforms of Cervical Cancer. *J Biomed Mater Res A* **2023**, *111* (6), 747–764. https://doi.org/10.1002/jbm.a.37522.

(603) Lam, J.; Carmichael, S. T.; Lowry, W. E.; Segura, T. Design of Experiments Methodology to Optimize Hydrogel for iPSC-NPC Culture. *Adv Healthc Mater* **2015**, *4* (4), 534–539. https://doi.org/10.1002/adhm.201400410.

(604) Wu, D.; Eugenis, I.; Hu, C.; Kim, S.; Kanugovi, A.; Yue, S.; Wheeler, J. R.; Fathali, I.; Feeley, S.; Shrager, J. B.; Huang, N. F.; Rando, T. A. Bioinstructive Scaffolds Enhance Stem Cell Engraftment for Functional Tissue Regeneration. *Nat. Mater.* **2025**, *24* (9), 1364–1374. https://doi.org/10.1038/s41563-025-02212-y.

(605) Shi, M.; Dong, R.; Hu, J.; Guo, B. Conductive Self-Healing Biodegradable Hydrogel Based on Hyaluronic Acid-Grafted-Polyaniline as Cell Recruitment Niches and Cell Delivery Carrier for Myogenic Differentiation and Skeletal Muscle Regeneration. *Chemical Engineering Journal* **2023**, *457*, 141110. https://doi.org/10.1016/j.cej.2022.141110.

(606) Walker, M. J.; Xu, X.-M. History of Glial Cell Line-Derived Neurotrophic Factor (GDNF) and Its Use for Spinal Cord Injury Repair. *Brain Sci* **2018**, *8* (6), 109. https://doi.org/10.3390/brainsci8060109.

(607) Gantner, C. W.; de Luzy, I. R.; Kauhausen, J. A.; Moriarty, N.; Niclis, J. C.; Bye, C. R.; Penna, V.; Hunt, C. P. J.; Ermine, C. M.; Pouton, C. W.; Kirik, D.; Thompson, L. H.; Parish, C. L. Viral Delivery of GDNF Promotes Functional Integration of Human Stem Cell Grafts in Parkinson's Disease. *Cell Stem Cell* **2020**, *26* (4), 511-526.e5. https://doi.org/10.1016/j.stem.2020.01.010.

(608) Lang, A. E.; Gill, S.; Patel, N. K.; Lozano, A.; Nutt, J. G.; Penn, R.; Brooks, D. J.; Hotton, G.; Moro, E.; Heywood, P.; Brodsky, M. A.; Burchiel, K.; Kelly, P.; Dalvi, A.; Scott, B.; Stacy, M.; Turner, D.; Wooten, V. G. F.; Elias, W. J.; Laws, E. R.; Dhawan, V.; Stoessl, A. J.; Matcham, J.; Coffey, R. J.; Traub, M. Randomized Controlled Trial of Intraputamenal Glial Cell Line-Derived Neurotrophic Factor Infusion in Parkinson Disease. *Ann Neurol* **2006**, *59* (3), 459–466. https://doi.org/10.1002/ana.20737.

(609) Kambey, P. A.; Kanwore, K.; Ayanlaja, A. A.; Nadeem, I.; Du, Y.; Buberwa, W.; Liu, W.; Gao, D. Failure of Glial Cell-Line Derived Neurotrophic Factor (GDNF) in Clinical Trials Orchestrated By Reduced NR4A2 (NURR1) Transcription Factor in Parkinson's Disease. A Systematic Review. *Front Aging Neurosci* **2021**, *13*, 645583. https://doi.org/10.3389/fnagi.2021.645583.

(610) Sun, M.; Kong, L.; Wang, X.; Lu, X.; Gao, Q.; Geller, A. I. Comparison of the Capability of GDNF, BDNF, or Both, to Protect Nigrostriatal Neurons in a Rat Model of Parkinson's Disease. *Brain Res* **2005**, *1052* (2), 119–129. https://doi.org/10.1016/j.brainres.2005.05.072.

(611) Reid, J. A.; Dwyer, K. D.; Schmitt, P. R.; Soepriatna, A. H.; Coulombe, K. L.; Callanan, A. Architected Fibrous Scaffolds for Engineering Anisotropic Tissues. *Biofabrication* **2021**, *13* (4), 045007. https://doi.org/10.1088/1758-5090/ac0fc9.

(612) Sousa, J. P. M.; Stratakis, E.; Mano, J.; Marques, P. A. A. P. Anisotropic 3D Scaffolds for Spinal Cord Guided Repair: Current Concepts. *Biomater Adv* **2023**, *148*, 213353. https://doi.org/10.1016/j.bioadv.2023.213353.

(613) Xing, J.; Liu, N.; Xu, N.; Chen, W.; Xing, D. Engineering Complex Anisotropic Scaffolds beyond Simply Uniaxial Alignment for Tissue Engineering. *Advanced Functional Materials* **2022**, *32* (15), 2110676. https://doi.org/10.1002/adfm.202110676.

(614) Roam, J. L.; Nguyen, P. K.; Elbert, D. L. Controlled Release and Gradient Formation of Human Glial-Cell Derived Neurotrophic Factor from Heparinated Poly(Ethylene Glycol) Microsphere-Based Scaffolds. *Biomaterials* **2014**, *35* (24), 6473–6481. https://doi.org/10.1016/j.biomaterials.2014.04.027.

(615) Eggers, R.; de Winter, F.; Hoyng, S. A.; Roet, K. C. D.; Ehlert, E. M.; Malessy, M. J. A.; Verhaagen, J.; Tannemaat, M. R. Lentiviral Vector-Mediated Gradients of GDNF in the Injured Peripheral Nerve: Effects on Nerve Coil Formation, Schwann Cell Maturation and Myelination. *PLoS One* **2013**, *8* (8), e71076. https://doi.org/10.1371/journal.pone.0071076.

(616) Jalloh, U. S.; Gsell, A.; Gultian, K. A.; MacAulay, J.; Madden, A.; Smith, J.; Siri, L.; Vega, S. L. Synthesis and Photopatterning of Synthetic Thiol-Norbornene Hydrogels. *Gels* **2024**, *10* (3), 164. https://doi.org/10.3390/gels10030164.

(617) Krakora, D.; Mulcrone, P.; Meyer, M.; Lewis, C.; Bernau, K.; Gowing, G.; Zimprich, C.; Aebischer, P.; Svendsen, C. N.; Suzuki, M. Synergistic Effects of GDNF and VEGF on Lifespan and Disease Progression in a Familial ALS Rat Model. *Mol Ther* **2013**, *21* (8), 1602–1610. https://doi.org/10.1038/mt.2013.108.

(618) Vila, O. F.; Qu, Y.; Vunjak-Novakovic, G. In Vitro Models of Neuromuscular Junctions and Their Potential for Novel Drug Discovery and Development. *Expert Opin Drug Discov* **2020**, *15* (3), 307–317. https://doi.org/10.1080/17460441.2020.1700225.

(619) Chen, D.; Philippidou, P.; Brenha, B. de F.; Schaffer, A. E.; Miranda, H. C. Scalable, Optically-Responsive Human Neuromuscular Junction Model Reveals Convergent Mechanisms of Synaptic Dysfunction in Familial ALS. *eLife* **2024**, *13*. https://doi.org/10.7554/eLife.95388.1.

(620) Urzi, A.; Lahmann, I.; Nguyen, L. V. N.; Rost, B. R.; García-Pérez, A.; Lelievre, N.; Merritt-Garza, M. E.; Phan, H. C.; Bassell, G. J.; Rossoll, W.; Diecke, S.; Kunz, S.; Schmitz, D.; Gouti, M. Efficient Generation of a Self-Organizing Neuromuscular Junction Model from Human Pluripotent Stem Cells. *Nat Commun* **2023**, *14* (1), 8043. https://doi.org/10.1038/s41467-023-43781-3.

(621) Moysidou, C.-M.; Afonso Martins, I.; El-Shimy, I. A.; Bicci, I.; Cea, D.; Bukas, C.; Mekki, I.; Rusu, M.-C.; Nebol, A.; Lahmann, I.; Piraud, M.; Klotzsch, E.; Gouti, M. Enhancing Maturation of Human Neuromuscular Organoids via Electrical Stimulation. *Adv Sci (Weinh)* **2026**, e22762. https://doi.org/10.1002/advs.202522762.

(622) Zhang, Y.; Zhao, F.; Chen, S.; Li, B.; Dong, J.; Chen, Y.; Liu, Y.; Qiao, A.; Chen, M. Melt Electrowriting-Enabled Hybrid Platforms: Toward Functional Biomimetic Scaffolds for Cellular Interaction and Tissue Regeneration. *Acta Biomater* **2026**, *213*, 21–61. https://doi.org/10.1016/j.actbio.2026.02.015.